

An International  
Forum For  
The AE Science  
and Technology

# JOURNAL OF ACOUSTIC EMISSION

Vol.18/January-December 2000

2000  
VOLUME 18  
**JOURNAL OF  
ACOUSTIC EMISSION**

An International  
Forum for the  
AE Science &  
Technology

Endorsed by  
AEWG  
EWGAE

Published by  
Acoustic Emission Group  
Encino, CA USA

ISSN 0730-0050  
Coden JACEDO  
30 November 2000

1. View or print articles in PDF format using Acrobat Reader®.
2. You can install a free copy of Acrobat Reader®. Open READ-ME file for further instruction. (Acrobat Reader©1987-99 Adobe Systems Inc. All rights reserved.)
3. Use Adobe Acrobat® for full-text search of this disk.

Copyright © 2000 Acoustic Emission Group

Endorsed by  
AEWG  
and  
EWGAE

Published by  
Acoustic Emission Group  
Encino, CA USA

# JOURNAL OF ACOUSTIC EMISSION

**Editor: Kanji Ono**

**Associate Editors: A. G. Beattie, T. F. Drouillard, F. C. Beall and M. Ohtsu**

## 1. Aims and Scope of the Journal

Journal of Acoustic Emission is an international journal designed to be of broad interest and use to both researcher and practitioner of acoustic emission. It will publish original contributions of all aspects of research and significant engineering advances in the sciences and applications of acoustic emission. The journal will also publish reviews, the abstracts of papers presented at meetings, technical notes, communications and summaries of reports. Current news of interest to the acoustic emission communities, announcements of future conferences and working group meetings and new products will also be included.

Journal of Acoustic Emission includes the following classes of subject matters;

A. Research Articles: Manuscripts should represent completed original work embodying the results of extensive investigation. These will be judged for scientific and technical merit.

B. Applications: Articles must present significant advances in the engineering applications of acoustic emission. Material will be subject to reviews for adequate description of procedures, substantial database and objective interpretation.

C. Technical Notes and Communications: These allow publications of short items of current interest, new or improved experimental techniques and procedures, discussion of published articles and relevant applications.

D. AE Literature section will collect the titles and abstracts of papers published elsewhere and those presented at meetings and conferences. Reports and programs of conferences and symposia will also be presented.

E. AE Program and Data Files: Original program files and data files that can be read by others and analyzed will be distributed in CD-ROM.

Reviews, Tutorial Articles and Special Contributions will address the subjects of general interest. Nontechnical part will cover book reviews, significant personal and technical accomplishments, current news and new products.

## 2. Endorsement

Acoustic Emission Working Group (AEWG), European Working Group on Acoustic Emission (EWGAE), Committee on Acoustic Emission from Reinforced Composites (CARP), and Acoustic Emission Working Group of India have endorsed the publication of Journal of Acoustic Emission.

## 3. Governing Body

The Editor and Associate Editors will implement the editorial policies described above. The Editorial Board will advise the editors on any major change. The Editor, Professor Kanji Ono, has the general responsibility for all the matters. Associate Editors assist the review processes as lead reviewers. Mr. T.F. Drouillard is responsible for the AE Literature section. The members of the Editorial Board are selected for their knowledge and experience on

ISSN 0730-0050 Copyright©2000 Acoustic Emission Group

AE and will advise and assist the editors on the publication policies and other aspects. The Board presently includes the following members:

S.H. Carpenter	(USA)
D.A. Dornfeld	(USA)
P. Fleischmann	(France)
L. Golaski	(Poland)
M.A. Hamstad	(USA)
H.R. Hardy, Jr.	(USA)
R. Hill	(UK)
P. Jax	(Germany)
T. Kishi	(Japan)
O.Y. Kwon	(Korea)
J.C. Lenain	(France)
S.L. McBride	(Canada)
C.R.L. Murthy	(India)
H. Niituma	(Japan)
A.A. Pollock	(USA)
T.M. Proctor, Jr.	(USA)
I. Roman	(Israel)
C. Scala	(Australia)
C. Scruby	(UK)
A. Vary	(USA)
E. Waschkies	(Germany)
M. Wevers	(Belgium)
J.W. Whittaker	(USA)
B.R.A. Wood	(Australia)

## 4. Publication

Journal of Acoustic Emission is published annually in CD-ROM by Acoustic Emission Group, PMB 106, 16350 Ventura Blvd, Encino, CA 91436. It may also be reached at 6531 Boelter Hall, University of California, Los Angeles, California 90095-1595 (USA). tel. 310-825-5233. FAX 818-990-1686. e-mail: ono@ucla.edu

## 5. Subscription

Subscription should be sent to Acoustic Emission Group. Annual rate for 2000 and 2001 is US \$104.00 including CD-ROM delivery, by priority mail in the U.S. and by air for Canada and elsewhere. For additional print copy, add \$32. Overseas orders must be paid in US currencies with a check drawn on a US bank. VISA/MC accepted. Inquire for individual (with institutional order) and bookseller discounts.

## 6. Advertisement

No advertisement will be accepted, but announcements for books, training courses and future meetings on AE will be included without charge.

# Journal of Acoustic Emission

## Contents of Volume 18, 2000

### Selected papers from “EWGAE 2000, 24th European Conference on Acoustic Emission Testing”, published by CETIM, Senlis, France

Studies of the non-linear dynamics of acoustic emission generated in rocks by Z. Majewska and Z. Mortimer (Institute of Geophysics, University of Mining and Metallurgy - Poland)	1
Acoustic emission as result of tensile and shearing processes in stable and unstable fracturing of rocks by J. Pininska (Warsaw University - Poland)	8
Relation between acoustic emission signals sequences induced by thermal loading and the structure of sedimentary rocks by B. Zogala, and R. Dubiel (University of Silesia - Poland)	15
Acoustic emission/Acousto-Ultrasonic data fusion for damage evaluation in concrete by A. Tsimogiannis, B. Georgali, and A. Anastassopoulos (Envirocoustics S.A. - Greece)	21
Concrete Crossbeam Diagnostic by acoustic emission method by Z. Weber, P. Svadbik, M. Korenska and L. Pazdera (Technical University of Brno - Czech Republic)	29
Waveform based analysis techniques for the reliable acoustic emission testing of composite structures by M. Surgeon, C. Buelens, M. Wevers, and P. De Meester (Metalogic and Katholieke University Leuven - Belgium)	34
Optical fibres for in situ monitoring the damage development in composites and the relation with acoustic emission measurements by M. Wevers, L. Rippert, and S. Van Huffel (Katholieke University Leuven - Belgium).	41
Lamb-wave source location of impact on anisotropic plates by H. Yamada, Y. Mizutani, H. Nishino, M. Takemoto and K. Ono (Aoyama Gakuen University - Japan and University of Calif., Los Angeles [UCLA] - USA)	51
Characterisation of the damage and fracture mechanisms in $Ti_3SiC_2$ using acoustic emission by P. Finkel, R.K. Miller, M.A. Friesel, R.D. Finlayson, P.T. Cole, M.W. Barsoum and T. El-Raghy (Physical Acoustics Corp. and Drexel University - USA)	61
Evaluation of martensitic transformation dynamics of Cu-Al-Ni shape memory alloy single crystals by acoustic emission method by K. Yoshida, S. Kihara, and K. Sakamaki (University of Tokushima - Japan)	68
The identification of basic fatigue parameters on electroresonance pulsator with help of acoustic emission technology by P. Mazal, and J. Petras (Brno University of Technology - Czech Republic)	75

The phase of contact damage and its description by help of acoustic emission by J. Dvoracek, J. Pazdera, and L. Petras (Brno University of Technology - Czech Republic)	81
Acoustic emission monitoring of delayed hydride cracking in Zirconium by A. Barron and C. Rowland (Bodycote and Pancom - United Kingdom)	87
Examination of plate valve behaviour in a small reciprocating compressor using acoustic emission by J.D. Gill, R.D. Douglas, Y.S. Neo, R.L. Reuben and J.A. Steel (Heriot-Watt University - United Kingdom)	96
A new method of acoustic emission source location in Pipes using cylindrical guided waves by H. Nishino, F. Uchida, S. Takashina , M. Takemoto and K. Ono (Aoyama Gakuen University - Japan and University of Calif., LA - USA)	102
Acoustic emission method for pressure vessel diagnostics at a refinery by B.S. Kabanov, V.P. Gomera, V.L. Sokolov, and A.A. Okhotnikov (Kirishinefteorgsintez - Russia)	111
Optimisation of acquisition parameters for acoustic emission measurements on small pressure vessels by F. Rauscher (Vienna University of Technology - Austria)	118
Monitoring of weld's defects evolution submit to static and dynamic loading thanks to the acoustic emission method by C. Hervé, R. Pensec, and A. Laksimi, (CETIM - France)	125
Acoustic emission due to cyclic pressurisation of vessels with partially penetrated longitudinal seams by M. Bayray (Institute of of pressure vessels and plant Technology - Austria)	131
Inspection of LPG vessels with AE examination by P. Tscheliesnig, and G. Schauritsch (TÜV Austria - Austria)	138
Inspection of pressure vessels used in refrigeration and air conditioning systems by A. Skrabec, F. Zhang, M. Cherfaoui, and L. Legin (CETIM - France)	144
The new Russian standards in the field of acoustic emission by V.I. Ivanov, and L.E. Vlasov (Orgenergoneft - Russia)	150
Using acoustic emission to monitor metal dusting by F. Ferrer, E. Andres, J. Goudiakas, and C. Brun (Elf Atochem - France)	155
Use of acoustic emission to detect localised corrosion philosophy of industrial use, illustrated with real examples by A. Proust, and J. C. Lenain (Euro Physical Acoustics - France)	161
Inspection of flat bottomed storage tanks by acoustical methods. Classification of corrosion related signals by P. Tscheliesnig, G. Lackner, M. Gori, H. Vallen and B. Herrmann (TÜV - Germany, CEST - Italy)	167
Screening of tank bottom corrosion with a single point AE detector: AE-Simple by P.J. Van De Loo, and D.A. Kronemeijer (Shell Global Solutions - The Netherlands)	174
Case histories from ten years of testing storage tank floors using acoustic emission by S.N. Gautrey, P.T. Cole, and S.J. Schoorlemmer, (Physical Acoustics Limited -United Kingdom)	180

Acoustic emission detection of damage in reinforced concrete conduit by H.W. Shen, S. Iyer, M.A. Friesel, F. Mostert, R.D. Finlayson, R.K. Miller, M.F. Carlos and S. Vahaviolos, (Physical Acoustics Corp. - USA)	189
Comparison of artificial acoustic emission sources as calibration sources for tool wear monitoring in single-point machining by A. Prateepasen, Y.H.J. Au and B.E. Jones (Brunel University - United Kingdom)	196
Development of an equipment to monitoring and control the quality of resistance welding (CRAFT Project) by J. Catty, (CETIM - France)	205
A study of small HSDI Diesel engine fuel injection equipment faults using acoustic emission by J.D. Gill, R.L. Reuben, J.A. Steel, M.W. Scaife and J. Asquith (Heriot-Watt University - United Kingdom)	211
Unsupervised pattern recognition of acoustic emission from full scale testing of a wind turbine blade by D. Kouroussis, A. Anastassopoulos, P. Vionis and V. Kolovos (Envirocoustics S.A. - Greece)	217
Acoustic emission proof testing of insulated aerial man lift devices by A. Anastassopoulos, A. Tsimogianis and D. Kourousis (Envirocoustics S.A. - Greece)	224
BOXMAP - Non-invasive detection of cracks in steel box girders by J.R. Watson, K.M. Holford, A.W. Davies and P.T. Cole, (Cardiff University, Physical Acoustics Ltd - United Kingdom)	232
Monitoring failure mechanisms in CFRP orthopaedic implants during fatigue testing by A. Taylor, S. Gross, C. Rowland and P. Gregson (Finsbury, University of Southampton, Pancom - United Kingdom)	239
Continuous monitoring of rock failure by a remote AE system by T. Shiotani, S. Yuyama, M. Carlos and S. Vahaviolos (Tobishima Corp. – Japan, PAC - USA)	248
New AE signal conditioner for industrial use by H. Vallen, J. Forker and J. von Stebut, (Vallen Systeme GmbH – Germany and Ecole des Mines - France)	258
New software tools for the AE-practitioner by H. Vallen and J. Vallen, (Vallen Systeme GmbH - Germany)	265
Improved source location methods for pressure vessels by V. Godinez, S. Vahaviolos, R.D. Finlayson, R.K. Miller, and M.F. Carlos (Physical Acoustics Corp. - USA)	272
Neural network localization of noisy AE events in dispersive media by M. Blahacek, Z. Prevorovsky, and J. Krofta (Institute of Thermomechanics - Czech Republic)	279
Dynamics and damage assessment in impacted cross-ply CFRP plate utilizing the waveform simulation of Lamb wave acoustic emission by Y. Mizutani, H. Nishino, M. Takemoto and K. Ono (Aoyama Gakuin University – Japan and UCLA - USA)	286
Acoustic emission detection during stress corrosion cracking at elevated pressure and temperature by R. Van Nieuwenhove, and R.W. Bosch (Centre d'Etude de l'Energie Nucléaire - Belgium)	293
Detection of pitting corrosion of aluminium alloys by acoustic emission technique by H. Idrissi, J. Derenne, and H. Mazille (INSA de Lyon - France)	299

Reliability of acoustic emission technique to assess corrosion of reinforced concrete  
by H. Idrissi, and A. Limam (INSA de Lyon - France)

307

## **AEWG43 Presentation**

Theoretical Treatment of AE in Massive Solid....by M. Ohtsu

S1

Diagnosis of Concrete Structures by AE....by M. Ohtsu

S7

## **EWGAE 2000 (EWGAE.pdf)**

**SOMMAIRE** -- Content of EWGAE 2000 Proceedings

i - v

**AVANT-PROPOS** Mohammed CHERFAOUI, Christel RIGAULT

vi

**Présentation - EWGAE**

vii

**Authors Index** (18Auindx.pdf)

I-1 – I-2

**Contents of Volume 18, 2000** (18Conts.pdf)

I-3 – I-6

e-mail Addresses of Authors (e-mail.pdf)

EWGAE 2000 Participant List (Senlis.pdf)

# JOURNAL OF ACOUSTIC EMISSION, VOLUME 18

Two folders are provided for Windows 95/98/ME and for Macintosh. Each contains Adobe Acrobat Reader® Installer (ACRD4ENU.EXE or Reader Installer). If you don't have a software that can read a pdf-file, install one first. Adobe Acrobat®, which can be purchased from Adobe: [www.adobe.com](http://www.adobe.com), will enable you to utilize "Search" function using an INDEX file provided (in the Index folder). This allows you to perform full-text search (Launch Acrobat and choose Edit > Search > Quary.)

Contents are listed in 18Contsp.pdf (PC) or 18Conts.pdf (Mac). Authors Index is available from 18Auidxp.pdf (PC) or 18Auindx.pdf (Mac). Contents and preface of EWGAE2000 Conference Proceedings are given in EWGAEp.pdf (PC) or EWGAE.pdf (Mac), while lists of conference participants and selected authors' e-mail are available in Senlis and e-mail files.

ISSN 0730-0050 Copyright©2000 Acoustic Emission Group Coden JACEDO

## **2000/2001 SUBSCRIPTION RATE**

Base rate (CD-ROM) for one year	\$ 96.00
Add Postage of       U.S. - Priority rate	\$ 8.00
All others - Air mail rate	\$ 8.00
CD-ROM + printed copy, surface mail: add	\$ 32.00

VISA and Mastercard orders accepted. Payment must be in U.S. dollars drawn on a U.S. bank.  
Bank transfer accepted. (Account No. 080-03416470) at

**California Bank and Trust  
San Fernando Valley Office  
15250 Ventura Blvd,  
Sherman Oaks, CA 91403-3262**

One volume of four issues per year through vol. 17. Index included in the last issue. Back issues available at \$50 per volume for Vols. 1-3, \$90 per volume for Vols. 4-8, \$96 per volume for Vols. 9-17. US surface postage \$8 per volume. For Canada and overseas surface delivery, add \$11 and for air mail, add \$30 per volume (shipping charges will be adjusted for multi-volume order).

All orders should be sent to (or Fax 1-818-990-1686): [Please note the addition of PMB in address. This is a new US Postal Regulation and mails won't arrive without it.]

Acoustic Emission Group  
PMB 106, 16350 Ventura Blvd.  
Encino, CA 91436 USA

For inquiry through Internet, use the following address:  
Editor-Publisher  
Publication Date of This Issue (Volume 18):

# STUDIES OF THE NON-LINEAR DYNAMICS OF ACOUSTIC EMISSION GENERATED IN ROCKS

Zofia MAJEWSKA and Zofia MORTIMER

Institute of Geophysics, University of Mining and Metallurgy, Kraków, Poland

## ABSTRACT

The paper concerns the acoustic emission (AE) generated in rock specimens by fracture process of a variable origin and scale. Two different experiments have been conducted: uniaxial compression and gas sorption. Generalised correlation exponent dimension  $D_q$  of the distribution of AE energy rate have been determined and the reconstruction of the attractors of the phase space for the AE time series have been calculated. It was shown that  $D_q$  may also be associated with fracturing mode and that process of rock fracturing during compression is of lower order than that of coal fracturing induced by gas sorption.

## INTRODUCTION

AE techniques may be applied to a wide range of activities in the geotechnical area, e.g. mine safety, rock and soil slope stability, surface subsidence, in situ stress evaluation, underground storage, nuclear waste disposal, geothermal energy development and others too numerous to mention. In all these activities the rock failure is of prime importance. In general, AE techniques are used as a diagnostic tool but attempts are made to find the relationship between the AE characteristics and the basic physics of the phenomenon under study [1]. Recent studies have produced substantial evidence, which indicates that fractal statistics can be successfully applied to AE generated in rocks samples under stress [e.g. 2-8].

This paper is concerned with an examination of fracture process in rocks in terms of non-linear dynamics of observed AE during two very different types of tests - uniaxial compression and gas sorption on hard coal. Rock fracture in compression is a progressive process and AE characteristics together with the stress-strain curves in the pre- and post-failure regions can provide an insight into the failure process. The purpose of the gas sorption tests on hard coal was to study the specific interactions between coal matrix and gas molecules leading to coal fracturing, which is revealed as AE. Presented in this paper are studies of non-linear dynamics of AE from microfracturing monitored during uniaxial compression experiments and gas sorption tests comprised of:

- analysis of fractal /multifractal character of AE energy distribution [ $D_q(q)$ ],
- analysis of time variability of fractal dimensions  $D_2$  and  $D_\infty$ ,
- analysis of phase space of AE process (calculation of embedded attractors).

## EXPERIMENTAL

### Uniaxial compression tests

Three rock types were used in this study; coal, dolomite and sandstone. All specimens were cylinders 42 mm in diameter and 84 mm in length and were loaded uniaxially using the Instron 8500 stiff testing machine operated at constant strain rate  $10^{-6} \text{ s}^{-1}$  (axial or circumferential). The load and strain history of each specimen was obtained. AE was detected by Dunegan SE1000-HI transducer with an integral 40dB preamplifier mounted on the upper platen of the Instron. AE signals were further amplified by low-noise, high gain preamplifier and then fed to a microcomputer controlled AE analyser. AE monitoring system was operated with the following settings: filter 10 kHz – 100 kHz, gain 90 dB.

## Gas sorption tests

Studies have been conducted on two types of hard coal: high rank and medium rank, obtained from two Polish coal basins (Lower Silesia Basin and Upper Silesia Basin). Test specimens were 22 mm in diameter and 44 mm in length. Experimental facilities used in high pressure sorption of CO<sub>2</sub> on coal comprised a pressure vessel and associated pressurisation and monitoring systems. The coal specimen could be pressurised and depressurised using a system of pressure valves. AE from coal specimen was monitored by an externally mounted transducer on the cap of the test vessel. The other elements of AE monitoring system were the same as before. Each specimen was first vacuum degassed (10<sup>-4</sup> torr). Next, carbon dioxide from a gas cylinder was admitted into the vessel at a pressure of 4 MPa. AE measurements were carried out during fifty hours of gas sorption.

## THE BASIC CALCULATION PROCEDURE

In this study the generalised dimension  $D_q$  was estimated by means of the statistical moment of order q of the correlation integral [Grasberger and Procaccia, 1983]:

$$C(l, q) = \frac{1}{n} \sum_{i=1}^N \left[ \frac{1}{N-1} \sum_{j \neq i} \Theta(l - \|x_i - x_j\|) \right]^q \quad (1)$$

where  $N$  is the total number of measures  $\overset{\mu}{x}_i$  and  $\Theta$  is the Heaviside function. An object is multifractal if

$$\log C(l, q) \propto q D_{q+1} \log l \quad (2)$$

The linearity of the log-log plot indicates the existence of statistical self-similarity of events. The slope of  $\log C(l, q)$  vs.  $\log l$  plots gives  $D_q$ , the estimate of the generalised dimension. For  $q=2$  the generalised dimension is the correlation exponent dimension, denoted by  $D_2$ . The estimate  $D_\infty$  clears up information about the most intensive clustering in a heterogeneous fractal set. The difference between estimates  $D_2$  and  $D_\infty$  represents the degree of the heterogeneity of a heterogeneous fractal set. Here the  $D_{12}$  is taken as the estimate of  $D_\infty$ .

The  $D_q$  vs  $q$  relation characterises the specific conditions of the process under study. According to the Takens theorem, from the set of observations of particular values  $s(n)$  d-dimensional vectors  $\overset{\mu}{y}(n)$  with the delay co-ordinates (shifted by the time lag T) were created [e.g. Abarbanel, 1996]:

$$\overset{\mu}{y}(n) = [s(n), s(n+T), s(n+2T), \dots, s(n+(d-1)T)] \quad (3)$$

These vectors create d-dimensional embedded space, in which the reconstructed attractor is investigated. Single variable time series of the AE energy rate have been examined. The correlation dimensions  $D_2$ , for increasing embedding dimensions  $d$ , from 1 to 15, were calculated. When the Euclidean dimension reaches a certain value  $d$  beyond which the fractal dimension  $D_2$  no longer increases, that  $d$  value estimates the dimension of the reconstructed phase space and the dimension of the attractor. A small number of degrees of freedom confirms the deterministic chaotic behaviour of the process.

## RESULTS

Only selected results are presented due to the limited space. Acoustic emission and loading history of two specimens – dolomite (loaded with constant circumferential strain rate) and coal (loaded with constant axial strain rate) are shown in figs. 1 and 3a. There are characteristic changes of AE energy rate during loading cycle. The AE development is different for the two samples examined. In dolomite, the anomalous rapid initial increase in AE corresponds to high stress concentration arising still at crack

closure. During the linear elastic phase, AE energy slows down and rises significantly for the second time near the failure strength. Changes of AE energy rate follow that of load, both in pre-failure and post-failure regions.

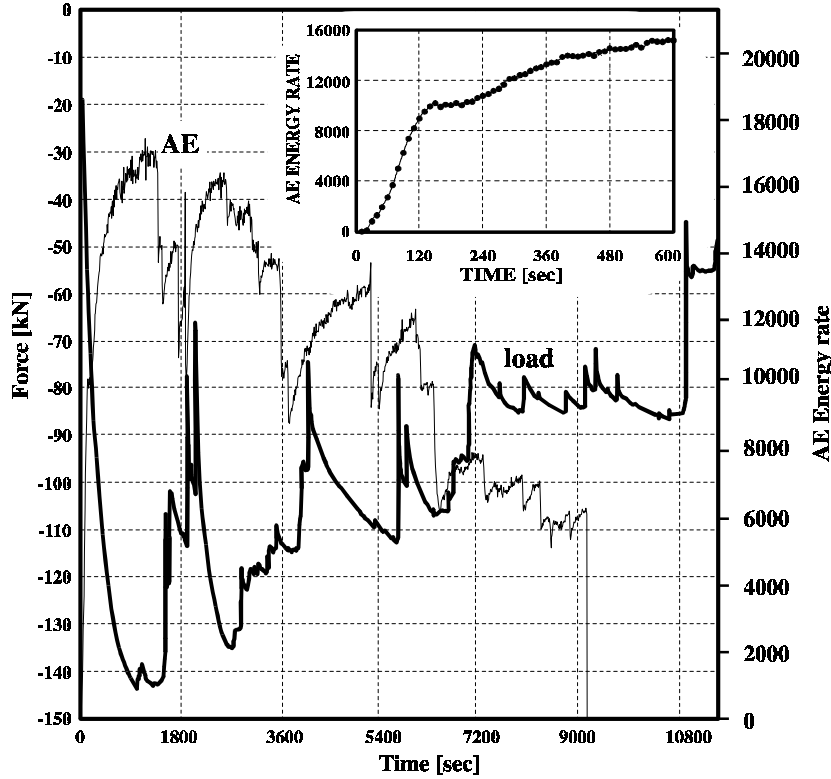


Fig.1 AE energy rate distribution for dolomite specimen under uniaxial compression test.

Coal, at the beginning of loading behaves in different way from the dolomite - only very few AE events are recorded and a marked increase in AE is evident but beyond fifty percent of the failure strength. A sharp rise in AE occurs at eighty percent of the failure strength and is followed by a drastic drop just before failure.

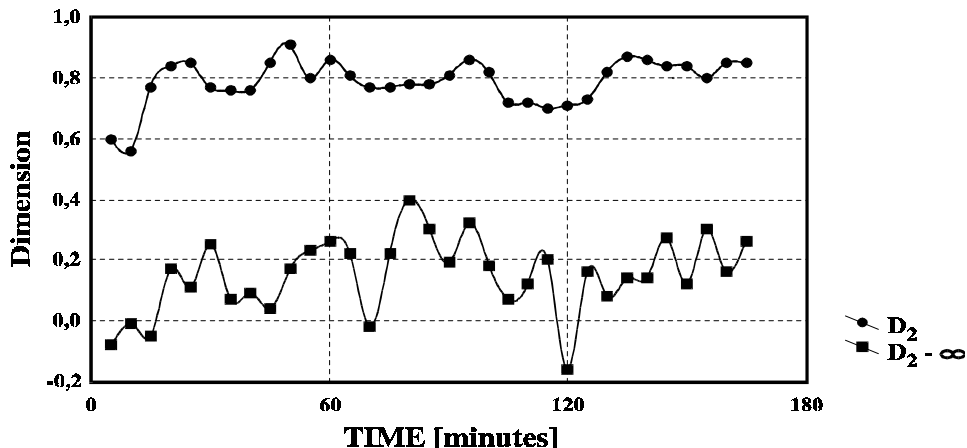


Fig.2 AE energy rate distribution and temporal changes of  $D_2$  and  $D_{2\infty}$  for dolomite specimen under uniaxial compression test.

Figures 2 and 3b reveal that temporal variations of  $D_2$  and  $D_{2\infty}$  indicate consecutive stages of specimen deformation. The pre-failure and post-failure regions for dolomite specimen are described by two different  $D_q$  vs  $q$  relations (Fig.6). The pre-failure region characterises monofractality and strong self-similarity of AE energy rate distribution while a weak multifractality and a weak self-similarity is observed in post-failure region. It seems that various focal mechanisms of AE are responsible for it. In uniaxial compression rock failure occurs in two modes [e.g. 11, 12]:

1. local fracturing predominantly parallel to the applied load,
2. both local and macroscopic shear failures.

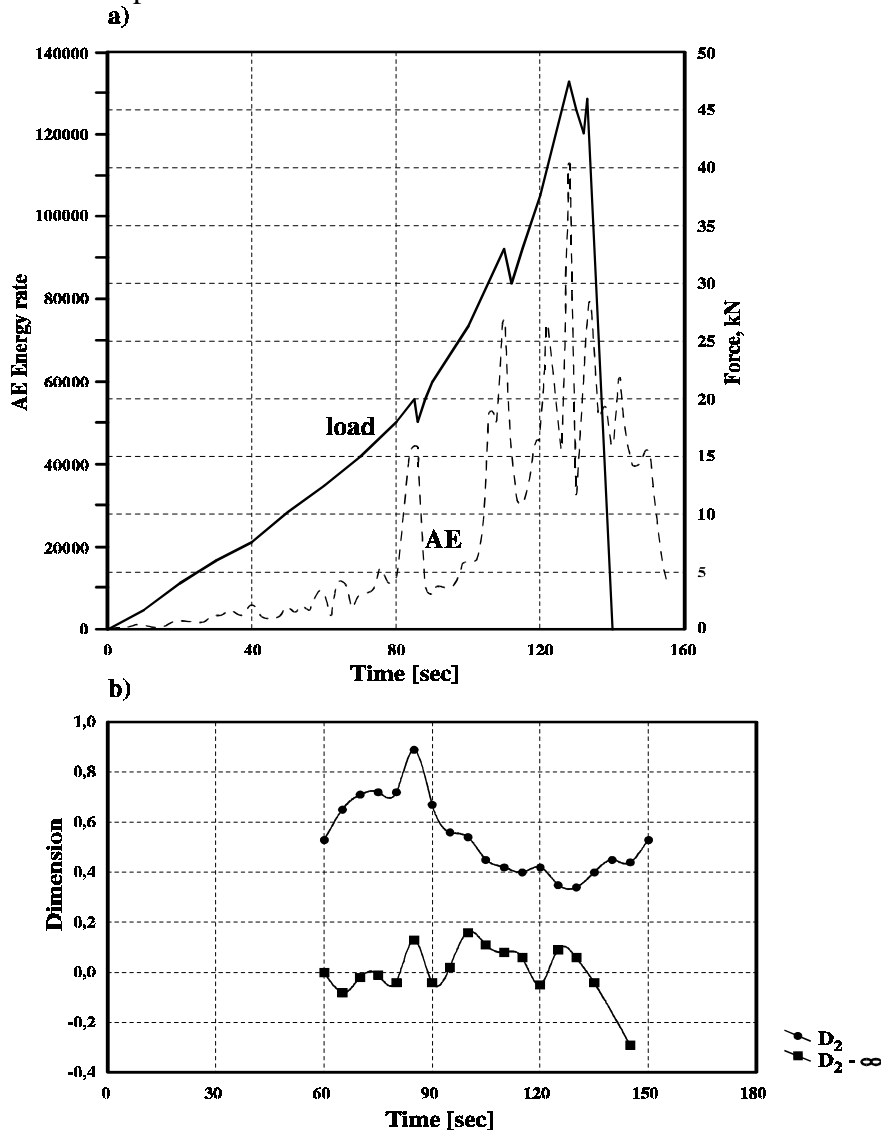


Fig.3 AE energy rate distribution (a) and temporal changes of  $D_2$  and  $D_{2\infty}$  (b)  
for coal specimen under uniaxial compression test.

For heterogeneous rocks, the first mode of failure is characteristic in pre-failure region whereas the consecutive development of faults at the boundary and in the interior of the specimen take place in post-failure region. The essential similarity of the plots  $D_q$  vs  $q$  for coal (which failed violently) and dolomite in the pre-failure region confirms the above explanation. Figure 7 shows that the embedded phase space of AE energy rate associated with rock fracturing under uniaxial compression is around six dimensional.

The AE phenomenon induced in hard coal by gas sorption can be explained, to some extent, on the basis of copolymeric model of coal structure [e.g. 13, 14]. From the model, hard coal consists of:

- a surface part (macro, meso-, micro- and submicropores),
- a volume part (macromolecular and molecular fractions).

Gas molecules can be deposited in coal structure on the surface of macropores (surface adsorption), located into mesopores (capillary condensation) and into micro- and submicropores (volumetric adsorption). Furthermore, some molecules may penetrate into macromolecular and molecular fractions (absorption). The sorption capacity of coal is made up of the submicropores, molecular fraction and macromolecular three dimensional cross-linked network.

Figures 4 and 5 show the AE energy rate and changes of  $D_2$  and  $D_{2\infty}$  estimates during  $\text{CO}_2$  sorption for two types of coal tested. In general, three subprocesses within the sorption of  $\text{CO}_2$  can be distinguished in the plots, namely: adsorption, adsorption – absorption and absorption. At first, the adsorption take place, then two simultaneous processes (adsorption and absorption) proceed at various rates, hereafter absorption is carried through. The difference in kinetics of  $\text{CO}_2$  adsorption and absorption is evident.

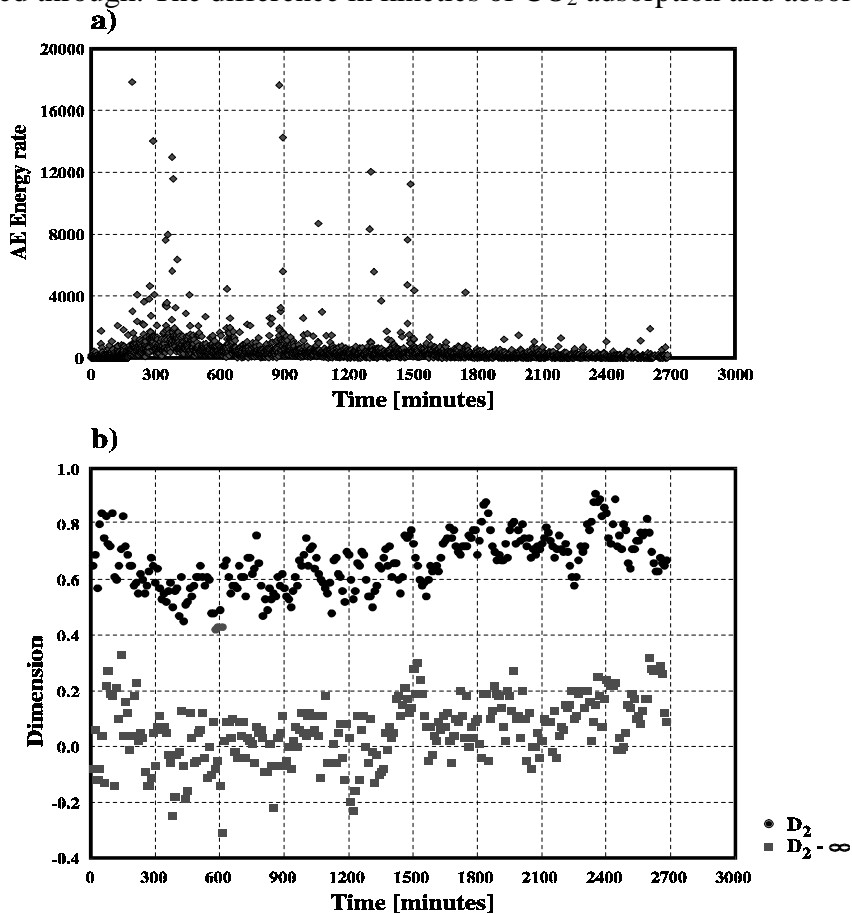


Fig.4 AE energy rate distribution (a) and temporal changes of  $D_2$  and  $D_{2\infty}$  (b) during  $\text{CO}_2$  sorption on specimen CA.

Plots  $D_q$  vs  $q$  (Fig. 6) show that sorption process in specimen CA (high rank coal) is more heterogeneous than in specimen CK (medium rank coal). Moreover, the reconstruction of the embedded phase space indicates that  $\text{CO}_2$  sorption in high rank coal is a chaotic process of lower order than it is in medium rank coal (Fig. 7).

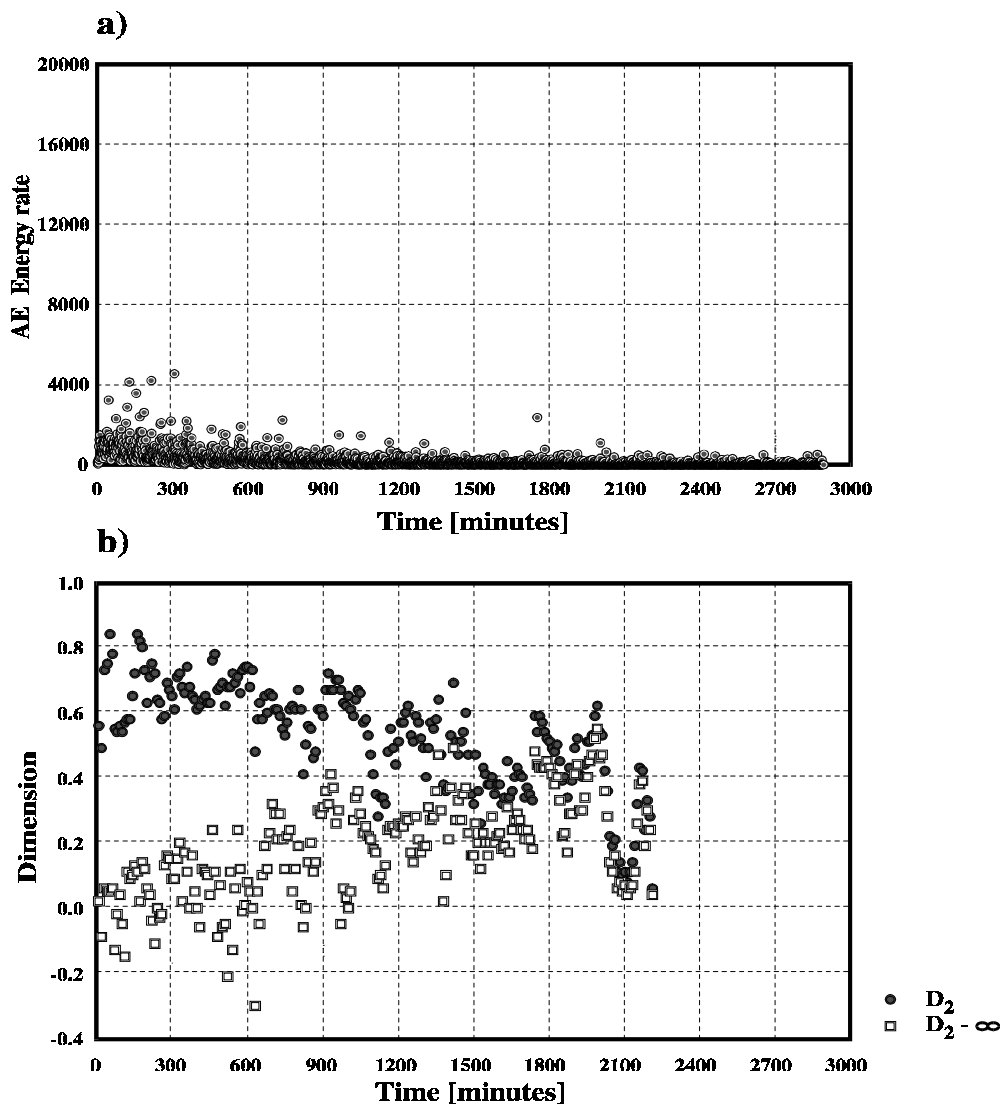


Fig.5 AE energy rate distribution (a) and temporal changes of  $D_2$  and  $D_{2-\infty}$  (b) during  $\text{CO}_2$  sorption on specimen CK.

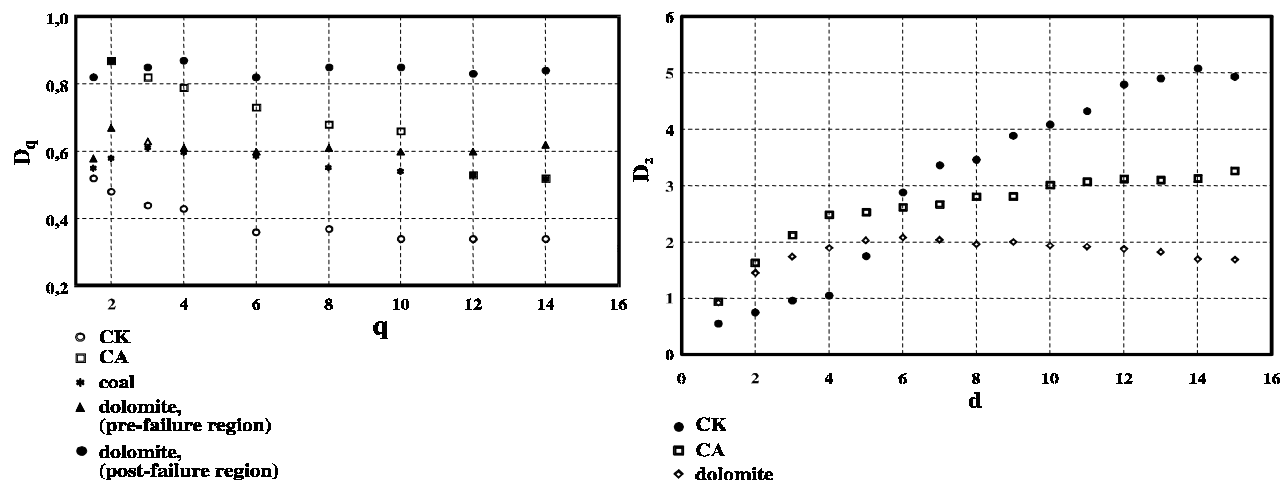


Fig. 6 Generalised fractal dimension of AE energy rate.

Fig. 7 Plots of correlation dimension  $D_2$  versus embedding dimension  $d$ .

The observed differences in behaviour of coal tested are interpreted as due to the direct impact of coal rank. In high rank coal, the content of a molecular fraction is low and a contribution of the aliphatic and heterocyclic cross – linked chains of macromolecular fraction increases, what results in structure stiffening. In contrast, the very high content of mesopores and slight amount of molecular size pores is peculiar to medium rank coal as a result of a marked differentiation in dimensions of coal structure. Therefore, for this coal, the contribution of the elastic absorptive part is lower than it is in high rank coal.

## CONCLUSIONS

- Multifractal analysis of the AE generated in rocks subjected to uniaxial compression shows that generalised fractal dimensions may also be linked with fracturing mode,
- the heterogeneity of fractal structure of the distribution of AE energy rate associated with CO<sub>2</sub> sorption on coal depends on coal rank and grows along with it, and
- process of gas sorption in high rank coal is a chaotic process of lower order than it is in medium rank coal.

## REFERENCES

1. Hardy H.R., 1998, In Proc. of 6<sup>th</sup> Conf. AE/Ma in Geologic Structures and Materials, pp. 599-609.
2. Lei, X., Nishizawa O. and Kusunose K., 1993, Geophys. J. Int., vol. 115, pp. 79-84.
3. Main J. G., Sammonds P. R. and Meredith P. G., 1993, Geophys. J. Int., vol. 115, pp. 367-380.
4. Hirata T., J., 1987, Geophys. Res., vol.92, pp. 6215-6221.
5. Smirnov V. B., Ponomarev A. V. and Zavyalov A. D., 1995, Physics of the Earth, vol. 1, pp. 38-58, (in russion).
6. Itakura K., Sato K., Nagano K. and Kusano Y., 1994, Progress in Acoustic Emission VII, JSNDI, pp. 255-260.
7. Majewska Z., Mortimer Z., 1988, Proc. of 14<sup>th</sup> IAES Conf., pp. 109-118.
8. Mortimer Z., Majewska Z., Lasocki S., 1999, Pol. Acad. Sc. M-22 (310), pp. 89-94.
9. Grassberges P. and Procaccia J., 1983, Physica 9 D, pp. 189-208.
10. Abarbanel H.D.I., 1996, Analysis of Observed Chaotic Data, Springer Verlag, Basel.
11. Wawersik W. R., Fairhurst C., 1970, Int. J. Rock Mech. Min. Sci., vol. 7, pp. 561-575.
12. Andreev G.E., 1995, Brittle Failure of Rock Materials, A.A.Balkema /Rotterdam/Brookfield/.
13. Hall P., Thomas K. and Marsh H., Fuel, 1992, vol. 71, pp. 1271-1275.
14. Milewska-Duda J., Fuel, vol. 72, 1993, pp. 419-425.

## ACKNOWLEDGEMENTS

This work was sponsored by the Polish Committee for Scientific Research under contract No 6PO4D05017.

# ACOUSTIC EMISSION AS A RESULT OF TENSIL AND SHEARING PROCESSES IN STABLE AND UNSTABLE FRACTURING OF ROCKS

Joanna PININSKA  
University of Warsaw, Warsaw, Poland

## ABSTRACT

*Uniaxial tests performed on rocks indicate that intra-, inter- or transgranular cracking can assume a number of forms, depending on the mineral composition and structure of the rock medium. Based on an analysis of deformation characteristics and the course of acoustic emission, one can infer as to whether the observed defects are a result of tensile or shearing processes, or both.*

## INTRODUCTION

Strength experiments in laboratory show that the main factors responsible for destabilisation of rock structure under compression are the size, geometry and strength of the mineral components of rock. These and many other properties of rock inhomogeneity influence the course of cracking (1-5). The character and course of cracking determine the rate, at which a rock loses its stability rapidly or with a delay and refers with the great similarity to the model of acoustic emission (AE) events.

The simulations of cracking processes in media having different structures recently presented by Napier and Peirce (6) show how much the advancement of tensile and shearing processes during cracking depends on a structure of the rock and dynamics of its deformation. In order to refer those models to the lithogenic divisions of rocks, they should be constructed in view of the basic characteristics of igneous, sedimentary and metamorphic rock structure. A general genetic review shows that the majority

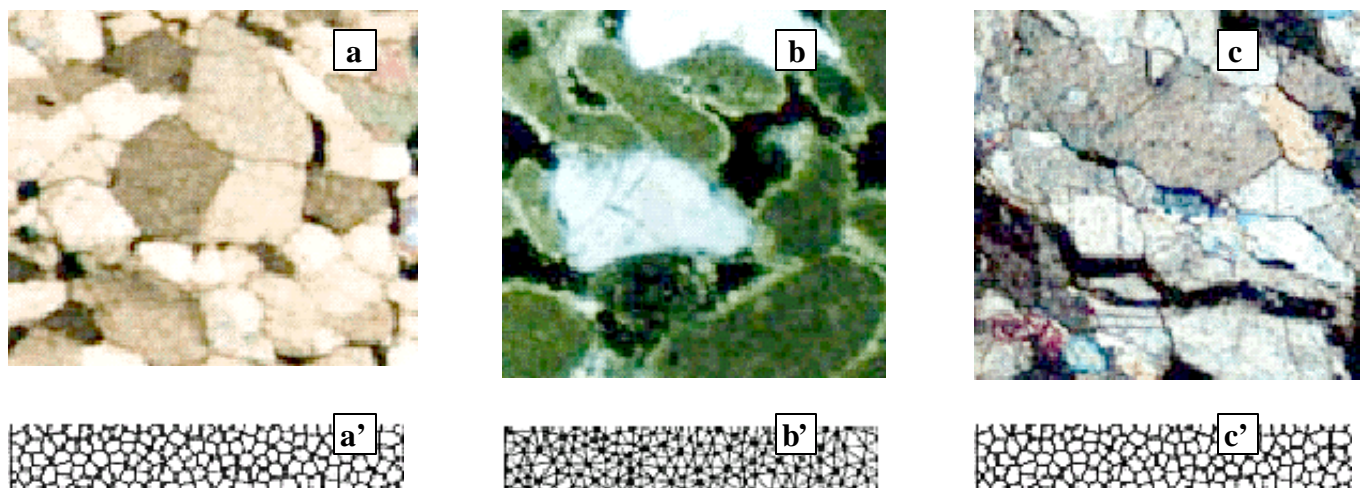


*Fig. 1. Example of characteristic genetic features of rock structures: a - periodic structure, regular grains; b - chaotic structure with a number of pores, irregular grains; c - directional structure of grains; a',b',c' - examples of random tessellation patterns after Malan & Peirce (7): a' and c' - medium of polygonal structure; b' - medium of trigonal structure,*

of igneous and equigranular sedimentary clastic rocks with homogeneous, massive structure and well-formed grains have the features of a periodic medium with quartz grains as the basic elements (Fig. 1a). Most of sedimentary rocks of organic origin have a random distribution of their basic elements; the geometry of grains is complex - irregular with numerous pores in between (Fig. 1b). Directional, strongly anisotropic positioning of grains is characteristic of metamorphic rocks (Fig. 1c).

Due to the inhomogeneity of rock structure, the process of cracking has a discontinuous character and varying dynamics. It can be accelerated or delayed depending on the local properties of the rock structure and the actual stage of stability. The hysteresis loops on the strain curve are a representation of oscillations resulting from the concentration and relaxation of stresses. Therefore, the process of cracking and its varying dynamics can be registered with the use of a deformation curve or an acoustic emission plot, provided the strength tests are conducted in a stiff testing machine with a strain rate control at the pre-failure and post-failure state (Fig. 2a and b).

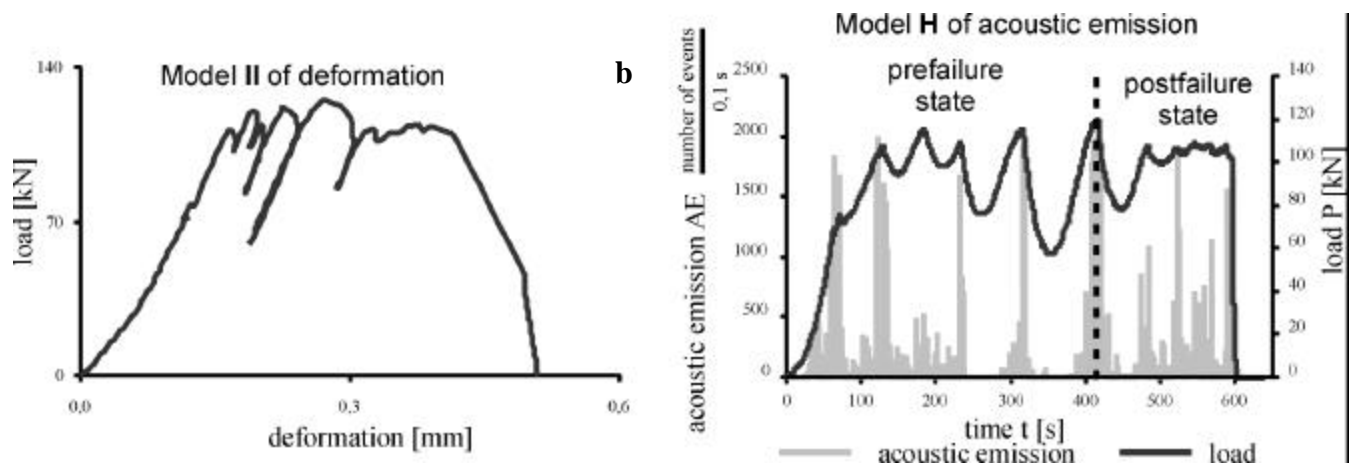


**Fig. 2. Varying dynamics of cracking registered at the prefailure and postfailure state in a stiff testing machine: a - from axial strains; b - from acoustic emission; (diabase from Niedzwiedzia Gora).**

In order to explain the mechanism of cracking and evaluate its dynamics and its acoustic emission path, it is necessary to study the features of the structure in relation to the observations of the shape of the centres of cracking, their initial orientation and its modification during their further development.

## EXAMPLES OF MANIFESTATIONS OF CRACKING

From strength testing of various lithologic types of igneous, sedimentary and metamorphic rocks from the Holly Cross Mts, the Sudetes and Jurrassic Uplands in Poland, the following rock structures/rock cracking relations were found: micro-fracture inside grains - intragranular cracking (Fig. 3a); micro-fracture around grains - intergranular cracking (Fig. 3b); and transgranular development of macro-fracture (Fig. 3c) with displacements along surfaces of discontinuity (Fig. 3d).

The character of the grain contacts in polymineral rocks influences the cracking mechanism; hence the distribution of very strong grains, quartz in particular is very significant. If the strong grains touch, stress concentrates on the contacts and these grains are destroyed first. The nuclei of cracking are formed as a result

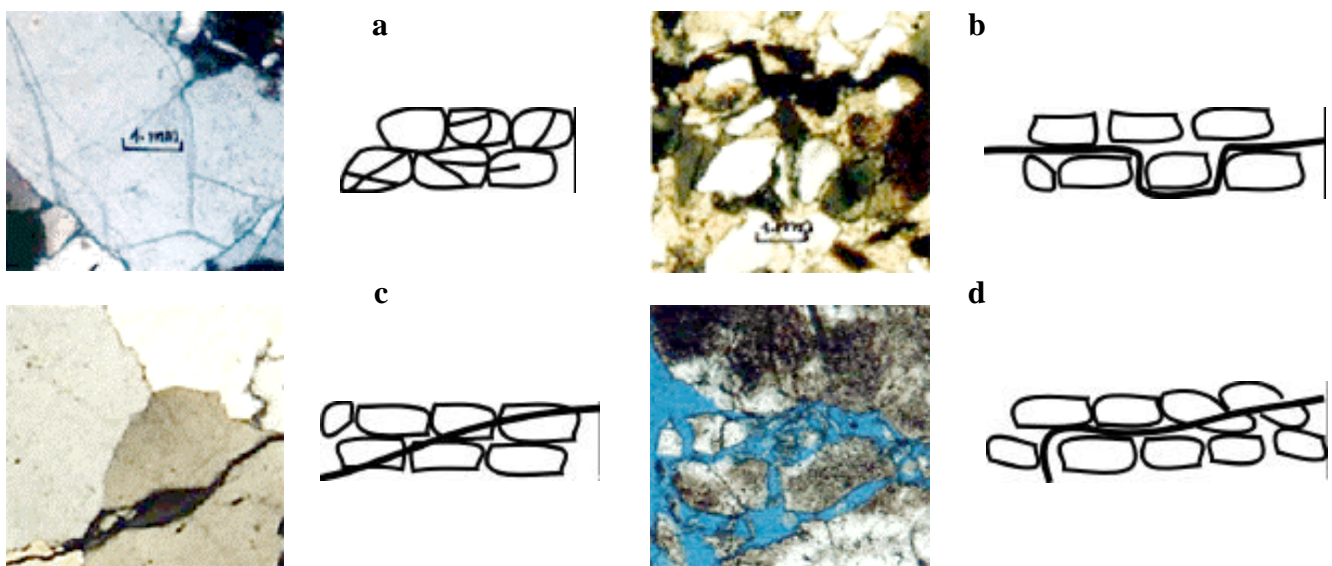


**Fig. 3. Formation of initial fissures in rocks:** a - intragranular cracking (sandstone with silicate cement); b - intergranular cracking (sandstone with carbonate cement); c - development of transgranular cracking (granite); d - development of cracking with a displacement (limestone).

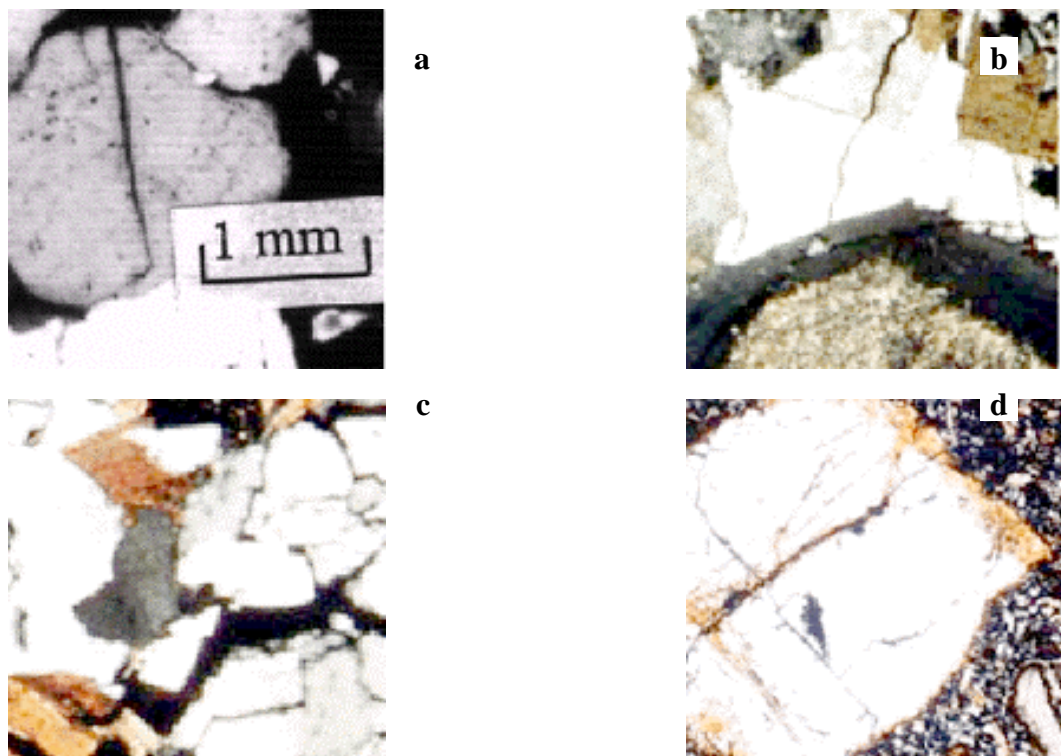


**Fig. 4. Nuclei of intragranular cracking:** a - Zerkowice sandstone; b - Michalowice granite (visible barrier in the way of the crack in the cover of a plagioclase grain); c - crystallising fissured grain of quartz (Kosmin syenite); d - fissured grain of olivine in undisturbed rock groundmass (Luban basalt).

of tension, being an intragranular separation of an individual grain. This is exemplified by the quartzite sandstones and the sandstones with siliceous cement (Fig. 4a), where the nuclei of cracking concentrate in the quartz grains and the silicate cement forms a barrier disabling further cracking. Similar phenomena can be observed in granites

(Fig. 4b) and other igneous rocks (Fig. 4c and 4d).

When the grains do not touch one another but are separated with a weak clayey ferruginous silicate or carbonate cement, the cracking takes place in the cement and is of intergranular character. This effect occurs in most of weak sedimentary rocks, for example in the Dwikozy sandstones with carbonate cement (Fig. 5a). Similar phenomena of intergranular cracking can be observed in carbonate rocks, especially organogenic rocks, for example in Pinczow limestones (Fig. 5b). The failure fracture in carbonate rocks usually has a very rough surface and displacements typical of shearing processes (Fig. 5c).

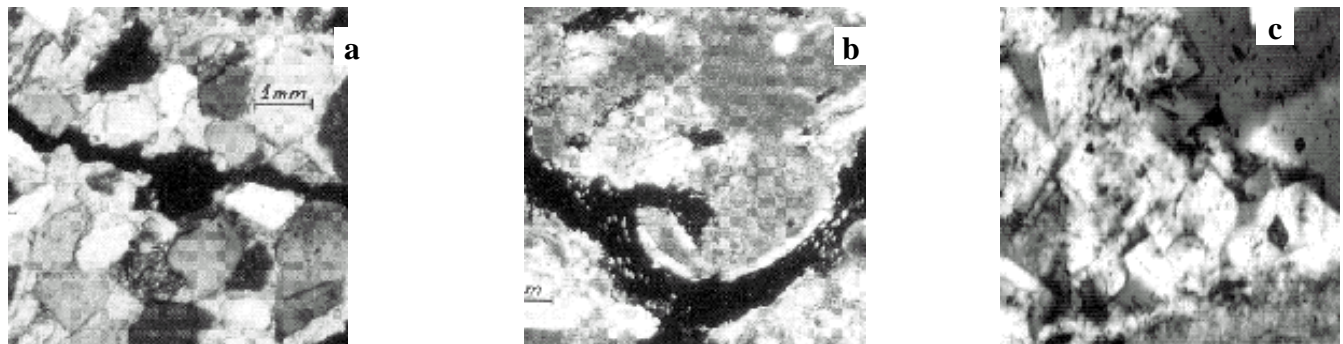


**Fig. 5. Formation of centres of intergranular cracking:** a - in clastic rocks with carbonate cement (Dwikozy sandstone); b - in organodetrital limestones (Pinczow limestone); c - fracture with displacements (Ogrodzieniec limestone).

Cracking in metamorphic rocks is conditioned by the anisotropy of the medium. Generally, it has an intergranular character and is concordant with the lamination. Cracking is connected with shearing, for example in the marble of Kletno (Fig. 6a). However, local intrusions of other stronger grains may form barriers modifying the propagation of the crack. Barriers originating from the intrusion of quartz in marble are presented in Fig. 6b.

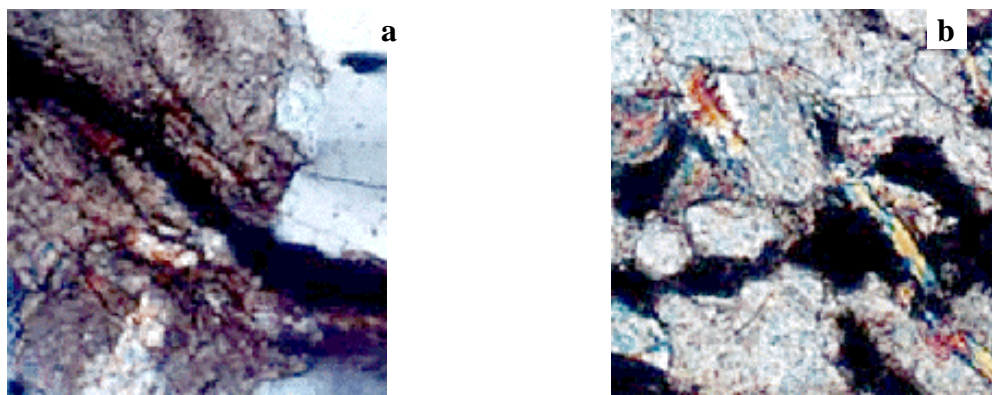


**Fig. 6. Example of fracture propagation in metamorphic rocks:** a – use of structural surfaces (coarse marble of Kletno); b - modification of crack propagation on accessory quartz grains.

Different grain sizes quantitatively influence the formation of defects in the rock; the destabilisation of a fine-grained rock structure can occur only when a greater number of fissures appears than is required in a coarse-grained rock. Therefore, e.g. the fine-grained Zimnik granites are stronger than the medium-grained Strzegom granites, and the fine-grained Przedborowa syenites are stronger than the coarse-grained Braszowice gabbro. The irregular shape of grains having complex geometry induces new processes of shearing of edges, which can

be observed, for example, in the Pinczow limestones (Fig. 5b). The cracking is of inter-, intra- and transgranular (with displacements) mixed-type character. The susceptibility to tightening of fractures increases (Fig. 7). The nuclei of microcracking concentrate and this leads to the formation of macrofractures and the development of unstable cracking. The process of macrofracturing can be locally modified with varying directions of anisotropy of individual grains or through transgranular cracking, which in the course of unstable cracking destabilises the structure of rock.

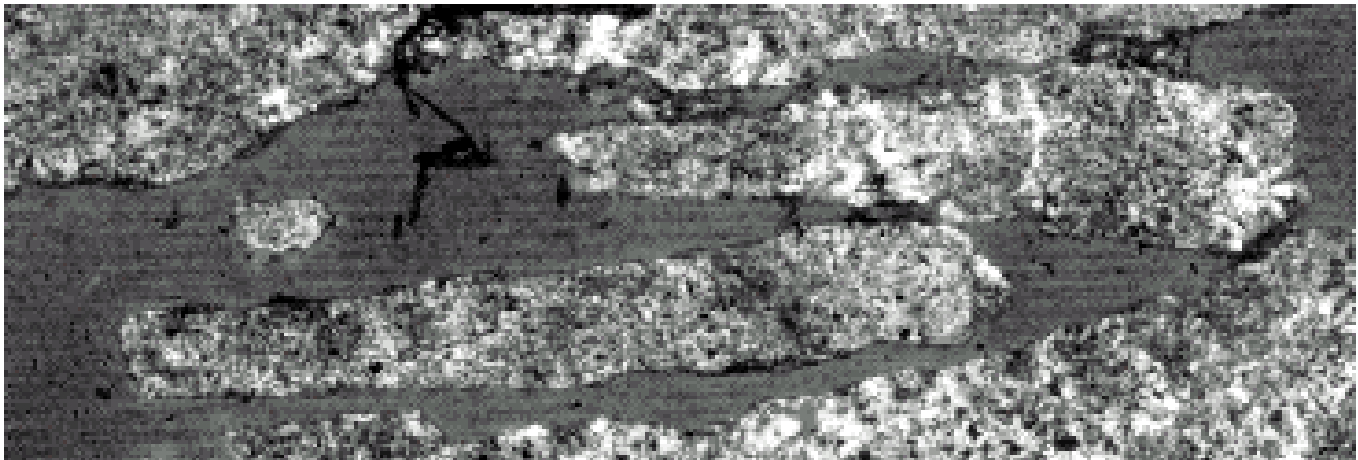


**Fig. 7. Transgranular cracking in limestones from Ogrodzieniec.**

#### RELATION OF THE MECHANISM OF CRACKING TO THE MODEL OF ACOUSTIC EMISSION

The above-discussed properties of the rock structure cause the formation of nuclei of microcracking and the development of macrocracking to have a varying dynamics, related to the given strain mechanism. They are followed by AE-event specific distribution. In the case of intragranular cracking of periodic media, cycles representing destruction of individual grains appear on the strain curve as repeatable results of relaxation and stress concentration, and as a continuos, regular increase and decrease of signal energy in acoustic emission on the micro and macro scale. The processes follow the model of deformation type  $M_{II}$  and model of postfailure acoustic emission type H (Fig. 8a).

In rocks with slip surfaces resulting from shearing, considerable post-critical volumetric strains are observed (Pininska, 1994, 1995). Eventually, in the course of final failure, local strengthening and slowing down of the process can take place.

The deformation curves and acoustic emission paths related to intergranular cracking in a medium with random composition of grains show irregular patterns of relaxation and concentrations of strain and energy emission. The processes follow the model of deformation type  $M_{III}$  and model of postfailure acoustic emission type M or L (Fig. 8b).

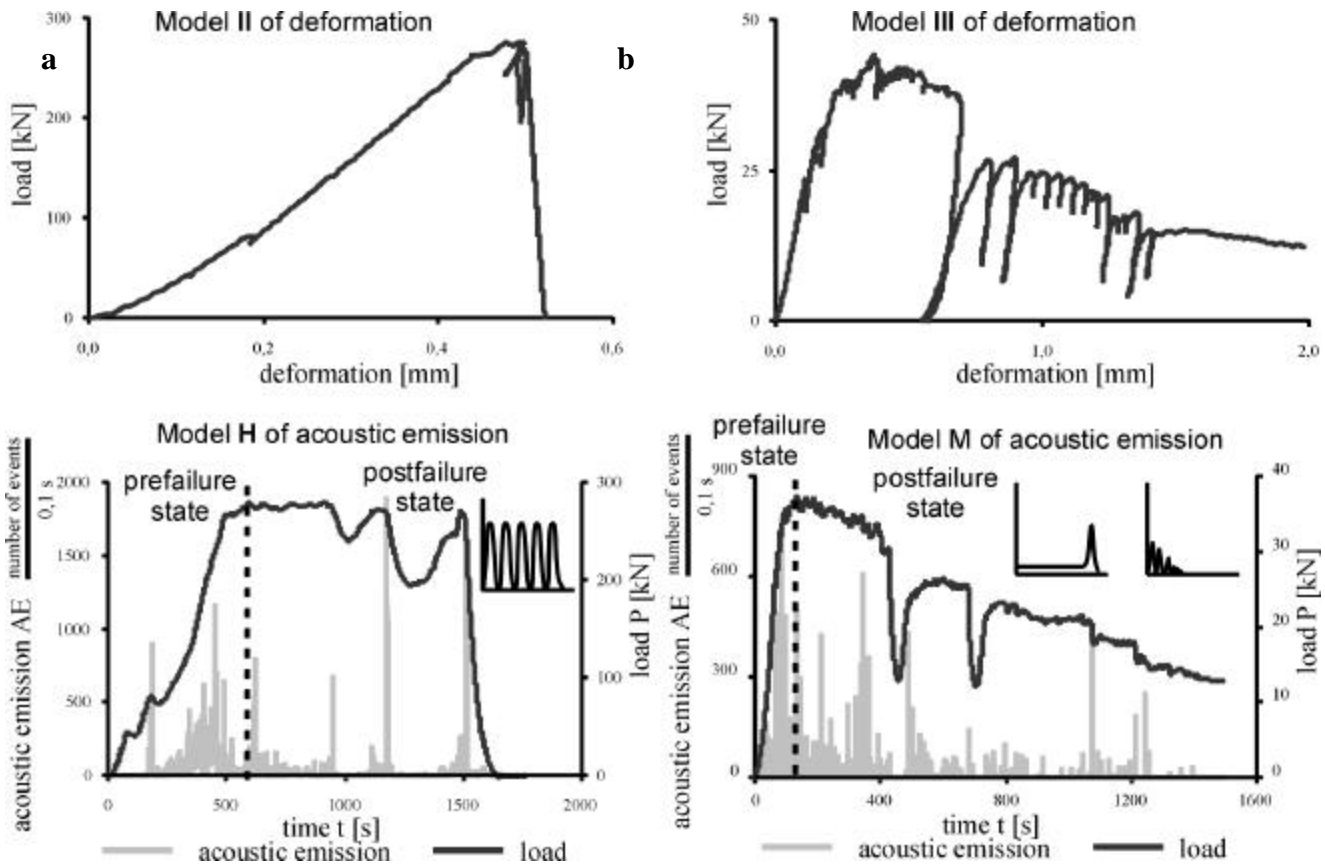


**Fig. 8. Regular (a) and irregular (b) effects of cracking registered on the strain curve and acoustic emission path and the models of deformation and acoustic emission (after Pininska (4)).**

As already mentioned, due to the influence of the shearing processes in intergranular cracking, considerable volume changes can be observed, the decrease of strength is slowed down and residual strength is significantly maintained. Intragranular cracking results in a rapid loss of strength. This is accompanied tightening of the fractures, which locally strengthens the rock, but no significant volume changes occur and the final destruction of the structure is usually violent.

## COMPARATIVE STUDY

The presented phenomena observed in the majority of rocks subjected to uniaxial compression can be interpreted in a view of simulation studies by Napier & Peirce (1995). They modelled the development of cracking in brittle materials having a polygonal and trigonal structure (Fig. 1a and b). The analyses showed that the finer the material, the higher the density of failure fissures and the state of mobilisation of all cracks causing final destruction of the structure at a given stage of strain is much lower in the fine-grained material than in its coarse-grained counterpart. This confirms the strength experiences in actual rocks, where unstable cracking in coarse-grained material takes place much faster. Less fractures are necessary to originate the unstable cracking process.

Fissures in the polygonal structure develop much harder than in the trigonal one, therefore the structure is much more stable than the trigonal one. However, this is true only to a certain extent as, at more advanced cracking, additional tensile centres caused by the stress of the displacing grains can occur. As a result of the additional

factor mobilising the new nuclei of cracking, the polygonal structures undergo a rapid decomposition without slipping displacements. In contrast, considerable zones of slipping, diagonal to the rock sample, are formed in the trigonal structure. The actual structure of rocks is more complex than suggested in the trigonal and polygonal models presented by Napier and Peirce. None the less, these models explain the way in which the structure is destroyed in most rock types. Rocks with carbonate mineral composition follow the description of the trigonal model, whereas the behaviour of clastic sedimentary rocks and igneous rocks corresponds to the polygonal model. These phenomena directly influence the general paths of cracking and acoustic emission.

The cracking mechanisms of polygonal models apply to polymineral clastic and crystalline igneous and metamorphic rocks with considerable quartz grains. On the strain curve they show regular oscillations of stresses related to intragranular tensile defects of seeds-point type. These models explain the reasons for the lack of extensive post-failure volume strains and low values of residual strength and represent repetitive acoustic oscillations model.

The cracking mechanism explained by the model of trigonal structure is characteristic of carbonate rocks, and clastic rocks with high feldspar or clayey material content, showing varying dynamics of stress and represent acoustic irregular oscillations model. This is related to intergranular cracking with a predominance of shearing processes and considerable postfailure volumetric strains and the pick of acoustic emission before the final destruction. It is accompanied by a considerable residual strength.

Acoustic indicators of rock structure degradation can be determined for crystalline rocks and carbonate rocks according to their varying acoustic emission along the rock deformation path. Especially diagnostics are the indicators for determination of the pre-failure thresholds of microdilatancy and macrodilatancy as well as for the stable fracturing range. These three indicators are strictly related to the grade of fracturing mobility and show the number of acoustic events at the limit of initial stable fracturing, and at the limit of stable fracturing - i.e. at the unstable fracturing threshold. In crystalline rocks the acoustic indicators are related to the volume density and strength of rock. In carbonate rocks they manifest the random pattern of fracturing and effects of attenuation by the shearing processes.

## REFERENCES

1. Brace W. F. and Bombolakis E. G. 1963. A note on brittle crack growth in compression. *J. Geoph. Res.*, **68**, Washington.
2. Cundall P. A. and Fairhurst C. 1986. Correlation of discontinuum models with psychical observations – an approach to the estimation of rock mass behaviour. *Felsbau*. 4.
3. Pininska J. & Lukaszewski P. 1992. Rock failure in acoustic emission spectre. Proc. XX-th Meeting of EWGAE, Leuven. Belgium.
4. Pininska J. 1994. Crack growth in the postcritical path of deformation of sedimentary rocks. *Mechanics of Jointed and Faulted Rocks-2*. Balkema. Rotterdam.
5. Pininska J. 1996. Some problems of the stress distribution on structural contacts in natural rocks bodies. Lvow University. *Sbornik Naucznych Rabot*. **36**. t.2. Lvow.
6. Napier J. A. L. and Peirce A. P. 1995. Simulations of extensive fracture formation and interaction in brittle materials. Proc. Mechanics of Jointed and Faulted Rock – MJFR. Balkema. Rotterdam.

# **RELATION BETWEEN ACOUSTIC EMISSION SIGNAL SEQUENCES INDUCED BY THERMAL LOADING AND THE STRUCTURE OF SEDIMENTARY ROCKS**

**Bogdan ZOGALA and Ryszard DUBIEL**  
**University of Silesia, Sosnowiec, Poland**

## **ABSTRACT**

*Sedimentary rock samples were subjected to thermal loading. During the heating both AE activity (number of counts per 100s) and temperature were recorded. The results showed that significant increases of acoustic emission activity and cumulative acoustic emission counts were different for various kinds of rocks. Four types of AE signals sequence were distinguished. The type of sequence is directly related to structure of sample regardless of the kind of rock.*

## **INTRODUCTION**

Mineral composition of rocks, lamination, porosity, fracturing and micro-fracturing directly influence their elastic properties. Thus, the structure of rocks influences the course of acoustic emission (AE) induced by mechanical (1) as well as thermal loading (2). A study carried out on sedimentary rocks subjected to thermal stresses showed that, for various kinds of rocks, AE significantly increased at different temperatures and various kinds of rocks are characterised by different AE activity (3). It was also shown that AE signal sequence depends on structure of rock (4). The goal of our investigation was to determine the relation among AE signal sequence and the structure and lithology for various kinds of sedimentary rocks.

## **MEASUREMENTS**

The measurements were carried out on sedimentary rock samples: mudstone, sandstone and limestone. All the samples were taken from the Upper Silesian Coal Basin and belong to carboniferous (sandstone and mudstone) and triassic (limestone) strata. The rock samples (cylinders of 100-mm diameter and 100-mm height) were obtained by cutting the cores. On each sample, two holes were drilled to the depth of 50 mm. In the first hole, the temperature gauge and in the second one the waveguide for AE transducer were installed. All the samples were heated in unconfined conditions up to 140°C. During the heating both the AE activity (number of AE counts per 100s) and temperature were recorded. The heating rate was approximately 2.1-2.3°C/min.

## **SAMPLES**

- Mudstones were composed of sharp edged quartz grains with admixture of silty minerals, ferric oxides and siderite grains. Some of investigated samples have been laminated whereas the other had chaotic and compact structure. Fracturing, variable granulation, and pores of several mm have also been noticed in some of the samples.
- Sandstones were medium and variable-size grained, laminated, and were composed of quartz, feldspars, micas, and chips of rock with argillaceous and calcareous cement. Quartz grains were chaotic oriented and sharp edged. Colour of the samples was light grey and grey.

- Limestones were compact, hard, unbedded, breccious structured. It was noticed that pores with calcite druses, cracks about 30 mm filled by sharp-edged chips of marlaceous and calcareous breccia. Some of the samples were composed of macroclastic breccia cemented by argillaceous substance. One also observed stylolitic sutures. Colour of the samples was white and light grey.

## DISCUSSION

Investigation concerned sixty rock samples: forty sandstone, ten mudstone and ten limestone samples. They were subjected to thermal loading to maximum temperature 140°C. Next, sequences of acoustic emission signals were analysed. Significant increase of acoustic emission activity was observed in different temperature range for various kinds of rocks (table 1):

- from 64.8 to 75.8°C for sandstone samples (average 70°C)
- from 60.4 to 103.7°C for mudstone samples (average 86°C)
- from 64.2 to 81.8°C for limestone samples (average 74°C)

Cumulative AE counts were also different for various kinds of rock. The largest for limestone samples (average 1950 signals), less for sandstone samples (average 1800 signals) and the least for mudstone samples (average 1700 signals) (see Table 1). One distinguished four types of acoustic emission signal sequences (Figs. 1, 2, and 3); these were found in all kinds of samples:

- type 1 – main shock (crack) is very strong and is not proceeded by foreshocks. The AE quickly decays.
- type 2 – main shock is not so strong as for type 1 and the foreshocks are observed
- type 3 – main shock is not observed. First the number of signals increases then decreases.
- type 4 – main shock is not observed. High AE activity is observed to the end of the heating.

Table 1 AE Signal Sequences

Rock	-1-	-2-	-3-	-4-	-5-	-6-	-7-	-8-	-9-
Sandstone	40	64.8-75.8	70	98-3847	1800	4	12	16	8
Mudstone	10	60.4-103.7	86	126-2687	1700	1	3	2	4
Limestone	10	64.2-81.8	74	225-3247	1950	1	3	4	2

1 – number of samples; 2 – temperature range of AE significant increase; 3 – average temperature of significant AE increase; 4 – range of AE cumulated count number for particular samples; 5 – average AE cumulated count number; 6 – number of samples for sequence type 1; 7 - number of samples for sequence type 2; 8 - number of samples for sequence type 3; 9 - number of samples for sequence type 4

The sequence type is found to relate to the structure of rock. Sequences of type 1 and 4 were obtained for homogenous rocks with low porosity and few cracks. The main feature of the rocks is uniform distribution of stresses. The heterogeneous cracked rocks with low porosity were characterised by sequence of type 2. Sequences of type 3 were obtained for extremely heterogeneous cracked rocks with high porosity. The stress distribution in these rocks is not uniform. The largest number of AE signals was observed for samples characterised by sequence type 3 and 4 whereas the least AE counts for samples characterised by sequence type 1. Figure 4 shows percentage shares of particular sequence types for tested rock samples; i.e., mudstone (a), sandstone (b) and limestone (c).

We also compared four AE signal sequences with sequences obtained in our previous research concerning the thermal memory effect in the course of AE (5-8). We found that the thermal memory

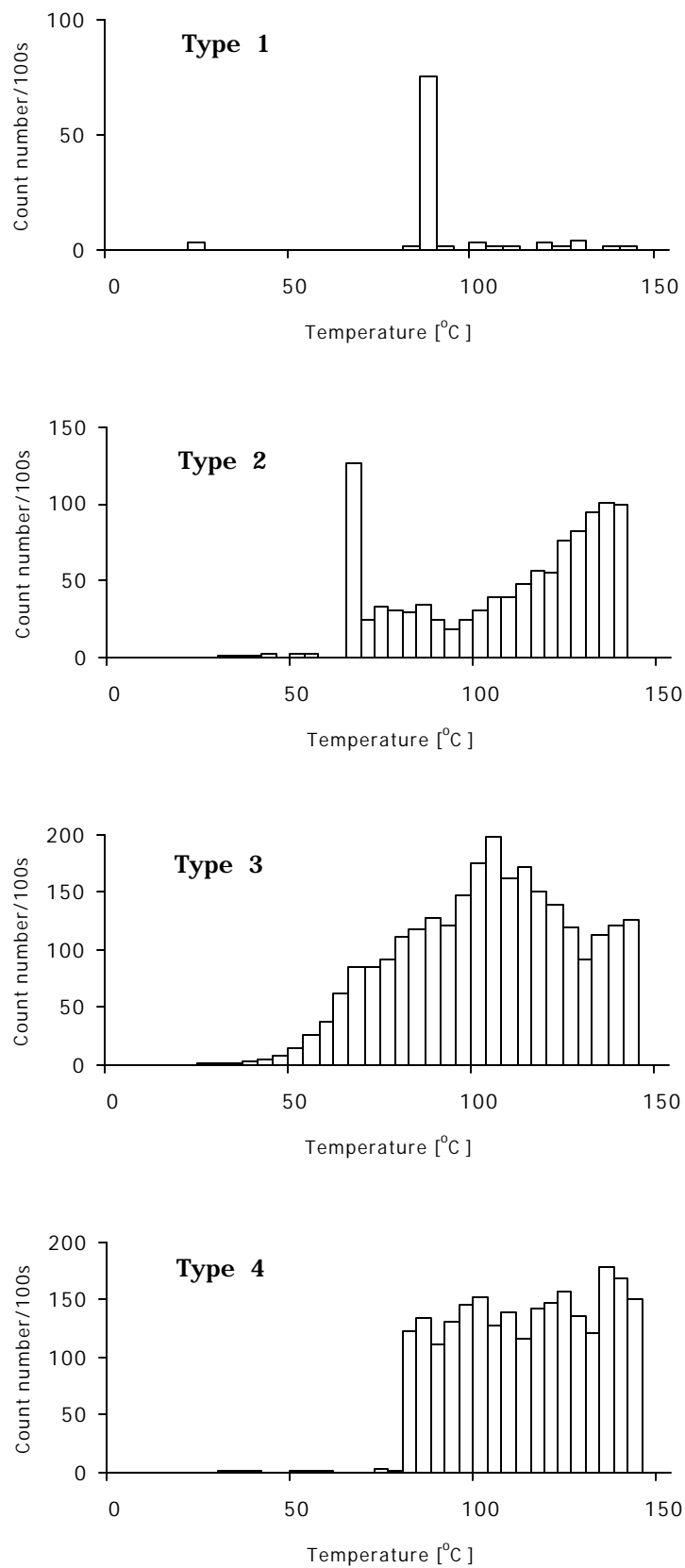


Fig. 1 Four types of sequences of AE signals for tested 40 sandstone samples.

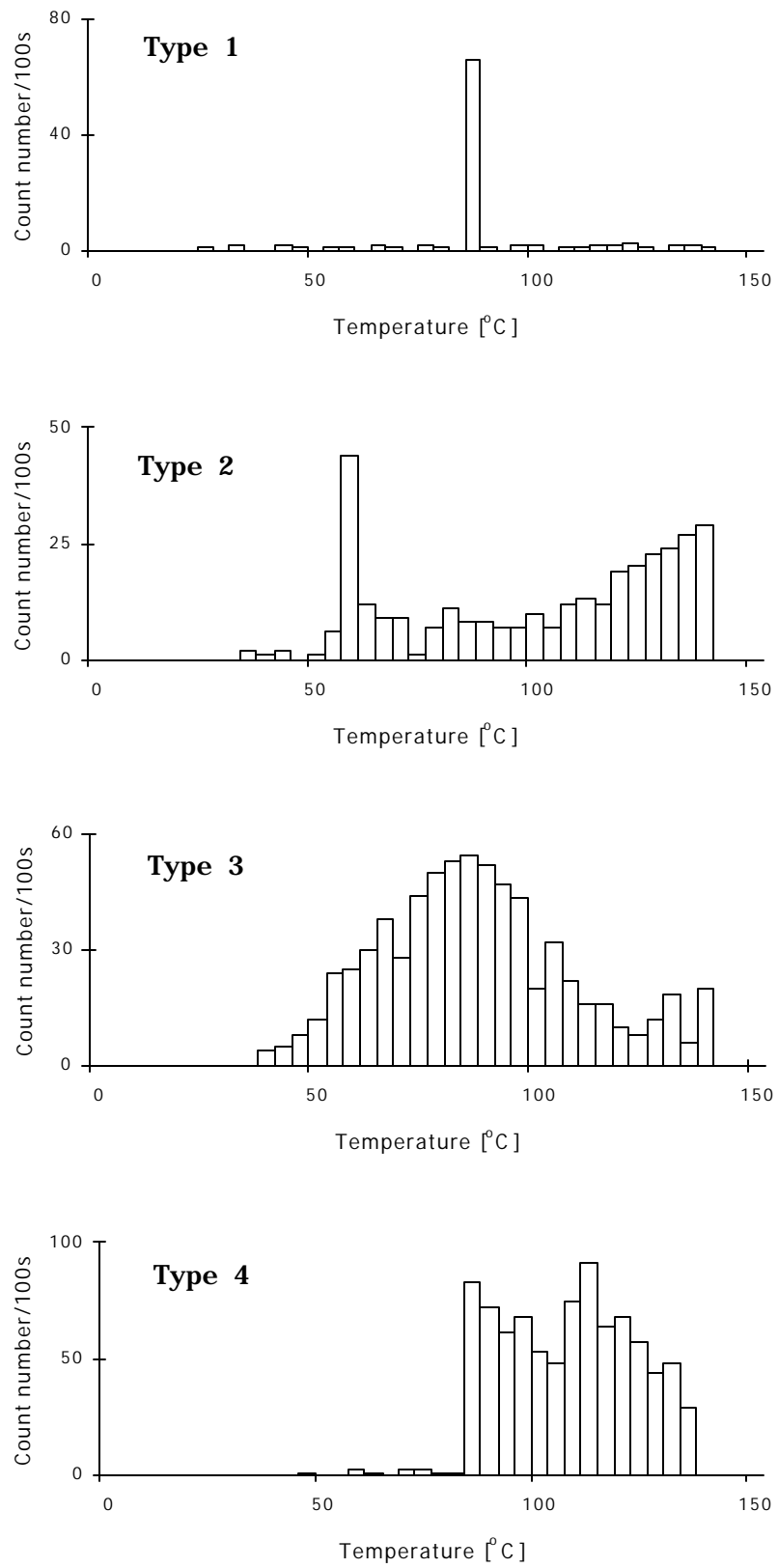


Fig. 2 Four types of sequences of AE signals for tested 10 mudstone samples.

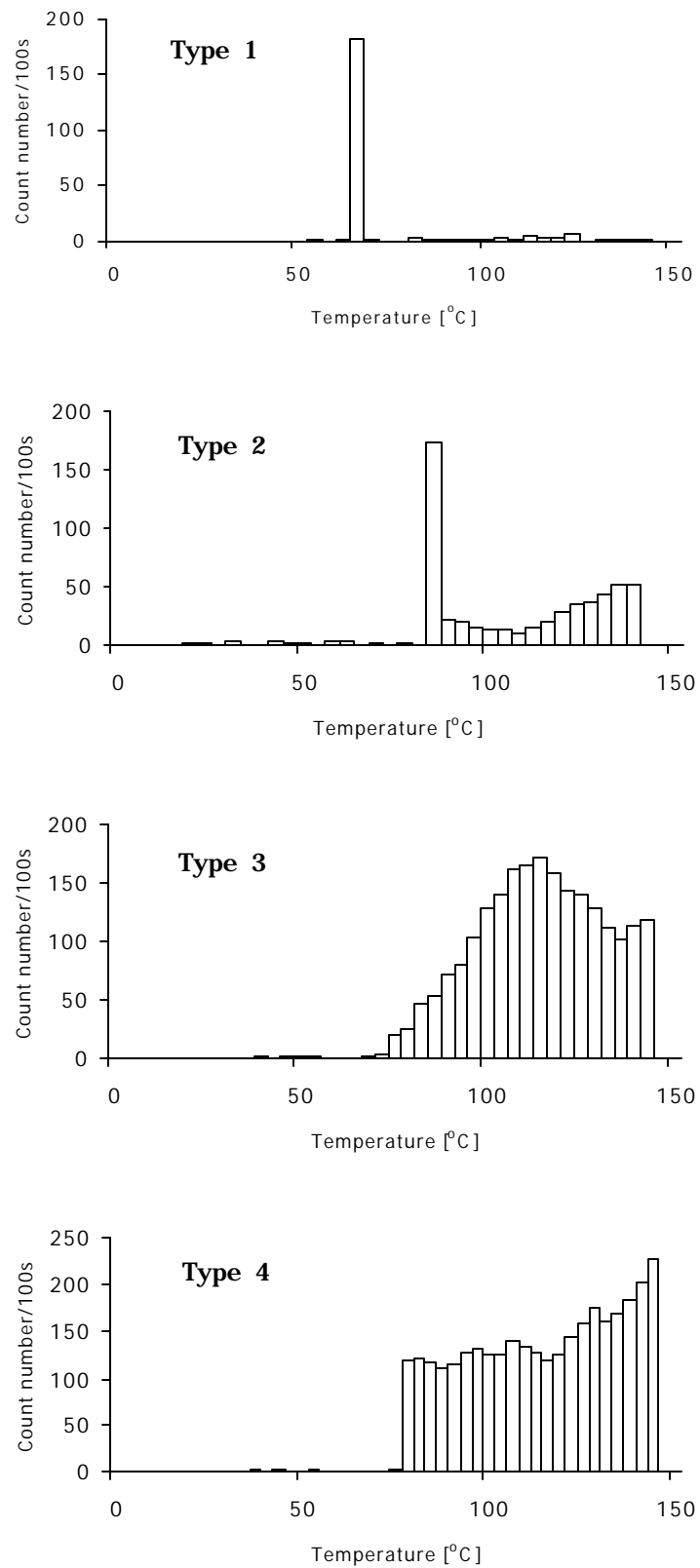


Fig. 3 Four types of sequences of AE signals for tested 10 limestone samples.

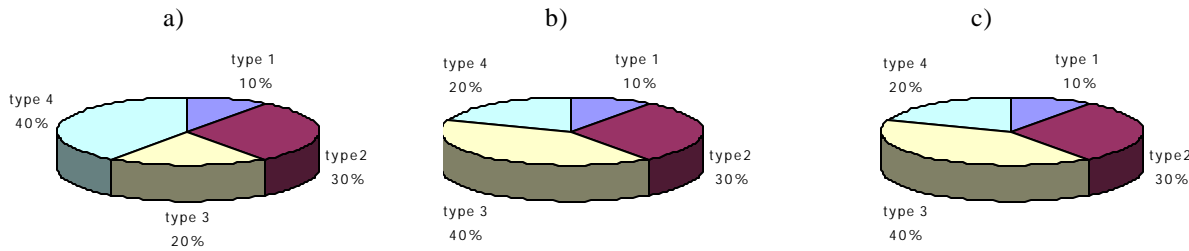


Fig. 4 Percentage share of particular sequence types for tested rock samples. a) mudstone samples, b) sandstone samples, c) limestone samples.

effect was observed in homogeneous and heterogeneous rocks (sequence type 2, 3, 4), but was not observed in extremely homogeneous rocks (sequence type 1).

## CONCLUSIONS

1. Thermal stresses induce four types of AE signal sequences in sedimentary rocks.
2. AE sequence type depends on the structure of sedimentary rock sample.
3. Cumulative AE counts are large for sequence type 2, 3 and 4 and the least for sequence type 1.
4. Previous and present research showed existence of the thermal memory effect in the course of AE for sequence type 3 and 4. For sequence type 1, the thermal memory effect is not observed

## REFERENCES

1. Mogi K., 1977: Dilatancy of rocks under general triaxial stress states with special references to earthquake precursors. *J. of Phys. of the Earth*, **25**, Suppl. 1977, 203-217.
2. Chen Y., Wang C., 1980: Thermally induced acoustic emission in Westerly granite. *Geoph. Res. Letters*, **7**(12), 1089-1095.
3. Zogala B., 1992: Application of AE for observation of sedimentary rock samples fracturing subjected to thermal loading. PhD Thesis, Faculty of Earth Sciences, University of Silesia, Katowice, (unpublished, in Polish)
4. Zogala B., Dubiel R., 1998: Analysis of acoustic emission signals sequence induced by thermal stresses in mudstone samples. Proc. 23rd European Conference on Acoustic Emission Testing, TUV, Vienna, 53-58.
5. Zogala B., 1999: Physical basis of the maximum temperature memory in the course of acoustic emission in sedimentary rocks. *Acoustics in Technology, Medicine and Culture*, Krakow, 85-90.
6. Zuberek W.M., Zogala B., 1996: Memory of maximum stresses and maximum temperatures during rock deformation. *Publ. Inst. Geoph. Pol. Acad. Sci.*, **M-18** (273, 133-138).
7. Zuberek W.M., Zogala B., Dubiel R., 1998a: Laboratory investigations of the maximum temperature memory effect in sandstones with measurements of acoustic emission and P-wave velocity. Proc. of 6th Conference on Acoustic Emission / Microseismic Activity in Geologic Structures and Materials, Trans Tech Publ. (ed. H.R. Hardy Jr.), 157-168.
8. Zuberek W.M., Zogala B., Dubiel R., Pierwola J., 1998b: Maximum temperature memory in sandstone and mudstone observed with acoustic emission and ultrasonic measurements. *Int. J. of Rock Mech. & Min. Sci.* **35**, No 4-5.

# ACOUSTIC EMISSION/ACOUSTO-ULTRASONIC DATA FUSION FOR DAMAGE EVALUATION IN CONCRETE

Apostolos TSIMOGIANNIS, Barbara GEORGALI\* and Athanassios ANASTASSOPOULOS

Envirocoustics S.A., Athens, Greece

\*Hellenic Cement Research Center Ltd., Athens, Greece

## ABSTRACT

*The nature of concrete poses a number of difficulties to conventional non-destructive testing (NDT) methods. Due to the existence of several geometric discontinuities, such as voids and particle interfaces, microscopic damage is not usually evaluated by NDT. To retrieve this information from concrete, techniques such as microscopy and chemical analysis are used. Damage accumulation on a microscopic level may not always affect the static behavior of a structure but is crucial for dynamic loading conditions. Although acoustic emission (AE) techniques can detect damage at early stages on structures that can be loaded to typical loads (bridges, piers etc.), they cannot be applied to structures that are not suitable for loading (buildings). In the present work, mortar specimens are monitored using, simultaneously, AE and Acousto-Ultrasonic (AU) techniques, during compressive strength tests. The purpose is to monitor damage by AE and evaluate this damage with AU measurements, a technique independent of load. The results show the efficiency of AU in characterizing the level of microscopic damage in mortar specimens and are in agreement with AE monitoring during loading. AU results are also compared against microscopy findings regarding the amount of damage in the specimens.*

## INTRODUCTION

The majority of modern infrastructure and buildings use reinforced concrete as the main construction material. It is of importance to monitor and evaluate the structural integrity of such constructions. Especially in areas with seismic activity, this becomes of crucial importance in order to ensure the safety of buildings and other concrete based structures. This is emphasized when the mechanical properties of concrete are considered: concrete is a delicate mixture requiring precise mixing of the various elements for each use, according to manufacturer's specifications, and care must be taken during solidification so as to achieve the desired properties. Microscopic damage in concrete caused under such conditions is difficult to monitor due to the nature of concrete (porosity, aggregates, etc.) although it can accelerate damage and weaken the structure to future adverse loadings. Conventional NDT methods [1] face a number of difficulties when applied to concrete and even more so when applied in an attempt to locate or characterize damage on the microscopic level. Therefore, it has been standard practice to assess the condition of concrete by the extraction of specimens and the use of optical microscopy and chemical analysis to assess the effects of adverse loads, environment, etc.

Acoustic Emission (AE) can provide information about developing damage at early stages and the application of advanced data analysis can provide crack orientation and mode [2,3]. As AE requires loading of the structure, it cannot be applied to buildings. Acousto-Ultrasonics (AU) can be used as a dynamic method to assess the level of damage as the interaction of an induced stress wave with the medium will introduce medium-related alterations to the original wave [4]. Based on this assumption experiments were performed using several techniques on mortar cement specimens.

The results are indicative of AU capabilities in assessing sustained damage. Furthermore, AU signal characteristics, as opposed to ultrasonic velocity measurements, have demonstrated high sensitivity to changes in the material at low loads. As a result, during the experiments, AU was considered as a means of non-destructively assessing some of the mechanical properties and behavior of concrete. The results are in agreement with the production of AE by the material and, also, with microscopy results of the unloaded specimens.

## MATERIALS

The mortar cement mixtures used for the present work are presented in Table 1 with some details regarding their composition. For each type and age, two specimens were tested. The specimens were kept in a 90% humidity controlled temperature environment as required by standards for concrete and were removed from this environment 2 to 3 hours prior to testing.

## INSTRUMENTATION & EXPERIMENTAL SETUP

The equipment used were a PAC MISTRAS-2001 AE system and a PAC C-101-HV pulser. The sensors used for pulsing and receiving were PAC R6, 60kHz resonant, with PAC 1220A preamplifiers. The sensors used were chosen for their high sensitivity, frequency response for concrete measurements [5] and their ability to be used for ultrasonic velocity measurements according to ASNT recommendations [1].

Microscopy results are available for specimens A for all three ages. Prior to the test each specimen was loaded to 150kN to remove AE produced from debris (dust, small particles etc.) on the surfaces of the specimen and to allow for any irregularities on its surface to settle. All specimens were compressed to failure and monitored throughout simultaneously by AE and AU. During compression one AE sensor was constantly receiving AE signals from the specimen. The pulses were generated at specific loads. Synchronous triggering of pulser and AE systems was used. The setup is shown in Fig. 1. The AE acquisition system recorded both features and waveforms for further analysis.

## MICROSCOPY

The application of by petrographic (microscopical) examination to building materials such as mortar cement or/and concrete, detects the quality of aggregates, cement paste characteristics, water to cement ratio (w/c), structure porosity, cracking and defects, etc. The procedure is according to ASTM standards [7]. The microscopic examination is performed on epoxy impregnated “thin sections” (thickness<25  $\mu\text{m}$ ), typically using magnifications of 30-250x. The results shown are for specimens A for all ages. The following parameters were measured:

ID	Age (days)	A/C	W/C
A	2	4	0.60
A	7	4	0.60
A	28	4	0.60
B	2	3	0.50
B	7	3	0.50
C	2	3	0.65
C	7	3	0.65

Table 1. Specimen specifications and data.

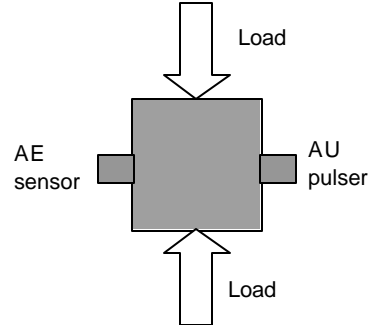
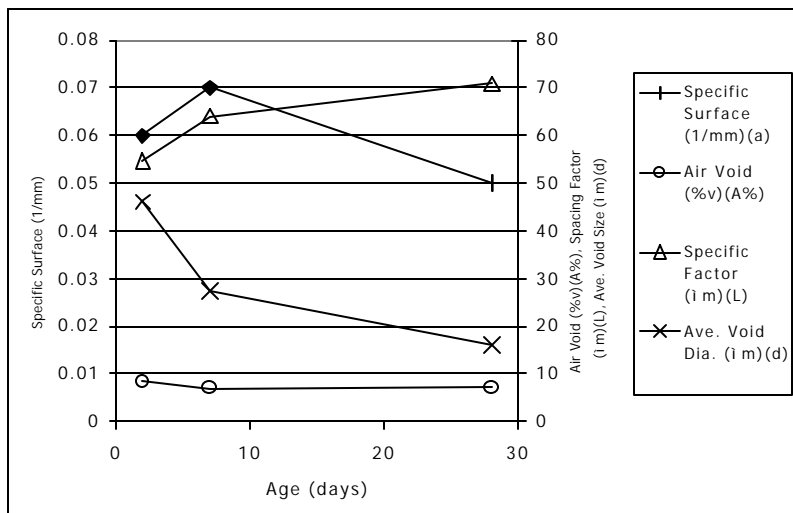


Fig. 1. Experimental setup.

Air void Size: The average air void size decreases with age as the size distribution of air voids shifts to smaller sizes with age. This can be explained, either by allocation of air voids, or by reduction of pore size, due to filling with hydration products (see Fig. 2).

Air void content: The air voids percentage can be said to remain constant, if the method error is considered.

Specific Surface and Spacing Factor: The spacing factor (the maximum cement paste distance from the air void) increases with mortar age. Air void specific surface increases with mortar age, giving confirmation of the decrease in air void size. Given the total air void volume as constant, this can be explained by the large pore allocation to smaller ones. It must be emphasised that with the petrographic examination the identified air void size is greater than 10  $\mu\text{m}$ , and as a result they don't enlist to the micro-pores category, which are filled by cement paste during the plastic stage.



*Figure 2. Microscopy results for mortar cement specimens A.*

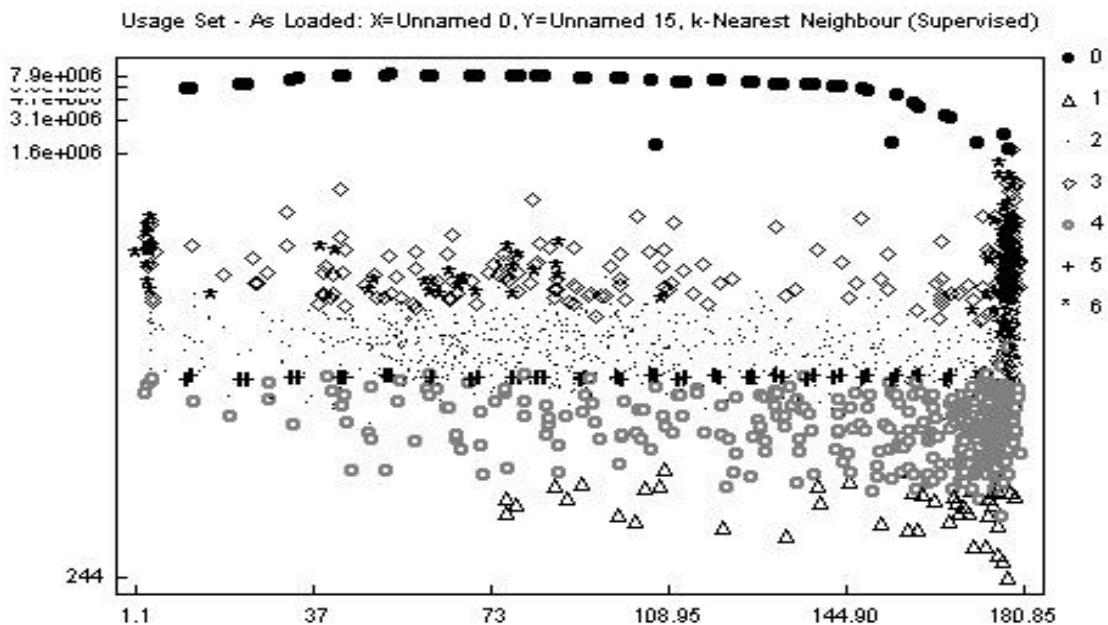


*Fig. 3. Clustering for specimens A. 2 days. Energy vs Time (s).*

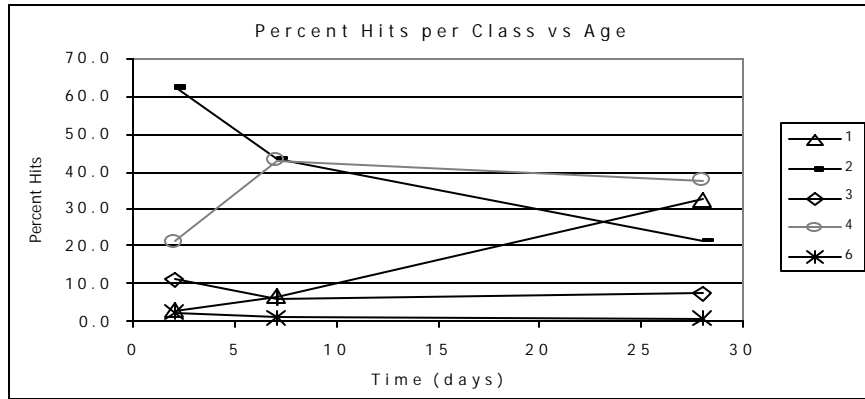


*Fig. 4. Percent of total hits per class for all ages.*

## ACOUSTIC EMISSION

The first observation regarding AE data is the fact that the specimens exhibited different behavior depending on their age. The 2 day specimens produced significant AE at lower load levels, with a subsequent decrease in activity until the fracture load is approached. As the specimens age (7 and 28 days) this behavior changes with most AE produced near the fracture load. In addition, aged specimens demonstrated the Kaiser effect. The onset of AE was clearly after the 150kN initial load. This can be justified taking into consideration the increased elasticity of the 7 days specimens and even more so the 2 day specimens. This can be observed repeatedly in all specimens with various aggregate to cement (A/C) and water to cement (W/C) ratios. To draw more conclusions from this type of behavior and to be able to assess the observed AU signals further, a more detailed analysis of the AE data is performed using NOESIS, a commercially available Pattern Recognition (PR) and Neural Networks (NN) Software package. The classification scheme is not for distinguishing among a number of failure mechanisms, but instead is used to separate data in different categories so as to review the behavior and progress of each type of signals among different specimens and improve the understanding of the data produced by each specimen. Some of these classes of signals may be related to a physical phenomenon and a discussion is made on this with results supported by AE, AU and microscopy findings. In addition general considerations regarding the behavior and aging of concrete are used in this respect.

Data from specimen A (2 days) were used for the initial clustering. The original data were normalized using a non-linear space transformation based on logarithmic functions. to avoid biasing due to large vector distances. In addition, a reduced set of six features (AMP, DUR, SIG, STRENGTH, CNTS, RSTM, ABS ENER) was used for the unsupervised algorithm. The algorithm used was the Max-Min Distance [6] algorithm as implemented in the Noesis software. The final classification is composed of 7 AE classes and the two AU classes. The results were then used to train a classifier so as to automatically apply to other data sets. The training method used was the k Nearest Neighbor Classifier (k-NNC)[6] using Octagonal distance type for optimized performance in the present type of data. Typical clustering results are shown in Fig. 3. Figure 4 presents the percentage of total hits per class for all ages of specimens A.

Class 1 comprises signals, which appear in older specimens. It is apparent from Figures 3, 4 and 8 that these are low energy signals, which appear throughout the compression test but mainly at fracture. The behavior of other type of specimens is similar but reduced A/C ratio samples produce more AE in class 1. This, along with the fact that class 1 appears in older specimens, may suggest that class 1 is related to mechanisms in the cement paste. These may also be related to air content as well as void size, parameters, which are affected by age.

Class 2 is another important class with medium energy signals which diminishes as the specimens age. This class of signals appears from low loads and demonstrates high activity at intermediate loads. The decrease of the number of signals in this class and its behavior with the applied load is indicative. The

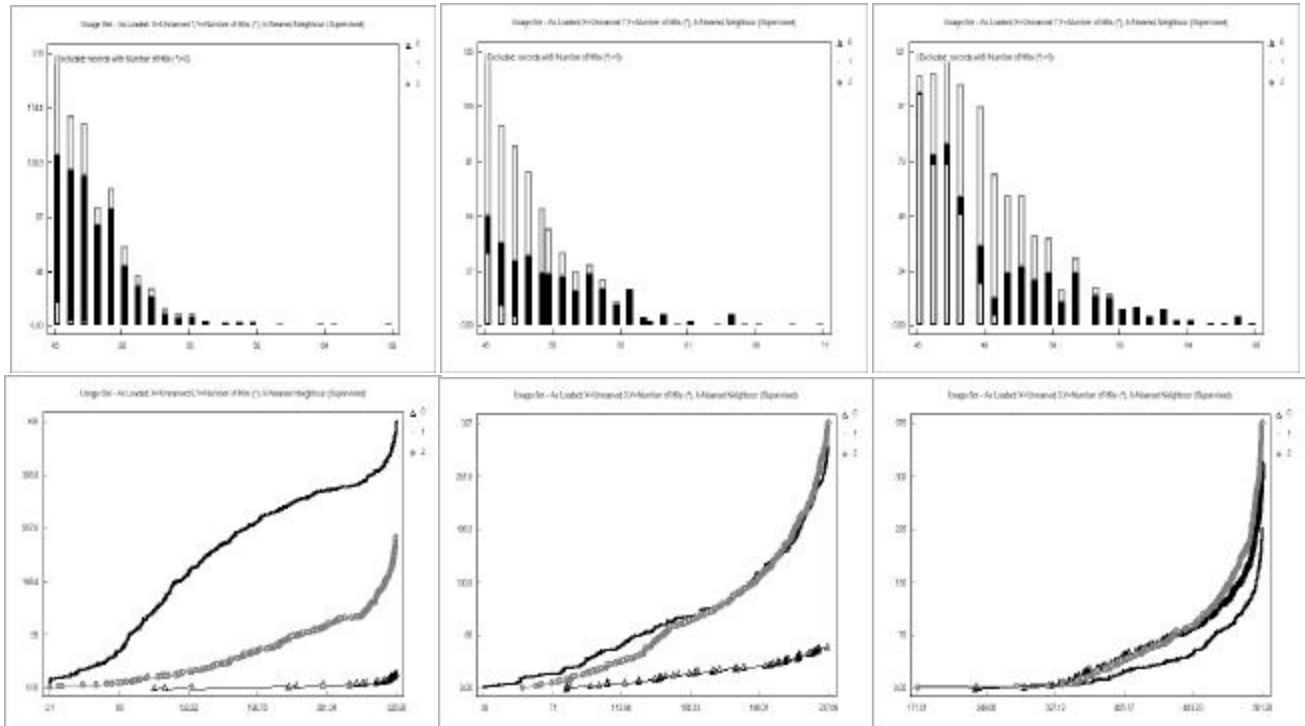


**Fig. 5. Class amplitude distribution (top) and cumulative hits (bottom) for all ages for specimen A (2, 7 and 28 days left to right)**

same reasoning holds for class 2, which appears at low loads and is more pronounced in new specimens. Class 2 appears to be produced by mechanisms related with the aggregates as it diminishes with age and with A/C ratio. The behavior of Class 3 is different and the phenomena, which cause it, seem to become after 7 days. This class may be related to internal friction as it appears only very early in the specimens' lives. Figure 6 illustrates typical amplitude distributions and hit cumulative plots for the three discussed classes. The above results will also be discussed in relation to the AU data, which can provide an impression of permanent or recoverable changes in the microstructure of the material.

## ACOUSTO-ULTRASONICS

The experiments conducted during the present work demonstrate clearly that AU signals can show oncoming failure at early stages. It is obvious from all specimens that AU signals weaken significantly after approximately 80% of maximum load. An important observation regarding AU measurements is their sensitivity at lower loads.

Throughout the loading procedure specimens produced AE depending mainly on their age and composition and AU data exhibited a significant variation indicating changes in the specimens, throughout each test. Transmitted AU energy increased as the load was applied, indicating that the

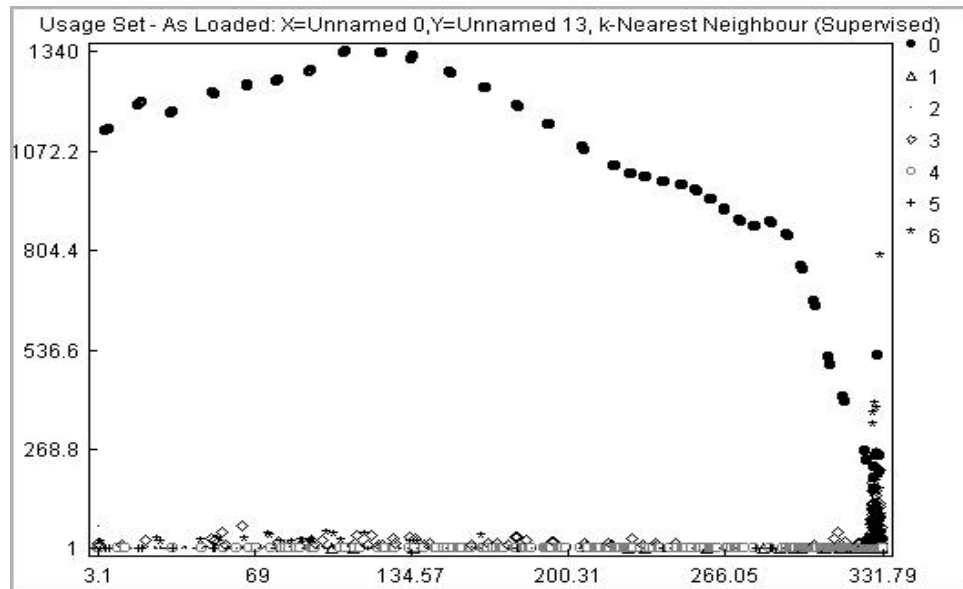


*Fig. 6. Signal Strength vs Time for specimen A 7 days.*

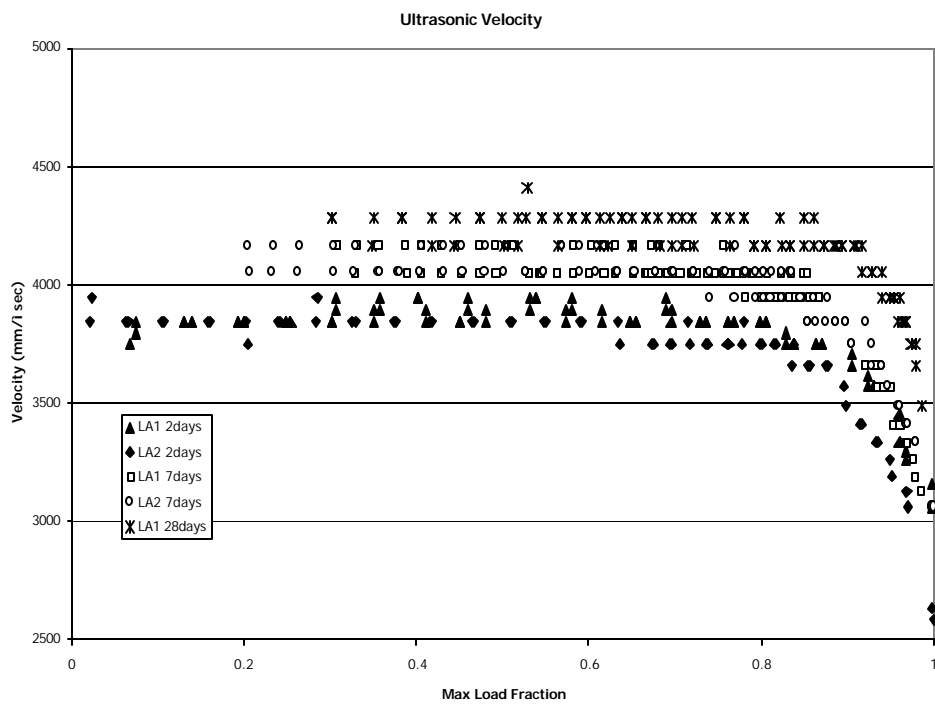


*Fig. 7. Ultrasonic velocity for various specimens. The velocity remains constant until approx. 0.8 of max load is reached.*

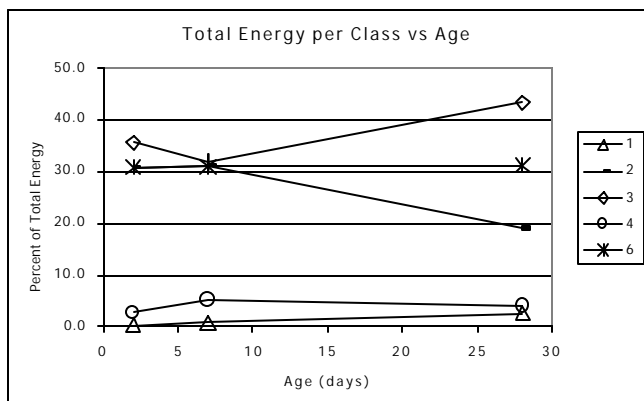


Fig. 8. Percent Total AE Energy per class.

specimens became better wave-guides, which may be an indication that they become denser. This may be related to the elasticity of concrete and the elastic or plastic collapse of voids. This was observed for loads up-to about 50% of maximum load. As specimens age, the initial behavior is of variations in AU energy with a general trend for decrease. The initial fluctuation and the general decrease tendency may indicate some sort of micro-structural damage.

Using ultrasonic velocity measurement [1], it can easily be observed that the velocity drops sharply at about 80% max load. Velocity measurements are insensitive, though, to any changes the material undergoes at relatively low loads and therefore the sensitivity of the technique in assessing minor damage cannot be determined. Other AU characteristics vary significantly as the load is increased from zero to some value whereas the velocity of the wave remains constant and can thus provide more information about the material's behavior.

## DISCUSSION

As mentioned, the behavior of AU signals is unique in the sense that the specimens become better wave guides as the load is applied. After a certain load some break-down appears to take place and the signals' energy decreases. Waveform analysis using Fast Fourier Transforms (FFT) did not indicate any significant change in the frequency spectrum. FFTs of AU signals throughout a number of tests were studied but the only information related to the total energy transmitted through the material with insignificant frequency changes or shifts.

The behavior of AU signals can in general be correlated to AE and microscopy results. It is interesting to observe the behavior of AU signals with respect to class 6. The increase or variations in the AU signals' energy appears at the same time with class 6, especially in younger specimens (2 and 7 days) (see Figure 9). Class 6 is composed of relatively high energy signals at small loads. The appearance of a high energy class at small loads along with the change in AU characteristics may indicate a change in the structure of the material, such as friction, void collapse etc. The energy contained in class 6 signals remains constant for all specimen ages.

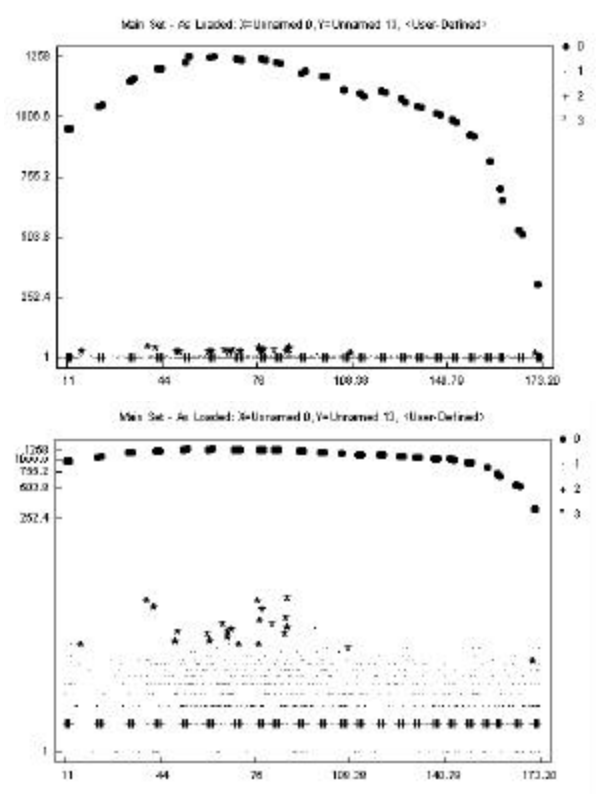


Fig. 9. Typical behavior of Class 6 (\*) and Class 2 (.) with AU energy in normal and log scale.

At early loads, when variations in AU characteristics occur, other classes of signals show variations in the amount of AE produced, such as classes 3 and 2. These classes, as mentioned, may be correlated with mechanisms in the material and can thus affect AU.

## CONCLUSIONS

It has been demonstrated in the present work that a combination of various techniques can provide important information and better understanding of the results of each technique. In addition, application of pattern recognition techniques has proven a powerful tool for signal discrimination as a means for advanced data analysis in Acoustic Emission.

The results are indicative of AU sensitivity and ability to assess damage in mortar specimens. AU can be related to physical changes in the specimens and can thus provide information regarding their internal structure. This is crucial for the use of AU techniques utilizing signal characteristics as opposed to ultrasonic velocity, in an attempt to assess early stages of damage in concrete. Although concrete is somewhat different in its behavior than mortar, initial work has shown similar behavior and research is being focused in that direction.

## REFERENCES

- [1] ASNT, Non-Destructive Testing Handbook, vol.7, “Ultrasonic Testing of Bridges and Buildings”, pp. 680-684.
- [2] S. Yuyama, T. Okamoto, M. Shigeishi, and M. Ohtsu, “Quantitative Evaluation and Visualization of Cracking Process in Reinforced Concrete by a Moment Tensor Analysis of Acoustic Emission”, *Materials Evaluation*, **53**(6), 1995, pp. 751-756.
- [3] S. Yuyama, T. Okamoto, T. Kamada, M. Ohtsu, T. Kishi, “A Proposed Standard for Evaluating Structural Integrity of Reinforced Concrete Beams by Acoustic Emission”, *Progress in Acoustic emission VIII*, The Japanese Society of NDI, 1996, pp. 295-304.
- [4] M. Uchida, T. Okamoto, T. Shibata, D. Mori, and M. Ohtsu, “Structural Integrity Evaluation on Reinforced Concrete Members”.
- [5] A. Tsimogiannis, A. Anastassopoulos, “Experimental Set-up Design for Acousto-Ultronics on Concrete Specimens”, MHKKYNES Project, Athens, 1999
- [6] Envirocoustics ABEE, “Noesis Reference Manual”, rev.0, 1999.
- [7] ASTM 856-83, “Standard Practice for Petrographic Examination of Hardened Concrete”.

# CONCRETE CROSSBEAM DIAGNOSIS BY ACOUSTIC EMISSION METHOD

Zdenek WEBER, Petr SVADBIK, Marta KORENSKA, Lubos PAZDERA  
Technical University of Brno, Brno, Czech Republic

## ABSTRACT

Centred cyclic bending load was applied to a reinforced concrete crossbeam. Crack controls were carried out by AE method and simultaneously by visual reference. Simultaneously, the rise and growth of the cracks were measured. The amplitude of AE events depends on the crack velocity, which itself depends on the stress intensity of the crack. The increase of AE energy and counts during cyclic loading indicated the absence of Kaiser effect in the reinforced concrete crossbeam. The frequency content of AE signals is the function of the transducer's frequency response. The experiment demonstrates high sensitivity of the AE method at monitoring stress states. These results provide information about behaviour of building structures in standard and extreme situations.

## INTRODUCTION

In a project of new variable bridge system with a span of 6 to 30 m, the most important connection was a steel concrete girder with a monolithic steel-reinforced concrete crossbeam (Fig. 1,2,3). The crossbeam model was designed and made at scale 1:1 and was tested all at Brno University of Technology. On the basis of positive results by numerical analyses and loading tests, it has resulted in building the integrated bridge system across the river Ploužnice in Stružnice at Ceska Lipa at end of year 1999. The experimental check of reliability of coupled girder, the detection of transmission of tension in the areas of negative moment under hold and ways to find fault of the construction before the exhaustion of the ultimate tensile capacity were the main aims in this work.

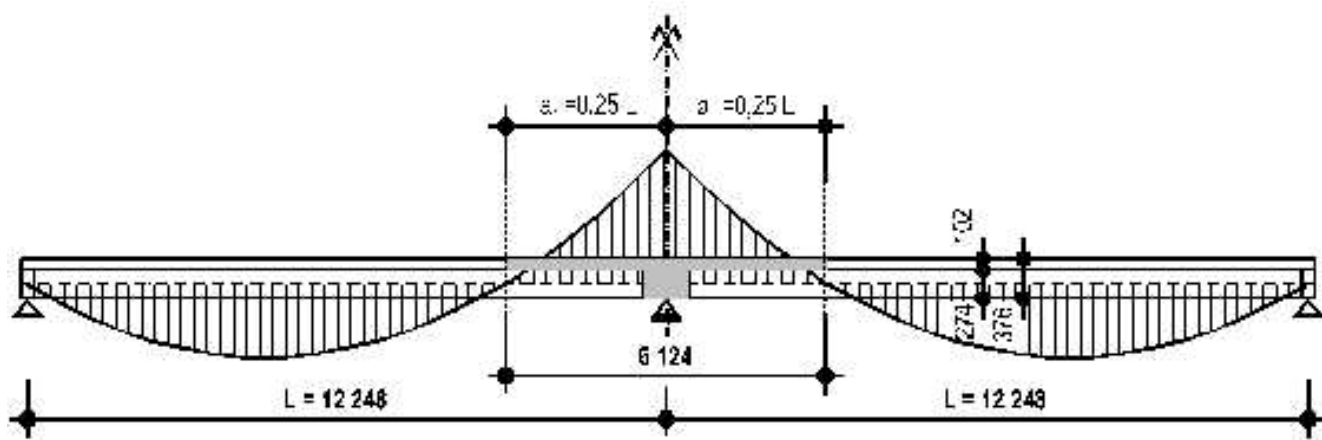
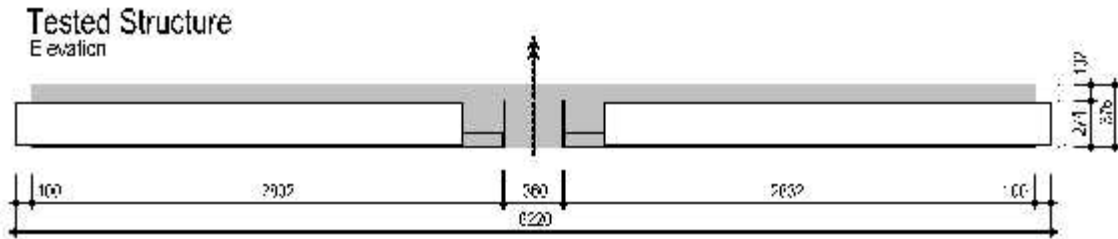


Fig. 1. Reason about segment test model in longitudinal direction.

A part of static load test of the model steel-concrete monolithic crossbeam was:

- a few cycled loading (100 cycles each) with subsequent measurement of its ultimate loading-capacity,
- the behaviour of the construction at cracks and their expansion (acoustic emission method)
- monitoring responses on this loading by X-ray non-destructive testing on the shear connector.



*Fig. 2. Select test model.*

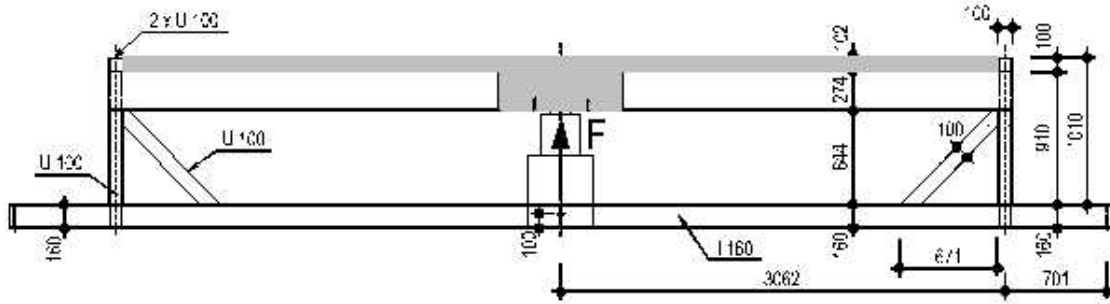


**Fig. 3. Tested model of composite steel concrete girder.**

This article describes measurement results and monitoring by acoustic emission (AE) method, verification of correlation between fatigue and AE activities, generated during the controlled cyclical load test.

The monitoring of AE, generated by cracks during the tests, proceeded on the test specimens aged 7, 28 and 90 days and further on the final crossbeam model from February to the end of April 1999 (*Fig. 4,5*).

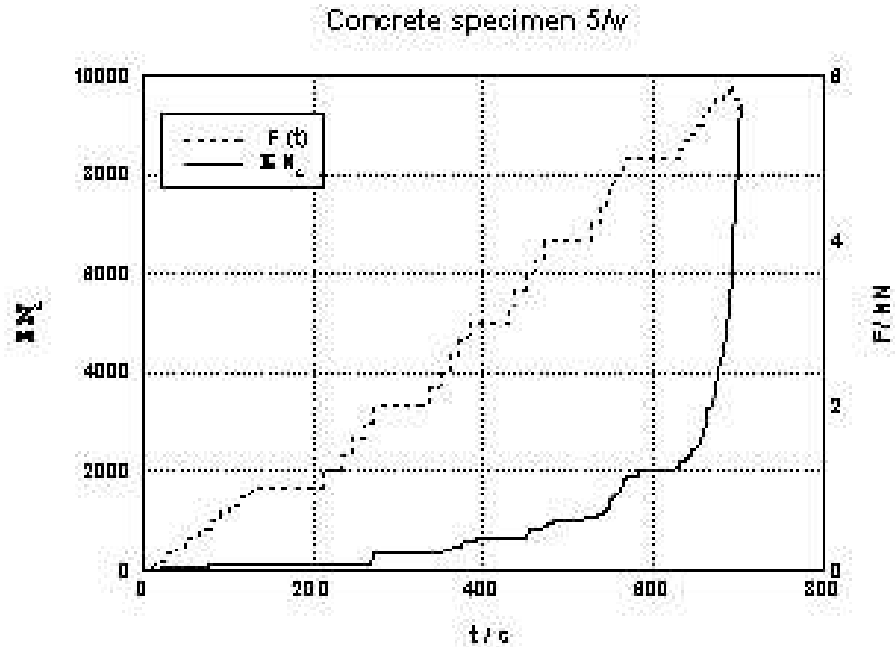


*Fig. 4. Age 7 days, three points bending load.*

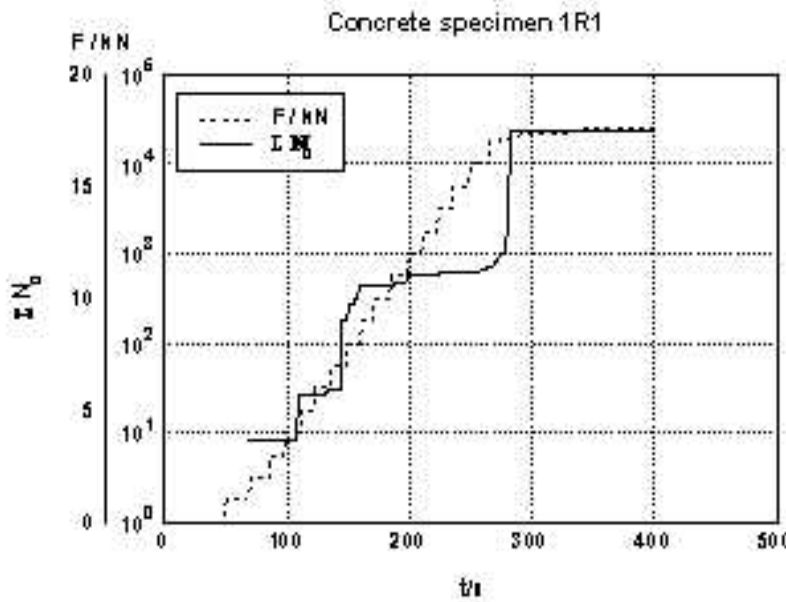


Fig. 5. Age 28 days, four points bending load.

## EXPERIMENTAL SET UP

Following AE systems were used in the cyclic tests:

- 6 channel PAC LOCAN 320 system with preamplifiers and filters. The four channels were arranged on planar localisation in the middle part of upper surface of the girder (in corners of area  $40 \times 60 \text{ cm}^2$ ). These were piezoelectric sensors with the resonance frequency of 225 kHz. The fifth channel with a broadband (from 100 to 1000 kHz) sensor and the sixth one with a resonance (225 kHz) sensor were placed at the bottom of the steel frame in the lower parts of the crossbeam.
- the notebook CARRY 6500 with an extension box containing 3 measuring cards for monitoring and sampling AE signals and collecting loading information.

## RESULTS

The measuring of ultimate tensile capacity of the model crossbeam was achieved with loading graded in % from theoretically computed ultimate load-carrying capacity. It is at 30, 60, 90, 100, 150 and 200 %. Simultaneously, the start and development of cracks were measured. The measurement results are shown in Fig. 6 to Fig. 11. The solid line in these graphs presents the cumulative AE, and the dot-and-dash line gives the level of force.

*Fig. 6:* The model was first step-by-step loaded to 20, 40 and 60 kN. Already from 40 kN, there are indicated structural disturbances, which were visually checked and drawn in after each stop of loading.

*Fig. 7:* The holds were removed and model was permanently loaded by dead weight (about 19.3 kN). Then, it was further super-loaded by a press to 60.8 kN. Recorded fall in tension load was caused by a defect of hydraulic pumps.

*Fig. 8:* In this period, the measurement model was subjected to 20 load cycles from 17.8 to 80.9 kN. In figure, it is evident that Kaiser phenomenon disappears in the initial three cycles.

*Fig. 9:* The model was put through variable loading in the remaining 80 cycles with the force range being the same as the previous experiment (below). The loading characteristic was deleted from graph to better show results.

*Fig. 10:* In this test period, the model was loaded step by step from 82 kN to 141.5 kN and then to 168 kN. There was model evaluation, visually recorded new cracks and then it was examined radiographically at the surroundings of selected shear connectors. The crossbeam loading continued until 252 kN; it is 1.5 times the theoretical ultimate load-carrying capacity. In this moment, the sample showed a deflection of 32 mm. The next load step was not applied by reason of double defects of the pump.

*Fig. 11:* In this last cycle, the model was loaded to the previous maximum value of 252 kN. After this, load was raised step by step to 275 kN. Shortly after reaching this value, the general collapse of the steel-concrete girder occurred; namely, first, local crushing of the lower left parts of pressured flange and followed by the local warp of the right parts of pressure flange. Very fast fall of force followed and experiment was finished.

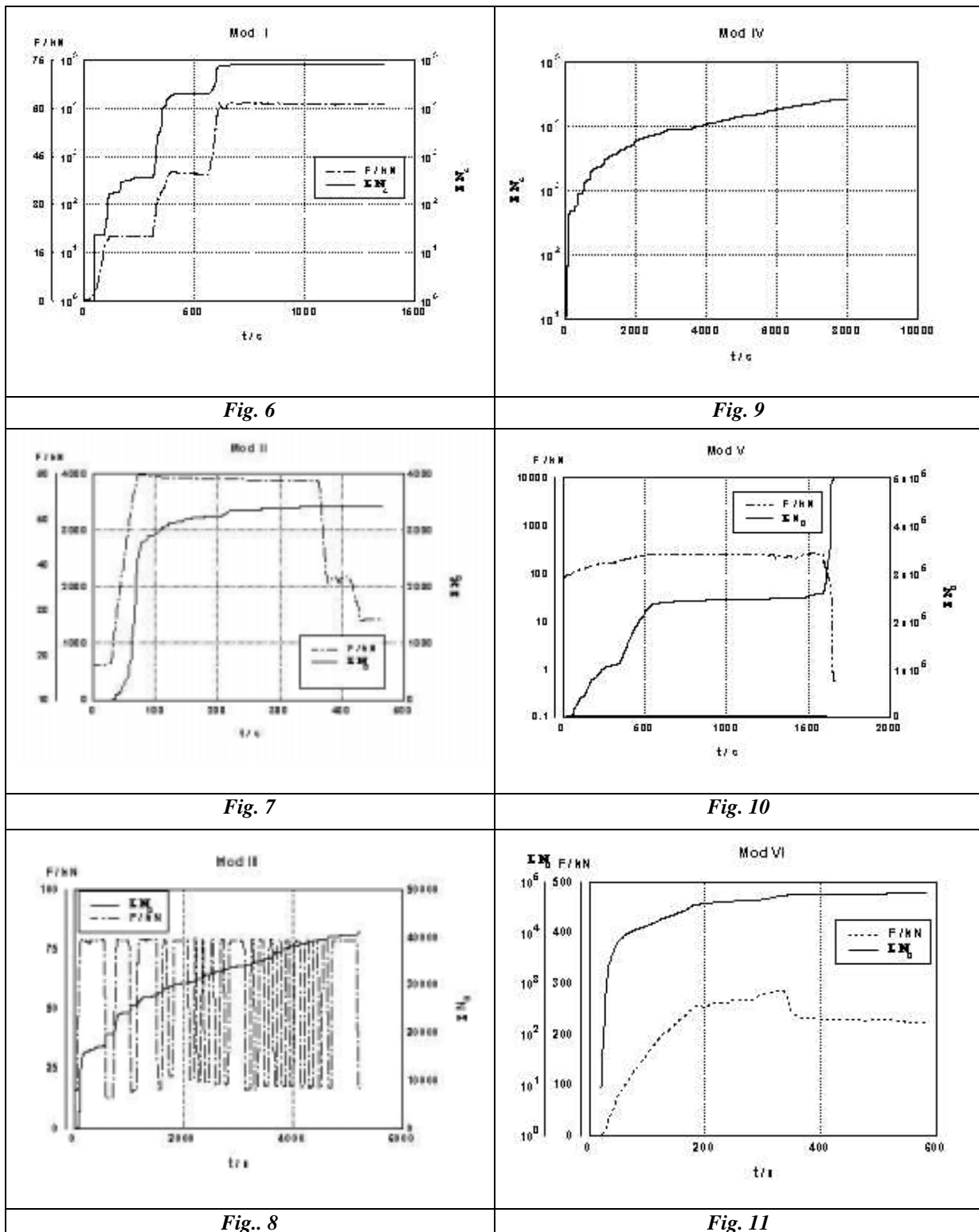
## CONCLUSION

The AE measurement demonstrates its extreme sensitivity to the start and successive development of bend and shear cracks in tested concrete specimens and the whole steel-concrete construction. AE signals contain information to enable the precise determination of cracks and their subsequent activities that affect the qualities of the tested structure. The loss of Kaiser phenomenon indicates accurately the moment of tested matters passing from the elastic to plastic material status. Here, AE signals have especially high amplitudes (over 70 dB).

This research has been conducted by CEZ J22/98 No.~261100007 and GACR 103/97/P140.

## REFERENCES

- [1] Strasky, J., Svadbik, P., Schmid, P.: Experimental Verifying of Reliability Coupled Steel Concrete Girder with Monolithic Crossbeam, CV/69/98, October, 1999, pp. 53.



# **WAVEFORM BASED ANALYSIS TECHNIQUES FOR THE RELIABLE ACOUSTIC EMISSION TESTING OF COMPOSITE STRUCTURES**

**M. SURGEON, C. BUELENS, M. WEVERS\*, and P. DE MEESTER\***  
**METALogic n.v., Heverlee, Belgium, \*KU Leuven, Leuven, Belgium**

## **ABSTRACT**

*Although the acoustic emission (AE) technique has now aged for more than thirty years, the analysis techniques that are used in practical field testing are still very basic. The last decade has seen a growing awareness of the dangers involved in reducing an AE signal to its basic parameters and thus eliminating most of the information. This awareness has resulted in the development of practical AE analysis techniques that are based on the complete waveform rather than on the parameters. These techniques also make use of a growing insight into the theoretical principles of AE signal generation and propagation, which is evidenced by e.g. the use of the classical plate wave theory. This paper will lay out the principles of the classical plate wave theory and will demonstrate how this simple theory combined with a complete waveform acquisition can lead to a more reliable testing of composite materials.*

## **INTRODUCTION**

The acoustic emission technique (AE) has for many years been considered as the prime candidate for structural health and damage monitoring in loaded structures. It offers the user a number of inherent advantages, the main of which are its continuous and *in situ* monitoring capabilities and the possibility to examine the whole volume of a structure simultaneously with a limited number of sensors.

The increasing use of composite materials in loaded structures and their complex damage development has created a need for an efficient and reliable NDT technique that can be used during the service life of these materials. AE clearly has the potential to serve as a continuous damage detection technique for composites and during the past decades many studies have been undertaken to develop the technique to higher levels of performance. Three main types of data analysis have been extensively explored so far. That is, AE activity analysis (focussing on the amount of signals that are detected during a test), AE parameter analysis (studying evolutions in the basic signal parameters like amplitude, duration or energy) and AE frequency analysis (analyzing the frequency content of AE signals). Although many applications can be envisaged in all of the areas where composite materials are being used or could be used, it is surprising to see that the number of practical applications exploiting the AE technique has remained relatively limited. The main reasons for this are the limitations of the analysis techniques discussed above, which make it difficult to extend laboratory results to industrial structures. Commonly encountered problems are the large amounts of gathered data, the difficult separation of noise from real damage signals, the material anisotropy, the large wave propagation paths, etc. Summarizing these observations, one can state that AE has remained mainly a qualitative technique and that its further acceptance and practical use require a more quantitative approach based on theoretical concepts, which can reliably take into account source phenomena and wave propagation effects.

Another attempt at providing a better theoretical background for AE testing is now known as modal acoustic emission (MAE) or waveform based acoustic emission. MAE starts from the observation that AE waves are mechanical in nature and should therefore be treated as such. Following the general

theory of wave propagation in solids, AE waves should propagate through a structure in a variety of modes. The separation of these modes at the sensor could make it possible to extract information about the source event that produced the wave. Additionally, wave propagation theory offers theoretical tools to study the influence of attenuation and dispersion.

This paper will first provide a simple, yet practical, theoretical background for AE signal analysis. It will then be demonstrated how this theory can be used to make composite testing more reliable by demonstrating, on a laboratory scale, how signal recognition and discrimination, noise elimination and source location can be performed in a more consistent manner.

## PLATE WAVE THEORY

A comprehensive overview of wave propagation theory as it applies to solid materials can be found in reference 1. Solutions to wave propagation problems in structures of arbitrary geometry can be obtained by using the three-dimensional equations of the elasticity theory. In the case of plate-like structures, however, a simpler theory can be used, i.e. classical plate wave theory. According to this theory, mechanical waves propagate through plate-like structures in three modes: the extensional mode (particle displacement in the plane of the plate and in the direction of wave propagation), the flexural mode (particle displacement perpendicular to the plane of the plate) and the shear mode (particle displacement in the plane of the plate and perpendicular to the direction of wave propagation). MAE has up to now made extensive use of the extensional and the flexural mode.

Based on the classical plate wave theory, the velocities of propagation of both modes can be calculated. Plate wave theory predicts a non-dispersion extensional mode: all frequency components of this mode propagate at the same velocity. Although practical results show that this is a reasonable approximation, it will not be satisfied completely. An analysis of the extensional mode based on higher order theories shows that the extensional mode exhibits limited dispersion behavior in which the velocity of propagation decreases with increasing frequency. For the flexural mode, plate wave theory predicts dispersion behavior in which the velocity increases with increasing frequency. A more detailed overview of classic plate wave theory and the way it has been applied in AE testing can be found in references 2-6.

## MATERIAL AND EXPERIMENTAL TECHNIQUES

All tests performed in this study made use of a carbon/epoxy composite material, which was produced in three different 8 ply cross-ply lay-ups:  $[0, 90_3]_s$ ,  $[0_2, 90_2]_s$  and  $[0_3, 90]_s$ . Tensile samples were used having a length of 150 mm, a width of 12 mm and a thickness of 1 mm. Tensile tests were performed on the MTS 810 loading frame. All tests were monitored by attaching two broadband AE sensors (Digital Wave Corp., B1025) to the specimens. The AE signals captured by these sensors were fed into a Fracture Wave Detector (Digital Wave Corporation) system.

## RESULTS

### Wave mode recognition

Figure 1 shows a signal that was generated by transverse matrix cracking in a  $[0, 90_3]_s$  laminate. The figure shows both the time and frequency domain of the signal. As is indicated on the time domain graph, the signal can generally be divided in two zones. The wave package that arrives first at the sensor shows a behavior in which the period of the subsequent cycles decreases with increasing time. The

frequency content of this mode increases with increasing time which also means that the lower frequency components arrived first at the sensor and propagated at the higher velocities. As was discussed before, this dispersion behavior is typical for the extensional mode. The wave package that arrives at approximately 40  $\mu$ s exhibits a behavior, in which the period of the subsequent cycles increases with increasing time. The frequency content of this mode decreases with increasing time and thus the higher frequency components arrived first at the sensor and propagated at the higher velocities. This dispersion behavior is typical for the flexural mode.

Both plate wave modes can be recognized in this signal. Generally, the extensional mode propagates at a higher velocity than the flexural mode and exhibits a higher frequency content. As is indicated on the frequency domain graph, the range between 400 and 800 kHz corresponds to the extensional mode and the range between 0 and 200 kHz to the flexural mode.

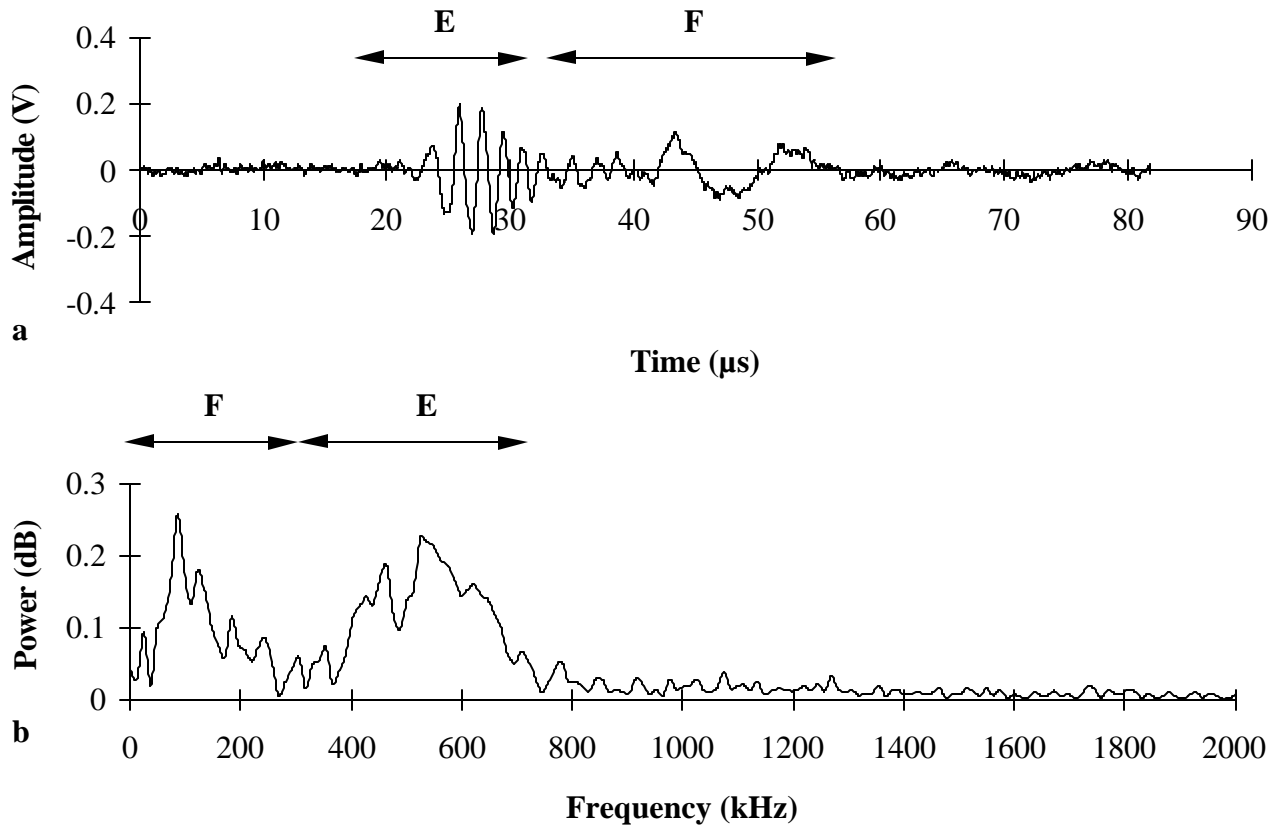


**Fig. 1: Matrix crack signal generated in a [0, 90]<sub>L</sub> sample: a) time domain, b) frequency domain  
(E: extensional mode, F: flexural mode)**

The wave package that arrives at approximately 40  $\mu$ s exhibits a behavior in which the period of the subsequent cycles increases with increasing time. The frequency content of this mode decreases with increasing time and thus the higher frequency components arrived first at the sensor and propagated at the higher velocities. This dispersion behavior is typical for the flexural mode.

Both plate wave modes can be recognized in this signal. Generally, the extensional mode propagates at a higher velocity than the flexural mode and exhibits a higher frequency content. As is indicated on the frequency domain graph, the range between 400 and 800 kHz corresponds to the extensional mode and the range between 0 and 200 kHz to the flexural mode.

## Discrimination between damage phenomena

The two main damage phenomena that are active during tensile testing of a cross-ply composite laminate are transverse matrix cracking at the early stages of testing and fiber fracture during the later stages of testing. An example of a matrix crack signal as it was generated in the [0, 90<sub>3</sub>]<sub>s</sub> lay-up was given in Fig. 1. Further investigation of the matrix crack AE signals revealed that the frequency content of these signals increased as the 90-ply thickness decreased.

Figure 2 shows a signal that was attributed to fiber fracture, due to the load level at which it appeared. The signal exhibits a dominant extensional mode and its main feature is its higher frequency content as compared to the matrix crack signal. This is reflected in the frequency domain: the signal exhibits large frequency components above 1000 kHz. This is in contrast with the matrix crack signal (see Fig. 1) in which no significant content could be observed above 1000 kHz. It thus seems feasible to base discrimination between different damage phenomena on the properties of the plate wave modes.

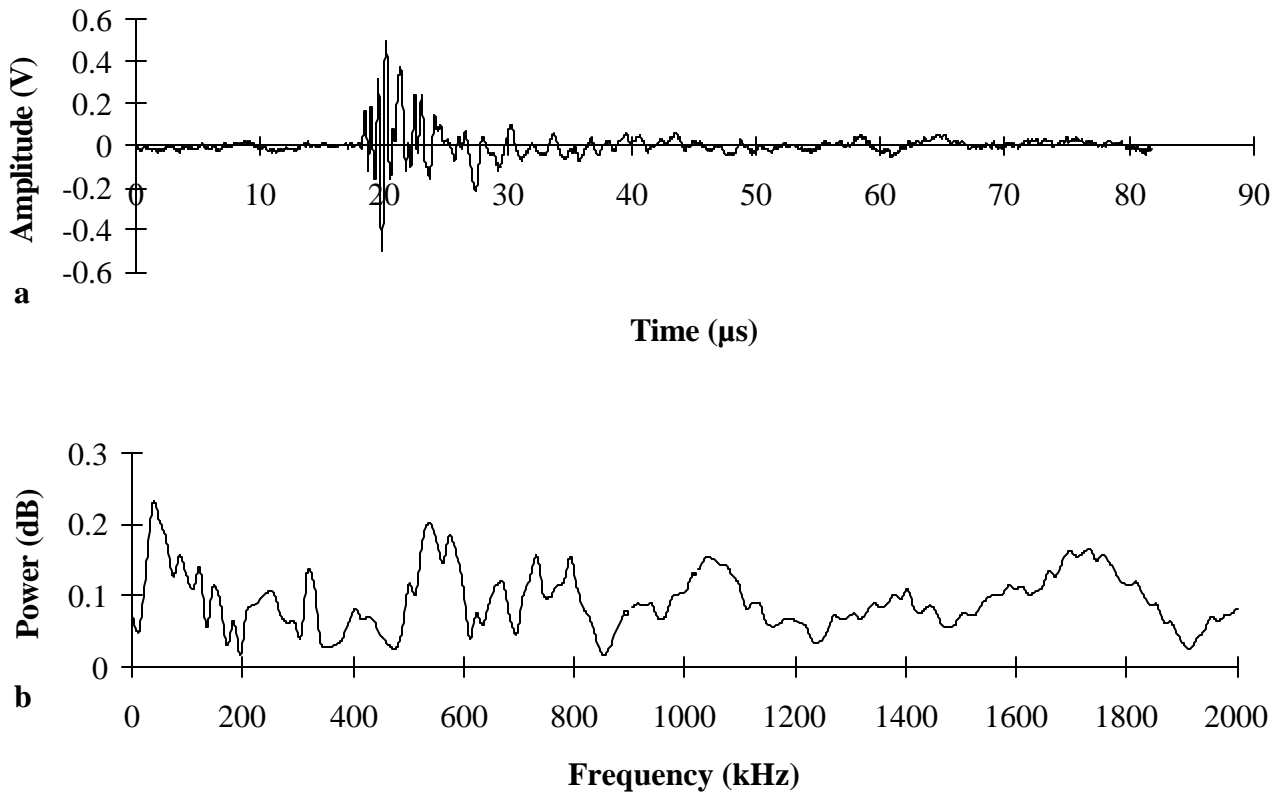


*Fig. 2: Fiber fracture signal generated in a [0, 90<sub>3</sub>]<sub>s</sub> sample: a) time domain, b) frequency domain*

## Noise elimination

One of the main problems preventing the widespread use of AE in practical applications is the elimination of noise signals from the data set. Based on the classic parameter based analysis procedures, this elimination has proven to be very difficult. As will be shown here, noise signals can be eliminated in a more consistent manner based on the complete waveform and the modal properties. The main noise phenomena that are active during laboratory type tensile tests are EMI (electromagnetic interference) and grip noise. Figure 3 shows an example of an EMI signal, measured by two sensors. The

shape of these waves is quite different from the ones shown above. Both signals are detected at exactly the same time. Additionally, the signals are very high frequent in nature and do no exhibit plate wave characteristics or propagation effects. It should be noted here that a traditional AE analysis would have treated this signal as a signal with amplitude comparable to the one of the real damage signals, a short duration and a high number of counts. Reducing the wave to these parameters would have made it very difficult to eliminate this noise type.

Figure 4 shows an example of a grip noise signal. A clear signal was only observed at sensor 2. The signal appears not have propagated to sensor 1, which suggests that it originated outside the sensor region, at the sensor 2 side. The signal at sensor 2 does exhibit plate wave characteristics, but they are markedly different from the ones of the damage signals as the low frequency content is much higher. Both examples demonstrate how more consistent noise elimination should be based on the complete waveform and the modal properties of AE signals.

### Source location

AE does not only offer the user the possibility to determine when damage occurs and what type of damage is active, but it also makes it possible to obtain information about the spatial location of the damage. Based on the arrival time of an AE wave at a limited number of sensors, a source location can be calculated, if the velocity of propagation in the material under study and the position of the different sensors are known. The key element in a good and accurate location procedure is the determination of the arrival times of the AE wave at the different sensors. Arrival times are traditionally determined by using a fixed threshold value: the arrival time of a wave is the point where it first crosses the threshold. This procedure is prone to an error as it does not take into account the modal nature of the AE wave. Using a fixed threshold, one can never be sure which part of the wave first reaches the threshold. A good location implies that the arrival times are determined on a part of the wave that has traveled with the same velocity to all of the sensors.

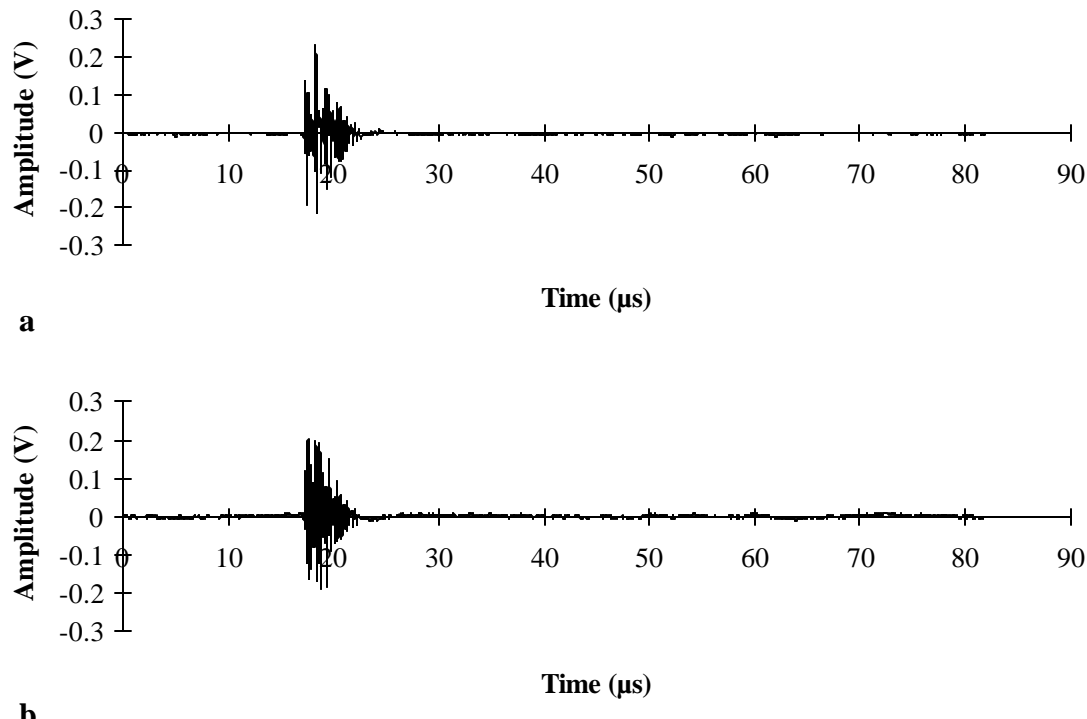


*Fig. 3: EMI noise signal: a) sensor 1, b) sensor 2.*

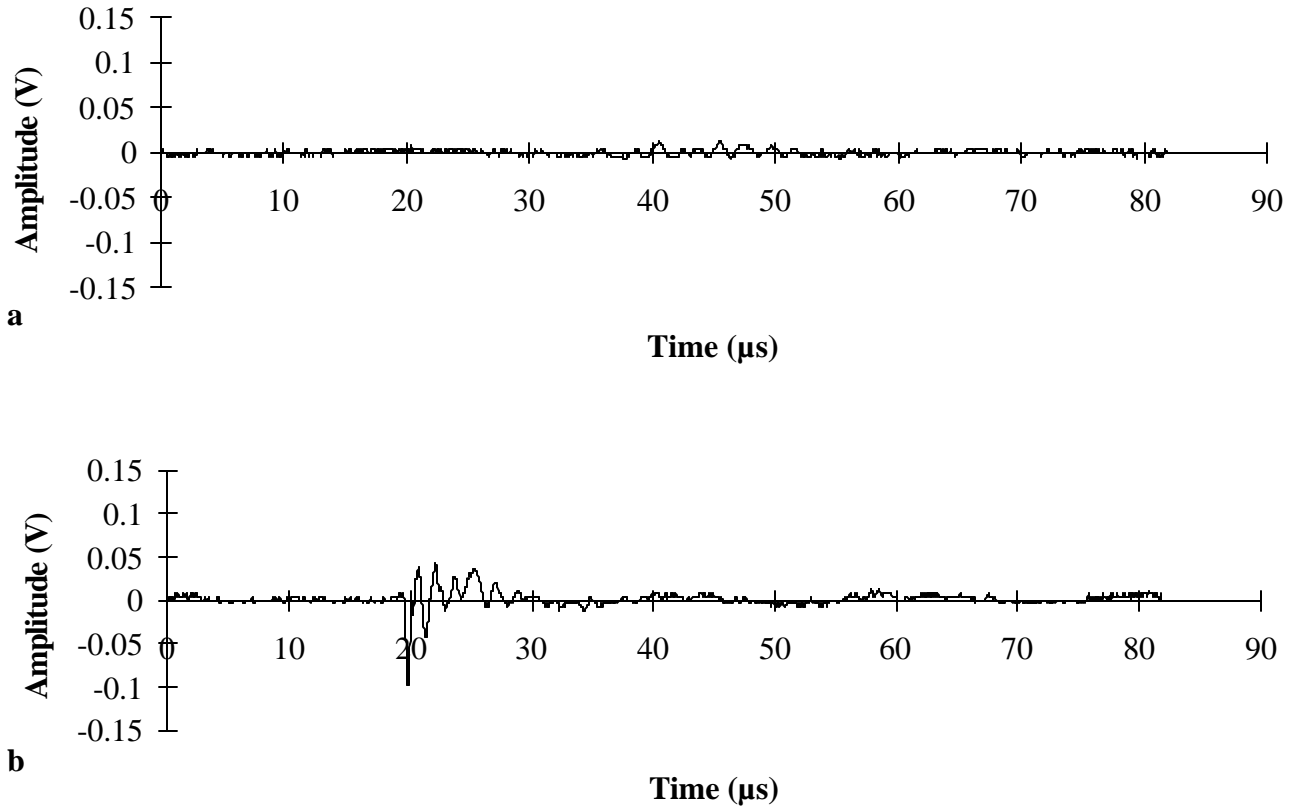


*Fig. 4: Grip noise signal: a) sensor 1, b) sensor 2*

A detailed discussion of this problem can be found in reference 8. During the tests performed in this work, two sensors were used and a linear location procedure was applied. Some signals were observed that could pose problems to the classic AE location procedure as for some threshold values, the arrival times are determined on the extensional mode at one sensor and on the flexural mode at the other sensor. Using a fixed wave velocity, this led to location errors up to 35 %. This demonstrates that for an accurate source location, the modal nature of AE waves should always be taken into account.

## CONCLUSION

Waveform based AE analysis techniques use simple theoretical concepts as a theoretical background to study AE signals generated in composite plates. Here, it was demonstrated how plate wave modes can be recognized in real damage AE signals. Furthermore, a number of examples showed how the technique can discriminate between different damage phenomena, how it can be used to consistently eliminate noise signals from the data set and how it can improve on the location procedures as they are offered by traditional AE systems.

On a more general note, it is believed that more reliable techniques are needed if AE is to further improve into a generally accepted testing technique. Potential users of the technique are still put off by the empirical nature of the classic analysis techniques, which lack a theoretical basis and a general validity. It is believed that the evolution into an analysis of the complete waveform and its properties can be a big step into the right direction.

## REFERENCES

- (1) Graff, K.F., *Wave motion in elastic solids*, Dover Publications, New York, 1975
- (2) Gorman, M.R., Plate wave acoustic emission, *J. Acoust. Soc. Am.*, 1991, **90**(1), 358-364
- (3) Gorman, M.R., Prosser, W.H., AE source orientation by plate wave analysis, *Journal of Acoustic Emission*, 1990, **9**(4), 283-288
- (4) Gorman, M.R., Ziola, S.M., Plate waves produced by transverse matrix cracking, *Ultrasonics*, 1991, **29**, 245-251
- (5) Prosser, W.H., Advanced AE techniques in composite materials research, *Journal of Acoustic Emission*, 1996, **14**(3-4), S1-S11
- (6) Ziola, S.M., Gorman, M.R., Source location in thin plates using cross-correlation, *J. Acoust. Soc. Am.*, 1991, **90**(5), 2551-2556

# **OPTICAL FIBRES FOR IN SITU MONITORING THE DAMAGE DEVELOPMENT IN COMPOSITES AND THE RELATION WITH ACOUSTIC EMISSION MEASUREMENTS**

**M. WEVERS, L. RIPPERT and S. VAN HUFFEL**  
Katholieke Universiteit Leuven, Leuven, Belgium

## **ABSTRACT**

*The complex damage development process in composite materials demands a system that could continuously monitor their damage state in particular structural applications. Fibre optic sensors embedded in the composite material could offer an alternative for the robust piezoelectric transducers used for acoustic emission (AE) monitoring. For simplicity and robustness reasons, intensity-modulated optical fibres were chosen to detect damage in CFRP composite laminates based on the microbending concept. Advanced signal processing techniques based on time-frequency analysis have been applied on the signals collected during loading of the CFRP composites. The short-time Fourier transform has been computed and noise reduction algorithms (adaptive filtering and spectral subtraction filtering) have also been used. The transient signals being detected can be correlated with AE signals, analysed with a modal AE system. The signals are attributed to the initiation of damage in the materials and thus the optical signal contains, besides the level of overall strain, information in the elastic energy released whenever damage is introduced in the host composite.*

## **INTRODUCTION**

The emergence of optical fibre communication technologies in the 1970's has enabled the development of embedded optical sensors for process condition monitoring and for smart materials/structures applications (1,2). We also initiated a study to incorporate optical fibres in carbon-fibre reinforced epoxy laminates in order to monitor the fatigue behaviour characterised by a gradual damage development. The method of embedding the optical fibres and their influence on the mechanical behaviour of the host material has already been evaluated for a number of laminates and the embedding positions have been optimised (3,4,5).

The present paper is focused on the signal processing of the optical fibre data, done in collaboration with the Department of Electrical Engineering. The signal processing has been done in order to find a relation with the internal strains in the composite produced on one hand by the external loading (stresses and temperature) and on the other hand by the internal damage development. Especially for the latter an attempt will be made to correlate the signals measured with the AE technique, in which we already have proven its competitiveness more than once (6,7) and the signals of the embedded optical fibres. With optical fibres embedded in composite materials and intelligent data processing of the optical fibre signals, one can integrate a NDT-system into this complex material, or derived component or structure, similar to the neural system in a human body.

The fibre optic sensors have several advantages compared to the electronically based sensors like piezo-ceramics such as light-weight, all passive configurations, low power utilisation, immunity to electromagnetic interference, high sensibility and bandwidth, compatibility with optical data transmission and processing, long lifetimes and low cost (as long as using silicon fibres). Disadvantages exist with reparability as long as optical

fibres have to be integrated into the material and placed according to major occurring stresses and strains to obtain reliable data.

## PRINCIPLE OF OPERATION

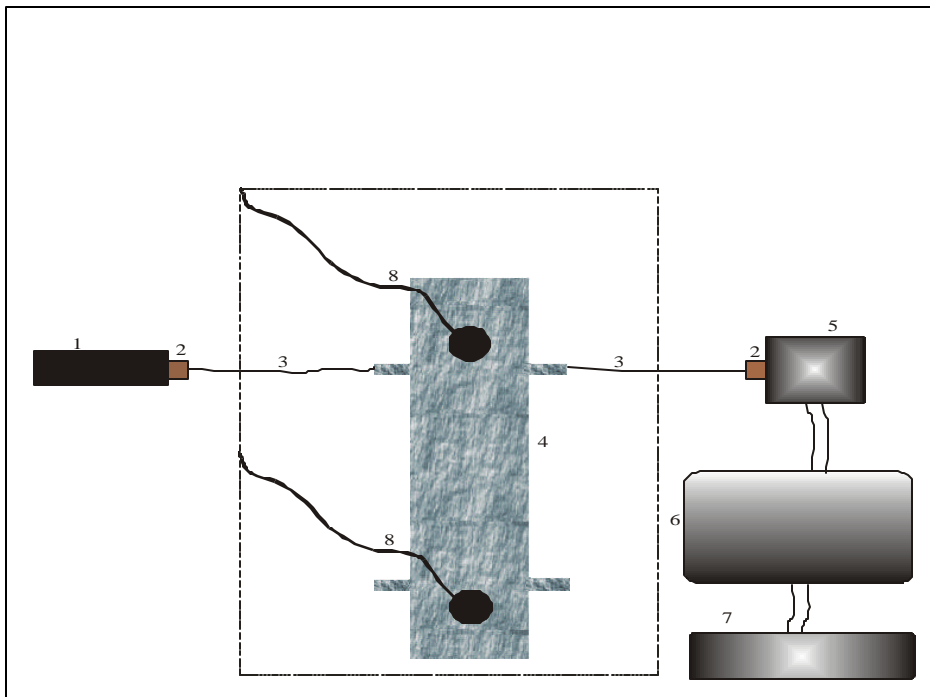
To detect damage, two kinds of optical sensors can be used: phase-modulated sensors (interferometers) and intensity-modulated sensors. The former is usually more sensitive but also very fragile. A sensing system, which is simple and robust enough for industrial use, is offered by intensity-modulated optical sensors. The intensity variations of the transmitted light are caused by a perturbing environment. If for instance the optical fibre is bent (8), small amounts of light are lost through the cladding because the condition of total reflection is violated. The amount of intensity loss depends on the amount of bending. The stress field in a composite material is influenced by the external loading and the internal damage in the material. This may cause the optical fibre to bend in the material so that a decrease in intensity of the transmitted light can be seen. Initiating and growing damage is associated with acoustic stress waves propagating in the material. When a wave encounters an optical fibre, this bends locally and so some light might also be lost. A high sampling rate (SR) can be used to detect those transient signals released by matrix cracking, delamination or fibre fracture phenomena. To reveal this information from the optical signals, signal analysis tools such as filtering, time analysis and time-frequency analysis is required.

## EXPERIMENTS

Our previous study addressed the choice of fibres, the embedding procedure and the influence of the optical fibres on the mechanical properties (monotonic tension, three and four point bending and tension fatigue) of different carbon-epoxy composite laminates. The next step was to evaluate the performance of the optical fibre NDT system.

*Fig. 1: The sensing system*

- 1 : Laser source
- 2 : Optical coupler
- 3 : Optical fiber
- 4 : Composite specimen
- 5 : Photodiode + amplifier
- 6 : Computer (oscilloscope card)
- 7 : Workstation
- 8 : AE sensor



Laminates were produced from a Vicotex 6376/35/137/T400 C/epoxy prepreg. The prepreg was cut and stacked into a  $(0_2^\circ, 90_4^\circ)_s$  lay-up. The optical fibre was embedded in the  $90^\circ$  direction in the middle plane of

the specimen. A polymeric bore tube was put around the optical fibre at its exit point from the composite specimen. It shrank around the fibre during the cure and so protected this weak point. The samples tested had the following dimensions: 150 mm length, 25 mm width and 1.2 mm thickness.

A He-Ne laser source was used to power the multi-mode optical fibre embedded in the carbon-fibre reinforced composite material. The output light intensity was collected by a photo-diode, and was sent to a computer via an oscilloscope card as seen in Fig. 1 of the sensing system.

The optical signal post-processing was done on a SUN workstation using MATLAB<sup>®</sup> software, in particular the signal processing toolbox. A program was written to filter the signal, to compute its STFT and to visualise the changes in its power spectrum over time (9). Additional tools were developed to extract damage related information from this time-frequency analysis.

An acoustic emission (AE) system was also used to monitor the damage development in this composite laminate: the Wave Explorer from Digital Wave Corp. This system is equipped with broadband sensors (Digital Wave B1025) with a nearly flat frequency response in the 50–3000 kHz frequency range. It uses the plate wave theory as a theoretical background and analyses the waves according to their mechanical nature, namely, extensional and flexural waves. It is called a modal AE (MAE) system (10,11). MAE allows a more convenient way to identify the kind of damage by looking at the frequency content of the acoustic waves produced. The presence (or absence) of extensional and flexural modes is the key to the damage mode characterisation. It has been proven to work in an efficient way for matrix cracking and fibre fracture (12). It also allows a clear recognition of noise grip and EMI.

On the oscilloscope card, three channels were used. One channel was used to collect the optical signal, another channel collected the optical signal filtered using a capacitor to get only the ac component amplified 11.5 times, and a third one to collect a trigger signal sent by the AE system each time an AE event is detected. The sampling rate (SR) was set to 10 kHz.

Tensile tests were performed on Instron 4505 universal testing machine with a 100 kN load cell. To prevent grip failure, aluminium end tabs were bonded to the specimens using a two-components Araldite 2011 epoxy glue. The displacement rate was 0.5 mm/min and a Labview program drove the tensile machine and the oscilloscope card.

## RESULTS AND DISCUSSION

Ten specimens were tested and at the beginning of each tensile test, pencil-lead break tests were performed for calibration purpose.

### Low pass filtering

The tensile load curve of one test is shown in Fig. 2. During the first 90 s, several pencil-lead break tests were performed to calibrate the AE system. Then, the loading was applied until the final fracture. After 261 s of test, there was a sudden decrease in the applied strain due to some damage near one of the aluminium tabs. Figure 3 shows the optical signal for the same test. A 4<sup>th</sup>-order low pass (LP) Butterworth filter was applied with a 5 Hz cut-off frequency. The curve has been reversed for better comparison with the preceding one. The optical

intensity starts to decrease when the loading starts to be applied. A low-frequency oscillation can be seen on the curve and is due to vibrations produced by the Instron machine. The final fracture is clearly seen and the strain release at 261 s also appears as a change of slope on the curve. It is thus shown that the optical signal contains information on the strain produced by external loading.

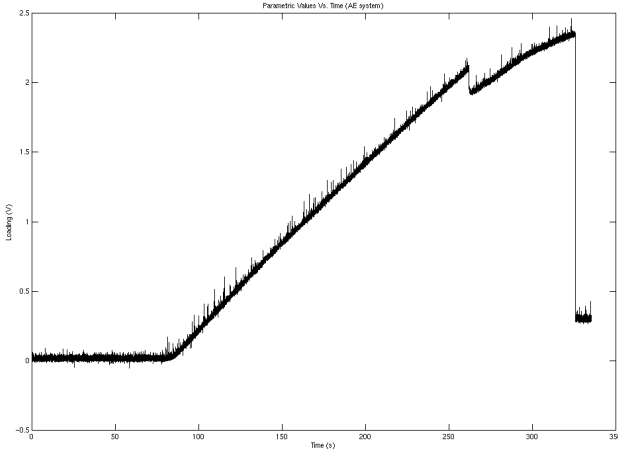


**Fig. 2:** The loading versus time curve.

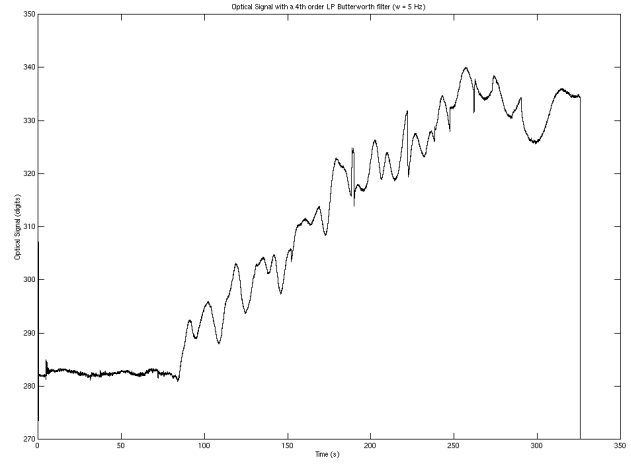


**Fig. 3:** The optical signal filtered with a low pass Butterworth filter.

Some sharp spikes are also hidden in the curve of Fig. 3. To see them more clearly, the same low pass filter was applied to the ac component of the optical signal (amplified 11.5 times). As can be seen on Fig. 4 the signal is constant except for some big spikes. The time instant at which those spikes appear is the same as the time of occurrence of some AE events. These AE events can be related to damage inside the material, so those spikes can also be related with the damage, which causes a sudden strain energy release in the material. By removing the 5 digits offset and taking the absolute value of this signal, a threshold can be set and damage detection is achieved.

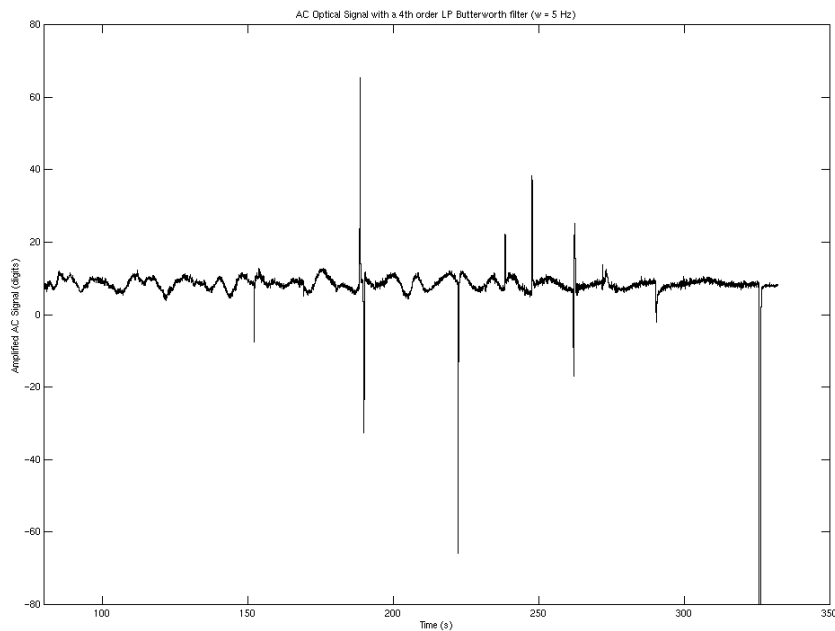


**Fig. 4:** The ac component of optical signal filtered with a low pass Butterworth filter.

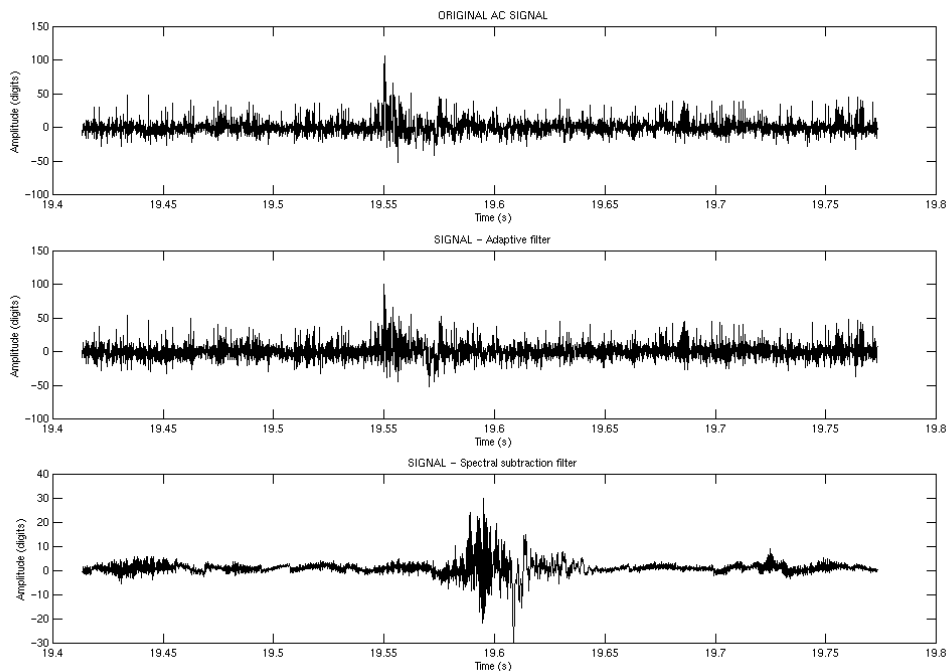
The main limitation is the sensitivity; the events detected by this method are only the most energetic ones. The less energetic events detected by AE cannot be seen on the optical signal or are smaller than the curve oscillations and can therefore not be detected by the threshold technique. Removing the polyimide coating from the optical fibre may increase the system sensitivity.

Most of the high-frequency components are filtered out with this low-pass filtering technique so the signal cannot be used for damage identification. Another drawback is that changes are less sharp and some delay may also appear. This method shows that damage detection is possible with intensity modulated optical sensors based on the microbending concept, but some more advanced signal analysis techniques are required to have information on the kind of damage so this low-pass filtering has to be replaced.

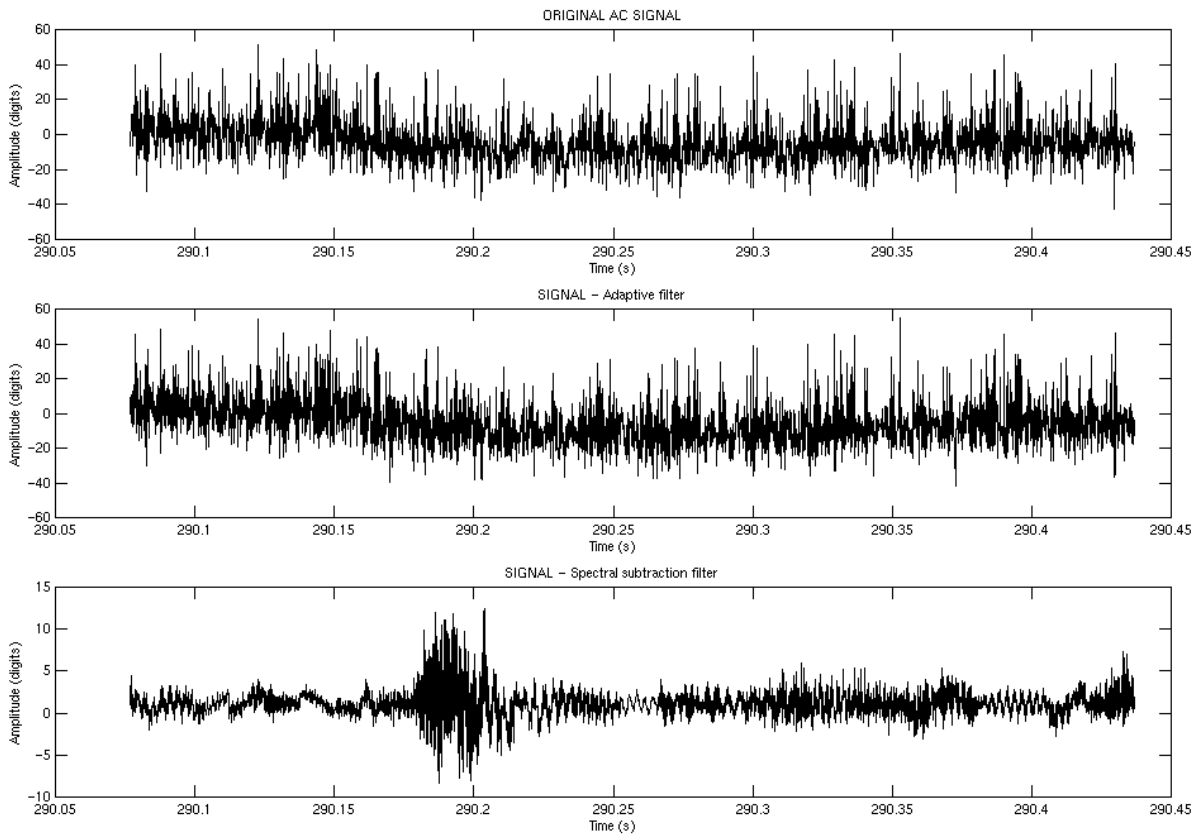
## Noise reduction

If one has to look for small effects on the optical signal the Signal to Noise Ratio (SNR) has to be increased. The biggest noise source is from the laser power supply (50 Hz and the harmonics from the net). An *adaptive filter* was used to remove this noise only up to 1 kHz (13) because this filter was computation time consuming. Subsequently, *spectral subtraction*, a filtering technique used in speech processing (14), was applied to see more clearly the expected ‘optical events’. This technique requires that the background noise environment remains locally stationary to the degree that its expected spectral magnitude value just prior to an expected event equals its expected value during the event. It is also assumed that significant noise reduction is possible by removing the effect of noise from the magnitude spectrum only.

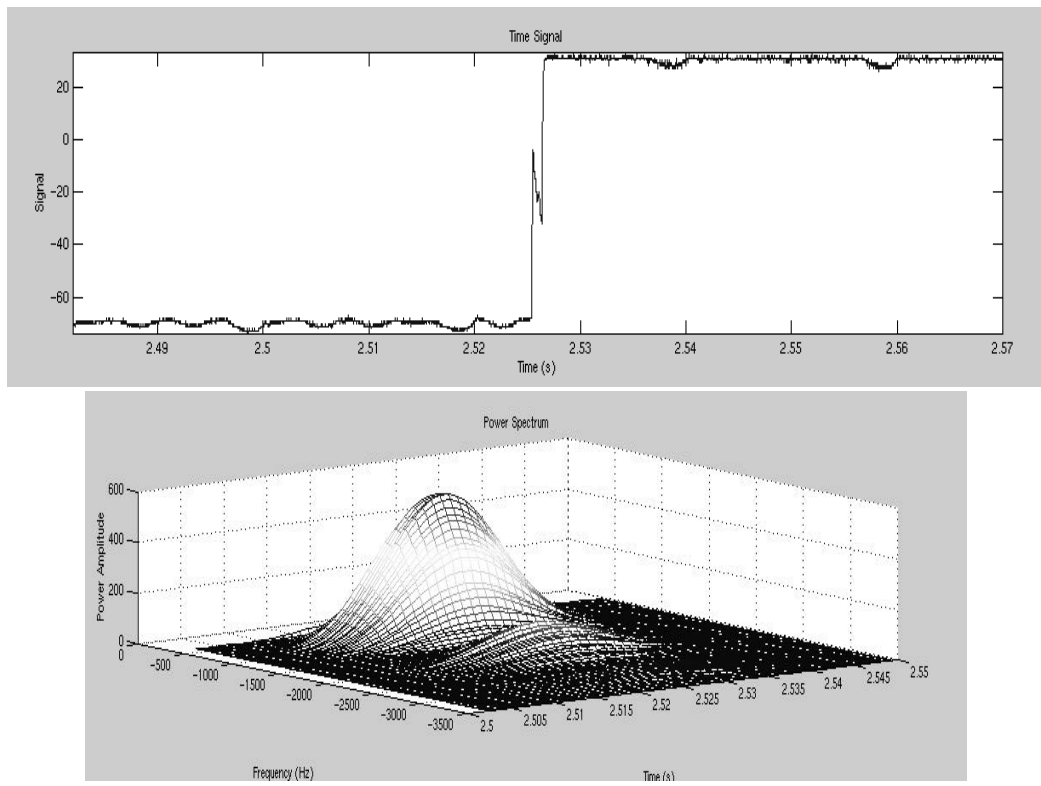
These techniques were applied to pencil lead break tests (Fig. 5) and on optical signals from real damage (as indicated by AE) during tensile tests (Fig. 6). They allow a good noise reduction without reshaping too much the signal.



**Fig. 5:** The original optical signal, the signal filtered with an adaptive filter and with the spectral subtraction method of a pencil lead break.



**Fig. 6:** The original optical signal, the signal filtered with an adaptive filter and with the spectral subtraction method of a real damage event.



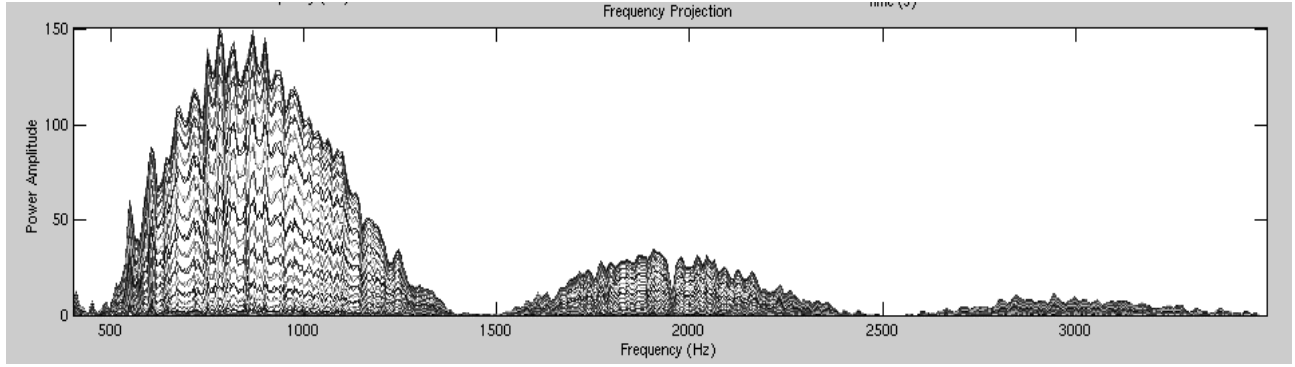


**Fig. 7:** Final fracture of a specimen in the time domain (top), its spectrogram (middle) and the frequency projection of the spectrogram (bottom).

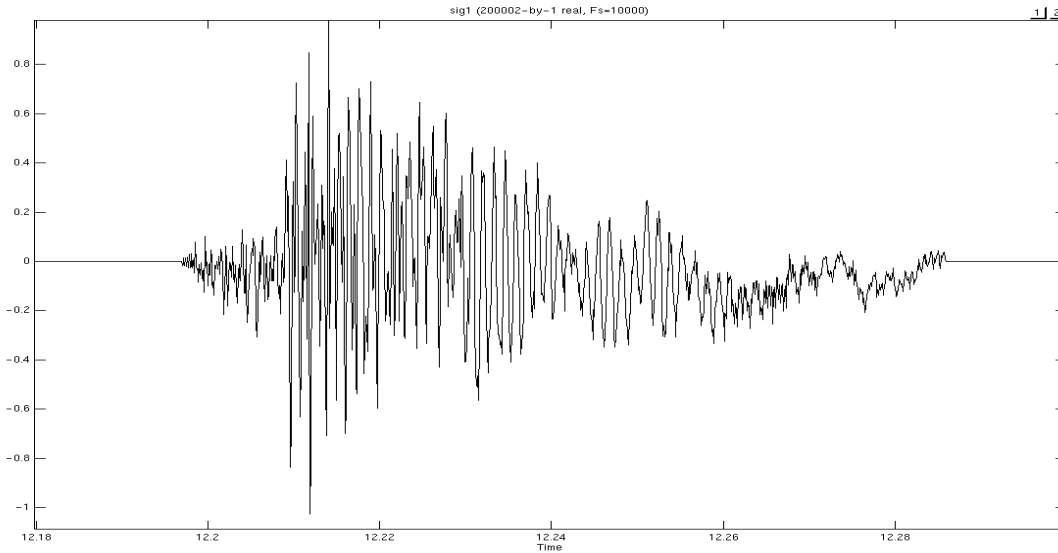


**Fig. 8:** The filtered optical signal of a pencil-lead break in the time domain.

### Time-frequency analysis: STFT

Since the expected signals were non-stationary (transient), their frequency content, visualised by the Fourier transform, varied in time. The short-time Fourier transform (STFT) can be used to visualise the frequency content of a signal over time (13). This so-called spectrogram is visualised in Fig. 7 (middle) for the 400–3500 Hz frequency range. This figure corresponds to the specimen final fracture event that can be seen in the time domain in the top curve. For better view and analysis, the frequency projection of the spectrogram can be computed (see bottom).

### Damage identification

The filtered optical signal corresponding to a pencil lead break was extracted and a time-frequency analysis (STFT) was performed. Both the AE time signal and the optical time signal (respectively seen in Figs. 8 and 9) show a small extensional component followed by a big flexural mode. This is coherent with what can be expected from a pencil lead break test done on the surface of the specimen. Waves produced by a pencil-lead break test are quite similar to those produced when damage occurs in a composite material.

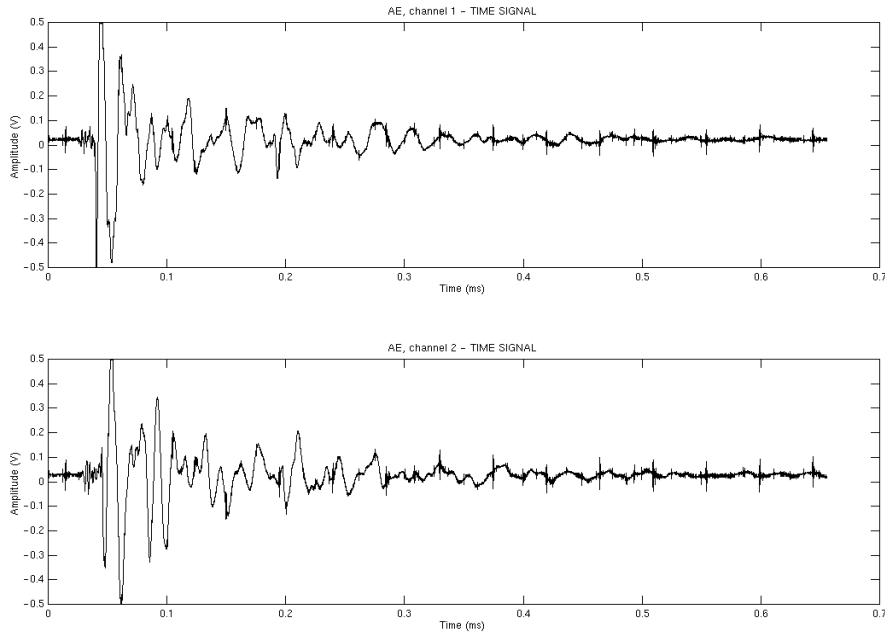


**Figure 9:** The AE signal in the time domain at two sensors typical for an in-plane lead break test.

Figures 10 and 11 show the ac optical signals corresponding to AE events recorded during the tensile test (middle and bottom). The time-frequency analysis clearly identifies special features in the signals, which can be attributed to matrix cracking or fibre fractures based on their time of occurrence.

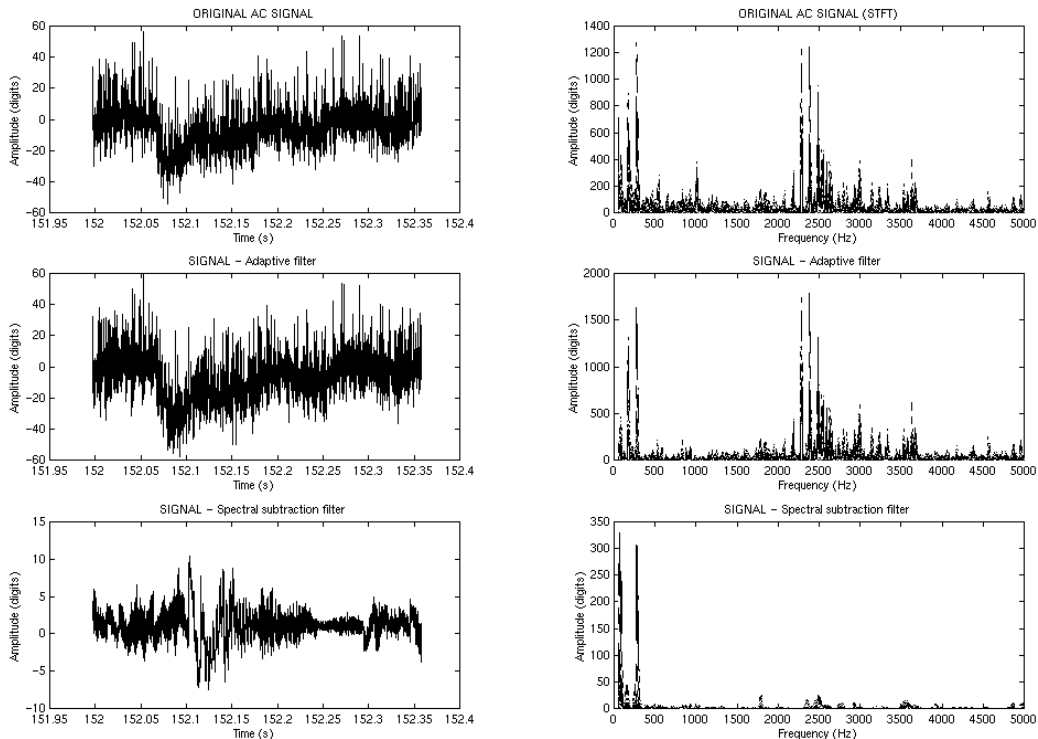


**Fig. 10:** The ac optical signal, the filtered signals (adaptive filter and spectral subtraction method) and the frequency spectrogram of an AE event detected in the middle of the tensile test.

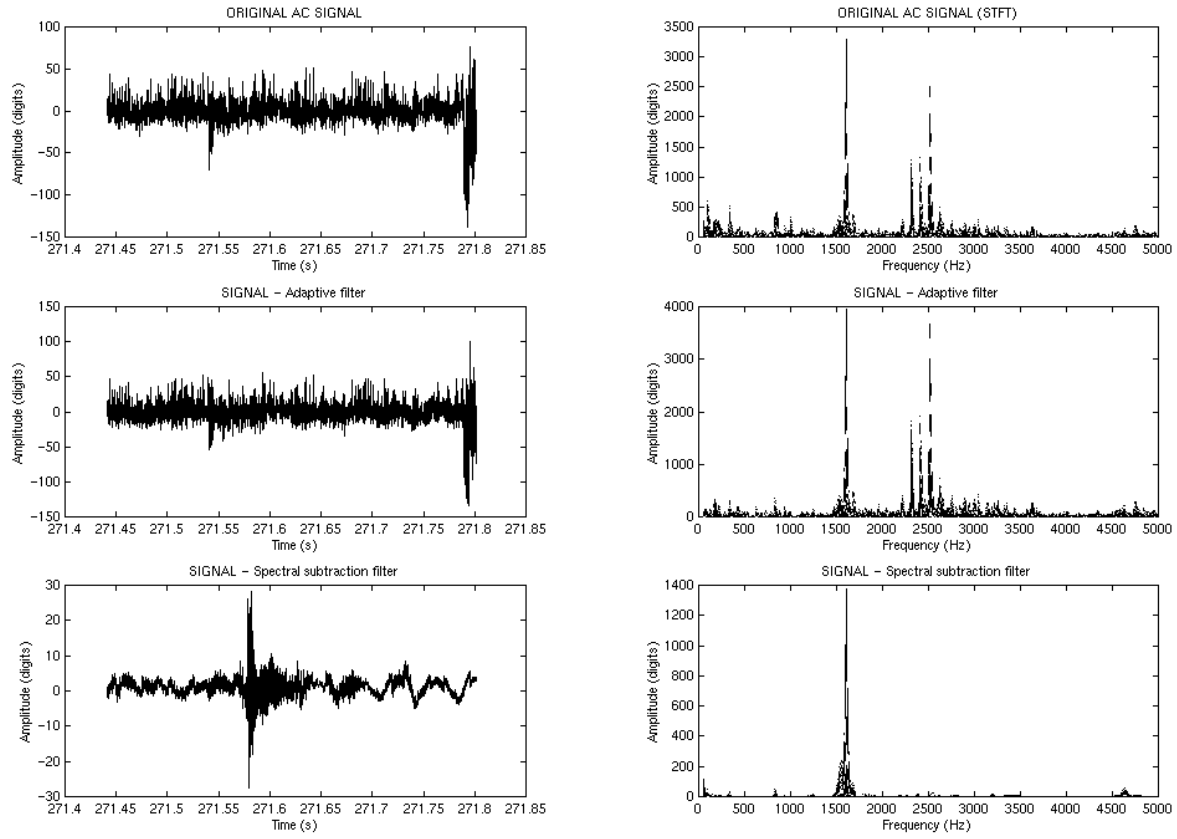


**Fig. 11:** The ac optical signal, the filtered signals (adaptive filter and spectral subtraction method) and the frequency spectrogram of an AE event detected at the end of the tensile test.

## CONCLUSION

It has been shown that an intensity modulated optical sensor based on the microbending concept can be used for continuous damage monitoring of a carbon-fibre reinforced laminate composite. The NDT system is simple and robust, but requires some advanced signal analysis tools like adaptive filtering, spectral subtraction filtering, and time-frequency analysis (STFT).

The intensity-modulated optical fibre sensor (microbending principle) can detect pencil-lead breaks, the overall strain in the composite and strain variations due to damage development during loading. The similarities between optical and MAE signals should permit damage identification. The damage location has not been studied so far, this may require to embed several optical fibres in the specimen.

## ACKNOWLEDGEMENTS

The authors would like to thank Ing. J. Vanhulst for his precious help with the data acquisition system, and K. Eneman for providing the code for the applied filtering techniques.

## REFERENCES

1. D. BUTTER, G.B. HOCKER, Applied Optics, **17**(18), (1978), 2867.
2. N.D. GLOSSOP and al., Optical fibre damage detection for an aircraft composite leading edge, Composites, **21**, (1990), 71-80.
3. SURGEON, M., WEVERS, M., Static and dynamic testing of a quasi-isotropic composite with embedded optical fibres, Composites Part A, **30**(4), (1999), 317-324.
4. SURGEON, M., WEVERS, M., Using optical fibre technology to develop a damage detection sensor for composite materials: preliminary research, Proc. the 7th ECNDT, Copenhagen, May 1998, Vol. 1, pp. 1048-1056.
5. SURGEON, M., WEVERS, M., Quantifying the damage state of a quasi-isotropic CFRP with embedded optical fibres during fatigue testing using acoustic emission and microfocus radiography, Proc. the 7th ECNDT, Copenhagen, May 1998, Vol. 1, pp. 193-200.
6. WEVERS, M., VERPOEST, I., DE MEESTER, P., Identification of fatigue failure modes in carbon fibre reinforced composites with the energy discriminating acoustic emission method, Journal of Acoustic Emission, **8**(1), 1989, S272-S276.
7. WEVERS, M., Listening to the sound of materials: acoustic emission for the analysis of material behaviour, NDE&E, **30**, 1997, 99-106.
8. BERTHOLD III, J. W., Historical review of microbend fiber-optic sensors, Journal of lightwave technology, **13**(7), 1995, 1193-1199.
9. S. VAN HUFFEL, J. CRAEMERS, B. LENARTS, H. DANIELS, G. NAULAERS, P. CASAER, Episodes of apnea and bradycardia in the preterm newborn: impact on cerebral oxygenation measured by near infrared spectrophotometry, Proc. EUROPTO Conf. on Photon Propagation in Tissues IV, Sweden, 1998, SPIE, Vol. 3566, pp. 112-123.
10. S. ZIOLA, I. SEARLE, Automated source identification using modal acoustic emission, Review of Progress in Quantitative Nondestructive Evaluation, 1997, Vol. 16A, pp. 413-419.
11. M.R. GORMAN, Progress in detecting transverse matrix cracking using modal acoustic emission, Review of Progress in Quantitative Nondestructive Evaluation, **17A**, 1998, 557-564.
12. SURGEON, M., WEVERS, M., Modal analysis of acoustic emission signals from CFRP laminates, NDT&E International, **32**, 1999, 311-322.
13. J.G. PROAKIS, D.G. MANOLAKIS, Digital signal processing: principles, algorithms, and applications, 3<sup>rd</sup> ed., Prentice Hall, Upper Saddle River, NJ, 1996.
14. S.F. BOLL, Suppression of acoustic noise in speech using spectral subtraction, IEEE Transactions on acoustics, speech, and signal processing, ASSP-**27**, N° 2, 1979.

# LAMB WAVE SOURCE LOCATION OF IMPACT ON ANISOTROPIC PLATES

H. YAMADA, Y. MIZUTANI, H. NISHINO, M. TAKEMOTO and K. ONO\*  
Aoyama Gakuin University, Tokyo, JAPAN, \*UCLA, Los Angeles, CA, USA.

## ABSTRACT

*This study reports the development of a new source location method using Lamb waves on anisotropic carbon-fiber reinforced plastic (CFRP) plates. We monitored Lamb waves produced by pencil-lead breaks and steel-ball impacts using four resonant-type AE transducers mounted on 300-mm square corners within 500-mm square plates and determined arrival time of 65 kHz A<sub>0</sub>-Lamb waves, extracted by using a wavelet transform. For square arrangement, source location was first narrowed into one of four quadrants by the first arrival to the nearest sensor. Next, the source location in the particular quadrant was determined by sequential iteration. Here, the measured arrival-time differences were matched with those computed by moving a virtual source position in selected steps. We developed an algorithm providing automatic determination of arrival times and coordinate computation. It takes less than one second for each source location identification. Orientation dependence of Lamb waves for the CFRPs are experimentally measured and included in the algorithm. Accuracy of the source location for a unidirectional-CFRP plate is better than 5.6 mm within the 300 x 300 mm square. The average error of 2.4 mm was obtained for a quasi-isotropic CFRP plate. Results for several other CFRPs will be reported.*

## INTRODUCTION

Accurate source location of an impact and fracture is an important engineering problem for the precise identification of a damaged area. The source location of acoustic emission (AE) signals is impractical for many structures of fiber reinforced plastics (FRPs) due to strong orientation and frequency dependence of wave velocities (anisotropy and dispersion) and large attenuation. The velocity anisotropy can be measured, and for samples of limited dimensions, we can achieve three-dimensional source locations within 1.0 mm of a microfracture source in unidirectional FRPs [1-3]. The source location in thin plate is reduced to a planar (two-dimensional) problem, but a difficulty arises due to the dispersive nature of the Lamb waves [4]. Strong orientation dependence of Lamb wave velocities poses another problem. Several recent studies [5-9] attempted to improve source location methods. For example, Kwon et al. [9] recently utilized wavelet and inverse-wavelet transform for locating lead-breaks on aluminum and cross-ply CFRP plates. They utilized the arrival-time differences with threshold crossing method of single frequency A<sub>0</sub>-component. This method improves the source location accuracy, but the anisotropy issue remains unresolved. We have developed a new method for the source location based on dispersive, anisotropic Lamb waves. Here, measured arrival-time differences are matched with those computed by moving a virtual source position in small steps. We report the algorithm for source location and source location accuracy of impact on CFRP plates.

## SOURCE LOCATION METHOD

The present source location method consists of the following steps; 1) Perform wavelet transform of detected waveforms, extracting the A<sub>0</sub>-mode component at a selected frequency. This frequency is chosen to be the major component of the observed signals and to best differentiate the desired wave mode from others. 2) Determine the arrival times of the detected waveforms. The arrival time is defined at the instant when the wavelet coefficient reaches 20% of the peak value. (The position of the peak

value, or peak-arrival time, can also be used.) 3) Select a zone. Utilizing the sequence of the arrival times, the source location is confined to a zone; e.g., one of the four quadrants for a square four-transducer arrangement. 4) Determine the source location by sequentially minimizing the differences of the measured arrival times and the arrival time differences computed by moving a virtual source position in the quadrant determined in the previous step. The position is moved by a preset amount (typically 10 to 20 mm) in the X- and Y-directions. When a minimum is found, the preset amount is halved and a minimum is searched again in the immediate neighborhood. This is repeated several times until a certain level of accuracy is achieved. 5) In the calculation of step 4, experimentally measured, anisotropic group velocity of  $A_0$ -mode Lamb waves is used. The velocity is frequency dependent and the values must correspond to those of the selected frequency.

## MATERIALS AND VELOCITY PROFILES

We used in experiment three types of carbon-fiber reinforced plastic (CFRP) plates of 500 mm square. One is 24-ply unidirectional (UD-)CFRP, where the X-direction refers to the fiber direction of UD-CFRP. The second plate is 32-ply and quasi-isotropic ( $0^\circ_4/45^\circ_4/90^\circ_4/-45^\circ_4$ s) and the X-direction is along the  $0^\circ$  top/bottom lamina fibers. The third type is cross-ply CFRPs ( $(0^\circ_n/90^\circ_n)$ s,  $n=4, 6, 8$ ) of various thickness (2.0, 3.0, 4.0 mm). We measured the orientation dependence of  $A_0$ -Lamb waves, produced by pencil-lead breaks. The waves were detected by two transducers (PAC, type PICO) located at 40 and 90 mm along the angle  $\theta$  (measured from the  $0^\circ$  fiber). Examples of detected waveforms and their wavelet coefficients at 65 kHz, in the direction of  $\theta = 0^\circ$  (fiber direction),  $30^\circ$  and  $90^\circ$  for UD-CFRP, are shown in Fig. 1.

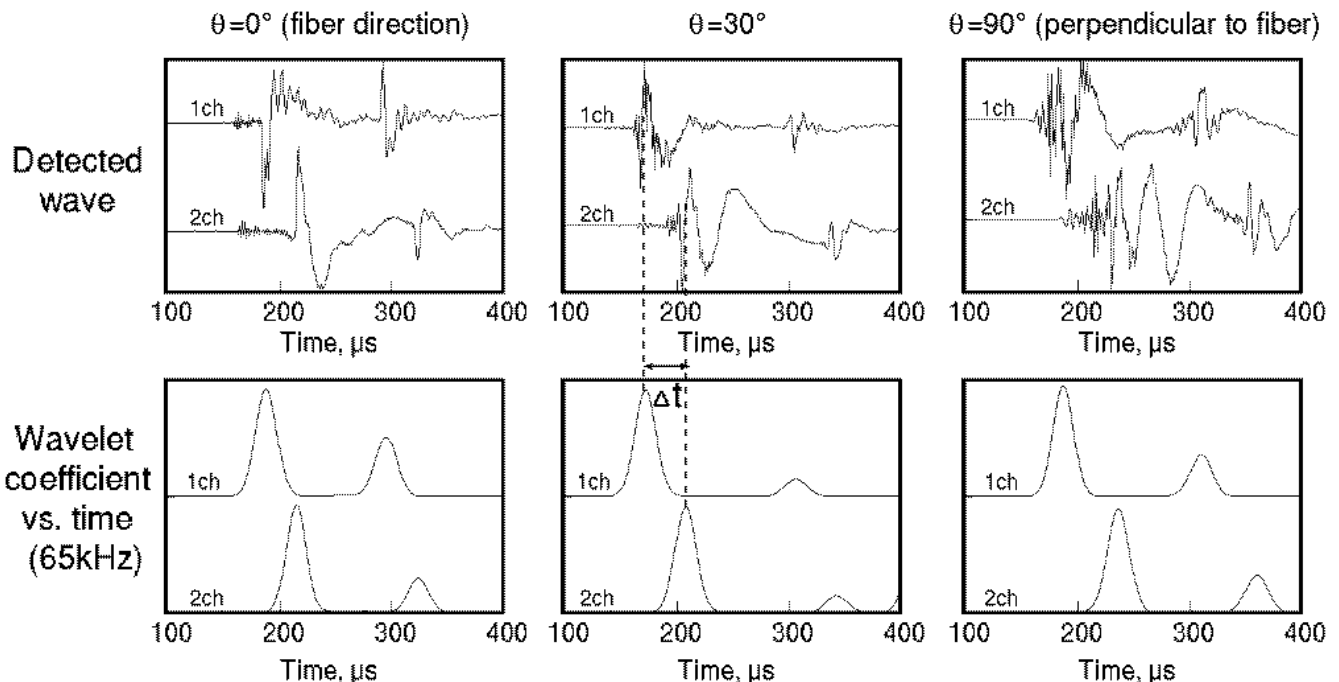


**Fig. 1 Examples of Lamb waves and their 65 kHz components in UD-CFRP plate as a function of the propagation direction  $\mathbf{q}$**

The wavelet coefficients were extracted by a wavelet transform with Gabor function as the mother wavelet. Velocities were measured by dividing the inter-transducer distance (50 mm) by the first-peak arrival time differences  $\Delta t$  of 65 kHz  $A_0$ -Lamb. Orientation dependence of 65 kHz  $A_0$ -Lamb velocities for UD-, quasi-isotropic and cross-ply (thickness=2.0 mm) CFRP are shown in Fig. 2. Measured data was approximated by a 6-th order polynomial equation (solid line). Velocity anisotropy of the quasi-

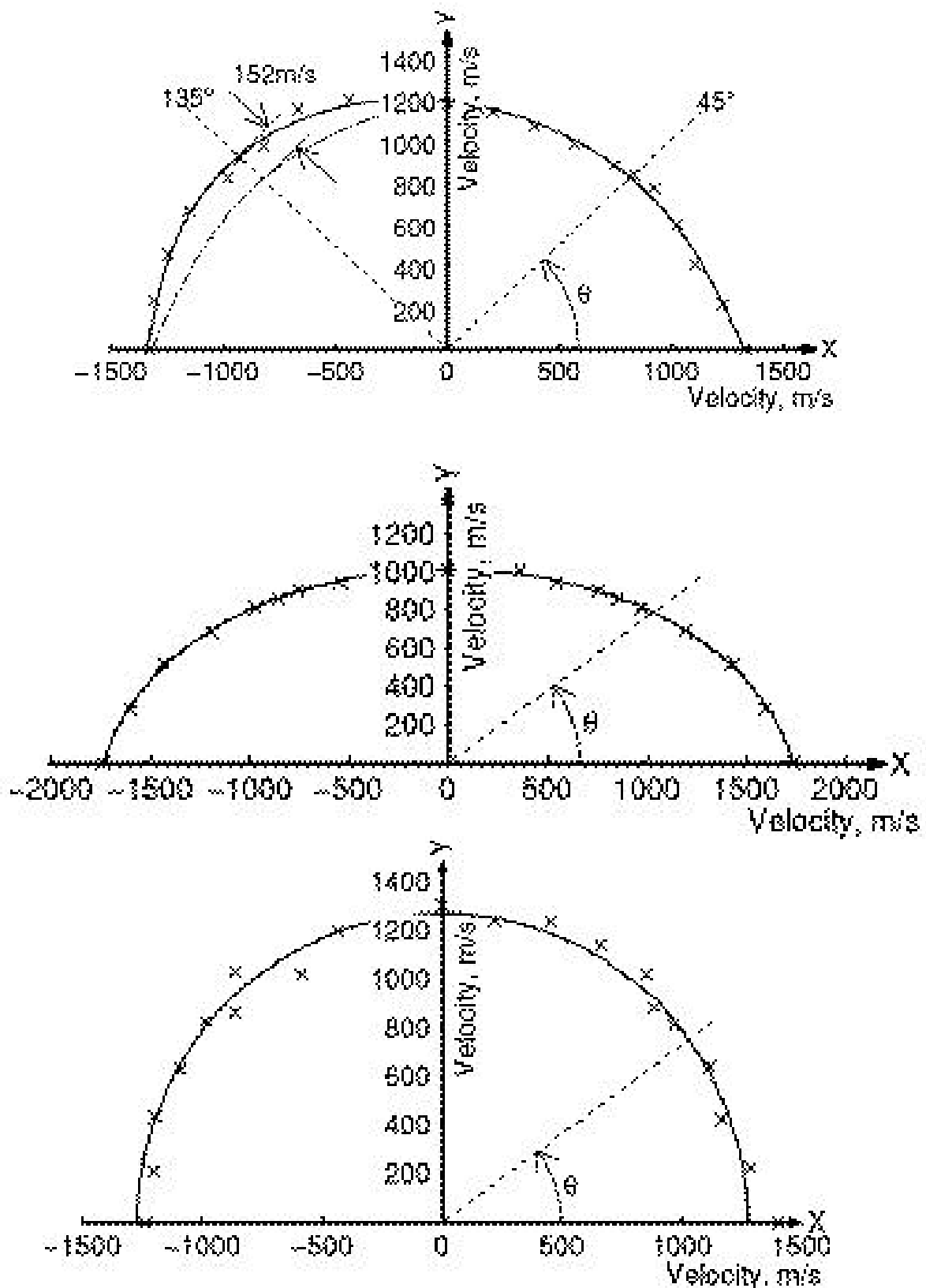
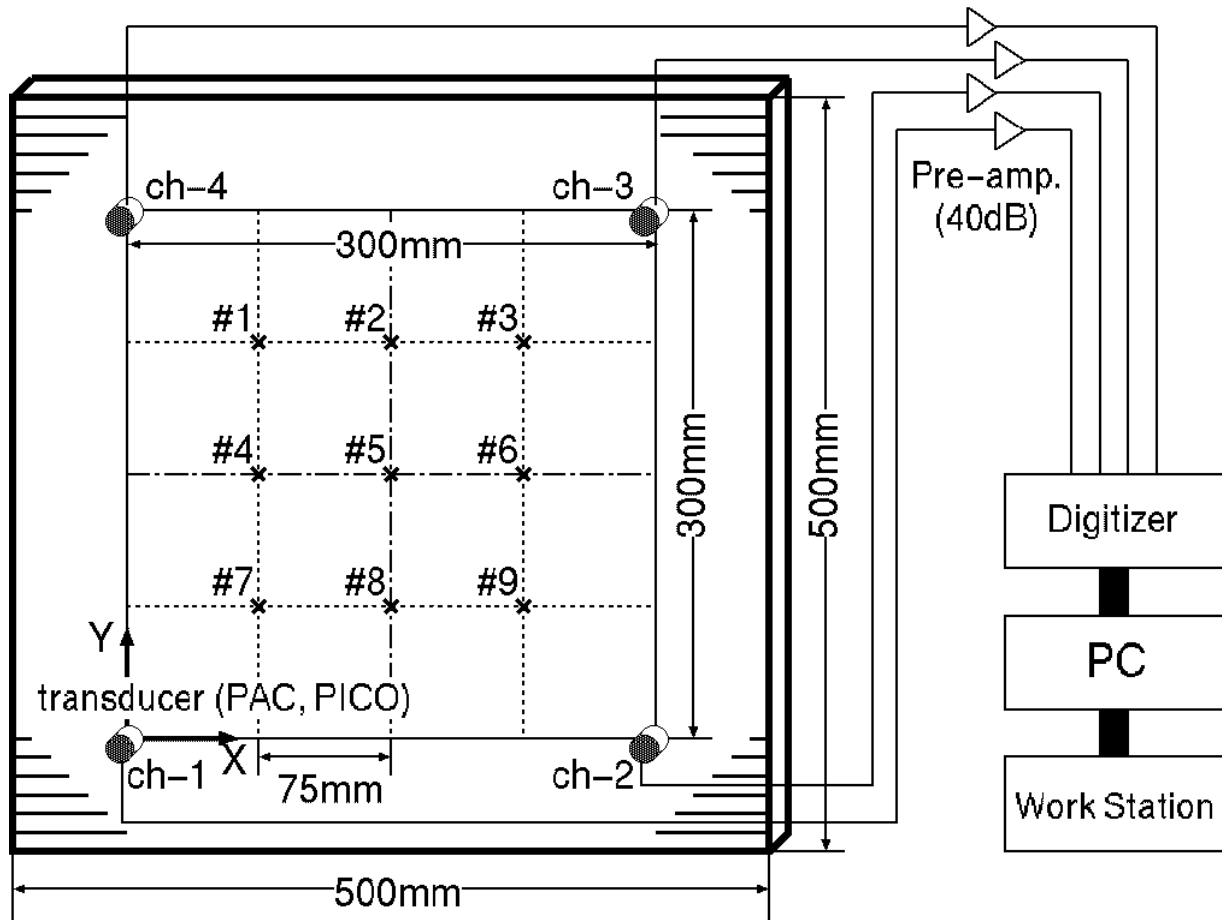


Fig.2 Orientation dependence of 65 kHz  $A_0$ -Lamb velocities in  $(0^\circ/45^\circ/90^\circ/-45^\circ)_s$  CFRP plate (top), UD-CFRP plate (the center), and cross-ply CFRP of 2.0mm thickness (bottom).

isotropic plate is small, or 6 %, whereas a strong velocity anisotropy exists for the UD-CFRP with the ratio of maximum to minimum velocities of 1.7. It is also noted that the velocity variation for the quasi-isotropic plate is asymmetric to the Y-axis. That is, the velocity at  $\theta = 135^\circ$  (1312 m/s) is faster by 152 m/s than that (1160 m/s) at  $45^\circ$  probably due to the eight -45° plies at mid-thickness.

## SOURCE LOCATION

Figure 3 shows the schematic illustration of source location method. Source location experiment used four AE transducers (PAC, type PICO; 4.0 mm diameter; nominal resonant frequency, 0.45 MHz). These were mounted on the corners of a 300 mm square on 500 mm square CFRP plates. The origin of the coordinate is set at the channel 1 transducer. Lamb waves were produced by simulated impacts (pencil-lead break and steel-ball drops). Outputs of the transducers were amplified 40 dB and digitized at an interval of 800 ns with 1024 points at 10 bit amplitude resolution, and fed to a work station (Sun Spark Station 5) for analysis. Wavelet transform is useful in getting arrival-time information with a high S/N ratio and sharp peak definition. Shown in the top row of Fig. 4 are examples of Lamb waveforms produced on the quasi-isotropic CFRP plate by a pencil-lead break (left) and a steel-ball drop (right) at #2 position, corresponding to the coordinate (150, 225). These waves were monitored by channel-4 transducer. The waves produced by the pencil-lead break contains both the  $S_0$ -Lamb component



*Fig.3 Schematic illustration of source location method of Lamb waves produced by impacts at #1 to #9 positions on CFRP plate.*

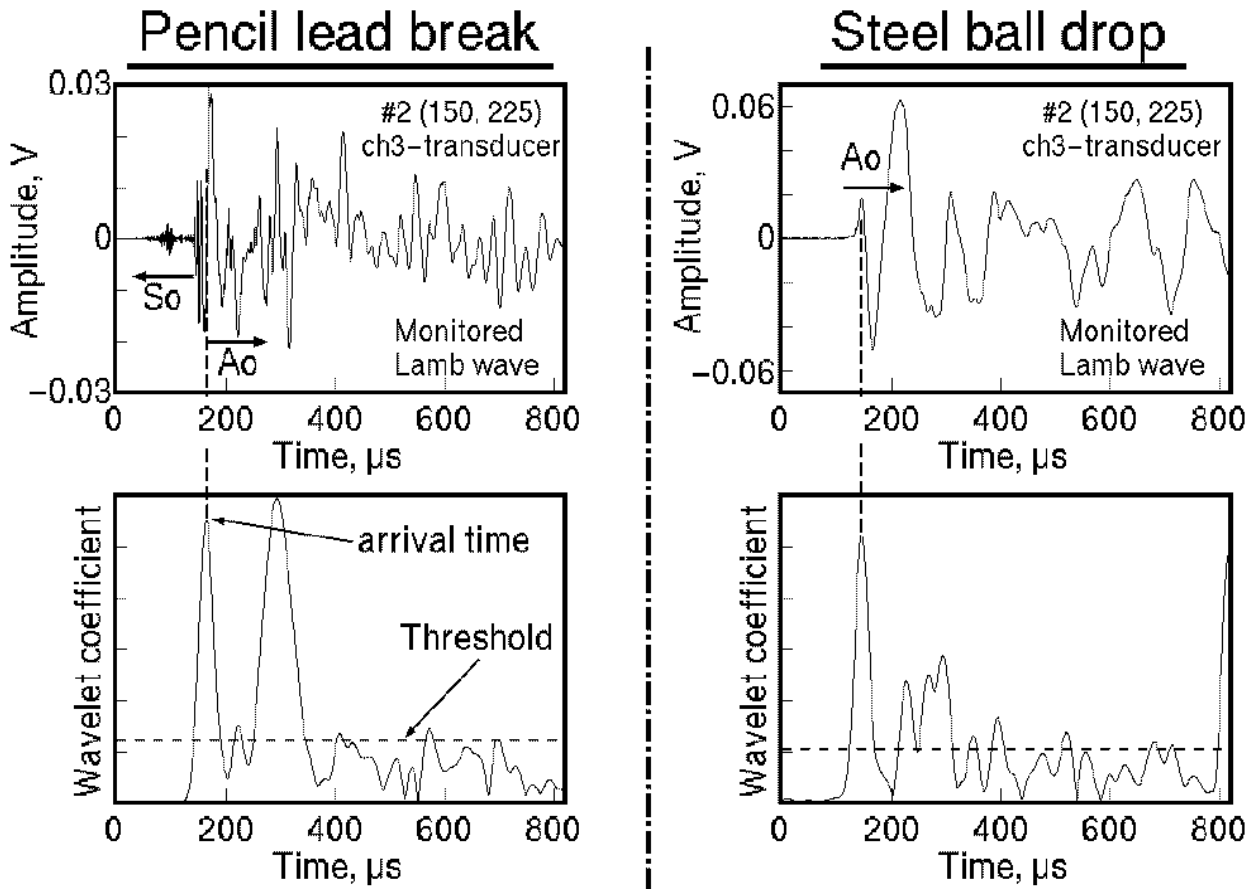


**Fig.4 Examples of Lamb waveforms (the top) produced by pencil-lead break (the left) and steel ball drop (the right) on  $(0^\circ/45^\circ/90^\circ/45^\circ)_s$  CFRP plate. The bottom two figures represent the time transient of wavelet coefficients at 65 kHz.**

(arriving first, high-frequency, low-amplitude) and the late-arriving large amplitude A<sub>0</sub>-Lamb component. The wave due to steel-ball impact contains only the A<sub>0</sub>-Lamb component, having lower frequency and large amplitude. The bottom two figures represent the time transient of 65 kHz wavelet coefficient, corresponding to the 65 kHz-components of the signals. The S<sub>0</sub>-components can not be seen in these figures because of their low amplitude.

Selection of a particular frequency component for the source location depends on two factors. One is to use the strong frequency components of propagating Lamb waves. This is affected by the mechanism of wave generation, wave propagation characteristics and transducer parameters. The other is a sufficient velocity difference of the S<sub>0</sub>- and A<sub>0</sub>-Lamb waves, so that the A<sub>0</sub>-Lamb arrival is adequately separated from the S<sub>0</sub>-Lamb wave component. For example, in the quasi-isotropic CFRP plate used here, the velocity of A<sub>0</sub>-Lamb at 65 kHz is calculated as 1.3 mm/μs while that of S<sub>0</sub>-Lamb is 5.5 mm/μs. These were obtained by Adler's matrix transfer method [10]. At 250 kHz, both velocities are similar and it is impossible to separate the A<sub>0</sub>-Lamb from the S<sub>0</sub>-Lamb waves. This means that the utilization of low frequency Lamb waves is better for determining the arrival times of impact-induced waves. The use of even lower frequencies is limited by the lack of transducer sensitivity, although the attenuation is lower. It is also expected that spatial definition becomes poor as the wavelength increases proportionately.

### a. Source Location on Quasi-isotropic CFRP Plate

The source location on a quasi-isotropic CFRP plate was determined by first exciting Lamb waves by breaking a pencil-lead and by dropping a steel-ball (7 mm diameter, 1.4 g mass, 20 mm height) at position #1 to #9 in Fig.3. Square transducer arrangement was used. The upper row of Fig. 5 shows typical waveforms excited by pencil-lead breaks at position #2 (150, 225) and monitored by four resonant transducers (ch.1 to 4). Their 65 kHz wavelet coefficients (or  $A_0$ -components in this case) are shown in the bottom row. From the wavelet coefficients vs. time curves, we determined the arrival

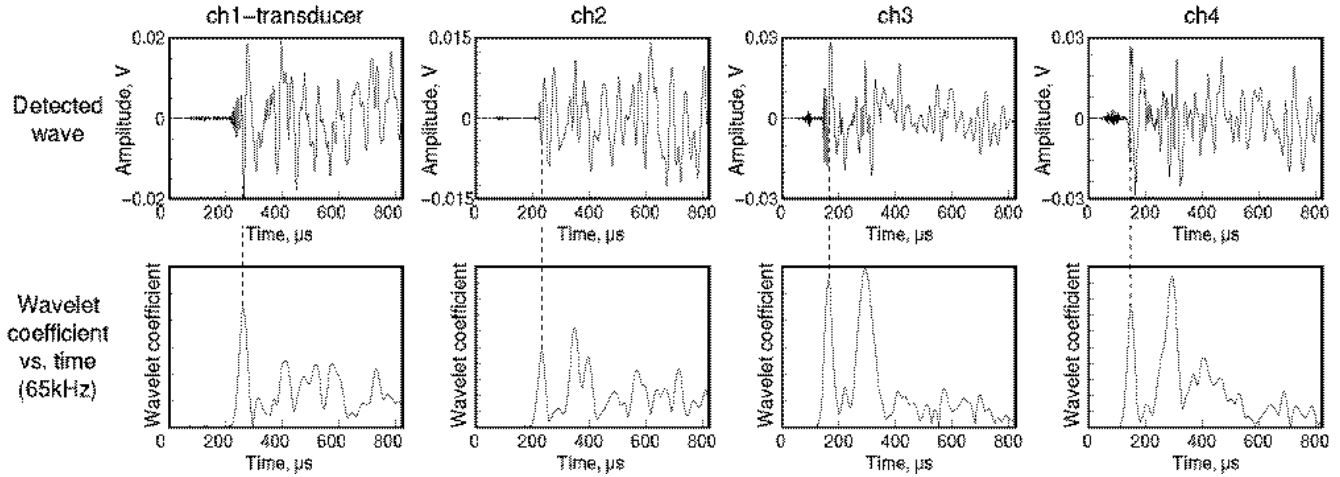


*Fig.5 Examples of Lamb wave (top) and their 65 kHz  $A_0$ -components (bottom) produced by pencil-lead break at #2 position and monitored by four AE transducers on  $(0^\circ/45^\circ/90^\circ/-45^\circ)_s$  CFRP plate.*

times of the detected waveforms, which were taken at the points in time when the wavelet coefficient reaches 20% of the peak value. This compensates for the attenuation of wave amplitude. We also compared them with the positions of the peak value, or peak-arrival times, but the 20%-threshold approach was slightly better in final location accuracy. Although the peak position coincides better with the arrival of the particular frequency component judging from the shape of the waveform, broadness of the peaks probably contributes to the observed discrepancy. The determination of the arrival time was performed as a part of computer program along with the wavelet transform. Owing to a good S/N ratio and sharply rising wavelet profiles, arrival times can be accurately identified. Using the arrival time data, we obtained next the sequence of the arrival times. This identifies the source location within one of the four quadrants for the square four-transducer arrangement used. The final step of this source location method is to use measured arrival time differences and orientation dependence of  $A_0$ -Lamb waves, and to estimate a source location. The differences of the measured arrival times are matched to computed arrival time differences, by using one of iterative processes. Results are shown in Fig. 6 for pencil-lead break (left) and steel-ball drop sources (right), which indicate an original position by a square and estimated source position by an X. The estimated source locations agree well with the given locations. The location results are given in Table 1. The maximum error of 6.8 mm and average error of 2.4 mm were obtained for pencil-lead break sources on this quasi-isotropic CFRP plate. For steel-ball drops, the maximum error of 6.3 mm and average error of 3.0 mm were obtained. Computation time was less than one second. The importance of utilizing anisotropic Lamb wave velocities can be demonstrated by a comparison with source location results with an isotropic velocity. Table 2 summarizes the results, which indicate the maximum error of 26.4 mm and average error of 17 mm. Even though 65 kHz  $A_0$ -Lamb velocities only varies from 1.17 mm/ $\mu$ s to 1.33 mm/ $\mu$ s (or 6%), this velocity variation decreases the location accuracy to an unacceptable level.

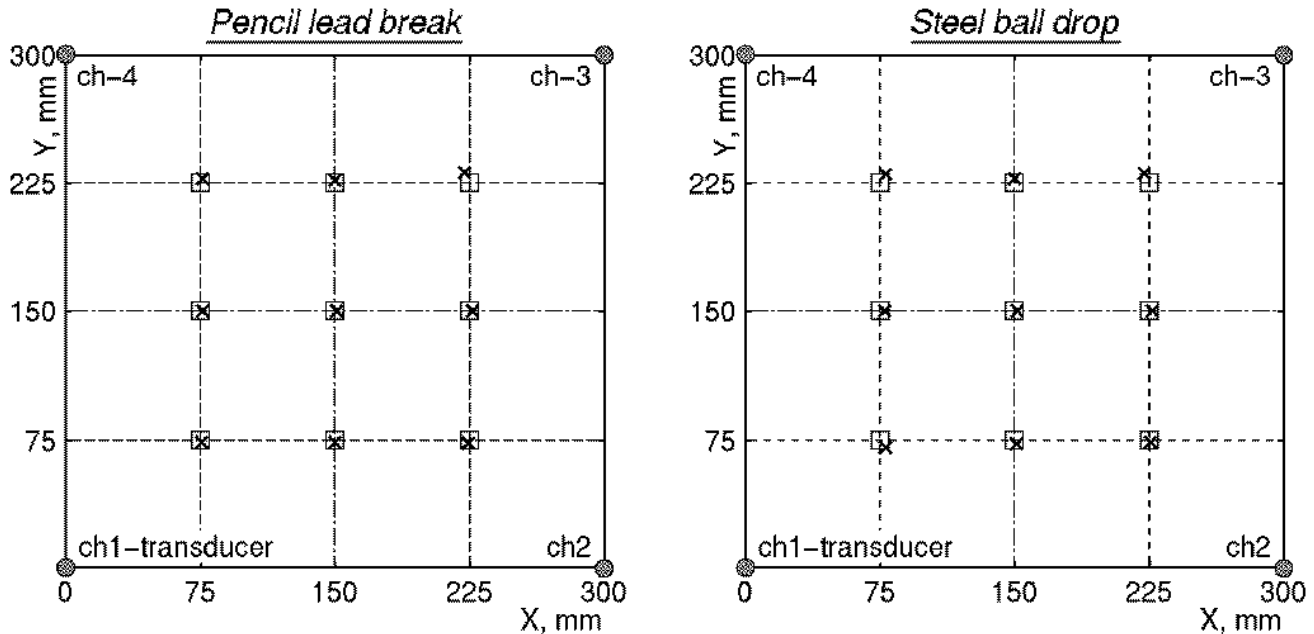


**Fig.6** Comparison of given source location (□) and estimated location (X) of pencil-lead break (the left) and steel-ball drop (the right) on  $(0^\circ/45^\circ/90^\circ/45^\circ)_s$  CFRP plate.

**Table 1** Source location of pencil-lead break (the left) and steel-ball drop (the right) on  $(0^\circ/45^\circ/90^\circ/45^\circ)_s$  CFRP plate.

### Pencil lead break

No.	Impact location		Estimated location		error (mm)
	x (mm)	y (mm)	x (mm)	y (mm)	
#1	75	225	75.9	224.0	1.3
#2	150	225	150.1	227.8	2.8
#3	225	225	222.0	231.1	6.8
#4	75	150	74.8	150.7	0.7
#5	150	150	151.0	151.6	1.9
#6	225	150	225.3	152.9	2.9
#7	75	75	75.6	72.9	2.2
#8	150	75	148.0	74.9	2.0
#9	225	75	224.8	76.1	1.1

Average error 2.4mm

### Steel ball drop

No.	Impact location		Estimated location		error (mm)
	x (mm)	y (mm)	x (mm)	y (mm)	
#1	75	225	77.6	227.2	3.4
#2	150	225	150.0	228.2	3.2
#3	225	225	223.2	229.0	4.4
#4	75	150	76.5	150.6	1.6
#5	150	150	150.9	152.2	2.4
#6	225	150	225.9	151.8	2.0
#7	75	75	78.4	69.7	6.3
#8	150	75	151.1	71.7	3.5
#9	225	75	225.3	75.0	0.3

Average error 3.0mm

## b. Source Location on UD-CFRP Plate

The source location analysis of pencil-lead breaks and steel-ball drops is performed on a UD-CFRP plate that has stronger anisotropy. Specimen size and transducers layout are the same as those used for the quasi-isotropic CFRP plate. Procedures are identical to those used earlier and 65 kHz A<sub>0</sub>-components were utilized. The source location results for pencil-lead breaks and steel-ball drops are summarized in Table 3.

**Table 2 Source location on  $(0^\circ/45^\circ/90^\circ/-45^\circ)_s$  CFRP plate using 65 kHz  $A_0$ -component assuming the symmetric velocity distribution to the Y-axis.**

No.	Impact location		Estimated location		error (mm)
	x (mm)	y (mm)	x (mm)	y (mm)	
#1	75	225	77	212.5	12.7
#2	150	225	140	208.5	19.3
#3	225	225	209	246	26.4
#4	75	150	77	149.5	2.1
#5	150	150	150	133.5	16.5
#6	225	150	203.5	144	22.3
#7	75	75	89.5	57	23.1
#8	150	75	159	90.5	17.9
#9	225	75	223	87.5	12.7

Average error 17mm

**Table 3 Source location of pencil-lead break and steel-ball drop on UD-CFRP plate.**

### Pencil lead break

No.	Impact location		Estimated location		error (mm)
	x (mm)	y (mm)	x (mm)	y (mm)	
#1	75	225	72.0	227.1	3.7
#2	150	225	150.9	226.4	1.7
#3	225	225	227.3	226.3	2.6
#4	75	150	69.5	151.2	5.6
#5	150	150	148.2	149.3	1.9
#6	225	150	228.3	150.0	3.3
#7	75	75	72.5	71.7	4.1
#8	150	75	151.7	73.1	3.8
#9	225	75	224.6	73.8	1.3

Average error 3.1mm

### Steel ball drop

No.	Impact location		Estimated location		error (mm)
	x (mm)	y (mm)	x (mm)	y (mm)	
#1	75	225	72.8	229.0	4.6
#2	150	225	150.9	229.0	4.1
#3	225	225	227.3	224.1	2.5
#4	75	150	66.6	150.8	8.4
#5	150	150	153.7	149.5	3.7
#6	225	150	228.0	150.9	3.1
#7	75	75	73.4	71.8	3.6
#8	150	75	148.3	71.0	4.3
#9	225	75	225.2	73.0	2.0

Average error 4.0mm

The source location for pencil-lead break was determined within 5.6 mm maximum error with the average error of 3.1 mm. Accuracy of source locations for steel-ball drops is also good, with the average error of 4.0 mm and 8.4 mm maximum error. The results demonstrate that, in spite of a higher velocity anisotropy of UD-CFRP, the source location can be accurately estimated by the present method.

### c. Source Location on Cross-ply CFRP Plates

The source location analysis of pencil-lead breaks is performed on cross-ply-CFRP plates of three different thickness (2.0, 3.0 and 4.0 mm). Specimen size and transducers layout is the same as those used for the quasi-isotropic CFRP plate. Procedures are identical to those used earlier and 65 kHz  $A_0$ -components were again utilized. The source location results for pencil-lead breaks are summarized in Table 4. The source location for pencil-lead break was determined within 6.5 to 11.8 mm maximum

**Table 4 Source location of pencil-lead break on Cross-ply-CFRP plates.**

Thickness: 2.0 mm					Thickness: 3.0 mm					Thickness: 4.0 mm							
No.	Impact location		Estimated location		error	No.	Impact location		Estimated location		error	No.	Impact location		Estimated location		error
	x (mm)	y (mm)	x (mm)	y (mm)	(mm)		x (mm)	y (mm)	x (mm)	y (mm)	(mm)		x (mm)	y (mm)	x (mm)	y (mm)	(mm)
#1	75	225	72.2	230.3	6.0	#1	75	225	73.5	229.0	4.3	#1	75	225	72.5	231.8	7.2
#2	150	225	150.0	232.0	7.0	#2	150	225	150.0	230.6	5.6	#2	150	225	148.9	236.7	11.6
#3	225	225	228.7	231.9	7.8	#3	225	225	228.7	227.8	4.6	#3	225	225	226.9	232.0	7.3
#4	75	150	67.4	150.0	7.6	#4	75	150	70.6	150.0	4.4	#4	75	150	70.8	150.6	4.2
#5	150	150	150.7	151.4	1.6	#5	150	150	149.3	152.1	2.2	#5	150	150	150.0	150.0	0
#6	225	150	234.4	152.2	9.7	#6	225	150	230.9	149.4	5.9	#6	225	150	229.5	149.4	4.5
#7	75	75	71.3	65.4	10.3	#7	75	75	68.9	72.7	6.5	#7	75	75	72.6	65.9	9.4
#8	150	75	148.9	70.3	4.8	#8	150	75	148.3	70.1	5.2	#8	150	75	148.9	66.9	8.2
#9	225	75	231.1	70.5	7.6	#9	225	75	228.8	72.8	4.4	#9	225	75	234.5	70.6	10.5

Average error 6.9mm

Average error 4.8mm

Average error 7.0mm

error with the average error of 4.8 to 7.0 mm for these plates. The results demonstrate that, in spite of a lesser velocity anisotropy of cross-ply CFRP plates, the source location accuracy was comparable to the other plates. This implies that the accuracy limitation is due to the lack of homogeneity in the plates used rather than the source location algorithm.

## CONCLUSION

We developed a new source location method applicable to anisotropic plates, and demonstrated its utility for the source location of quasi-isotropic, unidirectional and cross-ply CFRP plates with velocity anisotropy and dispersion. The orientation dependence of  $A_0$ -Lamb velocities for CFRPs plates was measured at selected frequencies by a wavelet transform of AE signals. This velocity data was incorporated for the source location analysis. The computer algorithm developed provides performing wavelet transform, determining the arrival time of a selected frequency  $A_0$ -Lamb component and computing the source coordinates. The source was first estimated to one of four quadrants within 4 transducers by using the arrival times, and then accurately determined by sequential iteration. Here, the measured arrival-time differences were matched with those computed by moving a virtual source position in pre-set steps. The source locations of pencil-lead breaks in 300 x 300 mm square enclosed by four transducers on both the quasi-isotropic and unidirectional CFRP plates were determined with the maximum (average) error of 6.8 (3.1) mm. Steel-ball drop sources were located with the average error of 3.0 mm for the quasi-isotropic plate and 4.0 mm for the UD-CFRP plate. Speed of the source location was less than one second in all the cases.

## ACKNOWLEDGEMENT

M. Takemoto is grateful for the financial support received from the Ministry of Education (10875130). A part of this research was supported by the fellowship to Y. Mizutani from the Japan Soc. for Promotion of Science.

## REFERENCES CITED

- [1] K.S. Downs and M.A. Hamstad, J. Acoustic Emission, 14(3-4), (1996), S61-S73.
- [2] W.H. Prosser, J. Acoustic Emission, 14(3-4), (1996), S1-S11.
- [3] T. Kinjo, H. Suzuki, M. Takemoto, JSME Int. Series A, 41-3 (1998), pp. 359-365.
- [4] M.R. Gorman and W.H. Prosser, J. Acoust Emission, 9, (1991) 283-288.
- [5] S.M. Ziola and M. R. Gorman, J. Acoustic Soc. Am., 90(5), (1991) 2551-2556.
- [6] K.Y. Hjang, W.H. Lee and D. Kim, Progress in AE, (1999) IV-58-65.
- [7] V. Venkatesh and J.R. Houghton, J. Acoustic Emission, 14(2)(1996)61-68.
- [8] Y. Promboon and T.J. Fowler, Source Location on Fiber Reinforced Composites, paper delivered at

6-th Int. Sym. on AE from Composite Materials at Texas, (1998, June).

[9] O.Y. Kwon and Y.C. Joo, Progress in Acoustic Emission, (1998) IV9-17.

[10] E.L. Adler, C.K. Jen, G.W. Farnell and J. Sloboszewicz, Ultrasonic Int. '85, (1985) 733.

# CHARACTERIZATION OF THE DAMAGE AND FRACTURE MECHANISMS IN $Ti_3SiC_2$ USING ACOUSTIC EMISSION

P. FINKEL, R.K.MILLER, M.A.FRIESEL, R.D.FINLAYSON, P.T.COLE,  
M. W. BARSOUM\* and T. EL-RAGHY\*

Physical Acoustics Corporation, Princeton Junction, NJ, USA

\* Drexel University, Philadelphia, PA, USA

## ABSTRACT

*In this paper we report on the study of the acoustic emission (AE) produced during room temperature deformation of polycrystalline, fully dense, bulk samples of the ternary carbide,  $Ti_3SiC_2$ . This material is a damage tolerant ceramic that deforms plastically by a combination of delamination of individual grains, shear, and kink band formation. To further evaluate the deformation and fracture mechanisms, AE was monitored during compression tests. The AE activity is a strong function of strain rate and grain size. Unlike regular metals, this ceramic does not exhibit a peak of AE activity associated with the point of non-linearity in the stress-strain curve. An attempt has been made to quantify the AE and correlate it to the various damage mechanisms occurring during room temperature compression. AE can be used to continuously monitor the evolution of the damage, and its onset.*

## INTRODUCTION

Acoustic Emission (AE) is a well-proven technology for studying the mechanisms accompanying deformation and fracture. The AE produced during deformation of solids is a function of their elastic moduli, temperature, and microstructural features such as grain size, strength and fracture toughness. The various damage processes (dislocation motion, crack initiation and propagation, plastic deformation, etc.) radiate elastic waves that can be detected by piezoelectric transducers. Typically, each of these mechanisms is accompanied by a different AE signature, and in principle it is possible to differentiate between them. Furthermore, AE activity can be used as an indication of the onset of failure. The determination of failure modes by various AE signals and their correlation with mechanical properties is a base for developing evaluation criteria for damage characterization of ceramic materials.

To date, two limitations have restricted the use of AE to study the fracture of brittle solids in general, and ceramics in particular. The first is the high AE event rates that sometimes exceed 1000/sec [1]. A solution to this problem is to use the MISTRAS-2000 system (Physical Acoustics Corp.) that is capable of performing waveform and signal recording with a maximum event rate exceeding 1200/sec. The second limitation, which is more difficult to overcome, is related to properties of ceramics being brittle and damage intolerant by their nature. Recently, however, a new class of materials was discovered, that are extremely damage tolerant [2-5]. The power of combining AE with this new class of materials is demonstrated in this work.

For the current study we selected the ternary carbide,  $Ti_3SiC_2$  recently fabricated and characterized in fully dense, bulk, single phase samples [2]. This material is rather stiff (Young's moduli  $\approx 300$  GPa [2,6,7]) but relatively soft (Vickers hardness,  $\approx 4$  GPa). At the same time, it is readily machinable by regular high speed tool steels with no lubrication or cooling required. In addition to the aforementioned characteristics,  $Ti_3SiC_2$  is also oxidation [8] and creep resistant [9]. Most relevant to this work is the fact that  $Ti_3SiC_2$  deforms by a combination of regular glide kink and shear band formation [10,11]. The dislocations are overwhelmingly confined to the basal planes [12], are mobile, and multiply at room temperature [11].

We have also shown that highly oriented macro-grained samples are ductile at room temperature and deform by forming macroscopic shear bands that, for the most part, extended across the samples tested. Because the deformation is constrained to the shear bands, the latter are areas of considerable upheaval, with delaminations, crack bridges and other evidence of intense deformation clearly obvious in post-deformation micrographs. The details and sequence of events that lead to the formation of the shear bands has not been studied in detail. The results presented in this paper, do shed some light on the problem. To date polycrystalline samples loaded in compression at room temperature failed in a brittle manner. In our most recent work, we demonstrated that the mechanical response of  $Ti_3SiC_2$  is a strong function of strain rate [13]. The results shown in this paper clearly show that when loaded slowly, even randomly oriented polycrystalline samples will exhibit some plasticity at room temperature. Finally, it is important to note that since  $Ti_3SiC_2$  does not possess 5 independent slip systems, it does not possess a yield point. The transition is thus one from elastic to in-elastic deformation, which is often not easy to determine from load deflection curves. The stress at which the transition occurs is henceforth referred to as the inelastic deformation stress or IDS.

This paper describes the quantitative results from application of the AE for determination of the role the microstructure and test parameters play during the deformation and fracture of  $Ti_3SiC_2$ . The goal of this work is to carry out a detailed study of the acoustic emission accompanying initiation and subsequent damage evolution in  $Ti_3SiC_2$  samples during compression. The analysis of AE data allows us to evaluate the effect of the grain size and strain rate on AE activity and also gain further insight into the deformation mechanisms of this material.

## EXPERIMENTAL PROCEDURE

The material for fabricating  $Ti_3SiC_2$  samples was prepared using reactive hot isostatic pressing (HIPing) [14]. In this work, three microstructures were tested: a fine grained (FG) with average grain size of 5  $\mu m$ ; a coarse-grained (CG) with average grain size of 100  $\mu m$ , and a duplex microstructure (DM) which consisted of very large grains of the order of 500-800  $\mu m$  plates, about 100  $\mu m$  thick, embedded in a matrix of 100  $\mu m$  grains. All tests were performed on cylindrical specimens (7 mm diameter and 15mm length) machined by electro-discharge machining.

Figure 1 shows the set-up of AE monitoring hardware used in this study. The compression tests were performed on an Instron-type testing machine at room temperature. The nominal strain rate was varied from 0.00056 to 0.0056  $s^{-1}$ . In a few samples the strain was measured with a specially designed fiber optic strain gage that attached to the lateral side of the specimen. The MISTRAS-2000 system (Physical Acoustics Corporation) used in this work is capable of performing waveform and signal recording with a peak event rate exceeding 1200/sec. The AE signal was recorded with a broadband PAC S9208 and resonant PAC R15 transducers mounted on the free side of the specimen under test.

## RESULTS AND DISCUSSIONS

Stress-strain curves of two CG samples tested at 0.00056  $s^{-1}$  are shown in Fig. 2. In both cases, a deviation from nonlinearity is observed at  $\sim 200$  MPa, which is followed by what can be best described as a region of distinct hardening, or in-elastic deformation, until failure at  $\sim 500$  MPa. One sample failed at a strain of 1.2 %, the other at  $\sim 2$  %. In these tests the strain was directly measured using the optical strain gauge. The reproducibility between the two runs is excellent. The straight line represents the stiffness calculated based on the measured modulus of 333 GPa [6]. Also plotted in Fig. 2 (lower curve) is the cumulative AE event rate for Sample # 1. Below 200 MPa, there is very little AE activity. Beyond the IDS, the AE activity (RMS, hit rates and energy) increases monotonically until fracture.

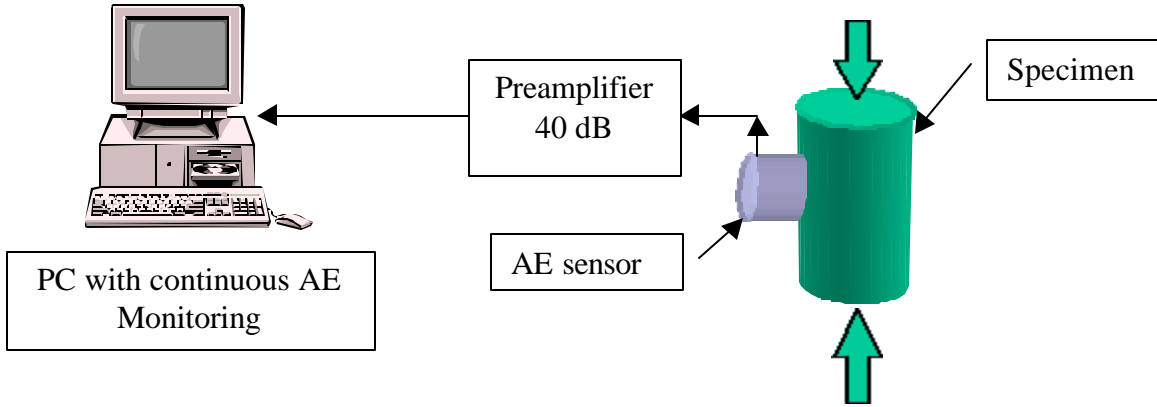


**Fig. 1. Set-up of the AE monitoring hardware used in this study.**

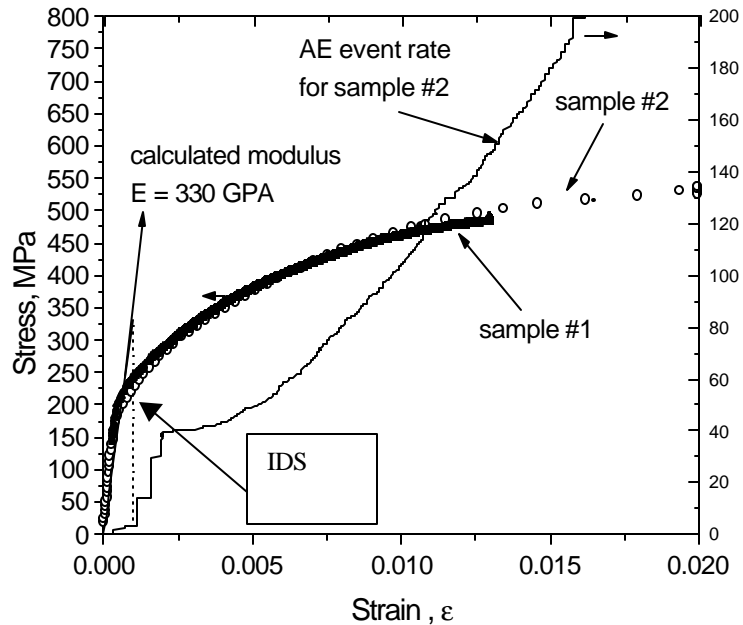


**Fig. 2. Stress – strain curve and cumulative AE events vs strain for CG sample.**

In order to evaluate the effect of experimental variables in this work, the AE was measured as a function of strain rate. Figure 3 shows the AE RMS voltage  $V_{\text{rms}}$  plotted as a function of strain rate ( $\dot{\epsilon}$ ) (cross-head speed) at 95% of the stress to failure. A least squares fit of the data (dashed line) yields a slope of  $\sim 0.6$ . The solid line represents (slope 0.5) the normal strain rate dependence  $V_{\text{rms}} \sim (\dot{\epsilon})^{0.5}$ . This normal strain rate relationship implies that the AE source mechanism, associated with moving dislocations, remains unchanged over the range of strain rates measured [15]. The origin of this behavior in  $\text{Ti}_3\text{SiC}_2$  is not clear yet and more work is required.

The results shown in Fig.4 demonstrate the effect of grain size on AE activity obtained during the monotonic compression test using a strain rate of  $0.00056 \text{ s}^{-1}$ . This figure displays the load (top set of curves), cumulative RMS (middle set of curves) and cumulative hits (bottom set of curves) versus time for the FG (a), CG (b) and DM (c), samples. As can be seen, cumulative hits and RMS increase with a grain size increasing. Note the change of scale of the y-axis when going from the FG to the CG and DM

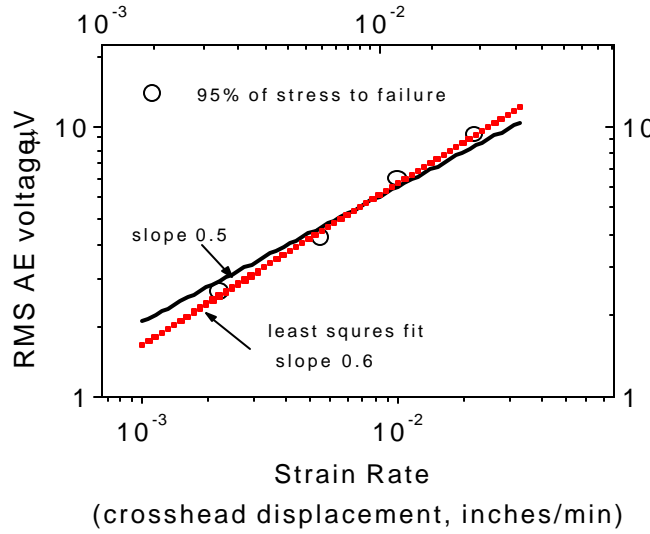


Fig. 3. RMS voltage vs. strain rate for CG sample.

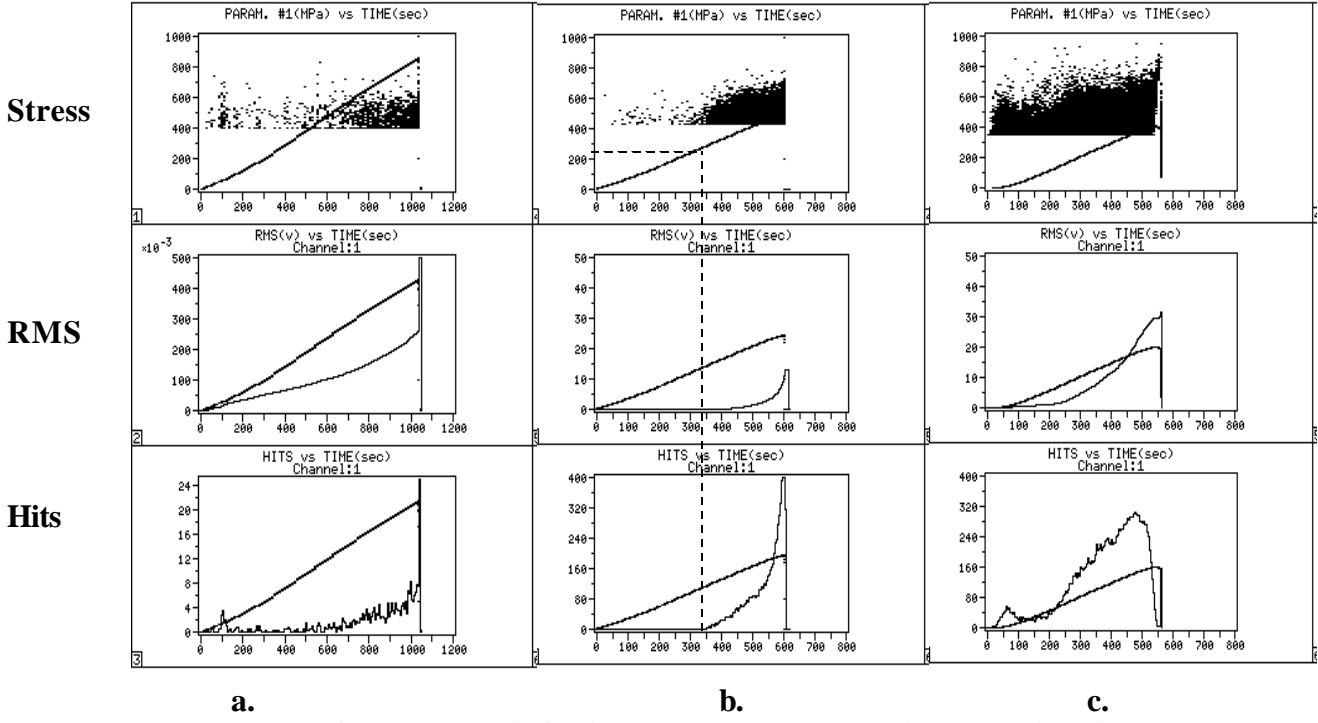


Figure 4. Time history AE results for three various grain size sample: (a), CG (b) and DM (c).

samples. These results clearly show that the AE activity is a strong function of microstructure. This is in a good agreement with the theoretical approach [16]. Furthermore, as the point at which the cumulative AE event rate increases dramatically (Fig. 4b, lowest curve) corresponds to a stress of  $\approx 250$  MPa, it is comparable to the IDS determined from Fig. 2 ( $\approx 200$  MPa), and the former must be associated with the initiation of damage. This can be used to quickly and accurately measure the IDS in these damage tolerant ternary compounds; a quantity that has not been easy to determine.

It is important to contrast the behavior of  $Ti_3SiC_2$  with that of ductile metals and other more brittle ceramics. In metals, including Ti, the AE activity and RMS are at a maximum at the yield point. Typical ceramics behave more like the FG response shown in Fig. 4a. The AE activity of DM samples starts at

early stages of deformation is almost an order of magnitude higher than that for FG samples. The AE behavior of the CG and DM samples is distinctly different (see Fig.4b and Fig.4c). In light of what is currently known about the deformation modes of  $Ti_3SiC_2$ , i.e. grain delaminations, kink and shear band formation in individual grains this is not too surprising.

It is reasonable to assume that the AE signature of the aforementioned deformation modes is different than that due to the simple glide of dislocations along basal planes that must precede them. In the CG and DM samples, it is also reasonable to assume that the first AE events occur at stresses that are much lower than those required for the formation of the first macroscopic shear bands. This in turn suggests that there may be several AE signatures. The analysis of individual waveforms and their spectra support this notion. Figure 5a and 5b show the AE hits amplitude distributions, waveforms and their spectra for CG sample at two levels of the applied stress: (a) initial stage I, ( $\approx 300$  MPa, just after IDS); (b) stage II (at  $\approx 450$  MPa, near failure stress). The AE signals measured at stage I were typically burst type with a relatively low energy per event and with dominant low frequency component centered around 150 kHz (Fig. 5a, lower curve). This AE is most likely due to dislocation motion, array formation and kink band formation and possibly initial delaminations. At the higher strains (Fig. 5b, lowest plot) the spectrum is distinctly different; the events are high energy and contain higher frequencies. These are AE signals of the second type. It is therefore reasonable to associate this AE signal with the formation of the macroscopic shear bands. The amplitude distribution plots (Figs. 5a,b, top plots) also indicate differences. The amplitudes in both stages have a peak between 40-50 dB. However, a second peak can be observed in loading stage II (Fig. 5b, top curve, marked with the arrow) between 60 and 70 dB. This indicates the presence of at least one other mechanism after the IDS. In order to distinguish AE signals from the different damage mechanisms, it is also possible to apply pattern recognition analysis.

The Physical Acoustics Corporation NOESIS software that was used for this purpose illustrates (Fig. 6) the evolution of the various AE features during the loading of a DM sample. The onset of the shear band can be clearly identified, as the signals forming cluster #1 have relatively low mean frequencies.

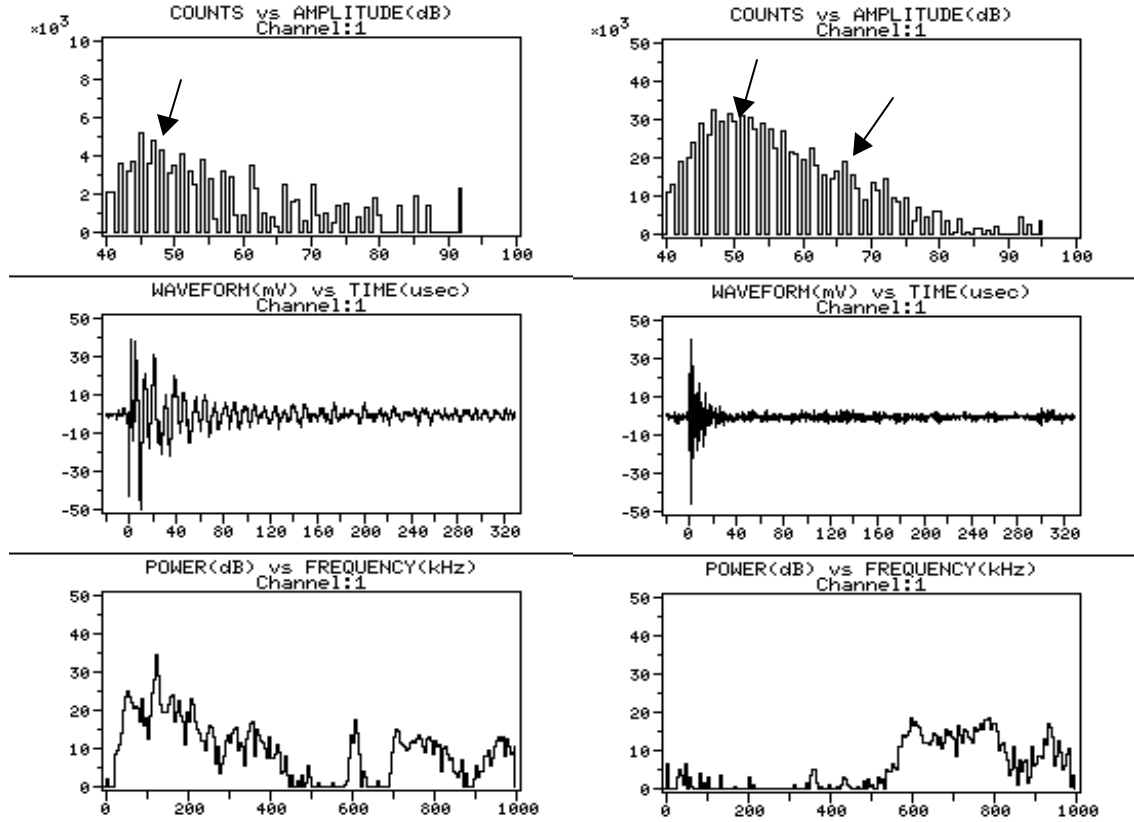
One important result of the performed study is that deformation induced AE is shown to be very effective and useful for the evaluation of fracture mechanisms in  $Ti_3SiC_2$ . Also, we have proved that AE frequency spectrum data and pattern recognition analysis could be used to characterize various AE sources associated to damage evolution of this material. The AE results demonstrate the unique damage tolerance characteristics of  $Ti_3SiC_2$ ; the amount of damage these solids can accumulate before failing is quite remarkable even at room temperature. Finally, our AE results clearly indicate that both the design stresses, which probably would have to be less than the IDS, and the amount of damage the material can withstand before failure, are strong functions of grain size and microstructure.

## CONCLUSIONS

In this study acoustic emission was used to evaluate the damage mechanisms occurring during room temperature compression of  $Ti_3SiC_2$ . The AE generated during compression tests of the  $Ti_3SiC_2$  samples has been measured and characterized. Three types of microstructures were investigated, and the measured AE was found to be dependent on the grain size and strain rate. Analysis of the AE signals suggests that more than one mechanism was responsible for the signal. Based on this work, AE can be effectively used to evaluate the fracture mechanisms and damage evolution in this material. Further studies on the quantitative correlation between AE and material micro-mechanics are under way and will be published soon.

## REFERENCES

1. A.Warner, et al, Monitoring of Deformation Induced Microcracking in Polycrystalline NiAl, *Mat.Res.Soc.SympoProc.*364, p.543, 1995.
2. M. W. Barsoum and T. El-Raghy, "Synthesis and Characterization of a Remarkable Ceramic:  $Ti_3SiC_2$ ", *J. Amer. Cer. Soc.* 79, [7] 1953-56 (1996).
3. T. El-Raghy, A. Zavaliangos, M. W. Barsoum and S. Kalidinidi, Damage Mechanisms Around Hardness Indentations in  $Ti_3SiC_2$ , *J. Amer. Cer. Soc.*, 80, pp. 513-516, (1997).
4. I. M. Low, S. K. Lee, B. Lawn and M. W. Barsoum, "Contact Damage Accumulation in  $Ti_3SiC_2$ ", *J. Amer. Cer. Soc.*, **81**, 225-28 (1998).
5. T. El-Raghy, M. W. Barsoum, A. Zavaliangos and S. Kalidindi, "Processing and Mechanical Properties of  $Ti_3SiC_2$ , Part II: Mechanical Properties", *J. Amer. Cer. Soc.*, **82**, 2855-2859 (1999).
6. P. Finkel, M. W. Barsoum and T. El-Raghy, "Low Temperature Dependence of Elastic Properties of  $Ti_3SiC_2$ ", *J. Appl. Physics*, **85**, 7123-7126 (1999).
7. R. Pampuch, J. Lis, J. Piekarczyk and L. Stobierski, " $Ti_3SiC_2$ -Based Materials Produced by Self-Propagating High Temperature Synthesis and Ceramic Processing", *J. Mater. Synthesis & Processing*, **1**, 93 (1993).
8. M. W. Barsoum, T. El-Raghy and L. Ogbuji, "Oxidation of  $Ti_3SiC_2$  in Air", *J. Electrochem. Soc.*, **144**, 2508-2516 (1997).
9. M. Radovic, M. W. Barsoum, T. El-Raghy, J. Seidensticker and S. Wiederhorn, "Tensile Creep Properties of  $Ti_3SiC_2$  in the 1000-1300 °C Temperature Range", Submitted for Publication
10. M. W. Barsoum and T. El-Raghy, Room Temperature Ductile Carbides", *Met. Mat. Trans.*, **30A**, 363-369 (1999).
11. M. W. Barsoum, L. Farber and T. El-Raghy, "Dislocations, Kink Banks and Room Temperature Plasticity of  $Ti_3SiC_2$ ", *Met. Mat. Trans.*, **30A**, 1727-1738 (1999).
12. L. Farber, M. W. Barsoum, A. Zavaliangos, T. El-Raghy and I. Levin, "Dislocations and Stacking Faults in  $Ti_3SiC_2$ ", *J. Amer. Cer. Soc.*, **81**, 1677-81 (1998).
13. M. Radovic, M. W. Barsoum, T. El-Raghy, J. Seidensticker and S. Wiederhorn, "Tensile Properties of  $Ti_3SiC_2$  in the 25-1300 °C Temperature Range", *Acta Mater.* in press.
14. T. El-Raghy and M. W. Barsoum, "Processing and Mechanical Properties of  $Ti_3SiC_2$ : Part I: Reaction Path and Microstructure Evolution", *J. Amer. Cer. Soc.*, **82**, 2849-54 (1999).
15. S. Y. Hsu and K. Ono, Proceedings of the Fifth International AE Symposium, pp.283, Japanese Society for Nondestructive Inspection, Tokyo, Japan.(1980).
16. H. G. N.Wadeley, C.B. Scruby, J. H. Speake, *International Metals Review*, **25**, No.2, p.41. (1980).



a.

b.

**Fig. 5. Two types of typical AE amplitude distributions, waveforms, and power spectra in CG sample corresponding to load stage I (a) and stage II (b) ( see text).**

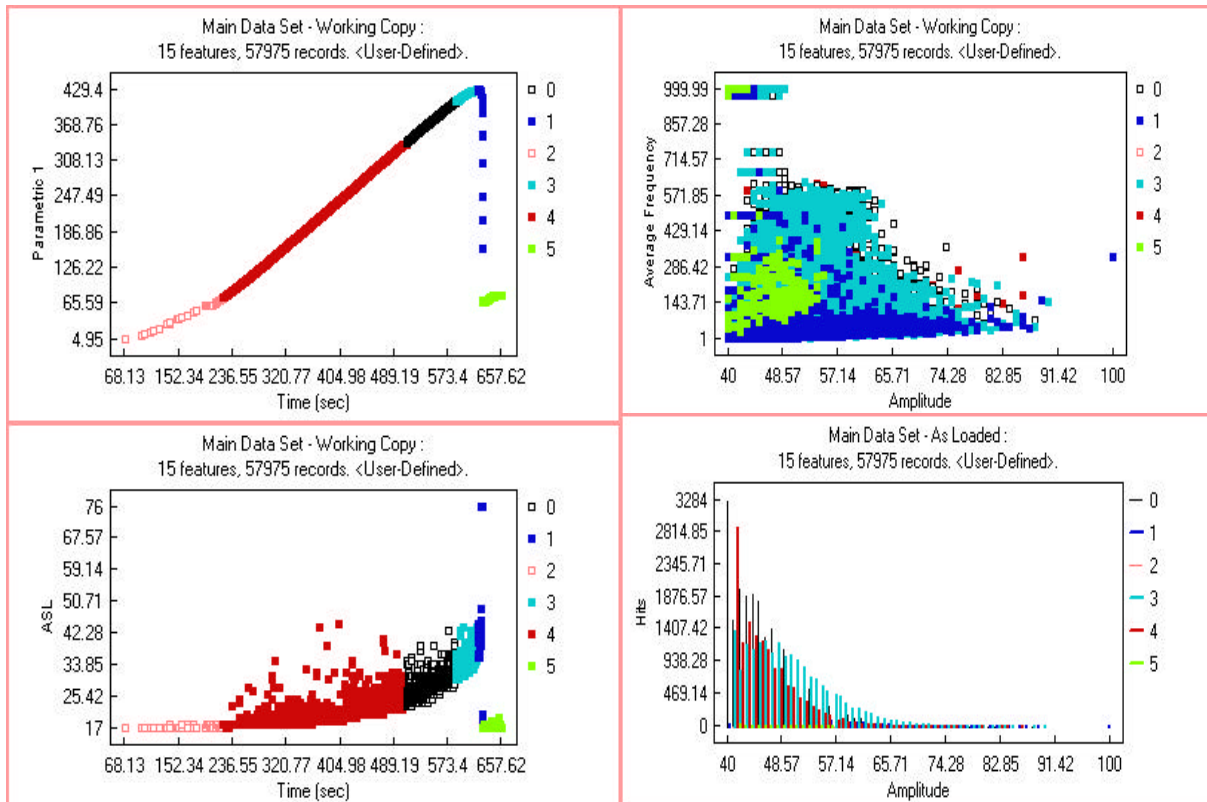


**Fig. 6. AE time history for DM sample analyzed with pattern recognition technique.**

# EVALUATION OF MARTENSITIC TRANSFORMATION DYNAMICS OF Cu-Al-Ni SHAPE MEMORY ALLOY SINGLE CRYSTAL BY ACOUSTIC EMISSION METHOD

Kenichi YOSHIDA, Shinichi KIHARA\* and K. SAKAMAKI

Department of Mechanical Engineering, Tokushima University, Tokushima, Japan

\*Yamaguchi NEC Corporation, Yamaguchi, Japan

## Abstract

*Cu-Al-Ni shape memory alloy exhibits a super-elasticity, which shows perfect recovery of plastic deformation. The super-elasticity used in this study results from a perfect reversible martensitic transformation. Acoustic emission (AE) behavior during the stress-induced martensitic transformation has been investigated using two types of specimens of Cu-Al-Ni shape-memory alloy single crystal, each of which has different stress concentration factors. AE total event counts generated during martensitic transformation did not depend on the specimen volume. AE event rate and the amplitude distribution were associated with the nucleation and growth of martensite plates during loading and their disappearance and shrinkage during unloading. Sequential change of AE waveforms during deformation was different in the two specimens because of differing martensite plate shapes. The martensitic transformation rate obtained by AE waveform analysis increased with increase of fatigue damage.*

## Introduction

Martensitic transformation is known as a transient shear process in materials. The dynamic property of the transformation must give an important information on the nature of the transformation [1]. In general, the martensitic transformation proceeds both by nucleation and growth of martensite plate [2]. The dynamic behavior of martensitic transformation phenomena has been measured by transient electrical resistivity change in Fe-Ni alloy [3], magnetic permeability change in Fe-Ni alloy [4] and AE method in 304 stainless steel [5,6]. These results have two weak points to explain the dynamic behavior of individual martensite plates. One is that the studies included the constraints due to grain boundaries because materials used were polycrystalline. Another is that these could not be distinguish between nucleation and growth of martensite plates because of difficulty of in situ measurement.

In this paper, the dynamic properties of the stress-induced martensitic transformation in two types of Cu-Al-Ni shape-memory alloy single crystal were investigated using AE method. The martensitic transformation used in this study was the  $\gamma_1$ '(DO<sub>3</sub> structure) $\leftrightarrow\gamma_1$ '(18R structure) transformation, which can be observed by an optical microscope during tensile deformation at room temperature. Therefore, the nucleation and growth behavior of martensite plates was examined in detail.

## Experimental procedures

Material used was a Cu-14.1mass%Al-4.1mass%Ni alloy ( $M_s=250K$ ,  $A_f=280K$ ) for stress-induced martensitic transformation. It was melted in argon in a high-frequency induction furnace and cast into a plate-shaped copper mold. It was next put into a graphite mold. An oriented single crystal of the Cu-Al-Ni alloy was grown using a seed crystal by the Bridgman method at a speed of 32 mm/h. They were solution-treated at 1273K for 1 hr. and then quenched into water at room temperature in order to keep

the  $\gamma_1$  matrix phase. Two kinds of tensile specimens (shown in Fig. 1) were prepared by an electron-discharge machine, polished mechanically and then electro-polished in a solution of phosphoric acid supersaturated with chromium trioxide. These were nearly smooth (specimen No. 1) and double-side notched (specimen No. 2) specimens. Stress concentration factors in these specimens were 1.01 and 2.65, respectively. For volume dependency on AE activity, rectangular samples (size: 12 mm x 4 mm x 0.9~1.8 mm were also used. The orientation of the single crystal specimen was determined by the back-reflection Laue method. The specimen had (001) surface and [100] tensile direction, respectively.

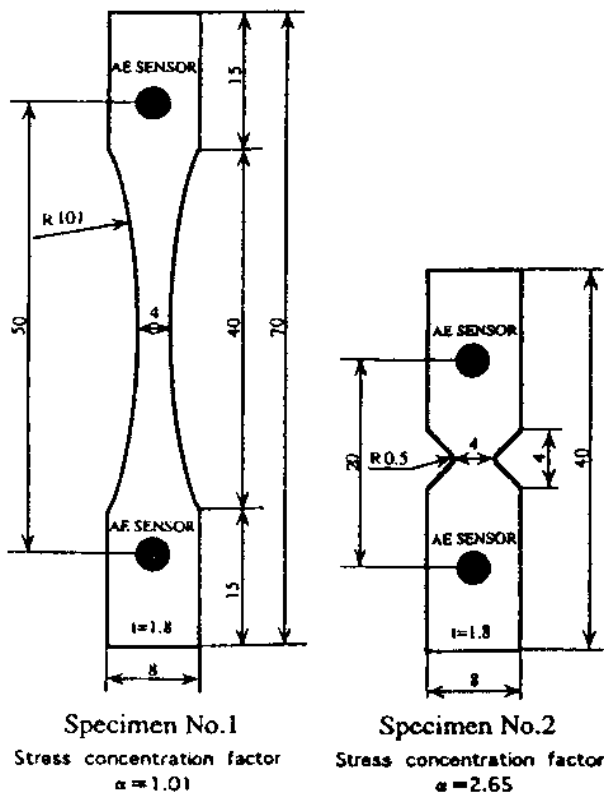


Fig. 1 Specimen shapes and AE sensor locations.

Tensile test was carried out with an Instron-type testing machine at a strain rate of  $5.6 \times 10^{-5} \text{ s}^{-1}$ . Fatigue test by plate bending was also carried out with a Schenck-type testing machine at a cyclic rate of 6 Hz. Surface appearance during tensile test was observed and photographed microscopically by an optical microscope.

Acoustic emission measurements were performed using 2-channel AE monitoring system (PAC: MISTRAS-2001). The AE signals were detected by two AE transducers (M5W) with wide frequency band. These were directly attached on the grip part of a specimen with a quick-acting glue. The distance between the two transducers was 50 or 20 mm. Detected AE signals were amplified by a constant gain of 60dB through a band-pass filter of 0.1 to 1.2 MHz. Acoustic emission parameters measured consisted of the AE events, the peak amplitude and the waveforms. Threshold level was 50dB, which corresponded to 316  $\mu\text{V}$  at the preamplifier input.

## Results and Discussion

### (1) Effect of specimen volume on AE activity

All the specimens exhibited super-elasticity and completely recovered the matrix phase upon unloading because of the lower  $A_f$  point of the material. When a given plastic strain is exclusively due to the martensitic transformation, an amount of transformation is considered as proportional to the given plastic strain energy. So effect of specimen volume on AE activity has been examined. All the specimens were given the same plastic strain energy per unit volume and an amount of transformation changed by the specimen volume. Results obtained during loading and unloading at the constant plastic strain of 2% are shown in Fig. 2. Total AE event counts decreased with an increase in the specimen volume. AE activity does not seem to depend on the amount of the martensitic transformation in material, but strongly depends on the dynamic behavior of the transformation. Especially the tendency becomes stronger under the reverse transformation. This indicates that it is possible to track nucleation and growth of transformation by AE method.

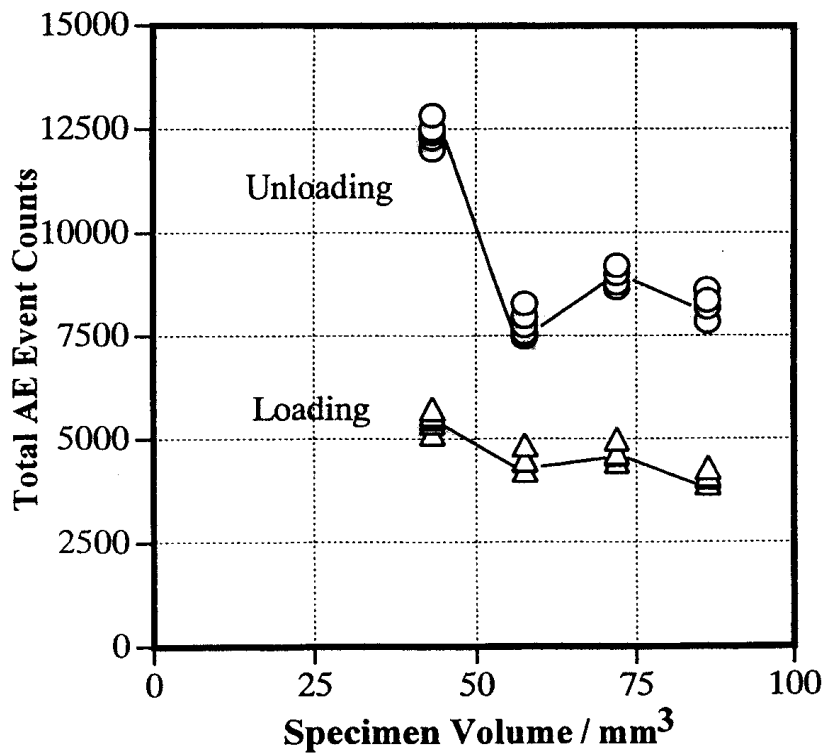


Fig. 2 Effect of specimen volume on total AE event counts (constant plastic strain of 2 %).

### (2) Difference of AE activity under different stress conditions

Relations between load-elongation curve, AE event rate and amplitude in the smooth (No. 1) and notched (No. 2) specimens during loading are shown in Fig. 3 and 4. Typical sequential surface appearances at the four elongation values by optical microscope are also shown. Less AE events were detected in the smooth specimen than those in the notched specimen, but higher AE amplitude was observed in the smooth specimen. According to the surface appearances in Fig. 3 and 4, the AE activity is related to the nucleation and growth of a few, large martensite plates in the smooth specimen and to the nucleation of many small martensite plates in the notched specimen.

### (3) Nucleation and growth behavior of the martensitic transformation

Acoustic emission behavior in the smooth specimen was different from that in the notched specimen in the early stage of the transformation as mentioned above. In the case of the smooth specimen, martensite plates extended to a single direction nucleated at first, and these grew in length and width directions and expanded through the thickness direction during yielding. Acoustic emission, which occurs sporadically during nucleation in the early stage of the transformation, had small amplitude, but AE changed to medium or high amplitude with the growth in length and width directions and still higher with expanded martensite plates. In the case of the notched specimen, many small amplitude acoustic emissions were detected when numerous small-sized martensite plates nucleated near the notch roots into two or three directions. There was only a small number of medium and high amplitude acoustic emissions because many martensite plates nucleated near the notch roots did not grow in the width direction because of stress concentration. Many higher amplitude acoustic emissions occurred with growth to the length and thickness directions.

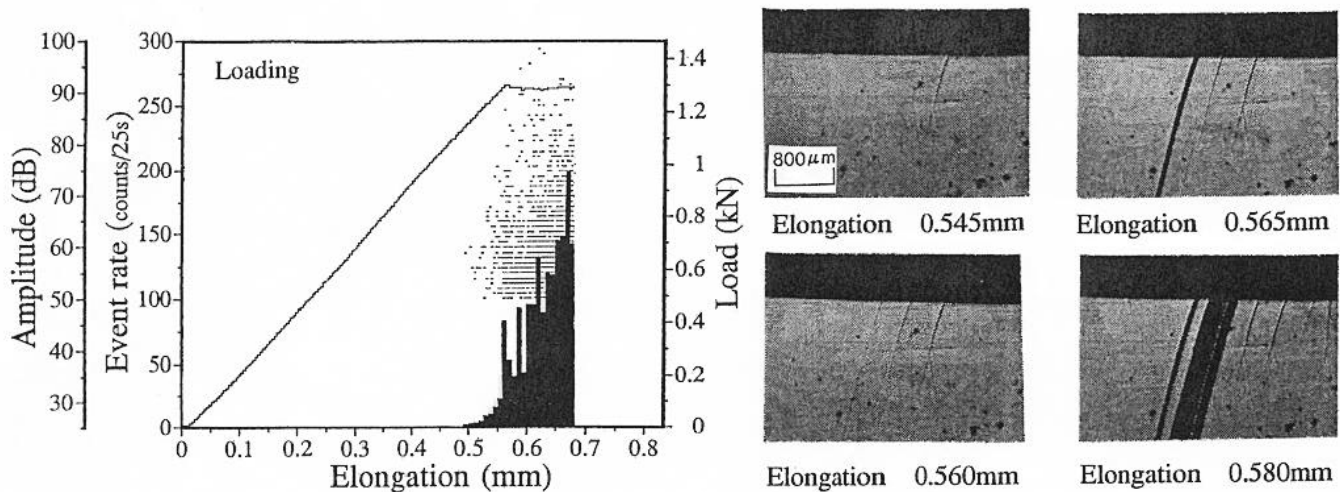


Fig. 3 Relations between load-elongation curve, AE event rate and amplitude during loading; in specimen No. 1 (smooth). Sequential surface appearance at different elongation by optical microscope.

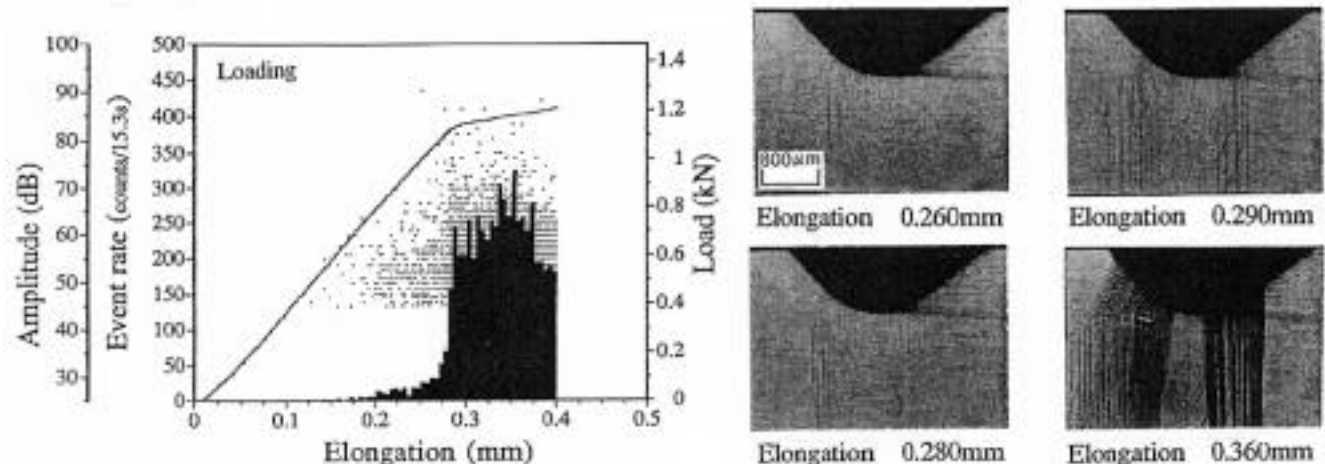


Fig. 4 Relations between load-elongation curve, AE event rate and amplitude during loading in specimen No. 2 (notched). Sequential surface appearance at different elongation by optical microscope.

Remarkable characteristics of acoustic emission waveforms in the smooth and notched specimens were found. In order to understand that, we divided into three stages the region from the loading start to yield point: Stage 1: starting point of loading to the nucleation region of martensite plates, Stage 2: mainly the growth region of martensite plates, Stage 3: near yielding. FFT analysis of detected AE waveforms has been performed in each transformation stage. A typical frequency spectrum of the waveform during tensile deformation is shown in Fig. 5. First and secondary peaks were selected as the characteristic parameters. Changes of these parameters during tensile deformation in the smooth and notched specimens are shown in Fig. 6 and 7, respectively.

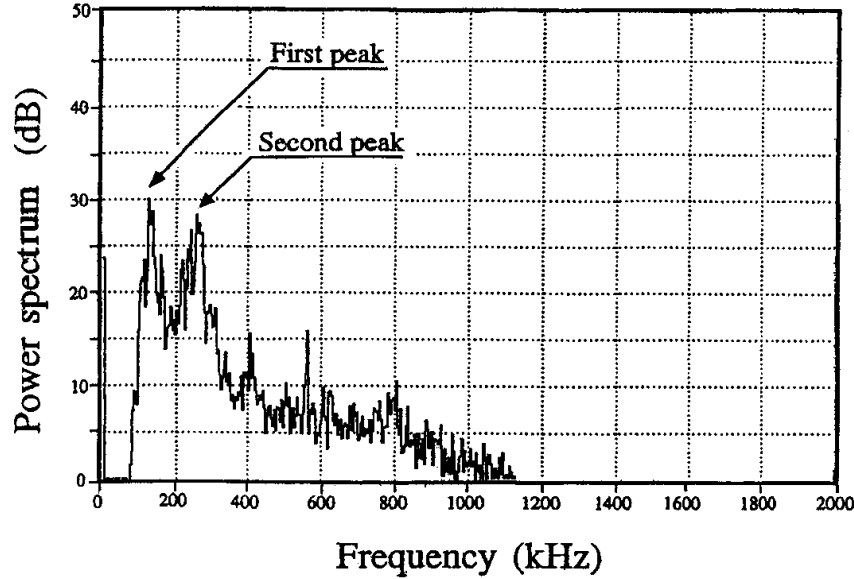


Fig. 5 A typical frequency spectrum of detected AE waveform.

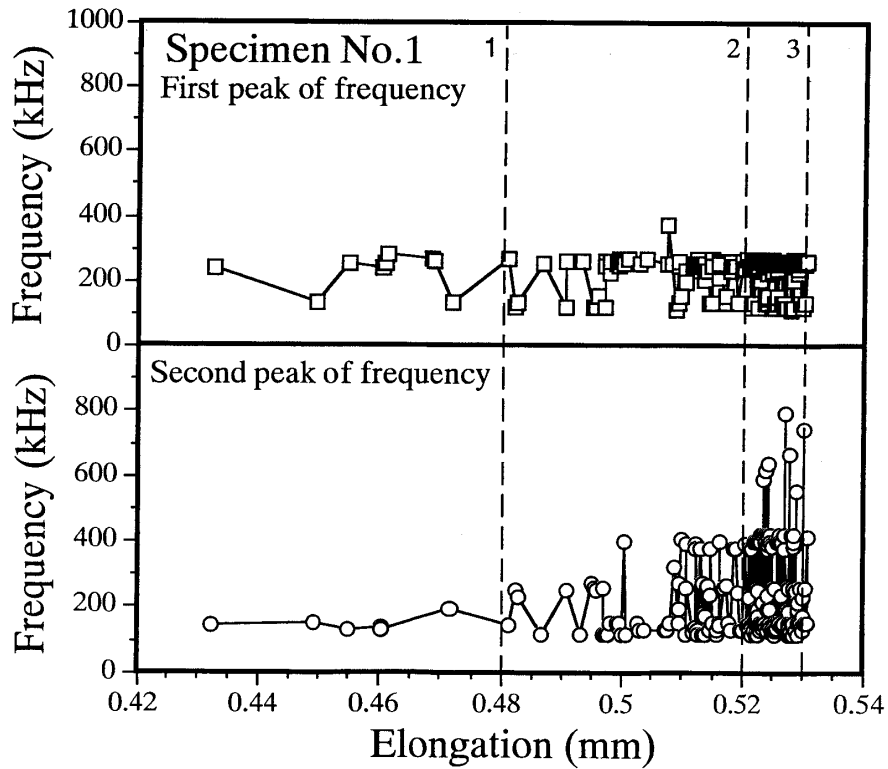


Fig. 6 Changes of first and second frequency peaks in waveforms detected in each stage during tensile deformation in Specimen No. 1 (smooth)

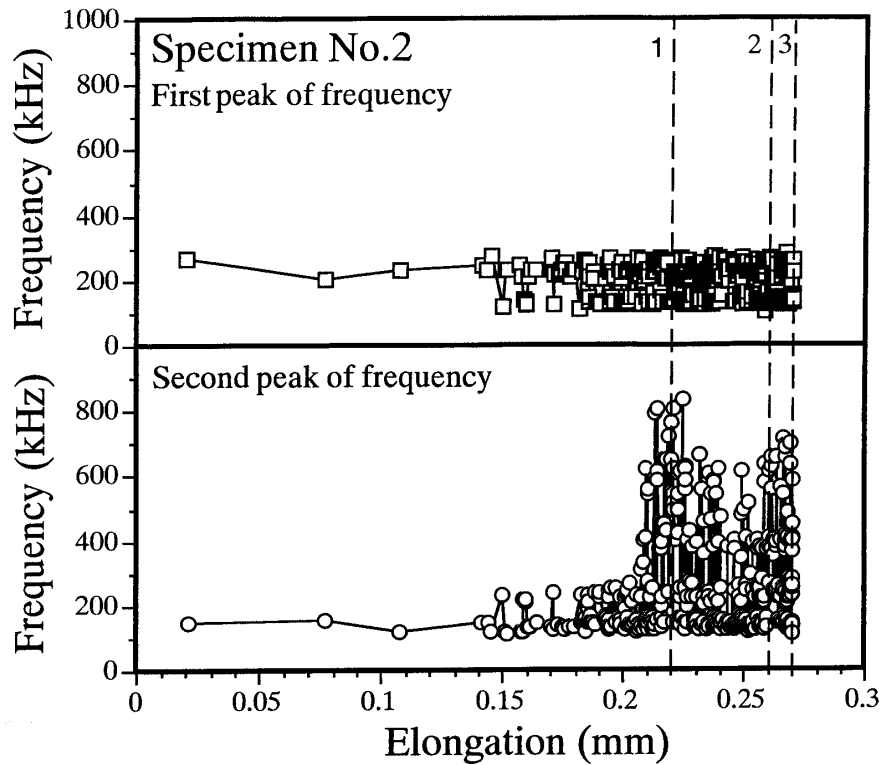


Fig. 7 Changes of first and second frequency peaks in waveforms detected in each stage during tensile deformation in Specimen No. 2 (notched).

First frequency peak is distributed near 200 kHz. This frequency seems to be characteristic of the martensitic transformation. The second peak frequency shifted to higher frequency in the latter half of Stage 2 in the smooth specimen but steeply to higher frequency in the latter half of Stage 1 in the notched specimen. The shift of the second frequency to higher frequency seems to depend on a degree of constraint against growth to length and thickness directions of the martensite plates. The shift suggests that the rise time in the martensitic transformation becomes short as discussed next.

#### (4) Rise time change of the martensitic transformation with fatigue damage

The rise-time analysis of the martensitic transformation has already been conducted using AE waveform analysis in the previous papers [7,8]. Takashima et al. tried to approximately conduct the source characterization using the dynamic Green's function in an infinite isotropic medium, assuming the Gaussian error function as the time shape function characterizing the dynamic property of the acoustic emission source. As a result, the mean rise time of the source was calculated by the gradient of the spectrum as the log-log expression in the frequency range of interest. Results obtained were apparently valid because the rise time of pencil-lead breaking as reference in this method was consistent with that in other method [9]. We applied the method to the martensitic transformation with fatigue damage. Change of the mean rise time due to the fatigue cycles in the smooth specimen during loading and unloading are shown in Fig. 8. Both of the mean rise times decrease with an increase in the fatigue cycles. Even if fatigue is given to 30000 cycles, we could not find out a macrocrack on the specimen surface. In this case, we could evaluate the growth rate of the martensite plates, which changed from 310 m/s to 500 m/s. The martensitic transformation is indicated to be able to occur more easily with increase of fatigue damage. Therefore, it is clearly possible to non-destructively evaluate the fatigue damage in the stage before crack formation in this type of material using AE waveform analysis.

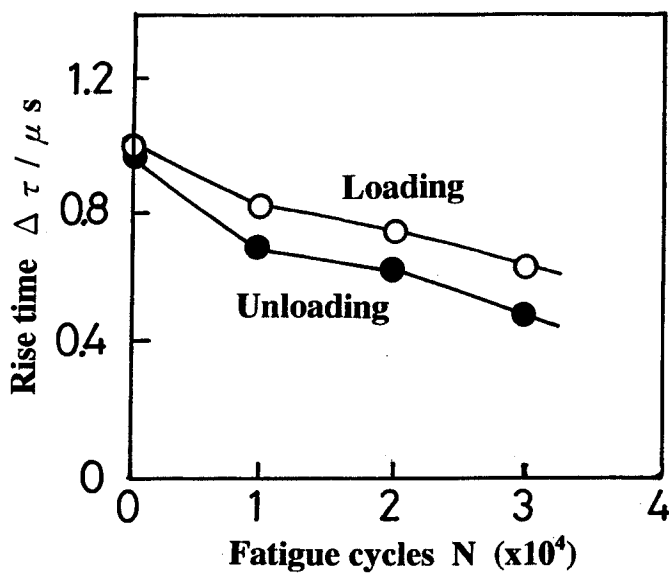


Fig. 8 Effect of mean source rise time on fatigue cycles in loading and unloading process. Mean source rise time was obtained by the acoustic emission wave analysis of Takashima et al. Decrease in mean source rise time corresponded to increase in growth rate of martensite plate of 310 to 500 m/s.

## Conclusions

Acoustic emission behavior during stress-induced martensitic transformation of Cu-Al-Ni shape-memory alloy single crystals, which exhibit super-elasticity, has been investigated using the smooth and notched specimens. Results obtained are as follows:

- (1) There is no effect of specimen volume on AE activity.
- (2) Sequential AE activity consisting of AE events, amplitude and waveforms in the smooth specimen is different from that in the notched specimen because of different stress concentration.
- (3) Acoustic emission method is effective to evaluate such dynamic processes as nucleation and growth of martensitic transformation.
- (4) It is possible to evaluate this type of material with fatigue damage using the acoustic emission waveform analysis.

## References

- 1) T. Saburi, C. M. Wayman, K. Takata and S. Nenno: Acta Metall., **28**(1980), 15-32.
- 2) K. Otsuka, C. M. Wayman, H. Sakamoto and K. Shimizu: Acta Metall., **24**(1976), 207-226.
- 3) R. F. Bunshah and R. F. Mehl: Trans. AIME, **197**(1953), 1251-1256.
- 4) T. Kakeshita, K. Shimizu, T. Maki and I. Tamura: Scripta Metall., **14**(1980), 1067-1070.
- 5) K. Takashima, Y. Higo and S. Nunomura: Phil. Mag., **49A**(1984), 231-241.
- 6) Z. Z. Yu and P. C. Clapp: Metall. Trans., **20A**(1989), 1601-1615.
- 7) K. Takashima, Y. Higo and S. Nunomura: Phil. Mag., **49A**(1984), 221-229.
- 8) K. Yoshida, H. Takagi and K. Sakamaki: J. JSNDI, **46-11**(1997), 821-829.
- 9) T. Ohira and T. Kishi: J. Japan Inst. Metals, **46-5**(1982), 515-525.

# THE IDENTIFICATION OF BASIC FATIGUE PARAMETERS ON ELECTRORESONANCE PULSATOR WITH HELP OF THE ACOUSTIC EMISSION TECHNOLOGY

Pavel MAZAL, Jiří PETRÁŠ – Brno University of Technology, Fac. of Mech. Engineering

Technická 2, CZ 616 69 Brno, Czech republic

## Abstract

*Exemples of chosen experimental results were introduced in the paper, that had been gained during the application of the technology of acoustic emission on the observing of fatigue failure of carbon steel and nodular cast iron with the surface treated by low temperature plasma nitriding. Gained parameters show that this non-destructive testing method is also suitable in the area of fatigue properties evaluation on the electro-resonance pulsators. Different types of AE data treatment are presented here.*

## 1. INTRODUCTION

One of the important research areas, which are being solved in the Institute of Design in BUT Brno is the problem of influencing of the fatigue limit and other fatigue parameters of materials by help of up-to-date surface treatment. Low-temperature plasma nitriding, oxinitriding, laser treatment of the surface etc. are examples of these treatments [1]. Electro-resonance testing machine RUMUL Cracktronic observes fatigue qualities of materials treated in this way. Technical solution of this pulsator makes possible only very restricted analyses of fatigue processes that really happen in loaded material.

Due to the fact that we have been dealing with the application of the acoustic emission technique (AET) in the area of contact loaded materials, we try to use this modern technology of non-destructive testing of damaged materials and constructions with such samples, that were loaded with classical fatigue on Rumul machine. First experimental results that proved the possibility to use AET for fatigue process observing on above mentioned pulsator have already been presented at the conference AE'99 [2]. First experiences have been deepened and the basic database of necessary AE parameters has been gradually created.

## 2. MATERIAL AND EXPERIMENTAL EQUIPMENT

In this paper, chosen results gained by cyclic loading of carbon steel ČSN 41 2060 (= C55) and nodular cast iron ČSN 42 2305 (= GJS-500-7), the surfaces of which have been treated by low temperature plasma nitriding (430°/26 hours) are introduced. By this heat treatment, the surface of material is saturated with nitrogen in gas atmosphere. The result of this quite complicated process is the appearance of very thin hard layer on the surface (so-called "white layer") and diffusion layers of various thickness (usually 0,2 – 0,3 mm – "dark layer"), that are gradually getting into basic structure. The example of metalographic cut of plasma nitrided nodular cast iron with appointed areas can be seen in figure 1.

By a number of materials, plasma nitriding causes important growth of microhardness and especially development of favourable pressure stress in surface layer. Fatigue limit of the material usually grows due to these changes. The area of so-called time fatigue limit is very important for common construction application. In this area, the moment of the initiation of microcracks and especially the length of following period of growth of fatigue crack is an important criterion. These parameters are very difficult to identify on electro-resonance loading equipment.

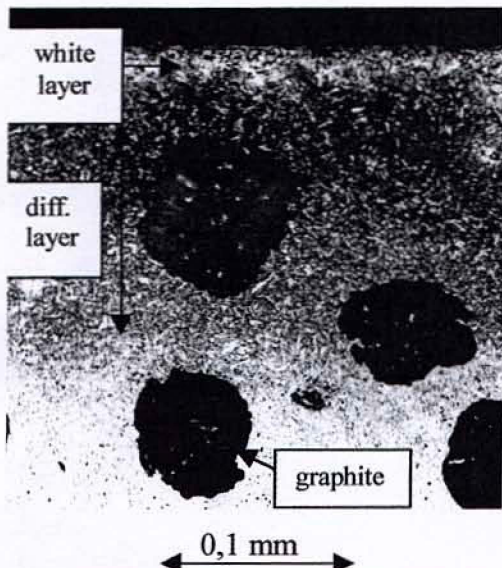


Fig.1 Example of tested plasma nitrided structure (nodular cast iron) (Nital)

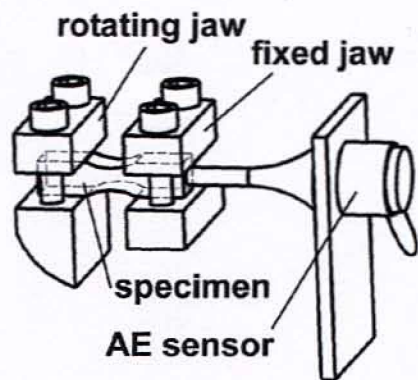


Fig. 2 Schematic illustration of fatigue test arrangement with AE sensing

Three types of AE analysers have been used for analysing of possibilities of distinguishing individual phases of fatigue process in our case. The process of testing itself was described in details in another paper [2]. Schematic illustration of fatigue tests arrangement with using of acoustic signal sensing can be seen in figure 2. The pulsator works in the area of flat four points bending with the frequency of loading about 130 - 150 kHz. Symmetric alternating loading cycle was used for all experiments. AE sensors with waveguide had to be used due to the limited size of samples.

### 3. EXAMPLES OF EXPERIMENTAL RESULTS

Samples of typical possibilities of AE signal processing in the area of fatigue loading are shown in following pictures.

In picture 3 there are summation curves, in which counts from the beginning of loading are gradually added. This curve can be drawn even for individual levels and gradual connecting of higher individual measured levels of the signal can be seen. Individual basic periods of fatigue process can usually be seen quite well on the curve.

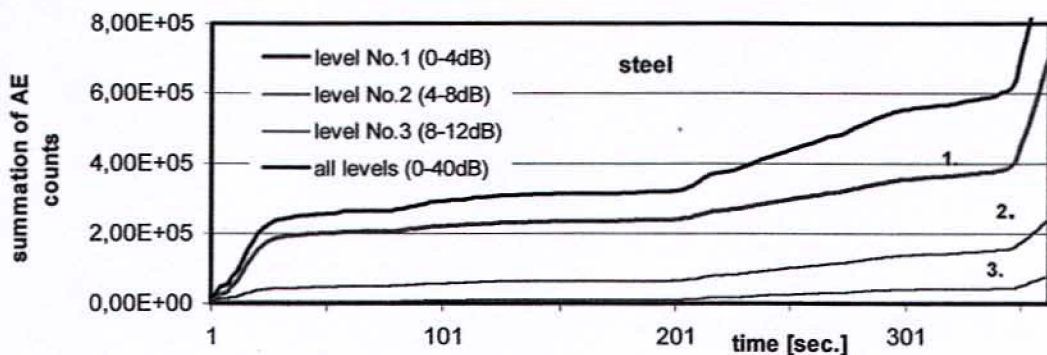


Fig.3 Records of total number of AE counts during fatigue loading in all levels and levels No. 1,2,3.

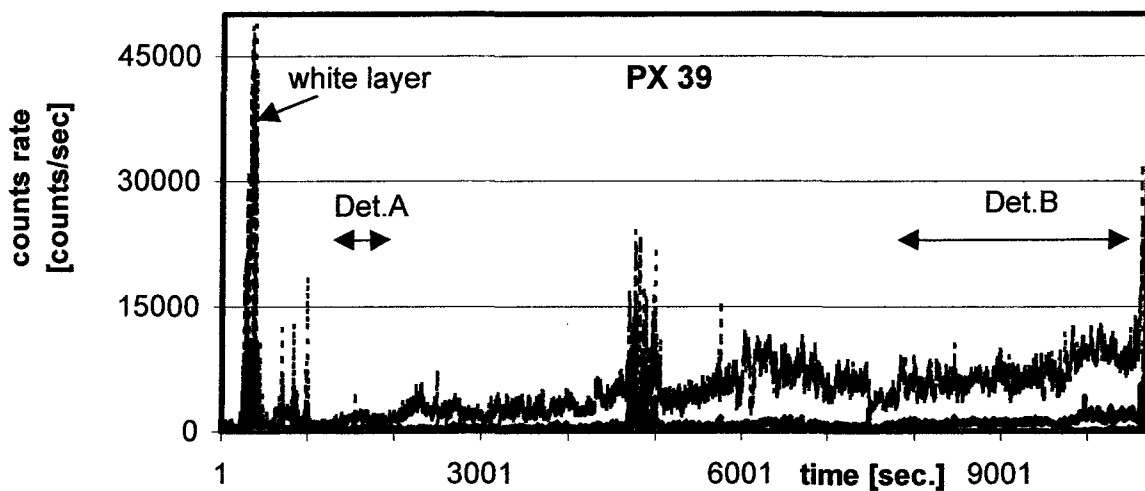


Fig. 4 Counts rate record in nodular cast iron in the whole process of fatigue test (AE 10C, levels 1-3)

Further possibility how to show acoustic activities in cyclic loaded material is its expressing by so called counts rate. In this case the number of counts measured in certain time period is drawn in graphic.

In picture 4 a record can be seen that was gained on nodular cast iron with surface treated by plasma nitriding. Mentioned sample was loaded in the area of so-called time fatigue limit (durability cca 150000 cycles). On the basis of quite detailed knowledge of behaviours of this material, we suppose that individual parts of the record can be interpreted as follows:

- 1) Slight softening of the whole volume of the material appears in the initial period (Fig.5).
- 2) Thin surface layer, which is very hard and fragile, cracks in case that the amplitude of loading is high enough. This process shows important growth of the number of recorded AE counts in the record.

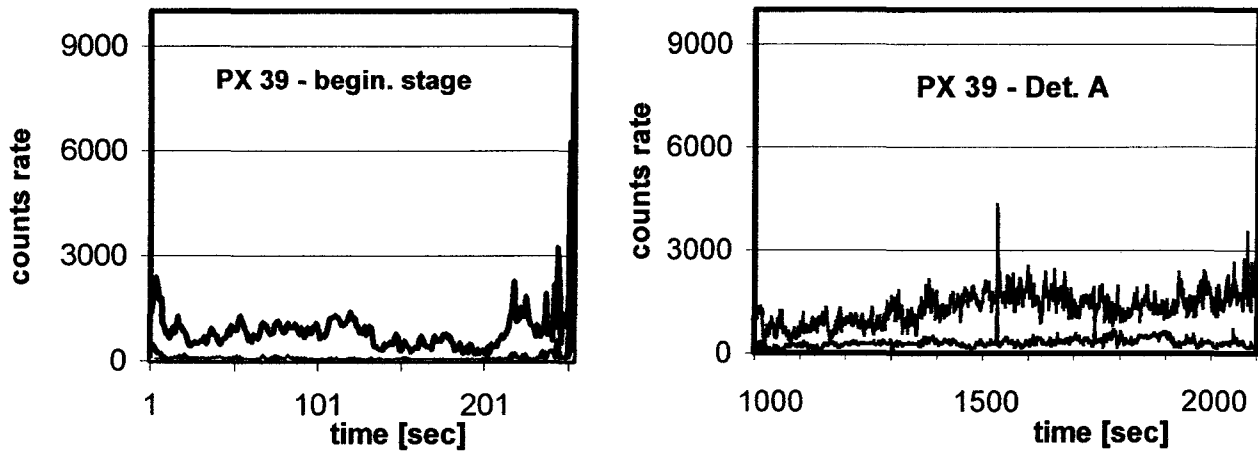


Fig.5 Detail of initial period of growth of fatigue crack in nodular cast iron - the area of crack of white layer (left) and following difficult spreading in nitrided layer (right) - Det A in Fig.4.

3) This obstacle is followed by comparatively quiet period in which damage in diffusion layer (dark layer) under the white layer is gradually cumulated. Due to the important oversaturation of the structure by nitrogen, quite high-pressure stresses appear, that restrict effective value of fatigue loading and, lower amplitudes of loading can stop spreading of fatigue cracks. Higher amplitudes cumulate sufficient energy cumulated for new re-starting of the whole fatigue process – Fig.5 - right.

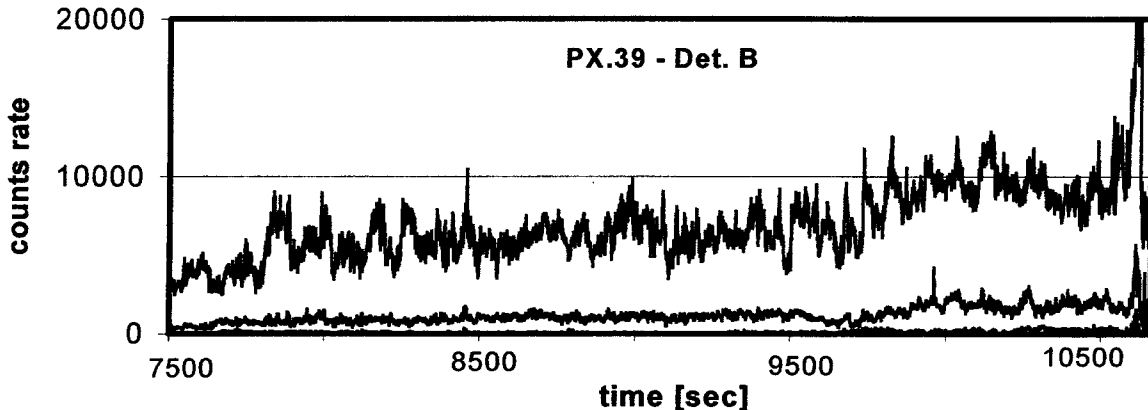


Fig.6 Counts rate in the last period of the fatigue test (nodular cast iron) – Det. B in Fig.4.

4) In the graphical dependence the releasing of energy and the beginning of spreading can be seen again. In the period of fatigue cracks spreading step shape of records can be seen by nodular cast iron. We suppose that this character of AE corresponds with jump damage of nodular cast iron. Fatigue cracks by its spreading do not grow regularly, but they gradually get over individual areas of basic material between graphitic globules and they are gradually connected into the only one main crack. Step character of AE records could correspond with these jumps.

The activity in higher levels is gradually being increased with the development of fatigue damage. It might be possible to get certain information for objective evaluation of the state of fatigue damage of material from so called histograms, in which AE activities in individual levels (mV) of recorded signal are observed.

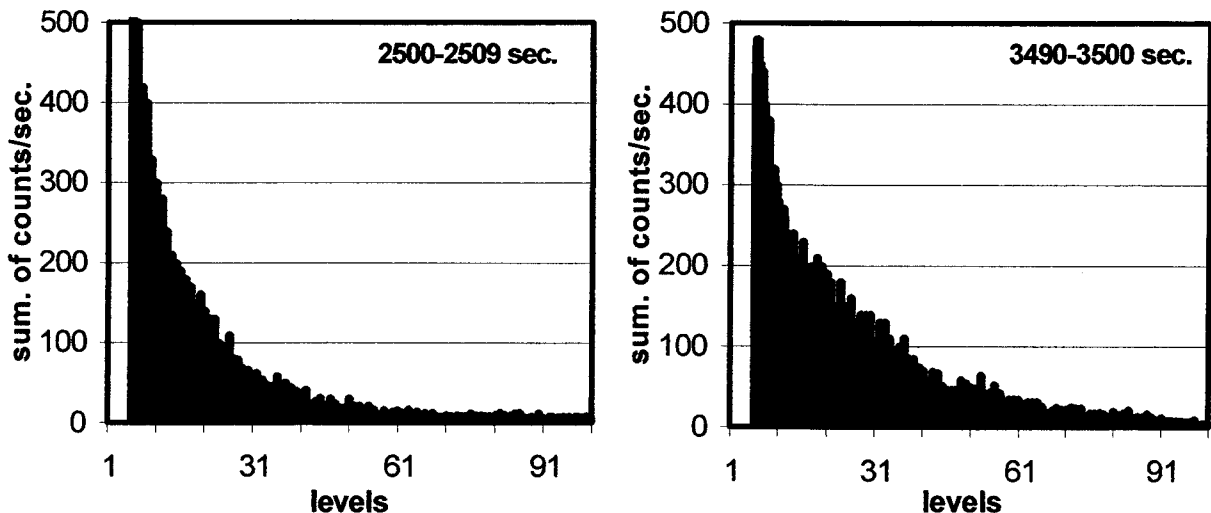


Fig.7 Typical amplitude distribution – histograms - from the different periods of fatigue loading (levels 1-100 = 0 – 800 mV) (analyser AED FTA4).

The shape of the AE events itself can be considered to be an important source of information about fatigue process in progress. Our up-to-date knowledge shows that it is possible to watch very important differences in the shape of the event in individual phases of fatigue process. Typical examples of characteristic shapes of this parameter are introduced in figure 8. To be able to make use of this characteristic it is necessary to gather much wider sets of information than those that are available up to now.

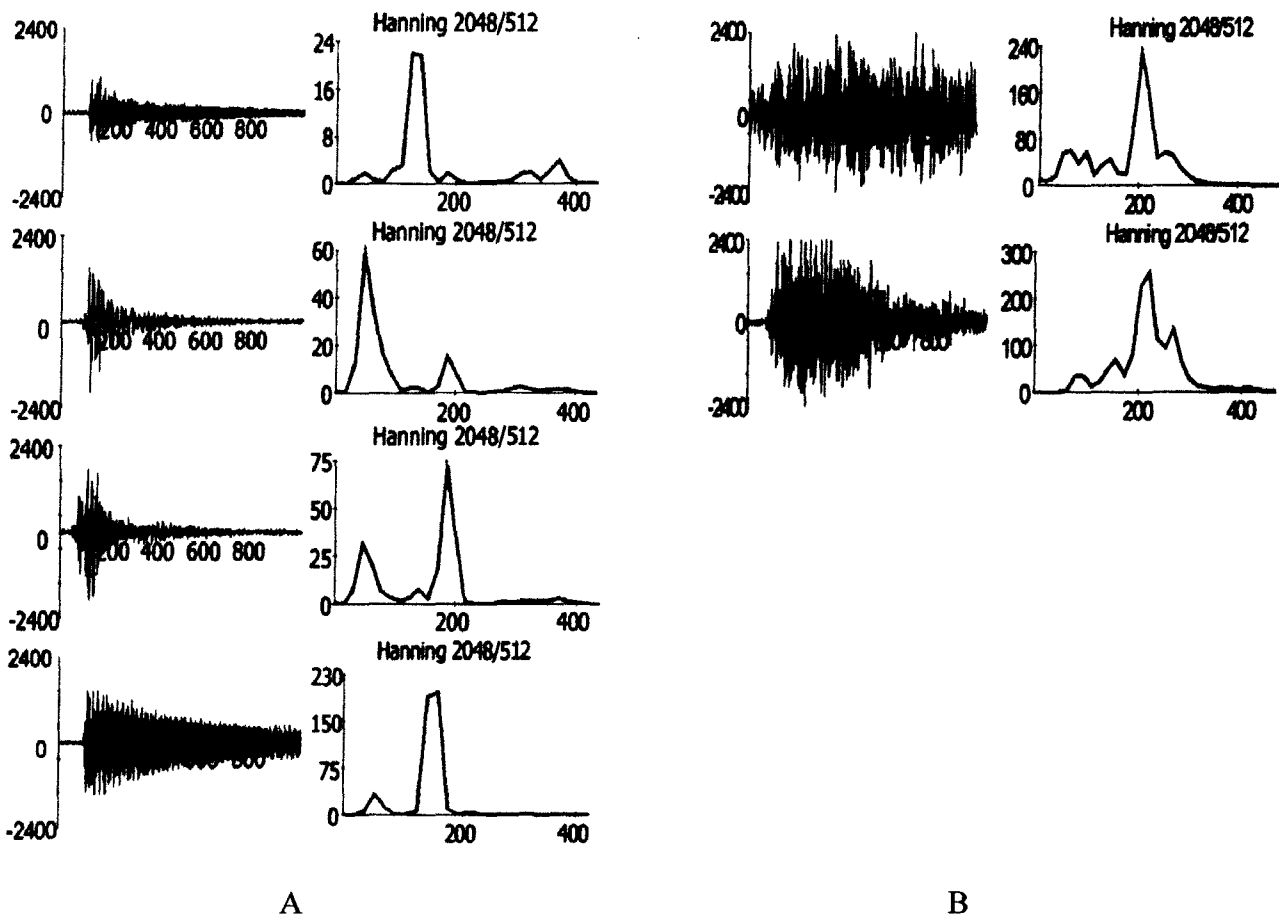


Fig.8 The shape of the typical events in initial area of fatigue loading and in the area of spreading of main fatigue crack (material A - carbon steel, material B - nodular cast iron) – coordinates: amplitude [mV] vs. time [μs], amplitude vs. frequency [kHz].

#### 4. DISCUSSION ABOUT RESULTS AND CONCLUSION

Introduced results of chosen typical ways of acoustic emission signal treatment show wide possibilities of application of this modern NDT method for the identification of fatigue process even on the electro-resonance fatigue testing machine. Mastering and automation of measuring with use of AE signal might enable more detailed analysis of cyclic process in quite complicated structural states, e.g. materials with various surface treatments.

The technology of acoustic emission makes possible observing of status in the whole loaded volume of material and it might enable observing of cracks that appear under the surface. These cracks are difficult to detect up to now. Precious working out of the process and mastering the elimination of undesirable influences to AE signal, it might enable to evaluate the intensity of initial softening, eventually hardening of material and especially, it might enable to identify the moment of the initiation of microcracks and the beginning of spreading of short cracks.

Processing of above-mentioned procedure will require a lot of experimental work and subsequent software processing of common trends. This work requires a lot of time and material. That is why it is recommendable to co-ordinate the work in this field on international level. We would appreciate any information about other places dealing with similar problem.

#### *Acknowledgements:*

*Work in this field have been made possible thanks to the support of Grant Agency CR - Grant project nr. 101/96/K264.*

#### **References et literature**

- 1) MAZAL,P.- STUCHLIK, J.- DLOUHÝ,I.: Fatigue properties of structural materials with plasma nitrided and lasered surfaces. In:11<sup>th</sup> Congres of IFHT, Florence, 1998, Vol.3, p.91-100.
- 2) MAZAL,P.- RICHTER,J.: Application of AET on fatigue testing machine Rumul. In: Acoustic Emission'99, Brno, 1999, p.157-164.
- 3) HUANG,M. et al: Using Acoustic Emission in Fatigue and Fracture Materials Research. JOM, Vol.50, No.11, November 1998, web page.
- 4) WEVERS,M. et al: The fatigue failure of steel wires monitored with acoustic emission. In: 23<sup>rd</sup> EC on AE testing, Vienna, p.114-119, TUV Austria, 1998.
- 5) LEE,C.S. et al: AE measurement of fatigue crack closure. Scripta Metall. et Mater., Vol.32, No5, pp.701-706, 1995.
- 6) SIEDLACZEK,J. et al.: AE of the 45HNMF structural steelduring Low Cycle fatigue. Journal of AE, Vol.10, No.3/4, p.1-11, 1992.

# THE PHASE OF CONTACT DAMAGE AND ITS DESCRIPTION BY HELP OF ACOUSTIC EMISSION

Jirí DVORÁCEK, Jirí PETRÁŠ, and Luboš PAZDERA  
Technical University of Brno, Brno, Czech Republic

## Abstract

*Characteristics of acoustic emission (AE) signal from individual phases of contact damage are explained in the contribution. The shape of AE signal by running-in and by permanent damage of the sample surface are described. Their comparison of emission duration, time of running-in, number of overshooting, maximum value of amplitude and energy of emission event is done on a sample of typical changes of AE signals in time. A sample of amplitude resolution of AE signal for individual phases of the test is shown. AE signal was sensed by testing of material resistance against contact fatigue on testing stations. The samples that underwent contact loading had been made of standard bearing steel. The contact was lubricated by plastic lubrication. AE signal was sensed and processed by 16-channel acoustic emission analyser AE FTA16. For the signal analyses, we selected not only the frequency analysis with utilisation of the Fourier transform, but the time-frequency transformation, the Wigner–Ville transform.*

## Experimental equipment

The experiments were done on the experimental testing stations Axmat. It is located in the laboratories of the Institute of Design of the VUT FSI in Brno. This equipment is designed for tests of bearing material resistance against the contact fatigue. Test principle consists in loading of a flat sample through layer of rotating balls by force, which develops contact stress of 5 GPa. The contact is lubricated by plastic lubricant. The test runs until when a permanent damage, so called pitting, occurs on the sample. This time is recorded and statistically evaluated. Sample surface deterioration process was observed by the introduction of the AE signal and its evaluation by a suitable mathematical system. In the contribution are presented results of sample from bearing material tests. The AE signal at a running-in and at a permanent surface damage is described.

## Theory

For the signal analyses, we selected not only the frequency analysis with utilisation of the Fourier transformation, but the time-frequency transformation of the Wigner–Ville transform. Calculation of the Wigner–Ville transform  $WV(\tau, f)$  is done by means of the correlation function by the integral relation:

$$WV(\tau, f) = \int x(t + \tau/2) \cdot x(t - \tau/2) \cdot \exp(-j2\pi ft) \cdot dt,$$

where  $\tau$  is the time parameter,

$f$  is the frequency parameter,

$x(t)$  is the signal being analysed.

This transform belongs among the basic time-frequency distribution, which is not limited by the Heisenberg's uncertainty relation. However its disadvantage is, similar to the Fourier transform, interference at the calculation and especially the necessary high calculation performance.

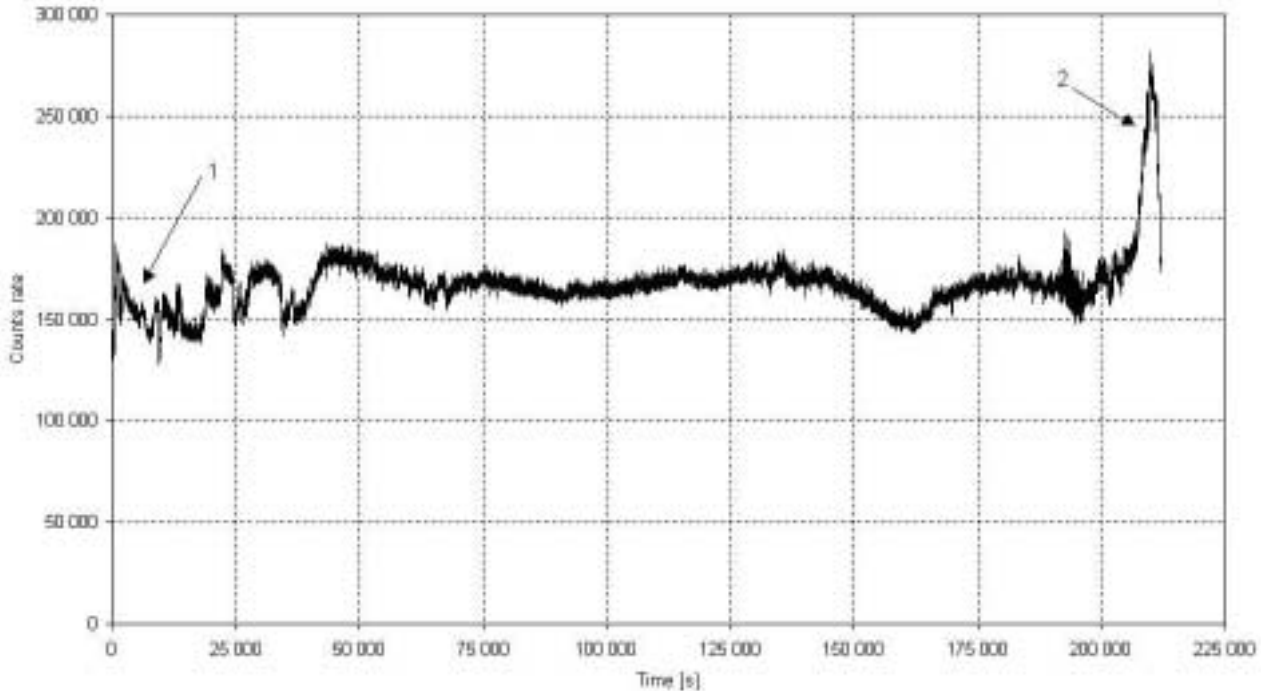


Fig. 1 History of AE

### Description of results

Experiment results are shown in the Figs. 1 to 11. In Fig. 1 is demonstrated the whole course of the test. AE count rates in 5 seconds intervals are recorded. In Fig. 1, areas 1 and 2 are marked out, from which were taken samples of the AE signals for further analysis. Signal analyses of the area 1 are introduced in Figs. 2, 4, 6, 8 and 10 and they are from the running-in phase. Signal analyses of the area 2 are shown in Figs. 3, 5, 7, 9 and 11. These are from the phase, where permanent surface damage occurred.

From the Wigner-Ville spectrum from the AE signal of the area 1, we find significant frequency, especially in the band around 1 MHz in time of about 20 to 30  $\mu$ s, and further around 2 MHz in time of about 5  $\mu$ s. This is in coincidence with both the frequency spectrum and the time change, where it may be the burst type of acoustic emission signal. The higher values in area over 2.5 MHz correspond probably an electric noise.

For the AE signal from the area 2 (Fig. 1), pitting occurred on the surface. By the Wigner-Ville spectrum, the most meaningful frequency range is estimated between 0.5 to 1.5 MHz and that in time intervals of about 15  $\mu$ s and further between 24 and 32  $\mu$ s. Here, in contrast with the previous spectrum, no apparent maxima over 2 MHz are found.

### Conclusion

The time-frequency transformation, Wigner-Ville transform, enables more complex view on the acoustic emission signals than the Fourier transform and time change. It significantly improves information about the acoustic emission signal.

## **Publications**

- 1) Mazal, P., Dvorácek J., Kolár, D.: *Determination of Contact Fatigue Properties by Acoustic Emission Technique*, 7th ECNDT, 1998, Copenhagen, Denmark.
- 2) Dvorácek J., Petrás J., Mazal P., Kolár, D.: *Acoustic Emission and Contact Properties of Surface Layers of Materials*, 23<sup>rd</sup> European Conference on AET, 1998, Wien.
- 3) Kolár, D., Mazal P., Dvorácek, J.: *Tribology characteristics and contact fatigue of structural steel and grey cast iron with laser and plasma nitrided surface in comparison with bearing steels*, 11th IFMT-4th ASM Europe, 1997, Paris.
- 4) Mazal, P., Kolár, D., Dvorácek J.: *Acoustic Emission Technique Utilisation for Pitting Observation of the Grey Cast Iron with Heat Treated Surface*, 11<sup>th</sup> IFMT - 4<sup>th</sup> ASM Europe, 1997, Paris.
- 5) Dvorácek J., Mazal P., Kolár, D.: *Diagnostic possibilities of contact loaded surfaces by Acoustic emission utilisation*, International science-technical conference „Machinery technology and rolling bearings '97“, 1997, KTU ŽU, Žilina.
- 6) Mazal P., Dvorácek J., Petrás J.: *Method and technique of Acoustic emission development in the Institute of Design of the Technical University in Brno*, Zborník referátov Medzinárodnej XXXVIII. konferencie katedier astí a mechanizmov strojov, 1997, SjF STU, Bratislava.
- 7) Mazal P., Dvorácek J., Petrás J.: *Acoustic emission at contact loading of grey iron with heat treated surface*, Quality and reliability of machines, 1997, KSS SPU, Nitra.
- 9) Mazal P., Dvorácek J., Kolár, D., Petrás J.: *Detection of the contact failure stage by Acoustic emission*, Defektoskopie 97, 1997, NDT, Praha.
- 10) Dvorácek J., Mazal P.: *Utilisation of the Acoustic Emission for Discovering of Material Pitting*. In: 4th Symp. DESIGN 96, 1996, University of Rijeka, Vol.1., Opatija, Croatia.
- 11) Mazal P., Dvorácek J., Petrás J., Dušek F.: *Experiences with AE10C device utilisation at contact fatigue tests*, Acoustic Emission 96, 1996, VUT, Brno.
- 12) Korenská M., Pazdera L., Smutný J., Weber Z.: *Application of Acoustic Emission Method on the Loaded Timber with Different Humidity Analysed by Wigner Spectrum*, CIB W 40 Meeting, proceedings, Czech Technical University, Faculty of Civil Engineering, Prague, August 30 – September 3, 1999, pp. 165-170.
- 13) Smutný J., Pazdera L.: *Philosophy of Measurement and Time-Frequency Analysis of Vibration from Railway Transport*, Railway Engineering '99, 2<sup>nd</sup> International Conference, London, UK, 25-26 May, 1999, (pp. 1-10) CD, ISBN 0-947644-39-3.

## **Acknowledgement**

The contribution was elaborated in frame of complex program of the GACR No. 101/96/K264 - Limit states of construction materials with utilisation of non-standard test methods. This research has been conducted at the Department of Physics as part of research project of Grant Agency Czech Republic GACR No. 103/97/P140.

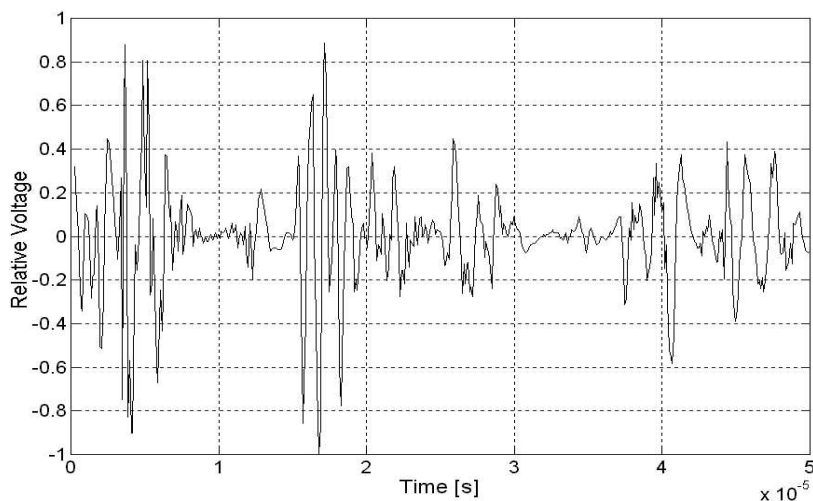


Fig. 2 Signal AE by running-in.

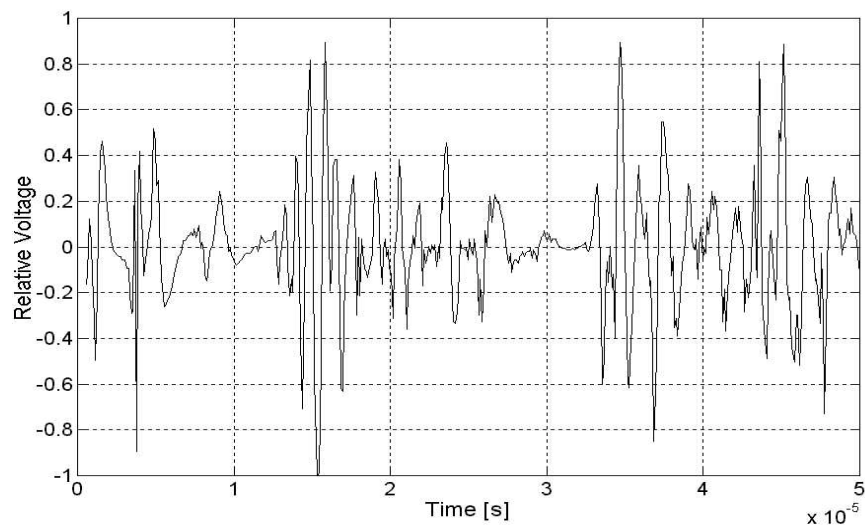


Fig. 3 Signal AE by permanent damage.

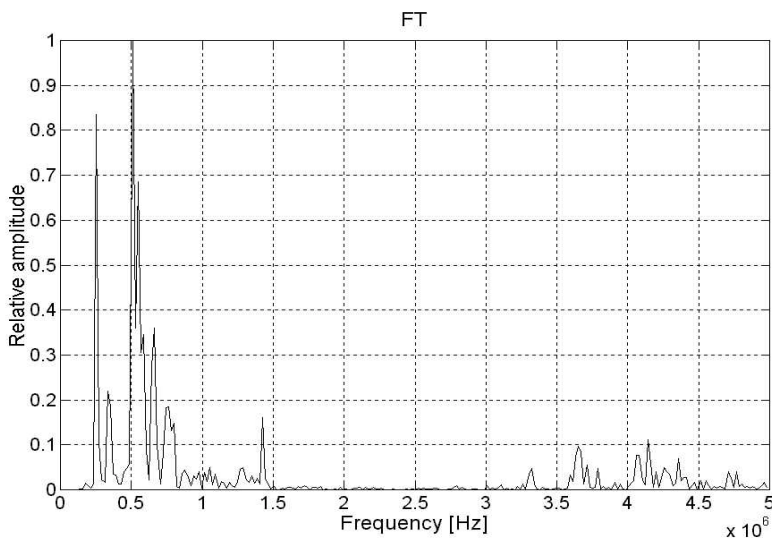


Fig. 4 Fourier transform of signal in Fig. 2.

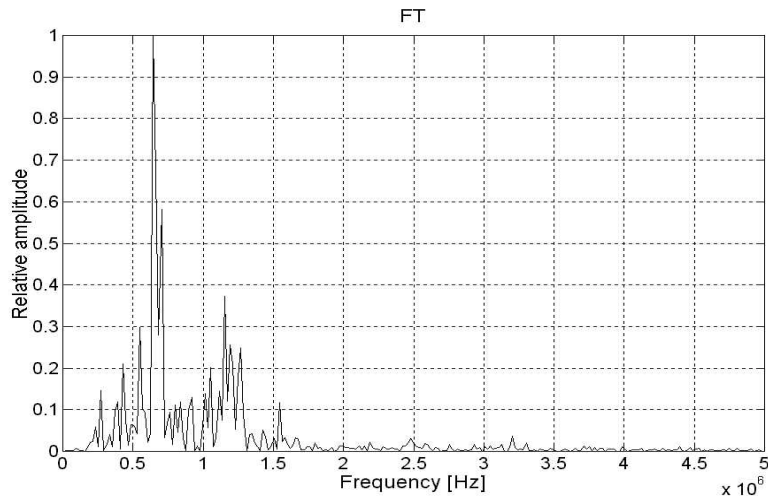


Fig. 5 Fourier transform of signal in Fig. 3.

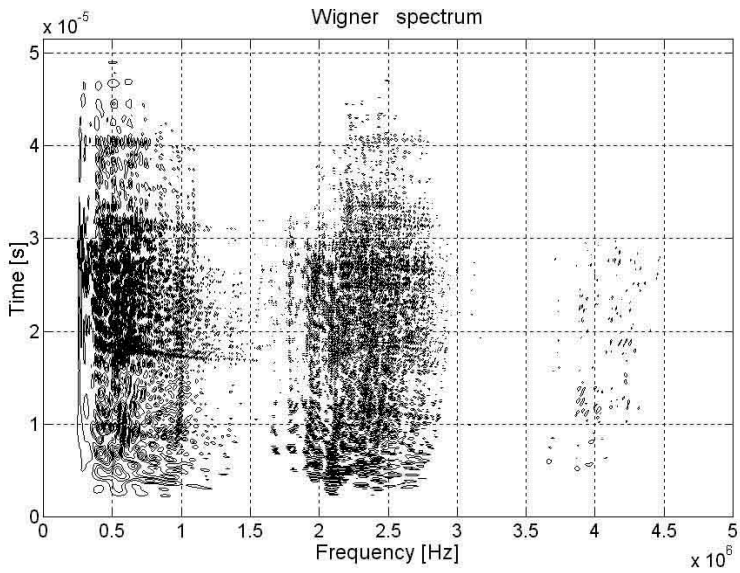


Fig. 6 Wigner-Ville spectrum contour graph.

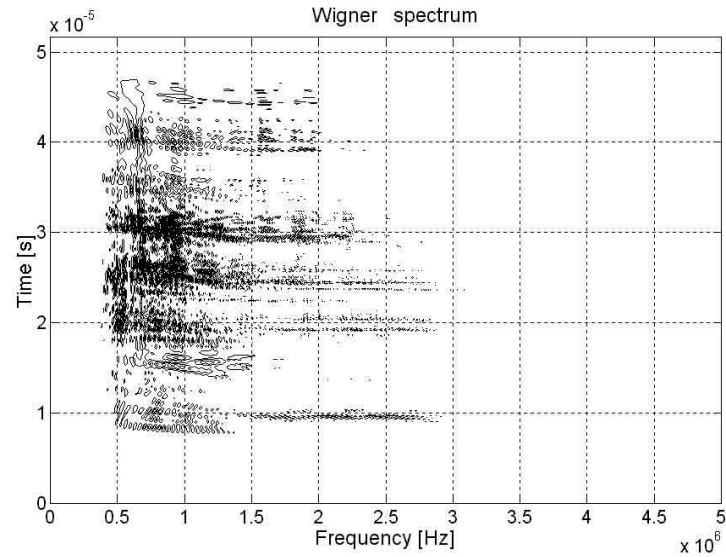


Fig. 7 Wigner-Ville spectrum contour graph.

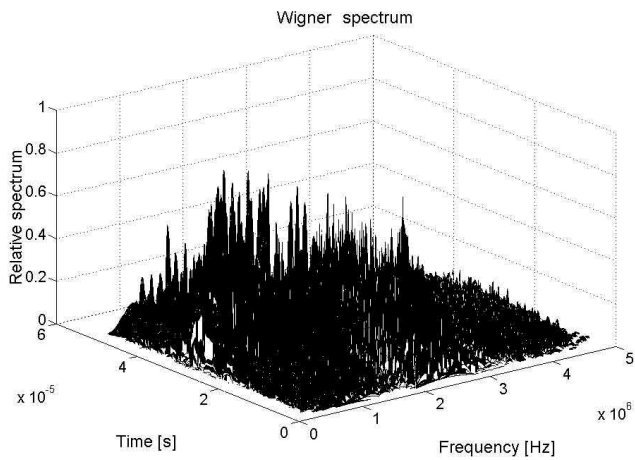


Fig. 8 Wigner spectrum 3D graph.

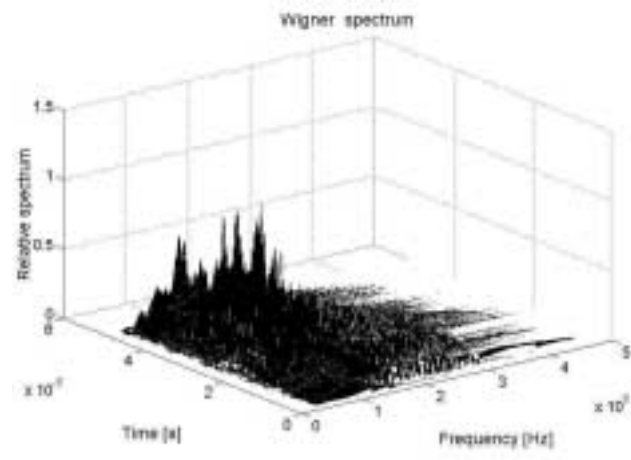


Fig. 9 Wigner spectrum 3D graph.

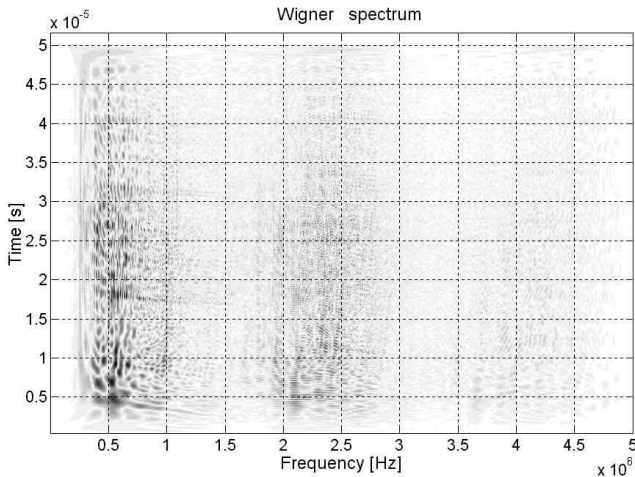


Fig. 10 Wigner spectrum image graph.

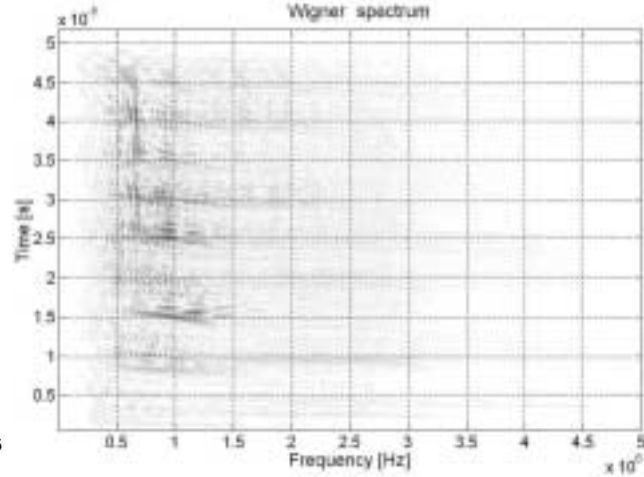


Fig. 11 Wigner spectrum image graph.

# ACOUSTIC EMISSION MONITORING OF HYDRIDE CRACKING IN ZIRCONIUM

A. BARRON and C. ROWLAND\*  
Bodcote, Daventry, UK and \*Pancom, Cambridge, UK

## ABSTRACT

*This paper describes the use of acoustic emission (AE) to detect the onset of delayed hydride cracking (DHC) in hydrogen damaged zirconium laboratory notched specimens. The onset of the DHC is an important factor in the integrity of an in-service component. The testing method described will help to quantify the number of cycles required to initiate the DHC and determine the critical section of the thermo-mechanical duty cycle, at which the DHC mechanism would initiate. The DHC mechanism and the experimental method of AE monitoring during thermo-mechanical cyclic loading are discussed. The development of on-line linear location via wave-guides proved to be vital to eliminate extraneous noise because of the test environment. The advantage of AE over the previous use of the DC potential drop technique is shown and the detection of DHC on the negative temperature slope of the thermo-mechanical cycle is demonstrated.*

## INTRODUCTION

### General Background

In service, zirconium alloy components may be subjected to loads induced from thermal warm-up and cool-down cycles, causing cyclic stresses and strains, which are potentially a significant factor for the integrity of these components due to the possible onset of delayed hydride cracking.

Zirconium alloy components can accumulate high levels of hydrogen pick-up during their service lifetime. In zirconium and its alloys, excess dissolved hydrogen precipitates as zirconium hydrides. These zirconium hydrides are brittle, and tend to precipitate preferentially at high stress points such as discontinuities or notches in stressed components subjected to thermal cycles. If failure of either the hydride or the hydride interface occurs the surrounding ductile material matrix will arrest crack growth. As hydride formation is enhanced by the application of stress, another and possibly larger hydride can then form at the newly generated crack tip. Further crack propagation can then occur, caused by this repeated hydride formation and failure cycle until total fracture of the component occurs. This mechanism of crack initiation and slow propagation is called delayed hydride cracking (DHC).

### The Hydride and Thermo-Mechanical Problem

As part of the design justification for DHC of certain zirconium alloy components, there is a need to characterise the hydride behaviour of the zirconium alloy material under simulated service conditions. To create a realistic, although worst case scenario, notched laboratory specimens were subjected to a thermo-mechanical cycle, which represents the major, and most damaging, events in the service cycle.

The definition of a thermo-mechanical cycle is when the stress intensity at a stress concentration changes simultaneously with the temperature. The combination of stress and temperature is the key factor. Hydrogen is concentrated by the stress field below the notch, and on cool down, hydrides precipitate locally in this area. These brittle hydrides can then be ruptured by either an increase in the stress intensity on cooling or by the local stresses applied as the brittle hydride phase precipitates.

Careful manipulation of the hydrogen level in the material and the thermo-mechanical cycle applied can hopefully mimic (in test specimens) the actual service conditions experienced when the material is in its deteriorated condition. A specially developed pulsed DC potential drop (DCPD) system had been used previously to monitor fatigue crack initiation on similar notched bend specimens under isothermal test conditions [1]. The early detection of hydride cracking, rather than fatigue cracking at its very initial stages, is essential if laboratory techniques are to be used in characterising the damaging thermo-mechanical hydride formation fracture process. The use of acoustic emission (AE) was therefore considered necessary as it was thought that the temperature changes in the thermo-mechanical cycles would render the potential drop technique impractical. There is also a possibility that the hydride cracking may initiate sub-surface, and of a localised nature, which would prove difficult to detect with DCPD.

## Literature Review

Work on material more susceptible to hydride precipitates [2] observed that the temperature at the onset of AE production during hydride formation in Nb, Ta and V was dependant upon the level of hydrogen concentration. It was concluded that the AE detected was due to cracking of precipitate particles rather than phase transformation or plastic deformation phenomena.

Investigation into brittle crack growth in metals [3] concluded that in some materials a one-to-one relationship exists between macroscopic crack movements and AE. A correlation was also derived between the amplitudes of the emissions and the energy release or size of the cracking event.

A study of stress corrosion cracking in high strength steels [4] used an electrical resistance technique (DCPD) and AE for simultaneous measurement of the stress corrosion cracking. No particular problems were highlighted in operating the two systems, although the testing was all performed at room temperature. The AE system was found to be more sensitive to the initiation of the stress corrosion cracking than the DCPD system and this was attributed to non-uniform crack propagation during the early stages of cracking. Initial cracking took the form of localised tunnelling, but eventually the crack front broadens across the test piece thickness and then propagates as a whole. As the DCPD technique effectively averages the crack length under its field of view it will therefore underestimate the length of the crack growth in the early stages. The AE technique, being sensitive to the elastic stress waves generated by the initial cracking, will therefore be better at detecting crack initiation in the brittle material.

Research work has been performed on the influence of hydrides on the ductile fracture of zirconium alloy [5]. Using AE techniques and static tension tests, two types of hydride induced embrittlement were identified. The first is the delayed hydride cracking process caused by stresses below the yield stress of the material and at comparatively low temperatures (<100°C). The other is the whole scale reduction of the alloy toughness due to the precipitation of a large number of hydride platelets. The fracture toughness ( $K_{IC}$ ) of the zirconium hydride was found to be  $1 \text{ MPa}\sqrt{\text{m}}$  at room temperature and  $3 - 4 \text{ MPa}\sqrt{\text{m}}$  at 300°C.

Fracture initiation studies on zirconium hydrides [6], again using AE and static tension tests, showed that if, at room temperature, the average hydride platelet length was in excess of approximately 50 - 100  $\mu\text{m}$  that a critical applied stress was the governing factor in the failure initiation of the hydride. Subsequent investigation [7] studied the initiation behaviour at elevated temperatures. Although the static tension tests performed in this study were under isothermal conditions this is the first reference to the use of AE at significant elevated temperature (300°C) to measure hydride cracking.

The results from the specimens showed that up to 100°C to 150°C cracking at the hydrides was initiated at slightly below the yield stress of the material. When the hydrides fractured, bursts of AE events occurred in large numbers. However, at higher temperatures, the hydrides were able to flow with the ductile matrix without cracking, and hence very few AE events were recorded.

All the reviewed work used AE techniques either at room temperature or at elevated isothermal conditions, recording cumulative AE data to display damage trend analysis. The work reported in this paper involves AE techniques to detect the individual failure initiation of reoriented hydrides, in notched specimens, using thermo-mechanical cycling to create a delayed hydride cracking mechanism

## OBJECTIVES

- To develop laboratory techniques to allow the AE activity from the initiation of delayed hydride crack formation in Zr-2.5Nb alloy to be detected during thermo-mechanical loading.
- To develop laboratory techniques to allow the simultaneous use of AE and DCPD crack detection techniques during thermo-mechanical loading.

## TEST ARRANGEMENT

The notch specimen (see Fig. 1) was loaded by a cantilever configuration and mounted in an insulated hot chamber. Wave-guides and the DCPD are attached to the specimen as shown in Fig. 3, showing the AE sensors outside the hot chamber. The heating method was a forced air circulation system, where heating and cooling rates of at least 1°C/min. was achieved to perform the thermo-mechanical cycle.

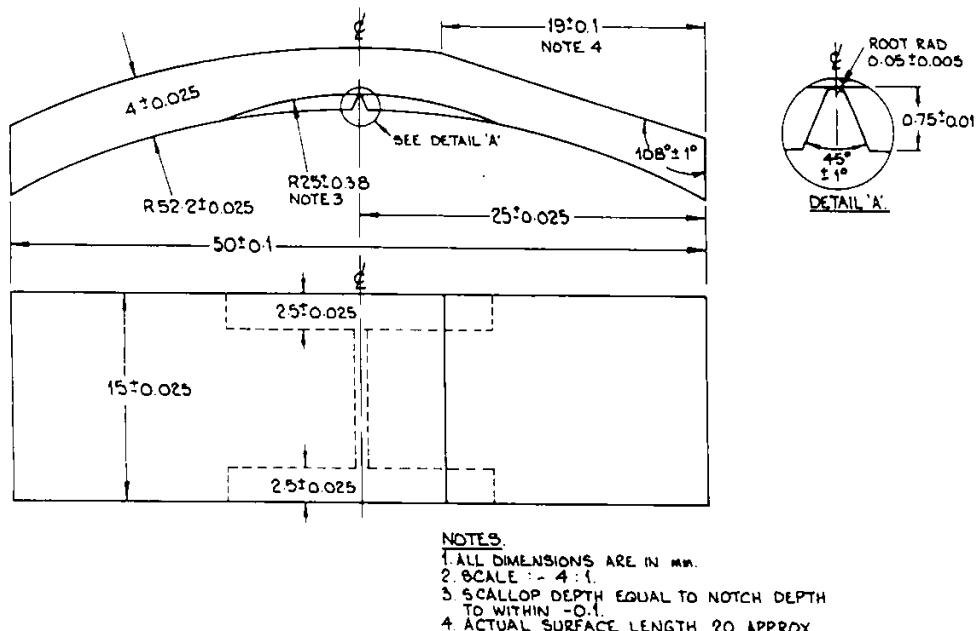


Fig. 1: Notch specimen.

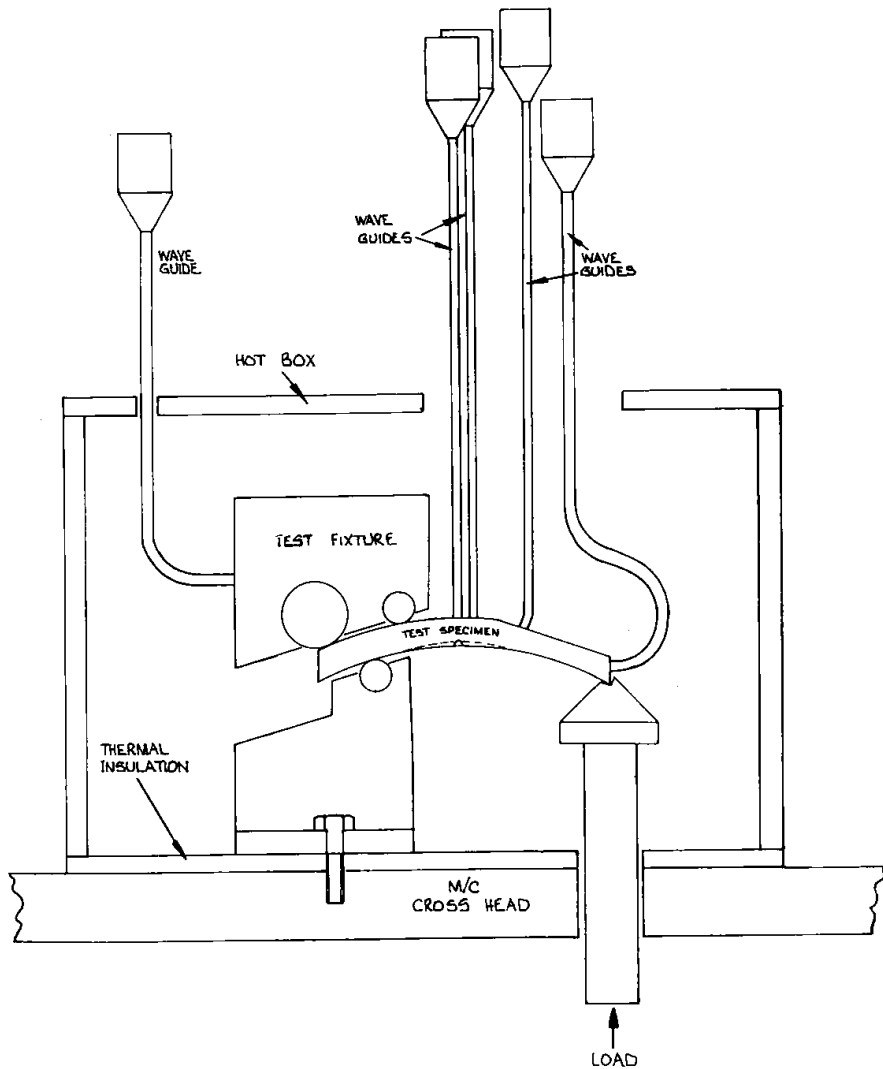
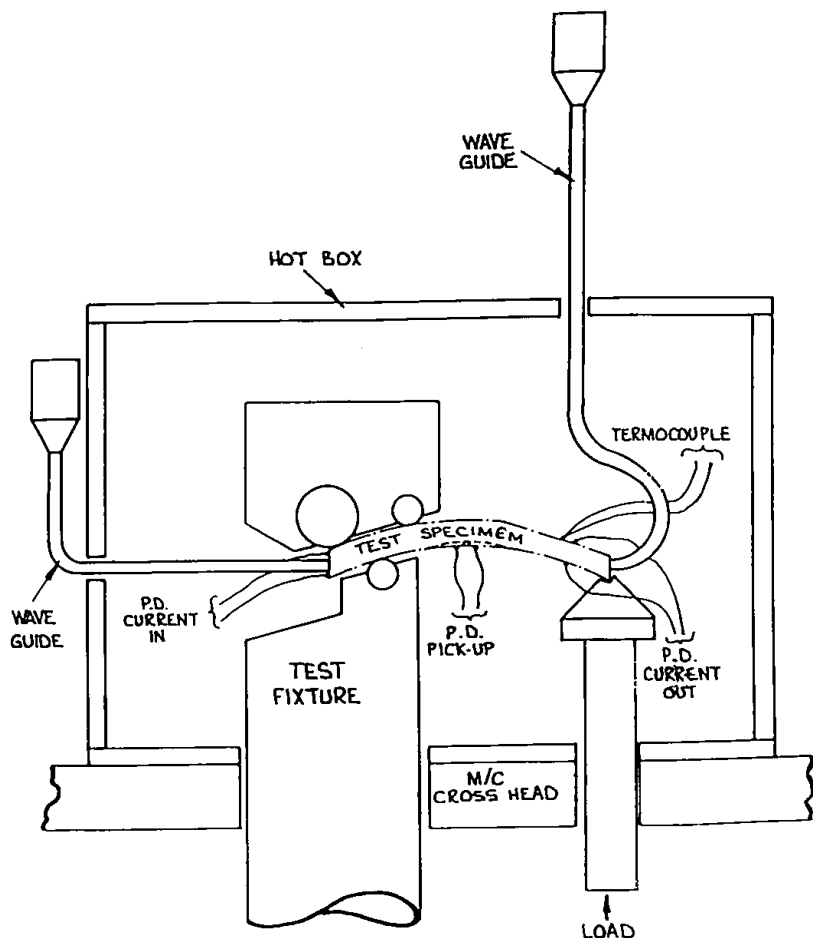


Fig. 2: Location calibration test rig.

The AE sensors (model Pancom P15W) are resonant at 150 kHz. To avoid coupling interface problems the element of the sensor is embedded into the conical head and was screwed on to the 6 mm mild steel wave-guide to provide easy removal and a consistent interface. Likewise the junctions of the specimen and wave-guide are also threaded joints. The AE system provided *on line location analysis* of the AE activity; this was very important because of the high background noise from the rollers, PD and thermocouple wiring, plus differential expansion activity at the test rig interfaces. The test arrangement was also designed with different lengths of wave-guides on either side of the test specimen. This arrangement was used to shift the null point of the specimen and wave guide assembly to some point remote to the notched area on the test sample, thereby any spurious electrical noise hitting both AE sensors simultaneously would then not resemble an AE event at the notch. To verify the ability to locate signals coming from the notch during the feasibility study, a calibration specimen was used which had three wave-guides directly attached to the specimen, see Fig. 2.

Two test parameters were fed to the Vallen AE instrument AMSY4; the load output from the servo hydraulic testing machine and the temperature from a 'K' type thermocouple, the latter being connected directly onto the specimen. The preamplifier gain was 34 dB and the threshold of AMSY4 set to 50 dB.



*Fig. 3: Test arrangement.*

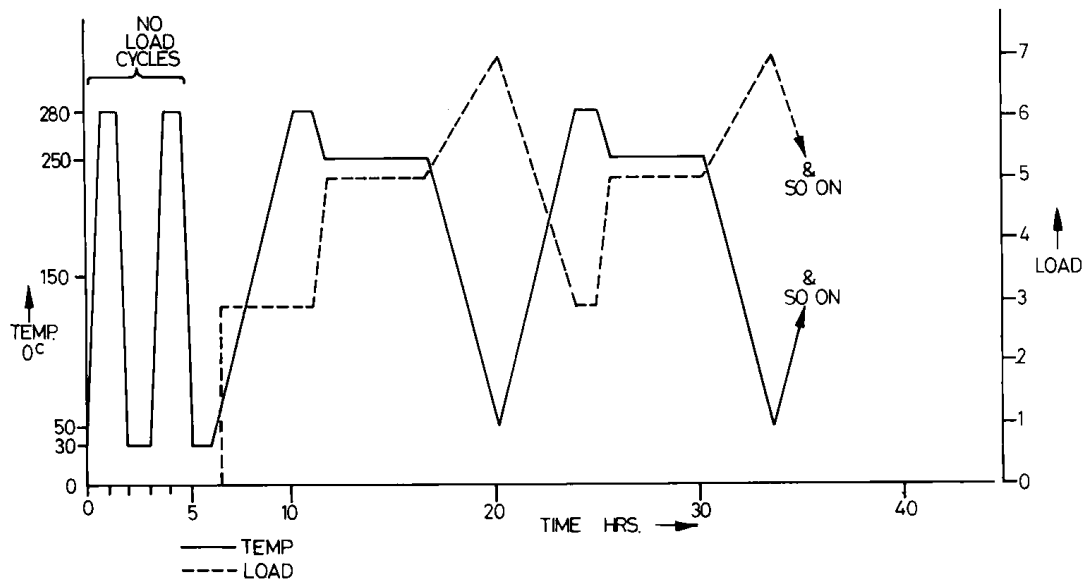


*Fig. 4: Thermo-mechanical cycles.*

A typical example of the thermo-mechanical cycle is shown in Fig. 4, noting the initial temperature cycles at no load to provide 'shakedown' of some of the mechanical elements in the system.

## RESULTS

Location calibrations were performed using pencil-lead breaks (2H, 0.7 mm diameter x 2 mm length) on the special external wave-guides (see Fig. 2), at room temperature and various elevated temperatures up to 290 °C. The results of the calibration showed that location could be obtained around the notch to an accuracy of  $\pm 6$  mm. This correlates well within the maximum theoretical accuracy expected when taking into consideration:

1. the depth of the specimen (4 mm)
2. the two different velocities of mild steel and zirconium.
3. wave mode changes introduced at the material/structure interfaces.

Sources of erroneous noise found during the initial thermo-mechanical trials included:

- a) the interface between the jig and the hot box.
- b) the high temperature ceramic based adhesive to secure the DCPD current pick up leads.
- c) wave-guide and specimen junctions
- d) reaction points of the specimen.

The noise from a) was greatly reduced by transferring the main rig reaction point outside the hot box, then it was not subjected to the thermal cycling as shown in Fig. 2. Extensively modifying the method by which the specimen wiring was restrained removed the noise condition of b). The remaining noise from c) and d) was overcome by using *on line linear location*, which allowed analysis of the data without stopping the test. Calibration using pencil-lead breaks were made at the beginning and the end of the test at the notch. A repeatability of  $\pm 4$  mm was obtained.

Initial trials using thermal cycling at a high constant load showed that the DCPD changed linearly with temperature at an approximate rate of 1  $\mu\text{V}/^\circ\text{C}$ . There was a correlation between the AE output characteristic of hydride failure and a change in the DCPD output. Although the DCPD system used was stable and sensitive (typically 5  $\mu\text{V}$  change for 50  $\mu\text{m}$  fatigue crack growth) it became apparent the AE was more sensitive, being able to detect isolated hydride failure.

The following results show a typical thermo-mechanical test. Figure 5 shows the total energy against the load and temperature applied to a specimen over nine full thermo-mechanical cycles. It can be seen from Fig. 5 that there are two main regions of AE activity;

- 1) combination of low temperature/high load and
- 2) combination of high temperature/ low load.

The result of filtering the data on those two criteria is shown in Figs. 6 and 7, respectively. Figure 6 shows that the cracking at the notch, occurring on the rising slope of the load and whilst the temperature is falling. Whilst from Fig. 7 there is no activity at the notch. All the data in Fig. 7 is erroneous noise from the reaction points and the wave-guide specimen interface, generally associated with fatigue cycling during the steady state section.

Hydride cracking was first found in the 4<sup>th</sup> cycle as shown by Fig. 8, with the load rising (196 N) and the temperature falling (100°C). This demonstrates the effectiveness of parametric filtering of the data, which enhanced the ability to show clearly an individual hydride cracking at the notch.

Performing a series of these tests has allowed the interaction of the crack tip stress intensity (K) and the number of cycles to the initiation of the DHC mechanism to be investigated. The critical section of the thermo-mechanical duty cycle, at which the DHC mechanism would initiate has also been identified.

## CONCLUSIONS

The background level of AE associated with temperature and load cycling was such that a twin sensor, linear location method of AE testing was necessary. The linear location method enabled AE activity from the notch area of the specimen to be distinguished from the rest of the AE activity. This linear location method was not sensitive to temperature cycling.

Two crack detection systems, AE and DCPD, were completely compatible. The instrumentation associated with each technique did not influence the results obtained from the other. This was achieved for thermo-mechanical cycling conditions. There is a high degree of confidence that an AE signature associated with hydride failure for this specimen configuration has been identified. This characteristic signature was found to be extremely repeatable.

The conventional DCPD technique failed to discriminate individual hydride failures and ultimately was unable to find small hydride cracking. The conclusion is that a stage has been reached when the AE system can detect hydride cracking, which cannot be found using conventional DCPD or metallurgical techniques.

The test program showed that manipulation of the crack-tip stress intensity during the thermo-mechanical cycle influenced the time to initiation of the DHC and the subsequent rate of DHC mechanism. Under static load conditions, the initiation of hydride failure was consistent with expected ductile-to-brittle transition temperature. The developed AE technique was able to establish the thermo-mechanical conditions, at which the DHC mechanism would initiate.

It can be concluded that this programme of development has produced an AE testing technique, which is capable of detecting the initial stages of spontaneous hydride cracking characteristic of the DHC. The sensitivity of the system is such that localised hydride failure can be detected at a stage not normally possible using existing techniques, which are compatible with thermo-mechanical cycling.

## REFERENCES

- [1] Bodycote Materials Testing Ltd, 1996, Isothermal Notched Fatigue Testing, Unpublished Report.
- [2] G. Cannelli and R. Cantelli, 1979, Acoustic Emission Stimulated by Hydride Formation in Niobium, Tantalum and Vanadium, *Advances in Acoustic Emission*, Dunhart Publ., Knoxville, Pages 330- 335.
- [3] J.C. Radon and A.A. Pollock, 1972, Acoustic Emission and Energy Transfer During Crack Propagation, *Engineering Fracture Mechanics*, 4, 295 - 310.
- [4] G. Green, P. McIntyre, 1981, A Study of Stress Corrosion Cracking in High Strength Steels Using Acoustic Emission Techniques, 5th International Conference on Fracture, *Advances in Fracture Research*, 4, 2049 - 2057.
- [5] S.A. Nikulin, M.A. Shtremel, V.G. Khanzhin, B.M. Fateev, V.A. Markelov, 1993, Influence of Hydrides on Ductile Fracture in the Zr-2.5 Nb Alloy, *Nuclear Science and Engineering*: 115, 193-204.
- [6] M.P. Puls, 1987, The Influence of Hydride Size and Matrix Strength on Fracture Initiation at Hydrides in Zirconium Alloys, *Metallurgical and Materials Transactions*, 19A, June 1988.
- [7] R. Choubey and M.P. Puls, 1993, Crack Initiation at Long Radial Hydrides in Zr-2.5Nb Pressure Tube Material at Elevated Temperatures, *Metallurgical and Materials Transactions*, 25A, May 1994.

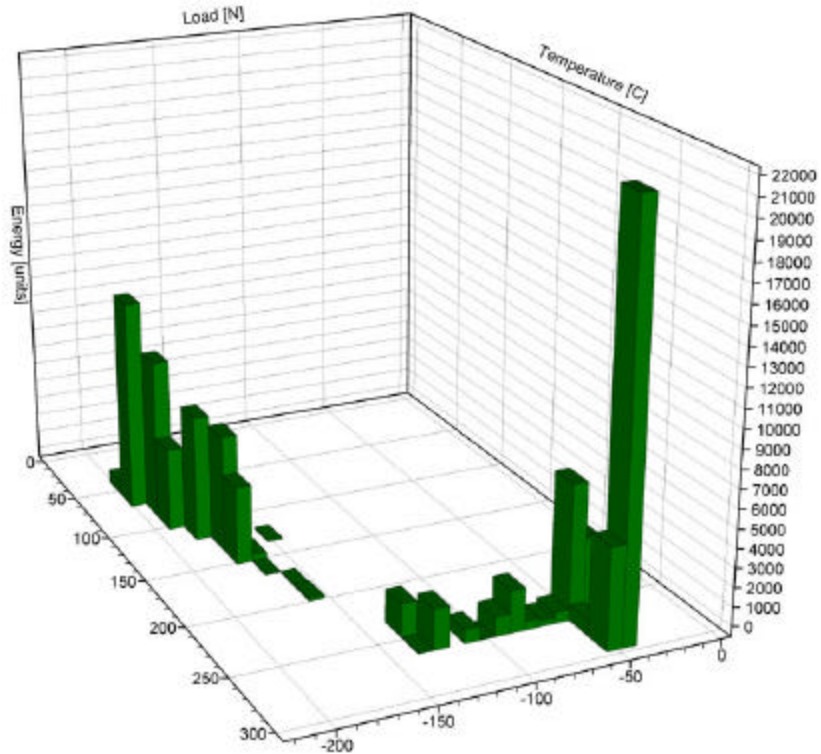


Fig. 5: Summation of AE energy from nine thermo-mechanical cycles, showing two regions of activity; 1) combination of low temp/high load & 2) combination of high temp/low load.

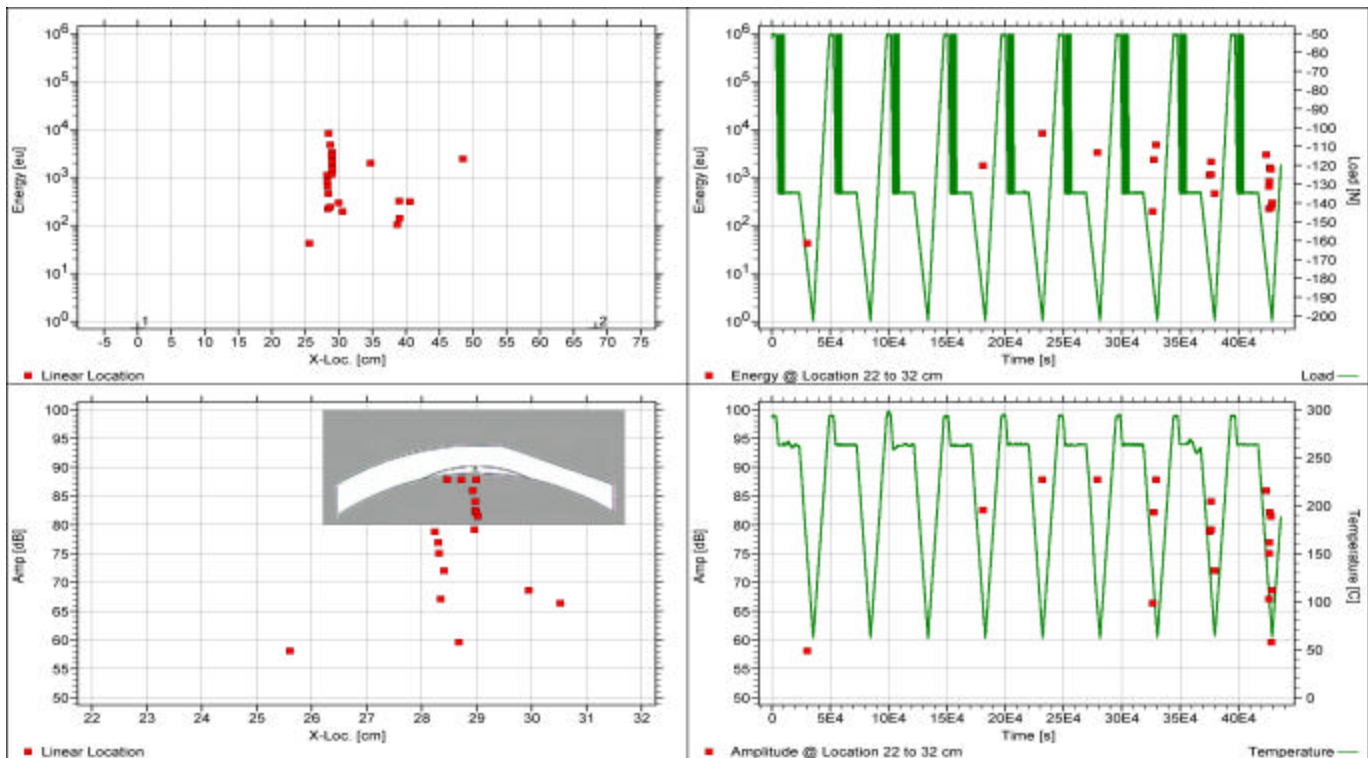
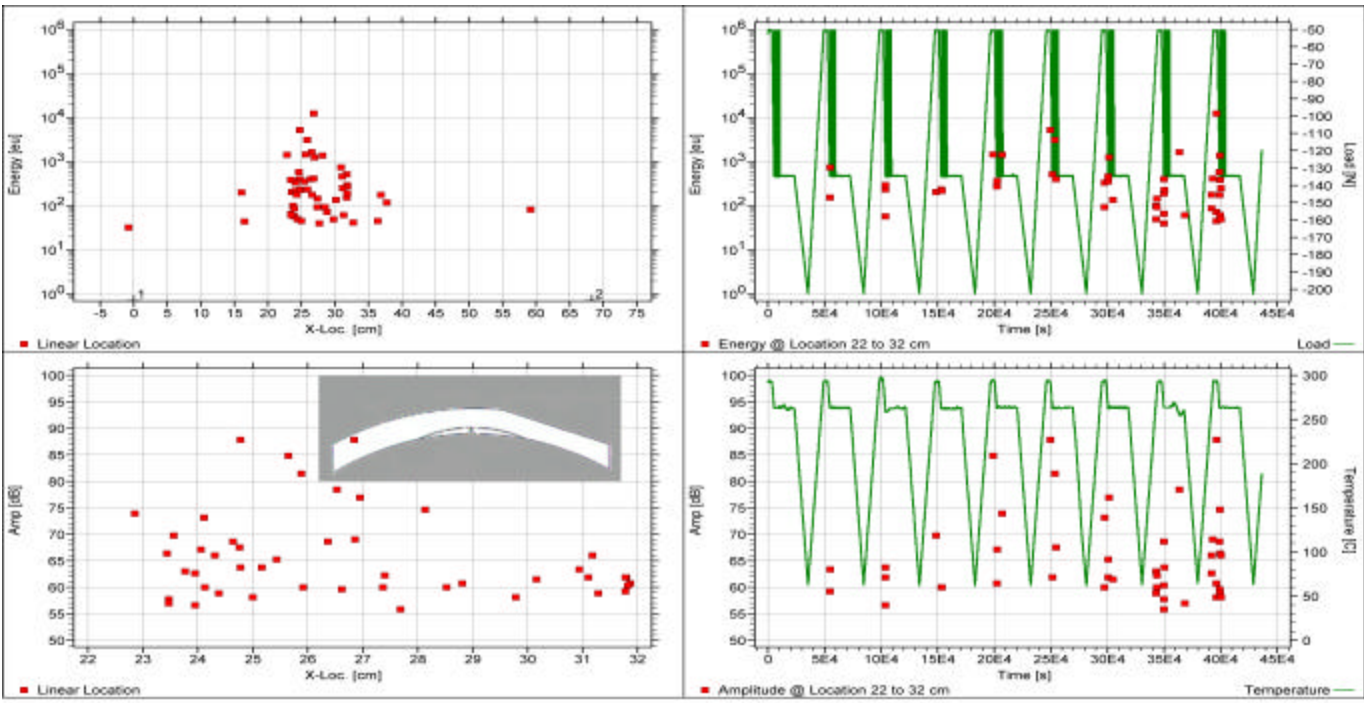
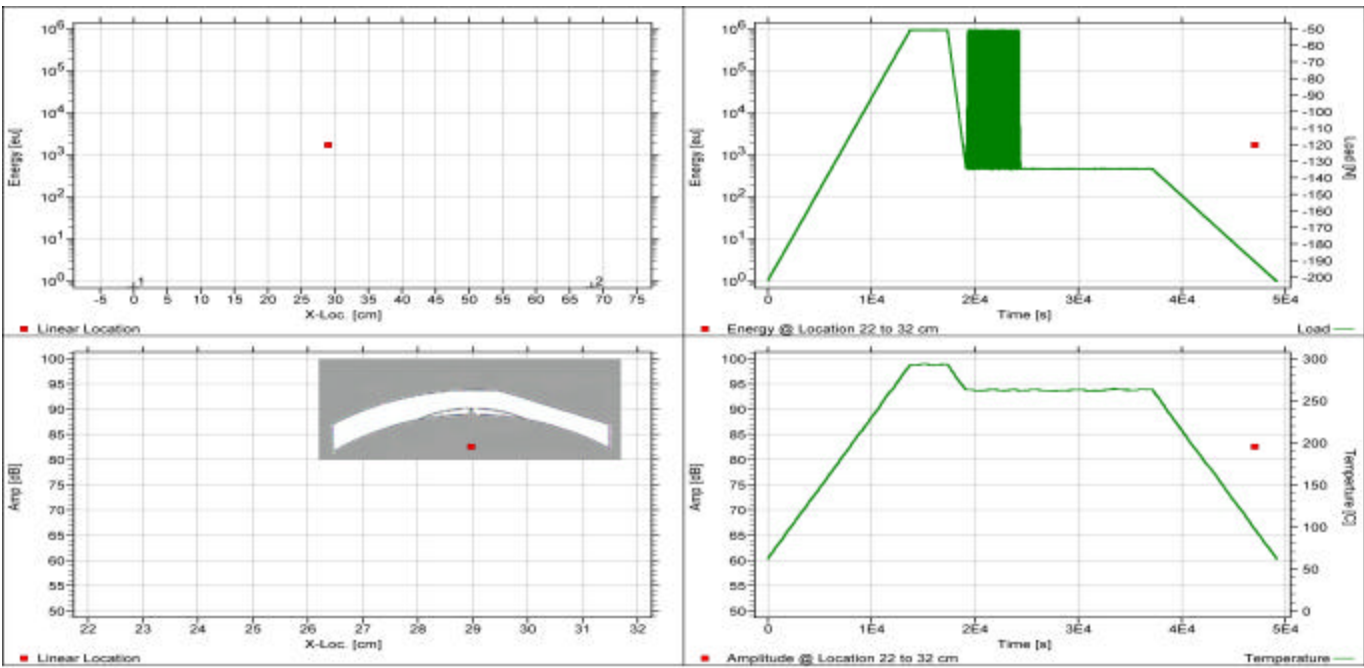


Fig. 6: Showing cracking at the notch with rising load and falling temperature.



*Fig. 7: Showing erroneous noise at low loads and high temperatures.*



*Fig. 8: Showing the initial crack at the notch during the fourth thermo-mechanical cycle.*

# **Examination of Plate Valve Behaviour in a Small Reciprocating Compressor using Acoustic Emission**

J.D. Gill, R.M. Douglas, Y.S. Neo, R.L. Reuben and J.A. Steel

Dept. of Mechanical and Chemical Engineering, Heriot-Watt University, Edinburgh. EH14 4AS.

## **SUMMARY**

*The gradual failure of compressor valves due to spring failure or damage to the valve face or seat can lead to loss of plant efficiency. It would be ideal for plant operators to be able to ascertain the condition of the valves on a continual basis to avoid expensive shutdowns or extremely conservative replacement procedures. The use of a non-intrusive detection technique, such as offered by acoustic emission, has proved to be the least influenced by machine resonances and other external sources of vibration. By examining the acoustic emission signal associated with the operation of the valves it has been possible to detect discernable differences resulting from changes in the condition of the valve.*

## **INTRODUCTION**

Compressors are, in theory, quite simple machines with few components to malfunction. The majority of compressors in operation today employ plate valves that open in response to the pressure in the compression chamber as opposed to a timed mechanical force. Whereas acoustic emission monitoring has been successfully applied to large compressors employing poppet valves [1] no work has yet been published on smaller compressors employing the more common plate-type valves. Common faults in such valves are delay in valve opening, fluttering of the valve while in the open position and delay in closing [2,3], each of which are associated with valve degradation or process conditions. The effective timing of valves has been regularly used to signify faults in the operation of compressors [4,5], but this requires the use of pressure measurements. A large percentage of industrial compressors in use today operate in hazardous environments and/or compress hazardous gases and so the use of intrusive sensors is not ideal as leakage of the gas into the atmosphere may occur, or a costly shutdown of the machine may be necessary to fit the transducer. Acceleration measurements have long been used to detect the condition of the compressor valves. However, it has been found that the signal recorded by a transducer mounted on the external surface of the compressor, is so affected by reverberation and dispersion that the signal is no longer recognizable as the originating force [3]. The use of acoustic emission monitoring, which utilises a much higher propagation frequency and across a much larger bandwidth tends to overcome this problem. This is because a great deal of the interference in the vibration signal is caused by low frequency structural resonances.

## **EXPERIMENTAL APPARATUS**

A series of tests were carried out on a Broom & Wade two cylinder, reciprocating compressor (Figure 1a), during which both acceleration and acoustic emission were monitored. Two Physical Acoustics D9203 acoustic emission transducers with outputs band-pass filtered between 0.1 and 1 MHz were mounted on the cylinder head studs (Figure 1b) using aluminium clamps which also allowed a Brüel & Kjaer 4334 accelerometer to be fitted in the same axis as the piston. The signals from the two acoustic emission sensors were fed through a signal conditioning unit which allowed the gain and averaging time (as required) to be adjusted. Both raw and RMS data was acquired with a shaft encoder signal to allow the signal to be re-sampled with respect to crank position. All calculations involving timing of mechanical events were averaged over ten cycles and all RMS measurements were sampled with an averaging time of 40 µs. A Kistler 6121A1 in-cylinder pressure transducer was also fitted to give detailed information on the behaviour of the valves during the tests.

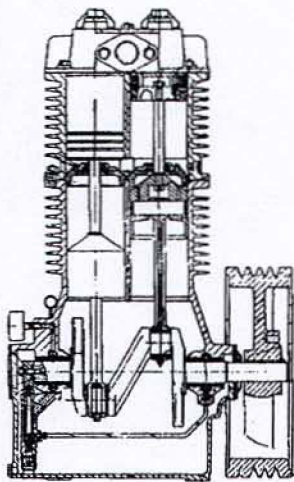


Figure 1a: Broom & Wade D41W Reciprocating Compressor Cross-Section

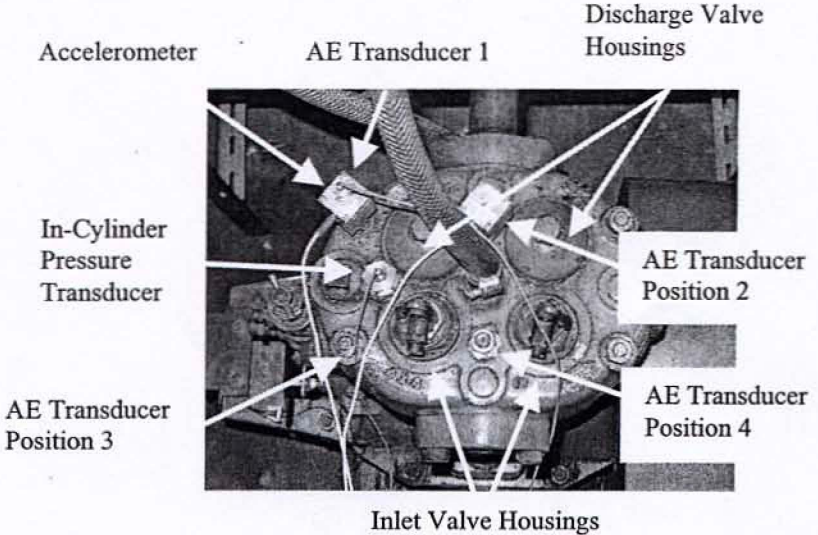


Figure 1b: Compressor Cylinder Head Set-up

Two discharge valve and one inlet valve conditions were examined to simulate; a damaged discharge valve seat face, a discharge valve sticking partially open as a result of the ingress of dirt into the system and progressive fatigue failure of the inlet valve spring. As the valve seat and face are both metal even the slightest damage to either face will cause gas to leak past the valve. The inlet and discharge valves are identical and consist of the valve seat and guard, two single-coil helical springs and the valve plate (Figure 2a).



Figure 2a: Valve Assembly

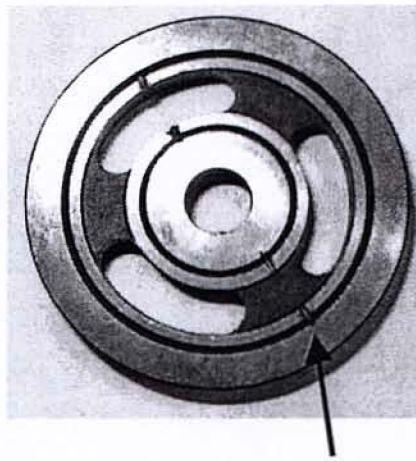


Figure 2b: Damaged Valve Seat

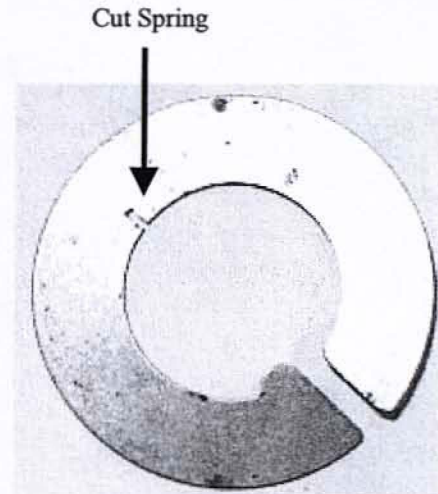


Figure 2c: Cut Valve Spring

The seat failure was simulated by introducing a small groove (Figure 2b) into the seat to allow gas to leak past the valve. The second experiment consisted of attaching a shim, 0.5mm in thickness, to the valve seat to prevent the valve from seating properly simulating foreign matter on the valve face. The

fatigue simulation consisted of gradually reducing the spring stiffness by introducing a series of cuts of varying depth into one or both of the springs (Figure 2c).

## NORMAL OPERATION

Figure 3a shows the behaviour of the valves and a p-V trace of a typical reciprocating compressor, and Figure 3b shows the RMS signal obtained from the acoustic emission sensor attached at position 1 (Figure 1b).

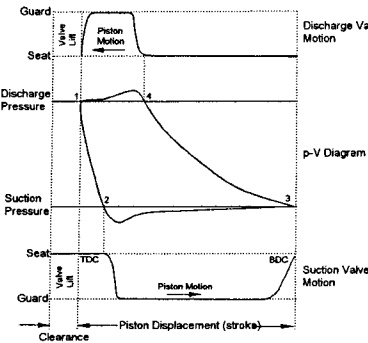


Figure 3a: Typical Reciprocating Compressor Behaviour

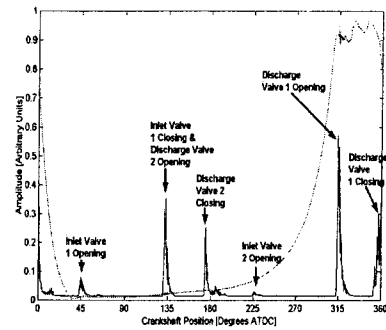


Figure 3b: Re-sampled RMS Normal Running AE Signal.  
AE Sensor Position 1 & Cylinder Pressure Trace

Superimposed on this is the in-cylinder pressure trace used to determine the general operation of the compressor. The large AE peaks with high rise time correspond to each of the main valve events, as labelled. The size of these peaks varies and, because of the timing of the mechanical events in the two cylinders, some AE peaks coincide

## FAULT CONDITIONS

The following sections describe the effects that each of the fault conditions has on the AE and pressure record of the compressor.

### Grooved Discharge Valve Seat

Figure 4a shows the cylinder pressure trace with the compressor operating with the damaged valve seat (Figure 2b) while Figure 4b shows the AE and pressure trace for the compressor operating with the damaged valve seat. The compressed air is discharged into a common manifold (i.e. both valves discharge into the same pipe), which is then allowed to discharge to atmosphere through a relief valve, maintaining a peak pressure (there are two peak pressure pulses in the cycle caused by each of the two cylinders) of approximately 8.6 bar in the manifold. As a result of this, when there is a fault causing the discharge valve not to seat correctly, pressure in the manifold will cause compressed air to leak back into the cylinder and also reduce slightly the pressure in the manifold. This effect has a number of influences on all valves on the compressor. The pressure differential between the inlet manifold (effectively atmospheric) and the cylinder pressure (directly related to the work done by the piston) is reduced. Therefore, more work is required by the piston to open the valve i.e. the valve opens later in the cycle. For the same reason, the inlet valve closes earlier in the cycle although this is masked in the acoustic emission record by the discharge valve in the adjacent cylinder closing. At bottom dead centre (BDC) and the beginning of the compression stroke the pressure in the cylinder should be approximately atmospheric. However, as a result of the poor seating of the valve, the pressure is marginally greater and steadily increasing as the pressure in the discharge manifold slowly leaks back into the cylinder.

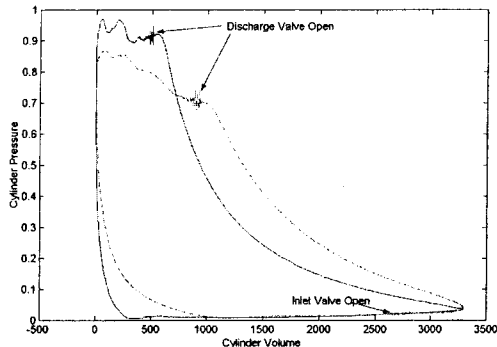


Figure 4a: p-V Diagram - Normal Operation (solid line)  
Damaged Seat (dashed line)

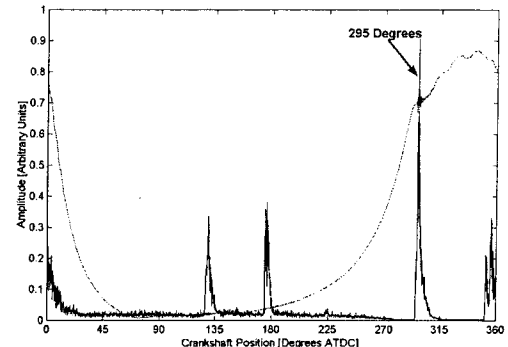


Figure 4b: Re-sampled rms AE & Cylinder Pressure Trace  
for Damaged Valve Seat (Sensor Position 1)

The air in the discharge manifold continues to leak into the cylinder until the piston has done enough work to overcome the pressure differential (between cylinder pressure and inlet manifold pressure) and open the discharge valve. This increase in the cylinder pressure by the leaking valve (and also the reduced pressure in the discharge manifold) causes the valve to open earlier in the cycle. The groove in the valve seat causing leakage into the cylinder causes an 11% reduction in peak pressure in the discharge manifold.

Using the acoustic emission signal it is possible to detect the change in timing of the discharge valve opening. In the case of the grooved valve seat the discharge valve opens at 295° as opposed to 312.5° for normal running. It is also possible to detect the valve opening time using the acceleration data. However, the acceleration data, although it detects mechanical events in the cycle (i.e. opening and closing of the valves) does not detect the fluid mechanical noise generated by the leaking of gas into the cylinder. This is seen in the AE signal as a high frequency portion beginning as soon as the discharge valve closes at approximately top dead centre (TDC). This low amplitude high frequency signal continues until approximately 270° after BDC when the cylinder pressure equals the pressure in the discharge manifold. At this point the flow of gas into the cylinder ceases.

### Unseated Discharge Valve Plate

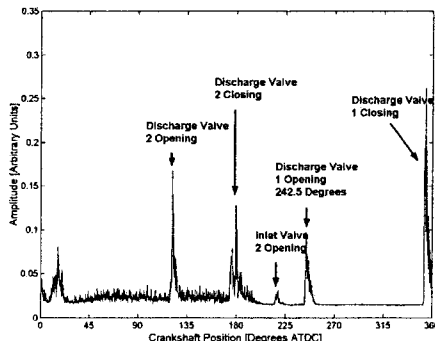


Figure 5: Re-sampled rms AE - Acquired from Position 1 with Valve Closing Fault

Figure 5 shows the AE signal acquired from position 1 (Figure 1b) with the shim attached to the valve seat. As can be seen the much more severe fault that prevents the valve from seating completely has caused the discharge valve opening point to be advanced to 242.5° (an advance of 70°). The high frequency content of the signal during the inlet stroke has increased in amplitude as a result of the greater flow of gas into the cylinder during this period of the stroke.

## Fatigued Inlet Valve Spring

Figure 6a shows the rms AE signal obtained from position 4 with a normal spring and a broken spring. The compressor is operating under no load conditions i.e. it is venting to atmosphere.

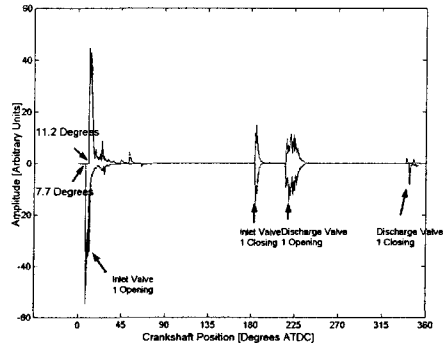


Figure 6a: Re-sampled rms AE Normal Running & Weakened Inlet Valve Spring (signal inverted)

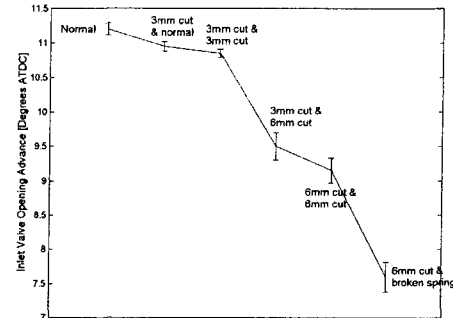


Figure 6b: Inlet Valve Opening Times versus Fault Condition

As the spring pressure is gradually weakened the compressor is required to do less work to overcome the inlet valve spring. Therefore, the valve opens earlier in the cycle (Figure 6b). However, this condition is only detectable under no load conditions. When the compressor is operating under load the cylinder pressure immediately after the discharge valve closes (i.e. approximately TDC) is marginally less than the discharge pressure. Therefore, the compressor has to do more work to open the inlet valve i.e. the piston has to move further down the suction stroke. At a working pressure of 8.6 bar the inlet valve opens at 45° after top dead centre (ATDC). At this point the piston is moving with a much greater velocity as a result of the reciprocating motion. This causes the valve to open more suddenly and therefore, it has not been possible to detect the change in spring stiffness while the compressor is under load. However, in larger machines, the behaviour has been found to be more akin to no-load conditions in terms of the inlet valve opening timing. Therefore, it is expected that it would be possible to detect weakened springs on large industrial machines under load conditions.

## Valve Flutter

The final experiment involved reducing the speed of the compressor to induce valve flutter. Valve flutter damages both the valve spring and, in particular, the valve face and seat, due to the increased

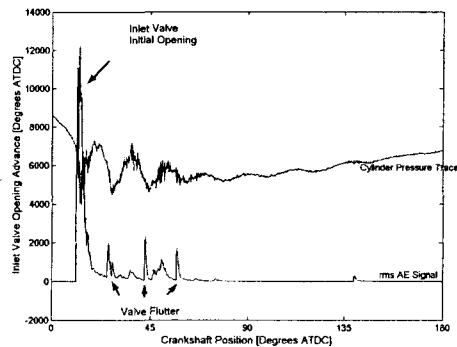


Figure 7: Re-sampled rms AE & Cylinder Pressure Trace with Inlet Valve Flutter

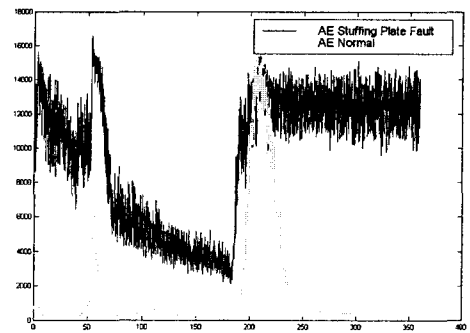


Figure 8: Ethylene Compressor rms AE Trace – Normal Running & Stuffing Box Gas Leakage

number of impacts. Figure 7 shows the effect that this has on the AE signal. As can be seen in the pressure signal the valve opens and closes a number of times after initial opening. This is clearly detected in the AE signal as three pulses.

## CONCLUSIONS

Acoustic emission has been demonstrated to be a suitable replacement for cylinder pressure measurements for cases where the environment will not permit such measurements to be made. It has proved capable of detecting the mechanical operation of the valves on a small, two-cylinder compressor. Furthermore, it has been shown that, whereas vibration measurement can only detect mechanical events [3], acoustic emission measurements can be utilised to detect gas flow within the compressor. This has already been shown to be useful on a much larger scale [1]. Measurements (reported elsewhere) have been made on a large, two-stage, horizontally opposed reciprocating compressor used to boost the pressure of ethylene from 260 barg to 3200 barg. Although this machine was fitted with poppet valves as opposed to plate valves, the AE response due to gas leakage shows very similar characteristics to those observed here. The compressor was found to have ethylene leaking past the stuffing plate into the sump of the machine. This was detected using the acoustic emission as a prolonged high frequency burst (Figure 8), although in this case the amplitude was much greater because of the increased working pressure.

Work is still being carried out on the Broom & Wade compressor with further work required to gain a full understanding of the effect that various faults have on the acoustic emission signal. However, it would appear that, at present, it is possible to detect certain faults that could not be directly detected using vibration data. It is also possible to detect the faults that can be detected with vibration measurements with greater confidence.

## ACKNOWLEDGEMENTS

The authors gratefully acknowledge the funding provided by the EC under its Brite-Euram programme, Project number BE96 3491.

## REFERENCES

- [1] Gill, J.D. *et al. Monitoring of a Large Reciprocating Compressor. Condition Monitoring and Diagnostic Engineering Management (COMADEM) '98.* 1 pp. 317-326, 1998
- [2] Matsumura, M. *et al. Behavior and Analysis of Reciprocating Compressor Valve. Kobelco Technology Review.* 14 pp. 20-24
- [3] McCarthy, D.J. and Lyon, R.H. *Recovery of Impact Signatures in Machine Structures Mechanical Systems and Signal Processing.* 9(5), 1995, pp. 465-483
- [4] Wang, D. S. and Pin, L. *Vibrational Analysis of the Motion Process of Compressor Ring-Valve Plates. Purdue Compressor Engineering,* Lafayette, Jul 1984, pp. 203-217
- [5] Li, C. J. and Yu, X. *High Pressure Air Compressor Valve Fault Diagnosis using Feedforward Neural Networks. ASME: Winter Annual Meeting,* New Orleans, 1993, pp. 375-380 (ASME: Manufacturing Science and Engineering).

# A NEW METHOD OF AE SOURCE LOCATION IN PIPES USING CYLINDRICAL GUIDED WAVES

Hideo NISHINO, Fukutoshi UCHIDA, Sunao TAKASHINA  
Mikio TAKEMOTO and Kanji ONO\*

Faculty of Science and Engineering, Aoyama Gakuin Univ., Setagaya, Tokyo JAPAN

\*Dept. Materials Science and Engineering, UCLA, CA, USA

## SUMMARY

We have developed a novel location method of damage in a pipe using cylindrical guided waves detected by a single AE sensor mounted on the pipe. For the source location in the axial direction, we use arrival time difference between  $L(0, 1)$  and  $F(1, 1)$  modes at a certain frequency, extracted by wavelet transform. The locations in an aluminum pipe are identified within an average error of 5% for wave propagating distance of up to 500 mm. For location along circumferential direction, we utilize both the amplitude and phase information of  $L(0, 1)$  and  $F(1, 1)$  modes. A good relation between the amplitude ratio of  $L(0, 1)$  and  $F(1, 1)$  modes and the circumferential source position is shown.

## I. INTRODUCTION

Analysis of guided waves in a hollow cylinder poses much difficulty due to the complex circumferential modes in comparison to plate (Lamb) waves. Gazis [1] first provided the theoretical background of cylindrical guided waves (cylinder waves). Three modes of the cylinder waves are Longitudinal (L-), Flexural (F-) and Torsional (T-). Experimentally, Fitch [2] first generated and verified the dispersion of L- and lowest F-modes using a pair of piezoelectric sensors. Several studies have been attempted since utilizing the unique characteristics of a low energy leakage of the cylinder waves. Long range interrogation of pipes was attempted by using cylinder wave techniques [3-5]. Selective generation of a specific mode of the cylinder wave was applied by Alleyne et al. [6] for nondestructive testing of piping in chemical plant. They reported that the cylinder wave can propagate several tens of meters in a 76-mm steel pipe. Rose et al presented [7] analysis of the cylinder wave attenuation due to energy leakage into liquid around a steam generator tube. Our group made quantitative analysis of guided waves to determine the location and dynamics of environmental assisted cracking in metallic rod [8].

We propose here a novel source location method of AE signals from pipe damage. The method can obtain the source location of AE signals propagating as cylinder waves. The AE signals are monitored by a single AE sensor mounted at the end of the pipe. First, we estimate the source location along the axial direction using the arrival time difference of  $L(0, 1)$  and  $F(1, 1)$  modes. For source location along circumferential direction, their amplitude and phase information was used.

## II. GUIDED WAVES IN A HOLLOW CYLINDER

We introduce the vibration mode and velocity dispersion of the cylinder wave. Phase velocity of the cylinder wave is computed from the characteristic equation, in a 6x6 matrix form derived from the wave equation in the cylindrical coordinates with the stress free boundary condition at the inner and outer surfaces [1]. Vibration modes are Longitudinal (L-), Flexural (F-) and Torsional (T-) modes. These modes

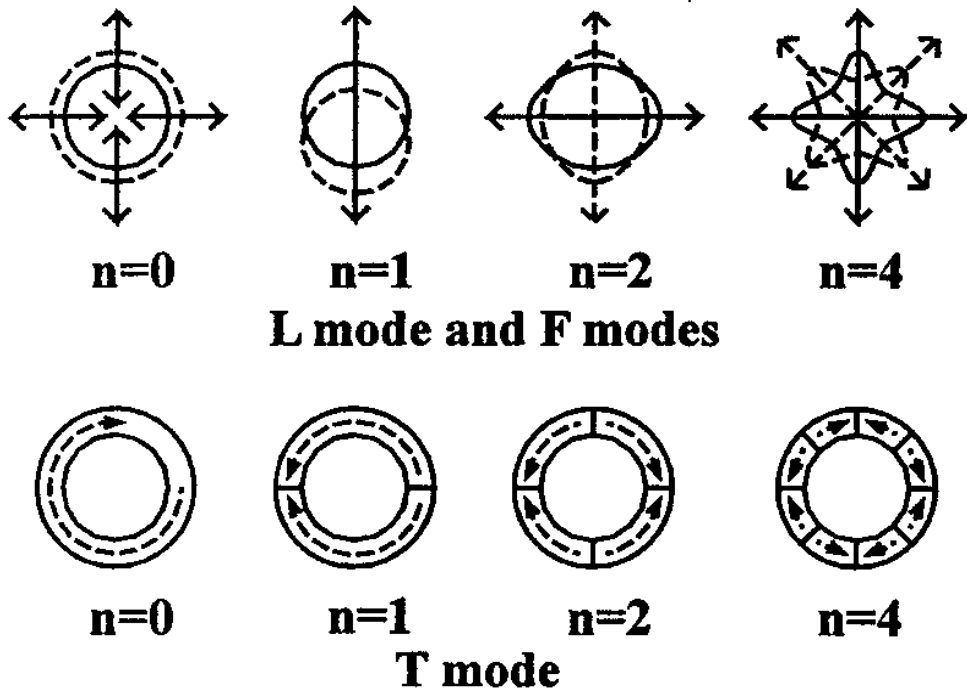


Fig. 1. Circumferential vibration mode.

are described as  $L(0, m)$ ,  $F(n, m)$  and  $T(n, m)$ , where  $n$  and  $m$  are the circumferential and radial (thickness) mode parameters, respectively. L-mode is axially symmetric, sometimes called as a breathing mode. Schematic illustrations of circumferential modes are shown in Fig. 1.

Meitzler [9] and Silk et al. [3] classified all the high order circumferential modes as the F-mode. In their classification, T-mode had only the circumferential fundamental mode ( $n=0$ ). It is natural, however, that the  $n$ -parameter of T-mode is not limited to zero. Each high order T-mode is coupled only with a SH wave at the cut-off frequency (the so-called *longitudinal-shear wave* in [1]). This new classification allows us to correlate the three cylinder modes to plate waves at diminishing wall thickness-to-outer diameter ( $t/d$ ) ratios; i.e., L- and F-modes to Lamb waves and T-mode to SH mode plate wave [10].

Figure 2 shows phase velocity dispersion of L- and F-modes for an aluminum pipe of 5 mm diameter and 1 mm thickness. They were computed for the longitudinal wave velocity of 6400 m/s and the shear wave velocity of 3040m/s. Velocity dispersions of  $A_0$  and  $S_0$  Lamb waves for 1 mm thick aluminum plate are also shown. Shape of the dispersion curves is identical for constant  $t/d$ . Therefore, the horizontal axis is normalized by the product of frequency ( $f$  in kHz) and wall thickness ( $t$  in mm). This behavior is the same as that of Lamb wave dispersion curve [11].

Figure 3 indicates the characteristic features of the velocity dispersions. Effects of  $t/d$  on the velocity dispersion of  $L(0, 1)$  and  $L(0, 2)$  modes are shown for  $t/d = 1/2, 1/3, 1/5, 1/10$  and  $1/16$ . Note  $t/d=1/2$  is for a solid cylinder or a rod. With reducing  $t/d$  or increasing frequency-thickness product  $ft$ ,  $L(0, 1)$  and  $L(0, 2)$  modes approach the velocity dispersions of  $A_0$  and  $S_0$  Lamb waves in a plate whose thickness is equal to  $t$ . At diminishing  $ft$ , the dispersion curves converge to that of a rod. This demonstrates that the cylinder waves have the characteristics between the rod waves and Lamb waves [12].

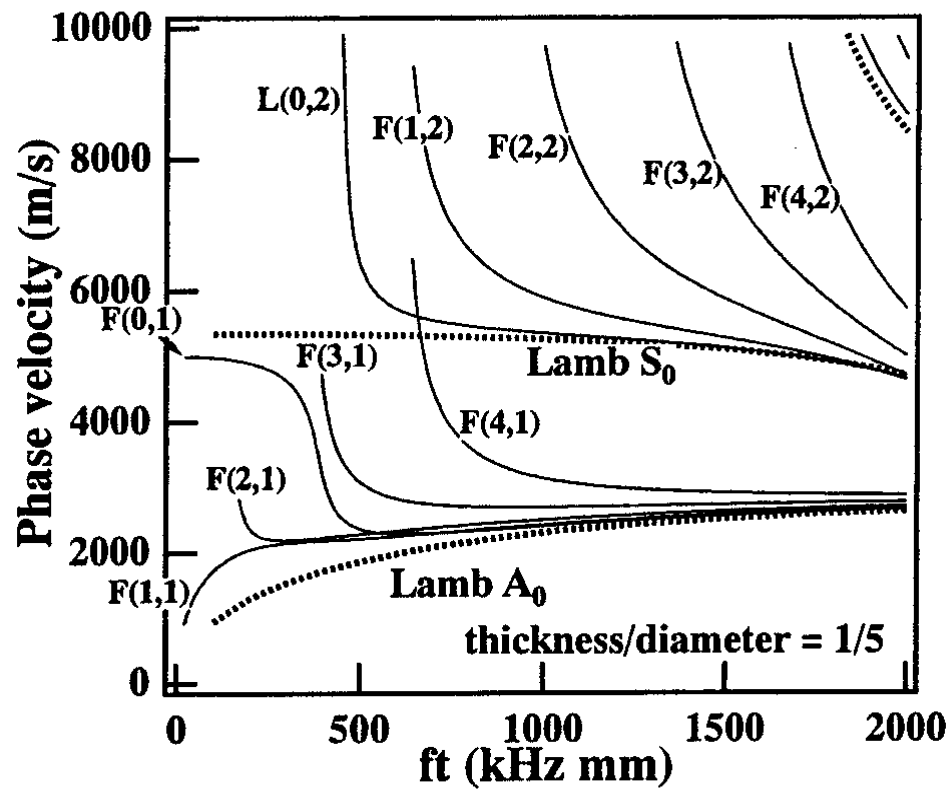


Fig. 2 Phase velocity dispersion of cylinder wave (Aluminum pipe,  $d = 5 \text{ mm}$ ,  $t = 1 \text{ mm}$ ).

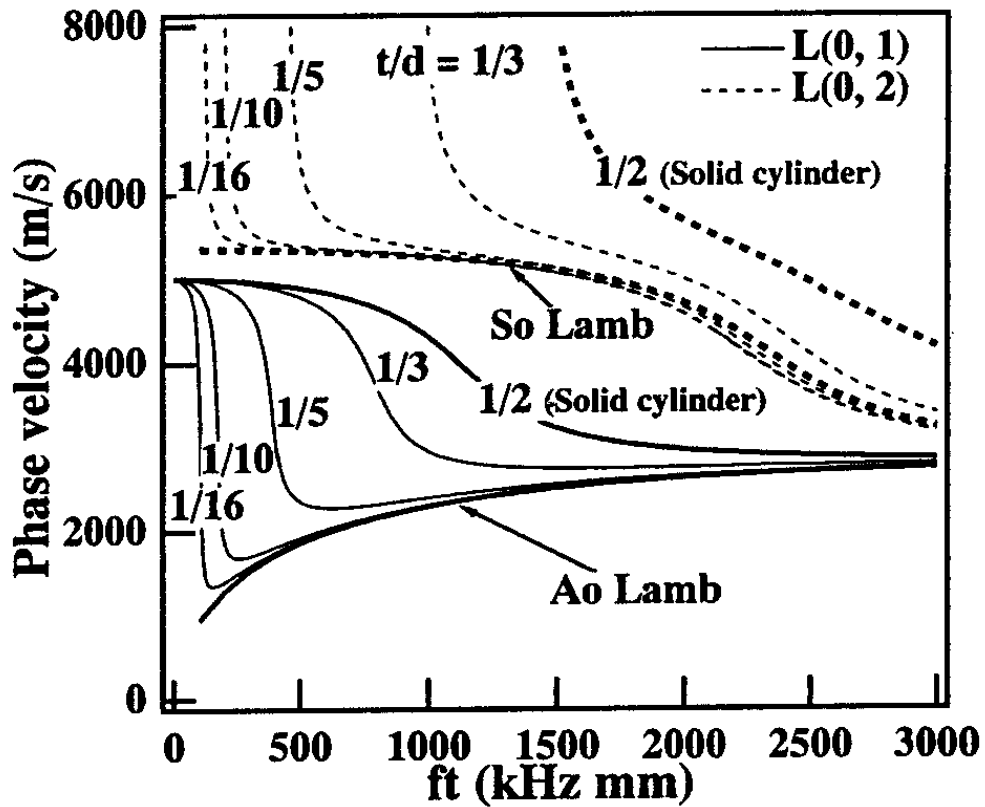


Fig. 3 Phase velocity dispersion of  $\text{L}(0, 1)$  and  $\text{L}(0, 2)$  modes for pipes with different  $t/d$ .

### III. AXIAL SOURCE LOCATION

#### 3-1 Method of source location

We obtain the source location of an AE signal using the velocity difference of L(0, 1) and F(1, 1) modes monitored by a single AE sensor. As shown in Fig. 4 for a 1 mm thick aluminum pipe of 5 mm diameter, we observe a large group velocity difference of L(0, 1) and F(1, 1) modes at low frequency range. Here, we select the frequency  $f = 140$  kHz, at which F(1, 1) velocity shows a maximum. Utilizing the group velocity  $v_L$  of L(0, 1) mode and  $v_F$  of F(1, 1), the source location along the z axis (z being the distance from the sensor in Fig. 5) is given by equation (1),

$$z = \frac{v_L v_F}{v_L - v_F} t, \quad (1)$$

$t$  is arrival time difference between L(0, 1) and F(1, 1) modes at the selected frequency. Though F(2,1) modes exists in the same frequency range, a large arrival time difference between F(1, 1) and F(2, 1) modes makes the separation of F(2, 1) from F(1, 1) possible.

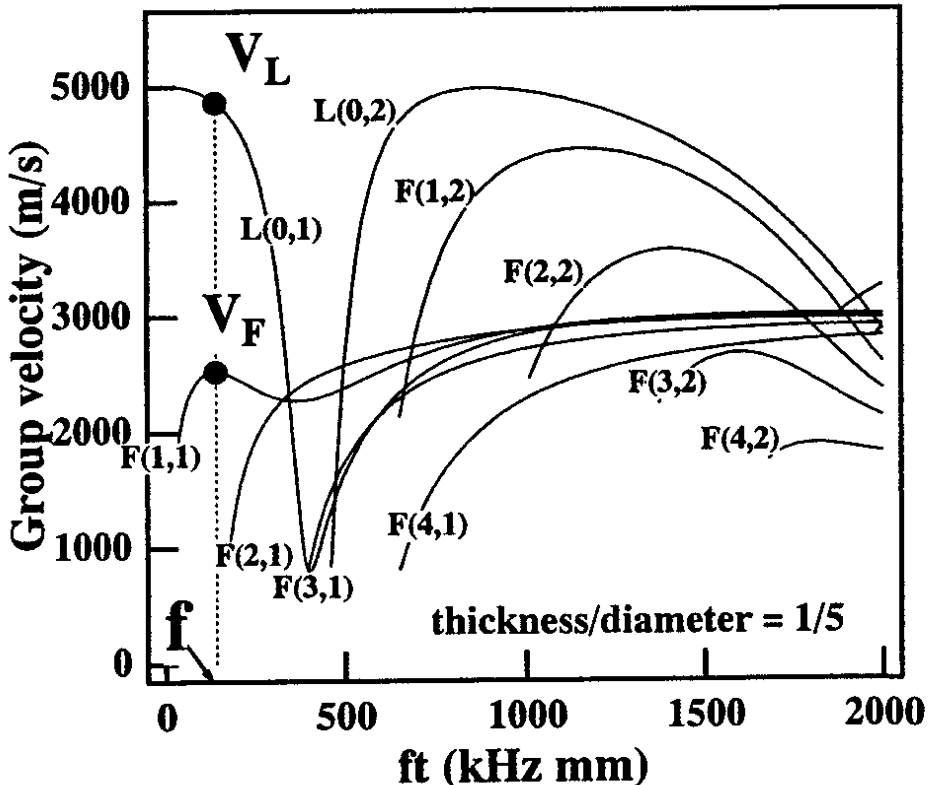


Fig. 4 Group velocity dispersion with  $V_L$  and  $V_F$  at frequency  $f$ .

#### 3-2 Experiment and results

We monitored cylinder wave signals by a Mach-Zehnder type laser interferometer (BMI, SH-140) having the 20 MHz bandwidth and by a small AE sensor (PAC, PICO, nominal center frequency 0.5 MHz) at 100, 200, 300, 400 and 500 mm from the distal plane (see Fig. 5). Four aluminum pipes with  $d$  of 4, 5, 6 and 8 mm and  $t$  of 1 mm were used. The specific frequencies were selected for the F(1, 1) velocity maxima and were theoretically determined as 210, 140, 100 and 80 kHz, respectively. Cylinder wave signals were generated by a point focused pulse YAG laser irradiation at the distal of the pipes.

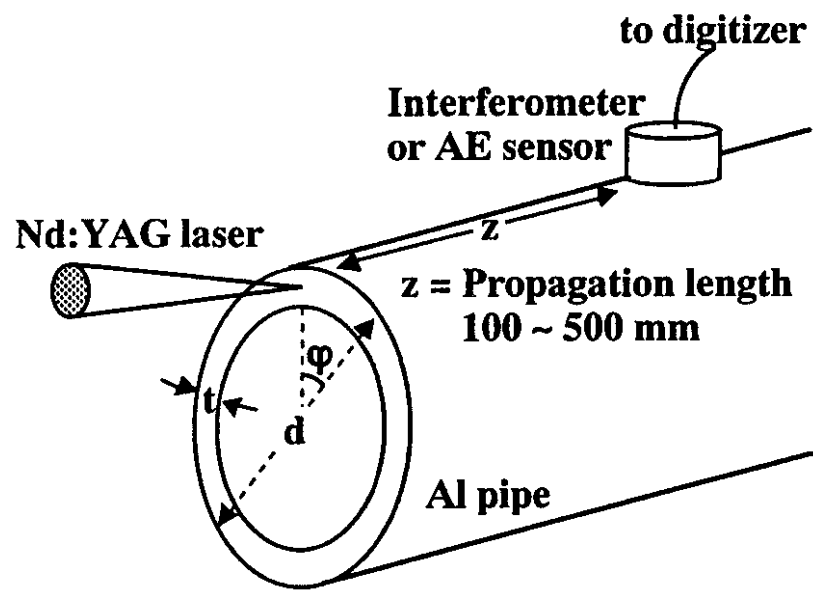


Fig. 5 Experimental apparatus of verification.

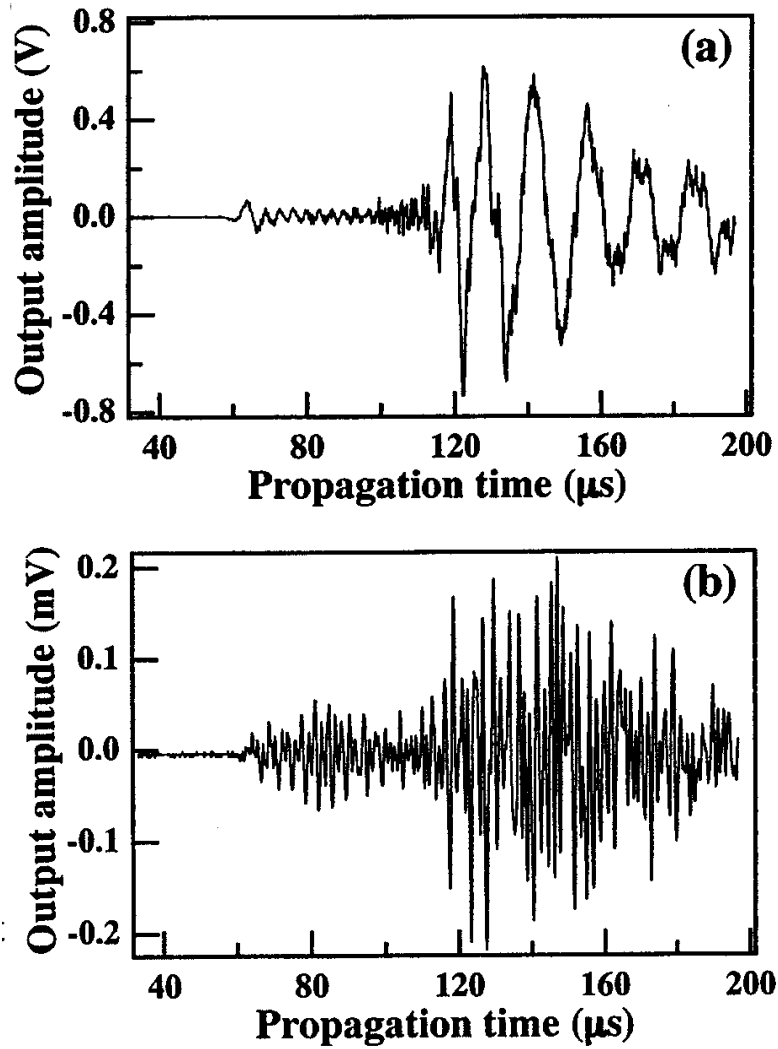


Fig. 6 Waveforms of the cylinder wave AE's detected (a) by interferometer and (b) by AE sensor.

Figures 6(a) and (b) show cylinder wave signals monitored by the interferometer and the AE sensor at  $z = 300$  mm for 5 mm diameter pipe. The interferometer output is radial displacement, while AE output is expected to be velocity. The first portion of the wave around  $60 \mu\text{s}$  is dominant to the  $L(0, 1)$ , and second around  $120 \mu\text{s}$  is the  $F(1, 1)$  mode for each AE signal. Time transients of 140 kHz components of the two waveforms, extracted by wavelet transform, are shown in Figs. 7(a) and (b), respectively. First peaks at  $63.6 \mu\text{s}$  of the interferometer and at  $63.9 \mu\text{s}$  of the AE sensor represent  $L(0, 1)$  mode, and second peaks at  $120 \mu\text{s}$  represent  $F(1, 1)$  mode. Using the  $t$ 's of  $56.4 \mu\text{s}$  and  $56.1 \mu\text{s}$ , the source distance  $z$ 's were estimated as 297 mm (1.0% error from 300 mm) with the interferometer signal and as 293 mm (2.2% error) of the AE sensor output, respectively. Here, the theoretically group velocities  $v_L$  and  $v_F$  at 140 kHz were 4860 and 2520 m/s.

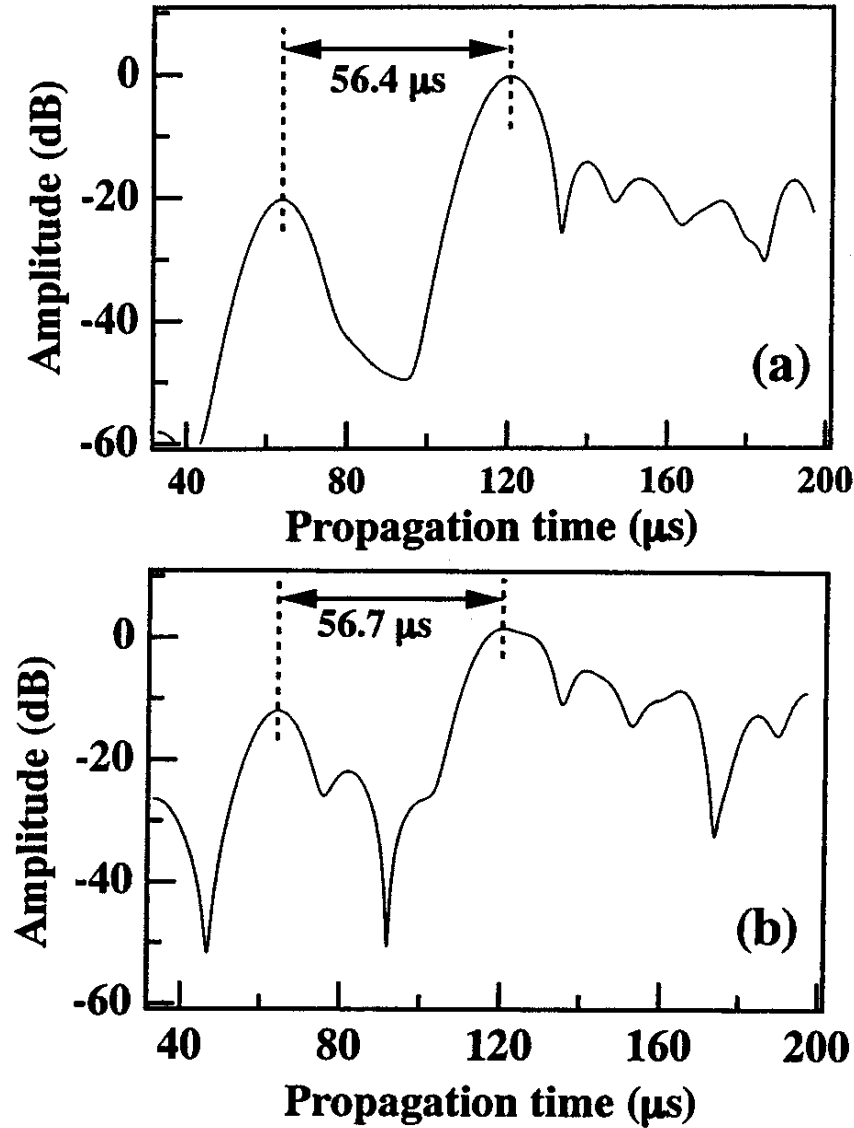


Fig. 7 140 kHz wavelet coefficient of AE signal detected (a) by interferometer (a) and (b) by AE sensor.

Location errors for another pipe diameters and source distances are summarized in Table I (interferometer signals) and Table II (AE sensor output). Several source location attempts for 100 and 200 mm distances were not successful due to the difficulty in separating the  $L(0, 1)$  and  $F(1, 1)$  modes. Average error of all the results obtained using the interferometer was 3.5%, while that using the AE sensor was 4.9%. The

latter was slightly larger due to a larger sensing area. Despite non-flat response of the AE sensor, we can estimate the source location in the axial direction with high sensitivity at lower frequency ranges. This finding can be applied to the AE inspection of slender pipes and tubing, significantly reducing the cost of damage inspection.

**Table I Errors (%) of source location using the cylinder wave detected by the wide-band Interferometer.**

Outer diameter	propagation length z (mm)				
	100	200	300	400	500
<b>8 mm</b>	-(%)	-	3.3	3.8	7.0
<b>6 mm</b>	-	-	2.0	3.3	3.6
<b>5 mm</b>	10	4.3	1.0	0.30	0.20
<b>4 mm</b>	5.0	2.5	2.3	3.8	4.0
(Thickness=1 mm)					

**Table II Errors (%) of source location using the cylinder wave detected by the resonant type AE sensor.**

Outer diameter	propagation length z (mm)				
	100	200	300	400	500
<b>8 mm</b>	-(%)	5.5	6.7	1.5	4.6
<b>6 mm</b>	-	-	2.0	9.5	9.2
<b>5 mm</b>	-	5.0	2.2	1.3	1.8
<b>4 mm</b>	7.4	6.0	2.3	7.5	6.0
(Thickness=1 mm)					

#### IV. CIRCUMFERENTIAL SOURCE LOCATION

Although the source location in the circumferential direction is less critical, we present here a method for the source location over the circumference of a pipe. The method relies on the amplitude ratio of  $F(1, 1)$  to  $L(0, 1)$  modes. Amplitude of  $F(1, 1)$  mode (see Fig. 1) changes depending on the source location, while that of  $L(0, 1)$  mode is independent on the location. This is one of "the initial-value problem" of the wave equation. Out-of-plane displacement in circumference of  $F(1, 1)$ -mode is presented by a sinusoidal function  $A \cos(2\pi f_z z + \phi)$ .  $A$  is peak amplitude,  $\phi$  indicates the circumferential source location and  $z$  the relative circumferential position between the source and sensor. The largest amplitude is obtained for  $\phi = 0^\circ$  and the amplitude is the smallest at  $\phi = 90^\circ$  (Fig. 8).

An aluminum pipe of 5mm diameter and 1mm wall thickness was used in the experiment. Using the system shown in Fig. 5, we monitored cylinder wave signals produced by laser irradiation at five circumferential positions ( $\phi = 0, 45, 90, 135$  and  $180^\circ$ ). Detected waveforms are shown in Fig. 9. Amplitudes of first peak A, due to  $L(0, 1)$  mode, were almost independent of  $\phi$ , and the phase showed no change. In contrast, the phase of peak B, due to  $F(1, 1)$  mode, changed at  $\phi = 90^\circ$  and amplitude was the smallest at  $\phi = 90^\circ$  (in fact, buried in other unidentified high-frequency modes). Figure 10 shows the amplitude ratio of  $F(1, 1)$  and  $L(0, 1)$  modes as a function of  $\phi$ . Closed circles indicate experimental data. At  $\phi = 90^\circ$ , error bar is inserted because no clear  $F(1, 1)$  component at  $\phi = 90^\circ$  was detectable. Solid curve

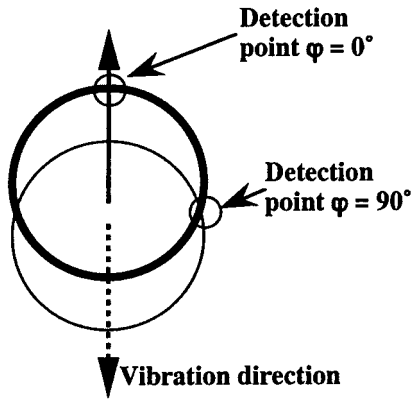


Fig. 8 Schematic illustration of  $F(1, 1)$  vibration and detection point .

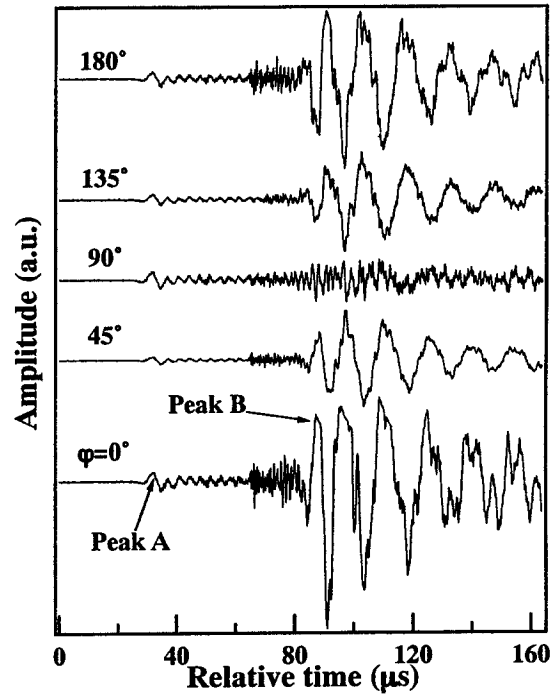


Fig. 9 Detected signals of cylindrical guided waves for different source position .

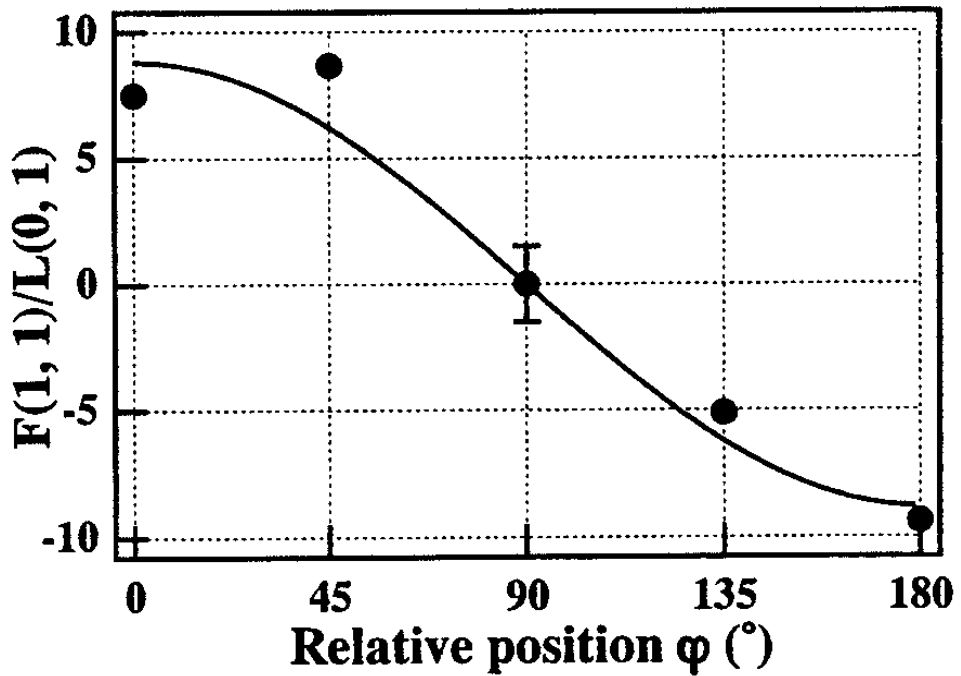


Fig. 10 Amplitude ratio of  $F(1, 1)$  and  $L(0, 1)$  as a function of probe position .

represents a theoretically predicted amplitude variation. Here, the peak amplitude A was determined as 8.8 by a least square fit to the experimental data except the amplitude  $F(1, 1)/L(0, 1) = 0$  at  $90^\circ$ . Experimental data agrees well with the theoretical prediction.

The present result demonstrates the feasibility of monitoring  $F(1, 1)/L(0, 1)$  and comparing it to the reference in order to identify AE source location in circumference.

## V. CONCLUSION

We have demonstrated a new source location method of the hollow cylindrical guided waves. The source location along the axial direction can be determined by utilizing the arrival time difference between L(0, 1) and F(1, 1) modes. Utility of this method was verified for laser-induced signals monitored by a wideband interferometer and an AE sensor. The axial source location was determined within 5% error using the AE sensor for up to 500 mm. Owing to the low energy loss of the cylinder waves, the present method is applicable to pipe inspection over a long distance.

We also showed a method for the source location in circumference. It utilizes both the amplitude and phase information of L(0, 1) and F(1, 1) modes. A good relation between the amplitude ratio of L(0, 1) and F(1, 1) modes and the circumferential source position was shown.

The application to the source location of real AE signals in long pipes remains as future challenge.

## REFERENCE

- [1] D. C. Gazis, J. Acoust. Soc. Am., 31, (1959) 568.
- [2] A. H. Fitch, J. Acoust. Soc. Am., 35, (1963) 706.
- [3] M. G. Silk and K. F. Bainton, Ultrasonics, 17 (1979) 11.
- [4] W. Bottger, H. Schnerder and W. Weingarten, Nucl. Engr. Design, 102 (1987) 356.
- [5] M. J. S. Lowe, D. N. Alleyne and P. Cawley, Ultrasonics, 36 (1998) 147.
- [6] D. N. Alleyne and P. Cawley, J. NDE, 15 (1996) 11.
- [7] J. L. Rose, J. J. Ditri, A. Pilarski, K. Rajana and F. Carr, NDT & E Int.. 27 (1994) 307.
- [8] M. Takemoto, F. Uchida, T. Sato, Y. Mizutani, H. Nishino and S. Yamazaki, J. Jpn. Soc. Corrosion Eng., 48 (1999) 733, in Japanese.
- [9] A. H. Meitzler, J. Acoust. Soc. Am., 33 (1961) 435
- [10] B. A. Auld, "*Acoustic fields and waves in solid*", 2nd ed., Krieger, (1990) New York.
- [11] I. Victrov, "*Rayleigh and Lamb wave*", ed. Lewis, Plenum Press, (1967) New York
- [12] H. Nishino, S. Takashina and M. Takemoto, to be submitted.

# **AE METHOD FOR PRESSURE VESSEL DIAGNOSTICS AT A REFINERY.**

**B.S. KABANOV, V.P. GOMERA, V.L. SOKOLOV AND A.A. OKHOTNIKOV**  
**Kirishinefteorgsintez, Kirishi, Leningrad region, RUSSIA**

## **ABSTRACT**

Kirishinefteorgsintez was the first refinery in Russia, which introduced AE methods. Due to the advantages of the AE method for increase of reliability of equipment and the desire to test more equipment units in less time, own AE group was created and hydraulic and pneumatic tests of pressure vessels are accompanied by AE testing. The localization of defective zones by the AE method has proved to be more effective than the application of traditional NDT methods. Per Russian regulations, all pneumatic tests must be accompanied by AE testing. There is a big demand for the replacement of hydraulic tests by pneumatic tests, as the refinery operates many special vessels, which cannot be pressurized by water. For interpretation, the traditional AE criteria are used: the localization of AE sources, verification of the Kaiser effect, pressure holding AE etc. AE source location with different wave velocities in the relatively thin shells (the different Lamb waves modes) and some cluster analysis algorithms are also used. 205 vessels have been tested since 1992. 29 of these vessels had been repaired due to the result of the AE testing. An AE test database has been formed and includes results of the AE testing and the corresponding follow-up inspections.

## **EXAMPLES OF AE TEST METHODS IMPLEMENTATION FOR VESSELS**

The importance of the AE method used for testing the refinery's equipment shall be demonstrated by examples of defect detection. The capability to detect these defects with traditional control test methods, without AE was miserable. The results are obtained with AMSY4 from Vallen-Systeme, although the refinery has used and still uses a LOCAN AT, manufactured by PAC.

### **EXAMPLE 1**

Test subject is a heat-exchanger shell made of carbon steel with stainless steel cladding; thickness: 20 mm; pneumatic test (scheme is presented in Fig. 1). Some results of planar location are shown in Fig. 2. They had been used for the inspection of vessel shell areas with AE source location analysis. Other instruments of post-analysis had been applied for more precise localization and classification of AE activity zones. For example, some parts of such analysis are shown in Fig. 3. Left diagram shows amplitude vs. counts of 3 channels in different colors, and indicates much higher amplitude at channel 14 compared to channel 6 and 13. These high amplitude signals (85-94 dB) indicate that the source might be quite near the channel 14. Right diagram in Fig. 3 illustrates the use of information about rise time in interpretation of planar location results.

The final positions of zone activities and the positions of the AE-sensors are indicated in Fig. 4. These zones had been classified according their nature as follows: Zone 1 was generated by relaxation in the weld between shell and fixed support; Zones 2 and 3 were generated by relaxation in the welding zones between shell and inside elements. (Note that processes of relaxation were usually correlated in Zones 2 and 3; therefore, the signals from different sources were generating the superposition of signals and the superposition was being registered by sensors from the location group, formed by channels 13, 14, 6, 10.); in Zone 4, by means of traditional NDT methods, with search priority near sensor 14, the defect has been detected inside the vessel at the welding zone around a dead-end boss (it was 45 mm in diameter). The defect has developed as a result of corrosion cracking to 8-10 mm in depth.

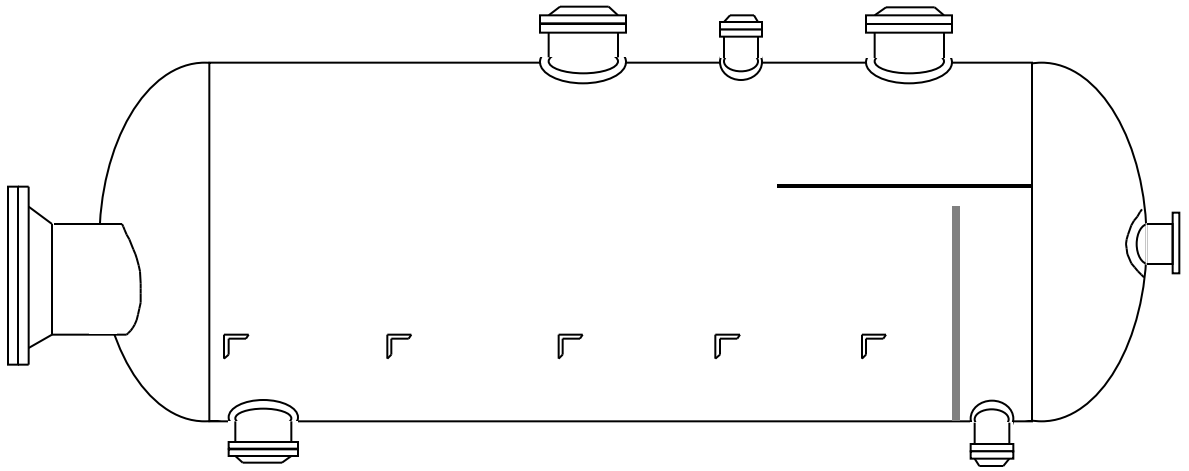


*Fig. 1. Heat exchanger scheme with construction elements producing the registered AE signal main array at pneumatic test of the vessel.*

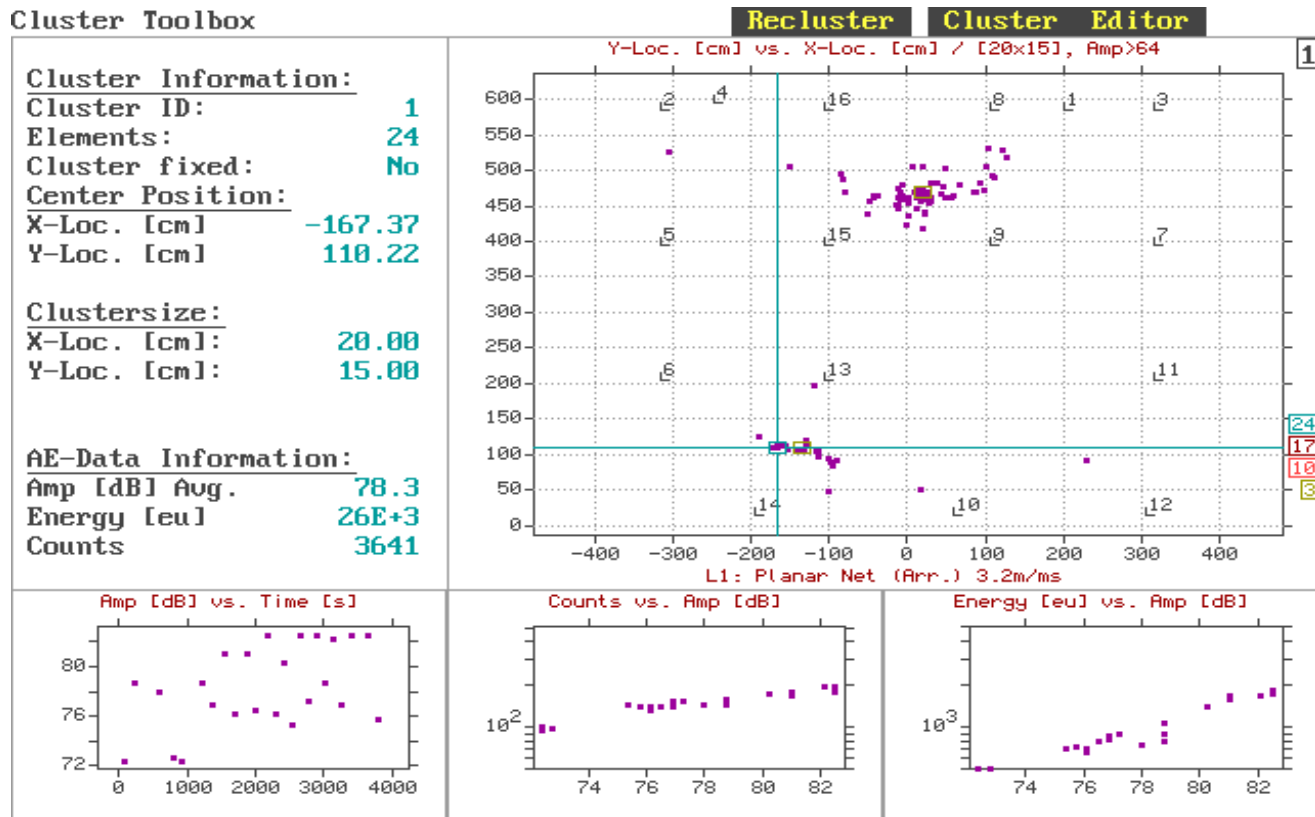


*Fig. 2. Location cluster parameters, corresponding Zone 1.*

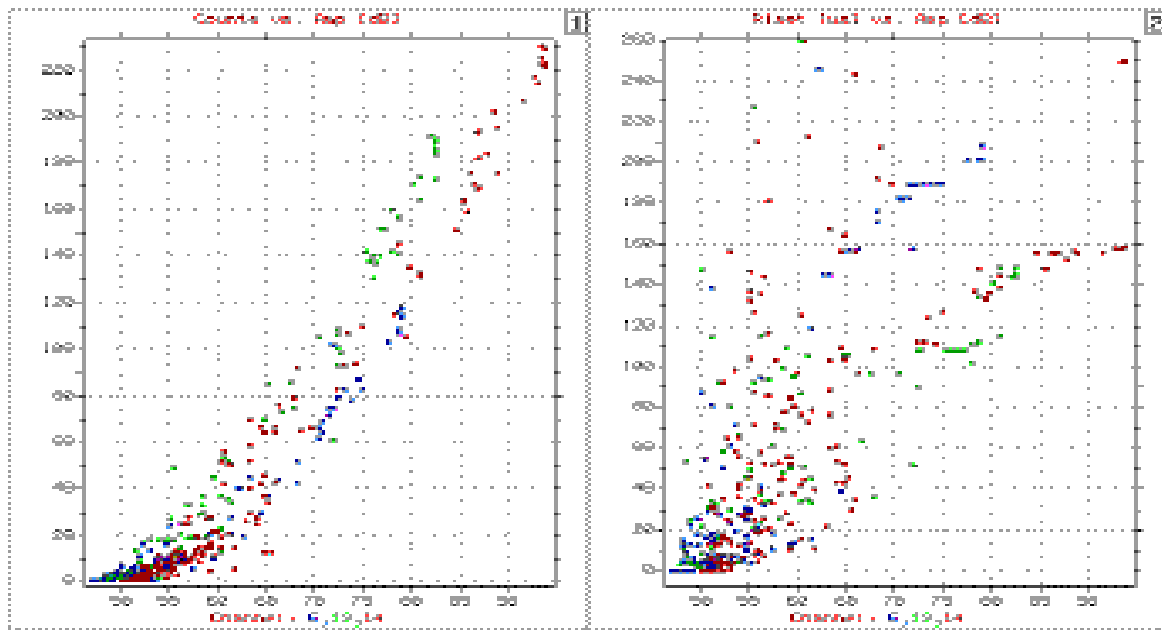


Fig. 3. Some diagrams, used for data interpretation by correlation; Counts vs. Amplitude [1] and Rise Time vs. Amplitude [2] for channels #6,13,14.

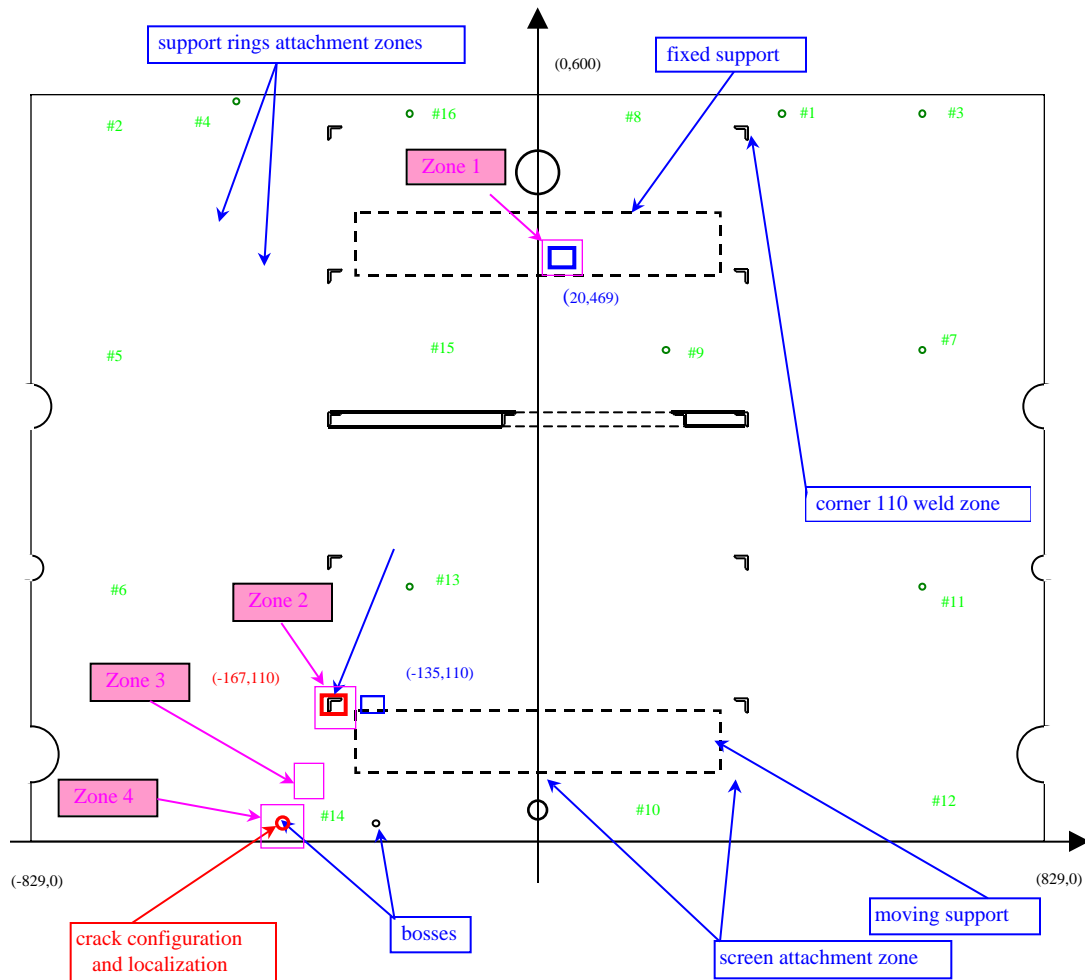
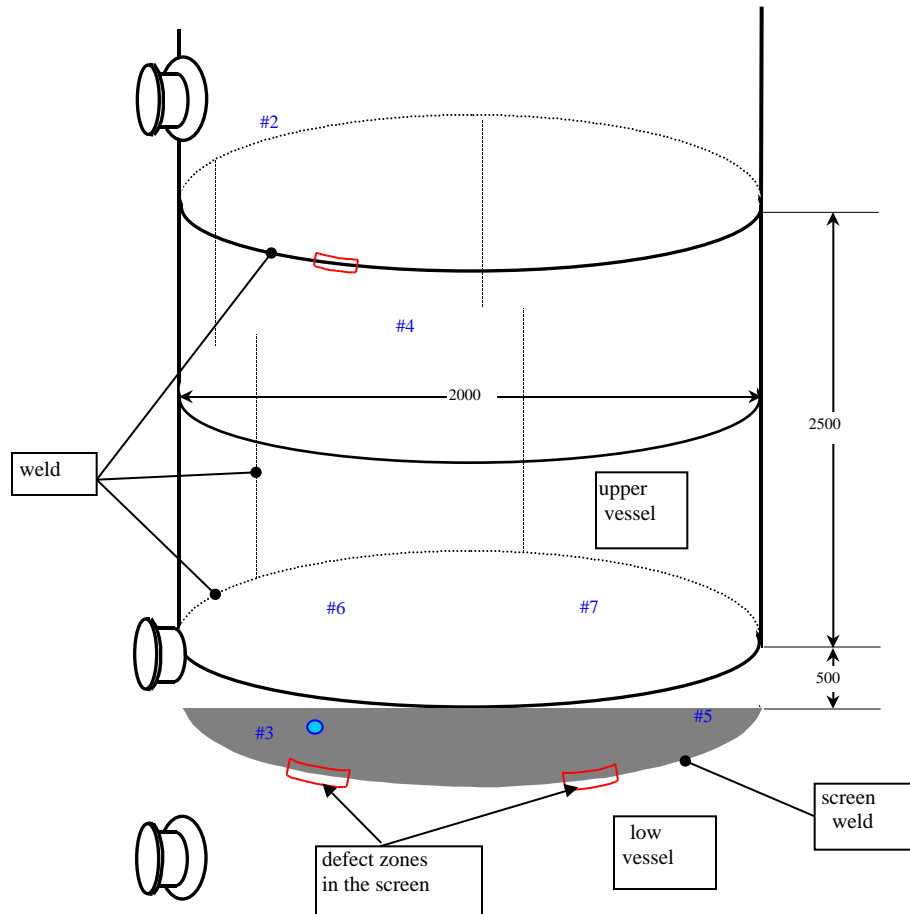


Fig. 4. AE sensor location at the shell reamer (inside view). The most active AE sources are shown.

## EXAMPLE 2

Test subject was a vertical vessel, located in the same shell with the other vessel. Both vessels are divided with the flat one-piece screen shown in Fig. 5. AE test accompanied the hydro-test of the upper vessel. The tested vessel material was carbon steel with cladding. Wall thickness was 16 mm.

Due to the operation stresses, perforation at some points around the perimeter of the screen had developed: in the weld between shell and screen, cracks were open. These cracks opened only under the inner pressure and that is why they could not be detected with the traditional inspection methods during shut down. Some characteristics of detected AE signals from the low band indicated that there had been leakage. Some of them are shown in Fig. 6. However, outside of the shell, the leakage could not be observed visually. In addition, the defects in the welds could not be detected with the other test methods. For the problem resolution, additional information had been received with the help of signal shape visualization functions, which in turn were used for AE source quality estimation by signal shape analysis.



*Fig. 5. Scheme of vessels for inspection (two vertical vessels, divided with a screen).*

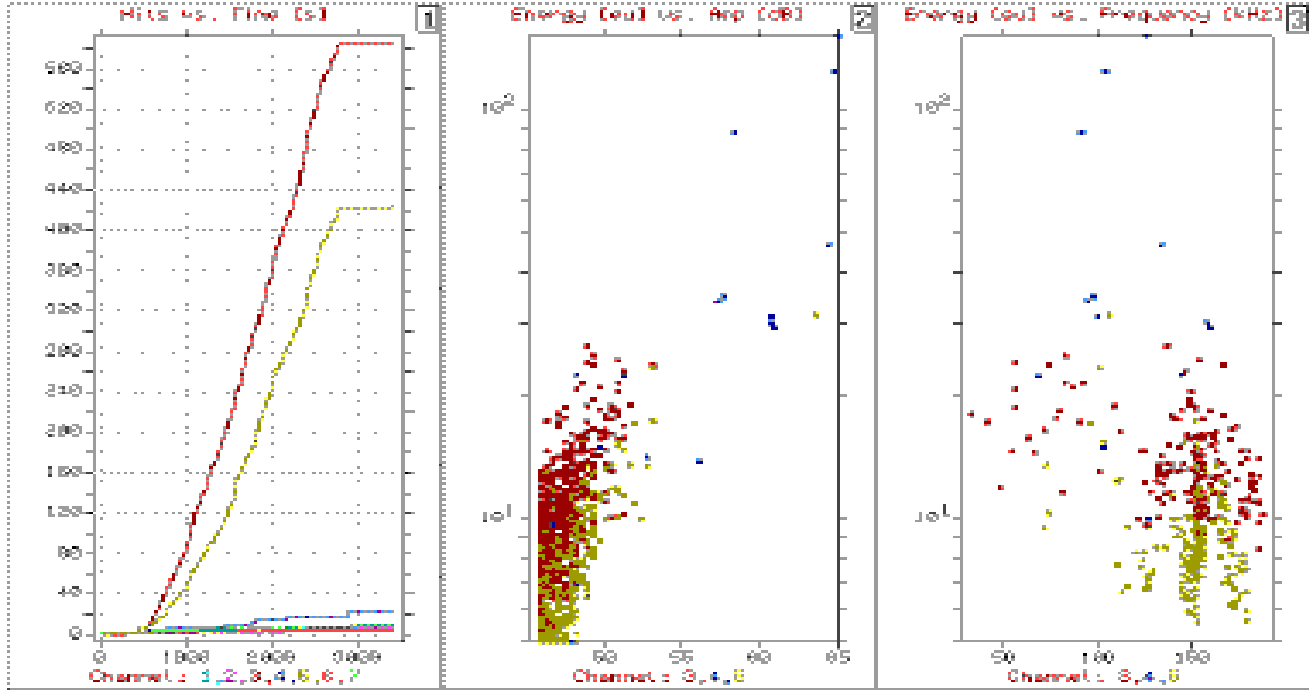


Fig. 6. Some diagrams for signal parameters, used for data analyses.

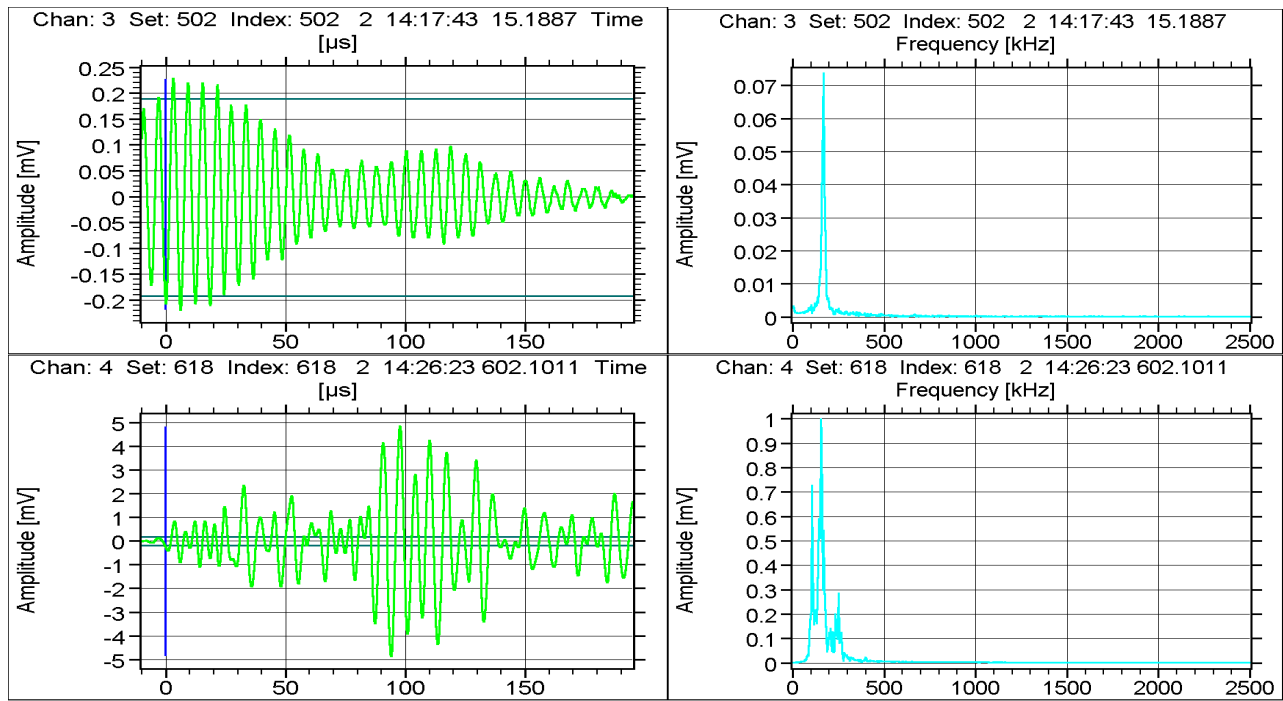


Fig. 7. Examples of AE signal from leakage (Chan. 3) and crack indication (Chan. 4).

Figure 7 shows an example of two typical signal shapes for different source types. Sensor #4 (bottom signal of about 5 mV or 74 dB amplitude) was located near the weld with some, not large, corrosion defects. Sensor #3 (top signal, just above threshold) was located near the screen and it registered periodic leakage through the open cracks of the defective weld. It is necessary to notice that the low vessel was also filled with water (prepared for hydro test). Water, pumped into the upper vessel for pressurization, increased the pressure till the stress in perforation sites reached the value necessary to open the cracks. Then, the water from the upper vessel leaked into the lower vessel until the pressure in

both vessels was equalized. Since the defect was only active while the pressures in both vessels differ, no other NDT methods would have a chance to detect the defects. AE seems to be an optimal method to detect such defects.

In the considered example, other types of defects were successfully detected and the defect locations were also determined.

### EXAMPLE 3

AE effectiveness is high for large vessels with places that are not easily accessible. For such kind of vessels, the combination of different location algorithms, as offered by the AMSY 4 system, is most effective. For example, good results were obtained with a combination of spherical and zonal location at large spherical vessels.

Vessel characteristics: material - carbon steel, thickness - 16 mm, diameter – 10.5 m, cubic capacity - 600 m<sup>3</sup>. AE testing accompanied the hydro test. Due to AE inspection, there were two corrosion zones detected at the vessel shell. One of the zones was detected with the help of a spherical location algorithm (Fig. 8). The second zone (weld piece) was determined by zonal location. Some data, characterizing the high relative AE activity of sensor #8, is shown in Fig. 9. AE results were confirmed with ultrasonic inspection and the defects were removed.

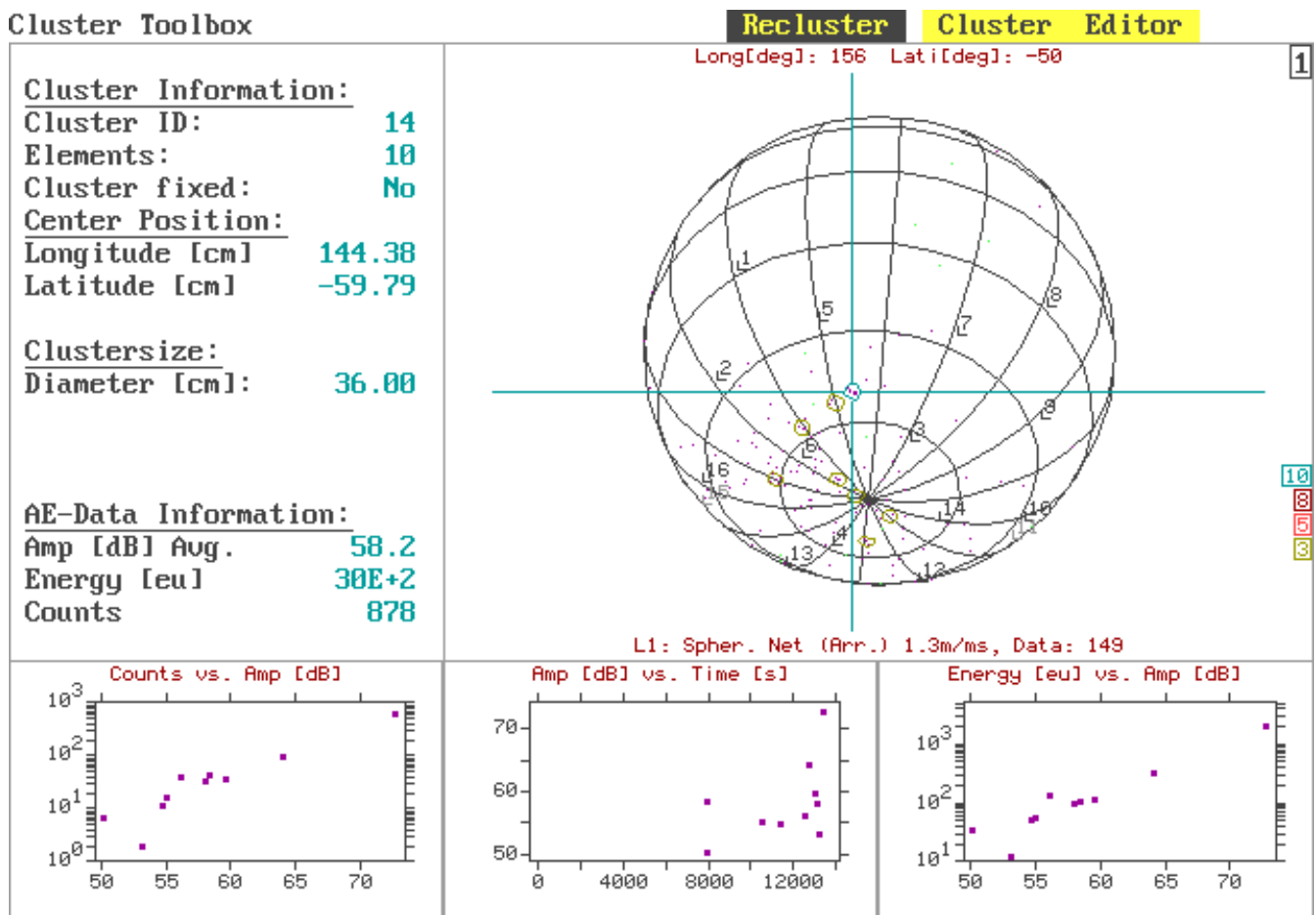


*Fig. 8. Location determination of corrosion defects of the vessel shell with sphere location algorithm.*

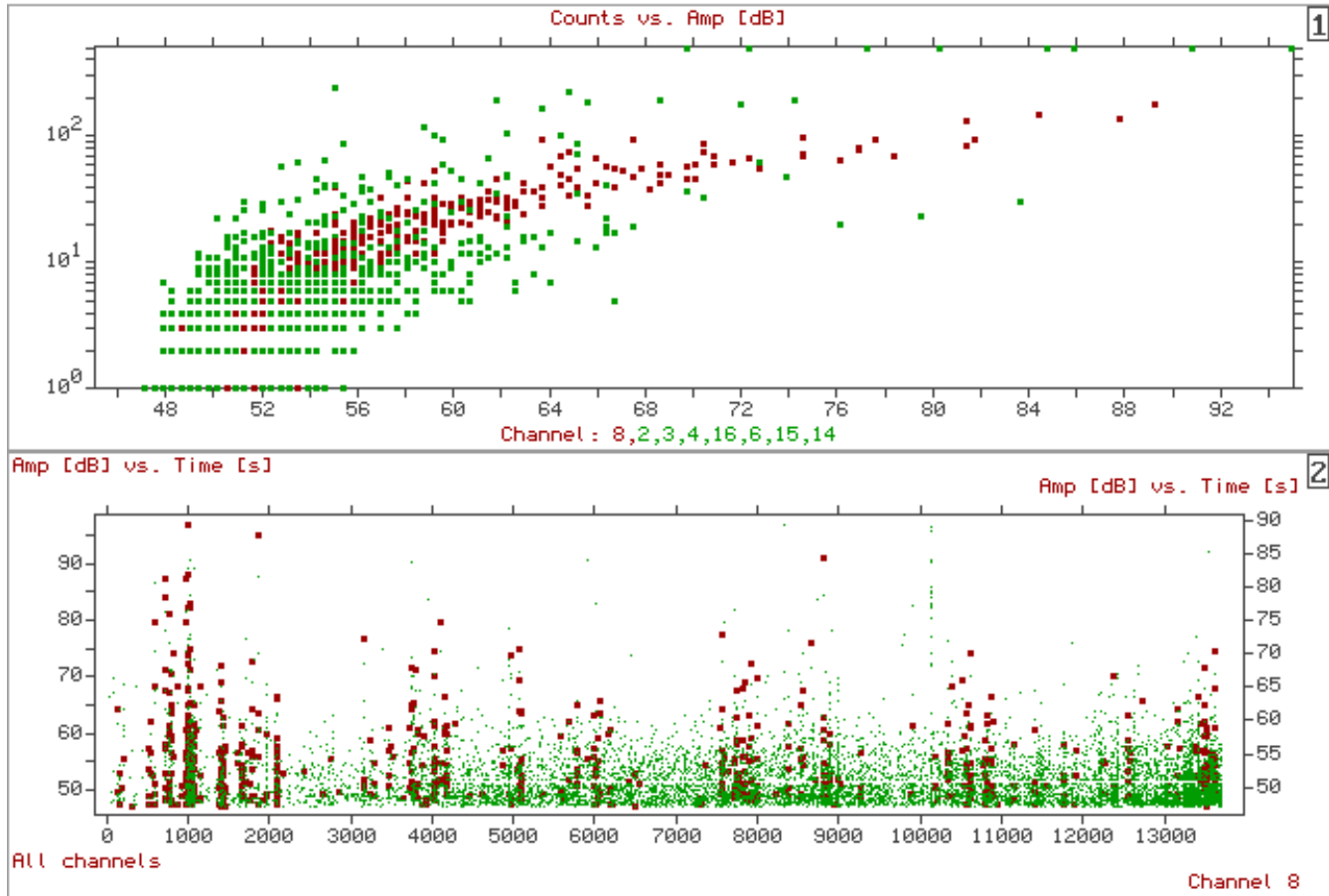


*Fig. 9. Example of graphic form, used for corrosion defect location determination of the vessel shell with zonal location algorithm.*

## CONCLUSION

AE methods are currently included in the nondestructive testing program of the plant and supplement the traditional methods successfully. Recognizing the effectiveness of AE implementation, the management has expanded the areas of its use and continues making investments in AE development at the refinery.

# OPTIMIZATION OF ACQUISITION PARAMETERS FOR ACOUSTIC EMISSION MEASUREMENTS ON SMALL PRESSURE VESSELS

Franz RAUSCHER

Institute of Pressure Vessel and Plant Technology  
Vienna University of Technology, Vienna, AUSTRIA

## ABSTRACT

*For acoustic emission (AE) measurements on small pressure vessels, it is important to perform proper location calculation for low and high amplitude events. The rate of AE events, which can be properly located, is also important. Therefore, a test was developed to evaluate the amplitude of the weakest properly locatable event, and to evaluate the rate of properly locatable events as a function of the amplitude. For the test, electrical signals were generated by a digital signal generator and transformed to mechanical waves by a piezoelectric reference source. The test is used to adjust the acquisition parameters of the AE equipment.*

## NOMENCLATURE

rate	frequency of pulses within the sequence
test	number of sequences with predefined parameter variation
amplitude at source	amplitude of the electrical signal in dB with 1 µV reference at the piezoelectric source
amplitude of event	amplitude of the electrical signal in dB with 1 µV reference at first hit sensor

## INTRODUCTION

At the Institute of Pressure Vessel and Plant Technology, experiments on small water-filled pressure vessels, welded and non-welded ones, were performed. Weld failures and cracks at proof tests and crack propagation at cyclic loading have been investigated [1-3]. When acoustic emission (AE) measurement is used at such vessels, source location is necessary for the separation of signals coming from the phenomenon to be investigated from those coming from other sources.

At these vessels acoustic waves are reflected many times and run around the vessel more than once. Therefore, the signals need very long time to diminish. Use of low threshold levels in this situation leads to very long duration of the signals, in addition to the problems with regard to noise. The consequence is that the acquiring channels are busy for long time intervals, and simple location calculation for subsequent hits is not possible. In this situation, it is necessary to optimize the set-up: It must be possible to perform location calculation for low amplitude events, and for a reasonable rate of AE events of high amplitude hits. Therefore, a test for determining the amplitude of the smallest locatable event and the rate of locatable AE events (rate of hits) depending on the amplitude was required.

The intention was to use it as a standard tool in addition to pencil-lead breaks and auto-calibration. Therefore, it must be possible to automate the test with standard components, and to extract the results with the standard software used in AE testing.

## TEST FOR DETERMINING THE QUALITY PARAMETERS

A fully digital signal generator was used to generate well-defined, precisely repeatable electric pulses. By using the second channel of the signal generator for triggering the pulses, sequences consisting of a predefined number of pulses with a predefined rate can be generated. A computer program running on a PC was used to set the parameters of the signal generator, to transmit the parameters to the analog inputs of the AE-equipment (AMS3 from Vallen Systeme), and to trigger the sequence of pulses. The generated events with the parameters were recorded at the AE equipment.

In one test, the amplitude and the rate of pulses were varied within predefined ranges, and one sequence was executed with each parameter combination. The minimal amplitude for proper location and the maximal rates for proper location depending on the amplitude are extracted from diagrams, which can simply be drawn by means of the AE-software. With the used signal generator it is possible to control by software a range of 40 dB in the amplitude without having too much noise. For reaching higher dynamic in the amplitude, attenuators have to be used. The maximal amplitude of the signal generator, which is 10V, gives the maximum strength of the signal.

The piezoelectric source, which converts the electrical signal into a mechanical wave, and the coupling, which transfers the wave to the vessels, are the parts, which cause problems for the repeatability and comparability of the test. Two options for selecting the piezoelectric source seem to be suitable: The first is to select the same type as for the sensors and performing the tests similar to the reciprocity calibration method [4] used for sensor calibration. The second method is to use a broad band reference source. For the tests described in this paper, the second method was chosen, applying a V103 transducer from Panametrics. Coupling was done in the same way as for the sensors.

In some tests, the piezoelectric source was coupled in the neighborhood of locations from where the investigated signals are expected to come from (region of the failure, crack etc. - here called failure region). In other tests the piezoelectric source were coupled near locations from where the noise is expected (noise location).

### Waveform of the test signals (pulse)

It must be expected, that the spectrum of the test signal influences the result. For tests, which address the influence of the frequency, small band signals are used. In the case of the test described here, the variation of the frequency was avoided and a broad band signal was used. Therefore, a signal was constructed with a spectrum of rectangular form from 0.1 to 1 MHz (Fig. 1). The signal is based on the cosine function, and the signal length is ten times the period of the lowest frequency content (equation below). A phase shift was used to shift the maximum amplitude of the pulse to 0.25 times the signal length and having zeros at the beginning and the end of the signal.

$$T = 1E - 4$$

$$f_{\min} = 100000 \text{ Hz}$$

$$f_{\max} = 1 \text{ MHz}$$

$$n_{\min} = f_{\min} \cdot T \quad n_{\max} = f_{\max} \cdot T$$

$$F(x) = \frac{\sum_{i=n_{\min}}^{n_{\max}} \cos \left[ 2\pi i \cdot \left( x - \frac{1}{4} \right) \right]}{n_{\max} - n_{\min} + 1}$$

The test signal was digitized at 2048 points and transferred to the signal generator with a precision of 14 bits. The resulting frequency for the signal generator is 20.48MHz, large enough for this spectrum.

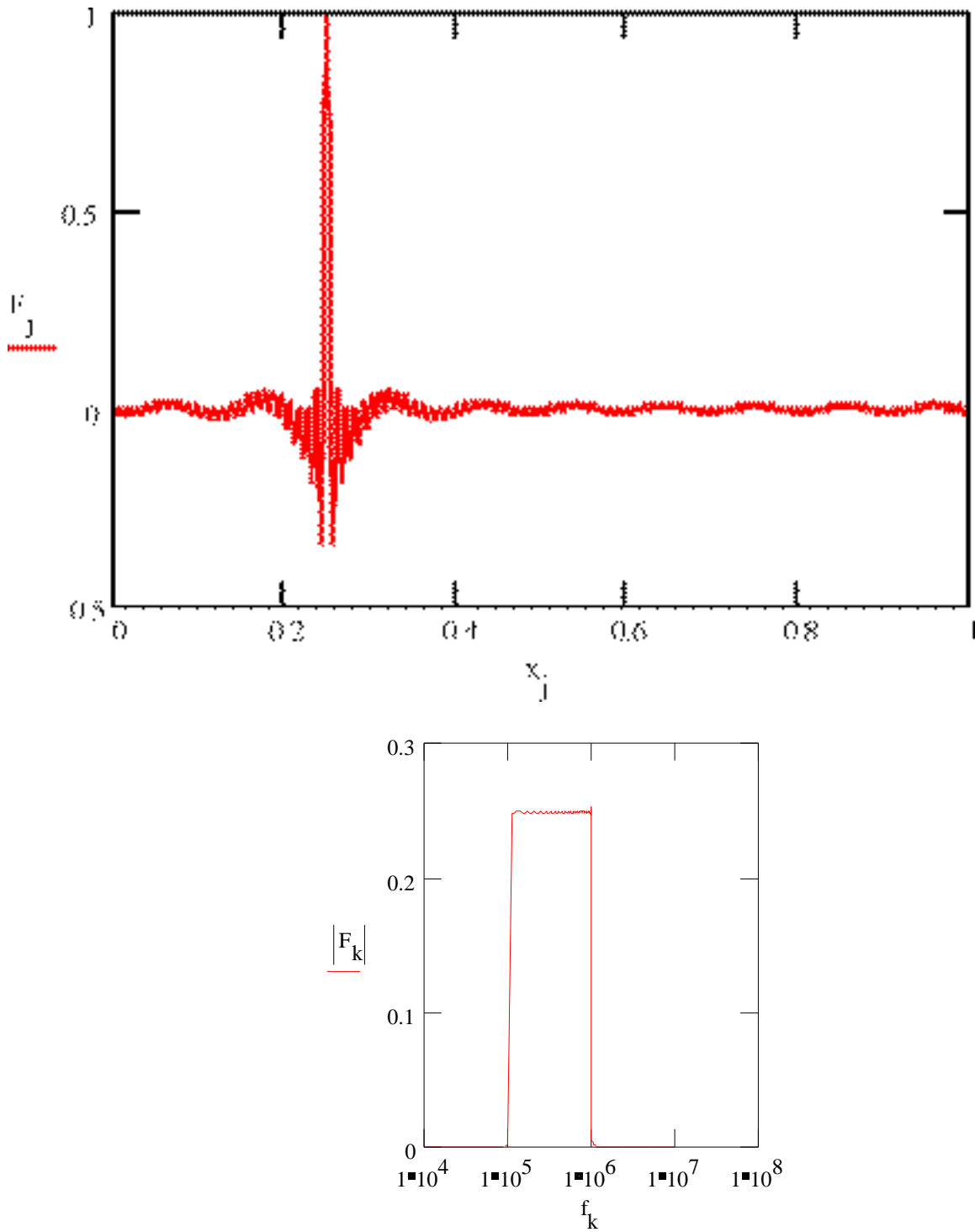


Fig. 1: Test signal (pulse) in time (top) and frequency (bottom) domain.

### Numbers for characterizing the test results

The number of properly located events at one sequence (10 pulses) determines whether proper location is possible for the used parameter combination of the sequence. The area in which an event must be

located, i.e. is properly located, must be chosen according to the goal of the acoustic emission measurements. In the experiments described below, a tolerance of  $\pm 10\text{cm}$  in x- and y-direction from the location of the source was specified. This is a rather large area for the investigated vessels, but in the planned experiments it is only important that the events are located in the correct region. A filter was used, to filter out the properly located events, and the number of properly located events is plotted versus the parameters, which are the amplitude and the rate (Fig. 2).

If ten events are properly located in one sequence (one parameter combination), the test is passed for this parameter combination. In this plot, the minimal amplitude at source for proper location is the amplitude of pulses at the utmost left clusters with 10 properly located events. The maximum rate for proper location depending on the amplitude at source is the largest rate with 10 properly located events at the corresponding amplitude. In the performed tests it seemed to be appropriate, to build a mean value, if for a parameter combination 8 or 9 events were properly located.

When AE-measurements are performed for monitoring cracks or failures only the amplitude at the receiver is known. Therefore, for the interpretation of location quality, it is sometimes more useful to use the amplitude at the receiver (Fig. 3). According to this diagram, similar numbers as above can be extracted with the amplitude of the recorded event instead of the amplitude at source.

A very good impression of the quality of the location calculations is given by the location plot y vs. x of the located hits (Fig. 4) for all sequences performed in one test.

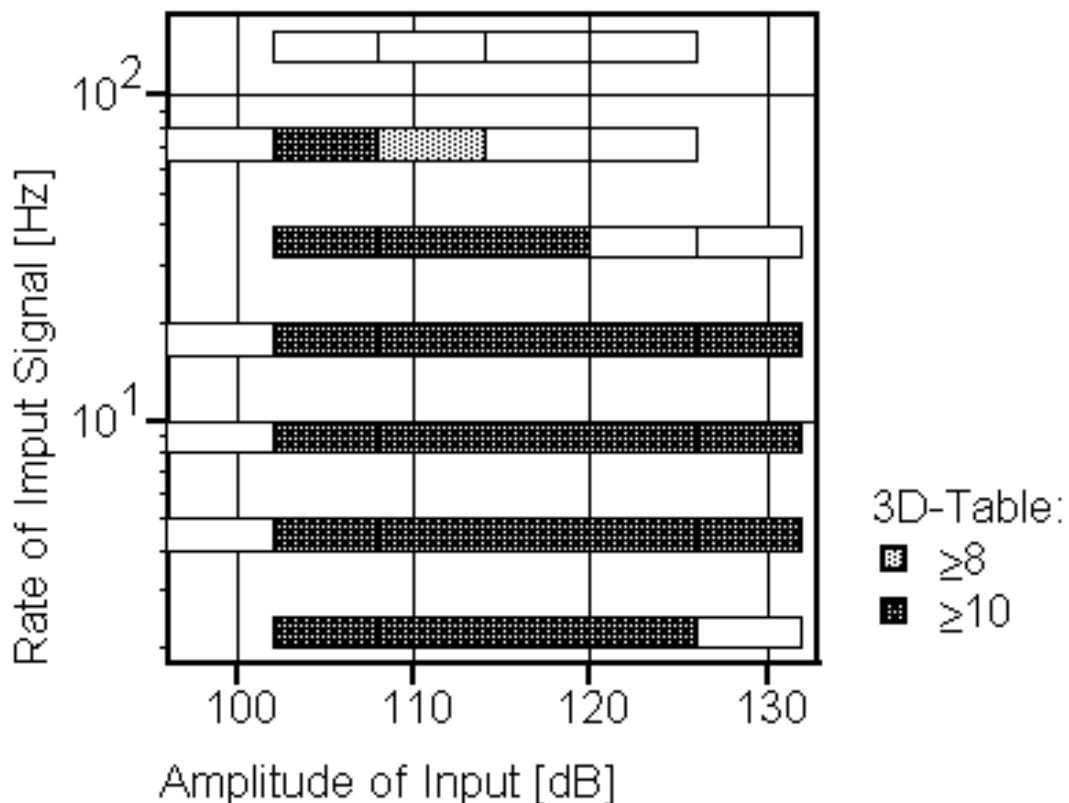


Fig. 2: Number of properly located hits versus amplitude at source and rate of pulses.

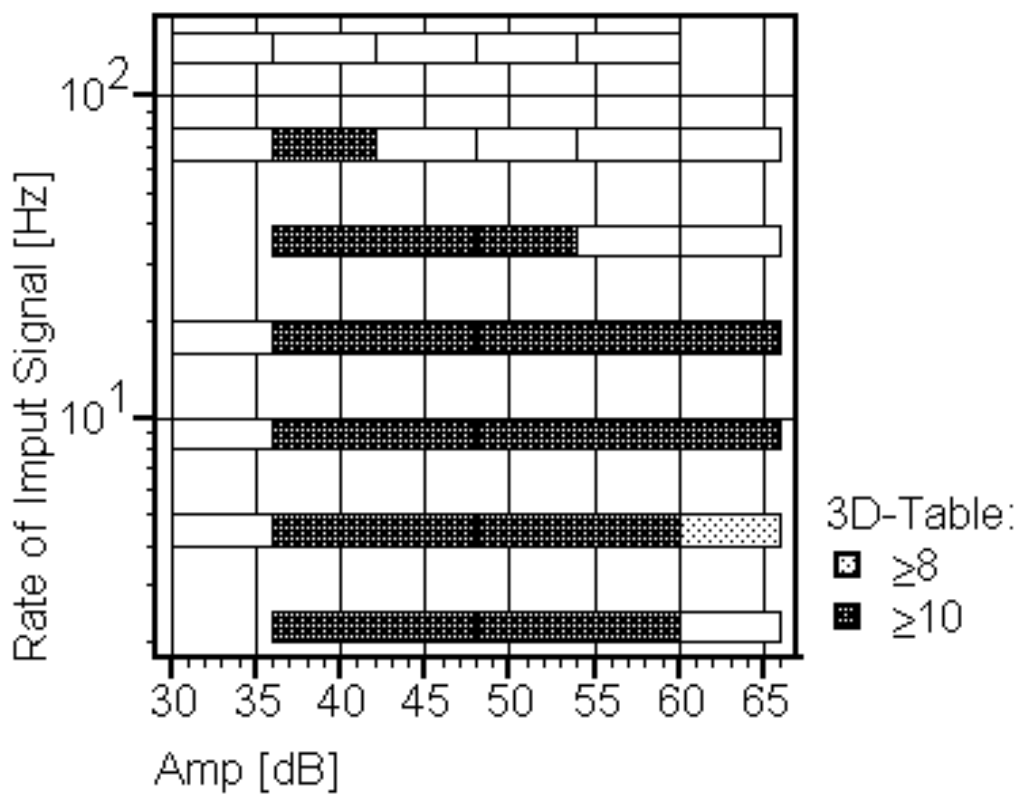


Fig. 3: Number of properly located hits versus amplitude of event and rate of pulses.

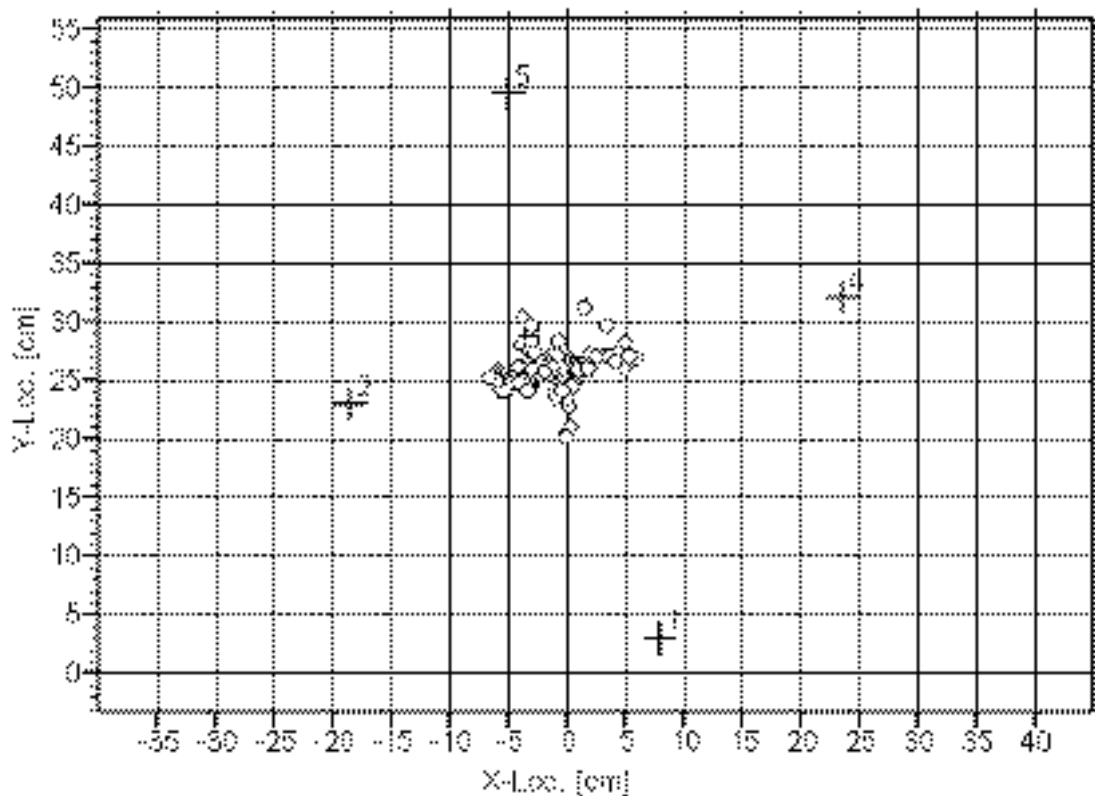


Fig. 4: y versus x of located events at one test with the source at x=2 and y=26.

There are three additional numbers, which are considered for the evaluation:

- Total number of events (located and not located ones) in the test.
- Total number of located events in the test
- Total number of properly located events in the test

### Optimization of the acquisition parameters using the test above

There are two important acquisition parameters, which determine how the hits are built from the incoming signal. The threshold level determines the sensitivity of the arrangement. The time span for which the channel is blocked by one hit is determined by the rearm time together with the threshold level.

To find a good combination of both parameters, the test described above was performed, for some combination of the two parameters. The pulse amplitudes of the test ranged from 100 to 130dB in steps of 6 dB and the rate of the pulses range from 2 to 128Hz increased from one step to the next by a factor of two. Therefore, 42 sequences á 10 pulses were used in one test.

The piezoelectric source was coupled near to an artificial notch, which is the expected failure region. The most important location for noise was the nozzle for the pressurization. The piezoelectric source was coupled to this region for another test. The results of some of the tests are listed in Table 1.

*Table 1: Tests for optimization of the acquisition parameters.*

Investigated acquisition parameters		Min. amplitude for proper location [dB]		Max. rate for proper location [Hz] Amplitude at source:		Max rate for proper location [Hz] Ampl. of event:		Number of events located in failure region	Number of events	Number of located events
Thres -hold [dB]	Rearm time [ms]	source	receiver	112dB	130dB	45 dB	63 dB			
27.7	0.41	106	39	32	16	32	16	261	2050	261
27.7	1.18	106	39	64	16	32	12	266	1187	266
27.7	3.021	106	39	48	16	32	16	269	543	269
27.7	5.99	106	39	32	16	32	12	249	393	249
27.7	11.98	106	39	32	12	32	12	252	362	252
27.7	24.013	106	39	32	16	32	12	254	368	254
29.6	3.021	112	45	64	16	48	16	244	437	245
31.2	3.021	112	45	64	16	64	16	263	458	263
33.7	3.021	112	45	64	16	64	16	242	380	242
36.4	3.021	118	51	64/118Db	32	64/51dB	54	212	393	212
27.7	3.021	Test with source at noise location (near nozzle)						0	520	154

The results show a slight decrease of the maximal rates for proper location when the rearm time is increased. An exception is the rearm time of 0.41ms, for which this rates are slightly decreased. When looking at the number of events it can be seen that the number of events can be decreased from 2050 to 543 by increasing the rearm time to 3.021ms, without reducing the number of properly located events. A

further increase of the rearm time reduces the number of events further, but the number of located events decreases also slightly and the maximum rates for proper location decrease also slightly. Increasing the threshold levels leads, as expected, to a reduction of minimal amplitude for proper location, but also to an increase of the maximal rate for proper location. Within these tests, it was not possible to decrease the threshold to a level at which a serious decrease of the maximal rate for proper location occurs.

An additional test, with the source at the expected noise location, shows that events from that location are not mapped into the failure region.

## CONCLUSION

A test for the quality of AE arrangements, which focus on the location calculation, was developed. The most important problems considering repeatability and comparability of the procedure are the piezoelectric source and the coupling of the source to the vessel. The preparation of the surface, where the source is coupled, is also important. In the case of the tests described here, a reference source was used, and it was coupled to the vessel in the same way as the sensors were coupled. The problem, that the user must perform the test in relatively short time when preparing experiments, was solved by fully automating the procedure, by controlling a digital signal generator with PC-software, and gaining the resulting indicators in a simple way from standard AE-diagrams. A limit for the automation of the procedure is the limited dynamic range of the signal generator, which can be solved by inserting attenuators manually into the cable. The maximum amplitude of the signal generator is another limit.

Indicators were developed, which quantify the weakest properly locatable event, and the maximum rate of locatable AE events, depending on the amplitude. With these indicators, it is possible to adjust the arrangement, acquisition and the location parameters and to test proper filters. The adjustment of the acquisition parameters with this test was shown.

## REFERENCES

- [1] Rauscher F., Schwarz M.: Schallemissionsmessung an Druckbehältern mit fehlerhafter Längsnah bei zyklischer Belastung sowie bei der Druckprobe. Bericht Nr. 5, Technische Universität Wien: Institut für Apparate und Anlagenbau (1995)
- [2] Rauscher F.: Acoustic emission of vessels with partially penetrated longitudinal seams. International Conference Acoustic Emission 1999 at Brno University of Technology, 15.-17.June 1999.
- [3] Bayray M.: Acoustic Emission (AE) due to cyclic pressurisation of vessels with partially penetrated longitudinal seams. European Conference on Acoustic Emission Testing 24-26 May 2000, Senlis France.
- [4] Nondestructive Testing Handbook, Vol. 5: Acoustic Emission Testing. American Society For Nondestructive Testing, 1987.

# **MONITORING OF WELD'S DEFECTS EVOLUTION SUBMIT TO STATIC AND DYNAMIC LOADING THANKS TO THE ACOUSTIC EMISSION METHOD**

**C. HERVE, R. PENSEC\* and A. LAKSIMI\*,  
CETIM, Senlis, France, \*UTC, Centre de Recherche de Royallieu, Compiegne, France**

## **ABSTRACT**

*Acoustic emission is a method especially suitable for the pressure vessels monitoring. The purpose of this study is to determine some patterns of flaw evolution via an original experimental approach. Static and fatigue cycles have been combined in order to duplicate accurately the loading undergone by a pressure vessel in service. Moreover, many parameters have been studied: different materials, several kinds of flaws, different forms of flaw. The research allows us to understand microscopic evolutions of some defects, to determine the efficiency of the acoustic emission method applied to the flaw detection according to the evolution state, and to evaluate the harmfulness of weld defects from their acoustic emission during the successive proof test simulation.*

## **INTRODUCTION**

The regulation requires that the pressure vessels be subjected before any use to a proof test and periodically every ten years thereafter. In general, this test consists of a hydrostatic pressure test. If this kind of test allows one to check the ability of a vessel to withstand its maximum pressure service, it does not allow to detect the presence of all the growing defects. Moreover, the Pressure Equipment Directive 97/23/CE [1] and the work of the TC54 (in particular the draft standard prEN 13445) introduce the possibility to replace the hydrostatic test by another proof test, hydraulic or pneumatic. All this explains the will of manufacturers and industrialists to lay out a method able to evaluate the vessel integrity during the different proof tests and also to guarantee the safety of such a test especially when the test is a pneumatic one.

The final objective of the research program is to replace the first proof test (hydrostatic or otherwise) or to propose a method of vessel re-qualification by some in-service test, pneumatic or hydraulic, monitored by acoustic emission (AE). The first part of this program deals with tension tests on specimens to study the behavior of welding defects subjected to a cycle of loading representative of what a pressure vessel can bear during its life, from the point of view of their mechanical behavior and of their AE.

In the present case, to study:

- 1) the fatigue behavior of one defect, a long and shallow notch;
- 2) the abilities of detecting by AE the defect during the pressure vessel lifetime;
- 3) the evaluation of the harmfulness of a defect by the AE, and
- 4) the estimation of the life duration of a structure from the AE recorded during a proof test or following tests.

## **EXPERIMENTAL SET UP**

### **Specimens and defects features**

The research relates to large-sized tensile specimens drawn from a 6-mm thickness sheet of a carbon-manganese steel, (C: 0.17%; Si: 0.02%; Mn: 0.7% and YS = 336 MPa; TS = 469 MPa). A weld seam has been produced in the center of the sample by a TIG technique, and at its foot, a long and shallow notch has been made by EDM.

### The AE equipment

Four sensors, manufactured by CETIM and resonant at 180 kHz, are connected to an AMSY4 AE acquisition system from Vallen Systeme. They form a linear mesh around the weld seams, the two external sensors eliminating the noise coming from outside. The location of the events is very sharp and the signals resulting from the weld area, with or without defect, can be located easily.

One of the main difficulties encountered during the AE survey of fatigue tests comes from the noise generated by the hydraulic system of the fatigue machines since significant mechanical vibrations can mask the AE generated in the center of the test-piece by saturating the sensors. To avoid this problem, a system of vibration insulation has been designed and set between the piston rods and the hydraulic wedge grips. This system allowed the detection threshold decrease from 55 to 34 dB.

### Cycle of loading representative of a pressure vessels life

In order to simulate more precisely the flaw evolution during the life of a pressure vessel, a combination of proof and fatigue tests has been applied to the specimens (Fig. 1).

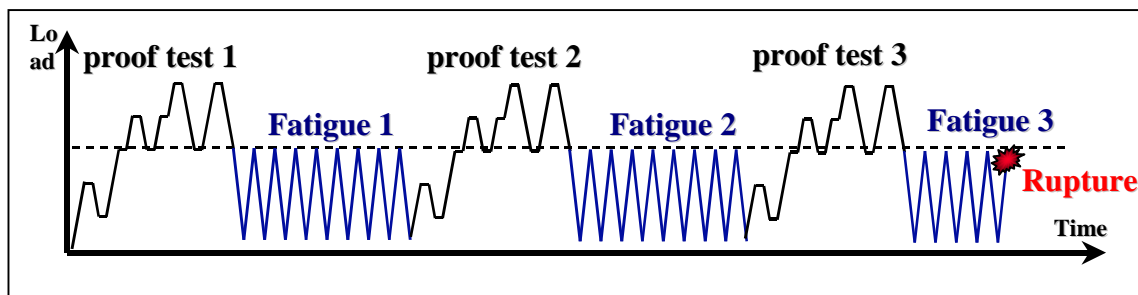


Fig. 1 Combination of cycles of tests and tests in fatigue applied to the specimens.

During the cycle of loading representative of a proof test, all the loads are compared to  $P_c$ , the design pressure. The maximum of load reaches  $1.5P_c$ , which is equivalent to 90% of the yield stress of the base material. The fatigue cycle is composed of sinusoidal oscillations at a 5-Hz frequency; the maximum of the load corresponding to  $P_c$ . The ratio between the minimal and maximal loads is 0.2. The number of cycles applied between two successive tests corresponds to a several daily uses of the vessel.

### DEFECT BEHAVIOR DURING FATIGUE LOADING ONLY

Under only fatigue cycling, the life duration of the specimens is expected from 86000 to 93000 cycles. The AE resulting from the defective zone is often masked during the fatigue cycles by a general emission of the specimen related to the resonance of the fatigue test machine. The vibration insulation system was unable to filter the significant vibration, and the signals of amplitude lower than 55 dB are not detected. Some of the specimens tested show an amplification of the emission recorded around the defective area to the two-thirds of the cycle. The rate of events and the average energy of the signals can increase then temporarily on a few thousands of cycles in the middle of the cycle. However, for each specimen, a final increase of the AE, in a number of events and in energy, is observed in the last thousands of cycles (Fig. 2).

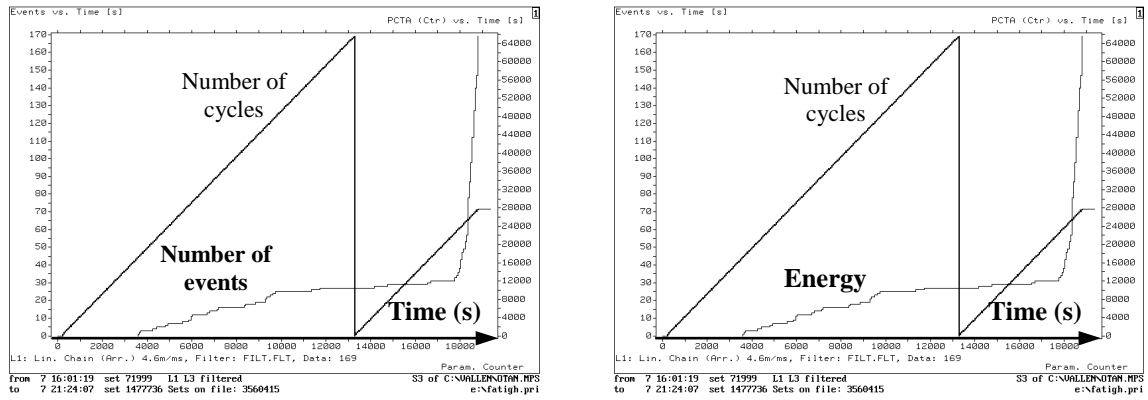


Fig. 2. Acoustic emission recorded on the level of the defective zone during cycling in fatigue;  
(a) Amplitude of the events. (b) Rate of true energy.

### Correlation between the mechanical behavior and the recorded acoustic emission

The mechanical behavior of the defect is composed of three successive stages: the initiation, the stable propagation and the final unstable propagation. The phenomenon of initiation features some ridges regularly laid out on the defect's initial boundary, which is synonymous with several starting points. The boundary of the defect quickly becomes uniform and propagates in the form of a succession of small striation and micro-cracks. Not very visible in the first half of the fatigue cycle, the striation becomes increasingly clear as the speed of the crack propagation increases. During the last stages of the stable cracking, the face presents a tangle of striation and dimples, synonymous with the appearance of a static tearing. Finally, the fatigue crack propagation becomes unstable, and a static fracture of the remaining ligament happens.

The stable propagation at low speed is undetectable by AE under the test conditions. Only the last stage of the stable propagation is clearly identifiable. It results in a rate of events and a rate of energy much more significant, the average amplitude of the signals remaining moderate. The small dimples thus do not generate events of strong amplitude. Schematically, the propagation speed of the crack, the rate of events and/or the rate of energy vary in time in a similar way and show in particular a strong increase during the last thousands cycles. The increase of the acoustic emission observed on some specimens at the two-thirds of the fatigue cycle is not related to a specific mark on the face of the crack.

## DEFECT DETECTION BY AE DURING THE LIFE OF A PRESSURE VESSEL

### Defect detection during the first proof test

Some previous studies [2,3] have shown that the long and shallow crack, submitted to a proof test, generates few AE and that the majority of the emission appears mainly in the second part of the loading cycle. However, different situations happen in the present case: Figure 3a shows a crack that generates a significant AE, but whose detection is paradoxically late since few insignificant events are observed until the load overtakes  $P_c$ . The detection of the defect is certain only during the last load rise towards  $1.5P_c$ . Figure 3b shows on the other hand a specimen far less emissive on the whole of the cycle, and whose events are not clearly indicative of the presence of a defect in the specimen.

In comparison with the behavior of a sound weld seam, the presence of a long and shallow crack in the vicinity of the weld is detected mainly by the amplitude of some of the recorded signals and by the temporal density of the AE appearance. The aspect of the Kaiser effect and the recurrence of the emission are not in the present case some criteria, which could allow us to detect the presence of the crack. Emission during holds is sometimes detected, but in a random way, which does not make it possible to be a relevant criterion.

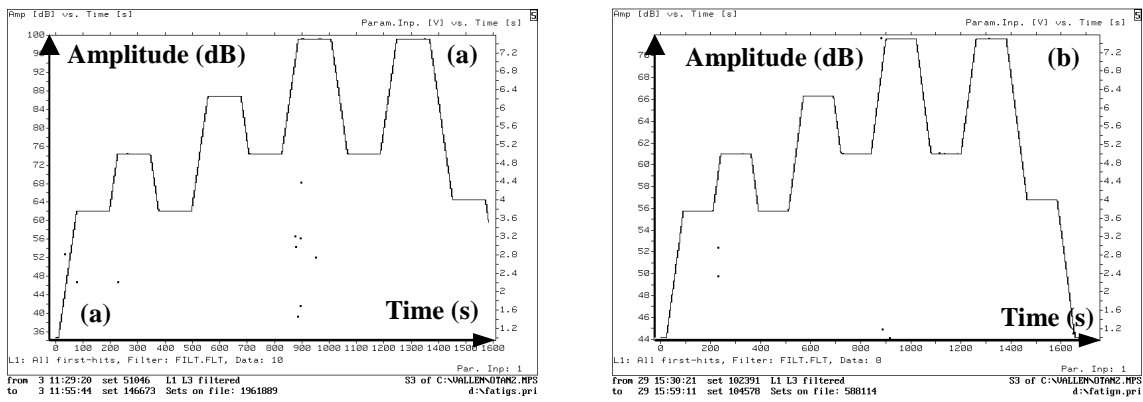


Figure 3: AE amplitude recorded during the first cycle of loading applied to two specimens containing a long and shallow crack.

### Detection of the defect from one proof test to another

Several specimens containing a long and shallow crack at the foot of their weld seam are submitted to a succession of proof and dynamic loading as described in Fig. 2.

In this situation, the fracture topography shows the following features (Fig. 4):

- The first proof test is not visible.
- The post-proof test behavior is typically like overloads and generates plastic deformation at the crack tip more significant in comparison with each previous fatigue cycle. The proof tests can be visually located on the fracture topography by a ribbon of smooth and bright surface. The width of this ribbon increases with the propagation of the crack since, the deeper is the crack, the bigger is the plastic deformation created ahead of the crack for a same load. Some ribbons are also accompanied by small dimples.
- Between the marks of the proof tests, the fatigue surface described in the first paragraph is observed. The width of these areas increases in time, whereas the number of cycles between the tests remains constant, thus representing the increase of the propagation speed of the crack in time.

The AE recorded during the second and the third successive proof tests undergone by the same specimen is described in Fig. 5 below (the first proof test of this specimen is related in the Fig. 3a).

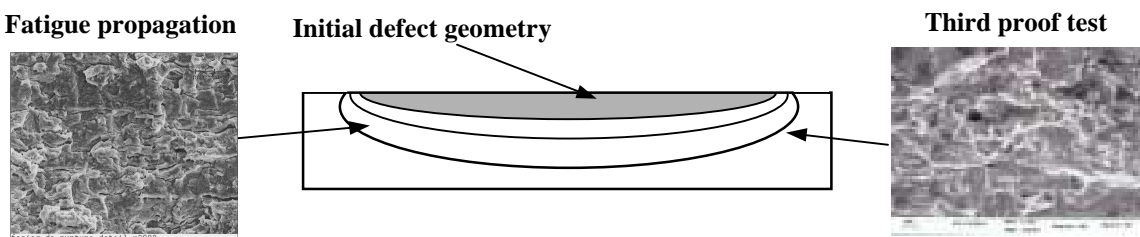


Fig. 4 Schematic fracture topography of a specimen which has undergone a succession of proof tests and fatigue loading.

The maximum of load reached during the fatigue cycling is equivalent to  $P_c$ , whereas it reaches  $1.5P_c$  during the different proof tests. The AE increases from a proof test to another since it is connected without any ambiguity to the volume of plastic deformation created during the overload. An increase, in quantity more than in quality, of the AE recorded from one test to the following is clearly correlated to the presence of a defect. However, as shown in the following paragraph, every defect is not announced

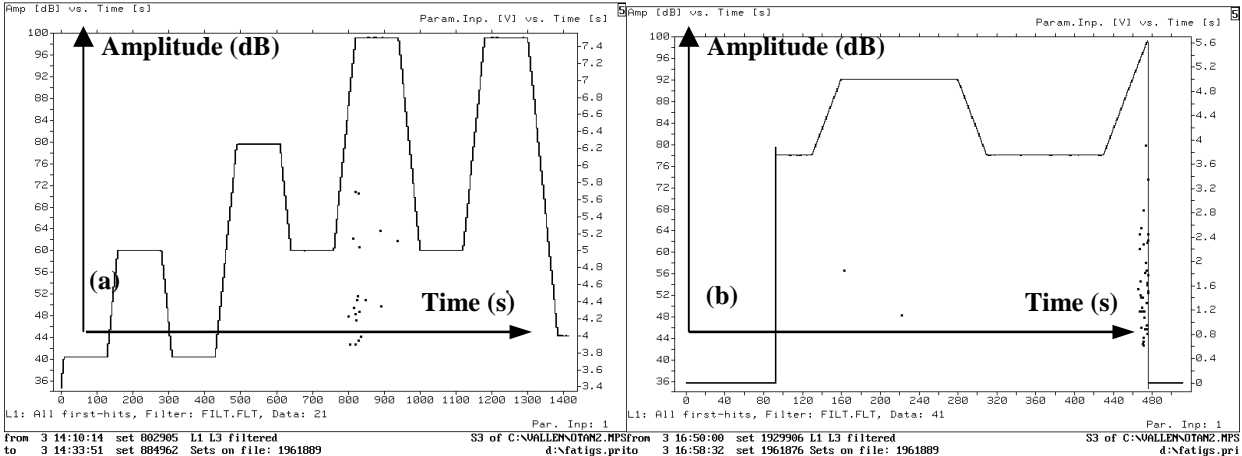


Fig. 5 Evolution of the acoustic emission (event amplitude) recorded during the second and the third proof tests undergone by a specimen (the first one corresponds to the Fig. 3a).

systematically by an increase in its AE from one test to another. That means that the comparison of the AE recorded from one test to another does not always make it possible to detect a growing defect.

During the second proof test, some AE can be recorded exclusively between  $P_c$  and  $1.5P_c$ , which means that the Kaiser effect can be observed whereas the defect propagates itself significantly during the previous fatigue loading (Fig. 5a). Some emission on the two holds at  $1.5P_c$  exist and, even if only two events appear clearly in the middle of these two stages, the emission observed on a hold is a best criterion for defect detection than the Kaiser effect can be. The final static fracture of the specimen happens during the third proof test at  $1.1P_c$ . Among the many tests performed, this is the only one where the Kaiser effect has not been observed (Fig. 5b).

The quantity of AE recorded during a test is thus in direct relationship to the level of damage undergone by the specimen and depends on the stage of evolution of the defect.

## ESTIMATION OF A DEFECT HAMFULNESS BY ACOUSTIC EMISSION

Three specimens, containing the same long and shallow crack are subjected to the same cycle of loading of Fig. 2. Although the defects are similar, the life duration of the third specimen is quite higher than the other two (+30%). Figure 6 represents below the number of events found during the different proof tests for each specimen.

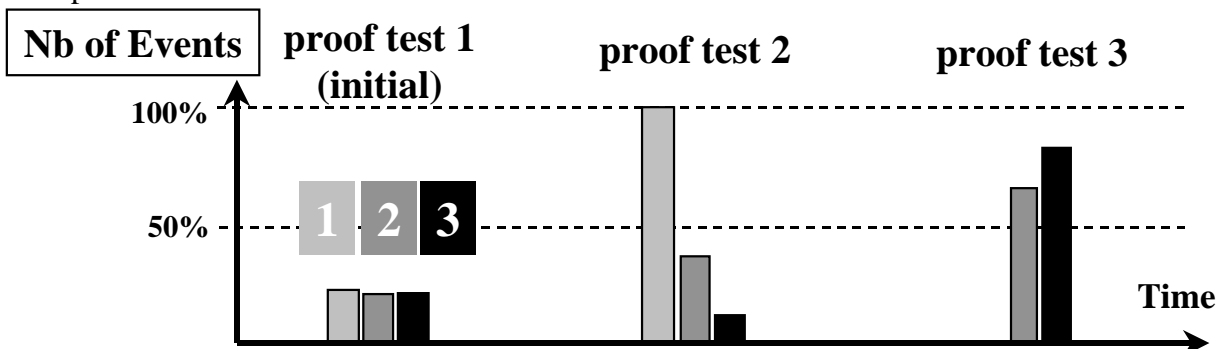


Fig. 6 Comparison of the number of events emitted in the defective area by three specimens during the three proof tests.

During the first proof test, the acoustic emission of the three specimens is relatively similar. After the first fatigue loading, the AE recorded during the second proof test is quite different among the three specimens. The specimen 1 is very emissive, and generates four times more events than during the first test. The specimen 2 shows a significant but limited growth in its AE. For the third specimen, the AE recorded during this second test is less than during the first one.

Compared to the evolution of the recorded emission from the first to the second, specimen 1 will break during the second fatigue test. The specimen 2 will complete its second fatigue load but will break during the third proof test and only the specimen 3 will bear the third proof test and will undergo a good part of a third fatigue test before breaking.

It is not thus possible to deduce the fatigue life-time of a specimen according to the AE, which it emits during the first proof test. The quantity of AE (in number of events or in energy) recorded during the second test appears to correlate to the life-time of the specimens if it is compared with the emission of the first test. The harmfulness of the defects is absolutely not quantifiable by the AE recorded at the time of the first test. Only the comparison of the acoustic emissions recorded during tests 1 and 2 gives a real indication of the tendency to the growth of a defect and thus of its harmfulness. Some defects being propagated significantly in fatigue cannot be detected during a proof test.

## **CONCLUSION**

By combining two kinds of loading, the experimental setup makes it possible to understand the real evolution of the defect during the life of a pressure vessel. The tests show that the AE emitted is directly correlated to the evolution stage of the defects. There is then a real relation between AE and the damage of the structures. The first test does not make it possible to have an idea of the harmfulness of the defects. On the other hand, the AE recorded during the second test is directly in correlation to the number of cycles borne by the structures up to the fracture. Furthermore, it is the comparison of the appearance of the AE between the two tests, which makes it possible to give an idea of the tendency to the growth of the defects and thus of their harmfulness.

## **REFERENCES**

- [1] European directive 97/23/CE, "Parliament and Council's directive related to the adjustment of the different European States' regulations, concerning the pressure vessels", 1997.
- [2] R. PENSEC, M. CHERFAOUI, C. HERVE and A. LAKSIMI, "Monitoring of defects evolution in pressure vessels. Application to the Improvement of the AE detection criteria", AES99, p. 187, Brno, 1999.
- [3] R. PENSEC, M. CHERFAOUI, C. HERVE and A. LAKSIMI, "Discrimination of flaws evolution patterns during pressure vessels static and dynamic cycles of loading thanks to the acoustic emission method", QNDE 99, Montreal, 1999.

# **ACOUSTIC EMISSION (AE) DUE TO CYCLIC PRESSURISATION OF VESSELS WITH PARTIALLY PENETRATED LONGITUDINAL SEAMS**

**Mulu BAYRAY**

**Vienna University of Technology, Vienna, Austria**

## **ABSTRACT**

*Experiments have been conducted at the Institute of Pressure Vessel and Plant Technology on a series of vessels with partially penetrated longitudinal seams. A pressure test and subsequent cyclic pressurisation were carried out on the vessels. AE statistical analysis of the pressure tests was reported in the previous EWGAE meeting. In this paper the AE signal due to the cyclic pressurisation of the vessels will be discussed. The aim of the paper is to present the experimental results obtained in investigating the crack growth using the AE data. Possible sources of noise during data acquisition were identified and ways of filtering the noise implemented. The AE data that is expected to be from the crack growth was then analysed. Results of the data analyses indicate that the AE intensity (e.g. cumulative counts) increases rapidly before burst. The AE data prior to burst are in agreement with crack growth measurement using strain gauges. It is also observed that the AE events occur mostly during the increasing pressure phase, well before reaching the maximum pressure.*

## **INTRODUCTION**

Experiments have been conducted at the Institute of Pressure Vessel and Plant Technology on a series of vessels with partially penetrated longitudinal seams [1]. AE statistical data analysis of the pressure test part of the experiments was reported in [2]. This current paper deals with AE data analysis due to cyclic pressurisation on vessels of series BC (16 vessels BC02-BC18 excluding BC07).

The objective of this paper is to present the AE data analyses during the cyclic pressurisation; especially, to investigate possible sources of noise and establish ways of filtering noise, to investigate the AE events due to fatigue crack growth and to investigate the possibility of monitoring the fatigue crack growth. The experimental procedure will be briefly described in the first section. The second section deals with the presentation of results and discussions. Finally concluding remarks will be forwarded.

## **EXPERIMENTAL PROCEDURE**

The description of the experimental set-up, test vessels and procedure are discussed in [1-2]. The experimental procedure will be briefly discussed here for convenience. The vessels with outer diameter 351 mm, overall length 600 mm, and thickness 3.5 mm were made of St52-3 DIN 17100 base material. The vessels were manufactured with intentional lack of penetration on the longitudinal weld. The lack of penetration was on the inside (root) of the one-sided weld and was about 240 mm long. The external

weld excess of the longitudinal weld was ground off. This region was the expected failure area during the loading of the vessels under internal pressure.

The general procedure of the experiment was to conduct a pressure test followed by cyclic pressurisation until failure. The pressure test was carried out as near as possible to the burst pressure and was monitored using strain as break-off criteria (Pressure at break-off,  $P_{bo}$ , was at 0.2% mean strain over 20 mm gauge length for BC02 and 0.5% for the rest). Then the vessel was cycled, sinusoidal at frequency of 1 Hz, for the first 10,000 cycles with  $P_{bo}/2.45$  as maximum pressure. For vessels surviving 10,000 cycles, the maximum pressure was increased and cycling continued up to the next 10,000 cycles. This procedure was repeated until failure. AE and strain gauge measurements were carried out during both the pressure test and cyclic pressurisation.

Five sensors (four 150 kHz resonant and one 900 kHz wideband) with Vallen Systeme AMS3 instrumentation were used to acquire the AE data. Preamplifier gain of 34 dB and threshold of 27 dB with 6 dB crest factor was utilised during the data acquisition.

## **EXPERIMENTAL RESULTS AND DISCUSSION**

### **Calibration**

The auto-calibration option of the AE instrumentation was utilised to calibrate the sensors. Difference in sensitivity among sensors was obtained by comparing two sensors and their response when one is used as a calibration input and the other as a receiver, and vice versa. An average and the maximum difference in sensitivity in the array of sensors were used as comparison criteria. Comparing the calibration data of all the vessels, the variations were not far from each other. Also, the average sensitivity of the sensors during the tests were in the range of the ASTM recommendation of  $\pm 4$  dB [3]. Thus, data collected during the respective cyclic pressurisation can be assumed as acquired at similar sensor conditions.

### **Signal – Noise Discrimination**

The possible sources of noise identified were due to electrical interference (EMI), pressurisation noise at inlet/outlet, friction at supporting brackets, and noise from circumferential welds (joggle joints). A large amount of data was acquired during the experiment, so that investigation and classification of the source of noise was difficult. Thus, we utilised methods of filtering and extracting the useful AE (due to the damage/failure). The filtering methods were: (1) Frequency filter: data was already acquired with high pass filter of 100 kHz integral with the preamplifier. (2) Amplitude filter: amplitude filter of 40 dB was used to suppress low-amplitude hits, which cannot be properly located. (3) Duration filter: hits having less than 30  $\mu$ s were filtered out to suppress any short duration electrical interference. (4) Location filter: after location of events using the above filters a filter which considers only events from the expected failing region was utilised. The filter was between  $-5 < X < 5$  and  $10 < Y < 40$  (cm), which describes the expected failing region. The data extracted using the noise filtering methods outlined above was considered for further analyses.

Table 1 below compares number of events extracted as useful data and total number of events acquired employing the first three filtering methods described above. The amount of useful data varies from one vessel to another, but was less than 8 % of the total amount of data acquired.

*Table 1 Extracted events and total number of events acquired.*

Vessel	Total no. of events (located and not located)	Events located inside expected region	% total
BC03	12,687	118	1.0
BC16	27,040	448	1.7
BC08	25,056	709	2.8
BC11	16,571	1,204	7.3

### Cumulative Counts versus Number of Cycles

In order to examine the history of the AE hits, cumulative counts and cumulative energy of all first hit channels were investigated (AE data discussed in the coming sections will be based on all first hit channels of the four 150 kHz sensors). In most cases, the cumulative counts and cumulative energy were found to have similar trend. In further discussions, only the cumulative counts will be considered. However, similar discussions could be made on the cumulative energy data.

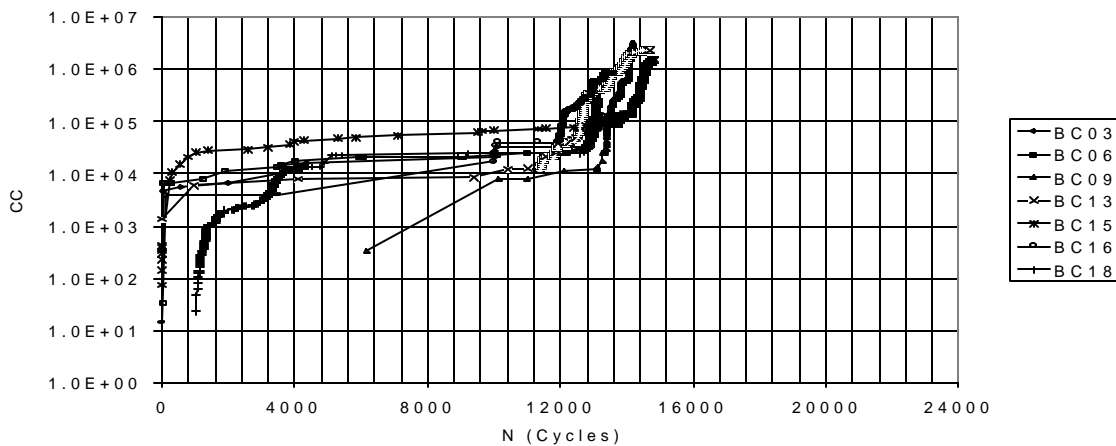


*Fig. 1 Cumulative counts versus number of cycles: Group I.*

Figures 1 to 3 show the AE activity in terms of cumulative counts (CC in logarithmic scale) throughout the life of the vessels (N). The plots are shown for the vessels in group for simplicity of viewing. The plots have in general three distinctive phases. The first phase, at the beginning of the fatigue cycles, is characterised by few events and few counts. The second phase, mid and major portion of the fatigue cycles, is characterised by low or no AE activity in almost all vessels. The third phase, few cycles before failure, is characterised by high rate of AE activity and hence the cumulative counts rose within

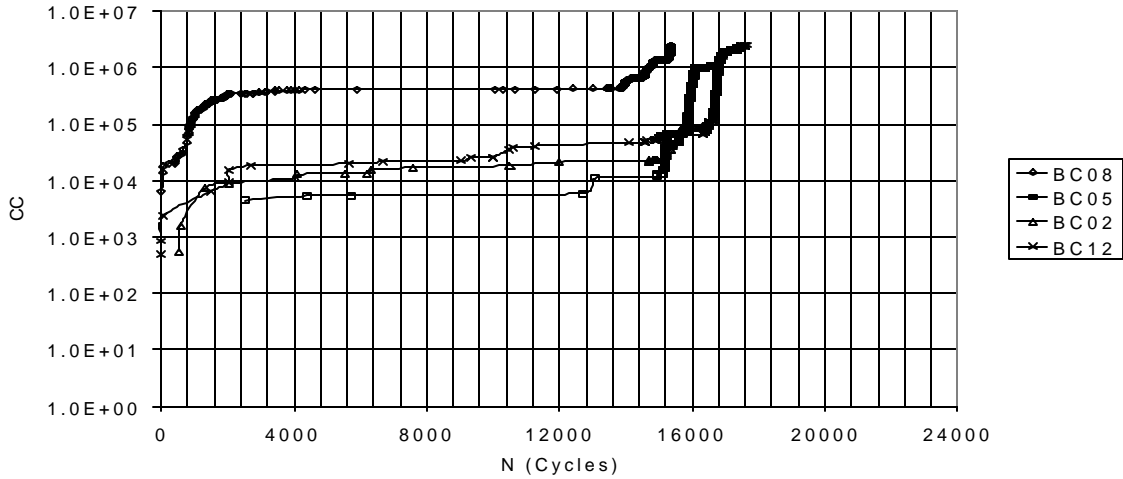


*Fig. 2 Cumulative counts versus number of cycles: Group II.*

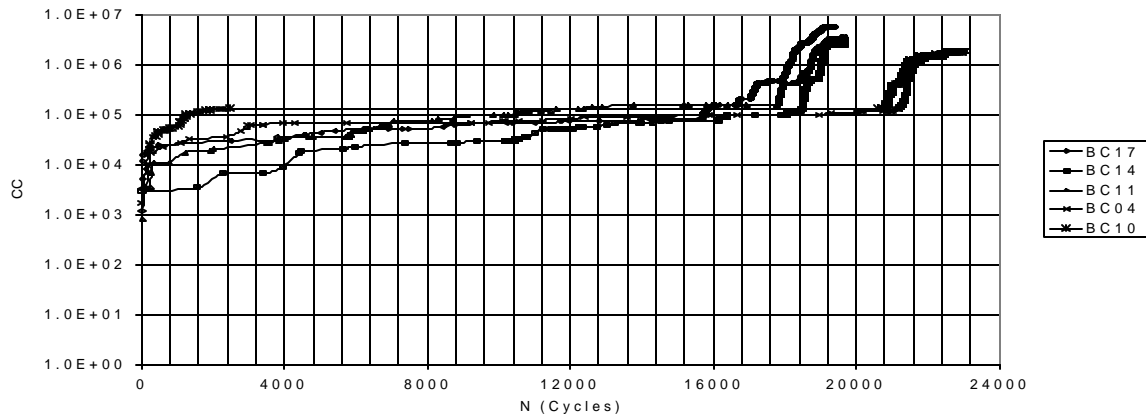


*Fig. 3 Cumulative counts versus number of cycles: Group III.*

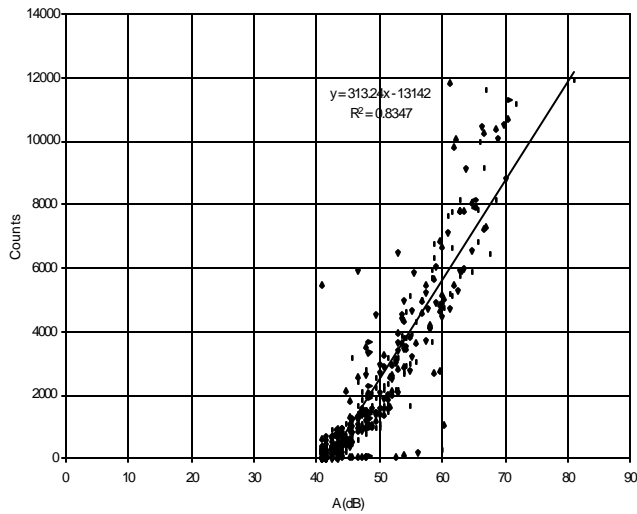
relatively few numbers of cycles. The sudden rise of AE cumulative counts was observed to happen after about 85 – 95 % of the total cyclic life of the vessel.

### Number of Counts versus Amplitude

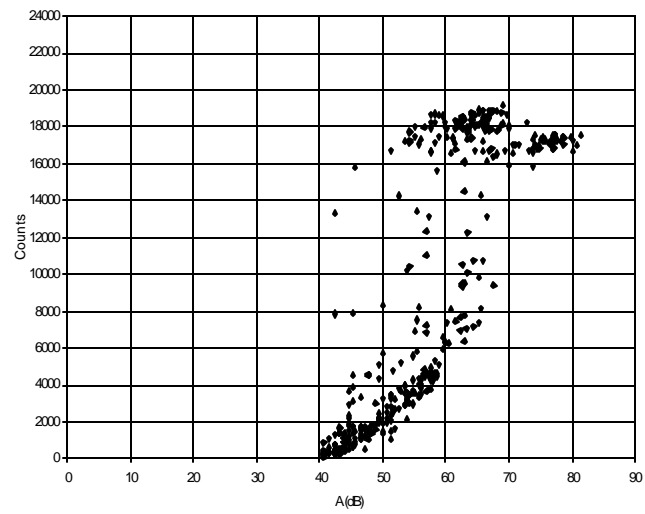
To look into the similarity and difference in characteristics of events in each vessel, the number of counts with the respective amplitude of hits were investigated. The plots of number of counts versus amplitude for vessels BC06 and BC09 are shown in Fig. 4.

It can be noted that the plot for BC06 shows a good linear relation between the number of counts and the amplitude. A trend line, including its regression function and coefficient of determination ( $R^2$ ), is shown in Fig. 4a. Such a trend is observed in most vessels although the scatter was variable from one vessel to another. A linear relationship between the number of counts and the amplitude (in dB scale) means an exponentially decaying signal. The plot for BC09 (also for BC08) shows a number of events with high number of counts ranging from low to high amplitudes (Fig. 4b). This means no relation between the

number of counts and the amplitude of the hits. This is expected from leak-type AE events, which are characterised by continuous emission. Hits of such type, whether low amplitude or high amplitude, have high number of counts. The last few cycles of vessel BC09 were, therefore, leak-type hits. In fact, when numerical filtering was used to suppress the last few cycles, linear tendency is obtained. The rms voltage level was also high during the last few cycles, and it confirms the existence of leakage before burst.



a) Vessel BC06.



b) Vessel BC09.

Fig. 4 Number of counts versus amplitude.

### Comparison between AE Cumulative Counts and Strain Gauge Data

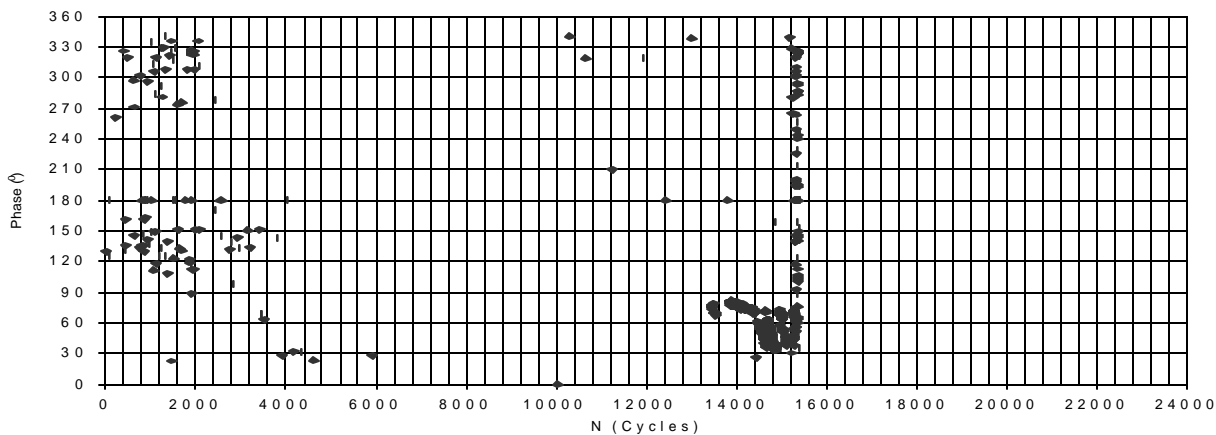
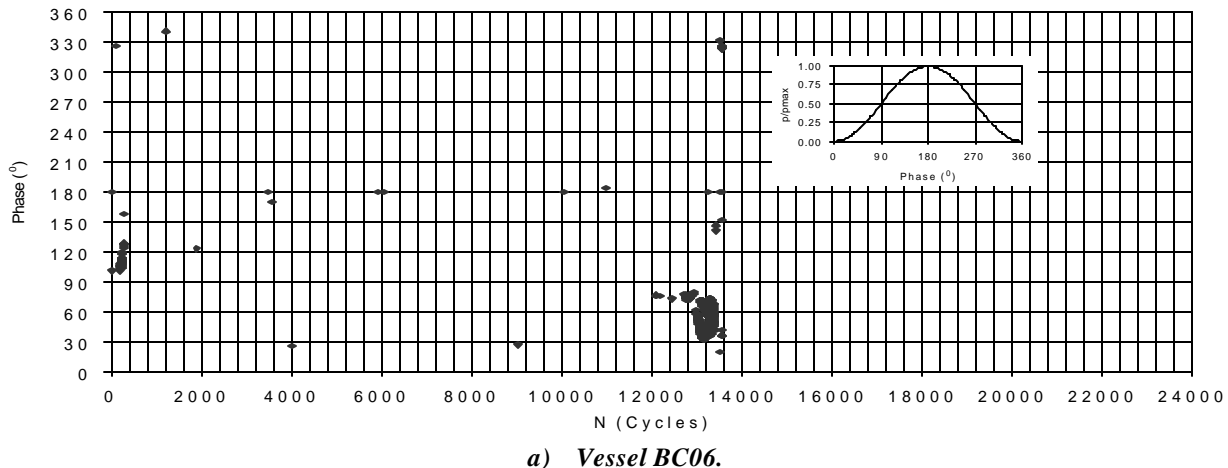
The cyclic pressurisation was also monitored using strain gauges attached close to the failure region. The strain gauge instrumentation was capable of recording data online. The AE cumulative counts data compared with strain gauge measurement data show similar trend. The strain gauge data recorded high rate of increase at the same time when the AE recorded high rate of counts.

### Occurrence of Events with Respect to Phase of Load Cycle

During the data acquisition, it was observed that most AE hits occur at lower pressure than at the maximum pressure of the cyclic load. The cyclic pressurisation was sinusoidal type of loading (phase 0 – 360°) alternating from minimum value (0° phase) just above 0 bar up to the maximum value (180° phase) and back to minimum value (360° phase), see insert of Fig. 5a. Utilising the cycle slope flag of the AE system and the pressure (parametric input), the occurrence of the events with respect to the phase of loading cycle was determined.

In most cases, the majority of events occurred during the phase where the load was increasing. Few events occurred near the maximum pressure and during the phase where the load was decreasing (with exceptions outlined in the next section). The AE data can be analysed by looking at the phase, at which the events were recorded as the number of cycles increases until burst. Figure 5 is such a plot for vessels BC06 and BC08. On most of the vessels, the following can be observed. (1) The majority of the events were recorded in the range 30-90° phase in most of the vessels. This means that those events were

recorded during the increasing pressure phase. After such events are observed, most vessels failed within a small number of cycles (400-3800 cycles). (2) In most of the vessels, the phase at which the events were recorded decreases as the number of cycles gets closer to burst. (3) In most vessels, a number of events were recorded around the maximum pressure ( $180^0$  phase). (4) Events were also recorded randomly on the increasing and decreasing phase of loading at the cycles close to final burst.



*b) Vessel BC08.*

*Fig. 5 Distribution of event occurrence with phase and number of cycles.*

Exceptions to the above observation:

- (a) Hits with low amplitude and low number of counts were recorded in vessels BC06, BC11, BC14 and BC18. Those hits can be identified on the amplitude versus phase and counts versus phase plots. The occurrence of the events was irregular and the source of the events might be noise.
- (b) Hits with varying amplitude and number of counts were recorded at early cycles in vessels BC08 (see Fig. 5) and BC10. The events were recorded near the maximum pressure ( $180^0$  phase), and in the decreasing pressure phase towards the minimum ( $300-360^0$  phase). The rms voltage level during this time was higher than the normal background noise level. The source of the events was not identified.

(c) Even though in most vessels events near burst were recorded throughout the load cycle, vessels BC08 and BC09 (see Fig. 4b) recorded abnormally many events. The hits were with high number of counts irrespective of the amplitude. Those events were due to leak just before burst.

## CONCLUSION

The signal–noise filtering method has extracted useful AE data due to crack growth. The exponentially decaying type of hits observed and confirmation of crack growth through strain gage measurement imply that the majority of the extracted data was from crack growth. However, the percentage of useful data as compared to the total amount of data recorded during the experiments was too small. Improvement in the percentage of useful data is expected by optimising the acquisition parameters. Studies in progress of improving the location of events on AE experiments of such small vessels is reported in [4].

The AE cumulative counts data showed that the growth of the crack could be monitored in most of the vessels. The cumulative counts increased at higher rates during crack growth, which could be seen on the plot of cumulative counts versus number of cycles. However, the number of cycles from the crack growth phase before failure was variable from one vessel to another.

Most of the AE events just prior to failure were found to be at the increasing phase in the cycle but lower than the maximum pressure. Though events were also recorded near the maximum pressure, the events at low pressure show that load gating may result in missing data related to crack growth. Further study would be necessary to investigate this observation and to look at utilising it as means of monitoring the crack growth.

Based on the AE data analysed, it seems that in the vessels considered here, no crack growth was observed until 10,000 cycles.

## REFERENCES

- [1] Project Report, “Pressure Vessels: The determination of the relation between the fatigue strength and hydro test pressure,” Vienna University of Technology, Institute of Pressure Vessels and Plant Technology, unpublished.
- [2] Rauscher, F., “Acoustic emission of vessels with partially penetrated longitudinal seams,” Proceeding of the EWGAE conference AE’99, Brno Czech Republic, June, 1999.
- [3] ASTM Standard, ASTM E 976.
- [4] Rauscher, F., “Optimisation of acquisition parameters for acoustic emission measurements on small pressure vessels,” Proceedings of the 24<sup>th</sup> European Conference on Acoustic Emission Testing-EWGAE 2000, Senlis, France, May, 2000.

# INSPECTION OF LPG VESSELS WITH AE EXAMINATION

P. TSCHELIESNIG and G. SCHAURITSCH  
TÜV Austria, Wien, Austria

## ABSTRACT

Since 1992 the required main inspection can be replaced by a pneumatic loading monitored with acoustic emission (AE). The data evaluation, which started with ASTM Standards, has to be changed, because new results showed that the specific kind of defects in joggle joints and all disturb noise make an active evaluation method inappropriate. An evaluation method based on the different AE characteristics, combined in a Cluster Evaluation Factor (CEF) and implemented in the on-line monitoring, gives us and in specific the test inspector the opportunity to detect the criticality of a vessel very early and stop the test without any problem for the environment.

## INTRODUCTION

It's obvious, that today gas is beside crude oil the most important basis for the production of energy. Because the establishment of the necessary network of transportation lines for natural gas is expensive the common alternative is the use of liquefied petroleum gas (LPG). This LPG is stored at the end-user, often private houses or medium and small enterprises, in small storage tanks up to 15 m<sup>3</sup>. Since these storage tanks (pressure vessels) have to be inspected before they go into service and periodically during their lifetime, we found defective storage tanks, which lead, due to defects in the welds, to the escape of LPG even during the normal service period. These defects occurred in the circumferential welds (joggle joints) caused by stress corrosion cracking (SCC). The Technical Inspection Hessen (BRD) investigated these phenomena and discovered that the reason for it has been the filling of these vessels with methanol during storage before they went into service. Because the TÜV Austria has experience with AE-testing of these types of vessels since 1992 and has tested and investigated similar defects, which occurred in France in 1995/96, it was invited to help devise a proper testing method for these specific defects.

## BASEMENT AND DEMANDS ON THE TECHNIQUE

Based on the experience with the specific type of defects we have had the following cracks in the joggle-joints, the heat-affected zone and even in the remaining overlapping part of the material.

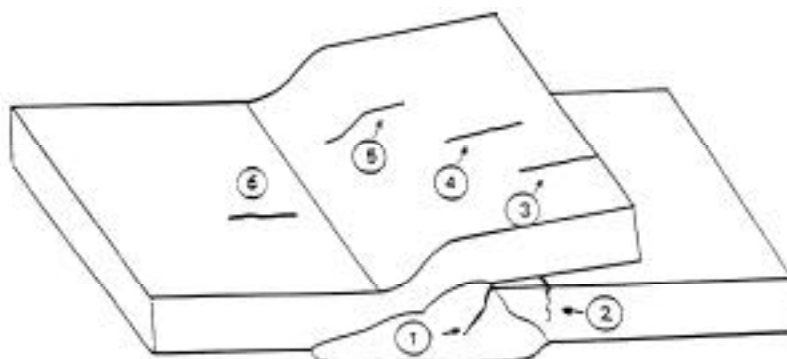


Fig. 1: Specific defects in the joggle-joint.

Due to technical and economical reasons, a planar location system is inapplicable, especially for those vessels, which are buried. These buried vessels are only accessible within the “dome” region, which are situated the man-hole (e.g. Germany, Switzerland and Austria) or only through connection-lines (e.g. France). On the other hand, the application of a one-sensor technique was improper based on the shadowing effect and the high attenuation of the buried vessels, because one sensor could not possibly inspect an area of up to  $30\text{ m}^2$ . Based on the high noise level coming from the environment and the pressurisation device, the TÜV Austria used for vessels up to  $5\text{ m}^3$  a two-channel system with a linear correlation technique.

The loading during the tests were performed up to 1.1 times of the design pressure with the stock product (LPG) itself. During this measurement the activity of the AE was controlled, but also the intensity was evaluated.

Because AE can only detect those defects, which become active during the stimulation, it was clear that the defects #3 and 4 (see Fig. 1) cannot be detected by AE. However, these cracks were not dangerous for the vessels, because these parts of the vessel will not be stressed during the test or the normal service. The most dangerous defects for the remaining lifetime of the structure are the cracks #1 and 2.

## **EXPERIENCES WITH THE AE TESTS**

From 1997 till 1999, 39 vessels from these production lots, where these specific types of defects could be expected, were tested in Germany. Of those 54 % was flagged by AE and has to be re-tested by other NDT-methods. During this test-period one of the vessels became leaky at 1.61 MPa. These specific results will be discussed later.

In Austria we tested during the same time period 75 vessels of the same series and 16 % of those vessels with the most significant defects were taken out of service and under-went re-tests by other NDT-methods. In this case no cracks were found, but unacceptable welding defects (e.g. lacks of fusion) were detected.

The difference between the vessels in Germany and Austria has been the drying of the vessels in Germany. The formic acid, produced from methanol and water, appeared in the vessels in a higher concentration in German vessels. In Austrian vessels, the acid was diluted due to the higher amount of residual water. But in both test series we found the same production defects and those initiated the SCC in combination with the specific geometry of the joggle-joints.

## **AE-TEST RESULTS**

The most interesting example was an LPG tank, which has a storage capacity of 2.3 ton, with the diameter of 1.6 m. The material was StE 355 with a wall thickness of 5.6 mm. The tank was situated underground and protected with epoxy-resin against corrosion.

The loading was performed by the evaporation of the liquefied gas from the working pressure of 850 kPa and was controlled with AE. At 1.5 MPa, the safety relief valve started to open and was blocked. After this the pressurisation was continued. At 1.58 MPa the test-inspector detected a high AE activity

and stopped the test. A crack (type 1 defect) was unstable critically at this stage and de-pressurisation was too slow, the tank became leaky. Most of the gas could be pumped back in the service truck, but the area around the vessel has to be blocked till the gas was diluted under the explosion barrier.

A post-test AE-data evaluation indicated that the crack propagation, which was initiated at a very low pressure, could be detected at 1.35 MPa according the AE activity. But this didn't show a large increase of the rate. Much clear increase of the AE intensity occurred. See Fig. 2. A few events with a high amplitude and energy, which consequently also resulted in a rise for the ring-down counts (with event duration of over 100 ms).

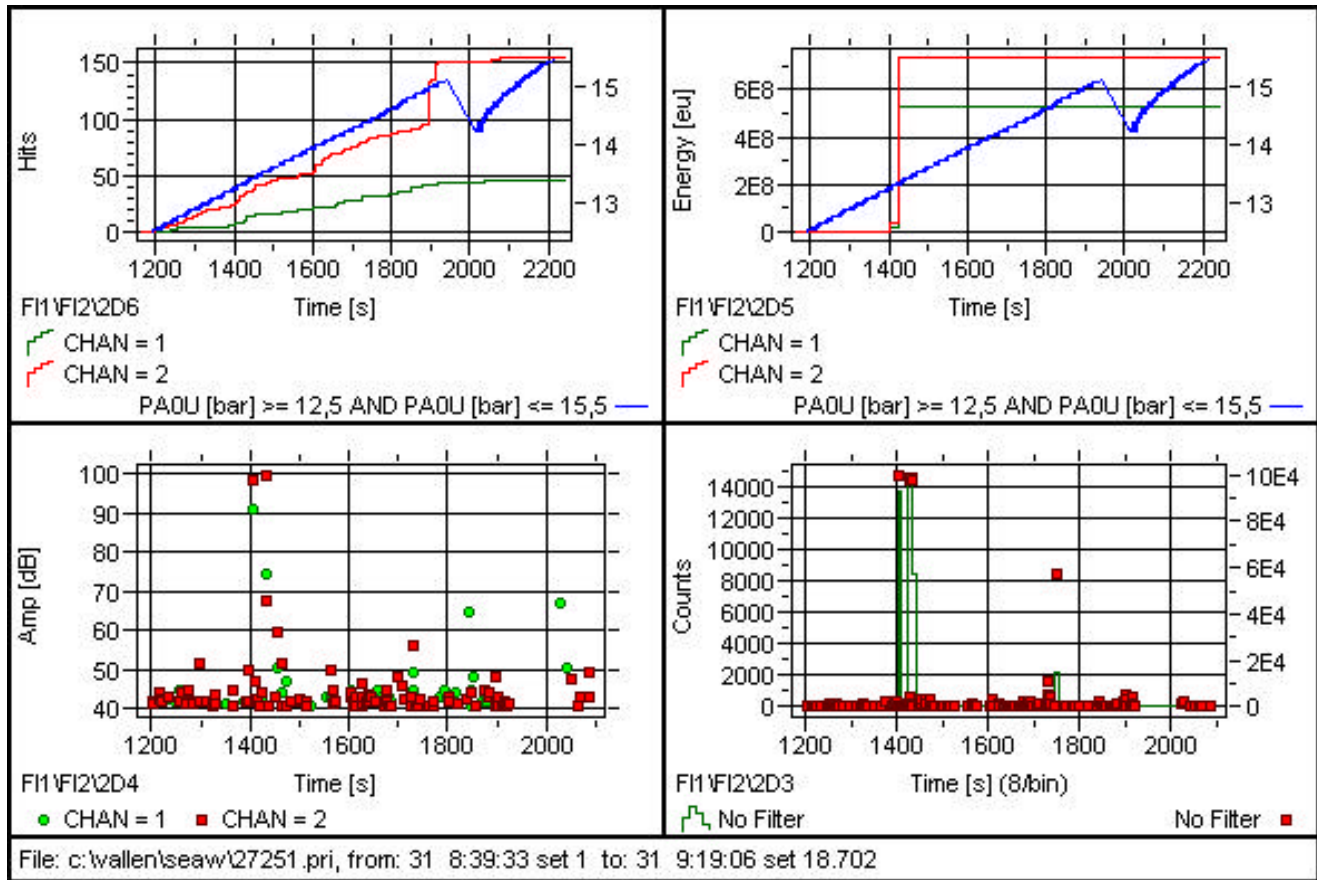
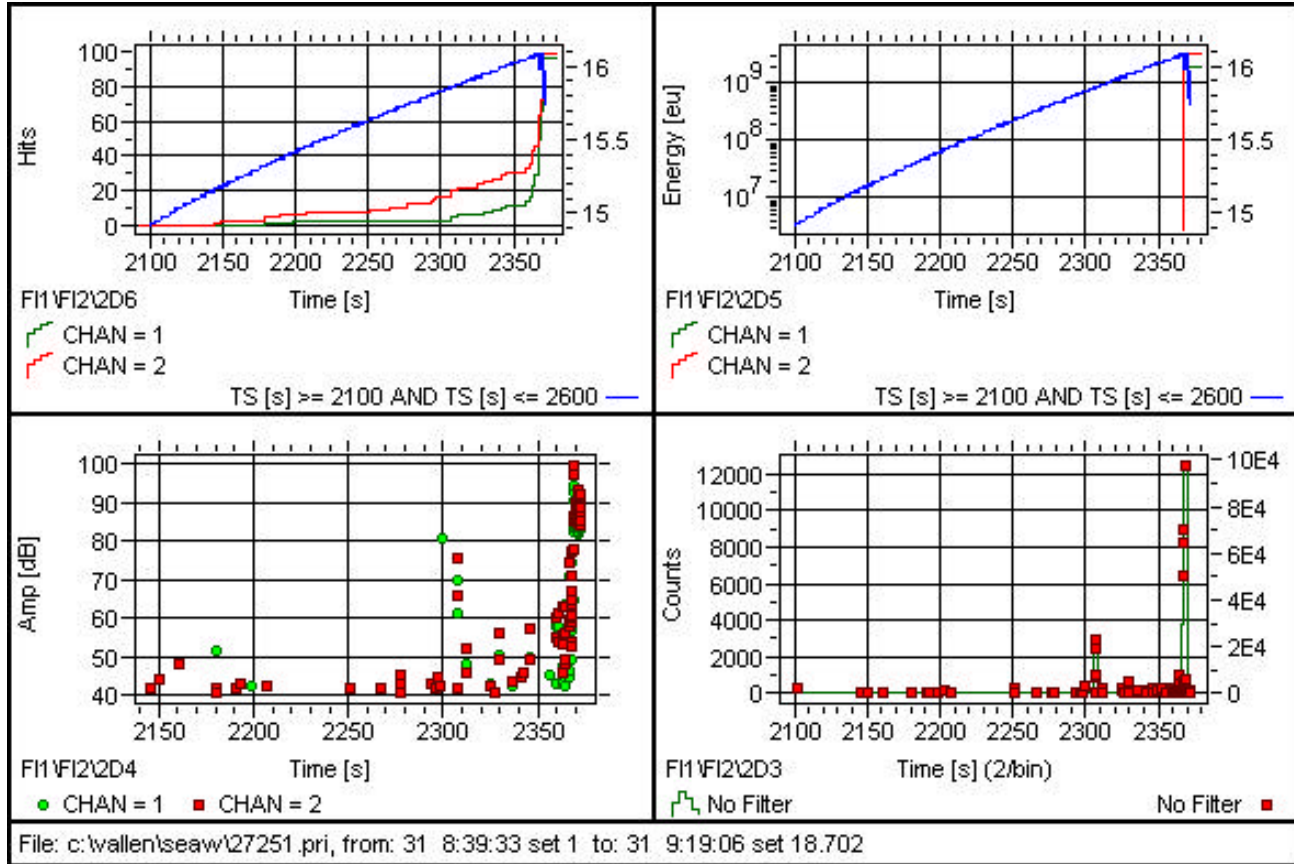


Fig. 2: AE-graphs starting from 1.2 MPa.

A more detailed evaluation of the data starting from the blocking of the safety relief valve showed that till 1.58 MPa only a smooth increase of the hit- and count-rate was found (Fig. 3). A few high energy events with consequently also high amplitudes led to a rapid increase in the energy and also count rate above 1.58 MPa. At 1.61 MPa the crack became critical and the pressure relief followed couldn't stop the crack propagation.

After the test, the tank was dug out and we found a 40-cm long crack of type 1 caused by stress corrosion cracking in the circumferential weld in the 6 o'clock position. The welding showed a massive pre-damage and the residual wall-thickness of 1 mm fractured spontaneously by the loading.



*Fig. 3: AE-graphs for the last period (1.50 MPa till 1.61 MPa).*

Such a big crack, which penetrated through more than 90 % of wall before the loading, showed in the AE behaviour no increase in the AE activity rate until the crack started to propagate. This is caused in this specific case by the joggle-joint geometry. This kind of welding produces a lot of interference noise due to remaining slag and other metallic particles in the over-lapping part of the weld, while any extension of the weld in circumferential direction of the weld is extremely restricted. Because the cracks are open from the beginning, no AE from crack opening movement could be detected.

From 1.5 MPa till 1.58 MPa, a few but very energetic signals could be detected. These were produced by crack propagation. This crack can be detected with AE and shall lead to a safe “stop” of the test. To take this into account, a specific factor, which gives us a possibility to classify a tank or even a specific area quantitatively in the post analysis, has to be obtained. This “Cluster Evaluation Factor (CEF)” refers to the specific characteristics of the AE-signals for the pre-selected cluster produced by a correlation between the two sensors used. Due to the small sensor-to-sensor distance, a definite location is impossible, but this time correlation gives us the possibility to filter out the noise and to weight the factor for a specific area. Under this presupposition, that is, for this type of vessels the defects are always in the same region, we can recalculate the energy of the event to the place of its origin or take this into account for the threshold of this factor. This evaluation factor is calculated according to the following formula:

$$CEF = \frac{1}{z} \sum_{n=1}^z f_{p_n}$$

where  $f_{p_n}$  is weighting-factor for the different AE characteristics,  $p_n$  is used AE characteristic (e.g. maximum amplitude, true energy) and  $z$  is number of used signal characteristics

This formula gives us a quantitative expression about the specific cluster of the test object. This factor will be implemented into the testing procedure as an alert-value and/or a stop-criteria and will be used on-line during the pressurisation.

In the example shown (Fig. 4), the CEF demonstrates the criticality of the vessel at 1.16 MPa, which gives enough time to stop the loading.

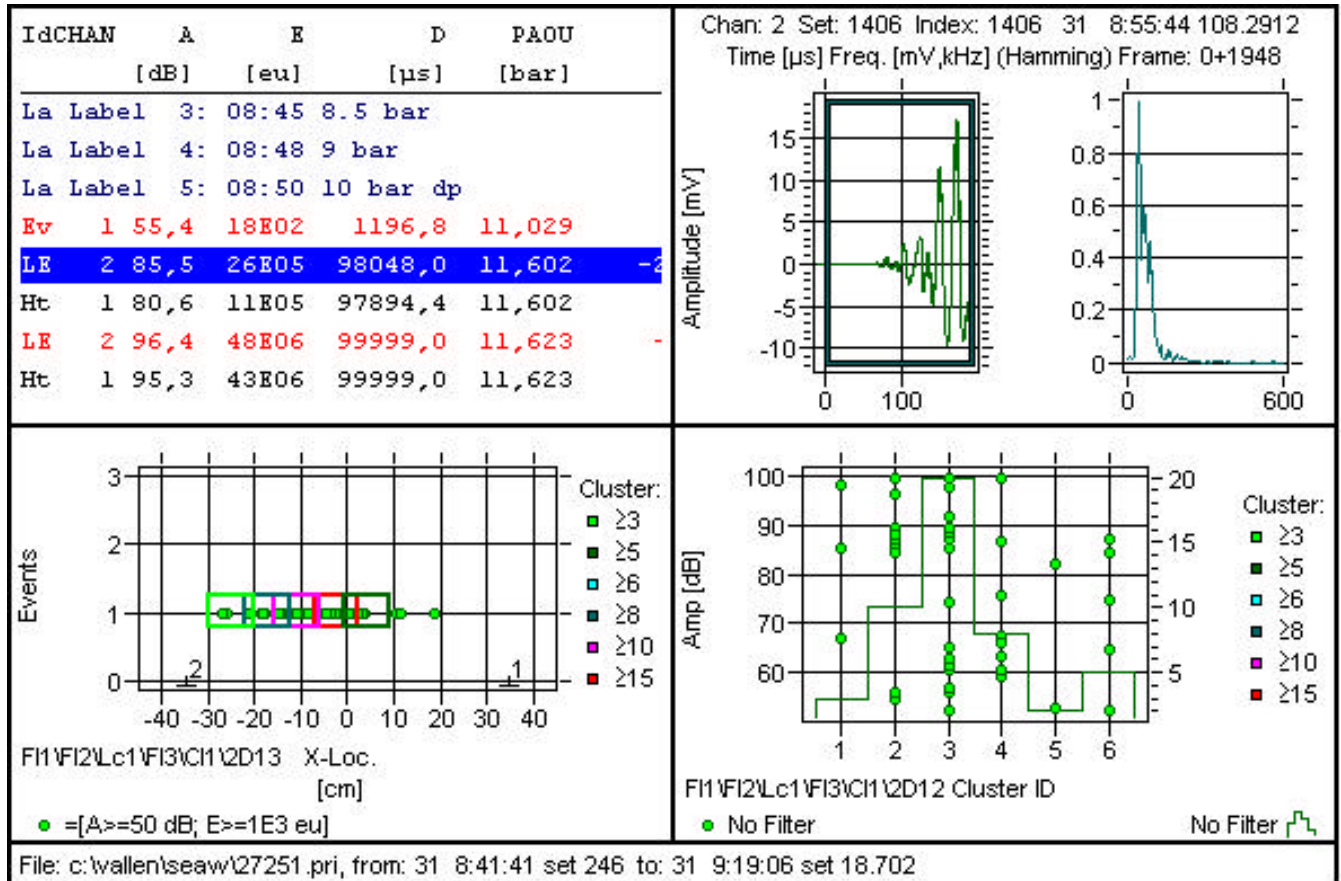


Fig. 4: Example of CEF.

Beside a clear test procedure, the previous feasibility check and a clear value for the CEF, the test inspector needs not to weight the different AE signatures of the vessel and gains therefore the necessary reaction-time to stop the pneumatic loading in time. This is an absolute requirement for this kind of tests.

## CONCLUSION

Since 1992 the mandatory inspection (hydrotest and visual inside inspection) can be replaced by a pneumatic test monitored with acoustic emission. The data evaluation started at the beginning has to be done according the ASTM E 569-82 "Standard Practice for Acoustic Emission Monitoring of Structures During Controlled Stimulation". This requirement is still valid for the accreditation and bring also a

sufficient result and pre-warning time, if only stable crack propagation appears. If you also have unstable, critical crack propagation, it is absolute necessary to add to this standard a specific test modification.

This test modification has to be adapted on the problems of joggle-joints as circumferential welds. These welds have specific defects, caused by stress corrosion cracking, but the AE behaviour is also distorted by the hindered elongation and the noise. Even though the structure produces enough AE for the pre-warning, the number of AE events is small and the AE test-crew must be highly alert during the pressure test.

For the on-line monitoring, one needs a pre-evaluated factor, which gives a simple quantitative value of the safety of the structure. The TÜV Austria used a specific cluster evaluation factor, which gives us the opportunity to include all necessary AE characteristics into a quantitative guideline to stop or continue the test.

## REFERENCES

1. P. Tscheliesnig, G. Schauritsch, G. Krenn; „Die Anwendung der Schallemissionsprüfung bei der wiederkehrenden Untersuchung von Flüssiggasbehältern“, TÜV Österreich (former Wien), presented at the 9. Kolloquium „Schallemission“ of the DGZfP in Zittau, 1992.
2. P. Tscheliesnig, G. Schauritsch; „Erfahrung und Weiterentwicklung bei der Prüfung von kleinen Lagerbehältern mittels der Schallemissionsprüfung“, TÜV Österreich, presented at the 11. Kolloquium „Schallemission“ of the DGZfP in Jena, 1997.
3. J.M. Capreau (Institute de Soudure), E. Eberhard (Butagaz), G. Schauritsch, P. Tscheliesnig (TÜV Austria), „Testing LPG Tanks By Acoustic Emission“, presented at the 23<sup>rd</sup> European Conference on Acoustic Emission Testing in Vienna, 1998.
4. P. Tscheliesnig (TÜV Austria), J. Liska (Skoda JS), “The testing of LPG vessels with Acoustic Emission Examination“, presented at the International Conference of Acoustic Emission in Brno (CS), 1999.

# **INSPECTION OF PRESSURE VESSELS USED IN REFRIGERATION AND AIR CONDITIONNING SYSTEMS**

**Alain SKRABER, Fan ZHANG, Mohammed CHERFAOUI and Laurent LEGIN\***  
**CETIM, Senlis, France and \*TRANE**

## **ABSTRACT**

*The survey consists in developing a monitored method, which uses the acoustic emission technique, allowing the overall quality of the structure to be assessed during testing while warranting the reliability of such a test when conducted pneumatically. The results given in this paper refer to tensile test runs on specimens and in-laboratory pressurization tests on refrigeration capacities. These tests have proven the fitness of acoustic emissions to detect growing defects on tanks made of a material for which the production processes (chemical pickling, shot-blasting, etc.) allow the surface oxide layer resulting from rolling to be eliminated. A space-time criterion allowing the discrimination of the signals representative of changes in a crack during the testing cycle has been developed.*

## **THE INDUSTRIAL PROBLEM**

In France, the statutory hydraulic test that serves for qualification purposes is advantageous in that it allows one to ensure that the vessel will withstand the maximum operating pressure. But it is costly as it involves the use of the whole plant and careful, lengthy cleaning operations even though it provides only a few pieces of information on the structural condition. The major drawbacks of the hydraulic test without any particular control are to make the defects vary without detecting them and to adversely affect the capacity performance owing to a residual humidity. The effects may alter the vessel life span and lead to extra costs.

Some mechanical industries especially those dealing with refrigeration equipment have been very much interested in the development of a method allowing the overall quality of the structure to be assessed during testing while warranting the reliability of such a test when conducted pneumatically.

Establishing a monitoring method would allow industrialists:

- to cope with the impossibility of using cryogenic fluids R11 and R113,
- to assess the overall quality of the structure,
- to eliminate any corrosion hazards,
- to reduce the lockout time during statutory re-testing with the possibility of making routine checking less frequent,
- to gain the experience required to adapt themselves to ever changing European standards and rules.

## **OBJECTIVES**

The survey consists in developing a monitoring method, which uses the acoustic emission technique and has two objectives, namely to assess the overall quality of the vessels while ensuring the reliability of pneumatic pressure tests.

The monitoring method would allow one to decide whether the vessel pressurization should be continued or stopped from the moment when any growing defect of a hazardous nature has been reliably detected and located in real time.

The results given only concern a portion of the project that consists in proving the method capability to meet this two-fold objective and in defining its limits and performances.

## APPROACH

At the end of various field test runs, it has first been proven that integrating an acoustic emission control system into a production line capable to adapt itself to environmental perturbations and production requirements was feasible.

A series of tensile tests on welded specimens has established a database representative of the behavior of the various welding defects. Tests aimed at adapting criteria obtained during the tests conducted on welded specimens have been carried out on pressure vessels of different size, made from different materials and of which the surface condition varied. It has, however, been impossible to directly transpose the criteria determined from welded specimen tests owing to the specific behavior of the various material surface conditions. The behavior differences will be explained by complementary tests conducted on «model» capacities and on specimens. These tests are described in the test result presentation.

The portion of the project that consists in defining a testing procedure and the associated software for automatic release of safety alarms is on the way. The results given in this paper refer to complementary tensile test runs on specimens and in-laboratory pressurization tests on capacities, which have allowed the method performances and limits to be evaluated.

## TESTING CONDITIONS

### General characteristics

The testing conditions described in Table 1 have been defined for in-laboratory tests conducted on cylindrical "model" capacities, upon which the analysis results described below are based. The table summarizes the main characteristics of tested capacities and of defects obtained by electro-discharge, and the test pressures ( $P_e = 1.5 \text{ Ps}$ ) reached.

*Table 1: Testing conditions*

Geometry(mm)			Nb of capacities	Test pressure	Defects: electroerosion	Nb of defects per capacity
dia.	thck.	Ig.			length(mm)	
400	6	1*600	7	60	100	1 or 2
168	3	1*280	12	50	10; 30; 50	1
168	4	1*185	22	80	50	1
600	6	2*260	3	30	50	6

### Testing cycle

The testing cycle represented on Fig. 1 consists of successive rises and plateaus. The vessel is subjected to pressure variations throughout the testing cycle twice before linear pressure loading takes place and until a burst occurs.

### Sensor layout

In most cases, the device used on all the tanks includes eight sensors, two of which are located on the

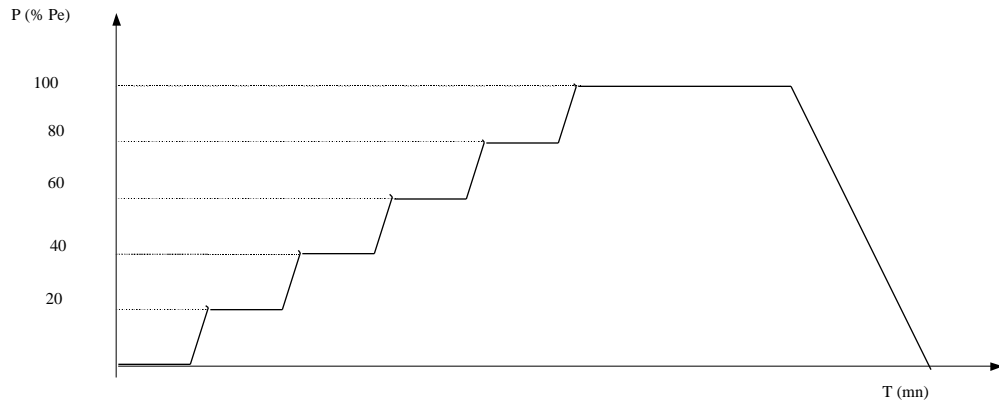


Fig. 1: Testing cycle

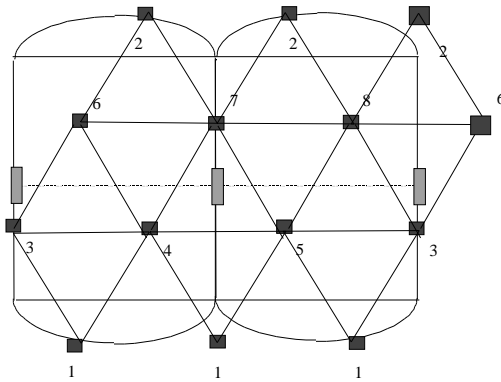


Fig. 2: Sensor layout on a developed view of the tank.

vessel bottom. The other six are set in two rows of three sensors each equally spaced so that the notches fall within an equilateral triangle as seen on Fig. 2.

## Instrumentation

The acquisition chain used is a VALLEN multi-channel system for characterization and localization of acoustic emission sources. The sensors are of the 180 kHz resonant type. Preamplifiers with a gain of 34 dB and a high-pass filtering at 20 kHz are located between the sensors and the acquisition system.

The acquisition system ensures the following functions in real time:

- signal localization
- threshold acquisition of impulse signal shape parameters (amplitude, energy, number of bursts, number of alternations, duration, rising time, frequency),
- periodical acquisition of continuous emission and of tensile test effort

## TEST RESULTS

### Correlation between specimen testing and capacity pressurization tests

Specimen testing has been initiated so as to be able to understand the problems arising from the transposition of criteria obtained through welded specimen tests to capacity pressurization tests.

Specimen testing with (and without) any rectification of their surface prove that the oxide layer which covers some capacities delivers many acoustic emission signals while it is cracking (Figs. 3 and 4). The tensile test on specimens and the capacity pressurization test have both shown that the start of oxide layer cracking was fundamentally different:

- tensile tests on specimens show that specific phenomena develops only when the yield strength has been exceeded (see Fig. 4: only a very small burst emission located on the specimen usable portion: between 2 and 11 mm in the resilient domain);
- during a capacity pressurization test, the oxide layer cracking occurs much before the yield strength is reached (see Fig. 5).

This could explain the difficulties met with the transposition of criteria determined from welded specimen testing.

### **Capacity testing - Signal analysis**

The analysis methods developed from various data processing operations (classifying, discrimination, neuron networks, etc.) do not allow growing defect signals to be discriminated from the many other signals generated during testing. As all these methods use the same data: shape parameters (duration, amplitude...), one can deduce that the oxide layer cracking signals and defect variation signals cannot be distinguished by applying analysis methods based upon conventional shape parameters.

On the contrary, as regards the tanks made of a material for which the production processes (chemical pickling, shot-blasting, etc.) allow the surface oxide layer resulting from rolling to be eliminated, in-laboratory capacity tests have proven the fitness of acoustic emissions to detect growing defects.

Figure 6 shows the start of signals representative of growing defects on surface oxide-free capacities. A defect regarded as non noxious (bursting outside of a defect) cannot be detect when the pressure is lower than the test pressure as the stress level reached does not suffice to make it vary. On the contrary, any noxious defect (burst occurring on the defect and reduction in the burst pressure) generates acoustic emission signals when the pressure is lower than the test pressure. The feasibility of the technique used to assess the overall quality of the vessel is thus proven by the variation in emission start vs. defect size curve. The start of emission of signals located on the defect increases with the defect noxiousness. We also see that the burst pressure always exceeds the test pressure even with the deepest defects. One can therefore deduce that the pressure equipment used in refrigeration systems is amply oversized.

A data analysis shows that for the type of capacity tested, applying a space-time criterion allows one to discriminate the signals representative of changes in a crack during the testing cycle defined under the conditions described above. The space-time criterion is reached when the threshold corresponding to a number of signals located within a small space (cluster) and of which the occurrence takes place in a small period of time is exceeded. In some cases, the so-called "multi-criteria" combination of the space-time criterion with another criterion based upon a shape parameter allows the diagnostic to be sharpened. For the type of capacities considered, adding this additional criterion allows one to eliminate "excessive false alarms" insofar as the space-time criterion suffices to detect all the tested growing defects.

Let us also specify that the above results have been achieved on capacities showing man-made defects of the electro-discharge type, which are certainly easy to make and calibrate but of which the applicability is questionable.

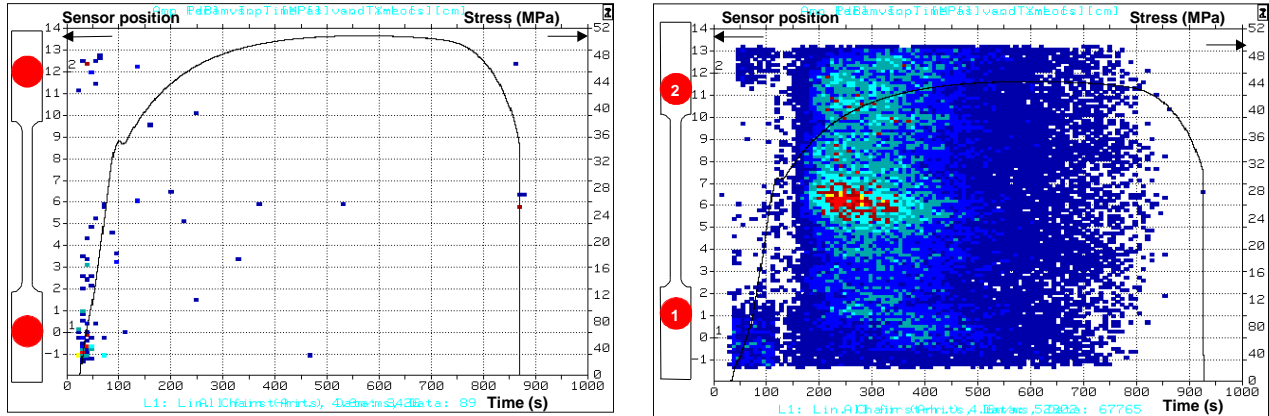


*Fig. 3: Difference of burst emission between an oxidized specimen and an oxide-free specimen.*

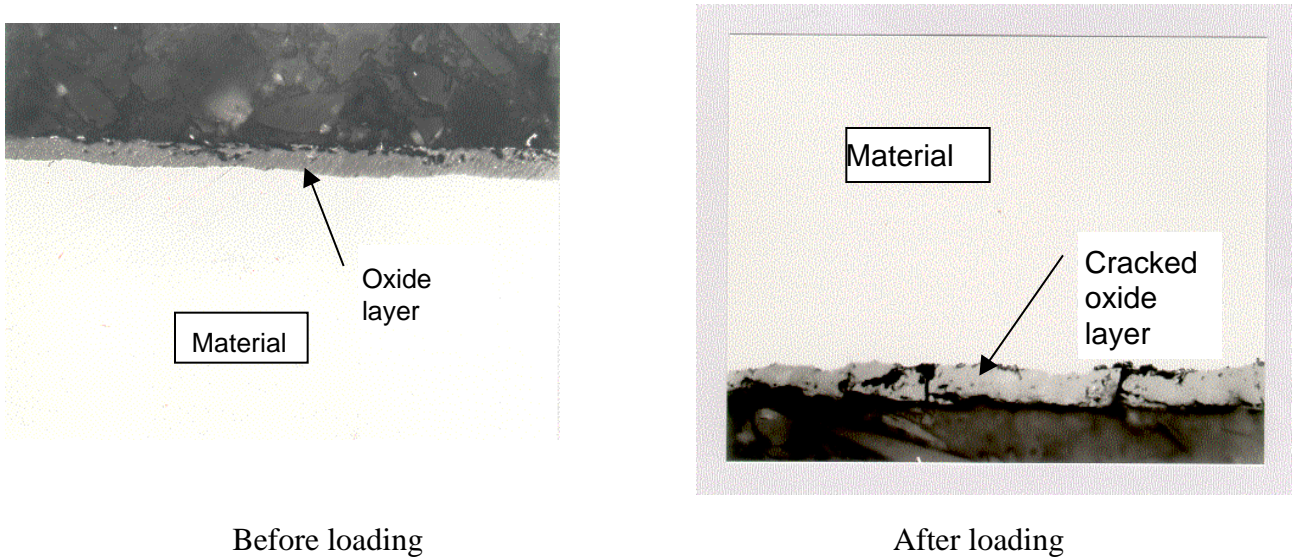


*Fig. 4: Oxide layer cracking.*

## FUTURE PROSPECTS

By using the acoustic emission, the procedure proposed by CETIM would allow conventional hydraulic tests to be replaced by pneumatic tests depending on the surface condition of the material used. The method performance in assessing the vessel overall quality during a pressurization test could be of service in new applications. The next step could consist in transferring the method to industry by integrating the CETIM system into the measuring sequence and the performance of validation tests (robustness test).

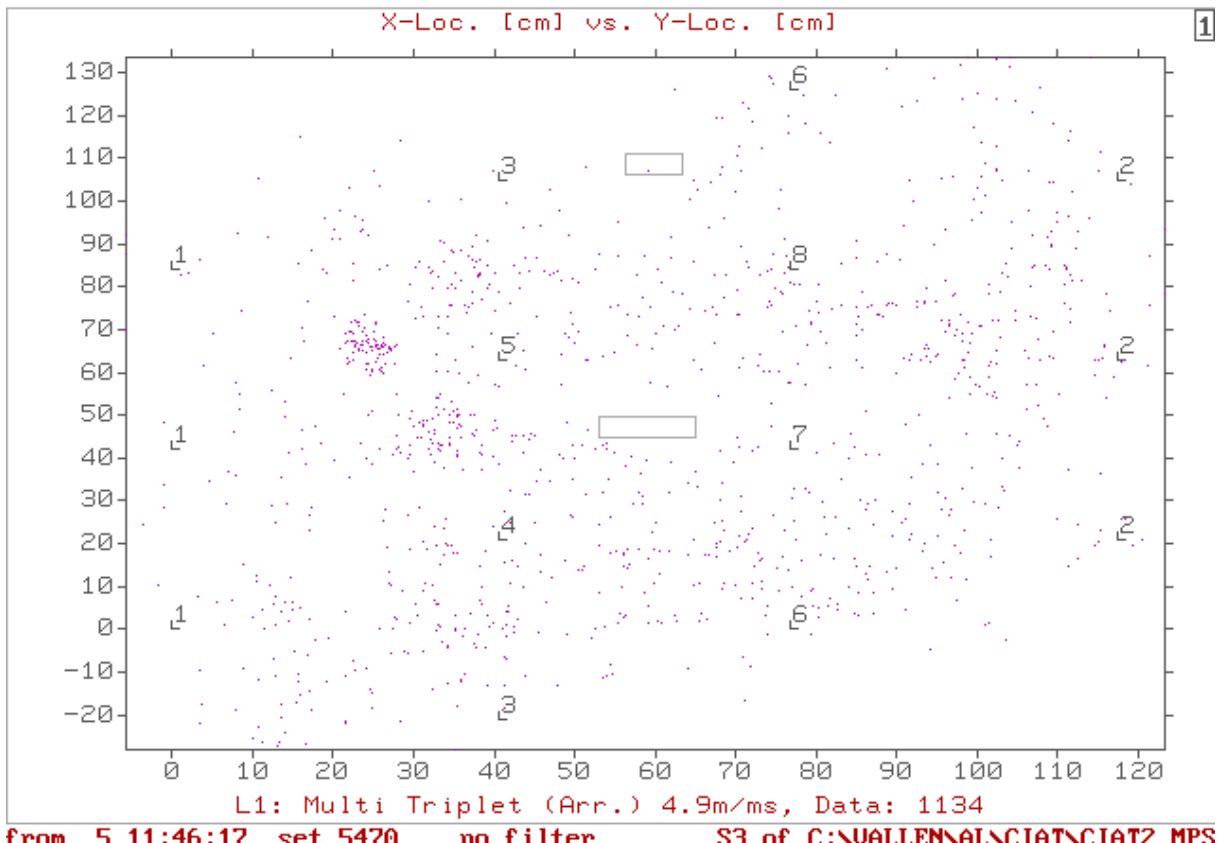
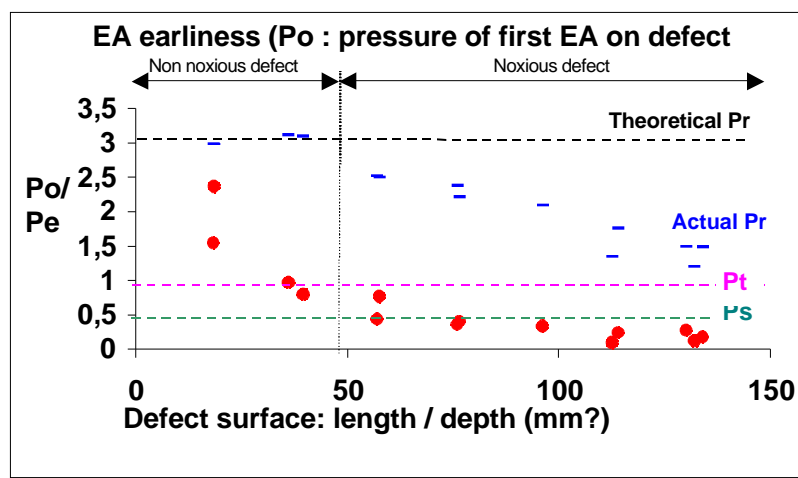


Fig. 5: Events localized on the tank during testing cycle.



Where      Pr : burst pressure  
 Pt : test pressure  
 Ps : operating pressure  
 Po : 1st emission pressure on defect

Fig. 6: Start of occurrence of signals representative of growing defects on capacities of which the material production mode allows the oxide to be removed.

# THE NEW RUSSIAN STANDARDS IN THE FIELD OF ACOUSTIC EMISSION

**Valery I. IVANOV and Igor E. VLASOV**  
**Orgenergoneft, Moscow, Samara, Russia**

## Abstract

*Three AE standards are created in Russia in recent years: 1) Regulation of organising and carrying out of AE testing of pressure vessels, apparatus, boilers and industrial pipelines, 2) Requirements to acoustic emission instrumentation used for monitoring of hazardous production facilities, 3) Requirements to acoustic emission sensors used for monitoring of hazardous production facilities. These standards have been approved by the main state agency of supervision over industrial safety in Russia - Gosgortekhnadzor of Russia. These are used for testing hazardous production facilities.*

## Introduction

Any evolution meets the crisis. Crisis generates problems but at the same time it stimulates new approach, which in Russia includes burst Acoustic Emission NDT Method (AEM) application in industry. Setting standards is a problem that we would like to discuss here.

AEM provides suitable classification of defects in an object under testing. AEM is increasingly operated in industry and widely used for safety maintenance of hazardous facilities. AEM operation is approved by "Regulation of Set-up and Safety Maintenance of Pressure Vessels" [1]. In USA AEM application for industrial facilities is regulated by ASTM, ASME and other technical societies. There are standards of AEM application in several other industrial countries.

During 1996-99 we have developed three basic Standards for Russian industry:

- Regulation of organising and carrying out of AE testing of pressure vessels, apparatus, boilers and industrial pipelines. RD 03-131-97 [2].
- Requirements to an acoustic emission instrumentation used for monitoring of hazardous production facilities. RD 03-299-99 [3].
- Requirements to an acoustic emission sensors used for monitoring of hazardous production facilities. RD 03-299-99 [4].

All these documents have been approved by the main state agency of supervision over industrial safety in Russia - Gosgortekhnadzor of Russia.

## The First Standard

«Regulation of AE Testing» states principles and procedures of AEM application and lists the facilities that can be examined by AEM. Special attention is drawn to preparation of AE work activities. It is recommended to perform the great amount of preliminaries before AE. It includes familiarity with or evaluation of material AE and wave-guide characteristics and that of careful choice of AE source classification system and rejection criterion. The entire recommended criterion is indicated in non mandatory Enclosure.

“Regulation of AE Testing” is a procedural and technical-organizational norm document, which contains orders, regulation and information. These provide AE testing of hazard facilities of oil-

chemical, gas, power and other industries. "Regulation of AE testing" consists of nine basic issues and eight Enclosures. The main issues are: General Provisions; Requirements to Organizational Management, Requirements to Executors and Procedure of Preliminaries to AE, Requirements to Outfit and Equipment, Testing Procedure, Data Accumulation, Processing and Analysis; Estimated Results; Record-Keeping on Testing Results; Safety Guidelines and Responsibility for "Regulation" Violation. Enclosures: AE sources classification system and criteria of examined subject status condition; Enumeration of reference documentation and literary sources, Requirements to Examination Report's contents, Forms of records (protocol) and report of examination results, Standard load diagram, Terms and definitions.

General Provisions contain documents purpose and range of its application. There is information about AE examination, its characteristics, and advantages and disadvantages (limitations). Division "Plan of AEM application" contains recommendation on how to use AEM in combination with other nondestructive testing (NDT) methods and its independent application. The original division is "Requirements to Organizational Management, requirements to executors and procedure of preliminaries to AE". It specifies scope of client's and contractor's work activities during decision making on carrying out of AE testing of the object and after it. Specification of major preliminary effort to AE examination should help to carry out the inspection in accordance with necessary requirements and provide the qualitative results.

Organizations to carry out the AE testing should meet several requirements to provide high performance level. It should be certified by Gosgortekhnadzor. The inspection personnel shall be properly trained and licensed/certified. The Issue "Outfit and Equipment Requirements" states the conventional requirements encountered in the majority of similar documents. The issue "Examination Procedure" specifies technology of the inspection, including such stages as installation of AE sensors, performance check of equipment and channels calibration (set-up), loading of the object, location of AE sources, noise analysis.

"The Regulations" specify that if there is no possibility of reducing the noises to required value, the AE examination should be stopped. The most important part of "The Regulation" is "The Estimated examination results". During AE examination, AE sources are registered, identified, classified and AE sources that exceeded threshold level are evaluated. Executor fixes admissible class of AE sources while preliminaries to AE inspection. So, "The Regulations" define 2-stage approach to estimated examination results:

1. Classification of AE sources
2. Identification of the source as acceptable or not

Classification of AE sources should be carried out on single or few parameters of signal: cumulative counting, amount of impulses, amplitude, power, counting rate, activity, AE sources concentration and time. Detected and identified AE sources are divided into four classes (categories):

- I class - passive source;
- II class - active source;
- III class - critical active source;
- IV class - catastrophic active source.

I class source: source registration for the purpose of its impact analysis of future development. II class source: registration and observation over development in process of examination, keep records and make notes on recommendation of for carrying out additional inspection by other methods. III class source: registration, observation over development, taking actions on preparation the possible load rejection. When IV class source would be detected, the following activities should be performed: immediate

unload to 0 or to the value when AE source class would come down to II or I. After unload, the object should be examined and the other methods of testing should be used if necessary. AE source should be identified and future-testing safety should be stated.

If the results of AE examination indicate that the estimation of the object's technical status was acceptable or no other AE sources were registered, application of additional nondestructive testing would not be required. If AE examination result interpretation was not clear, additional kinds of nondestructive methods should be used.

Executor should choose system of AE sources classification and criteria estimation of testing results and submit it to client's approval. Parameters of AE sources classification system and criteria of testing results estimation should be chosen from classification systems described in the Attachment especially for each object. That is why AE testing safety performance and future safety of the object under testing depend on Executor's qualification and experience.

"Regulations" state instructions on record-keeping of testing results. This document contains requirements to Examination Report's contents. In addition, there are forms of protocol and testing results and conclusion. Examination Results Report should contain the information, which would allow to estimate the object and confirm qualification level of organization and specialists carrying out the examination. Based on this, it will be possible to estimate the reliability of results.

## **Requirements to AE Instrumentation**

Standard "Requirements to AE instrumentation" contains the following items: methods of classification of AE examination, parameters and technical characteristics of AE equipment, requirements to parameters and technical characteristics and methods of its determination. Technical characteristics of AE instrumentation should be determined for each AE system (device) during certification and calibration.

Methods of AE examination are divided into devices and systems depending on its complexity.

AE instrumentation is divided into four classes following information volume received during AE examination. Since the dynamic range of AE signals may achieve 100 dB or more during AE testing, it is advisable that dynamic range of the equipment would be the same. Range of equipment working frequencies should be of 10 kHz – 1.0 MHz. Irregularity of frequency – amplitude characteristics should not exceed  $\pm 3$  dB. Error of AE signal amplitude measurement should not exceed  $\pm 2$  dB. Input range of threshold regulation: 20 - 80 dB (in reference to 1  $\mu$ V of channel input), discrimination 1 dB. Regulation of all others equipment parameters together with exact parameter values are proposed in the Report.

## **Requirements to AE Sensors**

AE signal interpretation, estimation of testing results and decision making to a great extent depend on values of AE signal parameters. Characteristics of AE sensors (AES) influence greatly the parameters of registered signal. The knowledge of AES characteristics should be obligatory. AES is a complex electro-acoustic system, which converts acoustic signal to electrical one. In Standard "Requirements to AE Sensors" the basic parameters are chosen and methods of its measurement are given. There are four parameters of AES: pulse characteristics: sensitivity (or transduction factor), impulse characteristics, fundamental frequency and energy characteristics, which reflects such characteristics as impulse signal energy transmission. All the above-mentioned parameters are real and are measured during calibration, and they are applied in most of criteria for AE sources classification.

Sensitivity of AES – “s” is determined as ratio of “ $u_m$ ” – Maximum value of AES impulse characteristics - to “ $u_1$ ” - acoustic signal maximum value (particles displacement of standard block or object under testing surface) of standard source directly under AES or close to it: “ $s = u_m / u_1$ ”.

Standard contains AES classification based on different parameters, including sensitivity, applied frequency range, frequency. AES are divided into four classes based upon sensitivity: I class sensors possess sensitivity less than  $50 \cdot 10^6$  V/m; II class sensitivity range  $(50-100) \cdot 10^6$  V/m; III class sensor sensitivity range  $(100-200) \cdot 10^6$  V/m; IV class sensors possess sensitivity exceeding  $200 \cdot 10^6$  V/m.

Various methods of parameter determination have been worked out for AES calibration, including analytic approaches and experimental principles of parameter values measurement. The following items have been assumed as a basis of experimental methods of parameter determination: AES reaction on dynamic displacement, standard surfaces of calibration block (object) on which AES was installed. Different stimulation sources of AE signal have been described, advantages and disadvantages of one or another calibration signal have been estimated. Methods of AES parameter measurement are similar to methods applied in existing standards (ASTM E 1106).

Various systems of measuring and parameter estimation of AES have been described; advantages and disadvantages of these systems have been fixed. Requirements to the following calibration means have been settled: calibration signal source, calibration blocks and devices, which are used for calibration.

During development of the Standards, needs of discussing principal issues became evident. At present, physical aspects of AE are more or less clear. That is, AE signal generation, its propagation, transformation and so on. The present authors believe the AE physics have been already created. Now it is time to work out the basis of AE examination. These are the fundamental problems of worldview. Besides there are scientific, technical and organizational questions which we would like to discuss.

Brief list of AE testing problems (just as for any other nondestructive testing and technical diagnostics) includes such items as personnel, Standards and equipment. In any case these problems exist all over the world. If we would not pay attention to borders we can say that these are the problems of the united AE society:

- precise program of method's development and cooperation on coordinated programs
- involving new (young) people in AE field
- interchange of ideas and personnel.

The important issue is what factors would influence AE examination results. These results might be more disastrous because AEM is closer to disaster than any other method. The question is “for how closer?”

Development of techniques and standards in AE field requires the international efforts. Many teams should work on one program. To start with, for example, program which will allow receiving from each team for each examination information about examination's reliability and about possibility of these data comparison. It should be appreciated to make an agreement (under condition of confidentiality) on interchange of examination results and to work out a system of receiving and submitting the data. It is necessary to have a group of teams to carry out analysis and analysis system. At the moment the weakest point of AEM is not the lack of standards, but an operator. Certainly, standards require important revision and amendments.

## **References**

1. Regulation of Set-up and Safety Maintenance of Pressure Vessels. PB 10-115-96. Gosgortehnadzor of Russia. 1996.
2. Regulation of organising and carrying out of acoustic emission testing of vessels, apparatus, boilers and technological pipelines. RD 03-131-97. Gosgortehnadzor of Russia. 1997.
3. Requirements to acoustic emission instrumentation used for monitoring of hazardous production facilities. RD 03-299-99. Gosgortehnadzor of Russia. 1999.
4. Requirements to acoustic emission sensors used for monitoring of hazardous production facilities. RD 03-300-99. Gosgortehnadzor of Russia. 1999.

# USING ACOUSTIC EMISSION TO MONITOR METAL DUSTING

Fridiric FERRER, Eric ANDRES, Jean GOUDIAKAS and Claude BRUN\*

Elf Atochem, Saint-Avold Cedex, France, \*Elf Atochem, Lacq, France

## ABSTRACT

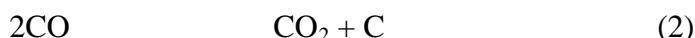
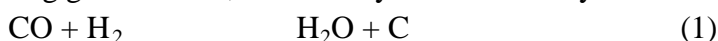
Metal dusting is a catastrophic form of carburization, which can lead to rapid wastage as the affected metal disintegrates into a mixture of powdery carbon and metal particles. The phenomenon occurs in gaseous atmosphere, which is strongly carburizing in the temperature range of approximately 400°C to 850°C with a carbon activity greater than one. The corrosion behavior of electropolished alloy 800H tubes was investigated in H<sub>2</sub>-85%CO gas mixture at 650°C. The metal dusting is preceded by internal carburization, whereby the chromium is tied up. The remaining Fe-Ni matrix then reacts to form unstable intermediate carbide M<sub>3</sub>C, which decomposes to metal particles and carbon. Acoustic emission (AE) sensors were coupled with the tested material during the experiments. Thus, corrosion evolution and pit distribution were monitored on-line and correlated with acoustic parameters. The introduction of organic sulfides in the process gas produced a significant decrease in the corrosion phenomena.

## 1. INTRODUCTION

In highly carburizing atmospheres (e.g. H<sub>2</sub>/CO/CO<sub>2</sub>/H<sub>2</sub>O), between 400°C and 850°C, materials such as carbon and stainless steels, as well as nickel-base alloys, can be affected by a damaging phenomenon called "metal dusting". In fact, a part of the material is rapidly turned into dust, which is composed of particles of metal and graphite. This degradation process can be very detrimental in environments such as those encountered in thermal cracking or ammonia plants.

The typical feature of a material damaged by metal dusting depends on the nature of the material. In all cases, the corrosion products are composed of the previously described dust, but for carbon steels or low-alloy steels, the corrosion develops uniformly, while for stainless steels or nickel-base alloys, it grows by pitting.

The mechanism of the phenomenon has recently been described in several papers [1,2]. It has been demonstrated that the carbon activity of the atmosphere must be greater than one. In classical carburizing gas mixtures, this activity is controlled by the following chemical reactions:



For plain carbon or low-alloy steels, five states of development can be distinguished. Firstly, there is an over-saturation of the metal with carbon. Secondly, cementite M<sub>3</sub>C forms at the surface. Thirdly, graphite is deposited on the cementite surface. Fourthly, the cementite decomposes to metal plus carbon (M<sub>3</sub>C → 3M + C). Finally, there is further graphite deposition on the fine metal particles formed in the previous state.

For high-alloy steels or nickel-base alloys, this mechanism is complicated by the existence of a protective chromia layer. In this case, metal dusting may start at some defects on the scale, which causes local attack and pitting [1]. The protection against this pernicious corrosion phenomenon requires either the choice of a resistant material or the use of inhibitors. This paper deals with the latter solution. In particular, some organic sulfides, known for their ability to decrease the amount of coke formation on metal surfaces during cracking processes [3], could also have an inhibiting effect on metal dusting [4]. The DMDS is one of these organic sulfides. However, the problem with high-temperature corrosion is the instantaneous determination of corrosion rate.

For that purpose, a method for on-line monitoring of corrosion evolution is needed. Recent work has demonstrated that AE could be a powerful tool for studying low or high temperature corrosion phenomena [5-8]. Accordingly, this technique has been chosen.

## 2. EXPERIMENTAL

The experimental device used in this study (Fig. 1) consists of a furnace, in which a metal sample tube is inserted and a controlled gas mixture feeding system. An AE acquisition system is composed of waveguides coupled to the metal sample, two wideband sensors (Vallen SE900) linked to preamplifiers (Vallen AEP4) and to a Vallen AMSY4 AE system. A hygrometer is used to follow H<sub>2</sub>O evolution due to the chemical reaction (1). AE calibration is done before and after each test. By using the Hsu-Nielsen acoustic source, we determined the waveguide attenuation to be about 15 dB.

Metal dusting tests were conducted during periods of ten days each. The principal experimental conditions chosen are brought together in Table 1. The chemical composition of the tested alloy is given in Table 2.

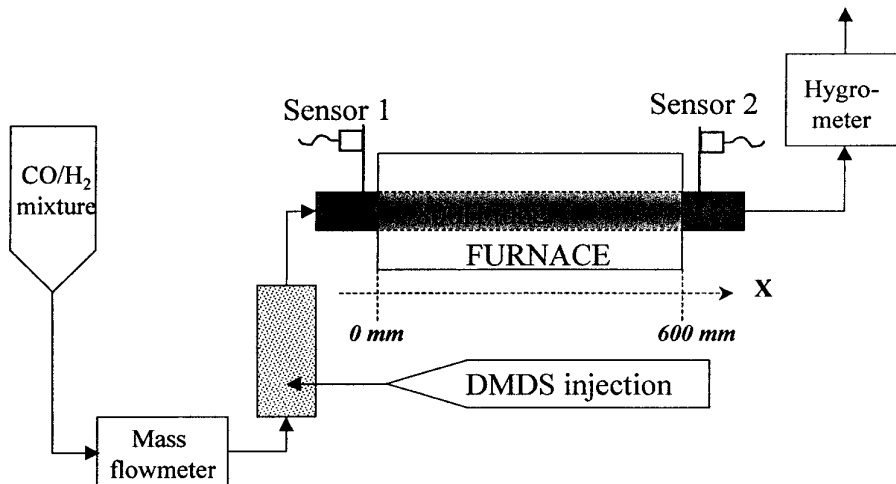


Fig. 1 Schematic representation of the experimental device.

## 3. RESULTS AND DISCUSSION

### 3.1 Test without DMDS injection

As a reference, the first test was conducted in a CO/H<sub>2</sub> atmosphere free of DMDS. After ten days in the hot carburizing gas mixture, the 800H tube was removed from the furnace and examined. Under a thick

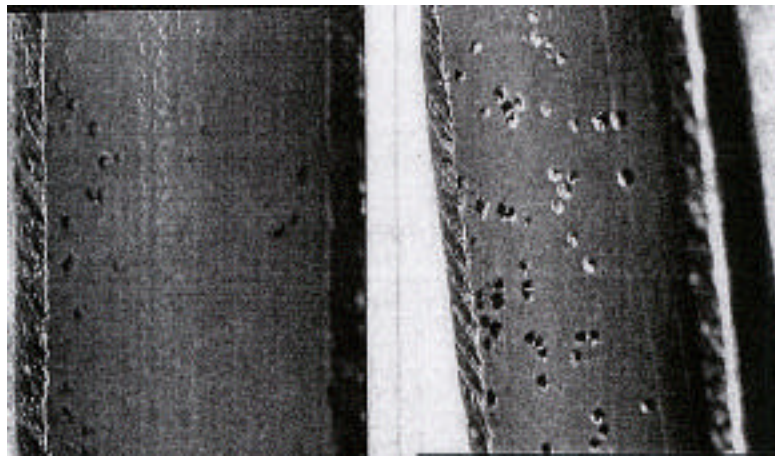


Fig. 2 Metal dusting pits generated during the test performed without DMDS (3.75x).

Table 1 : Experimental conditions.

Material	Tube dimensions	Temperature	Pressure	Gas mixture	DMDS	Flow rate
Alloy 800H	700*12*1 (mm)	650 °C	1 atm.	H <sub>2</sub> 85% / CO 15%	0 to 2000 ppm	50 L/h

Table 2 : Chemical composition of the tested 800H alloy.

Element	C	Si	Mn	S	Ni	Cr	Ti	Fe	Cu	Al
Wt. %	0.073	0.43	0.72	<0.001	<b>32.83</b>	<b>20.1</b>	0.47	43.63	0.41	0.50

coke layer, a distribution of numerous metal dusting pits was observed (Fig. 2). These pits were about 1 mm in diameter and 500 µm in depth. Further investigations by SEM and X-ray analysis allowed us to identify clearly the nature of the corrosion products: a dust composed of particles of metal and graphite.

The evolution of AE activity recorded during this test shows three periods (Fig. 3). During the first thirty hours, no AE could be detected: this corresponds to the incubation period of the phenomenon. Then, especially for channel 2, AE activity increased almost linearly. As long as the atmosphere was producing high carbon activity, the metal dusting was activated. When the gas flux was changed to N<sub>2</sub> flux, AE activity became weaker, or practically non-existent.

Acoustic parameters of the signals recorded during the emitting period are found in Table 3. Their values, relatively dispersed, do not show significant evolution with respect to time. Despite the use of waveguides, which have an attenuation of ~15 dB, the measured amplitudes are high enough to prove that the sound-generating mechanism is powerful.

Figures 4 and 5 show respectively the number of visually observed metal dusting pits and the number of localized AE events according to the X position on the tube (see Fig. 1). The pit distribution is characterized by two distinct populations (Fig. 4). The first one, between X = 100 and 350, is less important than the second one, between X = 350 and 600. The fact that there are two populations is due to the temperature profile of the furnace. Because of the latter, the optimal temperature for metal dusting is located in two critical zones of the tube, which explains the two pit populations.

Table 3 : Some acoustic parameters recorded during the metal dusting experiment.

Amplitude	Number of counts	Rise time	Average frequency
35 – 65 dB	1 to 1000	0 to 1500 $\mu$ s	80 to 350 kHz

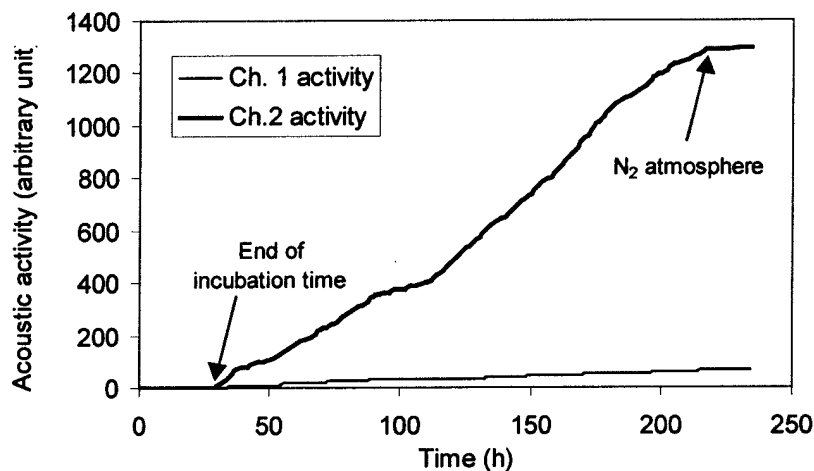


Figure 3 – Acoustic activities (two sensors) during the test performed without DMDS.

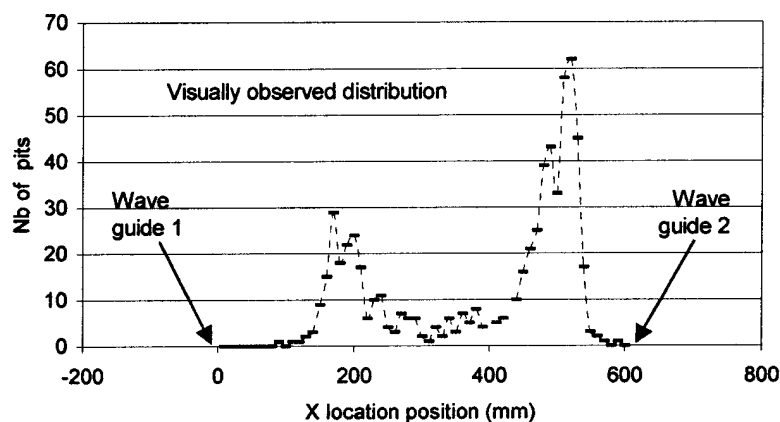


Figure 4 – Distribution of the visually observed pits according to the X location position in the tube.

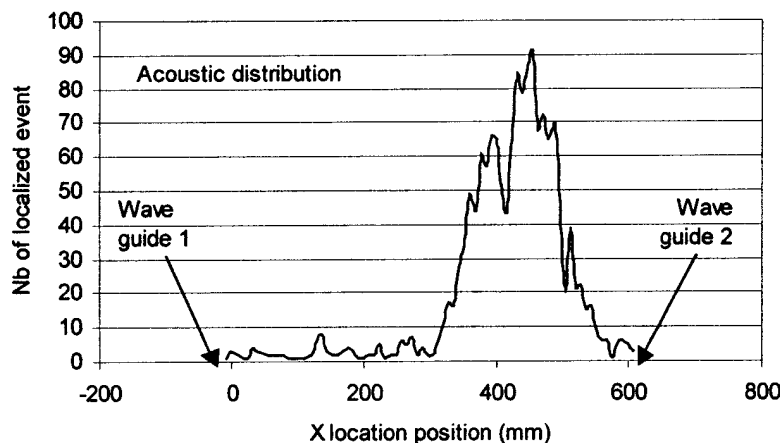


Figure 5 – Distribution of the localized acoustic events according to the X location position.

Figure 5 shows that the distribution of AE sources also has two populations. The second one is very similar to the second population in the pit distribution. On the other hand, the first population of localized AE events is almost non-existent. After the post-test AE calibration, we found that this lack could be attributed to an unfortunate loosening of the coupling of the sensor 2. The accuracy of the AE location of the damaged areas is then confirmed.

### 3.2 Tests with DMDS injection

Other tests were conducted in a CO/H<sub>2</sub> gas mixture with different quantities of added DMDS. After each of these tests, coke deposition, pit distribution and AE were examined. The results are summarized in Table 4, in comparison with the reference test. The DMDS injection indeed inhibits the metal dusting phenomenon. Moreover, AE monitoring corroborates perfectly these results. As no AE signals are recorded when coke deposition is observed, it can be concluded that the emitting mechanism is associated with the formation of pits and not with coking. A decrease in the AE acquisition threshold would perhaps allow for the detection of this carbon deposition.

Remark : During the test number 1, the relative humidity measured at the furnace exit varied in a similar way as AE activity but with a lower sensitivity.

**Table 4 : Influence of the DMDS on metal dusting.**

Test	DMDS	Coke deposition	Number of pits	Acoustic activity (hits/h)	Relative humidity evolution
1	Without	Thick layer	Numerous	> 100	High
2	2000	Very thin layer	None	< 1	None
3	200	Very thin layer	None	< 1	None

### 3.3 Interpretation

In AE studies of high temperature corrosion phenomena, the breaking of oxide scales is often assumed to be directly responsible for the ultrasonic wave generation. In the case of metal dusting, and especially for high-alloy steels or nickel-base alloys, this idea can be justified by the fact that damage takes place at scale flaws. Moreover, the metal dusting mechanism itself, i.e., the sudden decomposition of a carbon-over-saturated metal in the combination of metal and graphite must play a role in the AE activity. An extensive analysis of AE signal characteristics would help to distinguish between the two mechanisms.

Concerning the inhibiting effect of DMDS on metal dusting, investigation is planned to yield an accurate interpretation. In fact, following thermal decomposition of DMDS, sulfide compounds would fix on and deactivate the sites of the metal, which catalyze the phenomenon.

## 4. CONCLUSIONS

Experimental conditions were determined in order to develop a rapid metal dusting on 800H alloy. After ten days of testing, very significant damage, characterized by the presence of numerous pits, was observed.

The AE technique was tested as a possible monitoring technique. The AE signals are linked to the metal dusting pits formation, which generates relatively high energy ultrasonic waves in the material. The pit

formation can be detected following a passive acoustic period, which reveals the existence of an incubation time.

The use of organic sulfide DMDS was proposed to inhibit this serious corrosion phenomenon. In the presented experimental conditions, injection of small quantities of DMDS was sufficient to prevent the metal from being damaged or, at any rate, to retard the damage.

This work will be completed and followed by the examination of the preventive and arrestive properties of DMDS injection; in particular, for the assessment of minimum required dosage. For this application, acoustic emission monitoring will play an essential role.

## References

- [1] H.J. Grabke, C.B. Bracho-Troconis and E.M. Moller-Lorentz. "Metal dusting of low alloyed steels". Werkstoffe und Korrosion, 45, (1994), 89.
- [2] R.J. Gommans and T.L. Huurdeman. "DSM's experience with metal dusting in waste heat boilers". Paper 3b, Presented at the AIChE Ammonia Safety Symposium, Vancouver, BC, Canada, October 3-6, 1994, 20 p.
- [3] Cher Dip Tan and R. Terry K. Baker. "The impact of selected sulfides on coke formation on various metal and alloy surfaces". Published at the Department of Chemistry, Northeastern University, Boston, Massachusetts 02115, 1999, 14 p.
- [4] H.J. Grabke and E.M. Moller-Lorentz. "Effect of sulfur on the stability of cementite". Steel research, 66 (1995) No. 6, 254-258.
- [5] H. Mazille, R. Rothea, The use of acoustic emission for the study and monitoring of localized corrosion phenomena, Modelling aqueous corrosion, edited by K.R. Trethewey, P.R. Robarge. Netherland: Kluwer Academic Publishers, 1994, pp. 103-127.
- [6] F. Ferrer, H. Idrissi, H. Mazille, P. Fleischmann, P. Labeeuw. On the potential of acoustic emission for the characterization and understanding of mechanical damaging during abrasion-corrosion processes, Wear, 231 (1999), 108-115.
- [7] M. Schulte and M. Schütze. The role of scale stresses in the sulfidation of steels. Oxidation of Metals, 51, Nos. 1 and 2, (1999), 55-77.
- [8] A.S. Khanna and coworkers, Application of Acoustic Emission Technique in High Temperature Oxidation Studies. Key Eng. Mater., 20-28, no. 4, (1988), 3443-3451.

# USE OF ACOUSTIC EMISSION TO DETECT LOCALISED CORROSION PHILOSOPHY OF INDUSTRIAL USE, ILLUSTRATED WITH REAL EXAMPLES

Alain PROUST and Jean-Claude LENAIN  
EURO PHYSICAL ACOUSTICS SA, SUCY EN BRIE CEDEX, FRANCE

## ABSTRACT

*After several years of research in laboratory, the ability to detect active corrosion by acoustic emission technique has been successfully proven. More recently, the industrial feasibility has been established in the field, according to the requirements of two international chemical companies, on many cases of different pressure components and storage tanks. The goal was to make a diagnostic on the propagation of the localised corrosion, like pitting or stress corrosion cracking, on components during the process, on a restricted area in service components. This diagnostic has to be done immediately after the measurement, by a simple system and procedure, applied by a non-expert in acoustic emission. This need arises from unpredicted failures of industrial installations due to rapid propagation of corrosion damage, after a long period of initiation. The development of units, with multiple process, leads to complex problem upon the sensitivity of corrosion for an existing vessel exposed at various environments.*

*This paper presents several situations where CORPAC® technology can be applied, not only to detect and locate damage from corrosion, but also to: characterise the corrosion (evaluation), help to finalise the best choice of material, understand the part of the process cycle which produces, activates the corrosion, validate repairs, evaluate the efficiency of corrosion protection. Examples from different materials (stainless steel, carbon steel,...) on reactors, columns, piping, tanks are given.*

## INTRODUCTION

Localised corrosion cracking is an important damaging phenomenon in the chemical, petrochemical, and nuclear industries. Unpredicted failures occur in service, which have economic, safety, health and environmental consequences. Stress corrosion cracking, pitting and crevice corrosion are not easily detected with traditional non-destructive techniques. Furthermore, these damages are mostly detected during shut-down inspection and the periodicity of the inspection are not adapted to such a phenomenon which can take years to initiate and exhibit a significant speed of propagation. Material of the industrial devices are chosen to resist to corrosion, nevertheless localised corrosion take place due to unpredicted localised condition or transient state of process. Most of the time, the cause of localised corrosion is not clearly identified and at the opposite of general corrosion the kinetics are not easily predicted. When a subcritical corrosion damage is found, the inspection staff has to decided if they stop the production or if they can operate under survey because the propagation rate is low or more fortunately if the corrosion is stopped.

The detection of the propagation steps of localised corrosion has been first a beautiful dream of scientist before being demonstrated in laboratory scale. The AE signature of the "voice" of corrosion has been drawn from scientific studies including a European BRITE EURAM contract before to be transposed in industrial uses. The most difficult steps had been to extract automatically known signal from environmental noise of process.

This technology called CORPAC® has been achieved by building a database of SCC, pitting and crevice signal in a vessels configuration at several chemical plants.

## **ACOUSTIC EMISSION APPLIED TO THE SURVEY OF CORROSION PROCESS**

Acoustic emission (AE) is the result of sudden energy release within a material, which appears as elastic wave. This technique is widely used as a non-destructive testing technique for fitness for service evaluation in industrial field. AE is also a powerful tool to characterise and understand damage initiation and propagation. Most of all microscopic mechanisms has been studied and correlated with AE signals. Many authors have characterised the AE signature of many damage phenomena as localised plastic strain, twinning, ductile and brittle fracture for metallic alloys. Localised corrosion monitoring is more recently under the interest of researcher. It has been proved that many type of localised corrosion process can be detected by AE not only on laboratory scale [1] but also on industrial field conditions [2,5]. If AE sources from mechanical damage propagation are well accepted and understood, the mechanisms that generate elastic wave from corrosion process are sometimes not so clear. To better understand the effect of each corrosion process it has been necessary to identify recognised all parasitic signals coming from environmental effect like boiling, crystallisation, particle impacts...

### **Stress corrosion cracking (SCC)**

This phenomenon produces discontinuous “brittle” fracture surfaces in ductile material. SCC mechanisms have been deeply investigated and it has been found that AE signals are producing from both brittle crack propagation and plastic blunting of crack tip. In the case of transgranular crack propagation, the AE signal production is mainly a mechanical effect resulting from discontinuous crack propagation steps [3,4]. AE signals have been also detected and clearly identified from intergranular SCC crack propagation for instance in alloy 600 [6]. In this last case, it is not proved that this mechanism is purely discontinuous, but it gives raise to EA hits even in aluminium alloys.

### **Pitting corrosion and crevice corrosion**

A lot of mechanisms can be put forward to explain AE generation during pitting process, but many of them are not really realistic like metallic ion dissolution [5,7]. There is mainly 4 hypothesis which were maintained to explain elastic wave production: salt crystallisation inside pits, hydrogen evolution due to cathodic reaction, localised plastic strain at pit tip, spalling of corrosion products.

In the case of material type stainless steel the most probable mechanism is the formation and hydrogen evolution in the pit tip. For low carbon steel, the expansion of corrosion products can be the main phenomenon responsible of AE detection.

## **ADVANTAGES AND LIMITATIONS OF THE TECHNOLOGY**

Acoustic emission is the only non-invasive technique that can detect the initiation and propagation of SCC, pitting and crevice corrosion in-service and on-line. According to lab scale, small scale and full size studies one hour of monitoring is statistically enough to detect real case of corrosion encountered in industrial installation. A database is available for a wide range of stainless steels and carbon steels regard

to the SCC, pitting and crevice damage detection. The AE sensors are mounted on the external surface of the vessel wall and can withstand up to 170°C in standard conditions that cover most of the chemical process. A solution for higher temperature (maximum operation around 600°C) is under development and has given very good results for a SCC process at 250°C. Depending on the in service process noise installation corrosion damage can be detected from half a meter up 10 meters away from the sensor. A small access to the surface is needed and only local removal insulation has to be made before checking. The know-how, database and self-diagnostic algorithms are incorporated into a portable system requiring no expertise on the part of the user. This is crucial point because the tools have to be used with a periodicity related to corrosion risk and the industrial consequences defined by the risk based inspection policy of the plant.

The CORPAC® technology is able to detect only propagation corrosion process, which allows monitoring corroding plant as function of process conditions. The main limitation of this technology is a localised corrosion not detected if the corrosion process is stopped. For example, it is well known that propagation of SCC on austenitic stainless steel is not significant below 40°C in chloride environment. It has been verified with CORPAC® on a full size tank, with a continuous decreasing temperature rate, that AE activity from SCC is not more detectable below 50°C in a hot chloride environment. That is the major reason why AE has to be applied in service conditions. Also, this technique cannot determine if the corrosion is initiated from the inside or the outside.

## CASE HISTORY

Several case history are proposed to illustrate some uses of CORPAC®.

### Case 1 : Risk-based decision and characterisation of corrosion evolution (Fig. 1)

After several months of operation [8], internal visual inspection reveals significant pitting corrosion in a 19-25 HMo vessel and pitting and SCC in a 316 Ti vessel. These two brawn new different stainless steel vessels contain an organic product at 100°C. This product is supposed to be a non corrosive media stored under nitrogen flow. The corrosion study concludes that the corrosion could be due to the presence of few PPM of water. The production has to reduce as much as possible the content of water and the inspection staff has to find a way to confirm that corrosion has stopped. Periodic visual inspection of grinding area is practically difficult to achieve. Internal wall has to be first cleaned with steam introducing water not easily eliminated. Then, CORPAC® is used to assess the corrosion study conclusion. In summer 1996, the first CORPAC® evaluation showed that very few AE is detected confirming that corrosion has stopped when water content is drastically reduced. Furthermore a complete opposite diagnostic has been established six months later showing a strong corrosion activity at the liquid/gas interface.

This last conclusion has been explained later by an incident of production. One month before the examination, a dryer column has failed letting pass in the product a small amount of water. In 1998, the corrosion diagnostic was showing a strongly reduced rate of corrosion due to complete consumption of water. The CORPAC® analysis as confirm the corrosion expertise and has given tools to maintain a corroded structure in service. The non-conclusive internal inspection has been cancelled and replaced by low cost (no shut down) periodic survey with CORPAC®.



Fig. 1



Fig. 2

#### Case 2 : Damage area characterisation (Fig. 2)

A dye-penetrant inspection has detected that an 18-m high column presents some trough wall cracks. The micrographic examination shows clearly transgranular stress corrosion cracks in the austenitic stainless steel material. The first solution should be to replace the complete column. CORPAC® examinations have been performed on the complete wall of the column under service condition. SCC activity has been found only on a 2-m high section of the column corresponding probably to the level where the temperature is the most susceptible to promote SCC. This diagnostic has been partially confirmed on few 2-m squares with a pulsed eddy current technique. In this case, eddy current was able to detect only trough wall cracks or cracks near the surface. Because CORPAC® analysis demonstrates that defects are only propagated in a restricted area, the major part of this column has been conserved and the defective part cut and replaced by duplex stainless steel to better resist to SCC in these specific conditions.

#### Case 3 : internal coating and repair validation (Fig. 2)

CORPAC® has been performed on carbon steel railroad tank car and reactor with several types of vitreous or organic coatings (glass, ebonite...). At the occasion of a regular hydraulic proof test, a residual activity of corrosion was found before increasing the pressure. This unexpected phenomenon was due to some external repairs, which produce micro-cracks in the vitreous coating. The AE activity was due to general corrosion localised in the coating breakage area produced by industrial water.

In order to better understand and confirm this type of results, some experiments were performed on an old railroad tank car filled with water, which have been taken out of service. CORPAC® technology was able to detect corrosion activity not only where the coating was broken but also where electrical measurement did detect nothing.

The visual inspection reveals in this specific area the colour of the resins has changed. The permeation of industrial water through this non-effectively broken coating was sufficient to produce significant AE activity. 60 litres of hydrochloric acid were poured into the tank and within few min., AE activity of detected corrosion increases drastically showing that the corrosion rate is clearly correlated to AE measurements.

#### Case 4 : Help in material choice.

Introducing coupons on real industrial installation is common practice to finalise a material choice for corrosion resistance purpose. One of the major problems is to open the vessel periodically to withdraw coupons for observation. A CORPAC® unit was used to determine the corrosion initiation of several coupons on a by pass pipe. The only two things to take in consideration are that the coupons have to be in a same small area where the signature of each coupons can be mixed or also that the initial vessel is no subject to corrosion. The recorded activity is closely correlated to the damage propagation rate.

The development of units, with multiple process, leads to complex problem upon the sensitivity of corrosion for an existing vessel exposed at various environments.

## **CONCLUSIONS**

The propagation of localised corrosion such as pitting crevice and stress corrosion cracking is detectable industrially by Acoustic Emission without any variation of internal or external loading. The CORPAC® technology is rapid and easy to use and consists in ‘listening’ the process conditions. A pattern recognition algorithm is used to separate damage signature from process noise. The diagnostic of CORPAC technology reveals the existence of active or non-active localised corrosion. Useable by a non-expert in acoustic emission, it gives a rapid diagnostic on area, which a risk of localised corrosion is significant. The areas to check are mainly defined by the inspection staff or sometime by internal corrosion expert, according to several criteria. Most of the time the examination is decided by a risk based inspection plan but also according the site experience. As corrosion indications are found, CORPAC® allows to monitor and characterise their evolution and gives tools to understand the transient phase of process which gives rise to damage. As localised corrosion can be monitored, corroded structure can be kept in service with reasonable evidence of fitness for service and at least semi-quantitative information on corrosion rate.

## **REFERENCES**

- [1] PROUST A., Etude par la technique d’EA de la corrosion sous contrainte de trois nuances d’acier inoxydable (austénitique, ferritique et auténoferritique) en milieu chloruré chaud. Thèse GEMPPM, INSA Lyon, 1992

- [2] LENAIN, J.C., Evaluation de l'état de corrosion des fonds de bacs de stockage par Emission Acoustique, 3ème colloque Européen, Corrosion dans les usines chimiques et parachimiques. Lyon 14-15 Oct 1997.
- [3] PROUST, A., FLEISCHMANN, P., MAZILLE, H., ROTHÉA, R., Acoustic Emission monitoring of stress corrosion cracking on ferritic, austenitic and duplex stainless steels. Corrosion déformation Interaction. Les Renardières Septembre 1992.
- [4] YUYAMA, S., KISHI, T., HISAMATSU, Y., AE analysis during corrosion, stress corrosion cracking and corrosion fatigue process. J. Acoustic Emission, 1983, 2(1/2), 71-93.
- [5] POLLOCK, A., Acoustic Emission capabilities and applications in monitoring corrosion, Corrosion monitoring in industrial plants using non destructive testing and electrochemical methods, E. G.C. Moran et P Labine, Philadelphia, PA: ASTM, Special technical publication 908, 1986, P 30-42.
- [6] CASSAGNE, T., PROUST, A., MAZILLE, H., Initial results on stress corrosion cracking monitoring of alloy 600 in high temperature water using acoustic emission, ninth international conference on environmental degradation of material in nuclear power system-water reactors, Newport Beach, California, August 1-5 1999.
- [7] MAZILLE, H; ROTHÉA, R., TRONEL, C., An acoustic emission technique for monitoring pitting corrosion of stainless steels.
- [8] SOMMEN, J., RENAUD, L., L'Emission Acoustique : une aide au diagnostic efficace en cas de matériel corrodé. CEFRACOR 3ème colloque Européen Lyon, 14-15 Octobre 1997.

# **INSPECTION OF FLAT-BOTTOMED STORAGE TANKS BY ACOUSTICAL METHODS; CLASSIFICATION OF CORROSION RELATED SIGNALS**

**P. TSCHELIESNIG, G. LACKNER, M. GORI\*, H. VALLEN<sup>§</sup> and B. HERRMANN<sup>¶</sup>**  
**TÜV, Vienna, Austria, \*CESI, Segrate, Italy, <sup>§</sup>Vallen Systeme, Icking, Germany,**  
**<sup>¶</sup>Dow Germany, Stade, Germany**

## **ABSTRACT**

*Acoustic emission monitoring is applied during on-line inspection of flat-bottomed storage tanks to locate leakage in the bottom plates. Since location algorithms only handle signal arrival times, acoustic emission waveforms still have a relevant diagnostic potential. With a deeper knowledge of the links between the acoustic emission and the defects in a tank, this potential could be exploited in order to complement the location ability, and allow a more comprehensive evaluation of the tank. To investigate improved tank assessment methods and strategies, an EC funded project was started in 1997. This presentation highlights the feature analysis and pattern recognition applied to corrosion signals, gathered from tank plates submitted to corrosive fluids in the lab. The classifiers based on such database are now allowing a preliminary evaluation of acoustic emission signals from real tanks.*

## **INTRODUCTION**

The maintenance of flat-bottomed storage tanks, which suffer from corrosion, involves both economic and environmental matters. Early warning of degradation by corrosion should prevent leakage in the tank bottom. Actual leaks should be detected as early as possible, to avoid soil pollution or the sudden stop of the component. However, time-consuming and expensive off-line inspections, which require emptying and cleaning of a tank, would be unwarranted if the bottom condition is found good. Hence, on-line acoustic emission (AE) monitoring is performed as an interim test; so that, if the tank appears neither leaky nor seriously affected from corrosion, there can be enough confidence to delay the off-line inspection. The detection of several sources, when a tank is seriously affected from corrosion or the plant environment is very noisy, can make this decision rather difficult. In this case, additional evaluation methods would be needed to complement AE source location. Since arrival times only are analysed during location, AE waveforms still have a relevant diagnostic potential that could be exploited for this purpose. Moreover, a significant improvement would be reached if such evaluation methods can be based more on objective criteria and less on testing experience. Eventually, such improvements may further increase the reliability of the AE monitoring as demonstrated in the ECNDT '98 paper of Van de Loo and Herrmann [1], where in some cases the predictions of the tank bottom were not in full agreement with the actual conditions observed by off-line inspections.

The above considerations thus suggested a better understanding of the relationship between AE and tank damage. With the conviction that such knowledge can improve the diagnostic potential and reliability of AE monitoring, the EC funded project SMT4-CT97-2177 "Inspection of flat-bottomed storage tanks by acoustical methods" was started in October 1997.

## **PROJECT DESCRIPTION**

The project team comprises TÜV (coordination and testing), CESI (testing), Vallen Systeme (AE system manufacturer), and the industrial partners Shell - The Netherlands, and Dow - Germany, who support the project by arranging tests in plants and providing follow-up information after off-line inspections. This 3-years project includes the following main tasks:

- Laboratory tests to collect signals from leakage and corrosion processes,
- Evaluation of laboratory database using front-running and possibly automated analyses tools,
- Performance of field tests on storage tanks,
- Evaluation of field database using the methods developed after evaluation of laboratory database,
- Definition of a tank assessment strategy.

The preliminary results, gained in the first two tasks, allowed the prosecution of the project after mid-term assessment. This paper reviews the work done in such tasks, while field tests and data evaluation are in progress for the completion of the project. The final task is also intended to open the most significant results of this work to the European standardisation community.

## **PROJECT OBJECTIVES AND METHODS**

The relationship between AE and potential tank defects, like other subjects of practical importance for a tank evaluation, were considered for investigation and improvement by this project. For example, the discrimination of the actual stage of degradation of a tank bottom is very important for tank users [2]. Also relevant are discrimination between actual leaks and heavy corrosion spots, reliable clustering and positioning of AE sources, noise filtering. In fact, if a test is affected by noise from the tank structure or weather factors, the processing methods should also allow a better selection between noise and signals carrying the actual diagnostic information.

The focus on AE signal evaluation in this project has been emphasised by the use of feature analysis and pattern recognition methods. Reference laboratory tests were designed to provide a well-defined database to study the subjects, and develop improved methods for the assessment of real tanks.

In the frame of the project, the phenomena of leakage and corrosion were addressed, respectively, by testing partners TÜV and CESI. The contribution of Vallen Systeme allowed a common instrumental platform (AMSY4, VisualAE and VisualClass) at disposal of the testing partners, and has also granted support and upgrade actions during the progress of the project. The results presented in the followings have considered the analysis of the signals gathered by partner CESI from several tank plates submitted to corrosion tests in the laboratory.

## **LABORATORY CORROSION TESTS**

Through laboratory tests, a database of corrosion related signals was generated, made of AE waveforms associated to selected combinations of plate surface and corrosion environment. Test plates (area less than 0.5 m<sup>2</sup>, thickness about 10 mm) were cut from a corroded tank bottom. Some plates (label A) were "as found" to preserve their scaled surface (i.e. old corrosion); other plates (label B) were "grit blasted" to have a clean surface (i.e. new corrosion). The "old corrosion" and "new corrosion" surfaces were adopted to study the discrimination of the stage of degradation.

For the performance of the corrosion tests, four conditions were obtained by adding to plain water: 3wt%NaCl, 10%NaCl, acetic acid (pH=4), acetic acid (pH=4) and 3wt%NaCl, listed in order of increasing aggressive potential. The industrial partners suggested such conditions to simulate the actual (not accelerated) damage phenomena that may affect the tank bottom.

Corrosion was produced in a test pool (stainless steel) and AE monitoring was performed using different sensors provided from the technical partners. Such sensors are mainly resonant in the range 20-30 kHz, with a lower but still significant sensitivity at higher frequencies.

The combination of the above plate surface and corrosion conditions enabled 8 different corrosion tests. For the setting of signal classifiers, two additional tests were also considered, as two plates (45A and 45B), formerly tested under acetic acid, were submitted afterwards to the severer mix (acetic acid and NaCl) environment.

## **EVALUATION OF LABORATORY DATABASE - SIGNAL CLASSIFICATION**

To attempt a classification, the most significant differences among corrosion signals corresponding to the different plate-fluid combinations, have to be highlighted. This phase has to clarify two primary issues: the laboratory database must show a separation potential and the analysis tool must recognise and develop such potential to a rational form.

For the study of corrosion signal classification, the 10 reference tests were considered. As 10 data sets, each one identifying a corrosion test, were selected and fed separately to the program (Visual Class), a corresponding number of reference corrosion classes were "a priori" defined to attempt the desired signal classification. Each data set comprised 100-200 AE signals gathered from steady corrosion condition. Feature extraction was performed in a frequency band of 20-320 kHz and a time window corresponding to the whole recorded waveform (512 points at 1 MHz sampling rate).

The discrimination potential of the classifier can be evaluated according to the percentage of training signals, classified in each expected ("a priori" defined) class. The result for one classifier (one selected sensor) is presented in Fig. 1 where percentages, normalised to the actual number of signals in each data set, are within 50-90%. Similar results were found after evaluation of AE signals from one more sensor.

## **CLASSIFICATION TRIALS USING LABORATORY CORROSION DATA**

When the training session is deemed satisfactory, a classifier can be released for the classification of unknown signals. To assess the reliability of such classifiers, trials were performed using signals from the lab database, that were not used in the training session. All the lab tests performed were considered and, as a general rule, the classification was in agreement to the expected plate-fluid combinations.

Among such trials, the most significant one is related to the test "45Ba.a." (a plate with clean surface, corrosion under acetic acid). Since the test lasted several days, many data sets could be selected for a detailed description of the corrosion evolution after classification. The results are shown in Fig. 2: the trial data sets fed to the classifier are identified with a date and a label increasing with the test time.

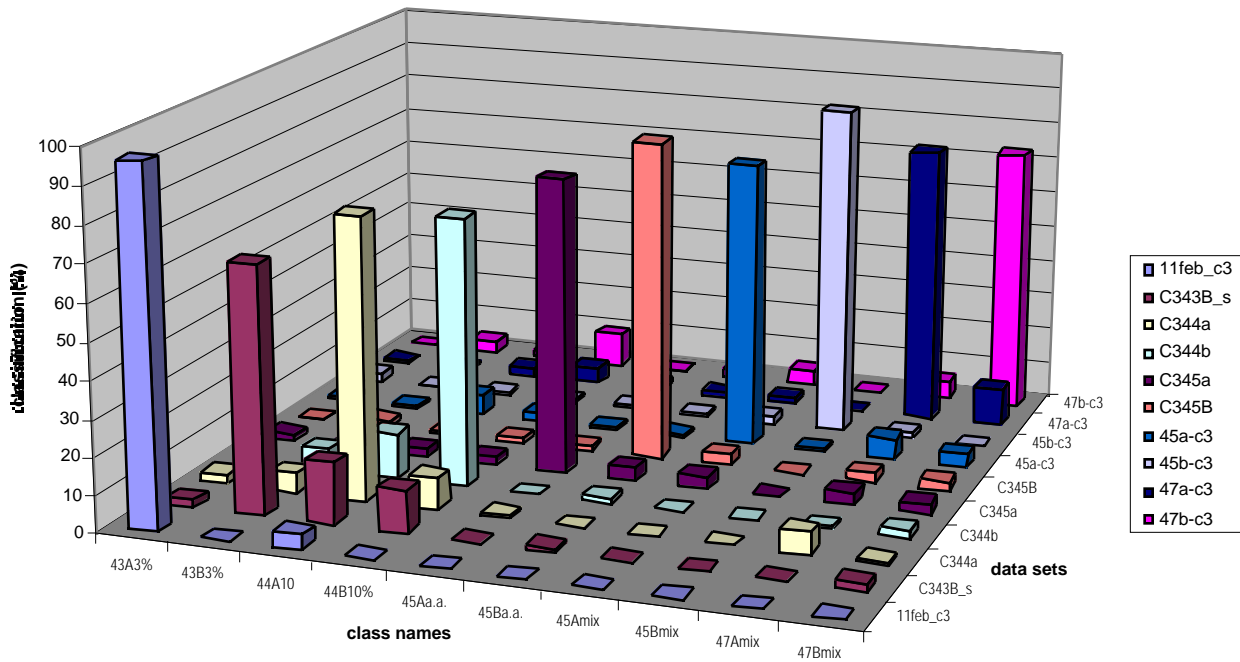


Fig. 1: "10-class" classifier based on corrosion signals. Distribution of training signals.

The results show that, at the onset of corrosion, signals mainly belong to the classes corresponding to less severe corrosion environment (3%NaCl and 10%NaCl). Afterwards, from the mid-phase of the test, more signals fall in those classes corresponding to the expected corrosion environment (acetic acid). This trend is better established as the test approaches its final stage (steady corrosion condition).

## CLASSIFIER UPGRADE

In the above classifiers, no specific class was defined to account for noise. If noise signals happened during a test, then the result of the classification would be confused.

Additional work was performed to provide signals representative of the following noise sources: bubbles (can arise from corrosion), water drops (may fall from tank roof), and rain (can be a very noisy source in a tank test). Bubbles and water drops were simulated in the laboratory. Rain signals were collected from a database recorded during a tank test. Then, one classifier was modified by adding these 3 "noise" classes to the existing 10 "corrosion" classes.

## TRIALS ON REAL TANK DATA

Trials have been performed to study the performance of the above mentioned classifiers. The example shown considers the same inspection, from which "rain" signals were extracted to upgrade the corrosion classifier. This time the trial data set was selected during a phase of the monitoring, in which rain was not expected to affect the test. Such data were analysed without pre-processing (Raw), and after filtering/locating (F&L). Figure 3 shows the results for the "corrosion" and the "upgraded" classifiers. In

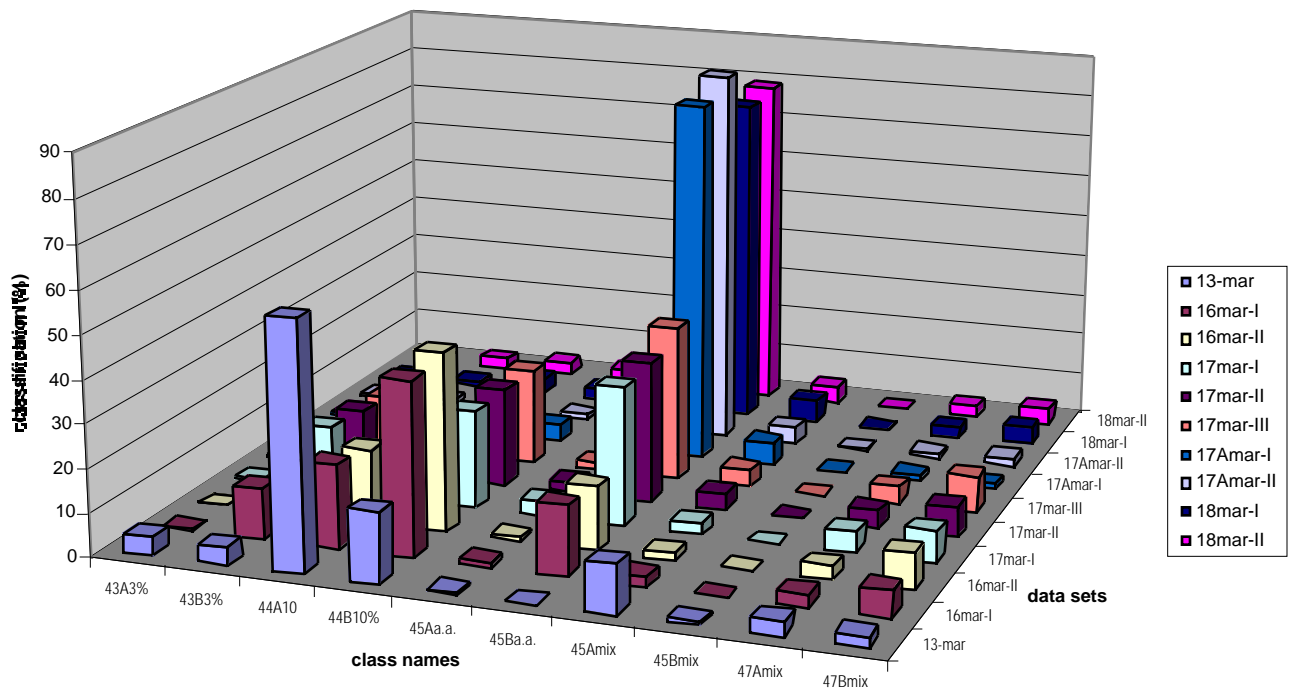


Fig. 2: Classification trial for test "45Ba.a.". Distribution of signals unknown to the classifier.

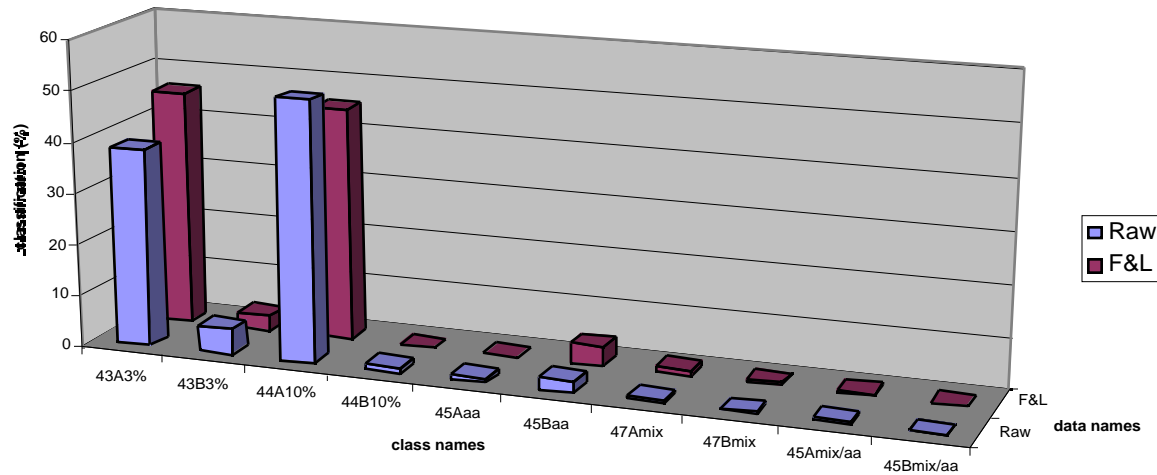
Fig. 3a ("10 class" corrosion classifier), the classification shows that only classes 43A3% (NaCl) and 44A10% (NaCl) are populated. In this case, a test operator should conclude that this tank suffers from some "old corrosion" (plate label is A), though the severity of the process seems not very serious. In Fig. 3b (13-class upgraded classifier), the classification highlights an unexpected though significant contribution from "rain-like" signals. In comparison to the performance of the 10-class corrosion classifier, 10% and 40% of the signals previously located, respectively, in class 43A3% (NaCl) and 44A10% (NaCl), are now collected in the "rain" class. The result also suggests a less severe corrosion (less data in class 44A10%), as compared to the one suggested by the 10-class corrosion classifier.

## CONCLUSIONS

This paper reported the evaluation of an AE database, made of signals gathered from corrosion laboratory tests, performed for different plate/fluid combinations. Feature analysis and pattern recognition could evaluate the separation of such corrosion-related waveforms. Noise signals were also considered for upgrading the corrosion classifier. The performance of such classifiers was assessed after classification trials. The results show that a suitably trained classifier, can sort out from a test database and classify, noise signals and signals relevant to corrosion of increasing severity.

On-line AE monitoring tests are currently performed in the SMT project. These tests are focusing tanks scheduled for off-line inspections in a short time period. Eventually, the reliability of the processing and evaluation method based on signal classification will be assessed on the basis of follow-up information.

(A)



(B)

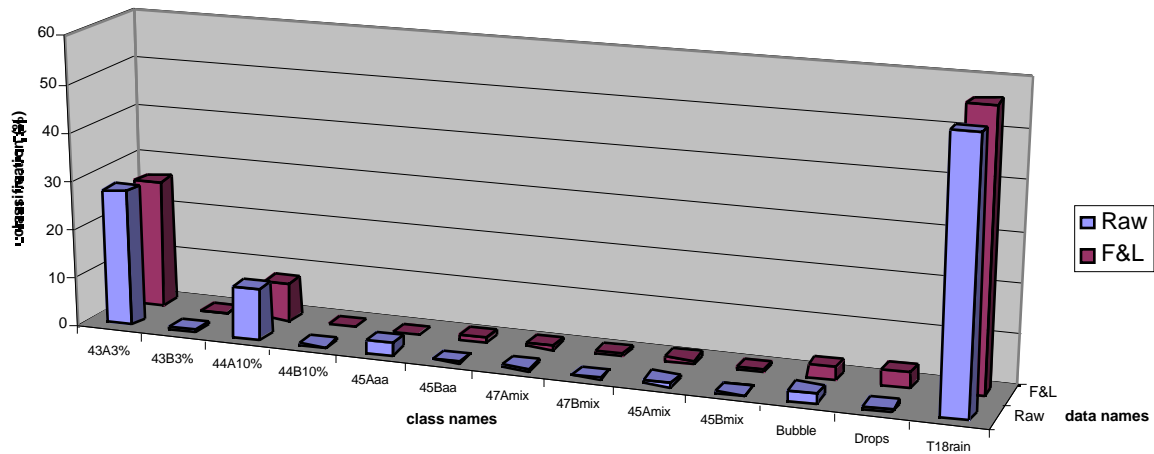


Fig. 3: (A) Shell Tank T18 - Inspection October 98. Results from "corrosion" classifier;  
(B) Shell Tank T18 - Inspection October 98. Results from "upgraded" classifier.

## **REFERENCES**

- [1] P.J. van de Loo, B. Herrmann, "How reliable is Acoustic Emission (AE) Tank Testing?" The Quantified Results of an AE Usergroup Correlation Study!", Proceedings of the 7<sup>th</sup> European Conference on Non-Destructive Testing, Copenhagen, 26-29 May 1998 - vol.1 - pp. 597-604.
- [2] D.A. Kronemeijer and P.J. van de Loo, "Acoustic Emission tank testing: How to discriminate between the onset of corrosion and further stages of degradation?", Presented at the European Conference on Acoustic Emission Testing, TÜV Austria, Wien, May 6-8, 1998.

## **ACKNOWLEDGEMENT**

The authors place a special acknowledgement to the European Commission (Directorate General XII) for supporting this SMT project. Many thanks also to the industrial partners Shell Global Solutions International B.V. (The Netherlands) and Dow (Germany) for their contribution to the project work. To Mr. Emilio Fontana for his efforts during the proposal of this project and to Mr. Fabrizio Cattaneo (CESI) who contributed to the work and results presented in this paper.

# **SCREENING OF TANK BOTTOM CORROSION WITH A SINGLE POINT AE DETECTOR: AE-SIMPLE**

**P.J. VAN DE LOO and D.A. KRONEMEIJER,  
Shell Global Solutions International B.V., CM Amsterdam, The Netherlands**

## **ABSTRACT**

*Tank bottom corrosion assessment with acoustic emission(AE) is a well-established non-intrusive testing technique. A drawback is that during the testing the weather conditions must be “ideal”. The mobilisation of qualified contractors is sometimes in conflict with the required test conditions. The tank owners felt the need to resolve this issue. Shell Global Solution launched the idea of a simple single point AE detector, to be applied by local inspectors at the best moment. A prototype instrument has been built, called AE-simple. Filter criteria are applied similar to those of the TANPKPAC test procedure. This paper describes the reliability investigation of this tool. The aim is to discriminate “A-grade” tanks (very minor corrosion activities) from “non A-grades”. This because earlier investigations showed a very good correlation between A-grades and tanks not requiring repair. We found that AE-simple scored 85 % correct in the A-grade class, whereas 13 % were “misses”, scored in class B (minor corrosion activities). The false call level is only 10%. This is judged as very promising, justifying further development into a simple portable field instrument.*

## **INTRODUCTION**

In the world of tank maintenance, the idea to shift from time-based to condition-based maintenance gets widely accepted. Attention is focusing on non-intrusive techniques. As such acoustic emission (AE) is now well established. A drawback of AE tank testing is that during testing the weather conditions must be “ideal”: no rain, weak wind, no operational activities. To plan the mobilisation of qualified contractors and to arrange the test period with Operations sometimes conflicts with the required test conditions. The tank owners felt the need to resolve this issue.

Shell Global Solutions launched the idea of a simple single point AE detector to be applied by local inspectors at the moment, which suits best. Through such a low threshold test, which can easily be repeated, insight can be gained in the tank bottom condition. One may then decide to organise a full AE test, or to postpone further inspection activities.

Main issue to investigate is the reliability of such a single point AE detector in comparison with a full analysis such as TANPKPAC (1), where use is made of a large number of sensors, covering the full circumference of a tank. The reliability of that method has been investigated by an industrial user group (2). Main result was that tanks graded as “A” appeared not to need any repair action. “E-grades” were indicative for serious damage, see Fig. 1.

## **APPROACH**

The first point investigated is the AE feature to be selected to assign a grade. In earlier work we identified the “duration” to be indicative for heavy corrosion spots with scale due to wall loss (3).

Although this observation is used for further detailed analysis (the “potential leak” data), for the assignment of an overall

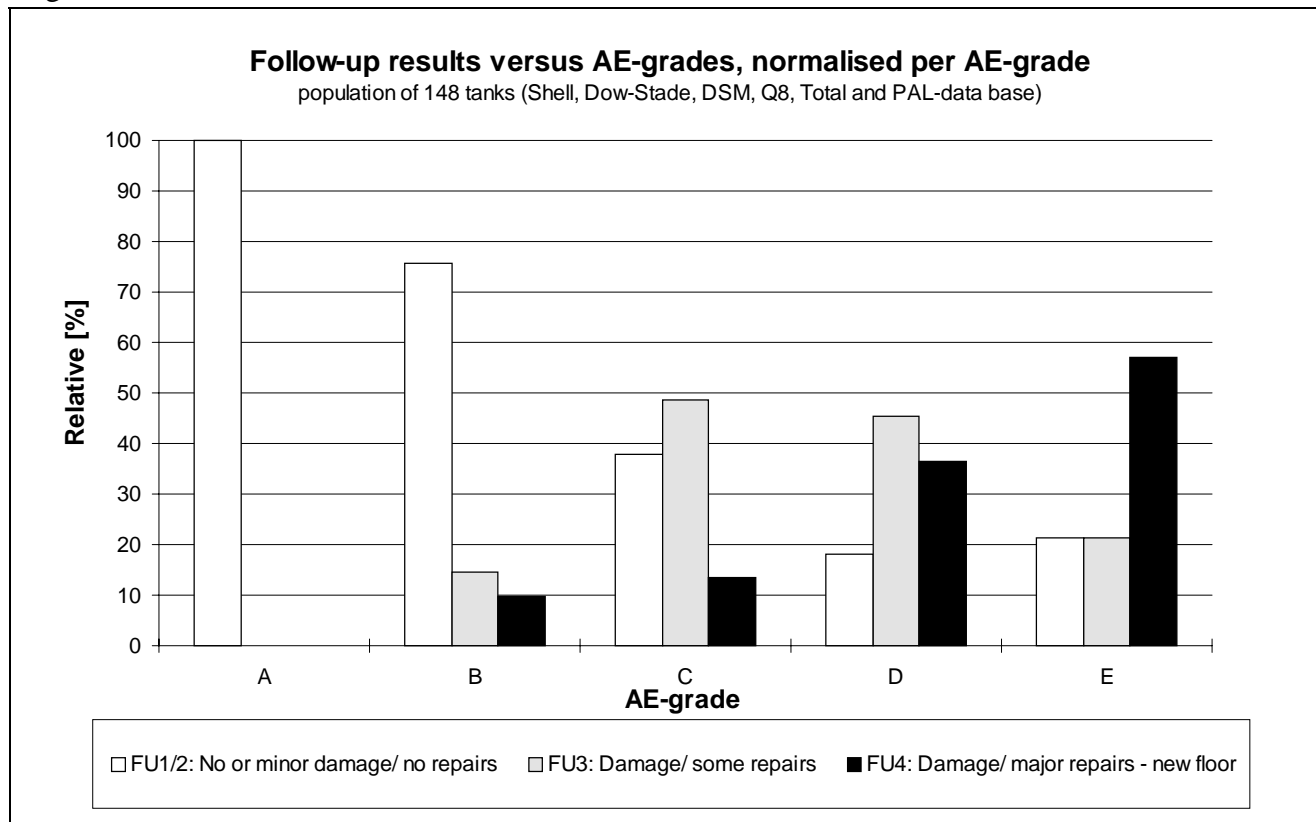


Fig. 1. Follow-up results versus AE-grades normalised per AE-grade (2).

grade, the most important parameter is the number of registered hits.

These hits are registered during a monitoring period of one hour. This period is based on the statistical occurrence (fluctuations in time) of the corrosion activities. Because for a handheld device, used by an operator, the favourable period should be as short as possible, we investigated the effect of shorter monitoring periods. As an outcome, we adopted the empirically derived conclusion from TANKPAC, that a monitoring period of one hour is optimum.

In the next chapter we will consider in full detail the variations in numbers of hits per channel as being representative for an arbitrary selected monitoring point.

## EXPERIMENTAL DATA

We started our investigation on a set of data obtained on 7 tanks of various diameters. The number of hits per channel is given in Table 1. We observed significant variations. These can not be related to the located corrosion spots.

Within TANKPAC these numbers are weighted, depending on tank size, viscosity of the product, applied threshold, etc. to end up with a grade. How this will be built-in into an AE-simple unit is out of the scope of this paper. We now only consider the assignment of a grade when based on the selection of a randomly selected position on the tank wall, for which we will take any channel to be representative. We will assume all other criteria unchanged.

Table 1. Number of hits per channel as registered on 7 tanks, various diameters, various overall grades as assigned by TANKPAC.

tank	I	II	III	IV	V	VI	VII
overall grade	A	A	A	B	B	C	D
Ch-1	313	185	254	1509	1425	2806	5009
Ch-2	245	164	134	387	1027	2256	2548
Ch-3	474	225	262	356	1312	2042	1663
Ch-4	27	219	748	391	950	818	2285
Ch-5	0	192	191	653	1464	1631	6837
Ch-6	406	314	561	447	966	2209	2956
Ch-7				444	843	1469	7380
Ch-8				689	599	1342	1681
Ch-9				492	744	1975	5254
Ch-10						1934	3903
Ch-11						3050	2704
Ch-12						2615	6249
average	244	216	358	596	1036	2012	4039

## STATISTICAL BACKGROUND

On the basis of the numbers given in Table I, but also on the numerous data available from all tanks tested with TANKPAC, it is justified to assume that the average number of hits per channel has a Gaussian distribution. This means that we may apply the “normal” statistical rules for probability intervals and standard deviations. The relevance of this is illustrated in Fig. 2.

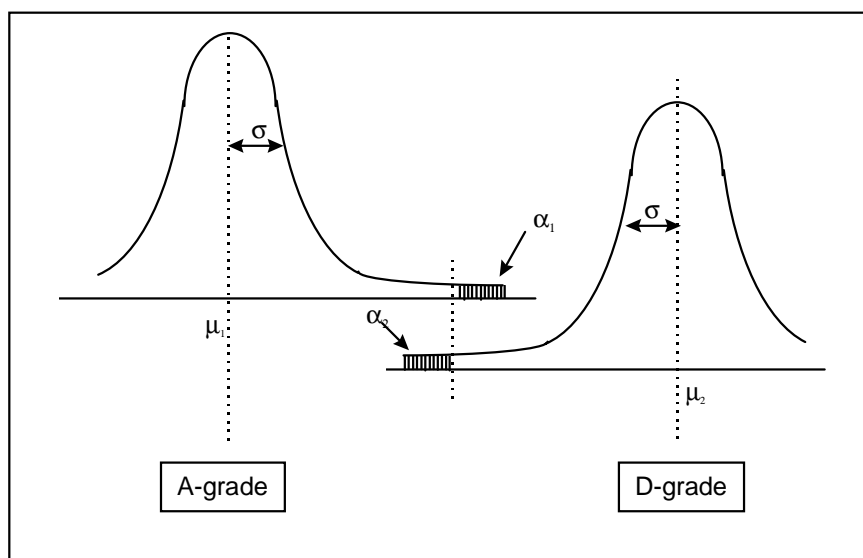


Fig. 2. Overlapping normal distributions of average number of hits per channel.

If the decision boundary is chosen as indicated in Figure 2, then  $\alpha_1$  is indicative for the percentage of “false calls”: although belonging to the class of A-grades, they are assigned to be non-A. The percentage is derived from the width of the distribution, expressed in the number of standard deviations (the factor t). Some examples are given in Table 2. For example, if the selected decision boundary is  $\mu_1+1.44*\sigma$ , the “right exceedance chance” is 7.5%.  $\alpha_2$  is indicative for the percentage of “misses: although belonging to the class of D-grades, they are left of the decision boundary, thus assigned to the population of A-grades.

Table 2. Interval width, t-factor and single sided exceedance chance.

1	interval width	68%	75%	80%	85%	90%	95%
2	factor t	1,0	1,15	1,28	1,44	1,64	1,96
3	single side exceedance	16%	12.5%	10%	7.5%	5%	2.5%

## STATISTICAL EVALUATION OF THE 7 TANKS AND FURTHER GENERALISATION

In Fig. 3, the average number of hits per tank is given, including the confidence intervals as given in Table 2. The dotted horizontal line, indicated as “criterion”, is the decision boundary. By shifting this line up and down, one can judge the effect on the false calls and misses. Where inspectors will actually put the decision boundary will depend on a more detailed consequence analysis, which is out of the scope of this paper. More important to discuss here is generalisation of this approach.

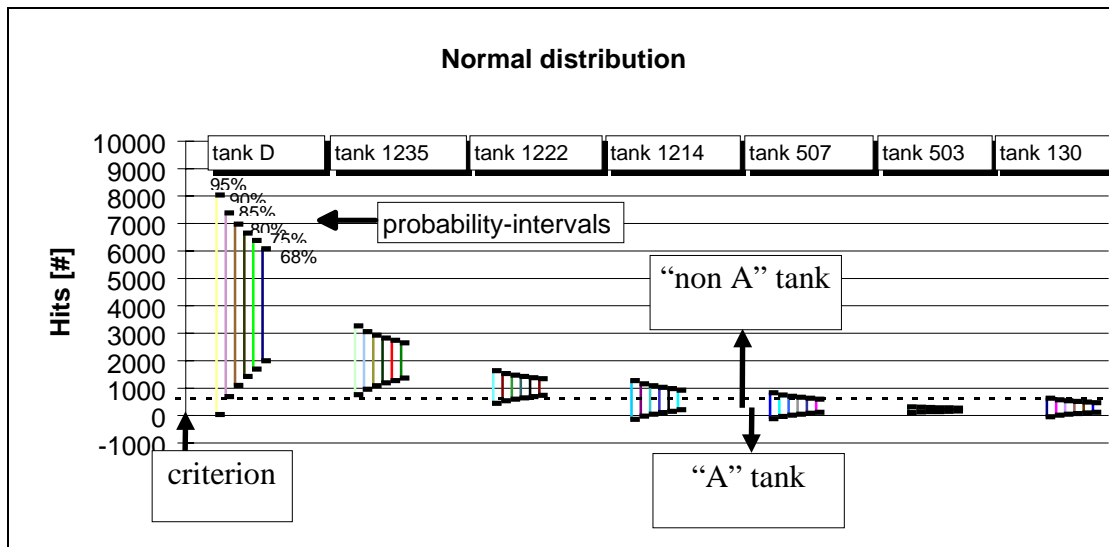


Fig. 3. Average number of hits and confidence intervals of the 7 tanks tested.

From the data of 46 graded tanks tested within Shell, we calculated the average number of hits per channel, shown in Fig. 4. If we apply the decision boundary for A- and non-A-grades of 400 hits, as indicated by TANKPAC, we observe that all assigned C-, D- and E-grades are indeed non-A-grades, the assigned B-grades show some false calls, whereas all A-grades are properly identified. This confirms that 400 hits is a good decision criterion.

To judge the scores for single point monitoring, we have to take the standard deviations into account. Via linear regression of the available data, we found as best approximation:

$$\sigma = 0.48 * \mu - 28$$

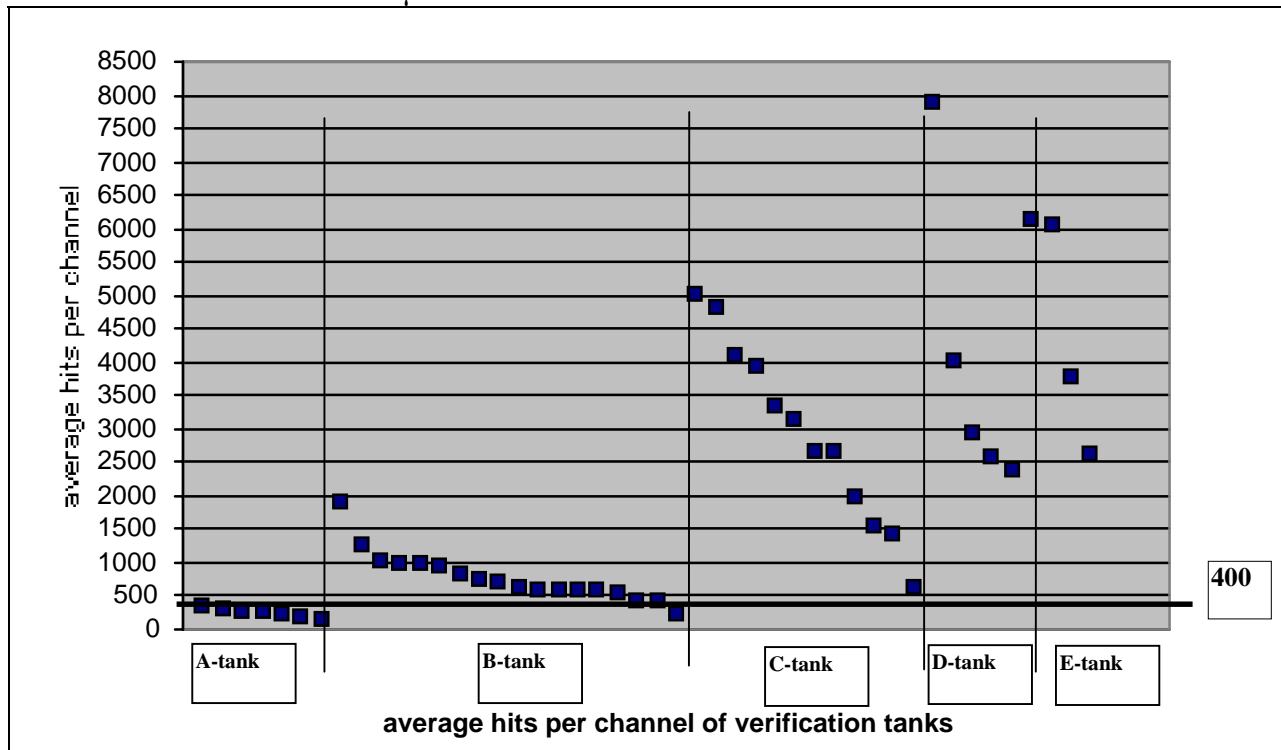


Fig. 4. Average number of hits per channel for 46 storage tanks tested at various Shell sites and application of 400 hits as decision boundary for A-grades

It should be realised that the chance of a miss or false call does not only depend on the measured average number of hits ( $\mu$ ) and standard deviation ( $\sigma$ ), but also on the likelihood of the occurrence of a certain grade! In other words:

$$(\text{probability of a good score}) = (\text{reliability of the technique}) * (\text{probability of occurrence})$$

Below we will illustrate this approach using the distribution of scores as found by PAL when they applied TANKPAC to more than 2000 tanks (Ref. 2. See Table 3). Tank owners know best their own tank farm, thus the potential occurrence of good or bad tanks. If required they can fine-tune or adapt the approach with their own figures.

Table 3. Distribution of grading scores obtained by PAL, when TANKPAC has been applied to all tanks of their customer database.

Assigned grade	A	B	C	D	E
statistical occurrence	34%	26%	25%	8%	7%

If we now combine the average number of hits and standard deviations per grade with the assumed most probable occurrence we can calculate the number of misses and false calls for any decision boundary. By way of example we show the results for a decision boundary is 400 hits, applied to the 7 tanks of Table 1 and an average E-grade value derived from the set of the 46 tanks used earlier (see Fig. 5).

The procedure applied is: subtract the average number of hits for a certain grade from the decision criterion. Divide that number by  $\sigma$  (which gives the factor  $t$ ). This determines the width of the

distribution. From the statistical t-tables the single sided exceedance chance can be determined. When this is multiplied with the chance of occurrence one gets the fraction of scores in the A class and the non-A class. When this is normalised to 100% above and below the decision boundary, one can express the scores in terms of percentages “misses” and “false calls”. We observe 85% good scores and no “serious” misses: 13 % are B-grades. Of the non-A graded tanks only 10% are false calls.

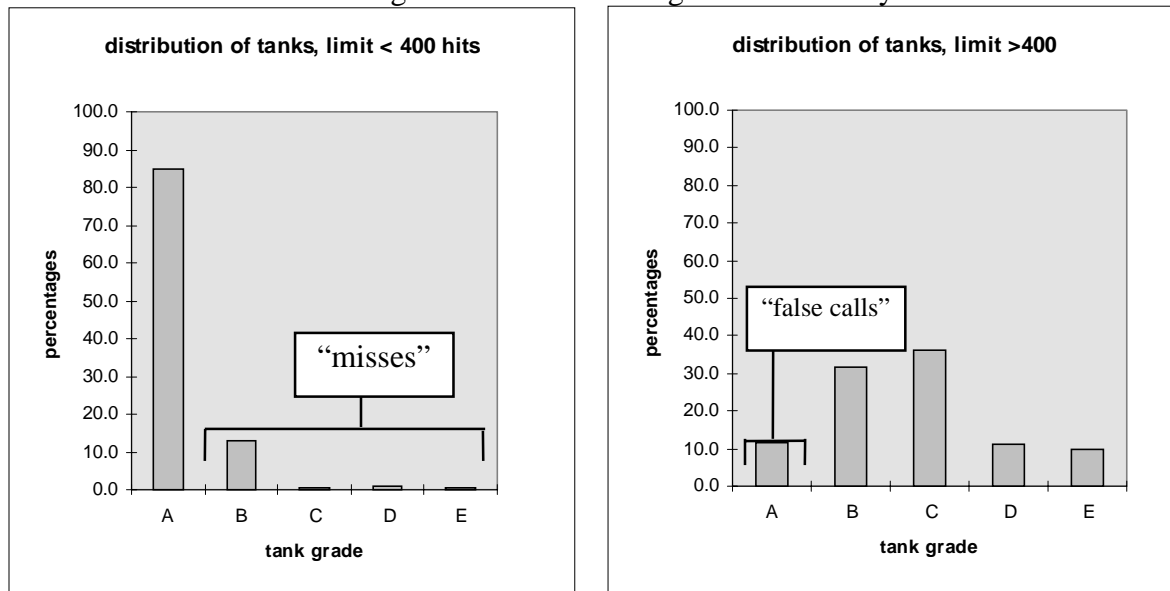


Fig. 5. Distribution of tanks: misses and false calls.

## CONCLUSION

To investigate the reliability of single point AE monitoring of tanks, we used the TANKPAC registered signals of any arbitrary single channel. When applying the average number of 400 hits as a decision criterion for assigning A-grade tanks (No follow-up recommended) and non-A-grades (full analysis recommended) we found that AE-simple scored 85 % correct in the A-grade class, whereas 13 % were “misses”, scored in class B (minor corrosion activities). The false call level is only 10%. This is judged as very promising, justifying further development into a simple portable field instrument.

## ACKNOWLEDGEMENT

We want to thank the student Arjan Schwartz for his contribution to the execution of the work. Also we would like to thank Physical Acoustics Ltd. (PAL) for supplying us with the detailed information of the tested tanks.

## REFERENCES

1. Physical Acoustics Group, “Acoustic Emission Testing of pressure systems and tanks”. Brochure PAL, Over/Cambridge, UK.
2. P.J.van de Loo and B. Hermann, “How reliable is Acoustic Emission (AE) Tank Testing? The quantified results of an AE Usergroup Correlation Study!” 7-th ECNDT, Copenhagen, May 26-29, 1998.
3. P.J. van de Loo and D.A. Kronemeijer, “Acoustic Emission Tank Testing: How to discriminate between the onset of corrosion and further stages of degradation?” European Conference on Acoustic Emission, Wien, May 6-8, 1998.



# CASE HISTORIES FROM TEN YEARS OF TESTING STORAGE TANK FLOORS USING ACOUSTIC EMISSION

Stephen N. GAUTREY, Phillip T. COLE, and H.J. SCHOORLEMMER\*  
Physical Acoustics Limited, UK and \*Physical Acoustics BV, Netherlands.

## ABSTRACT

*The enormous cost of opening and cleaning a storage tank for inspection of the floor is wasted if it is found to be in good condition. The system described here evaluates floor condition on-line by detecting active corrosion from the resulting acoustic emission. Evaluation of the emission against an experience-based database allows the floor condition to be established, and appropriate maintenance decisions made. This paper is a small cross-section of case histories from the past 10 years, taken from a database of thousands of tests.*

## INTRODUCTION

During operation, the only part of a tank that affects integrity, which cannot be inspected from the outside, is the floor. The enormous cost of opening and cleaning for inspection of the floor is wasted if it is found to be in good condition. In addition, environmental problems may result from the need to safely dispose of the waste inside many crude oil tanks. Major oil and chemical companies have worked with Physical Acoustics to develop a non-invasive method of evaluating floor condition, without removing the product. This method, known commercially as TANKPAC™, is widely reported in published papers, for example ref. 1 which looks at the reliability on 600 tank tests to June 1996, and ref. 2 which reports the cost savings resulting from its use as a maintenance planning tool.

The method involves mounting sensors on the tank wall and detecting the emission that results from active corrosion inside or underside the floor. Evaluation of the emission against an experience-based database allows the floor condition to be established, and appropriate maintenance decisions made. The system is not an NDT method but a maintenance planning tool, to tell when internal inspection is needed.

Iron, in the presence of water and oxygen combine to form a hydrated iron oxide, commonly called rust. This simple definition describes the one chemical reaction that probably costs industry more in losses and maintenance costs than any other. The emission detected during a test results primarily from the fracture and de-bonding of corrosion product as a result of the volumetric changes taking place, see ref. 3. Although corrosion is the prime source of interest, a leak may generate noise that masks the corrosion activity, and this is of course of interest to the tank owner, who is often unaware of the problem. This paper describes a selection of case histories from 10 years experience monitoring storage tanks for floor corrosion.

## CASE HISTORIES

All the case histories below show the results after processing to remove extraneous noise sources, which are inevitable at the high sensitivities being used. Sometimes only a few percent of the collected data is attributed to floor corrosion and shown in these plots.

#### A. Oil-Field Production Tank

This example is given first simply because it provides a good demonstration that the procedure does detect active corrosion. Many tanks with highly acidic and corrosive contents, such as those used in field production, have epoxy-coated floors backed up by large internal sacrificial anodes. These anodes provide protection when the coating has broken down, by corroding themselves; otherwise the floor would rapidly hole through. The anodes in this case are 1 metre x 0.5 metre rectangular zinc blocks. There are more than thirty in this tank, arranged in radial rings. Corrosion of zinc does not produce heavy scale, so the signals are small, but clearly detectable where the floor coating has locally failed and made them active. When the zinc has been consumed the activity becomes more dispersed and louder, as the floor corrodes away. The location system is so accurate that it almost shows the shape and orientation of these anodes, a remarkable result (Fig. 1). The same system is used to locate and orient tank inspection "robots". Naturally, it is important to confirm the anode locations from maintenance records in order to avoid incorrect interpretation.

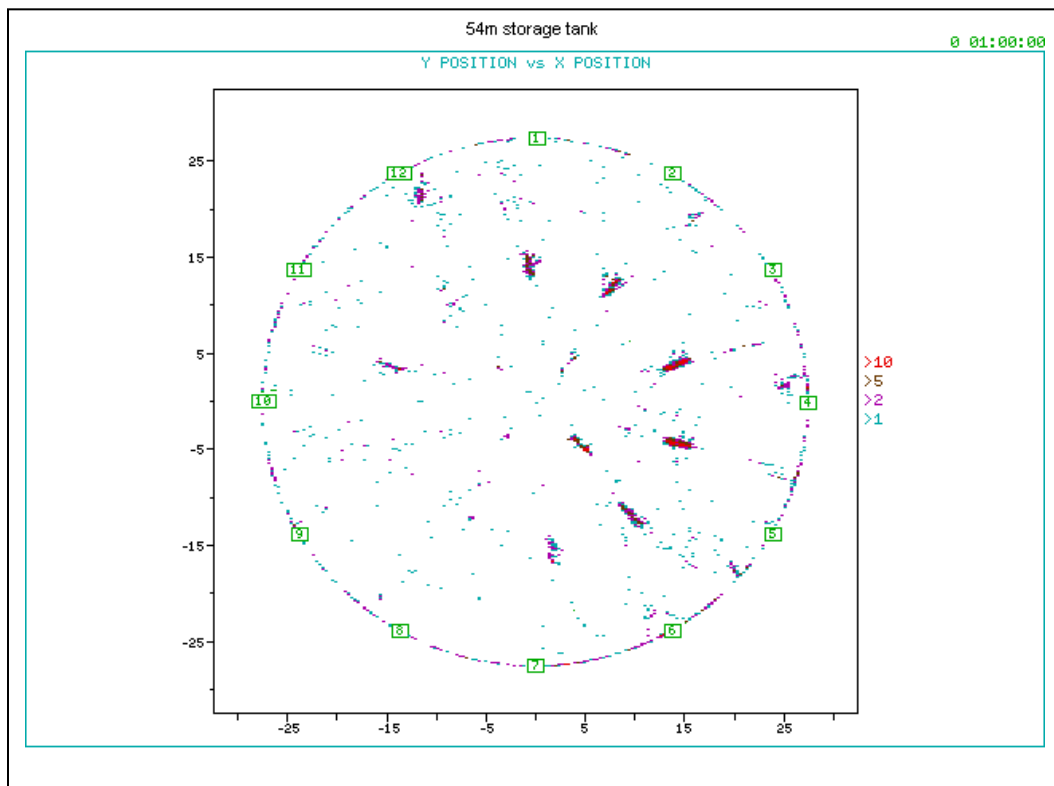


Fig. 1: 54 m diameter oilfield production tank showing location of "active" anodes.

#### B. 48-m Naptha Tank Before and After Repair

This tank was selected for maintenance as a result of testing and receiving the grading of "E", the highest priority. Approximately 90 patches were used in the repair of the tank, which, with the

benefit of hindsight, should have had a new floor; following repair the tank was returned to service, and a test carried out as a baseline. The "baseline" test showed that, despite extensive internal and magnetic field leakage (MFL) inspection, not all the problem areas had been repaired, and concentration of AE activity is shown, indicating potential future problem locations. (Fig. 2)

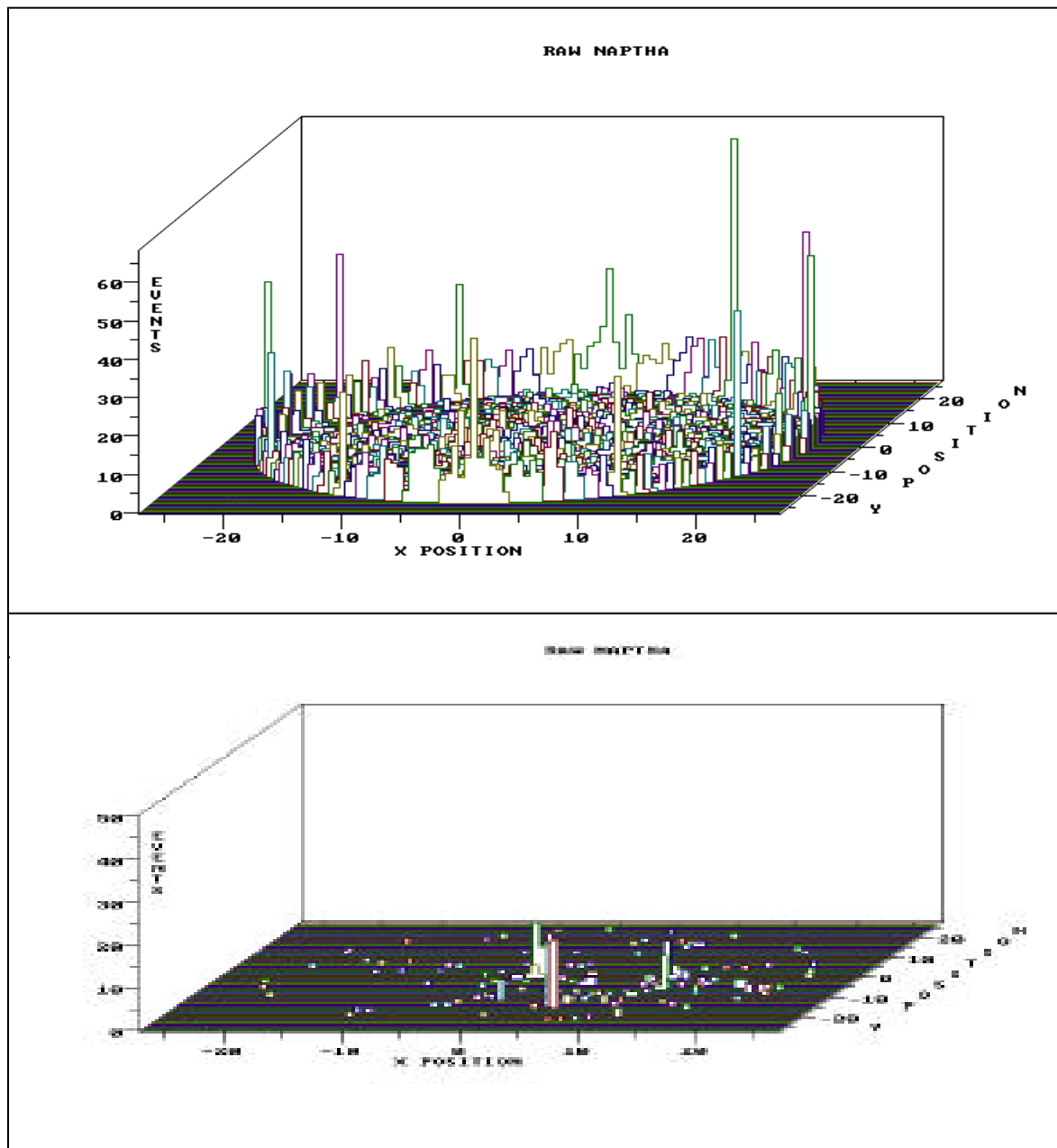


Fig. 2: Above: before repair; Below: after repair

#### C. 110-m GRP-lined Crude Oil Tank

The size of this tank and location of the damaged area some 40 metres from the nearest sensor make it of special interest. No damage was seen to the GRP liner, but MFL indicated >60% metal loss from underside in the active area, this was confirmed by plate removal. It was found that chlorides were present in the sand, which had possibly come from the beach rather than the depot!

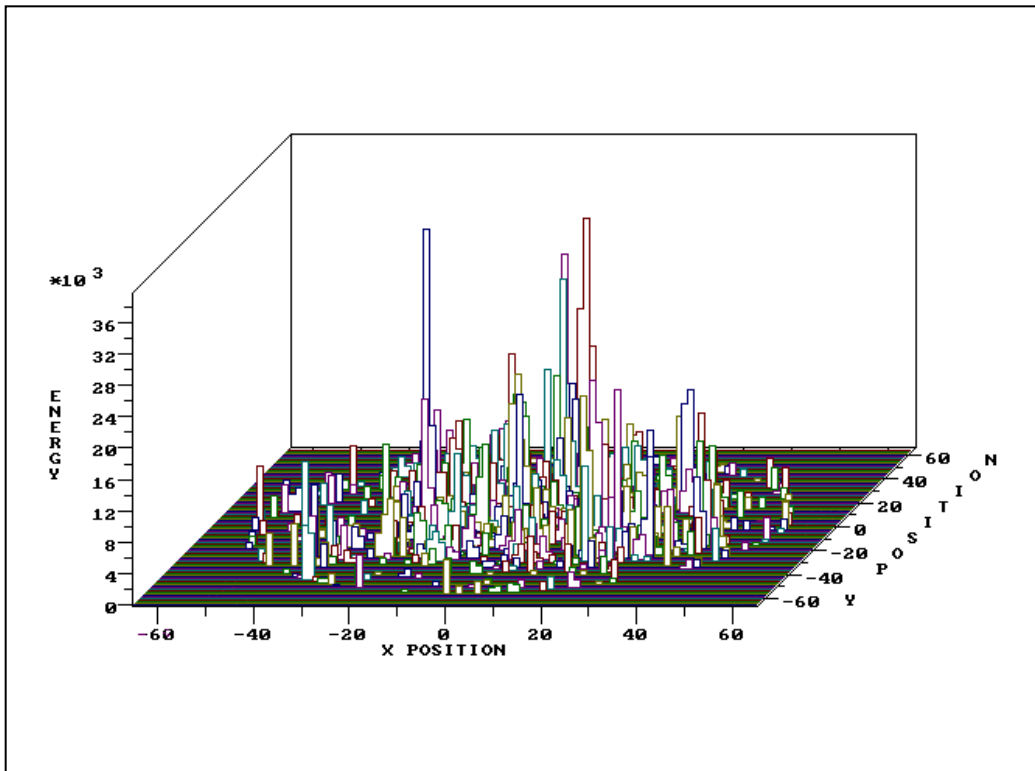


Fig. 3: GRP-lined Crude Oil Tank inspection.

#### D. Sulphur Tanks

A number of sulphur tanks have been tested, and the results have all been comparable, with 95-98% of the emission originating as a result of corrosion under the insulation on the tank wall. This makes it almost impossible to evaluate floor condition without resorting to complex 3D location methods to differentiate the two. Even then it is questionable if the floor result would be reliable. However, in all cases the wall was in exceptionally bad condition, threatening tank integrity, and in one case the tank was shut down shortly after the test and found to be corroded >90% through over large areas, and pin-holed in several locations, the tank was scrapped.

Of particular interest was the way corrosion was concentrated at the insulation support rings. Shown in the figure below is the vertical distribution of AE resulting from corrosion activity, showing pronounced peaks at the support ring locations. (Fig. 4)

#### E. Hot Fuel-Oil Tanks

Temperature plays a large part in corrosion rate, so it comes as no surprise that warm tanks suffer from higher corrosion rates once any corrosion barrier has broken down and conditions are right. Very hot tanks theoretically should not corrode, however a problem is found in the areas of temperature gradient, with locally high rates. In this case underside corrosion was more than 50% through floor around most of the annular ring, but over a very narrow band which was missed by the previous "spot" internal inspection. Tanks in similar service have failed catastrophically in service. (Fig. 5)

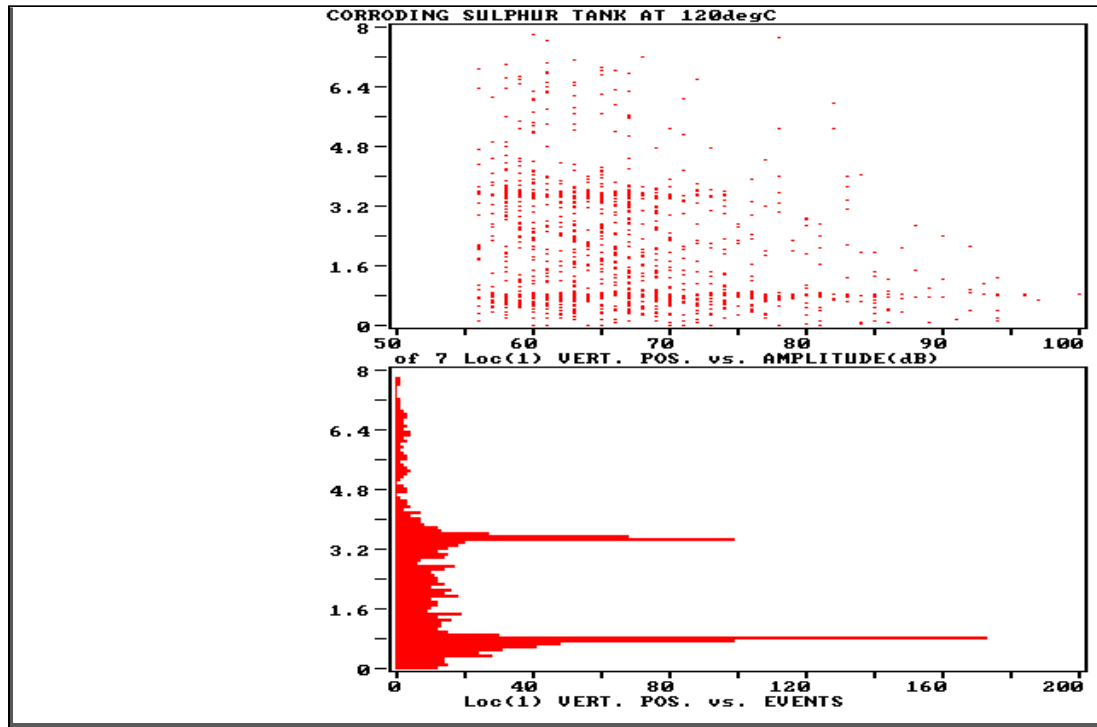


Fig. 4: Vertical distribution of AE resulting from corrosion. Lower plot: Y-axis is height in metres, X-axis is relative activity, peaks corresponding to severe corrosion at insulation support rings.

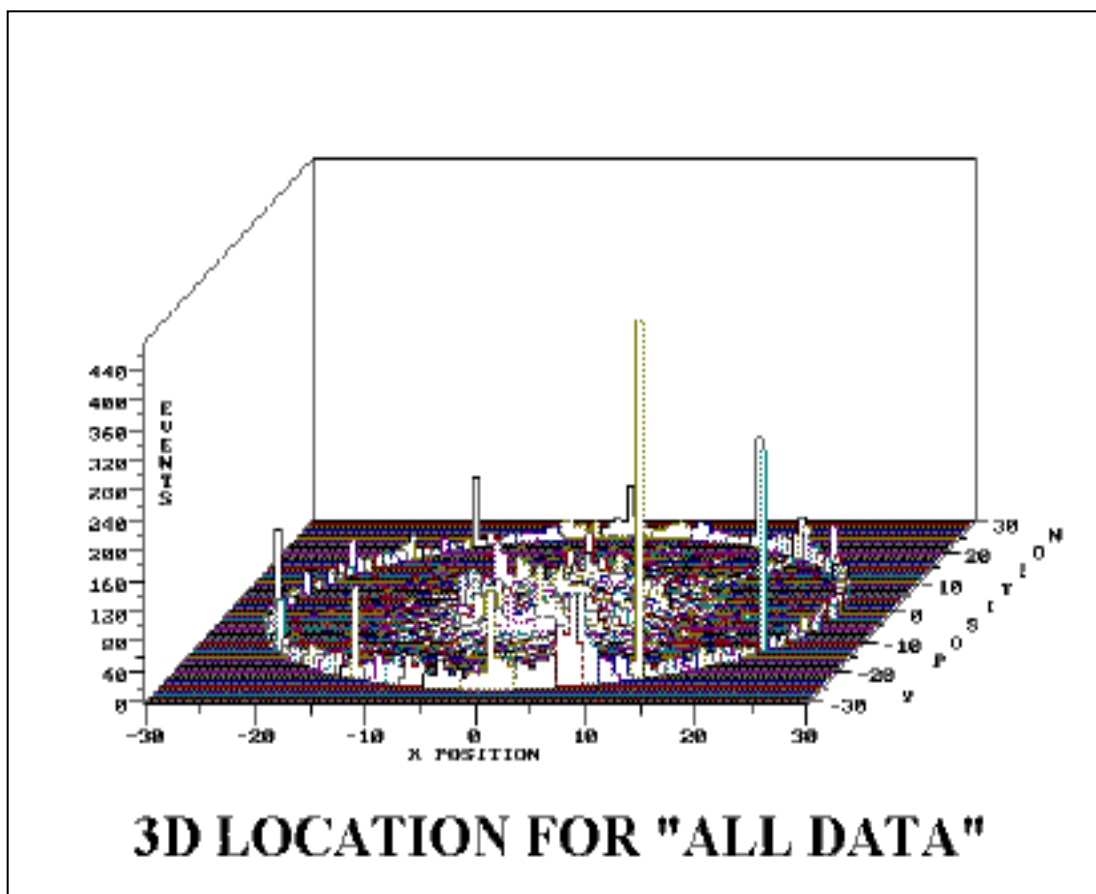


Fig. 5: Hot oil tank with severe annular corrosion.

## F. Crude Oil Tanks

Crude oil tanks are usually large, and have indeterminate amounts of sludge in the bottom. The depth and type of sludge can have a significant effect on the AE result and a number of tools are used to try and compensate for this, all based on experience and comparisons with follow-up inspection.

Sludge depth is possible to measure by dipping or sonar methods, but the type of sludge is more relevant. Some tanks have had a measured 3 m of sludge that had little effect on the results, transmitting sound easily. Others with "dense" sludge have a severe damping effect. Often of more importance is that the sludge is sometimes the only thing keeping the product in the tank, and over one hundred holes have been found in some floors of crude tanks after cleaning. Operators sometimes try to "re-suspend" sludge prior to cleaning, this is when the floor will often start to leak as the "sealing" sludge is removed.

GRP linings are very common in some areas, and have been found to have minimal effect on the test results. Very occasionally the lining de-bonds and breaks up, resulting in rapid corrosion and a high grade AE indications compared with comparable service tanks.

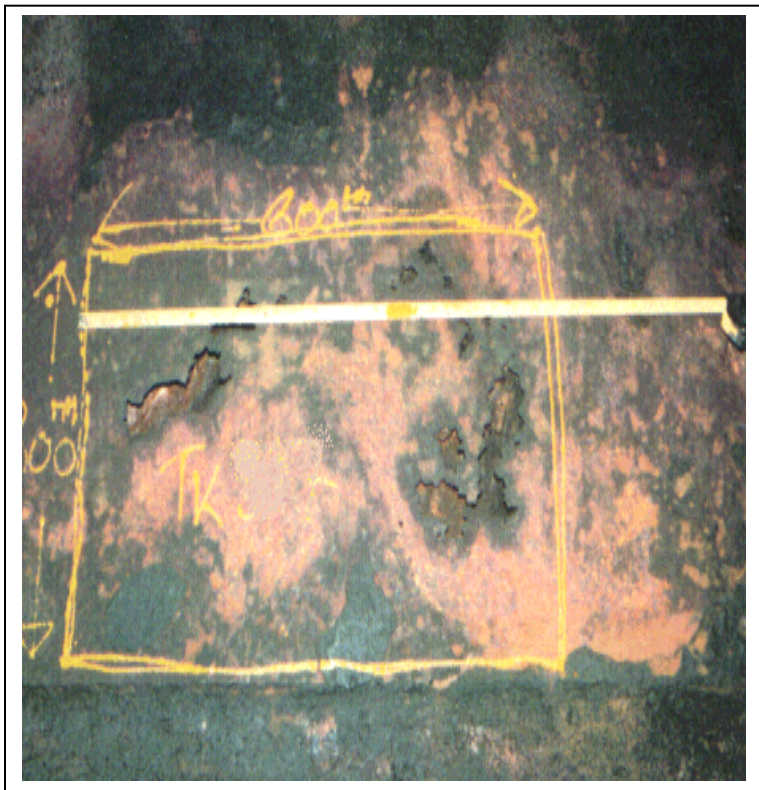


Fig. 6: One of 50+ holed areas in a crude oil tank, (not leaking in service because the sludge sealed the floor).

This also illustrates why "leak detection" is of limited use in professional maintenance planning. Leak detection only tells if the tank is leaking at the time of the test. In tanks with sludge, the leaks may stop and start on a random basis, over periods of seconds or minutes, or sometimes as a function of fluid height. Cracked plate welds may leak at low fluid level but seal at high fluid level.

Examples have been seen where the weld was completely missing over up to half a metre, but the tank had been in service for 15 years.

## G. Leaking Tanks

Leaking tanks fall into two categories; 1) those where the owner was not aware of a leak, and the leak was found as a by-product of the floor condition assessment, and 2) those where a leak was known or suspected, and confirmation or location was requested.

Assessment of floor condition is not possible in the presence of a significant leak, as the leak noise "drowns out" the corrosion activity. The "leak test" is a different procedure, when a significant leak is correctly located it is obvious, as the event rate is exceedingly high, with hundreds of events per second from one position; in this case, a few seconds of data is sufficient. Leak location on large tanks is difficult because insufficient tanks in the field actually leak for operators to gain the broad experience of the different situations that occur in the field. Laboratory tests can provide only very limited experience. Recent software and instrumentation developments, currently being field-tested, promise to assist in this area.

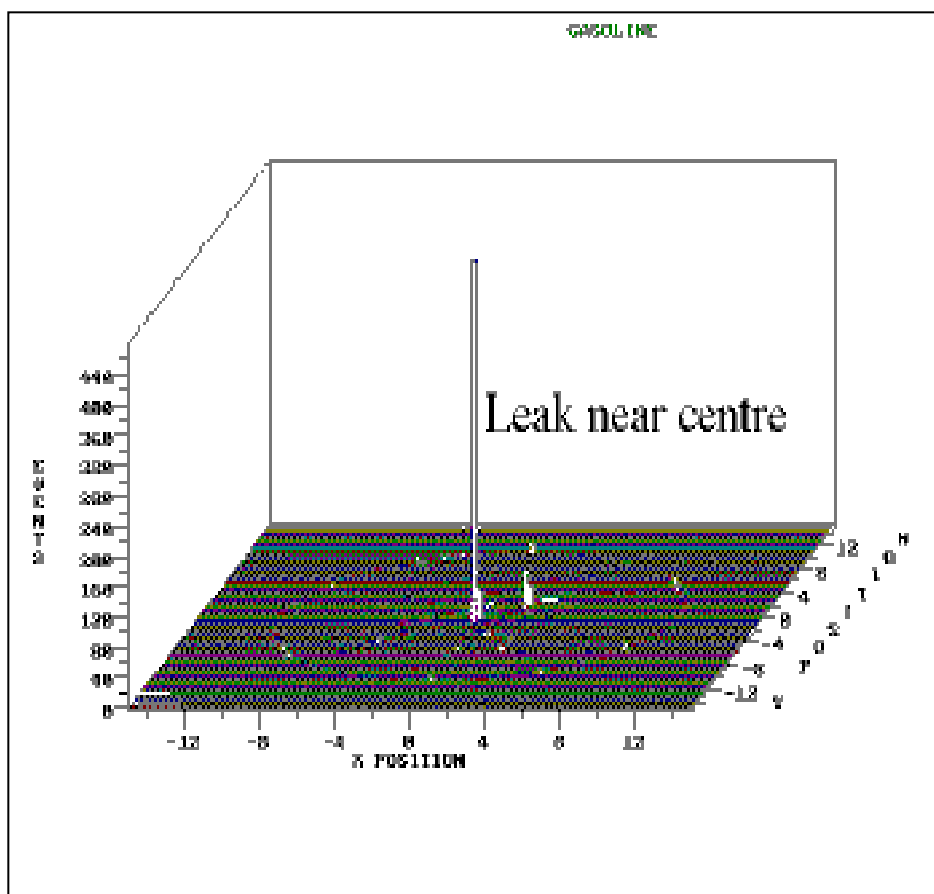


Fig. 7: Gasoline tank; owner did not know of its leak, which was found during a routine test.

The gasoline tank above had an epoxy coated floor. Where this failed locally, the floor had pin-holed, 1 mm in diameter when taken out of service about a month after the test, but the rest of the tank was in good condition.

In the following example, operations had calculated a 100 cubic metre per day loss from their naphtha storage farm, based on mass balance. Inspection felt it was a gauging error as there was no evidence of leakage, but at the request of operations requested our testing. The engineer found the leaking tank using a 5131-LF portable leak detector, then located the leak with the AE test system. The leak rate was so high, and generating so much noise, that the system amplifiers had to be switched off to avoid signal saturation. Opening the tank revealed a 1 cm hole due to MIC, (micro-biologically induced corrosion), and the floor was unsupported over a cavity "washed-out" by the leaking naphtha of several cubic metres. Some 700 tons of naphtha had gone into the ground since the leak was first suspected.

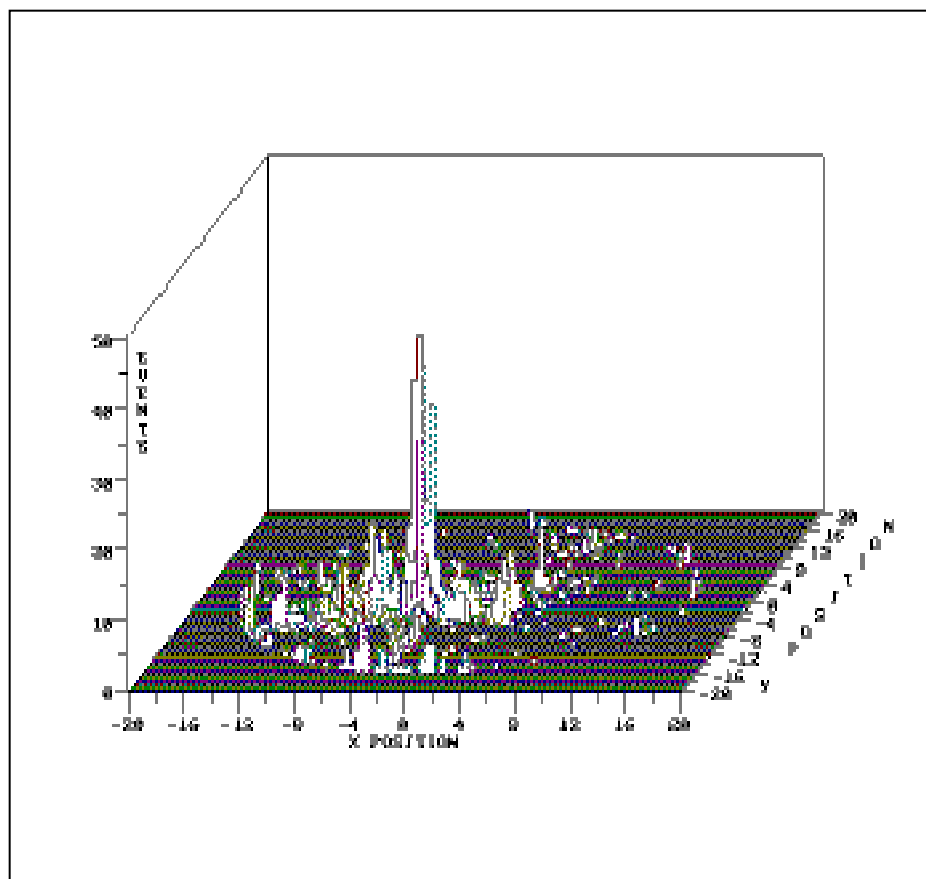


Fig. 8: A few seconds of data was sufficient to reveal the location of this 100 ton/day leak.

Other major leaks found in the field have been as a result of:

- Corrosion, the most common reason.
- A pipe rubbing at the edge of a sump, wearing a hole through the corner.
- Weld cracking, or no weld present.

Small leaks may not be detectable, either because they generate no noise, or the noise is drowned out by active floor corrosion. Multiple leaks in the same tank make location difficult or impossible, depending upon their individual characteristics.

## STATISTICS

These are reported overall in reference 1, and since that report on 598 tank tests, there has been no statistical change in the distributions. Overall statistics don't tell the individual picture though, and a few observations are worthwhile making:

- Some sites have nearly all "bad" tanks. The method is not a substitute for maintenance and it simply allows you to focus where it is needed most.
  - Some companies have over-maintained their tanks, and they stand to save a lot of money by using the method.
- <sup>a</sup> We can see there is no reason for tanks not to stay in service for very long periods, by combining all best practices this should be possible. We see some sites with only internal corrosion, some with only underside corrosion, but few have neither! Combining all best practices may achieve this.

## CONCLUSIONS

AE now plays a major part in tank maintenance planning for many oil companies, bringing benefits in safety, environment and cost. The TANKPAC™ procedure is very different from all conventional AE testing procedures for tanks and vessels, as there is no change in stress required, and the tank is simply monitored for a period of time. This makes the data interpretation and evaluation difficult, as there is not a parameter with which to correlate. The test is run at such a high sensitivity that proper noise recognition and elimination procedures are always required. The limitations and restrictions on its application are well documented; the benefits far outweigh these and have resulted in its rapidly increasing use world-wide.

## REFERENCES

1. P.J. van de Loo and B. Herrmann, "How Reliable is Acoustic Emission (AE) Tank Testing? The Quantified Results of an AE User-group Correlation Study", 7<sup>th</sup> European Conference For Non-Destructive Testing, Copenhagen, 1998.
2. S.D. Miller, J. O'Brien, D.L. Keck, "Implementation of Advanced NDT Technology Programs at Saudi Aramco," 7<sup>th</sup> European Conference For Non-Destructive Testing, Copenhagen, 1998.
3. Stephen N. Gautrey, Phillip T. Cole: "Acoustic Emission from Active Corrosion under insulation-A case history from a Sulphur Tank", Presented at the 22<sup>nd</sup> European Acoustic Emission Working group, Aberdeen, UK, 1996.

# ACOUSTIC EMISSION DETECTION OF DAMAGE IN REINFORCED CONCRETE CONDUIT

H. Warren SHEN, Subramanian IYER\*, Mark A. FRIESEL, Ferdinand MOSTERT, Richard D. FINLAYSON, Ronnie K. MILLER, Mark F. CARLOS and Sotirios J. VAHAVIOLOS

Physical Acoustics Corporation, Princeton Junction, NJ

\* Metropolitan Water District, La Verne, CA

## ABSTRACT

*Acoustic emission has been used to determine condition in reinforced concrete conduit. Acoustic data generated by PLB (pencil-lead break) were collected from both good PCCP (Prestressed Concrete Cylinder Pipe) and damaged PCCP as digital waveform files. These files were analyzed using the normalized frequency energy method. The results indicate that the energy in specific frequency segments can indicate the condition of the conduit, and with an appropriate tuning process, may show the type of damage; e.g., broken wire or delamination. A partial power function and a graphic alarm have been implemented in a standard AE instrument. A portable handheld sensor-head support structure has been designed and built to maintain a constant source-sensor distance spanning the width of the desired inspection region for a standard 1.2-m diameter PCCP.*

## INTRODUCTION

Prestressed concrete conduit is used for large volume residential and industrial water transport. The conduit is constructed of layered mortar and concrete, and has pre-tensioned wire windings embedded for added strength. Continual load and corrosion may cause the wire and concrete to fail, and may result in contamination and blockage of the conduit, and surface subsidence. A technique and instrument was developed which can reliably detect damaged conduit during periodic internal inspection.

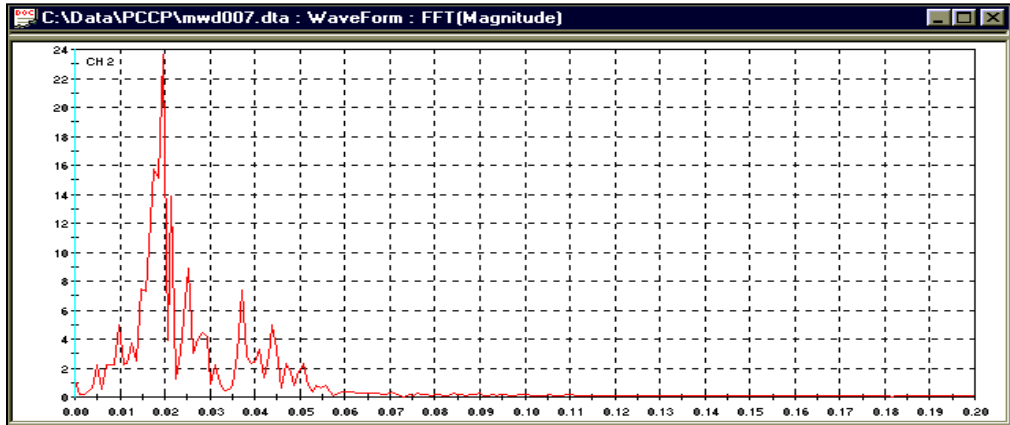
In December 1998, a preliminary study using acoustic methods to monitor PCCP was carried out, and promising results were obtained (1). The current work includes more detailed analysis using this existing data and new data collected in October 1999. Real-time results are presented later in the paper.

## ANALYSIS ON EXISTING DATA

Previously (1), it was concluded that frequency distribution is a potential approach for monitoring PCCP, as the high frequency response is significantly reduced when damage is present. Figures 1 and 2 compare the frequency spectra obtained from a good section of a pipe (Fig. 1) and a damaged section of a pipe (Fig. 2) using a PAC 30 kHz AE transducers. The spectra from the good pipe show significant energy around 40 kHz, with most energy between 10 and 30 kHz. The spectra from the damaged pipe have much lower energy near 40 kHz when compared to the energy in the 10 to 30 kHz range.

## PolyModal™ Frequency Envelop Feature

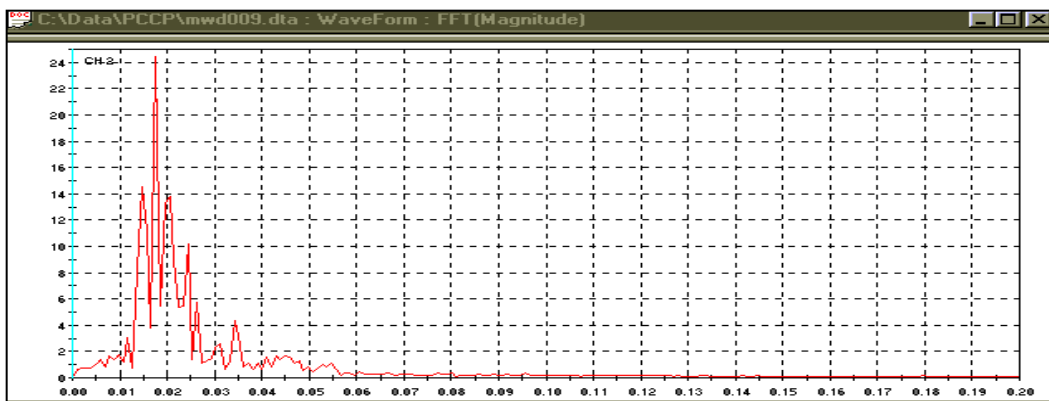
PolyModal (2) is a waveform toolbox software, which combines classical wave-mode analysis and digital signal processing methods with AE applications and test data. By using the Frequency Envelop Feature, up to 8 AE frequency based envelop features can be analyzed. Basically it breaks the spectrum down into (up to) 8 segments, where the area under the curve in each segment (partial power) is reported as a percentage of total area.



**PLB Performed at 10 O'clock Position from inside of the Good Pipe.**

**AE Sensor Located at 2 O'clock Position from inside of the Good Pipe.**

*Fig. 1 - AE spectrum (above) obtained from a good prestressed concrete pipe (bottom).*



**PLB Performed at 10 O'clock Position from inside of the**

**Stress Wire Damage Located at 12 O'clock outside of the Pipe.**

**AE Sensor Located at 2 O'clock Position from inside of the Damaged Pipe.**

*Fig. 2 - AE spectrum (above) obtained from a damaged prestressed concrete pipe (bottom).*

Table 1 is the partial energy presentation of the data from good pipe and from damaged pipe. The total frequency range is selected as 0 to 80 kHz, and each segment spans 10 kHz.

### Selection of Frequency Ranges for Partial Power Setup

It can be observed that four critical segments, namely, 0-10 kHz, 10-20 kHz, 30-40 kHz, and 40-50 kHz can be used to differentiate good pipe from damaged pipe by comparing partial powers. However, when more than one segment is used the differentiation can be enhanced. Table 1 shows that partial power segments 0-10 kHz, 10-20 kHz, 30-40 kHz, and 40-50 kHz give very good differentiation between PLB signals traveling through a good area and damaged area of concrete pipe. For example, in the 0-10 kHz segment, the signals of the damaged pipe ranged within 13% to 18% of the total energy while those of the good pipe ranged within 5 % to 10% of the total energy. In lower frequency ranges (0-10 kHz and 10-20 kHz segments) the signals show lower fractional energy in good pipe and higher fractional energy in damaged pipe. On the other hand, in higher frequency ranges (30-40 kHz and 40-50 kHz segments) the signals show higher partial power in good pipe and lower partial power in damaged pipe. The Mistras 2001 system (3) used for real-time monitoring can take up to 4 frequency segments for partial power (fractional energy) calculation, so the four frequency segments: 0-10 kHz, 10-20 kHz, 30-40, kHz, and 40-50 kHz were selected. It has also been determined that since the 0.5-mm lead carries more power and gives better differentiation than the standard 0.3 mm, the 0.5 mm pencil lead will be used.

Table 1

Table Showing the Differentiation between Damaged Pipe and Good Pipe Using the Partial Power Approach.

Signals were generated with the 0.5 mm PLB procedure from position 1 (10 o'clock) and received at position 5 (2 o'clock), and later from 5 to 1. R3I sensor was used.

	Part1	Part2	Part3	Part4	Part5	Part6	Part7	Part8	Total
Partial Power (kHz)	0-10	10-20	20-30	30-40	40-50	50-60	60-70	70-80	
	(%)	(%)	(%)	(%)	(%)	(%)	(%)	(%)	(%)
Transverse Damaged 1-5	14,55	22,13	17,23	13,16	13,81	8,67	4,98	5,48	100
	17,96	20,77	18,51	13,64	15,05	7,53	2,72	3,82	100
	18,28	21,77	16,56	12,89	13,44	9,08	4,38	3,60	100
Transverse Damaged 5-1	13,92	19,49	16,48	12,86	13,69	9,43	7,62	6,51	100
	13,66	21,47	17,98	12,63	13,50	9,52	5,58	5,65	100
	14,63	20,40	15,72	13,61	13,67	8,88	6,11	6,98	100
Transverse Good 1-5	8,10	19,57	17,74	16,08	14,84	9,34	7,28	7,06	100
	9,91	17,83	17,02	15,27	16,86	9,45	7,71	5,94	100
	8,02	17,58	17,49	15,71	16,61	9,78	7,96	6,85	100
Transverse Good 5-1	6,94	16,83	21,39	15,82	16,33	10,70	6,59	5,40	100
	5,91	17,21	22,91	16,74	17,40	11,03	4,74	4,08	100
	5,89	19,70	20,95	17,39	17,50	8,47	5,34	4,76	100

### EXPERIMENTAL PROCEDURE FOR NEW DATA

A field trip to the Metropolitan Water District, La Verne, CA was made in October 1999 to verify and demonstrate the instrument. It was the first time that a real-time partial power function was set up and activated to evaluate PCCP. The test configuration is shown in Fig. 3. Here, only signals generated at position 1 and received by sensor 2, and those generated at position 5 and received by sensor 1, are

discussed. The experimental procedure basically repeated what was performed as discussed earlier in this report. However, in addition to testing the real-time partial power function, two kinds of damage, namely, broken wire and delamination, were studied separately to see if the AE signals demonstrate a good classification on these two damage types.

The real-time partial power calculation was activated for the field experiment. This system function automatically calculates the partial powers in up to four preset frequency segments. By comparing the partial-power percentages of each segment, the condition of the pipe can be determined. With an appropriate adjustment of the partial-power settings, a classification of the damage type, e.g. broken wire or delamination, is achievable.

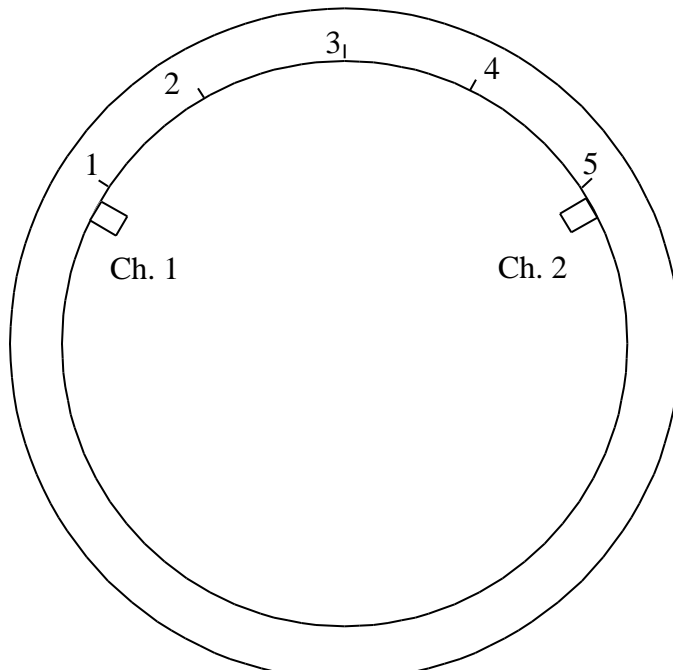


*Fig. 3 - Illustration showing the cross section of a PCCP conduit with the 2 sensor locations (Ch 1 and Ch 2) and the 5 signal source locations. In the current study, only data from PLB signals generated at Locations 1 and 5 are described.*

## RESULTS

Table 2 presents the results from the real-time partial power calculation of the PLB signals traveling in good pipe, pipe with broken wire damage, and pipe with delamination damage. It can be seen that the partial power in segment 3 (Part3: 30-40 kHz) and in segment 4 (Part4: 40-50 kHz) can differentiate between the good pipe and damaged pipe (either broken wire or delamination). Segment 3 (Part3: 30-40 kHz) can differentiate between delamination and broken wire but needs further adjustment (see below). Since this is the first time that the real-time partial power calculation was applied, the results shown in Table 2 can be considered promising.

## ADJUSTING THE PARTIAL POWER FUNCTION

The following steps describe how we adjust the system for the best PCCP evaluation and monitoring results. The adjustment should be carried out when monitoring different conditions, e.g. pipe material, pipe dimensions, buried pipe or underwater pipe.

1. Obtain the pipe diameter to calculate the distance between the PLB source and the receiving sensor.
2. Find the right threshold so the system can be triggered by a PLB signal even if it has traveled through badly damaged area. The threshold is set as low as possible to be sensitive, but it cannot be crossed by background noise. The procedure of finding the right threshold is through experimental trials.
3. Set the sampling rate and hit length to determine the time period of a waveform section being recorded and processed. For a 2-MHz sampling rate the time period being recorded and processed is 500  $\mu$ s. This should be determined if overlapping is acceptable or not.
4. Different sensors will respond in a different dominant frequency range, and the partial power frequency range must be adjusted accordingly.
5. In the Mistras system up to 4 frequency segments can be set up for partial power calculation. A standard procedure for identifying the best frequency bands is currently under development. With the PAC 30 kHz sensors, the total dominant frequency range can be set at 0 to 80 kHz. The 4 frequency segments are set at 0-20, 20-40, 40-60, and 60-80 kHz ranges for a general evaluation. After a first round trial there will be two segments giving good differentiation between the good and damaged conduit, e.g. 20-40 and 40-60 kHz ranges as was found here. The 4 frequency segments are then adjusted to 20-30, 30-40, 40-50, and 50-60 kHz ranges for a second trial. After identifying the damaged pipe, it may still be desirable to know what type of damage has occurred. Different damage types may show up more clearly in different frequency bands.
6. After the partial power parameters are determined, the graphic alarm is used to serve as an automatic warning system. The graphic alarm has a general threshold setting, and the user needs to enter a threshold. Whenever a signal generates partial power beyond the level (above or below), the alarm will be triggered.

## **CONCLUSION**

Partial power application for pipe damage evaluation and monitoring is a simple pattern recognition system. The four frequency segments can allow fast calculation and real-time classification. The partial power calculation in the Mistras 2001 can support up to four segments of frequency ranges. It has shown promise for differentiating between good and damaged pipes as well as different kinds of damage. For an in-situ real-time monitoring application, more than four segments might be required.

## **REFERENCES**

- (1) Friesel, Mark A., Shen, H. W., and Mostert, F., 1999, "Feasibility Study of Monitoring Prestressed Concrete Cylinder Pipe Using AE Techniques," Final Report, Physical Acoustics Corporation, Princeton Junction, NJ.
- (2) PolyModal Wave Toolbox: User's Manual, 1997, Physical Acoustics Corporation, Princeton Junction, NJ.
- (3) Mistras 2001 : User's Manual, 1997, Physical Acoustics Corporation, Princeton Junction, NJ.

**Table 2**  
**Data Showing the PLB (0.5 mm) Results Analyzed by the Real-Time Mistras Partial Power Method.**  
**R3I Sensor was Used for the Test.**

Partial Power (kHz)	Part1 0-10 (%)	Part2 10-20 (%)	Part3 30-40 (%)	Part4 40-50 (%)	Total of Part1 to Part4 (%)
Transverse Good 1-5	0	59	9	5	73
	0	59	8	5	72
	0	55	10	5	70
Transverse Good 5-1	0	53	8	3	64
	0	57	8	3	68
	0	53	9	3	65
	0	64	5	3	72
Transverse 1-5 Broken Wire	0	5	22	56	83
	0	6	22	57	85
	0	1	18	63	82
	0	6	24	54	84
	0	5	25	54	84
Transverse 5-1 Broken Wire	0	26	20	21	67
	0	25	22	19	66
	0	26	20	19	65
	0	25	22	19	66
	0	25	22	18	65
Transverse 1-5 Delamination	1	27	21	34	83
	4	24	18	37	83
	1	23	19	39	82
	0	17	14	42	73
	1	22	18	39	80
Transverse 5-1 Delamination	0	17	22	6	45
	0	24	10	12	46
	0	20	11	10	41
	0	24	12	8	44
	0	18	27	5	50

# **Meeting Calendar**

## **44th Meeting of AEWG**

June or July, 2001; Montreal, Canada: Program Chair: Robert Hay  
(BobHay@tisec.com)

Expect announcement shortly

## **E-GLEA II**

10-14 September, 2001; Laboratorio Ondas Elástica, Ensayos No Destructivos y Estructurales, COMISION NACIONAL DE ENERGIA ATOMICA, Buenos Aires, Argentina: see for detail at <http://www.cnea.gov.ar/cac/endye/glea.htm>

Proceedings of GLEA-I is available. See the web site.

## **25th EWGAE Meeting (EWGAE 2002)**

The second week September, 2002; Prague, Czech Republic: Program Chair: P. Mazal (mazal@cms.fme.vutbr.cz)

## **15th International AE Symposium (IAES-15)**

Date not fixed, but in 2002 at Tokushima, Japan; Symposium to be Organized by K. Yoshida (yoshida@me.tokushima-u.ac.jp)

# **COMPARISON OF ARTIFICIAL ACOUSTIC EMISSION SOURCES AS CALIBRATION SOURCES FOR TOOL WEAR MONITORING IN SINGLE-POINT MACHINING**

**A. PRATEEPASEN, Y. H. J. AU and B. E. JONES**  
**Brunel University, Uxbridge, Middlesex, UK**

## **ABSTRACT**

*Two artificial acoustic emission (AE) sources, an air jet and a pulsed laser, were evaluated in reference to their suitability as a calibration source for single-point machining and tool wear monitoring. The air jet source was found to have a more similar rms AE-spectrum to that obtained from machining than the pulsed laser source. The rms value of the AE signal (AE<sub>rms</sub>) produced by the air jet source was observed to be linearly proportional to the air pressure applied and sensitive to the torque used to tighten the insert onto the tool holder. When the applied torque was greater than 1.2 Nm, the AE<sub>rms</sub> remained constant. Thus, once the tightening torque is above this threshold, the AE<sub>rms</sub> value obtained from a sensor can be converted into an air pressure value. In this way, providing a set-up is calibrated using the air jet source under a defined condition, results obtained from different set-ups, having been identically calibrated, can be compared, thus facilitating a transfer and sharing of knowledge.*

## **INTRODUCTION**

Research into the use of acoustic emission (AE) for tool wear monitoring [1-10] has established that there exists a definite relation between AE and tool wear. Attempts were made to model the AE process in machining, but despite the fact that general trends could be predicted satisfactorily, the absolute values of AE produced in apparently identical machining processes could still differ markedly from one set-up to another.

The root cause of the problem is that the components that make up the AE transmission and measurement system as well as the interfaces between the components are highly variable. For single-point machining, typically, the components comprise an insert, a tool-holder and a sensor whereas the interfaces refer to those that occur between the tool insert and the tool-holder; and between the tool-holder and the sensor. Changes in either the components or the interfaces can produce a very different AE response. A striking example is the coupling between the insert and the tool-holder where, as will be reported in this paper, an increase in the clamping torque on the insert results in a significant drop in the root-mean-square value of the AE signal (AE<sub>rms</sub>). Consequently, AE results obtained from different research centres are not easy to compare making knowledge transfer at best difficult, if not impossible.

To achieve transferability of results and hence knowledge, some form of AE calibration is necessary. The process of calibration involves a measurement procedure carried out under specified conditions. Its objective is to establish the relationship between the value of a quantity as indicated by a measuring instrument and the corresponding value from a reference standard. When the result of the measurement can be ultimately related to a stated reference, such as a national or international standard, through an unbroken chain of comparisons all having stated uncertainties, then the measurement is said to be traceable to the standard.

It is important to note that the calibration of a sensor, as is conventionally done, in order to determine the AE at the sensing element of the sensor is not of much practical value. This is because one is often only interested in the character of AE at its source, for example, at the cutting edge in machining. What is immensely more useful is the calibration of the whole AE system with the location of the AE source known and the point of the sensor attachment decided. Understandably, once the layout of the source and sensor is changed, the system has to be calibrated again.

In this paper, two artificial AE sources, an air jet source and a pulsed laser source, were studied to assess their suitability as an AE calibration source for the single-point machining process. The effects on the AE were investigated of the clamping torque applied to the tool insert and a calibration procedure was suggested.

## ARTIFICIAL AE SOURCES

Based on the wave shapes, artificial AE sources can be classified into three different categories [11] as:

1. Noise – produced from, for example, helium gas jet impact, fracture of silicon carbide particles, stress corrosion cracking and phase transformation in AU-47.5% Cd;
2. Continuous waves - generated by exciting piezoelectric, electro-magnetic and electro-static devices;
3. Impulses – arising from sparks, breakage of glass capillary, breakage of pencil lead, dropping of a steel ball on a hard surface to produce an impact, point-contact resistive heating and laser pulse heating.

Berlinsky [12] used two artificial sources, a dropping ball and a pulsed laser, in the study of martensitic transformation in Fe-30Ni. McBride [13] used a helium gas jet to calibrate the AE system for measuring crack propagation in the vicinity of a notch. Evans [14] tested the diffuse field theory with a conical piezoelectric AE transmitter and sensor.

The American Society for Testing and Materials (ASTM) issued a standard guide E976-94 for determining the reproducibility and checking for degradation of AE sensors [15]. It recommended three artificial AE sources: an electrically driven ultrasonic sensor, a gas jet and an impulsive source produced by breaking pencil lead. The standard guideline E1106-86 [16] used a step point-force by breaking a glass capillary against a very large steel block.

To qualify as an AE calibration source in tool wear monitoring, the source should possess similar characteristics to the AE sources produced in machining, in addition to the also important characteristic of reproducibility. Here, similarity suggests that the comparing sources have rms AE-spectra that closely resemble each other in appearance.

The pulsed laser has been frequently used as an artificial AE source in the past two decades [17-20] for a number of reasons. Firstly, the laser source is broad-band and highly reproducible because the pulse parameters can be clearly defined and tightly controlled. Secondly, the energy of a laser pulse is readily quantifiable once the electrical parameters that drive the laser are known. Thirdly, laser can be delivered to remote locations via optical fibres. However, a pulsed laser is not without its drawbacks: it is expensive, requires stringent safety consideration and produces low power, hence weak AE, when, by necessity, operated within the thermo-elastic range so as not to cause damage to the impinged surface.

In many respects, an air jet source is similar to the helium jet source. The advantages of the air jet source are that it is non-contact, inexpensive, relatively safe, portable and readily available in a machine shop. The disadvantage is that the behaviour of an air jet in respect of the AE produced is affected by a host of environmental factors such as temperature and humidity.

## SIMILARITY COEFFICIENT

An n-point rms discrete AE-spectrum can be thought of as a vector  $\mathbf{u}$  defining a point in the n-dimensional vector space. By analogy with vectors in the three-dimensional space, the length squared of  $\mathbf{u}$  is the inner product of  $\mathbf{u}$  with itself. Thus, the length of  $\mathbf{u}$  can be computed from

$$|\mathbf{u}| = \sqrt{\mathbf{u} \cdot \mathbf{u}} = \sqrt{\sum_{k=1}^n u_k^2}. \quad (1)$$

This length is the same as the AErms of the signal from which the n-point discrete spectrum is derived. The vector  $\mathbf{u}$  can be normalised by dividing its elements by the length of the vector. A normalised vector, denoted by  $\bar{\mathbf{u}}$ , has a unit length.

Given two normalised vectors,  $\bar{\mathbf{u}}$  and  $\bar{\mathbf{v}}$ , in the n-dimensional space, the included angle  $\theta$  between them is related to the inner product of  $\bar{\mathbf{u}}$  and  $\bar{\mathbf{v}}$  as

$$\cos \theta = \bar{\mathbf{u}} \cdot \bar{\mathbf{v}}. \quad (2)$$

If the two vectors are identical, then  $\cos \theta = 1$ , whereas if they are orthogonal to each other, meaning that the projection of one vector on the other is zero, then  $\cos \theta = 0$ . Since the value of  $\cos \theta$  suggests the degree of similarity between the two vectors, it is named the *similarity coefficient*.

## AE COMPARISON OF AIR JET, LASER AND MACHINING

Three sets of tests were conducted to compare the shapes of the rms AE-spectra obtained from single-point machining, the air jet and the pulsed laser. The repeatability of rms AE-spectra from the air jet and pulsed laser sources was also assessed.

### Machining tests

Machining tests were performed with the cutting process variables changing as follows:

- Surface cutting speeds from 80 to 150 m/min;
- Feed rates from 0.1 to 0.4 mm/rev; and
- Depths of cut from 0.3 to 1.0 mm.

The work-piece was made from EN24T (0.35-0.45 % carbon) and measured 63.5-mm diameter by 150 mm length. Tool inserts of type GC 4035 DCMT 11 T3 04 UF and a tool shank of type SDJCL 1616H 11 (Sandvik Coromant) were used. Details of the insert geometry are: cutting edge length 11mm, insert thickness 3.97mm, insert shape 55°, rake angle 0°, clearance angle 7° and nose radius 0.4 mm.

A broad band AE sensor (125 kHz – 2 MHz) was mounted at the end of the tool holder with silicone rubber compound. A Hewlett Packard HP 89410A Vector Signal Analyser was used to produce a 401-line rms AE-spectrum with frequency from 0 to 1 MHz averaged over 70 consecutive spectra.

### Air Jet Tests

As shown in the block diagram of Fig. 1, air from an air supply passed through an air filter, a precision regulator, a precision pressure gauge, an on/off valve and a nozzle sequentially, emerging as an air jet. The air jet was directed normally at the top rake surface of the insert, 3 mm from the nose tip and equally distant from the leading and trailing edges of the insert. The insert was clamped to the tool-holder with a clamping torque of 2 Nm and the tool holder was, in turn, held in a fixture.

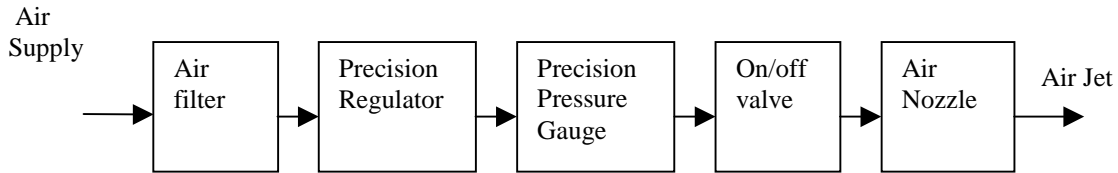


*Fig. 1. Block diagram of the air jet equipment.*

Both the stand-off distance from, and the location of the point of impact on, the rake face were controlled by micrometers. The measuring instruments and their settings were the same as those for the machining tests. Two resolutions of the frequency spectrum were used, namely 401 and 3201 lines. The schematic diagram of the AE signal propagation path is shown in Fig. 2.

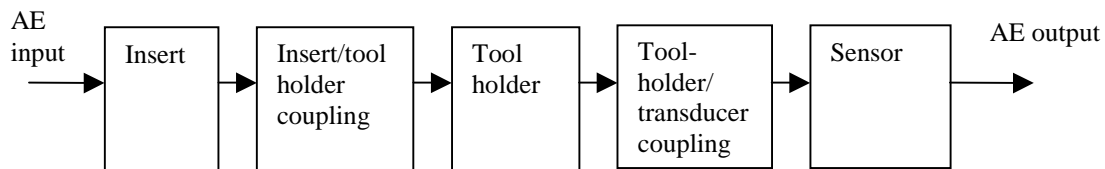


*Fig. 2. Schematic diagram showing the signal propagation path of AE in tool wear monitoring.*

The tests were performed with two different sizes of nozzle diameters: 1.0 mm and 1.4 mm. The stand-off distance was varied from 2 to 16 mm, in increments of 2 mm. The air jet pressure was varied between 1 and 5 bars, in increments of 1 bar.

### Pulsed Laser Test

A pulsed Nd:YAG laser system was used as the laser source. The energy of the laser was such chosen that it was insufficient to cause damage to the insert. The energy level of the laser was measured with a laser power meter, which registered a value of 3 mJ when the tip of the optical fibre was 2 mm away from the measuring matt black surface. The procedure and the set up of the measuring system were the same as those for the air jet tests excepting the spectrum resolution, which was 3201 lines.

### SIMILARITY OF ARTIFICIAL AND MACHINING AE SOURCES

All rms AE-spectra from the machining tests have similar appearance with the average spectrum as shown in Fig. 3.

Figures 4 and 5 show the typical AE time signals of the air jet and the pulsed laser. The air jet waveform is continuous whereas the pulsed laser is of burst type. Figures 6 and 7 show the RMS AE-spectra for the two different artificial sources. It is evident that both the air jet and pulsed laser sources produced sufficient frequency bandwidth, 100 kHz –500 kHz, for tool wear monitoring purposes but the energy level of the pulsed-laser source is much lower.

Using the machining RMS AE-spectrum as the reference, its extent of similarity compared to the air-jet source and the pulsed-laser source, expressed in terms of the similarity coefficients as defined in Equation (2), are 0.8653 and 0.5604 respectively. This result is to be expected as is apparent from the rms AE-spectra of Figs. 3, 6 and 7.

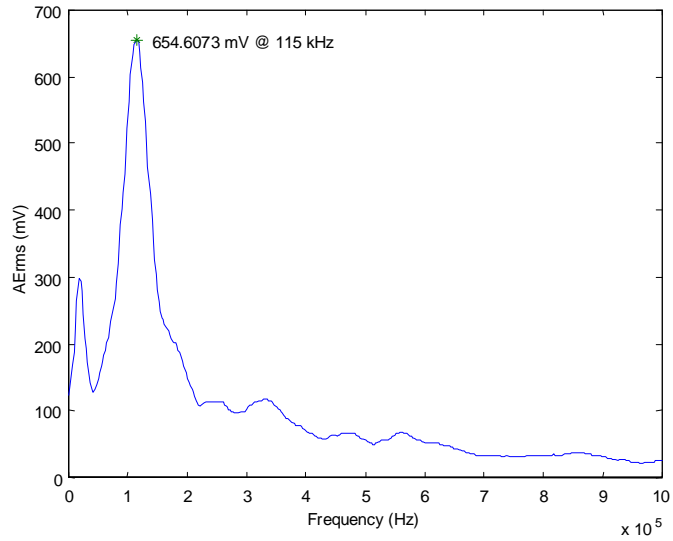


*Fig. 3. RMS AE-spectrum from machining EN24T with a GC 4035 insert.*

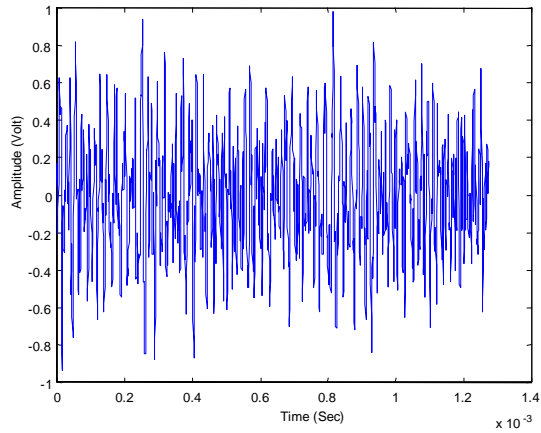


*Fig. 4. Time domain of the air jet.*

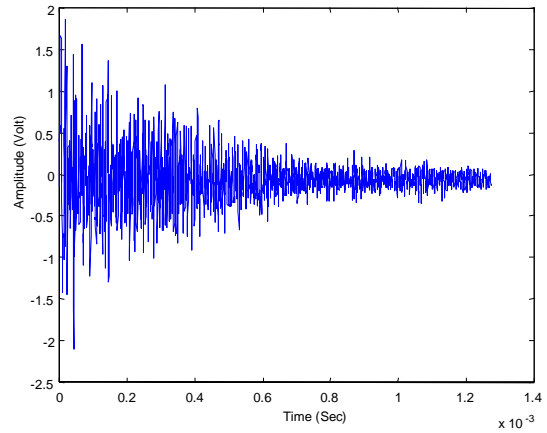


*Fig. 5. Time domain of the laser.*

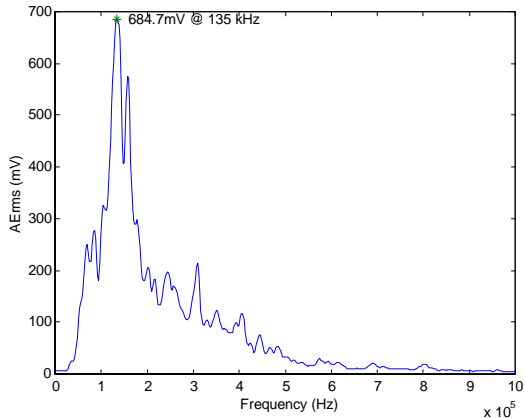


*Fig. 6. Power spectrum of the air jet.*

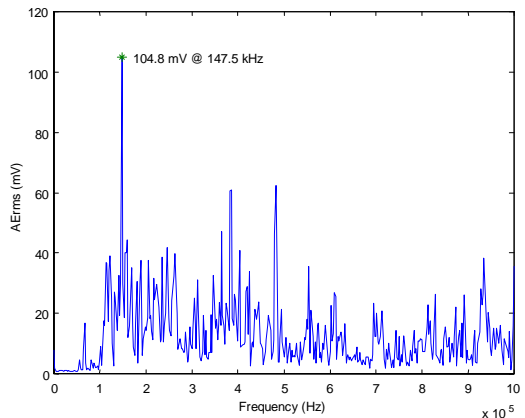


*Fig. 7. Power spectrum of the laser pulsed.*

## AE AND AIR-JET PRESSURE AT DIFFERENT STAND-OFF DISTANCES

Using Equation (1), the AE<sub>rms</sub> value of the AE signal was calculated. For the air jet tests, the relationship was established between the AE<sub>rms</sub> and the air-jet pressure at a stand-off distance from 2 to 16 mm, with bore diameters at the nozzle of 1 mm and 1.4 mm. The shapes of the rms AE-spectra at the two bore diameters were similar but the peak magnitude was higher for the bore diameter of 1.4 mm. On the other hand, the 1-mm diameter nozzle produced spectra that had lower variability. Using the 1-mm diameter nozzle, the relation between AE<sub>rms</sub> and the air-jet pressure for different stand-off distances is as shown in Fig. 8. The variability of the AE<sub>rms</sub>, defined as the  $\pm 1$  standard deviation divided by the mean, was  $\pm 2.62\%$ .

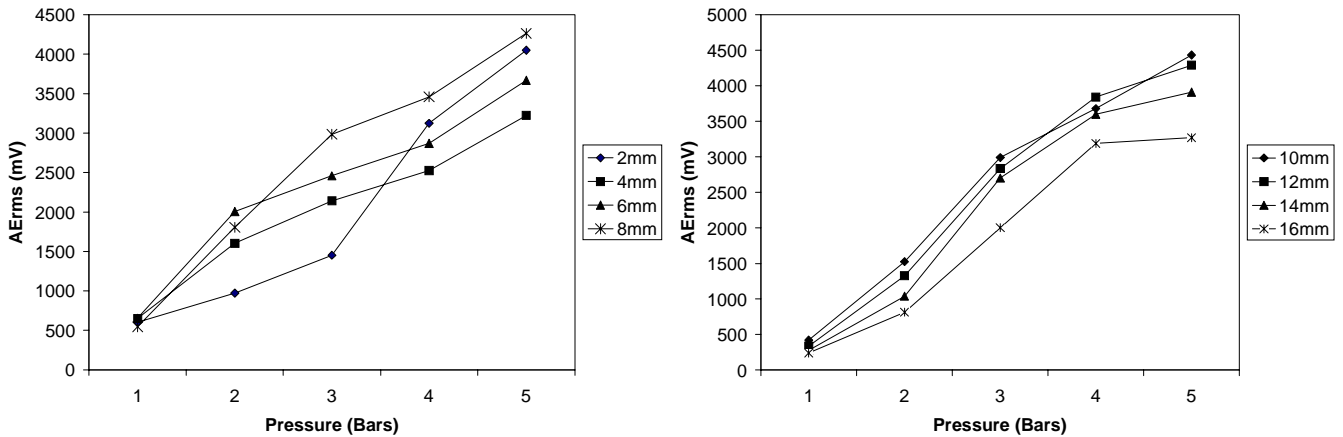


Fig. 8. AE<sub>rms</sub> of the air-jet at pressure, 1-5bars, at stand-off distances (a) 2-8 mm, and (b) 10-16mm.

The condition at the stand-off distance of 2 mm and pressure of 2 bars was chosen to show the variability of the measurements. These were the lowest values amongst the set of stand-off distances and pressures tested.

Peak amplitude on the rms AE-spectrum with 401-point resolution	$= \pm 5.05\%$
Peak amplitude on the rms AE-spectrum with 3201-point resolution	$= \pm 5.84\%$
AE <sub>rms</sub> from the rms AE-spectrum with 401-point resolution	$= \pm 1.14\%$
AE <sub>rms</sub> from the rms AE-spectrum with 3201-point resolution	$= \pm 1.27\%$

For the pulsed laser tests, the variability of the measurements at the stand-off distance of 2mm and laser energy of 3 mJ are:

Peak amplitude on the rms AE-spectrum with 3201-point resolution	$= \pm 2.02\%$
AE <sub>rms</sub> from the rms AE-spectrum with 3201-point resolution	$= \pm 1.92\%$

It is observed from these results that both artificial sources have similar variability.

## AE, AIR JET PRESSURE AND INSERT CLAMPING TORQUE

Air jet tests were conducted to study the effects of different sensor location and of different insert clamping torque on the AE<sub>rms</sub>. Similar to the air-jet tests in Section 4.2, the air jet was positioned vertically above the top rake face of the insert 2 mm inwards from both the leading and trailing edges of the insert, at a stand-off distance of 5 mm. Three pairs of AE sensors were mounted with the first of each pair on the tool holder and the second on the tool post, all held in position using a silicone rubber compound. These were all PAC sensors and the pairs were: WD and WD with response bandwidth of 100 kHz-1 MHz, UT1000 and UT1000 with response bandwidth of 60 kHz-1 MHz, R30 (100-400 kHz)

and R15 (50-200kHz). The outputs of these sensors were amplified by 60dB and band-pass filtered from 20 kHz to 1MHz. The Hewlett Packard HP89410A Vector Signal Analyser was used to produce an RMS AE-spectrum with 401-point resolution averaged over 70 successive spectra. The insert was tightened to three levels of torque, namely 0.4 Nm, 1.2 Nm and 2.0 Nm. The air-jet pressure was varied between 3 and 8 bars in 1-bar increments.

Results showed that the AE<sub>rms</sub> were linearly proportional to the air-jet pressure applied for all levels of clamping torque. It was also observed that the AE<sub>rms</sub> was the highest at the torque value of 0.4 Nm, therefore suggesting that the AE<sub>rms</sub> was sensitive to the torque applied. The graph for the clamping torque of 2.0 Nm is as shown in Fig. 9.

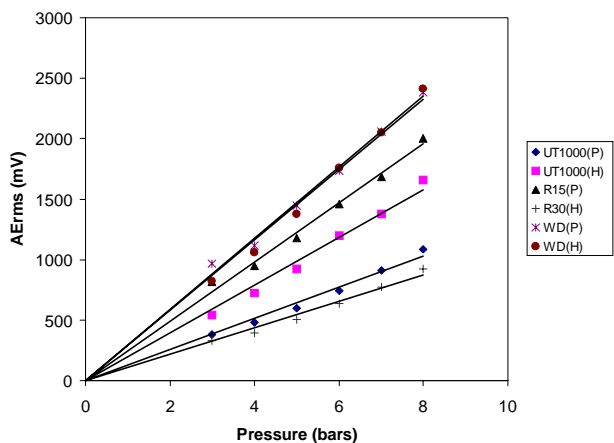


Fig. 9. AE<sub>rms</sub> related to air jet pressure for different sensors.

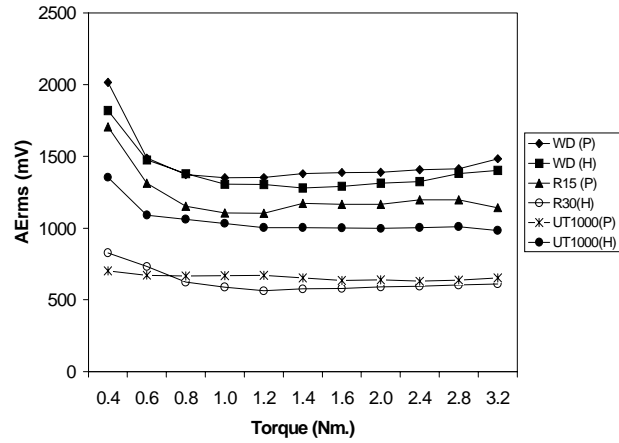


Fig. 10. AE<sub>rms</sub> related to clamping torque at constant pressure of 5

To study the relation between clamping torque and AE<sub>rms</sub>, the air-jet pressure was fixed at 5 bars whilst the clamping torque was changed from 0.4 Nm to 3.2 Nm using an adjustable torque wrench. The results, as in Fig. 10, show that the AE<sub>rms</sub> decreases as the torque increases from 0.4 to 1.2 Nm and then remains constant from 1.2 Nm to 3.2 Nm. The ratios of AE<sub>rms</sub> between the different pairs of sensors, one on the tool holder and the other on the tool post, were calculated for each value of clamping torque and they are as shown in the table below:

Sensor pair	Mean of ratios	Standard Deviation of ratios	Variability (%)
WD/WD	1.049	0.031	2.984
UT1000/UT1000	0.630	0.038	6.093
R30/R15	2.223	0.076	3.411

## CONCLUSION

Compared to the pulsed laser, the air jet is more suitable as an artificial calibration source for measuring systems used for machining study and tool wear monitoring. This is because the air jet source has an RMS AE-spectrum more similar to that observed in machining than the pulsed laser, is relative safe to use, is less expensive and is more readily available in a workshop.

For a fixed stand-off distance, the AE<sub>rms</sub> of the air-jet increases linearly with the air-jet pressure. The clamping torque applied to the insert can affect the AE<sub>rms</sub> if the torque value is low; but when the clamping torque exceeds 1.2 Nm, the AE<sub>rms</sub> remains constant. A safe clamping torque for the tool holder used in this research is around 2 Nm beyond which there is the risk of damaging the hexagonal head of the tightening screw.

In summary, a calibration procedure may be suggested as follows. With the insert clamping torque above 1.2 Nm, the AE<sub>rms</sub> value obtained from a sensor can be converted into an air pressure value using the calibration graphs such as Figures 8 and 9. In this way, providing a set-up is calibrated using the air jet source under a prescribed condition, results obtained from different set-ups that have been calibrated in the same manner can be compared.

## ACKNOWLEDGEMENTS

The authors wish to acknowledge support from the INTERSECT Faraday Partnership, the Engineering and Physical Sciences Research Council and the Royal Thai Government.

## REFERENCES

- (1) E.N. Diei and D.A. Dornfeld, "A model of tool fracture generated acoustic emission during machining", *Trans. ASME, Journal of Engineering for Industry*, 109 (3) (1989) 229-237.
- (2) E. Kannatey-Asibu, Jr. and D.A. Dornfeld, "Quantitative relationships for acoustic emission from orthogonal metal cutting", *Trans. ASME, Journal of Engineering for Industry*, 103 (3) 1981 330-340.
- (3) L. Dan and J. Mathew, "Tool wear and failure monitoring techniques for turning-a review", *1st J.Mach. Tools Manufact.*, 30 (4) (1990) 579-598.
- (4) R. Teti and D.A. Dornfeld, "Modelling and experimental analysis of acoustic emission from metal cutting", *Trans. ASME, Journal of Engineering for Industry*, 111(3) (1989) 229-237.
- (5) M.S. Lan and D.A. Dornfeld, "In-process tool fracture detection", *Journal of Engineering Materials and Technology*, 106 (2) (1984) 111-118.
- (6) T. Blum and I. Inasaki, "A study of acoustic emission from the orthogonal cutting process", *Trans. ASME, J. Engineering for industry*, 112 (1990) 203-211.
- (7) A.E. Diniz, J.J. Liu and D.A. Dornfeld, "Correlating tool life, tool wear and surface roughness by monitoring acoustic emission in finish turning", *Wear*, 152 (1992) 395-407.
- (8) J.J. Liu and D.A. Dornfeld, "Modelling and analysis of acoustic emission in diamond turning", *Journal of Manufacturing Science and Engineering*, 118 (1996) 199-206.
- (9) T.A. Carolan, S.R. Kidd, D.P. Hand, S.J. Wilcox, P. Wilkinson, J.S. Barton, J.D.C. Jones and R.L. Reuben, "Acoustic emission monitoring of tool wear during the face milling of steels and aluminium alloys using a fibre optic sensor", Part 1: energy analysis, *Proc Instn Mech Engrs*, 211(1997) 299-309.
- (10) K. Iwata and T. Moriwaki, "An application of acoustic emission measurement to in-process sensing of tool wear", *C.I.R.P. Annals*, 26 (1977) 21-26.
- (11) N.N. Hsu and F.R. Breckenridge, "Characterisation and calibration of acoustic emission sensors", *Materials Evaluation*, 39 (1981) 60-68.
- (12) Y. Berlinsky, M. Rosen, J. Simmons and H.N.G. Wadley, "A calibration approach to acoustic emission energy measurement", *Journal of Nondestructive Evaluation*, 10 (1) (1991).
- (13) S.L. McBride and T.S. Hutchison, "Helium gas jet spectral calibration of acoustic emission transducers and system" *Canadian journal of Physics*, 56 (1978) 504-507.
- (14) M. J. Evans, "The use of diffuse field measurements for acoustic emission", PhD. Thesis, Imperial College of Science, Technology and Medicine, 1997, 196 P.
- (15) The American Society for Testing and Materials (ASTM): Standard guide for determining the reproducibility of acoustic emission sensor response, E976-94, (1994) 374-379.
- (16) ASTM: Standard method for primary calibration of acoustic emission sensors, E1106-86 (reapproved 1992), 485-494.
- (17) Y. Berlinsky, M. Rosen, J. Simmons and H.N.G. Wadley, "A calibration approach to acoustic emission energy measurement", *Journal of Nondestructive Evaluation*, 10(1) (1991) 1-5.

- (18) A.M. Aindow, R.J. Dewhurst, D. A. Hutchins and S.B. Palmer, "Laser-generated ultrasonic pulses at free metal surfaces", *J. Acoust.Soc.Am.* 69 (2) (1981) 449-455.
- (19) C.B. Scruby, R.J. Dewhurst, D.A. Hutchins and S.B. Palmer, "Qualitative studies of thermally generated elastic waves in laser-irradiated metals", *J. Appl. Phys.*, 51(12) (1980) 6210-6216.
- (20) S. N. Hopko and I. C Ume, "Laser generated ultrasound by material ablation using fiber optic delivery", *Ultrasonics*, 37 (1999) 1-7.

# **DEVELOPMENT OF AN EQUIPMENT TO MONITORING AND CONTROL THE QUALITY OF RESISTANCE WELDING**

**J. CATTY**

**Technical Center for the Mechanical Engineering Industries (CETIM), Senlis Cedex, FRANCE**

## **ABSTRACT**

The resistance-welding process is widely used due to high productivity and economy. It is utilized strongly in the manufacturing of automotive components and structures. The automotive sector is particularly demanding in terms of quality standards, productivity levels and automation of production lines. The process of electrical resistance welding, however, suffers from persistent problems of inconsistent weld quality caused by variations in material composition, thickness and type of coatings, electrode wear and electrical supply fluctuation. There is a need to develop robust and reliable monitoring approaches either to predict or detect when the weld quality is beginning to decrease and/or defective welds have been produced. The need is to have a relatively low cost system that will accurately "verifies" the state of weld quality, assuring weld quality in real time.

The aim of the present project is to develop a low cost and robust prototype able to monitor and control the quality of resistance spot welding in industrial environment. Previous results have shown that the technique of acoustic emission (AE) is potentially very interesting, but in some industrial cases it gave less pertinent results. So, if the AE alone does not allow a reliable diagnosis in all configurations of welding, a multi-parameter approach seems to be a promising way. Based on these considerations, the prototype developed in the present project integrates two different technologies based on the monitoring of the electrical resistance welding parameters and AE control. Some results are presented in this paper.

Craft Project was funded by The European Community and includes as partners,

Incompol (PT), David Valente Almeida (PT), Gametal (PT), TECNA (IT), SOLRES (SP), MSC Technik (DE), Fleetguard (FR), EMT74 (FR), VPTech (FR), UTEC (PT), ISQ (PT), CETIM (FR).

## **INTRODUCTION – From the industrial approach to a new concept**

One of the basic requirements of a resistance-welding quality standard is that a peel or chisel test must be conducted at a frequency agreed with the customer. The resistance-weld quality control is usually carried out by conventional inspection techniques, destructive (metallographic and mechanical testing) and/or non destructive (ultrasonic or X-ray). Meanwhile, the welding conditions are based on tolerance parameters resulting from empirical/experimental results, some of which can be monitored. This common industrial approach, similar in the different end-users around Europe, fails to assure quality products and even leads to defective products. This situation has important implications on the productivity and cost effectiveness requirements for manufacturers.

The expected project outcome represents an important strategic advantage to both end-users and equipment manufacturers through:

- increase in the European industrial competitiveness through its capability to supply quality assured products,
- important savings in raw materials due to significant reductions in the number of destructive tests for quality control
- important contribution in the direction of the development of "intelligent welding machines".

## **FIELD OF THE STUDY – The coated steels, the main part of the market**

When the world of resistance welding is analyzed in terms of volume, it appears that the area of automotive industry and subcontractors is by far the greatest user of this process. In this area, most of the used materials are steels and coated steels. Aluminum alloys represent actually a small part of the market, but seems a promising field of development. The tests performed in this project are mainly based on coated steels (e.g., galvanized steels). Nevertheless, the concept of the monitoring system is able to be adapted to other welded materials.

## **METHODOLOGY**

The initial concept of the system is to take advantage of the combination of two types of measures (acoustic emission and electrical parameters). In order to achieve this goal, the methodology needs to determine:

- The best measurement parameters (type of sensors, filtering and acquisition),
- The most pertinent parameters, extracted and calculated from the signals from all the sensors.

The methodology adopted started with the development of a pre-prototype to be used in the spot-welding tests, flexible enough to support changes of sensors or pretreatment. Then, for each material and thickness, the experimental plan was the following:

- Welding with more than 35 different conditions of forces and currents. For each combination of current and force, obtain 5 shear-stress measures and 3 nugget diameter and 4 more for backup. (The welds must be obtained with electrodes in a good condition);
- For a selected ideal current and force, welds must be done from initial conditions (“good electrodes”) to deteriorated conditions in order to study the influence of electrode deterioration in spot weld quality and measured parameters.

The spot welds produced were evaluated in terms of spot diameter, penetration depth and mechanical strength, besides visual inspection.

Finally, a relationship between the recorded real-time parameters and the quality parameters (diameter, mechanical strength and explosion phenomenon) was searched to define a quality algorithm to be used in the prototype software.

## **TYPICAL RESULT ON STEEL**

### **Experimental conditions**

#### *Welding machines*

The spot-welding tests used for the data processing have been performed in laboratory environment, with TECNA Machines. These machines, a welding press and a welding gun, are representative of the most commonly used machines in the automotive industry (the welding gun for robots) and the subcontractors of this industry.

#### *The Prototype*

The prototype developed in the frame of the project (see photo 1) is based on a Compact-PCI industrial Computer (PXI system from National Instruments) equipped with an acquisition board. A specific interface board was developed, that ensures the following functions: Adaptation of the signals; Power supply of sensors if needed; Pre-treatment.

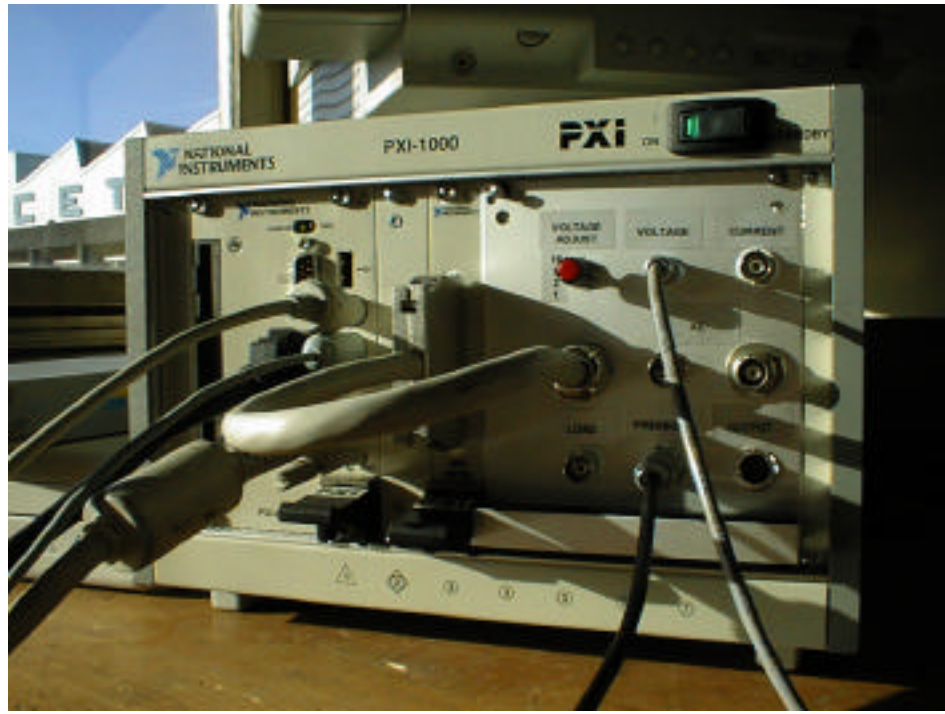


*Photo 1: Preprototype.*

The sensors specified in the definition of the prototype have been installed on the welding machine:

- Current Sensor: a toroid coil.
- Voltage Sensor: clamps fixed as closed as possible to the weld.
- Acoustic Sensor: a specific sensor developed for this application. It needs to be insensitive to the electromagnetic interference from the machine.
- Pressure or Force Sensor: a specific sensor was used for this application that enables us to measure the real force applied to the parts.

## Steps in the Data Processing

The aim of the data processing is to extract all the pertinent information from the real-time parameters, calculated from the signals coming from the sensors. In order to reach this goal, the data processing is divided into three steps:

- Step 1: Correlation between the parameters: In order to minimize the number of parameters used in the algorithm, we evaluate the correlation between all the parameters. When the correlation between two parameters is near unity, it means that the two parameters bring exactly the same information. Then, we can suppress one of the two parameters.
- Step 2: The prediction of the quality of the weld is divided into two objectives:
  - Prediction of the diameter of the (weld) point.
  - Prediction of the mechanical strength.
- Step 3: Prediction of the expulsion phenomenon.

## Application on an Electro-Zinc Steel

### Correlation between the parameters

This step allows us to suppress some parameters. After this step, we obtain less than 10 informative parameters.

### **Prediction of the diameter of the point**

In order to find the relation between the real time parameters and the diameter or mechanical strength of the point, we used a multiple linear regression algorithm. The result of the multiple linear regression performed to find the diameter of the point is represented in Fig. 1. This is a correlation diagram: on the X-axis, we found the predicted value; on Y-axis, the real (measured) values. The algorithm gives a global good prediction. An ideal prediction should put all the points on the line. Some points are placed out of the confidence ellipse. The pertinent parameters (used in the prediction) are linked to the welding stage.

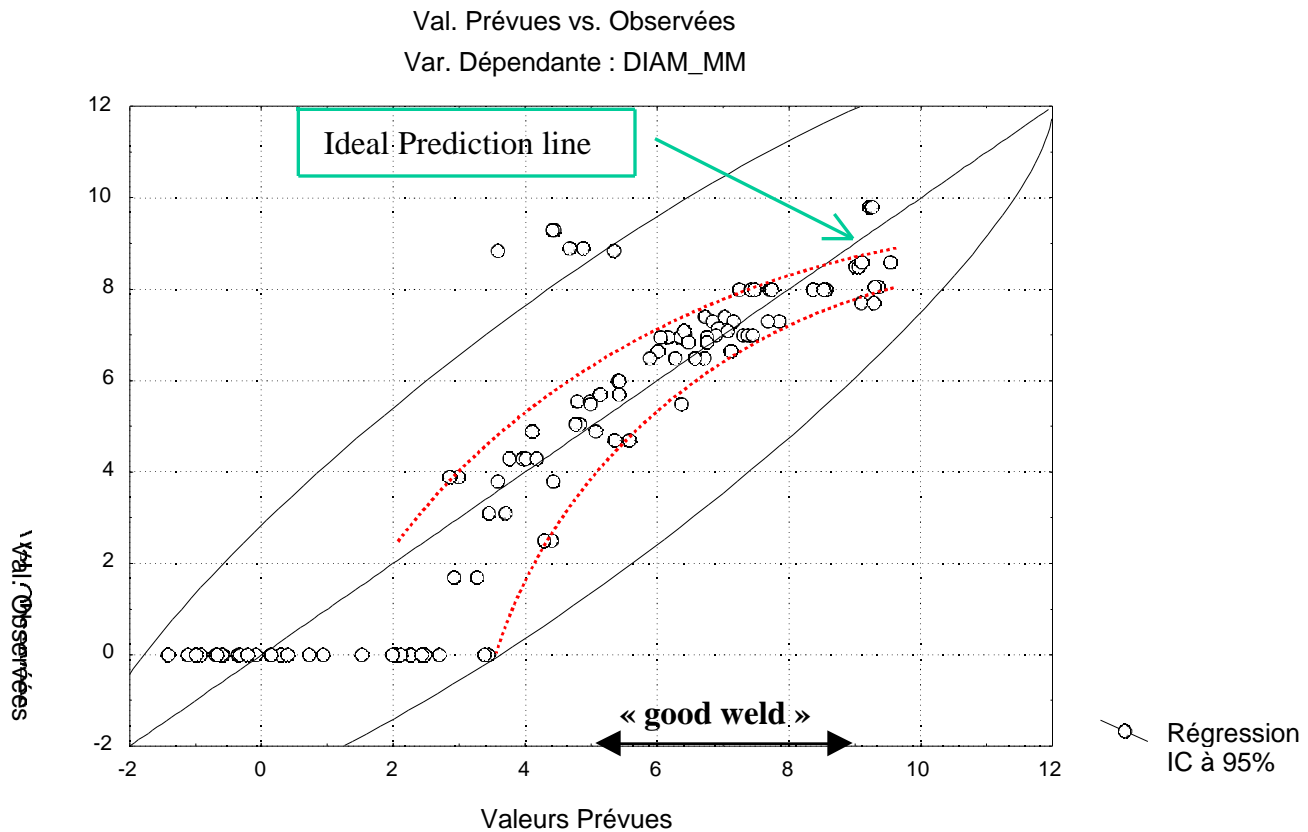


*Fig. 1: Result of the Multiple Linear Regression — Diameter of the Point.*

### **Prediction of the Mechanical Strength of the Weld**

We use the same multiple linear regression algorithm to find the relation between the real time parameters and the mechanical strength of the weld. The result of the process is represented in Fig. 2. The pertinent parameters (used in the prediction) are also linked to the welding stage. The algorithm gives a better prediction for the mechanical strength than the prediction for the diameter of the point.

### **Interpretation**

- This behavior has been observed in most of the cases studied (with different type of materials and thickness). It should mean that the real-time parameters are more linked to the mechanical strength than to the diameter. Thereby, we can suppose that the information included in the parameters is linked to the physical phenomenon of welding.

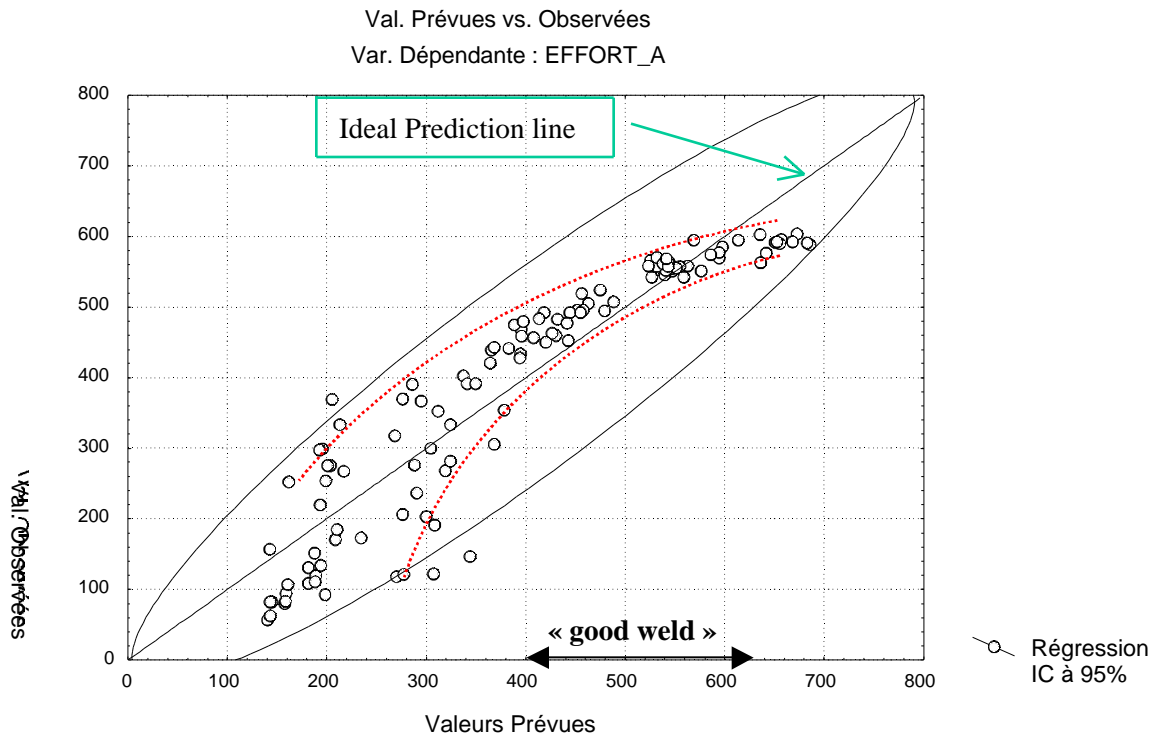


*Fig. 2: Result of the Multiple Linear Regression - Mechanical strength of the point.*

- We observe that the correlation seems to be non-linear, and more accurate for the points with high mechanical strength value. Although it seems hard to establish a direct relation between this remark and the process itself, we can assume that the resistance-welding process is often more reproducible in its «good working area» than for the «bad conditions». Then, the accuracy of the prediction is a criterion of good welding condition.

#### ***Prediction of the Expulsion phenomenon***

In order to control the quality of the resistance welding process, we need to detect the expulsion phenomenon. The system should give an answer – yes (expulsion) or no (no expulsion) -. The answer is only a binary value, 0 or 1. Then, the algorithm used is different from the one used to predict the diameter or mechanical strength. For this case, we use a discriminant analysis. This analysis is based on the same real time parameters than the previous analysis. The final result of the classification is given in Table 1.

*Table 1: Final result of the discriminant analysis*

Matrice de Classif. (incexp.sta)			
Lignes: classifications observ.			
Colonnes: classifications prévues			
	Total	G_1:0	G_2:1
	Correct	p=.53924	p=.46076
G_1:0	96.24	205	8
G_2:1	96.70	6	176
%	96.46	211	184

The global rate of good classification is high (96 %). It means that 96 % of the welds without expulsion are well classified (6 % of welds without expulsion are declared with expulsion). Moreover, 97 % of the welds with expulsion are well classified (3 % of welds with expulsion are declared without expulsion). The high rate of good classification is very promising, and industrially available.

## **CONSEQUENCE ON THE DEVELOPMENT OF THE PROTOTYPE**

From the tests performed on different type of materials, we observe that the results are very promising, but we note some differences, in term of quality of prediction and also in term of type of pertinent parameters used in the prediction.

From a general point of view, the quality of the prediction is better for the strength of the point than the diameter of the point. We can clearly observe that the relation is more linear and the prediction more accurate for the mechanical strength parameter. It seems to be an important result that shows that the prediction is really linked to the welding phenomenon: we can easily acknowledge that the parameter «Mechanical Strength» is more representative of the weld nugget than the parameter «Diameter of the point».

We can make another remark concerning the prediction results: the prediction is always more accurate for the welds with a correct diameter or mechanical strength. We observe that the points are very close to each other at the top of the curve and very scattered at the bottom of the curve («bad points»). From a theoretical point of view, it seems natural: it is well-known that good conditions of process (welding) are always more reproducible than bad conditions of process.

Concerning the pertinent parameters that allow the prediction, for each configuration, the relation is different in term of parameter and coefficient. However, this study allows us to show that the pertinent parameters that control or characterize the resistance-welding process are:

- Electric parameters,
- Load parameter and
- Acoustic parameters.

The monitoring system needs to have the information from all these sensors.

All these results show that the mathematical analysis of the real-time parameters gives pertinent information. The result of the prediction (diameter, mechanical strength or expulsion) is even higher than a direct analysis based on only one parameter.

We need next to consider the industrial transposition of this type of classification: The final relation that predicts the diameter, mechanical strength or expulsion requires several preliminary tests, because of the statistical nature of the data treatment. Actually, we don't know if a universal relation exists, independent of the nature of the welding machine or type of sheet, or shape, or thickness, but we are still searching. Nevertheless, the results achieved in this study will be exploited in a first «industrial prototype» that will be tested in industrial environment by industrial partners.

## **ACKNOWLEDGEMENT**

This CRAFT project is funded by all the industrial partners and the European community.

# A Study of Small HSDI Diesel Engine Fuel Injection Equipment Faults using Acoustic Emission.

J.D. Gill\*, R.L. Reuben\*, J.A. Steel\*, M W Scaife<sup>†</sup> and J Asquith<sup>†</sup>

\*Dept. of Mechanical and Chemical Engineering, Heriot-Watt University, Edinburgh.  
<sup>†</sup> Perkins Engines Co. Ltd., Peterburgh

## SUMMARY

*Acoustic emission measurements have been carried out on a Perkins T1004-4 high-speed, direct injection diesel engine. This is a turbocharged four-cylinder engine of approximately 1 litre per cylinder. The AE sensor was attached to the injector body of cylinder four. By examining the raw AE signal acquired from this transducer during the injection and combustion period it has been possible to describe the effectiveness of fuel injection of diesel into the combustion chamber. These measurements have also demonstrated the possibility of application to other factors affecting the combustion process.*

## ABSTRACT

Cylinder pressure, needle lift pressure and high pressure injection line pressures (at both pump and injector) have been acquired over the complete operating range of a Perkins T1000-4 turbocharged, four-cylinder high speed direct injection (HSDI) diesel engine. The engine is fitted with Perkins high-swirl 'Fastram' piston crowns and Bosch KD fuel injectors operated by a Bosch EPVE rotary fuel pump.

The work comprises a detailed study into the effect injector discharge pressure has on the acoustic emission (AE) response of the injector body. Two different fault conditions have been examined; injector discharge pressure reduced from 258 bar to 165 bar in all cylinders and injector discharge pressure reduced to 100 bar in cylinder 4 (instrumented cylinder). These two faults have been compared with the acoustic emission obtained under normal running conditions.

A comparison was also made with similar studies using vibration measurement, and it was found that the use of AE is more reliable at higher engine speeds and loads. This is due to the fact that the acceleration signal from the injectors suffers from severe interference caused by high amplitude, low frequency vibrations from structural resonances within the engine, specifically at high engine speed and load.

## INTRODUCTION

Arguably the most influential component of the diesel engine is the fuel injection equipment (FIE); even minor faults can cause a major loss of efficiency and an increase in engine emissions and noise. The FIE requires the tightest of manufacturing tolerances and effective combustion is very dependent on the successful operation of each of the component parts. With increased sophistication (e.g. higher injection pressures, pulse injection and electronic control) being required to meet continuously improving noise, exhaust smoke and gaseous emissions regulations, the FIE is becoming even more susceptible to failure. This is mainly as a result of the ingress of particles into the system causing excessive wear and, for this reason, it is no surprise that injection systems have been shown to be the largest contributing factor to diesel engine failure [1]. Methods for successfully measuring the

effective operation of the FIE have invariably relied upon the use of intrusive transducers to measure a related quantity, such as fuel injection pressure or cylinder pressure [2]. Some work has been undertaken to examine the use of vibration monitoring of the injector body [3] with the aim of using its response to diagnose the injector condition.

The largest problem with FIE is that small faults can easily manifest themselves without the end user being able to attribute these directly to the injection system [4,5]. This can be because they are not immediately noticeable or because the fault is so small that it does not necessarily show itself immediately in terms of a significant loss of power or increase in emissions. This generally happens with long-term wear and can allow damage to occur to other fundamental parts of the engine.

Both the vibration, and the significantly higher frequency acoustic emission responses of the injector are likely to contain valuable information pertaining to the overall condition of the injection system.

## EXPERIMENTAL SET-UP

The test engine was a Perkins T1004-4 turbocharged, four cylinder high speed direct injection (HSDI) engine developing 135 bhp at 2500 RPM. The engine was mounted on a skid and attached to a Froude eddy-current dynamometer to control engine load and speed. The engine was fitted with a Bosch EPVE rotary fuel pump and KD fuel injectors and was fully instrumented with injector pressure, in-cylinder pressure and needle lift transducers on the cylinder being examined (cylinder four) as shown in Figure 1. These were complemented by an array of acoustic emission (AE) transducers and accelerometers. All of the above transducers were synchronized with the angular position of the engine using a one-pulse-per-degree shaft encoder. After acquisition, the signal was re-sampled with respect to the shaft encoder signal to remove any effects of fluctuations in engine speed during the cycle. The AE sensors used were a combination of Physical Acoustics types D9203 and R30I. The signals from the transducers were bandpass filtered between 0.1 and 1 MHz and the rms AE signals were averaged at 25  $\mu$ s and sampled using a Microstar DAP 3000a/212 data acquisition board. The raw signals were sampled at 5 MHz so that after re-sampling of the signal it was possible to obtain a minimum resolution of 2.5 MHz to prevent aliasing of the signal.

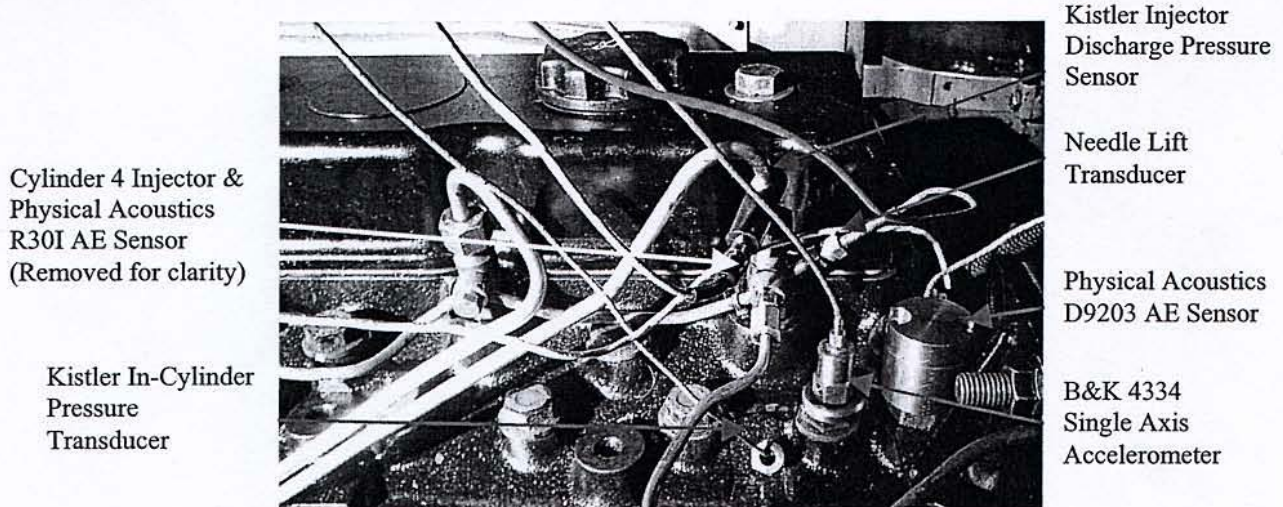


Figure 1: Perkins T1004 Cylinder Head Set-up

Raw and rms acoustic emission measurements were obtained simultaneously with all other measurements at engine speeds varying between idle and the full rated speed of 2500 RPM. Five different load settings were examined, calculated as a percentage of full load at that speed. These were

0%, 25%, 50%, 75% & 100% load. Three different injector discharge pressures were examined to simulate damaged injector springs.

## ACOUSTIC EMISSION MONITORING OF THE INJECTION PROCESS

Figure 2 shows a typical raw AE response from the injector body at 1500 RPM and 50% load for one full four stroke engine cycle re-sampled with respect to crankshaft position.

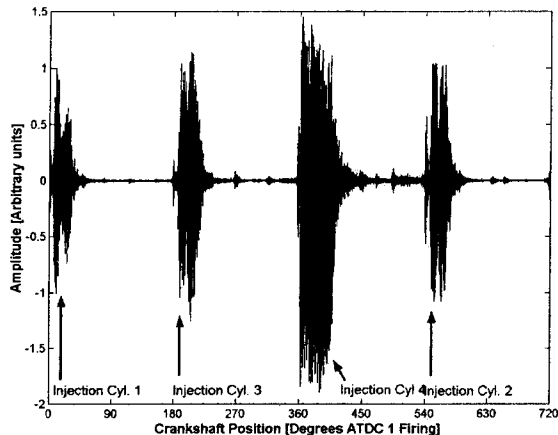


Figure 2  
Raw AE Re-sampled wrt Crankshaft Position at 2.5 MHz.  
AE Sensor Attached to Injector Body of Cylinder 4

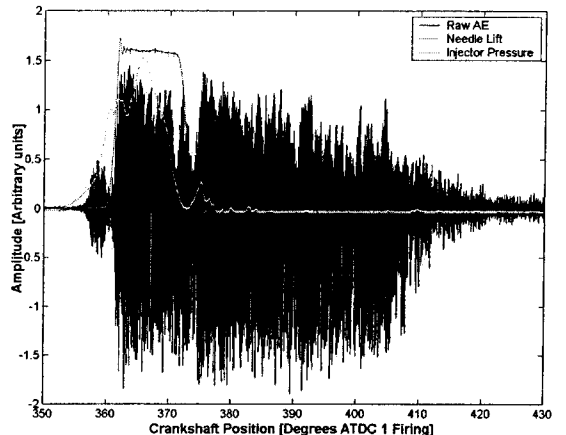


Figure 3  
Cylinder 4 Injection and Combustion Period - Raw AE,  
Injector Needle Lift and Injection Line Pressure

The injector discharge pressure was set at 165 bar, as opposed to the factory specification of 258 bar, but is otherwise in good condition. The AE signal can be seen to display four distinct bursts related to the injection and combustion period of each individual cylinder. The most significant burst is that due to the injection and combustion in cylinder four, the injector on which the AE transducer was situated.

If the signal obtained from the instrumented injector is examined in more detail, Figure 3, it can be seen that there is an increase in AE activity at approximately 356° after top dead centre (TDC) of the firing stroke of cylinder one. This is believed to be caused by the build-up of diesel pressure in the high-pressure pipe-work. This is in contrast to the vibration signal that does not appear to show any signs of the initial build-up of pressure immediately preceding the lifting of the injector needle.

## EXAMINATION OF FAULT CONDITION

Following examination of the normal operating condition, the injector discharge pressure in the instrumented cylinder (cylinder 4) was reduced to 100 bar to examine the effect this would have on the AE response. Figure 4 demonstrates the effect reducing injector discharge pressure has on the load speed curves for the engine. Much work has been carried out investigating, both mathematically and through visual examination, the effect injector pressure has on fuel-air mixing in the combustion chamber. It is agreed that, for an engine of this size, (1 litre/cylinder) impingement of the diesel spray with the wall occurs at between 8.5° to 11° after initial injection for an engine under full load. The majority of the air entrainment required for the mixture to reach the near stoichiometric condition occurs in the wall jet. Therefore, reducing the injector discharge pressure, as well as increasing droplet size, also increases the period before mixing of the fuel and air begins. The consequence of this is that

by the time the fuel is in a suitable state for ignition the peak cylinder pressure, and therefore temperature, has begun to fall.

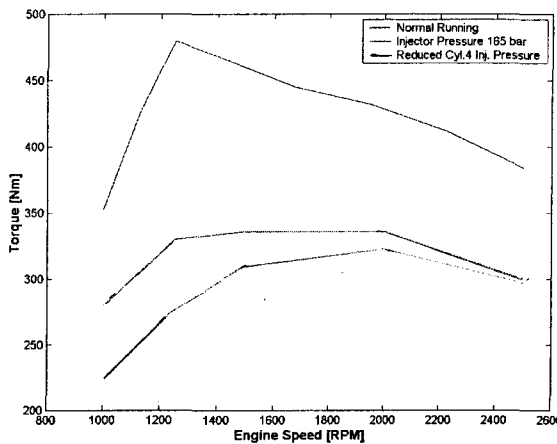


Figure 4: Load / Speed Curves for Perkins T1004-4 Diesel Engine

- Condition 1: Normal Running (Injector Discharge Pressure set at 258 bar)
- Condition 2: Injector Discharge Pressure Reduced to 165 bar in all Cylinders
- Condition 3: Injector Discharge Pressure Reduced to 100 bar in Cylinder 4

Figure 5 shows cylinder four injection and combustion period for normal running and for cylinder four injector discharge pressure reduced to 100 bar. The initial point of injection is earlier in the cycle for the reduced injector pressure and this is borne out in the AE response as the signal can be clearly seen to rise earlier than for the normal running condition.

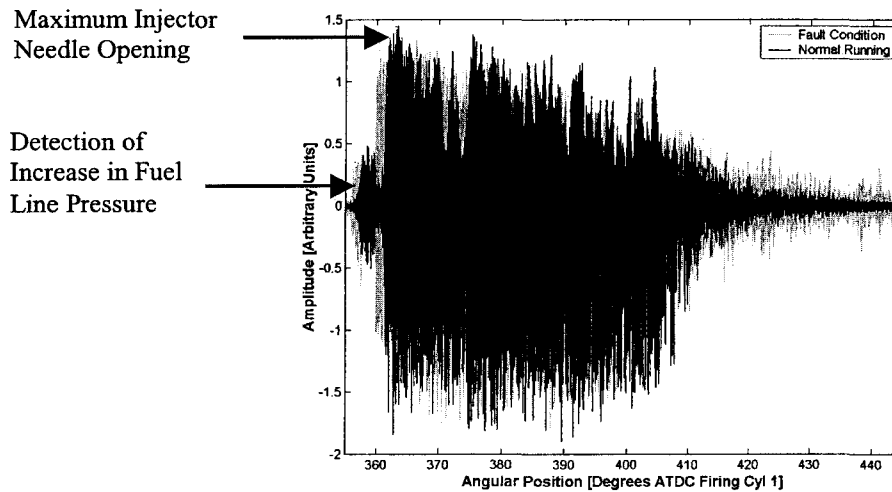


Figure 5: Raw AE from Cylinder 4 Injector Body showing Cylinder 4 Injection & Combustion Period

However, the lower amplitude AE response from the injector body associated with the combustion process is extended for the fault condition. It is believed that this is a result of the less efficient mixing of the fuel and air. This necessitates a longer period for the adequate entrainment of air with the larger fuel droplets causing more erratic burning of the fuel.

As the speed increases, the period between fuel injection and combustion increases in terms of crank angle as the fuel takes a certain time to mix and for ignition to commence. To compensate for this, the fuel pump control automatically advances the start of delivery. Figures 6 a-d show the point of detection of the increase in pressure in the fuel line and the point at which the injector needle becomes fully open for four different speed conditions across the range of loads. These were calculated by rms-processing of ten raw AE cycles for each condition with an averaging time of 40 $\mu$ s and then calculating the mean and standard deviation for each point. As can be seen, the point of fuel line pressure increase and the maximum opening of the injector nozzle needle detected by the AE transducer is advanced with reduced injector discharge pressure.

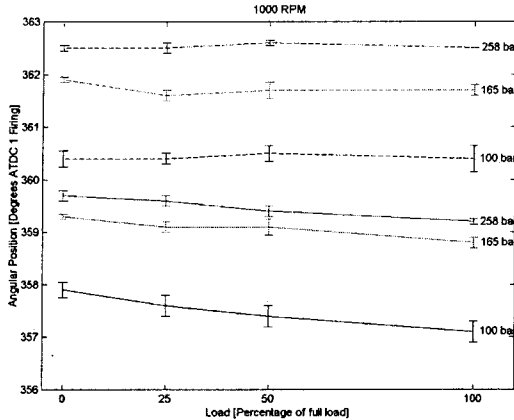


Figure 6a: AE Detection 1000 RPM

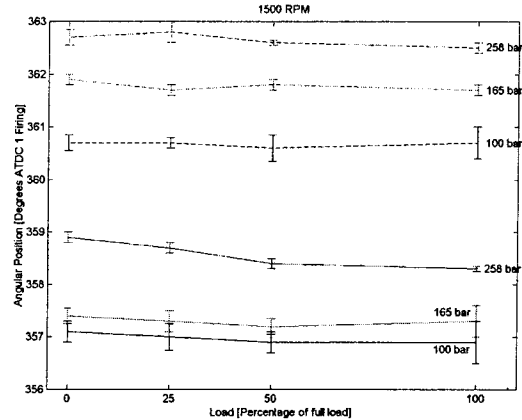


Figure 6b: AE Detection 1500 RPM

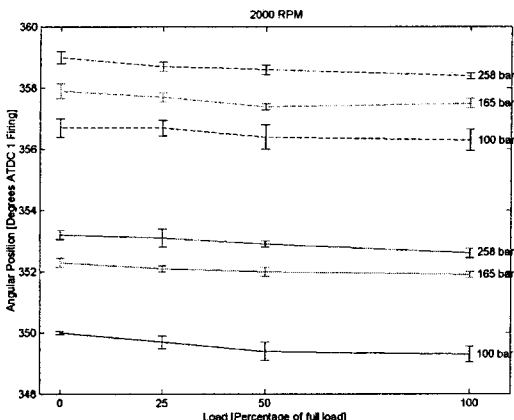


Figure 6c: AE Detection 2000 RPM

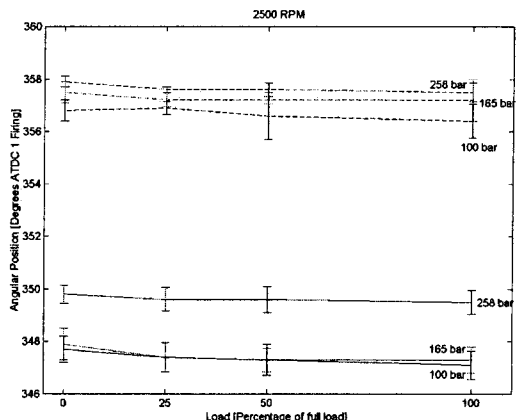


Figure 6d: AE Detection 2500 RPM

Detection of Increase in Fuel Line Pressure (solid line)  
Detection of Maximum Nozzle Needle Lift (dashed line)

## SUMMARY AND CONCLUSIONS

The effect of reducing injector discharge pressure on the AE recorded on the injector body has been quantified using measurements on a test bed engine. As has already been demonstrated by other authors, notably Gu and Ball [3], the injector vibration and stress waves in the injector body are caused by a combination of mechanical and fluid-mechanical events. These events consist of impacts caused by the needle opening and closing and also by the high-pressure diesel flow through the pipe-work and nozzle. A number of these events are more easily detected using acoustic emission, notably the build-up of pressure in the high pressure pipe immediately prior to the injection process commencing.

Examination of the point of detection of the increase in fuel pressure and opening of the injector nozzle using AE have been shown to be good descriptors of the injector discharge pressure. Using this measure it is possible to detect the nozzle opening pressure of the injector without the need for expensive and intrusive sensors. The advantage of acoustic emission measurement over vibration measurement in this type of application is the significantly higher frequency of signal detected. This overcomes problems associated with engine resonances and low frequency vibrations caused by the operating environment (e.g. mobile applications, such as vehicles).

## FUTHER WORK

Work is still being carried out into other fuel injector faults and the possibility of using a small array of acoustic emission sensors to detect a greater number of engine faults. Acoustic emission has so far been successfully applied to detect a variety of valve faults, gasket leakage and it has also been possible to reconstruct the cylinder pressure trace with an accuracy of  $\pm 5\%$ .

The largest problem to be overcome in terms of using acoustic emission to detect faults on small diesel engines is the complexity of the AE signal at high speeds and loads. As can be seen in Figure 1 the signal acquired by a sensor mounted on one cylinder does not just relate to that cylinder. To overcome this problem will require some form of filtering or another technique which is currently being examined. This technique uses the transfer function, calculated using a piezo-pulser as a source, of the individual machine to eliminate unwanted components of the signal.

## ACKNOWLEDGEMENTS

The authors gratefully acknowledge the funding provided by the EC under its BRITE-EURAM programme, Project number BE96 3491.

## REFERENCES

- [1] Roylance, B. J. and Zadeh, A. **The Development of Experimental Methods to Measure Film Deposit Formation on Diesel Engine Pistons**, *Experimental Methods in Engine Research and Development '91*, IMechE, London, 1991, pp. 67-74.
- [2] Shoji, T. **Effect of Cycle-to-Cycle Variations in Spray Characteristics on Hydrocarbon Emissions in a DI Diesel Engine**. *JSME: Series B*, 1997, **40**(2), 312-319.
- [3] Gu, F. and Ball, A.D. **Vibration Based Fault Diagnosis in Diesel Fuel Injection System**. *Diesel Fuel Injection Systems*. IMechE, London, 1995, pp. 89-98.
- [4] Lilly, L. C. R. **Diesel Engine Reference Book**, 1984, Butterworth & Co. Ltd.
- [5] Zahdeh, A. R. Henein, N. A. and Bryzik, W. **Diesel Engine Cold Starting: PC Based Comprehensive Heat Release Model: Part 1 - Single Cycle Analysis**. *ASME: Journal of Engineering for Gas Turbines and Power*, **113**, 464-473.

# **UNSUPERVISED PATTERN RECOGNITION OF ACOUSTIC EMISSION FROM FULL SCALE TESTING OF A WIND TURBINE BLADE**

**Dimitrios KOUROUSSIS, Athanassios ANASTASSOPOULOS,**

**Pantelis VIONIS\* and Vassilios KOLOVOS\***

**Envirocoustics S.A., Athens, Greece**

**\*Centre for Renewable Energy Sources, Pikermi, Greece**

## **ABSTRACT**

*In the present paper, acoustic emission (AE) data obtained during a static test of a 12-m FRP wind turbine blade was analyzed and classified into classes using various unsupervised pattern recognition (UPR) techniques. Class criticality was revealed by means of correlation of each class's activity with the applied load. Application of location techniques pinpointed the specific areas of activity of each class, on the blade. Using the UPR results, a supervised pattern recognition (SPR) method was trained, based on back propagation neural network, and applied to AE data obtained during a subsequent biaxial fatigue loading of the same blade. Similar classes appeared at the same regions of the blade, but were triggered at different phases of the loading cycle. The application of UPR on AE data proved to be a promising tool towards the characterization of damage evolution with monotonic or fatigue loading.*

## **INTRODUCTION**

Acoustic emission (AE) monitoring during full scale testing of FRP wind turbine (W/T) blades is a relatively new application. The difficulty in such tests arises mainly from the potentiality of different AE sources, such as delamination, matrix cracks, fiber breakage, etc., which, sometimes, occur concurrently and are expected due to the nature of FRP materials [1]. The separability of such material-failure mechanisms by means of UPR analysis of AE data has been demonstrated in the past [2,3]. However, the sophisticated structural design of modern W/T blades, containing reinforcement spars, internal cells and skin materials with different stacking sequences, introduces additional complexity in the understanding and characterization of the detected flaws. More specifically, particular sections of W/T blades (e.g. the internal spar ends) exhibit high AE activity, even at low load levels, due to local stress concentrations, but the corresponding mechanisms do not necessarily signify critical damage. Nevertheless, the same or another area of the blade might experience a different, more critical damage mechanism at higher loads, which has to be segregated and evaluated separately. Discrimination of the various damage mechanisms on FRP materials by means of conventional AE analysis imposes several restrictions and difficulties, as it is usually based on the location of the AE sources followed by tedious analysis of the characteristics of the located AE events. The analysis usually involves two-dimensional feature correlation (i.e. correlating two AE features at a time), as it is practically impossible to visualize the whole feature set. This approach does not always yield a reliable identification of the signatures of the various damage mechanisms. Even more so, it is not always possible to isolate a particular mechanism and monitor its activity in time, with increasing load, in order to assess its criticality.

The applicability of conventional AE analysis on full-scale testing of W/T blades was assessed by Sutherland et al. [4]. Further application of the AE technique proved to be successful in detecting and locating structural flaws on the blade, at very early stages and before they had become visible [5,6]. However, the necessity to discriminate and analyze the detected flaws by means of their AE features still exists and becomes even more apparent in the case of full-scale fatigue testing of a W/T blade [7]. The

purpose of this work is to separately investigate and compare the various classes of AE data, revealed by UPR techniques, which appear during static loading. Furthermore, application of neural networks for supervised classification of data obtained during fatigue loading of the same blade, offers a better insight into the nature of the existing flaws. Successful recognition of the different FRP damage mechanisms by means of their AE signatures could, ultimately, lead to the automation of the classification procedure for future W/T blade tests.

## EXPERIMENTAL SET-UP

For the present work, two different AE tests are considered. The first was a static test performed while the blade was previously unloaded. Conventional AE analysis has already been performed and has successfully pinpointed “weak” areas of the blade [5,6]. The second AE test refers to the monitoring of 23 cycles of biaxial fatigue loading at 0.1 Hz, which took place after the blade had undertaken several millions of fatigue cycles in the laboratory, and a visible crack had developed on the trailing edge of the blade between sensors 6 and 10 (see Fig. 1). All tests took place at the Centre for Renewable Energy Sources (CRES) Wind Turbine Blades Testing Laboratory. The blade was loaded on a single point by means of a hydraulic actuator (two in the case of fatigue testing), and AE data were recorded by a Physical Acoustics Corporation (PAC), ten-channel “SPARTAN 2000” AE system and the associated, PC-based data acquisition software. Ten 60 kHz resonant frequency PAC R6I AE sensors, equipped with a 40dB internal preamplifier, were mounted on the compression (suction) side of the blade. The sensor positioning and the corresponding AE channel numbers are presented in Fig. 1. During acquisition, basic AE signal features were recorded and stored in file by the AE system software (PAC-“SP2-LOC”), including channel number, hit arrival time, rise time, counts, energy, duration, amplitude, average frequency, average signal level and counts-to-peak. During the fatigue test, loads in both flap and edge directions were measured by the load cells between the blade and the actuators.

In the case of the static test, one hydraulic actuator was mounted underneath the blade and was exerting force perpendicular to the blade’s surface plane, so that the blade’s pressure side was under tension, as in real conditions. The load was applied at a flapwise position, 7 m from the blade’s root and at 25% chord station (Fig. 1), resulting in a triangular distribution of the bending moment along the blade’s axis, aiming to simulate the maximum operational load.

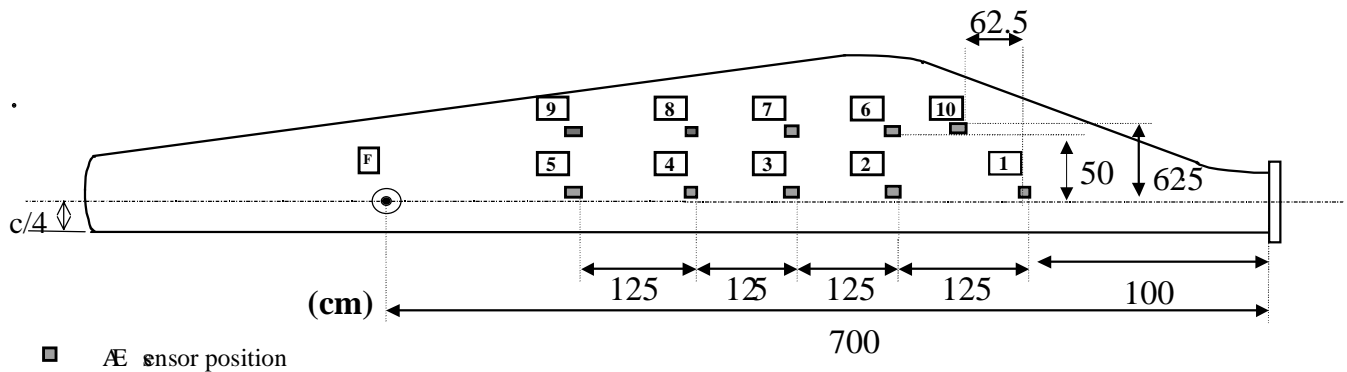


*Fig. 1: AE sensor position and channel numbers Load application point.*

In the fatigue test, two hydraulic actuators were used, at the same axial position as in the static test, one exerting force in the flapwise direction and the other in the edgewise direction. Both actuators were applying periodic force to the blade at the same frequency (0.1 Hz) and the resulting force had edgewise and flapwise components, with 90° phase shift, causing the blade to move elliptically.

## PATTERN RECOGNITION ANALYSIS

Unsupervised pattern recognition (UPR) was applied on the data of the first static test using the commercially available “NOESIS” pattern recognition and neural networks software for AE applications. A “first-hit” analysis was followed; i.e., only the first hit of each AE event was used. The first step before application of UPR was to select a representative set of AE features based on which the data would be segregated into classes, exhibiting similar characteristics. For that purpose, feature correlation analysis [8,9] was performed for all the available AE features.

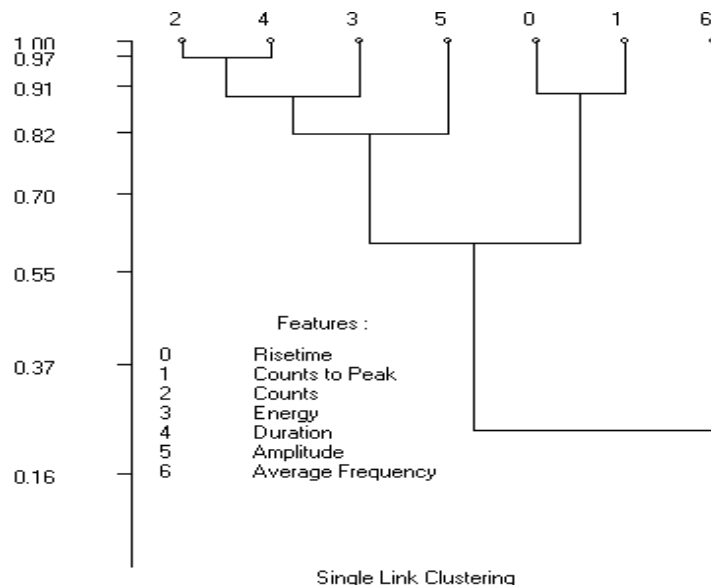


*Fig. 2: Feature Correlation Hierarchy.*

get indications for the data structure. Then, varying the number of the desired clusters, a parametric study was performed using the K-Means and LVQ-Neural Net algorithms, in order to assess the optimum number of classes by means of discrimination-efficiency heuristic criteria. Local minimization of the D&B  $R_{ij}$  criterion [9-11] occurred at seven classes for both the K-Means and the LVQ clustering algorithms. Therefore, the respective results were used to separate the data into seven classes.

For that purpose, feature correlation analysis [8,9] was performed for all the available AE features. The degree of correlation among features, presented in the dendrogram of Fig. 2, demonstrates very strong correlation for Counts and Duration. Subsequently, UPR was performed with a reduced set of AE features, comprising Rise Time, Counts to Peak, Energy, Duration, Amplitude and Average Frequency. Furthermore, all features were normalized individually to a range from 0 to 1, in order to avoid biasing the classification towards the feature exhibiting the highest physical dimensions.

Initially, UPR was performed using various clustering algorithms [8-10], to

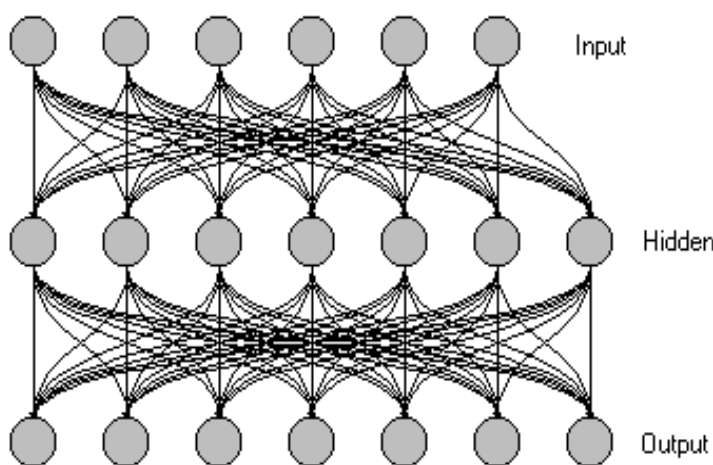


*Fig. 3: The BPNN classifier topology.*

Following the clustering performed by UPR on the static test data, a back-propagation neural network (BPNN) supervised classifier [8,11] was trained to correspond AE hits, from any given data set, to one of the seven classes (output layer) based upon the values of their AE features (input layer). Various trials were performed changing the number of hidden layers that connect the input and output layers and showed that one “hidden” layer (Fig. 3) was adequate. Success of training was assessed by applying this classifier on a subset of the static test data. The supervised classification yielded only 1% of misclassified hits in comparison to the desired UPR classification.

## FIRST STATIC LOADING

Figure 4 presents the cumulative AE energy vs. time for classes 4 and 6 with the loading envelope superimposed. It is observed that these classes exhibit similar activity trends. Comparing Fig. 4 with Fig. 5, which presents the cumulative AE energy vs. time for classes 1, 3, 5, it becomes evident that classes 4, 6 and are the only classes with continuous activity throughout the load holds. At the same time, although classes 3 and 5 exhibit high total AE energy, they totally cease at the end of the last load hold. Class 1 presents a burst of AE activity in the last load-hold (also observed in class 3) and then ceases. Classes 0 and 2 are generally very low in AE energy and inactive during load holds.

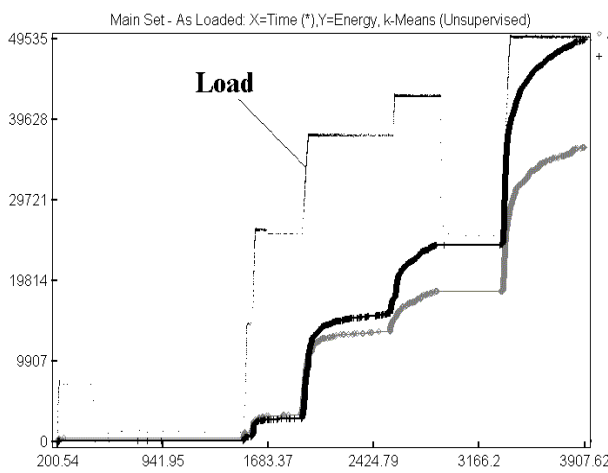


*Fig. 4: Cumulative AE Energy vs. Time  
(Classes 4, 6).*

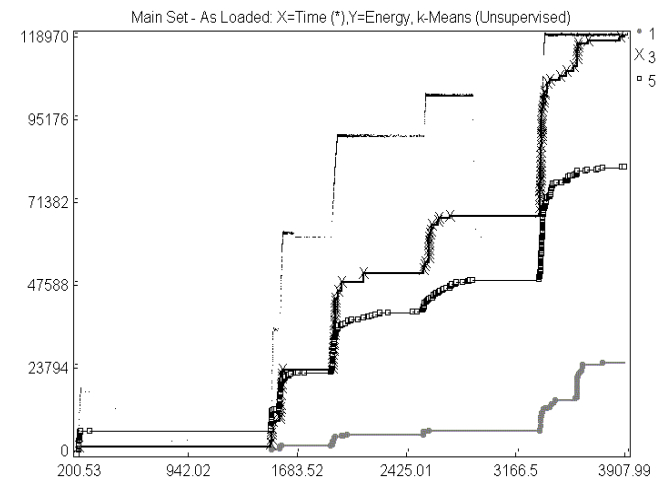


*Fig. 5: Cumulative AE Energy vs. Time  
(Classes 1, 3, 5).*

Feature correlation can be visualized in Figs. 6 and 7, which are scatter plots of Amplitude vs. Counts (in log scale) for classes 4, 6 and 1, 3, respectively. In these two-dimensional correlation plots, the overlapping between classes is strong in the low and medium Counts-Amplitude region where classes 4, and 6 coexist (Fig. 6). In the high-medium region, classes 1, 3 are better separated (Fig. 7).

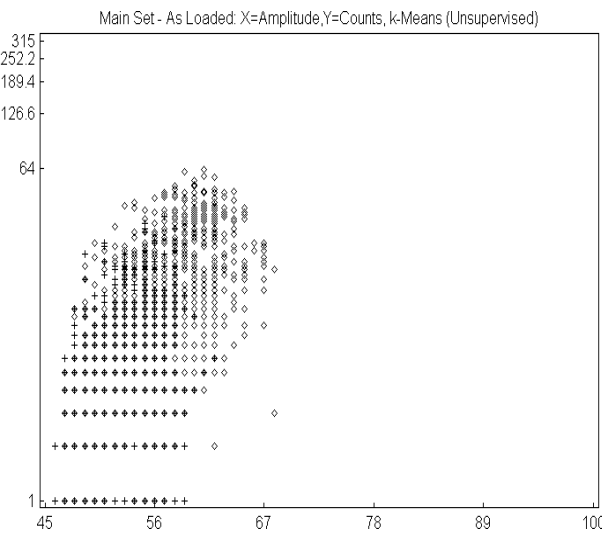


*Fig. 6: Amplitude vs. Counts (Classes 4, 6).*

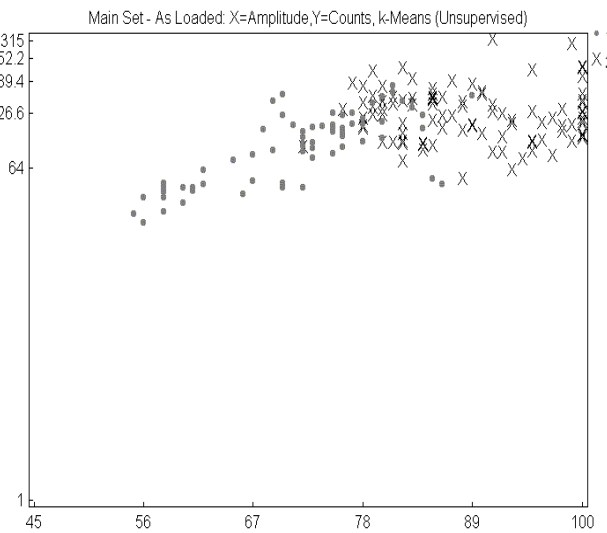


*Fig. 7: Amplitude vs. Counts (Classes 1, 3).*

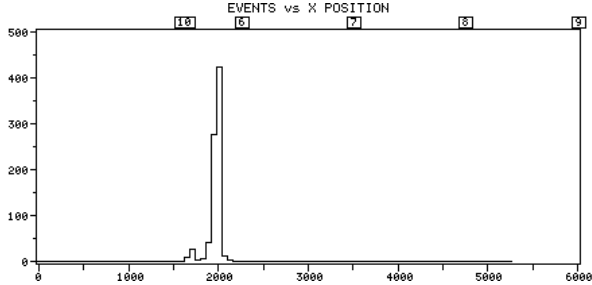


Fig. 8: Location of classes 4 and 6.

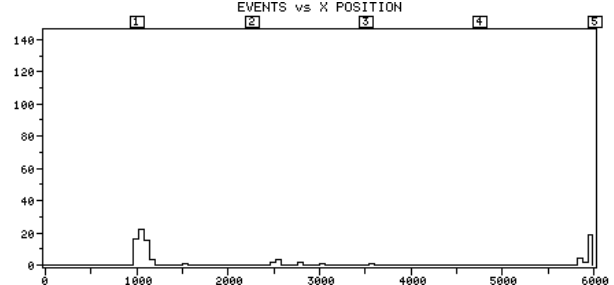


Fig. 9: Location of classes 1 and 3.

Aiming to correlate the different classes of data with particular areas of the blade, the linear location technique was applied separately for each class. For that purpose, the original data acquisition set of the test was used, which contained all-hits information. By means of specialized PAC software, this set was split into seven subsets, one for each class, each subset containing all-hits information only for its corresponding class. Two linear location groups were defined, one with sensors 1-5 and one with sensors 6-10 (see Fig. 1). Upon application of linear location, it was observed that: (a) Classes 4 and 6 were located mainly in the area between sensors 6 and 10 (see Fig. 8), (b) Classes 1 and 3 were located primarily very close to sensor 1 (see Fig. 9), (c) Class 5 was located right on sensor 5, which means that it might have been triggered anywhere from sensor 5 towards the load application point, and (d) Classes 0 and 2 gave very few locations.

## FATIGUE LOADING

Supervised classification was performed on the fatigue loading first-hit data. To gain a thorough insight as to whether particular classes appear at specific parts of or throughout the loading cycle, Figs. 10 and 11 present two scatter plots of the flapwise load vs. edgewise load. The shape of these plots is a good representation of the ellipsoidal movement of the blade at the load application point. For the plot of Fig. 10, data classes 4 and 6 were used, while Fig. 11 uses only classes 1 and 3 to generate the plot. Strong dependence of class activity with load is apparent only for classes 1 and 3. On the contrary, classes 4 and 6 appear more or less throughout the loading cycle.

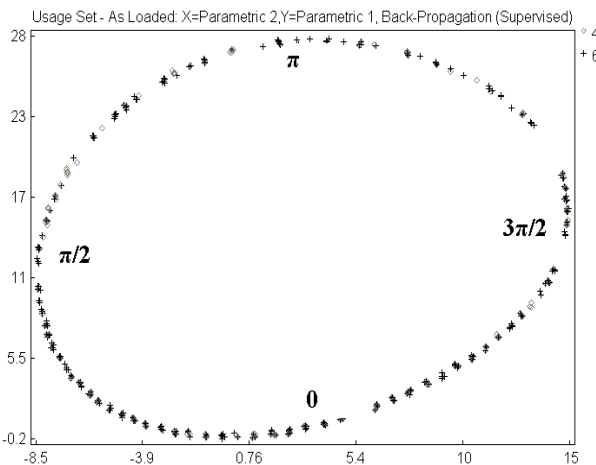


Fig. 10: Flapwise vs. Edgewise Load (Classes 4, 6)

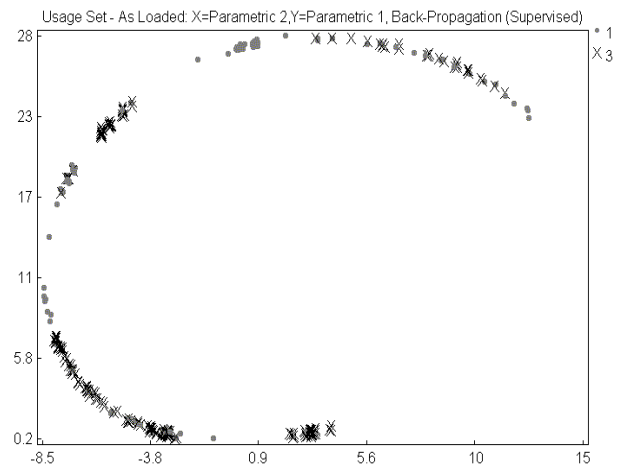


Fig. 11: Flapwise vs. Edgewise Load (Classes 1, 3)

These observations can be summarized for all classes by artificially dividing the loading cycle into four sections, based on the elliptical shape of the flapwise and edgewise loads correlation. Following the convention of Fig. 10, the loading cycle was divided to the parts (0 to  $\pi/2$ ), ( $\pi/2$  to  $\pi$ ), ( $\pi$  to  $3\pi/2$ ) and ( $3\pi/2$  to 0), where 0 and  $\pi$  coincide with the center values of the edge load and  $\pi/2$  and  $3\pi/2$  with the center values of the flap load. Table 1 summarizes the number of events per class, encountered on each section of the loading cycle.

	Section	Class 0	Class 1	Class 2	Class 3	Class 4	Class 5	Class 6	Total
1	0 to $\pi/2$	169	25	166	122	512	132	1231	<b>2357</b>
2	$\pi/2$ to $\pi$	36	52	103	37	168	80	302	<b>778</b>
3	$\pi$ to $3\pi/2$	59	23	43	27	177	10	337	<b>676</b>
4	$3\pi/2$ to 0	131	-	92	19	377	86	976	<b>1681</b>

*Table 1: Number of events of each class, per loading cycle section.*

Very appealing on Table 1 are the strong variations of each class's total events among the sections of the loading cycle. In total, the vast majority of AE is produced at the lower part of the cycle (sections 1 and 4). This trend is followed by all classes except for Classes 1 and 3, which seem to be very concentrated only on sections 2 and 1, respectively.

## CONCLUSIONS

Unsupervised pattern recognition on AE data obtained during the first static loading of a W/T blade yielded seven classes of data. Class criticality was assessed and it was demonstrated that classes 4 and 6 were the only active classes during the load hold periods. Although classes 1, 3 and 5 were more “intense” in terms of their AE features, their AE activity was rather occasional during static loading with sudden bursts of emission and emission during load increases. Further application of linear location indicated that different classes mainly originated from different areas of the blade. More specifically, classes 1 and 3 were located very close to sensor 1 where the internal spar ends. Classes 4 and 6 were located between sensors 6 and 10. In this area, although there were not any visual indications after the first static test, a crack was developed upon further application of several millions of fatigue cycles on the blade. Finally, class 5 was located on sensor 5 and it is believed to be associated with the skin damage that was observed at the load application point.

Based on the results of the UPR on the static test, supervised classification was performed on AE data obtained during fatigue testing of the same blade. Most classes exhibited strong periodicity and were active at particular sections of the loading cycle.

It is worth noting that segregation of the different classes, which was successfully performed with UPR, would be almost impossible with traditional AE analysis, because of the strong overlapping of the classes in any two-dimensional space defined by any two of the AE features. On the other hand, extracting first-hit information from the located AE sources still would not suffice, as one location of the blade might be associated with more than one damage mechanisms. Even more apparent is the need for pattern recognition in cases of fatigue loading since the complexity of the AE analysis increases.

## REFERENCES

- [1] Adams, R.D., Cawley, P., "A review of defect types and NDT techniques for composites and bonded joints", *NDT International*, Vol. 21, 1988, 207-222.
- [2] Anastassopoulos, A.A., Philippidis, T.P., "Pattern Recognition Analysis of AE from Composites", Proceedings of the 23<sup>rd</sup> European Conference on AE Testing, Vienna, 6-8 May 1998, pp. 15-20.
- [3] Anastassopoulos, A.A., Vahaviolos, S.J., Lenain, J.C., "Signature Recognition Of Acoustic Emission From FRP Structures", Proceedings. 7<sup>th</sup> ECNDT, Copenhagen, May 1998, pp. 2295-2302.
- [4] Sutherland, H., Beattie, A., et al., "The Application of Non-Destructive Techniques to the Testing of a Wind Turbine Blade", Sandia National Labs report, SAND93-1380. UC-261, U.S.A., June 1994.
- [5] Vionis, P., Anastassopoulos, A.A., Kolovos, V., Kouroussis, D.A., "Non-Destructive Testing of Full Scale W/T Blade by Means of Acoustic Emission Monitoring During Controlled Static Loading", European Wind Energy Conference and Exhibition, Nice, March 1-5, 1999.
- [6] Anastassopoulos, A.A., Kouroussis, D.A., Vionis, P., Kolovos, V., "Acoustic Emission NDE of a Wind Turbine Blade during Full - Scale Testing", *Insight*, Vol. 41, No. 6, June 1999.
- [7] Kouroussis, D.A., Vionis, P., Anastassopoulos, A.A., Kolovos, V, "Acoustic Emission Monitoring of a 12m Wind Turbine FRP Blade During Static and Fatigue Loading", Proceedings, 2<sup>nd</sup> International Conference on Emerging Technologies in NDT, May 24-26, 1999, Athens, Greece.
- [8] Envirocoustics A.B.E.E., "Noesis Reference Manual", rev. 0, October 1999.
- [9] Anastassopoulos, A.A., Philippidis, T.P., "Clustering Methodologies for the evaluation of AE from Composites", *J. of Acoustic Emission*, Vol. 13(1/2), 1995, 11-21.
- [10] Philippidis, T.P., Nikolaidis, V.N., Anastassopoulos, A. A., "Damage Characterisation of C/C laminates using Neural Network Techniques on AE signals", *NDT&E International*, Vol. 31(5), 1998, 329-340.
- [11] Anastassopoulos, A.A., Nikolaidis, V.N. and Philippidis, T.P., "A Comparative study of Pattern Recognition Algorithms for Classification of Ultrasonic Signals", *Neural Computing & Applications*, 1999, Vol. 8, 53-61.

# **UNSUPERVISED PATTERN RECOGNITION OF ACOUSTIC EMISSION FROM FULL SCALE TESTING OF A WIND TURBINE BLADE**

**Dimitrios KOUROUSSIS, Athanassios ANASTASSOPOULOS,**

**Pantelis VIONIS\* and Vassilios KOLOVOS\***

**Envirocoustics S.A., Athens, Greece**

**\*Centre for Renewable Energy Sources, Pikermi, Greece**

## **ABSTRACT**

*In the present paper, acoustic emission (AE) data obtained during a static test of a 12-m FRP wind turbine blade was analyzed and classified into classes using various unsupervised pattern recognition (UPR) techniques. Class criticality was revealed by means of correlation of each class's activity with the applied load. Application of location techniques pinpointed the specific areas of activity of each class, on the blade. Using the UPR results, a supervised pattern recognition (SPR) method was trained, based on back propagation neural network, and applied to AE data obtained during a subsequent biaxial fatigue loading of the same blade. Similar classes appeared at the same regions of the blade, but were triggered at different phases of the loading cycle. The application of UPR on AE data proved to be a promising tool towards the characterization of damage evolution with monotonic or fatigue loading.*

## **INTRODUCTION**

Acoustic emission (AE) monitoring during full scale testing of FRP wind turbine (W/T) blades is a relatively new application. The difficulty in such tests arises mainly from the potentiality of different AE sources, such as delamination, matrix cracks, fiber breakage, etc., which, sometimes, occur concurrently and are expected due to the nature of FRP materials [1]. The separability of such material-failure mechanisms by means of UPR analysis of AE data has been demonstrated in the past [2,3]. However, the sophisticated structural design of modern W/T blades, containing reinforcement spars, internal cells and skin materials with different stacking sequences, introduces additional complexity in the understanding and characterization of the detected flaws. More specifically, particular sections of W/T blades (e.g. the internal spar ends) exhibit high AE activity, even at low load levels, due to local stress concentrations, but the corresponding mechanisms do not necessarily signify critical damage. Nevertheless, the same or another area of the blade might experience a different, more critical damage mechanism at higher loads, which has to be segregated and evaluated separately. Discrimination of the various damage mechanisms on FRP materials by means of conventional AE analysis imposes several restrictions and difficulties, as it is usually based on the location of the AE sources followed by tedious analysis of the characteristics of the located AE events. The analysis usually involves two-dimensional feature correlation (i.e. correlating two AE features at a time), as it is practically impossible to visualize the whole feature set. This approach does not always yield a reliable identification of the signatures of the various damage mechanisms. Even more so, it is not always possible to isolate a particular mechanism and monitor its activity in time, with increasing load, in order to assess its criticality.

The applicability of conventional AE analysis on full-scale testing of W/T blades was assessed by Sutherland et al. [4]. Further application of the AE technique proved to be successful in detecting and locating structural flaws on the blade, at very early stages and before they had become visible [5,6]. However, the necessity to discriminate and analyze the detected flaws by means of their AE features still exists and becomes even more apparent in the case of full-scale fatigue testing of a W/T blade [7]. The

purpose of this work is to separately investigate and compare the various classes of AE data, revealed by UPR techniques, which appear during static loading. Furthermore, application of neural networks for supervised classification of data obtained during fatigue loading of the same blade, offers a better insight into the nature of the existing flaws. Successful recognition of the different FRP damage mechanisms by means of their AE signatures could, ultimately, lead to the automation of the classification procedure for future W/T blade tests.

## EXPERIMENTAL SET-UP

For the present work, two different AE tests are considered. The first was a static test performed while the blade was previously unloaded. Conventional AE analysis has already been performed and has successfully pinpointed “weak” areas of the blade [5,6]. The second AE test refers to the monitoring of 23 cycles of biaxial fatigue loading at 0.1 Hz, which took place after the blade had undertaken several millions of fatigue cycles in the laboratory, and a visible crack had developed on the trailing edge of the blade between sensors 6 and 10 (see Fig. 1). All tests took place at the Centre for Renewable Energy Sources (CRES) Wind Turbine Blades Testing Laboratory. The blade was loaded on a single point by means of a hydraulic actuator (two in the case of fatigue testing), and AE data were recorded by a Physical Acoustics Corporation (PAC), ten-channel “SPARTAN 2000” AE system and the associated, PC-based data acquisition software. Ten 60 kHz resonant frequency PAC R6I AE sensors, equipped with a 40dB internal preamplifier, were mounted on the compression (suction) side of the blade. The sensor positioning and the corresponding AE channel numbers are presented in Fig. 1. During acquisition, basic AE signal features were recorded and stored in file by the AE system software (PAC-“SP2-LOC”), including channel number, hit arrival time, rise time, counts, energy, duration, amplitude, average frequency, average signal level and counts-to-peak. During the fatigue test, loads in both flap and edge directions were measured by the load cells between the blade and the actuators.

In the case of the static test, one hydraulic actuator was mounted underneath the blade and was exerting force perpendicular to the blade’s surface plane, so that the blade’s pressure side was under tension, as in real conditions. The load was applied at a flapwise position, 7 m from the blade’s root and at 25% chord station (Fig. 1), resulting in a triangular distribution of the bending moment along the blade’s axis, aiming to simulate the maximum operational load.

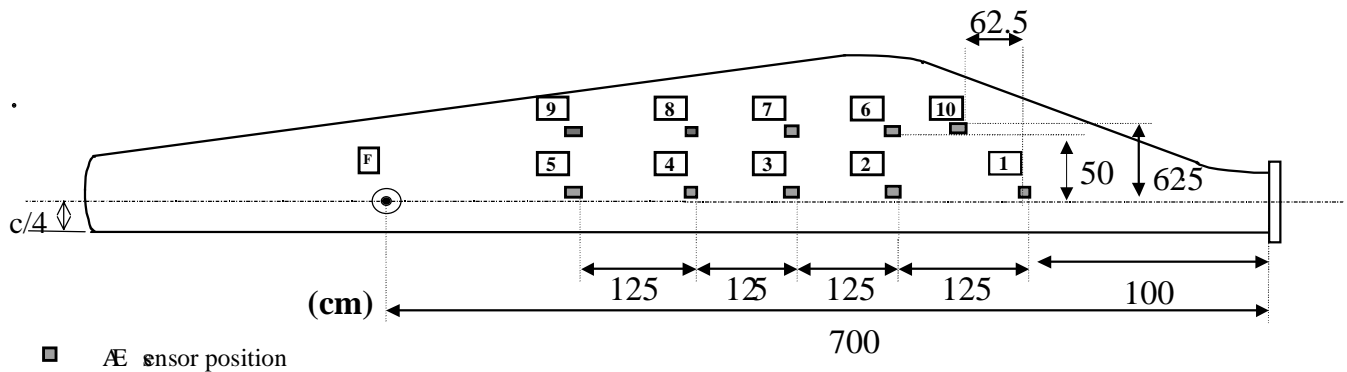


*Fig. 1: AE sensor position and channel numbers Load application point.*

In the fatigue test, two hydraulic actuators were used, at the same axial position as in the static test, one exerting force in the flapwise direction and the other in the edgewise direction. Both actuators were applying periodic force to the blade at the same frequency (0.1 Hz) and the resulting force had edgewise and flapwise components, with 90° phase shift, causing the blade to move elliptically.

## PATTERN RECOGNITION ANALYSIS

Unsupervised pattern recognition (UPR) was applied on the data of the first static test using the commercially available “NOESIS” pattern recognition and neural networks software for AE applications. A “first-hit” analysis was followed; i.e., only the first hit of each AE event was used. The first step before application of UPR was to select a representative set of AE features based on which the data would be segregated into classes, exhibiting similar characteristics. For that purpose, feature correlation analysis [8,9] was performed for all the available AE features.

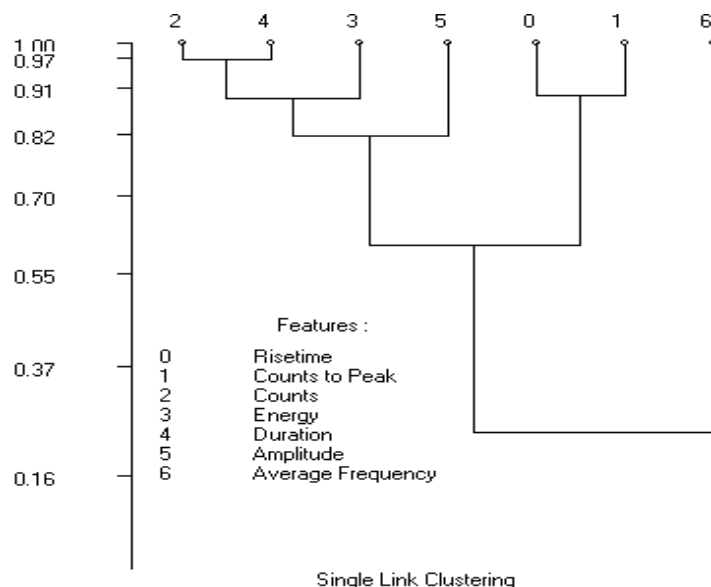


*Fig. 2: Feature Correlation Hierarchy.*

get indications for the data structure. Then, varying the number of the desired clusters, a parametric study was performed using the K-Means and LVQ-Neural Net algorithms, in order to assess the optimum number of classes by means of discrimination-efficiency heuristic criteria. Local minimization of the D&B  $R_{ij}$  criterion [9-11] occurred at seven classes for both the K-Means and the LVQ clustering algorithms. Therefore, the respective results were used to separate the data into seven classes.

For that purpose, feature correlation analysis [8,9] was performed for all the available AE features. The degree of correlation among features, presented in the dendrogram of Fig. 2, demonstrates very strong correlation for Counts and Duration. Subsequently, UPR was performed with a reduced set of AE features, comprising Rise Time, Counts to Peak, Energy, Duration, Amplitude and Average Frequency. Furthermore, all features were normalized individually to a range from 0 to 1, in order to avoid biasing the classification towards the feature exhibiting the highest physical dimensions.

Initially, UPR was performed using various clustering algorithms [8-10], to

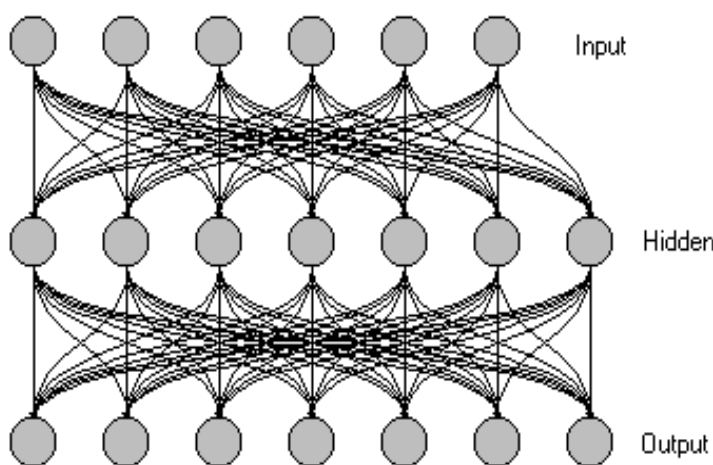


*Fig. 3: The BPNN classifier topology.*

Following the clustering performed by UPR on the static test data, a back-propagation neural network (BPNN) supervised classifier [8,11] was trained to correspond AE hits, from any given data set, to one of the seven classes (output layer) based upon the values of their AE features (input layer). Various trials were performed changing the number of hidden layers that connect the input and output layers and showed that one “hidden” layer (Fig. 3) was adequate. Success of training was assessed by applying this classifier on a subset of the static test data. The supervised classification yielded only 1% of misclassified hits in comparison to the desired UPR classification.

## FIRST STATIC LOADING

Figure 4 presents the cumulative AE energy vs. time for classes 4 and 6 with the loading envelope superimposed. It is observed that these classes exhibit similar activity trends. Comparing Fig. 4 with Fig. 5, which presents the cumulative AE energy vs. time for classes 1, 3, 5, it becomes evident that classes 4, 6 and are the only classes with continuous activity throughout the load holds. At the same time, although classes 3 and 5 exhibit high total AE energy, they totally cease at the end of the last load hold. Class 1 presents a burst of AE activity in the last load-hold (also observed in class 3) and then ceases. Classes 0 and 2 are generally very low in AE energy and inactive during load holds.

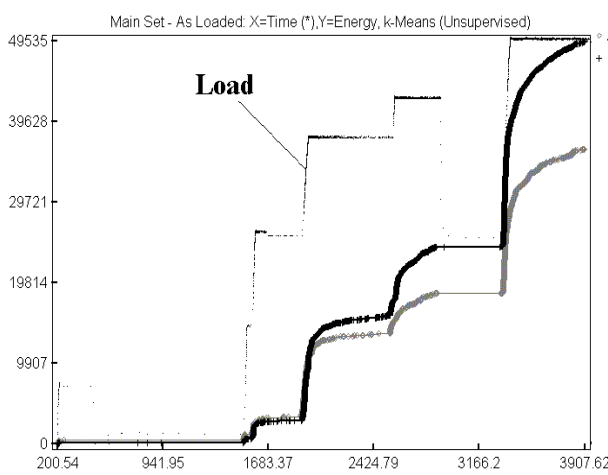


*Fig. 4: Cumulative AE Energy vs. Time  
(Classes 4, 6).*

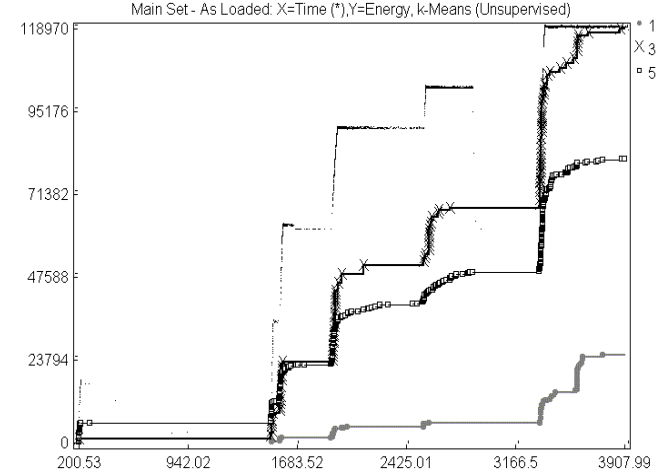


*Fig. 5: Cumulative AE Energy vs. Time  
(Classes 1, 3, 5).*

Feature correlation can be visualized in Figs. 6 and 7, which are scatter plots of Amplitude vs. Counts (in log scale) for classes 4, 6 and 1, 3, respectively. In these two-dimensional correlation plots, the overlapping between classes is strong in the low and medium Counts-Amplitude region where classes 4, and 6 coexist (Fig. 6). In the high-medium region, classes 1, 3 are better separated (Fig. 7).

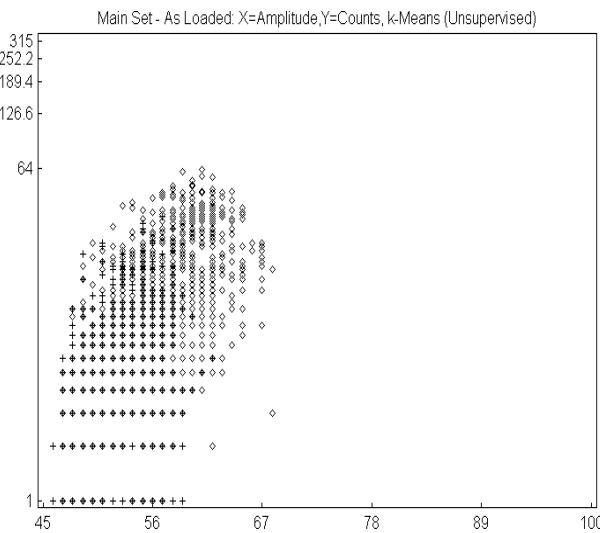


*Fig. 6: Amplitude vs. Counts (Classes 4, 6).*

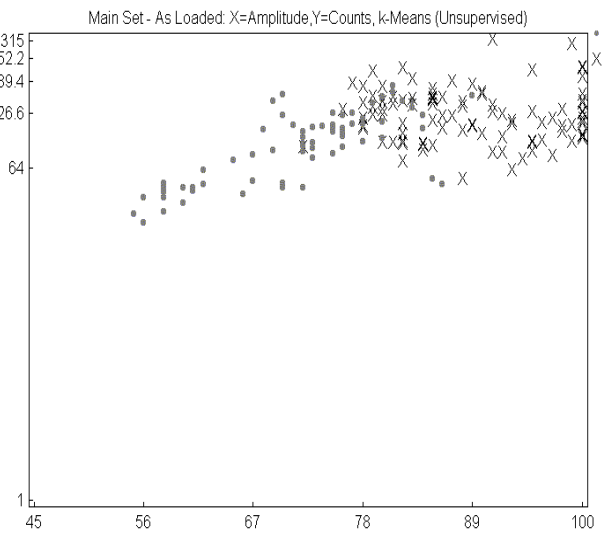


*Fig. 7: Amplitude vs. Counts (Classes 1, 3).*

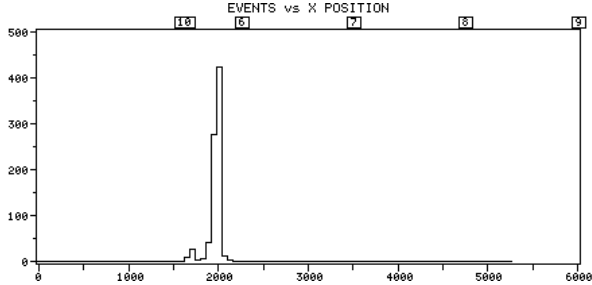


Fig. 8: Location of classes 4 and 6.

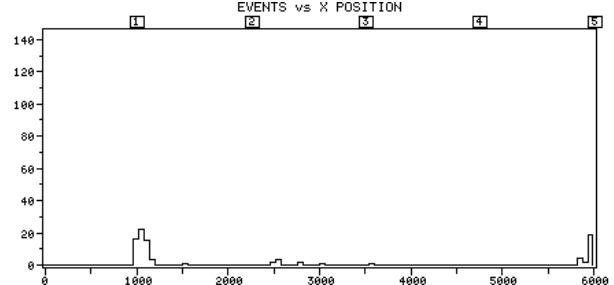


Fig. 9: Location of classes 1 and 3.

Aiming to correlate the different classes of data with particular areas of the blade, the linear location technique was applied separately for each class. For that purpose, the original data acquisition set of the test was used, which contained all-hits information. By means of specialized PAC software, this set was split into seven subsets, one for each class, each subset containing all-hits information only for its corresponding class. Two linear location groups were defined, one with sensors 1-5 and one with sensors 6-10 (see Fig. 1). Upon application of linear location, it was observed that: (a) Classes 4 and 6 were located mainly in the area between sensors 6 and 10 (see Fig. 8), (b) Classes 1 and 3 were located primarily very close to sensor 1 (see Fig. 9), (c) Class 5 was located right on sensor 5, which means that it might have been triggered anywhere from sensor 5 towards the load application point, and (d) Classes 0 and 2 gave very few locations.

## FATIGUE LOADING

Supervised classification was performed on the fatigue loading first-hit data. To gain a thorough insight as to whether particular classes appear at specific parts of or throughout the loading cycle, Figs. 10 and 11 present two scatter plots of the flapwise load vs. edgewise load. The shape of these plots is a good representation of the ellipsoidal movement of the blade at the load application point. For the plot of Fig. 10, data classes 4 and 6 were used, while Fig. 11 uses only classes 1 and 3 to generate the plot. Strong dependence of class activity with load is apparent only for classes 1 and 3. On the contrary, classes 4 and 6 appear more or less throughout the loading cycle.

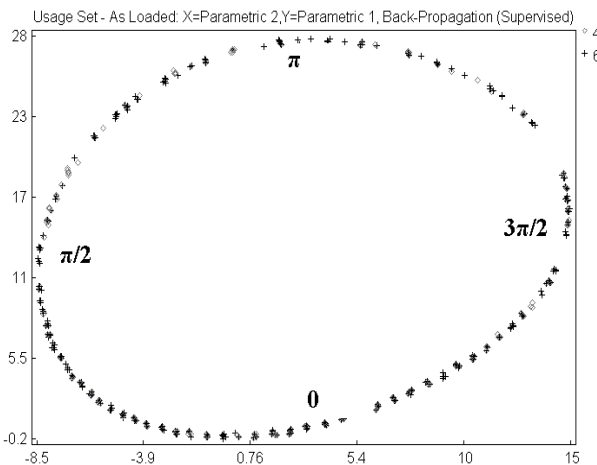


Fig. 10: Flapwise vs. Edgewise Load (Classes 4, 6)

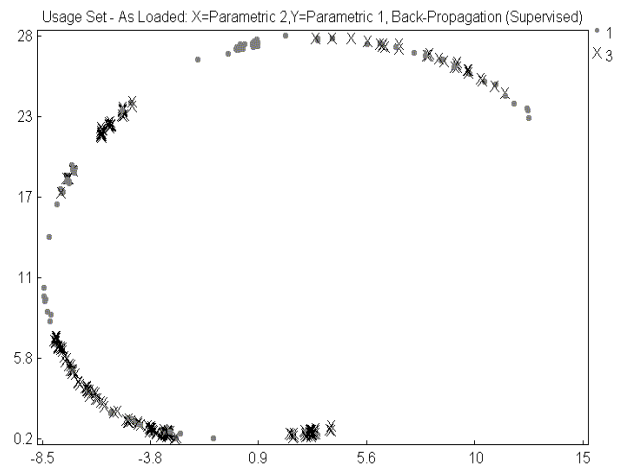


Fig. 11: Flapwise vs. Edgewise Load (Classes 1, 3)

These observations can be summarized for all classes by artificially dividing the loading cycle into four sections, based on the elliptical shape of the flapwise and edgewise loads correlation. Following the convention of Fig. 10, the loading cycle was divided to the parts (0 to  $\pi/2$ ), ( $\pi/2$  to  $\pi$ ), ( $\pi$  to  $3\pi/2$ ) and ( $3\pi/2$  to 0), where 0 and  $\pi$  coincide with the center values of the edge load and  $\pi/2$  and  $3\pi/2$  with the center values of the flap load. Table 1 summarizes the number of events per class, encountered on each section of the loading cycle.

	Section	Class 0	Class 1	Class 2	Class 3	Class 4	Class 5	Class 6	Total
1	0 to $\pi/2$	169	25	166	122	512	132	1231	<b>2357</b>
2	$\pi/2$ to $\pi$	36	52	103	37	168	80	302	<b>778</b>
3	$\pi$ to $3\pi/2$	59	23	43	27	177	10	337	<b>676</b>
4	$3\pi/2$ to 0	131	-	92	19	377	86	976	<b>1681</b>

*Table 1: Number of events of each class, per loading cycle section.*

Very appealing on Table 1 are the strong variations of each class's total events among the sections of the loading cycle. In total, the vast majority of AE is produced at the lower part of the cycle (sections 1 and 4). This trend is followed by all classes except for Classes 1 and 3, which seem to be very concentrated only on sections 2 and 1, respectively.

## CONCLUSIONS

Unsupervised pattern recognition on AE data obtained during the first static loading of a W/T blade yielded seven classes of data. Class criticality was assessed and it was demonstrated that classes 4 and 6 were the only active classes during the load hold periods. Although classes 1, 3 and 5 were more “intense” in terms of their AE features, their AE activity was rather occasional during static loading with sudden bursts of emission and emission during load increases. Further application of linear location indicated that different classes mainly originated from different areas of the blade. More specifically, classes 1 and 3 were located very close to sensor 1 where the internal spar ends. Classes 4 and 6 were located between sensors 6 and 10. In this area, although there were not any visual indications after the first static test, a crack was developed upon further application of several millions of fatigue cycles on the blade. Finally, class 5 was located on sensor 5 and it is believed to be associated with the skin damage that was observed at the load application point.

Based on the results of the UPR on the static test, supervised classification was performed on AE data obtained during fatigue testing of the same blade. Most classes exhibited strong periodicity and were active at particular sections of the loading cycle.

It is worth noting that segregation of the different classes, which was successfully performed with UPR, would be almost impossible with traditional AE analysis, because of the strong overlapping of the classes in any two-dimensional space defined by any two of the AE features. On the other hand, extracting first-hit information from the located AE sources still would not suffice, as one location of the blade might be associated with more than one damage mechanisms. Even more apparent is the need for pattern recognition in cases of fatigue loading since the complexity of the AE analysis increases.

## REFERENCES

- [1] Adams, R.D., Cawley, P., "A review of defect types and NDT techniques for composites and bonded joints", *NDT International*, Vol. 21, 1988, 207-222.
- [2] Anastassopoulos, A.A., Philippidis, T.P., "Pattern Recognition Analysis of AE from Composites", Proceedings of the 23<sup>rd</sup> European Conference on AE Testing, Vienna, 6-8 May 1998, pp. 15-20.
- [3] Anastassopoulos, A.A., Vahaviolos, S.J., Lenain, J.C., "Signature Recognition Of Acoustic Emission From FRP Structures", Proceedings. 7<sup>th</sup> ECNDT, Copenhagen, May 1998, pp. 2295-2302.
- [4] Sutherland, H., Beattie, A., et al., "The Application of Non-Destructive Techniques to the Testing of a Wind Turbine Blade", Sandia National Labs report, SAND93-1380. UC-261, U.S.A., June 1994.
- [5] Vionis, P., Anastassopoulos, A.A., Kolovos, V., Kouroussis, D.A., "Non-Destructive Testing of Full Scale W/T Blade by Means of Acoustic Emission Monitoring During Controlled Static Loading", European Wind Energy Conference and Exhibition, Nice, March 1-5, 1999.
- [6] Anastassopoulos, A.A., Kouroussis, D.A., Vionis, P., Kolovos, V., "Acoustic Emission NDE of a Wind Turbine Blade during Full - Scale Testing", *Insight*, Vol. 41, No. 6, June 1999.
- [7] Kouroussis, D.A., Vionis, P., Anastassopoulos, A.A., Kolovos, V, "Acoustic Emission Monitoring of a 12m Wind Turbine FRP Blade During Static and Fatigue Loading", Proceedings, 2<sup>nd</sup> International Conference on Emerging Technologies in NDT, May 24-26, 1999, Athens, Greece.
- [8] Envirocoustics A.B.E.E., "Noesis Reference Manual", rev. 0, October 1999.
- [9] Anastassopoulos, A.A., Philippidis, T.P., "Clustering Methodologies for the evaluation of AE from Composites", *J. of Acoustic Emission*, Vol. 13(1/2), 1995, 11-21.
- [10] Philippidis, T.P., Nikolaidis, V.N., Anastassopoulos, A. A., "Damage Characterisation of C/C laminates using Neural Network Techniques on AE signals", *NDT&E International*, Vol. 31(5), 1998, 329-340.
- [11] Anastassopoulos, A.A., Nikolaidis, V.N. and Philippidis, T.P., "A Comparative study of Pattern Recognition Algorithms for Classification of Ultrasonic Signals", *Neural Computing & Applications*, 1999, Vol. 8, 53-61.

# **ACOUSTIC EMISSION PROOF TESTING OF INSULATED AERIAL MAN-LIFT DEVICES**

**Athanassios ANASTASSOPOULOS, Apostolos TSIMOGIANIS and Dimitrios KOUROUSSIS  
ENVIROCOUSTICS S.A., Athens GREECE.**

## **ABSTRACT**

*Acoustic emission (AE) testing of insulated aerial man-lift devices has proved successful over the years and is widely accepted for testing both new and in-service vehicles. Although testing is relatively easy, data analysis and evaluation is a demanding process, since both metal and composite parts are simultaneously tested, while, the mechanisms used to manipulate the arm movements are potential noise sources. The existing standards for such type of testing do not outline pass-fail criteria for each structural part and material, and evaluation of the results relies basically on the experience of the analyst. The results of AE monitoring of five insulated aerial man-lift devices are reported in this work. Data analysis and evaluation is primarily based on multidimensional sorting and unsupervised pattern recognition techniques, which proved efficient for the discrimination of AE sources. Results from various unsupervised algorithms applied either on the AE feature set, or to its principal component projection, are discussed. Comparison of the proposed analysis process with traditional data treatment, is presented, as well. Supervised algorithms and neural networks were successfully trained, using the unsupervised pattern recognition results, and can be used for the classification of AE data from future tests.*

## **INTRODUCTION**

Periodic maintenance of aerial man-lifts is of outmost importance for the safety of personnel and for the economical operation of the device and the electrical utility. The inspection program usually comprises of structural integrity and dielectric tests in order to identify problems before they become critical [1]. Acoustic emission (AE) testing of insulated aerial man-lift devices has proved successful over the years and is widely accepted for testing both new and in-service vehicles [1-3]. Although AE was initially used to evaluate the structural integrity of the fiberglass booms [2], its applicability extended to the inspection and location of damage in the metal components as well. Through the years, AE has been used in identifying flaws in the new device, resulted from the manufacturing process, and in-service damage resulted from accidents, overload, fatigue and environmental conditions. AE testing of insulated aerial devices has become standard procedure for industries [1-3], supported by relevant standards [4,5]. However, the existing standards for such type of testing do not outline pass-fail criteria for each structural part and material, and the evaluation of results relies basically on the experience of the analyst. Furthermore, major industrial users [3] point out the variation in AE behavior between units of different design from different manufacturers.

The results of AE monitoring of five insulated aerial man-lift devices are reported in this work. Data analysis and evaluation is primarily based on multidimensional sorting and unsupervised pattern recognition techniques [6-8], in order to enhance the analyst efficiency in discriminating the different AE sources. Results from various unsupervised algorithms applied either on the AE feature set, or to its principal component projection are presented. Principal component projection proved to be an efficient pre-processing tool in pattern recognition analysis of AE data. Further automation of the evaluation process is achieved by neural networks [8,9], which proved suitable for classifying AE data and can be used to evaluate AE activity from future tests of similar devices.

## EXPERIMENTAL PROCEDURE

The aerial devices were loaded to 1.5 times the rated capacity. According to the guidelines of ASTM [4], two loading cycle were performed. The load was applied with the device in the position shown in Fig. 1. Thirteen (13) PAC-R15I 150KHz resonant sensors with 40-dB integral preamplifier were mounted at the positions shown in Fig. 2. Channels 1 to 5 were attached to the composite or insulated parts, while the remaining channels to the metal parts. A PAC Spartan-2000 AE system was used for real time data acquisition. Acquisition was performed at 40 dB threshold and 23 dB gain.



*Fig. 1: Test Position.*

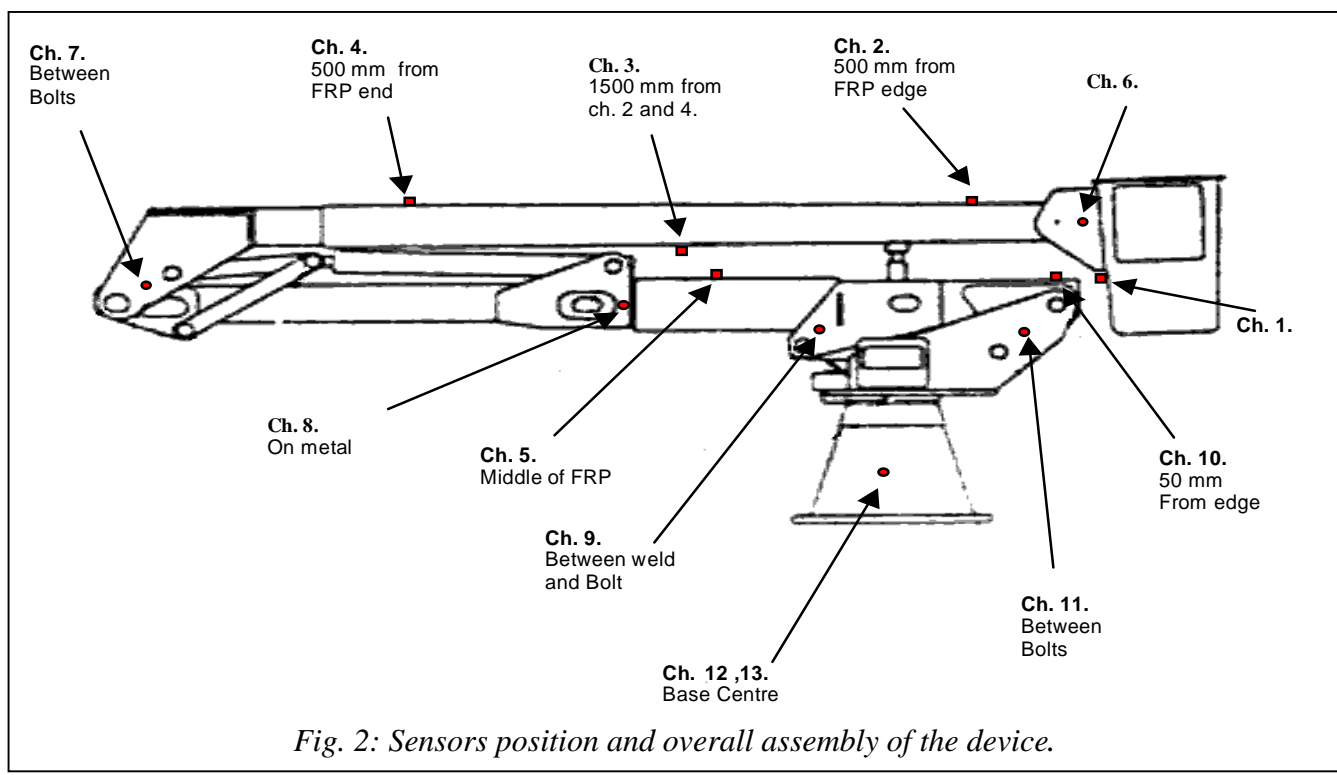


*Fig. 2: Sensors position and overall assembly of the device.*

Attenuation study confirmed the adequate coverage of the structure with AE sensors. Pencil breaks were used as simulated sources at various locations of the device, in order to measure arrival time differences for location purposes. ASTM [4] guidelines were used for immediate test termination in case of extreme damage. As indicated in ASTM, these criteria are not acceptance criteria.

## DATA ANALYSIS

Conventional data analysis and evaluation is usually [3-5] based on two different thresholds, named “low level” and “high level” threshold, with values of 40 dB and 70 dB, respectively. The total AE counts and the number of high threshold events (first hits) during the second loading and second hold period are used as evaluation criteria. The main problem associated with data analysis is the discrimination between genuine emission and the various potential noise sources, such as the mechanisms (usually chain and gears) used to manipulate the arm movements and the hydraulic system, which remain under pressure during testing. Furthermore since both metal and composite parts are simultaneously tested, signature recognition is becoming more complicated.

In the present study, unsupervised pattern recognition [6-8], applied on the data recorded from one aerial device, is used to discriminate the noise sources and establish a procedure for signature recognition of the structurally significant signal classes. Unsupervised pattern recognition is a numerical process aiming to group a data set of “N” patterns to a limited number of “C” sub-groups, called classes. The number of classes and their characteristics have to be determined by the unsupervised pattern recognition methodology. Features selection is a critical step in the analysis process and the results strongly depend on the completeness of feature set.

In the absence of any *a priori* information on the number of signal classes, features cannot be selected on the basis of discriminant analysis. Therefore, Amplitude, Duration, Energy (MARSE), Average Frequency, Rise Time and Counts to Peak, are selected from the eight recorded AE features and used as the default feature space in order to define a transformation and project the original data on a set of orthogonal axes where maximum variance is achieved [8].

The technique, known as principal component analysis, allows calculation of the “degree of fit” (as compared to the complete data set) when a subset of the transformed space is used [8]. The first three principal components, named PCA0, PCA1 and PCA2, resulted in a degree of fit of 95.52% and are further used for the unsupervised pattern recognition analysis and classifier design.

Four different clustering algorithms, K-Means, Max-Min Distance, Forgy and Cluster Seeking, were used for a parametric study in partitioning the AE data in classes ranging from two to twenty-five. The algorithms performance was evaluated by means of Rij and Tou criteria [6-8]. Both are heuristic criteria based on the ratio of average within-class distances to the distance between classes. The Rij criterion is an average measure of such a ratio, calculated using all of the different pair of classes, while the Tou criterion is defined by the ratio of the minimum distance between any pair of classes to the maximum of the average within-class distances. Therefore, the lower the value of Rij, (or the higher the value of Tou), the higher the discrimination efficiency of the resulting data partition. Furthermore, minimization of Rij or maximization of Tou criteria as a function of the resulting number of classes can be used to estimate the number of classes in the data [7].

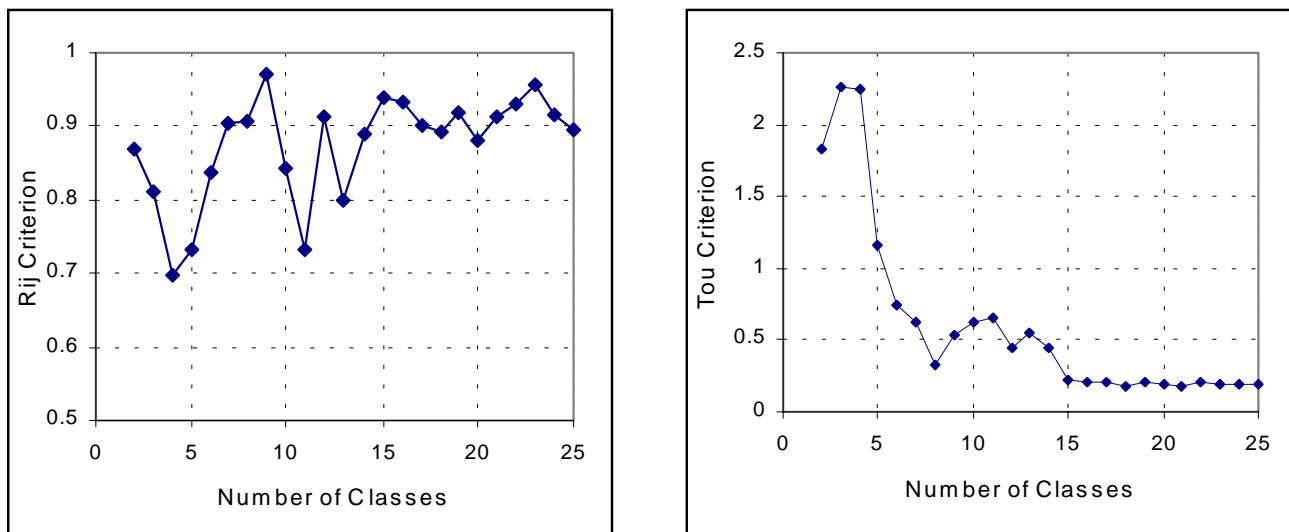
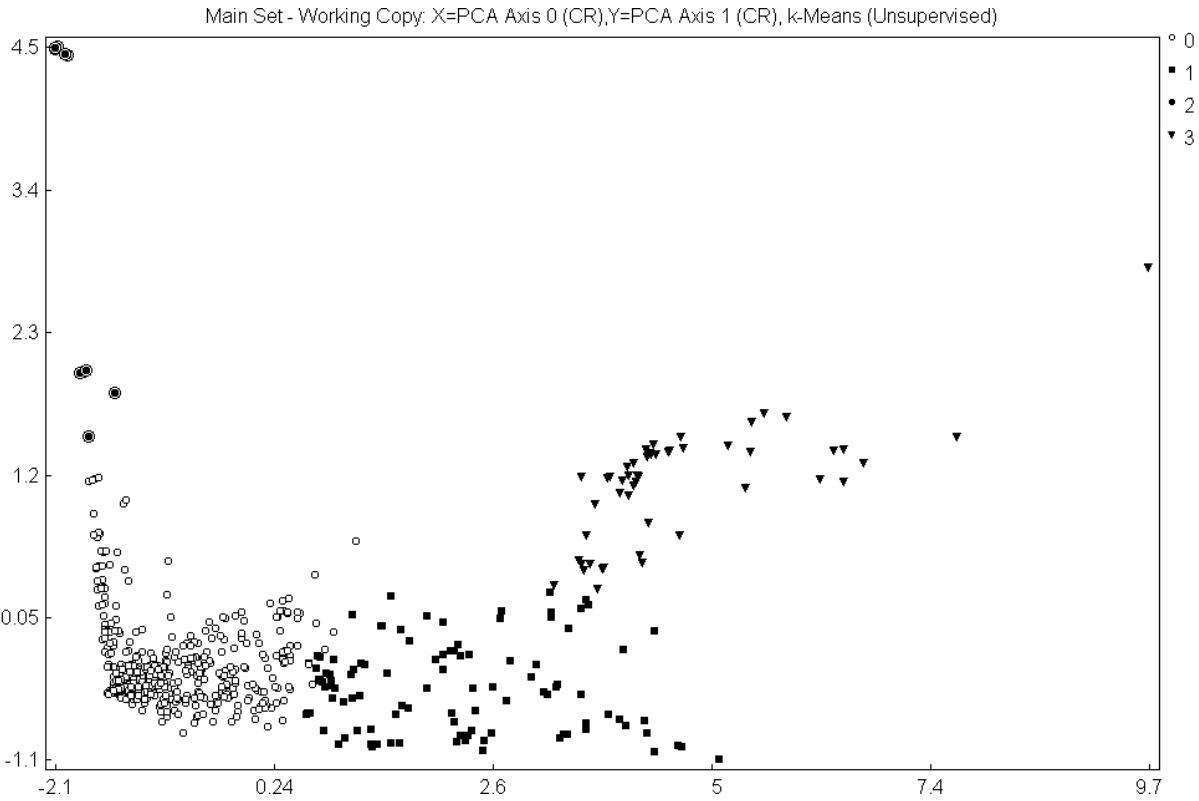


Fig. 3: Estimation of Number of Classes by means of Rij and Tou criteria.



*Fig. 4: Clustering results in the Principal Component Space.*

The results of the parametric study performed with K-Means clustering algorithm are presented in Fig. 3. As can be seen from the figure, Rij criterion is minimized at four classes (a second local minimum observed at eleven classes), while Tou criterion is maximized for three and four classes. From the numerical point of view, therefore, the resulting data partition in four classes was considered to be the most representative for the available AE data.

The respective clustering results are shown in Fig. 4, as scatter plot of the first vs. the second principal components. Figure 5 presents the same clustering results in the original feature space as AE Counts vs. Amplitude scatter plot.

A closer observation of Fig. 5 indicates an overlap between the resulting classes in the original space. However, this is an artifact of the specific projection since the clustering algorithms produce clearly separable classes. On the other hand, the indicated overlap emphasizes the increased efficiency of multidimensional analysis and clarifies the limitations imposed by amplitude-based classification with low and high threshold values.

Experimentation with the remaining clustering algorithms produced similar results. The Max-Min distance clustering algorithm produced better performance. This algorithm resulted in lower value of Rij for a seven-class partition. A closer investigation showed that the main classes of the selected K-Means partition remained the same, while some of the extreme classes were split. Selection between different clustering results and the ultimate validity of the resulting data partitions can be performed only in relation to the physical phenomenon under study. For this purpose, standard AE practices are used.

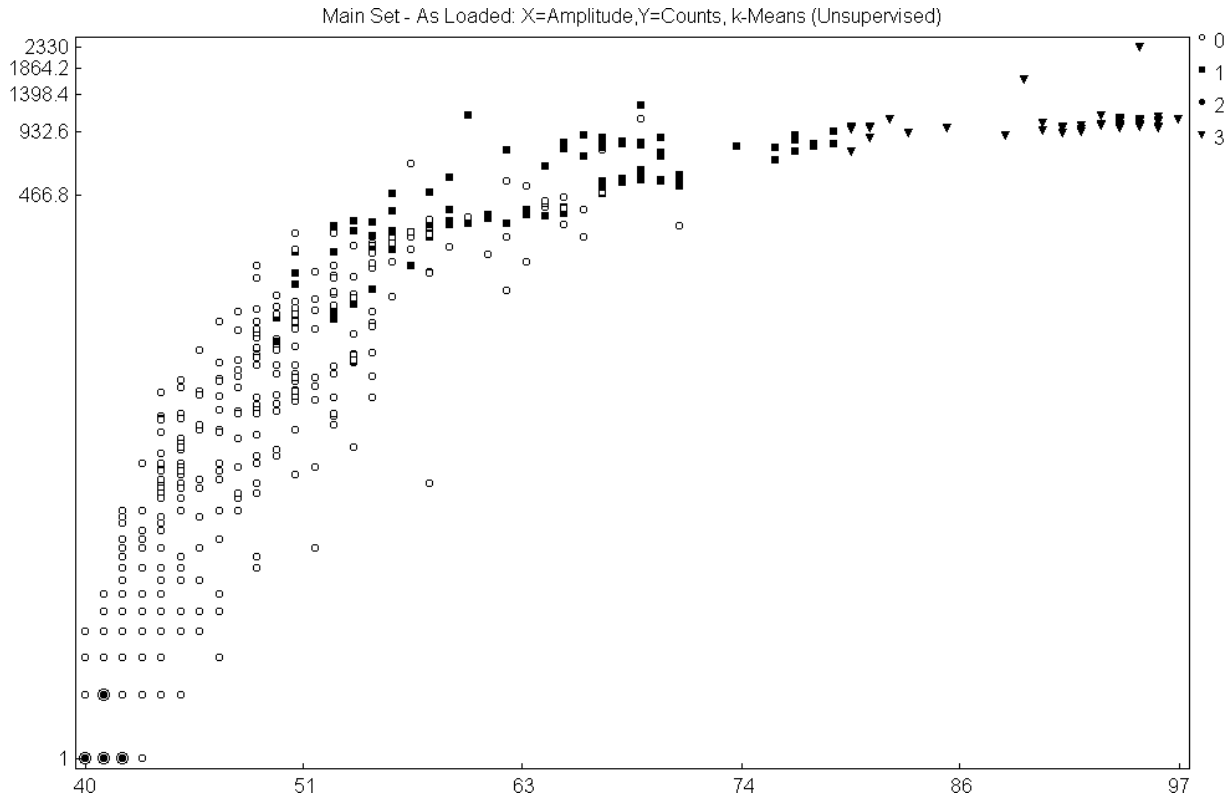


*Fig. 5: Clustering results in the Counts-Amplitude projection.*

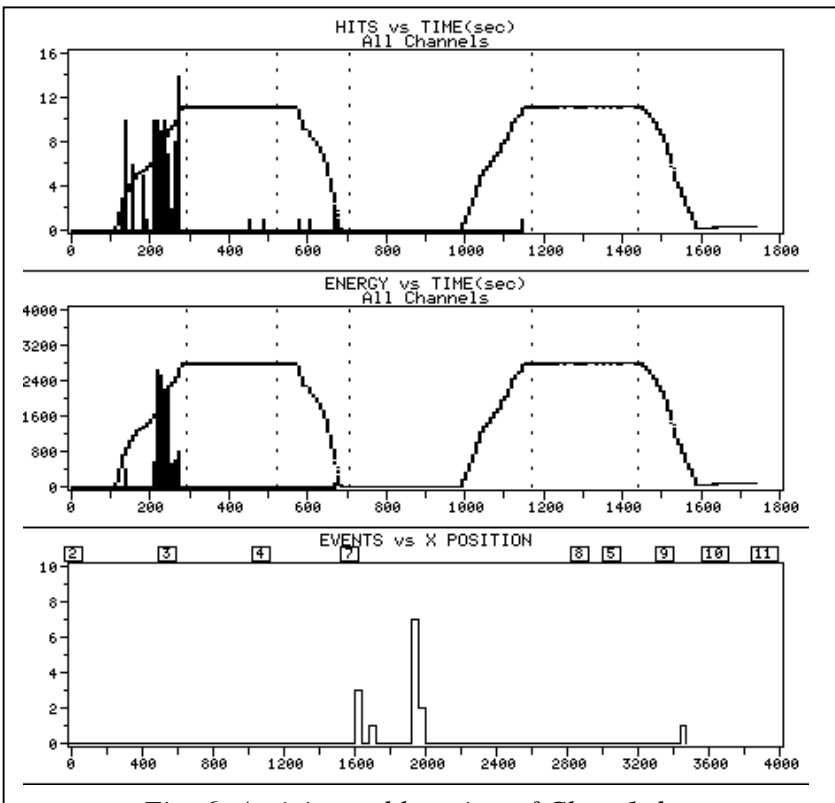


*Fig. 6: Activity and location of Class 1 data.*

The AE data from each class was replayed and evaluated by means of linear and zonal location, as well as by the activity during the loading stages. Figure 6 summarizes the results of class 1. In both hits vs. time (upper graph) and energy vs. time (middle graph) plots of Figs. 6 and 7, the load-time curve is superimposed.

Data of class 1, are well located, in the linear location group (bottom graph of Fig. 6), with high energy (middle graph presents energy rate of the located events). Furthermore, this class is active only during the first loading as can be realized from the hits versus time plot. From Fig. 5, the signature of this class comprises of hits, whose amplitude range from 47 dB to 80 dB. On the other hand, data of class 0, of which

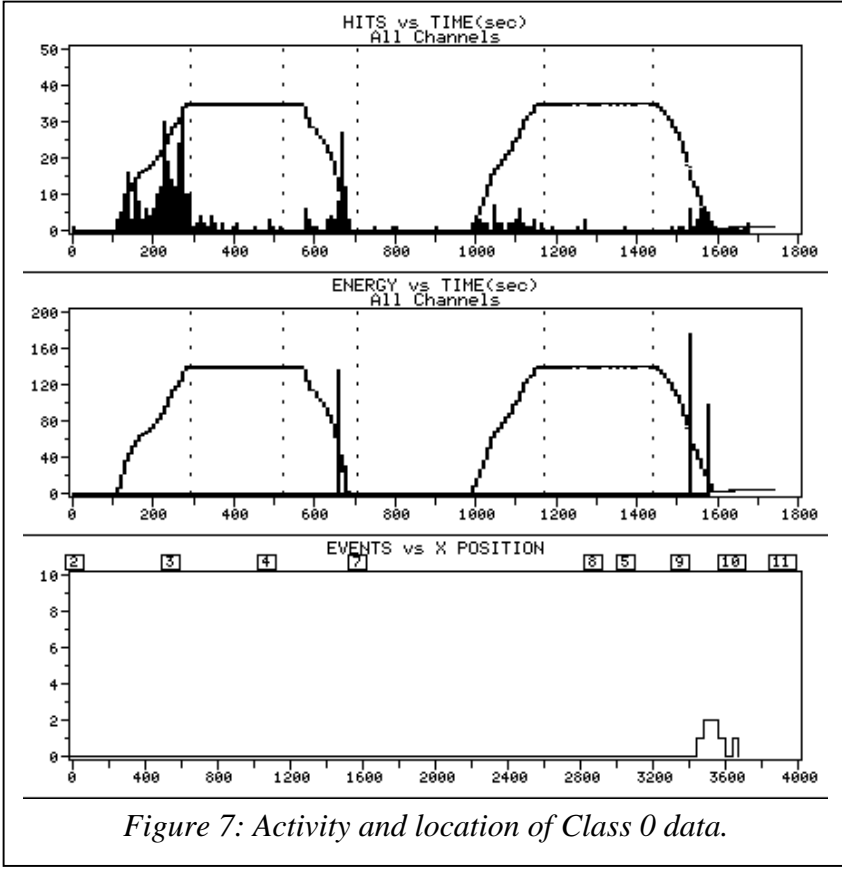


Figure 7: Activity and location of Class 0 data.

observed only in channels 6 and 7. As in the case of class 1, class 3 is active during the first loading, while class 2 has similar behavior with that of class 0; i.e., it remains active during the loading, load hold and unloading at both cycles.

Summarizing the results, classes 0 and 3 might be characterized as structurally insignificant or friction or noise related classes, while class 1 and 2 are considered as structurally significant classes.

## SUPERVISED PATTERN CLASSIFICATION

Based on the validated results of the previous phase, supervised pattern recognition [8,9] is performed for the classification of AE data recorded from the remaining four aerial devices as well as for the classification of AE data recorded in extremely noisy conditions. Two different supervised algorithms were investigated. The Nearest Neighbor classifier and a Back Propagation (BP) Neural Network with 1 input layer of three neurons, 1 hidden layer of four neurons and the output layer. The nearest neighbor classifier resulted in 1.57% (5 hits) misclassification error, while the BP neural network produced 0.63% (2 hits) misclassification error. The following table summarizes the classification results (AE hits per class and % of total test hits):

AE data were recorded without load (weight), while the device operator performed standard movements of the boom to place it to its normal position. Using the location set-up presented in Figs. 6 and 7, the AE data was located between sensors 9 to 11. The classifier assigned 97.3% of the total hits to the noise classes (89.7% in class 0 and 8.2% in class 1). The classification results for the case of hydraulic noise with load, where the device was operated (movements of the boom) with a weight hanging from the basket. In this case, 4.4% of the data were classified in classes 1 and 3.

amplitude ranges between 40 dB and 70 dB, locate between sensors 9 and 10, as can be seen from the bottom graph of Fig. 7. Furthermore, the class is active during all the different stages of the loading cycle as can be realized from the hits vs. time graph of Fig. 7. Most important is the fact that the located events from the linear location group (middle graph of Fig. 7) appear only during unloading.

AE data of classes 2 and 3 are not located by the linear location group. The zonal location results indicate that data of class 3 is located only by channels 6 and 7, while data of class 2 is located by the channels associated with the metal parts of the aerial device. Considering Fig. 5, class 2 has low amplitude and very few counts. Data of class 3 has amplitude greater than 75 dB and is

Table: Summary of the classification results.

Test Type	Class 0	Class 1	Class 2	Class 3
Training Data	438 (69%)	103 (16.2%)	44 (6.9%)	50 (7.9%)
AE aerial 2	210 (76.6%)	29 (10.6%)	32 (11.1%)	3 (1.1%)
AE aerial 3	650 (72.7%)	150 (16.8%)	79 (8.8%)	15 (1.7%)
AE aerial 4	386 (72%)	76 (14.2%)	50 (9.3%)	24 (4.5%)
AE aerial 5	714 (74.7%)	116 (12.1%)	84 (8.8%)	42 (4.4%)
Hydraulic Noise without load	6864 (89.7%)	20 (0.3%)	625 (8.2%)	142 (1.9%)
Hydraulic Noise with load (weight manipulation)	30980 (88.1%)	817 (2.3%)	2656 (7.6%)	724 (2.1%)

The number of hits classified in class 1 and class 3 can be used as evaluation criteria for the assessment of the structural integrity of the tested aerial device. At this point, it is worth noting that the device number 3 (indicated as “AE aerial 3” test), during the first loading cycle was accidentally loaded to load higher than 1.5 times the rated capacity. The overloading resulted in the highest number of hits classified in class 1 (and the highest percentage) among all the devices tested.

## DISCUSSION AND CONCLUSIONS

Unsupervised pattern recognition was used to characterize AE data recorded during the testing of five aerial man-lift devices. The analysis procedure resulted in four signal classes, two of which were considered to be noise. Comparison of the proposed analysis process with traditional data treatment, highlights the limitation of data evaluation by means of low and high amplitude thresholds.

Supervised algorithm, back propagation neural network, was successfully trained, using the results from unsupervised pattern recognition. It is worth mentioning that the high classification performance in case of hydraulic noise was achieved.

The analysis technique proved effective and can be used for the classification of AE data from future tests. In order to establish pass/fail evaluation criteria based on the recorded AE hits from each class, further experimentation is necessary in order to enrich the training set with additional AE sources. Verification of these sources with complementary NDT will allow generalization of the technique.

## REFERENCES

1. Kenneth Moore and C.A. Larson, “Aerial equipment requires thorough, regular inspection”, PAC Technical Report TR-107-2-1/84.
2. J.R. Mitchell and David G. Taggart, “Acoustic Emission Testing of Insulated Bucket Trucks”, Electric Utility Fleet Management, December/November 1983, pp. 41-50.
3. A.H. Bingham and William C. Veal, “Georgia Power Company Acoustic Emission Test Program”, ASTM STP-1139, “AE Testing of Aerial Devices and Associated Equipment Used in the Utility Industries”, 1992, pp. 1-21.
4. ASTM F-914-91, “Standard Test Method for Acoustic Emission for Insulated Aerial Personnel Devices”.
5. EN-61057: 1993, APPENDIX L (Informative), “Acoustic Emission on Aerial Devices with Insulated Booms – Test Method”.

6. A.A. Anastassopoulos, T.P. Philippidis, "Clustering Methodologies for the evaluation of AE from Composites ", J. of Acoustic Emission, Vol. 13, Nos. 1/2, 1995, pp 11-21.
7. T. Philippidis, V. Nikolaidis, A. Anastassopoulos, "Damage Characterisation of C/C-laminates using Neural Network Techniques on AE signals", NDT&E International, Vol. 31, No. 5, Elsevier 1998, pp. 329-340.
8. Envirocoustics S.A., "NOESIS reference manual", rev. 0, October 1999.
9. A.A. Anastassopoulos, V.N. Nikolaidis and T.P. Philippidis, "A Comparative study of Pattern Recognition Algorithms for Classification of Ultrasonic Signals", Neural Computing & Applications, 1999, Vol. 8, pp. 53-61. (Initially accepted April 1996 in J. of Systems Engineering).

# **BOXMAP - NON-INVASIVE DETECTION OF CRACKS IN STEEL BOX GIRDERS**

**J.R. WATSON, K.M. HOLFORD, A.W. DAVIES, and P.T. COLE\***

**School of Engineering, Cardiff University, Cardiff, UK**

**\*Physical Acoustics Ltd., Cambridge, UK**

## **ABSTRACT**

*Active defects, such as crack growth, produce acoustic emission (AE) signals. These signals can be detected by sensors spaced between 3 and 20 m apart, depending on the structure. The sensors are mounted directly onto the external surface and no paint removal is required for their mounting. The use of sophisticated data acquisition and analysis systems enables cracks to be located very early in life, long before they are detectable by the naked eye or other non-destructive testing methods. This paper presents BOXMAP technology, which has been developed by Physical Acoustics Limited and Cardiff University over the past 5 years, as a proven method for locating cracks in steel bridges. The methodology for monitoring structures is described in detail, highlighting strategic and practical considerations for the client and the engineer. These include access requirements, structural investigation and the filtering of any extraneous "noise" from crack data. One of the main benefits comes from data collected from continuous or intermittent monitoring, which can be used as structural fingerprints. These fingerprints can then be compared at regular intervals and the change in condition and/or rate of crack growth determined. This provides qualitative and quantitative information, from which repairs can be ranked and a priority-based maintenance strategy developed. The overall benefit is reduced whole-life costs. Details about the capabilities and limitations of different monitoring strategies are presented, along with examples from bridge trials with particular emphasis on source location and characterization.*

## **INTRODUCTION**

Bridge monitoring has the aim of providing information on the structural condition of a bridge, identifying and evaluating defects, to optimize maintenance work and maximize the impact of a limited budget [1]. Currently this is done by visual inspection [2] and monitoring using traditional methods such as strain gauging with conventional non-destructive testing methods used to evaluate suspected defects. Whilst this increases confidence in the integrity of the structures, many defects remain undetected until they reach an advanced stage [3-5].

There is a need for an assessment tool that is capable of identifying defects in their early stages, as risk and cost can be reduced by early intervention before large-area damage occurs. Monitoring systems using strain gauges and deflection transducers rely on various indicators such as deformation, strain and the vibration modes of the structure as a means of evaluation. These systems concentrate on detecting major structural changes that are caused by notable deformation and redistribution of stresses in the structure, by which stage severe damage has already occurred.

Traditional NDT techniques such as X-radiography, ultrasonics, magnetic particle and dye penetrant are widely used throughout industry but are generally cumbersome to use on site. All of these techniques assess local areas, which require good access to the structure and may entail working at height, above water, or in the proximity of fast moving traffic.

Indeed, some structures have areas that are so difficult to access that it becomes unfeasible, dangerous, or too costly to inspect. These techniques also provide a “snap shot” of defects and are unable to provide any more than speculative information about future behavior. They are ineffective and too costly as a “global” inspection method.

The benefits of acoustic emission (AE) are long known in the oil/petrochemical and aerospace industry, and are becoming increasingly recognized within the civil engineering industry. For 6 years, the Federal Highways Agency and Physical Acoustics Corporation in the USA monitored known defects and evaluated repairs on a number of bridges and produced a report with guidelines for the local monitoring of cracks and repairs [6]. Over the past 6 years during fatigue tests at Cardiff University’s School of Engineering, AE from large structural specimens has been studied to identify the characteristics of the different stages of crack growth [7-9].

Physical Acoustics Limited and Cardiff University have developed an AE-based condition monitoring technique for steel and composite bridges after a number of investigations and trials on a variety of bridges [10]. The AE system detects and locates active defects, such as crack initiation, anywhere in a structure using externally mounted sensors, positioned meters away from defects. This method allows non-invasive 100% volumetric assessment of structures and is therefore particularly effective for box girders, which has led to the development of the BOXMAP technique.

## **STRATEGIC CONSIDERATIONS FOR AE BRIDGE MONITORING**

Before carrying out an AE test, there are strategic considerations to be made. Three main factors, structural detail, the acoustical behavior of the structure and the monitoring strategy, namely Global, Semi-Global and Local, will dictate the number and location of sensors.

Box girders may have some of the following design features; diaphragms (with and without access holes), diagonal-bracing, stiffeners, and external access holes. All of these features influence the way that the elastic stress wave travels, decays and is located by the software. It is therefore necessary to review technical drawings to make use of structural details as wave-guides to ensure the full extent of the structure is monitored.

The location and number of the sensors to be used is a function of signal attenuation, which is affected by structural geometry, plate thickness, design, paint characteristics, and background noise. In every case, there will be unwanted “noise” from external sources such as traffic activity, expansion joint impact, bearing movement and airborne electromagnetic interference (EMI). It is essential to filter any extraneous emissions from collected data so that emission from defect growth is recognizable. Background noise is overcome using a range of methods; guard sensors are used to shield sensor arrays from sources of noise such as expansion joints; pattern recognition programs filter out identified noise sources that are incorporated into the cracking data. These methods have been developed using the experience gained during 6 years of bridge monitoring work with Federal Highways in the USA and during numerous bridge trials in the UK, and fatigue testing at Cardiff University.

Structures can be continuously or intermittently monitored with permanently installed sensors from the site or remotely via a modem. Technological advances and increased accessibility to the Internet allow “remote from site” real-time structural monitoring. Permanent mounting of cables and sensors with pulse and self-test capability eliminates the need for repeated access, giving rapid payback compared with the cost of aerial lifts and aerial walkways. Short duration on-site monitoring can provide

qualitative and quantitative information that can effectively assess the structure over a period of days using temporarily mounted sensors.

Three common monitoring methods are used to obtain differing levels of information:

- Global
- Semi-Global
- Local Area

“Global” monitoring using large sensor spacing still offers maintenance engineers the ability to identify damaged structures and focus further monitoring or inspection on areas sustaining damage. Trials have shown that an entire box girder can be monitored for one day and reveal a number of active areas. We are currently developing techniques to reduce the number of sensors required to globally monitor a structure.

“Semi-Global” monitoring provides precise source location, but requires an increased number of externally mounted sensors to give 100% volumetric monitoring, i.e. capable of locating damage anywhere in the structure, including shear studs, diagonal-bracing, welds, stiffeners and diaphragms.

“Local” area monitoring is used to assess active sources and known defects, using a small array of sensors around the area of interest. Crack orientation, length, activity, and position can be determined with accuracy over a short monitoring period, whilst continuous or intermittent monitoring at this level can identify the direction of crack growth and the rate of propagation. This information is essential for the bridge engineer to determine the status of the known defect and schedule maintenance or repair.

AE monitoring strategies all offer different levels of information about structural integrity and defects. AE monitoring using all of the strategies in conjunction may provide priority based assessment and maintenance methods where structures need to be fully assessed. “Global” monitoring is initially used to grade the structure according to its condition. Structures with active defects can then be “Semi-Globally” monitored to identify and locate significant sources, which in turn can be “Locally” monitored, or assessed using traditional NDT methods, where access is possible to acquire detailed information.

## **FIELD TRIALS**

One of the earliest AE tests of a steel bridge was carried out by Pollock and Smith [12] in 1972 on a military steel bridge. Since then there have been many more tests on a wide variety of structures, both steel and concrete. Huge experience was gained by Physical Acoustic Corporation during local area monitoring of identified defects and repairs for Federal Highways (F.H.W.A.). This work prompted Physical Acoustics to develop the Local Area Monitoring (L.A.M.) AE system.

Large area monitoring of steel structures have been developed by Cardiff University in conjunction with Physical Acoustics Limited. All tests and trials carried out used Physical Acoustics Corporation’s MISTRAS and SPARTAN AE systems, and sensors. The first trial on Trecelyn Viaduct in 1996 sought to establish the level of background noise typically encountered in bridge structures and to study the attenuation of signals in large structures. Emissions from expansion joint impact were found to “ring” throughout the structure, which required digital filtering. Bolted connections were found to significantly reduce the signal strength, yet artificial sources were adequately picked up at distances in excess of 20 meters.

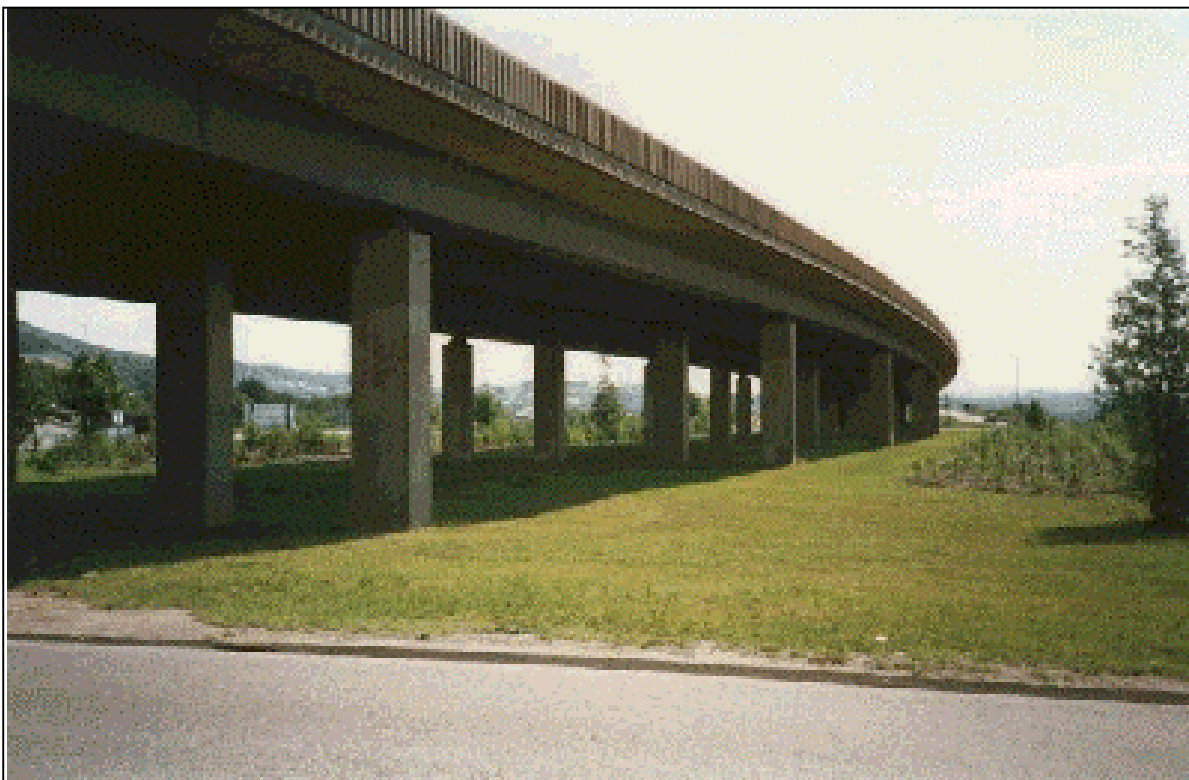


*Fig. 1: Salttings Viaduct.*

Extensive trials were carried out in 1997 on Salttings Viaduct, a 26-year-old composite box girder on the A465 near Neath, South Wales (Fig. 1). This study showed that active areas were identifiable at 10-metre sensor spacing, many of which coincided with internal diaphragms. Local monitoring of the most active diaphragm identified a strong source from the access hole cut into the plate. Recent Finite Element analysis [13] showed this to be an area of particularly high stress, which has led to on going fatigue tests on box girder sections with a variety of diaphragm designs.

## **MOTORWAY TRIAL I - PRELIMINARY INVESTIGATION**

During preliminary investigations, a composite box girder bridge was monitored during the morning rush hour. Prior to monitoring, an acoustic investigation was conducted using an artificial source to confirm location accuracy for a variety of details within the structure, including stiffeners, diaphragms and the internal welds. The bridge was monitored using a Semi-Global, externally mounted array. This test revealed that the bridge was in a very good condition with very few AE signals detected. This preliminary investigation enabled an optimum test set-up to be determined for the following major bridge trial.

## **MOTORWAY TRIAL II - MAJOR TRIAL TEST DETAILS**

A 40m span composite box girder was studied over a two-week period, during which it was semi-globally monitored for a one-week period between 5am and 10pm. The most significant AE sources, identified during investigations in the first week, were locally monitored during the second week. The girder lies underneath the cheveroned area between the 3 lanes south bound and the merging area of a two-lane slip road, Fig. 2. This girder was chosen since transverse deformation across the deck induces high stresses in the diagonal bracing members, Fig. 3.

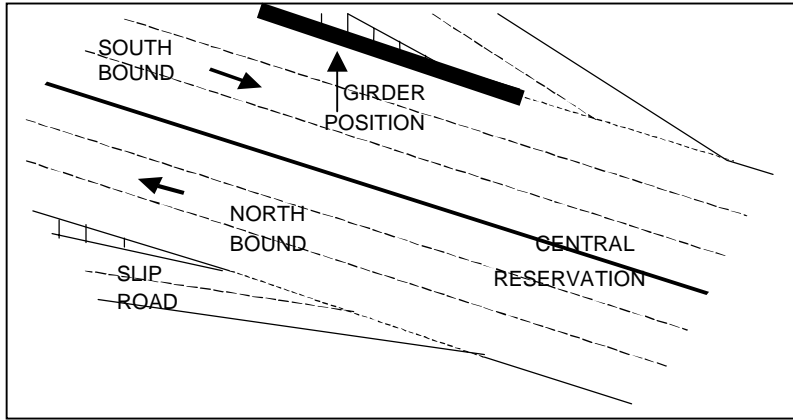


*Fig. 2: Position of box girder.*

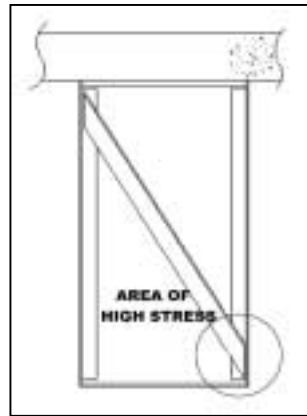


*Fig. 3: Box girder cross section.*

In order to identify any sources in the girder and attachments, the beam was monitored using a semi-global array that gave 100% volumetric monitoring. Two-dimensional location was achieved by “unwrapping” the structure, with damage locations shown on an “opened-up” diagram. Integrity of the cross braces was assessed using linear source location between sensors at either end of each cross brace. An initial AE study identified the expansion joint as a large source of extraneous noise. To filter this noise from the test data, guard sensors were placed to the ends of the girder. One-day trial monitoring in the first week identified 62 sources. Local arrays were set up around the two most active sources.

## RESULTS OF THE TRIAL

From the 62 identified sources, 18 were identified as significant and analyzed in detail. These were all found to be active on a daily basis. All but one of the 18 significant sources were found to be located at the end of the diagonal bracing. The main source “A”, identified by “Semi-Global” monitoring during the first day and subsequently monitored by a local array, is crack like and approximately 250 mm long, as illustrated in Fig. 4. It was located below the end of a diagonal bracing connection at the bottom of the flange. It is difficult to state whether the source is in the internal seal weld or bottom flange/web weld. The absence of emission from the central region of the suspected crack suggests that there is no further growth in this area.

AE activity showed a strong correlation with traffic flow. During periods of peak traffic flow, the average traffic speed dropped and at times traffic was stationary. These periods saw a reduced amount of emission. Most activity occurred when there was a high percentage of lorries travelling at a high speed, 55-65 mph. Figure 5 shows the correlation between strain due to free flowing traffic and AE events detected from the most active source, source “A”.

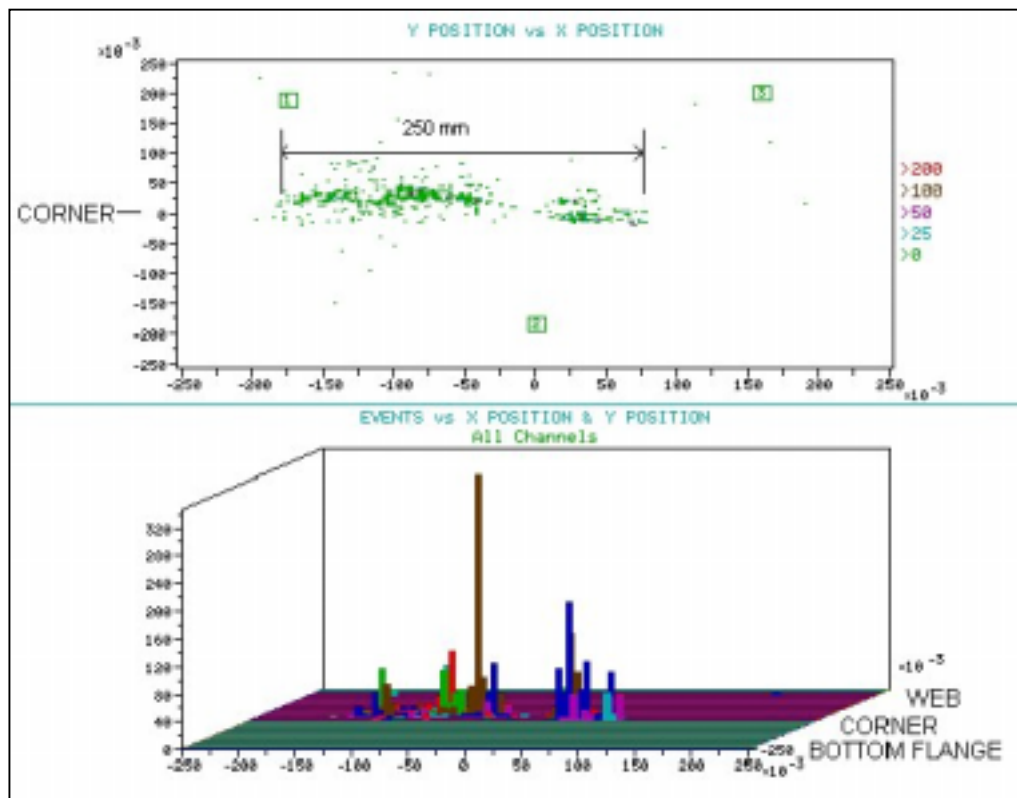


Fig. 4: Local monitoring location graphs for Source "A"; top graph shows activity in 2D, lower graph shows AE activity along the length of the crack like source.

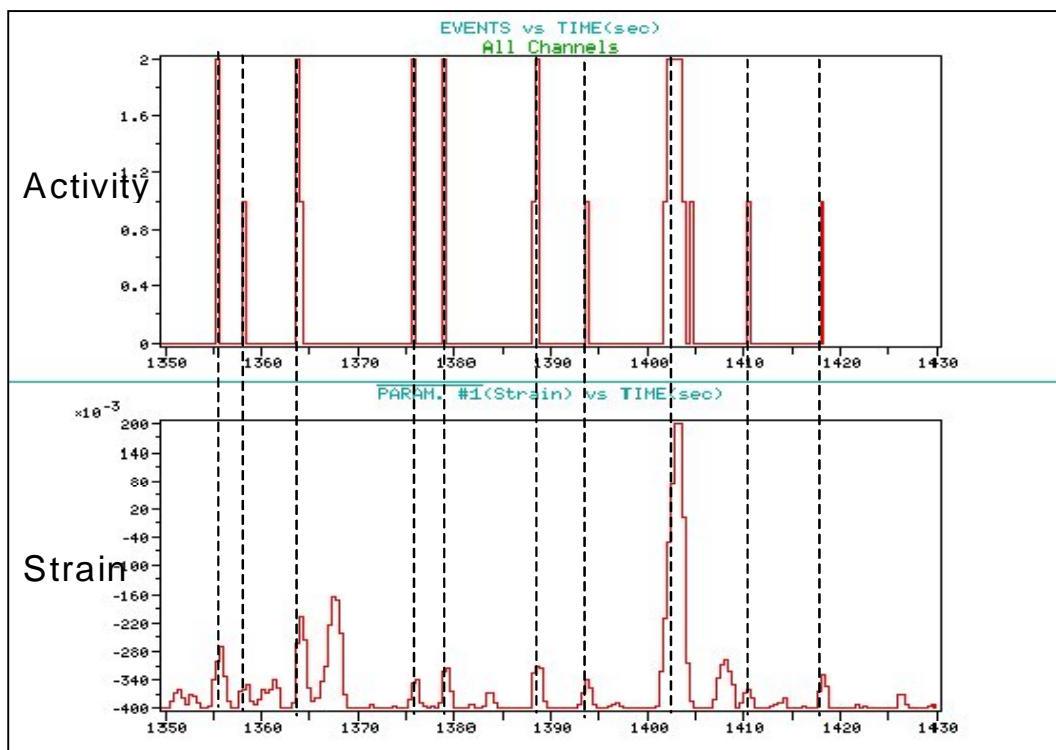


Fig. 5: Correlation between events from Source "A", and strain, over the same time period during peak but free flowing traffic conditions.

## CONCLUSIONS

Acoustic emission monitoring trials on motorway bridges using “Semi-Global” and “Local” sensor arrays have demonstrated that AE is a very effective method for detecting damage in bridges and steel structures, and for continuous monitoring of defect growth. A major advantage is that there is no need for internal access or paint removal. In addition, it is 100% volumetric testing, and damage location is achieved with relatively few sensors. Global monitoring has been developed as a method for identifying damaged structures; further research is being carried out by Cardiff University and Physical Acoustics Limited to develop this method to its full potential.

## REFERENCES

1. Bridle, R., “The Economics of Maintenance, Repair and Strengthening.” TRRL Document 1991.
2. DTp., “Bridge Inspection Guide”, HMSO – Department of Transport, 1984.
3. Russel, H., “Fears for Flyover as Cracks Appear”, New Civil Engineer, pp. 6, 30<sup>th</sup> July 1992.
4. Fowler, D., “Bridge Cracks Paralyse M50”, New Civil Engineer, pp. 5, 13<sup>th</sup> February 1992.
5. Fisher, J.W., “Hundreds of Bridges - Thousands of Cracks”, Civil Engineering, **55**(4), April 1985.
6. Physical Acoustics Corporation, “Acoustic Emission For Bridge Inspection” Report No. FHWA-RD-94, prepared for FHWA and U.S. Department of Transportation, June 1995.
7. Davies, A.W., Holford, K.H., Sammarco, A., “Analysis of Fatigue Crack Growth in Structural Steels by Classification of Acoustic Emission Signals”, Proc. 1994 Engineering Systems Design and Analysis Congress, PD Vol. 64.8.2, Vol. 8, Part B, ASME, USA, pp. 349-354. ISBN 07918-1280-4, 1994.
8. Davies, A.W., Holford, K.H., “Health Monitoring of Steel Bridges Using Acoustic Emission”, Structural Assessment: The Role of Large and Full Scale Testing, Joint Institute of Structural Engineers/City University, E and FN Spon. pp. 54.1-54.8. ISBN 0-419-224-904, 1-3 July 1996.
9. Yan, T., Holford, K., “Acoustic Emission Analysis Using Pattern Recognition Technique”, 23<sup>rd</sup> European Conference on Acoustic Emission Testing, Vienna, Austria, pp. 225-229, 1998.
10. Holford, K.M., Cole, P.T., Carter, D.C., Davies, A.W., “The Non-Destructive Testing of Steel Girder Bridges by Acoustic Emission”. 14<sup>th</sup> World Conference on Non-Destructive Testing, Vol. 4, pp. 2509-2512, ISBN 8120411269, 1996.
11. Carter, D., Holford, K.M., “I.M.A.G.I.N.E: Letting bridges do the talking”, INSIGHT, **38**(11), 775-779, November 1996.
12. Pollock, A.A., Smith, B., “Acoustic Emission Monitoring of a Military Bridge”, Non-destructive Testing, **5**(6), 164-186, 1972.
13. Pullin, R., Carter, D.C, Holford, K.M., Davies, A.W. “Bridge Integrity Assessment By Acoustic Emission - Local Monitoring”, Proc. 2<sup>nd</sup> International Conference on Identification on Engineering Systems, Swansea, pp. 401-409, ISBN 0860761584, 1999.

# **MONITORING FAILURE MECHANISMS IN CFRP ORTHOPAEDIC IMPLANTS DURING FATIGUE TESTING**

**A. TAYLOR, S. GROSS\*, C. ROWLAND<sup>†</sup> and P. GREGSON**  
**Finsbury (Development) Ltd., UK, \*University of Southampton, UK,**  
**<sup>†</sup>Pancom, UK.**

## **ABSTRACT**

*The success of an advanced CFRP hip prosthesis of highly anisotropic design is dependent on having a fundamental insight into its fatigue behaviour. Evaluation of damage under representative complex fatigue loading, conducted at various load levels, has been performed utilising non-destructive acoustic emission testing techniques. It has been demonstrated that the development of failure micromechanisms can be modelled by a discrete stage damage accumulation curve. Specialised feature extractions were generated from static tests and have enabled cumulative damage mode discrimination to be determined throughout the fatigue testing. The acoustic emission results have been correlated with complimentary inspection techniques.*

## **INTRODUCTION**

The design of an articulating hip implant from CFRP is attractive since functionally gradient biological and mechanical properties can be engineered to enhance the implant life. Specifically it is possible to reduce the interfacial shear stresses between implant and host tissue, thereby promoting more natural load transfer to adjacent bone. [1]

The CFRP implants are designed for the more active younger patient and will be subject to higher and more varied activity levels. Testing at the University of Southampton has been designed to simulate this loading. Damage accumulation throughout the fatigue loading is monitored by acoustic emission (AE) techniques. Prior to fatigue testing, AE signatures were determined from static test data to distinguish the various classic damage mechanisms.

The present paper focuses on the AE performance in damage mode recognition and location. It also provides information to formulate a damage development model.

## **METHODOLOGY**

The implant is based on a specifically designed dry carbon preform that accurately defines the complex fibre architecture. This preform combines various carbon fibres in unidirectional, woven and braided material formats to achieve the desired mechanical properties. The method of resin transfer moulding is employed to impregnate the dry carbon to obtain the bio-compatible load bearing implants. This method of production guarantees control over the entire external geometry.

Initial static tests were conducted in an Instron test frame with the implants embedded in a PMMA resin. The loading was applied at a compound angle, compliant with the ISO recommendations [2], to replicate the inclinations of the applied forces found in the body. Damage was monitored utilising a pair of

resonant 375kHz AE sensors during incremental loading. Off loading between steps facilitated detecting the change in Felicity ratio [3] on-line. A hold period at each load was carried out to determine the stability of any damage. All salient parameters of the AE events were recorded for characterisation on an AET5500 acoustic emission monitor.

Fatigue tests were conducted at 64%, 70% and 82% of the average static failure load and with a constant stress ratio of  $R=0.1$ . One sensor was positioned at the mounting interface and the other adjacent to the conic loading area, allowing damage location to be conducted based on the arrival time delay theory. Any signals detected by one sensor only or could not be located between sensors were filtered at the front end. All the AE signals, after passing over a set threshold level and through the valid event location filter, were measured to characterise the time-domain features; these include time of arrival, rise time, amplitude, count, duration and energy. From complimentary NDT methods, characteristic signal parametres were determined, which discriminated between the types of damage. Cross-correlation with micro-section microscopy was also conducted at locations where AE indicated damage.

## STATIC TESTING AND CLASSIFICATION OF DAMAGE MECHANISMS

A series of static tests were conducted in order to characterise and gain an understanding of the evolution of various failure mechanisms and obtain static mechanical data. The specimens tested in incremental steps to ultimate failure, achieved an average load level of 5.5kN. At this load, damage propagated in an increasing unstable fashion. The load level at which the Felicity ratio deviated from 1, indicating the onset of permanent damage, occurred at 90% of the ultimate load (Fig. 5). A clear change in damage mechanism can be observed between the loadings below and above the point where the Felicity ratio deviated from 1, both on the amplitude and energy of AE data (Figs. 1 to 4). Figures 1 and 2 clearly display a change in failure mechanism above 4.5kN with a notable shift in emission amplitude. Figures 3 and 4. Provide supporting evidence of an additional failure mechanism above 4.5kN with a marked shift in quantity and energy of emissions.

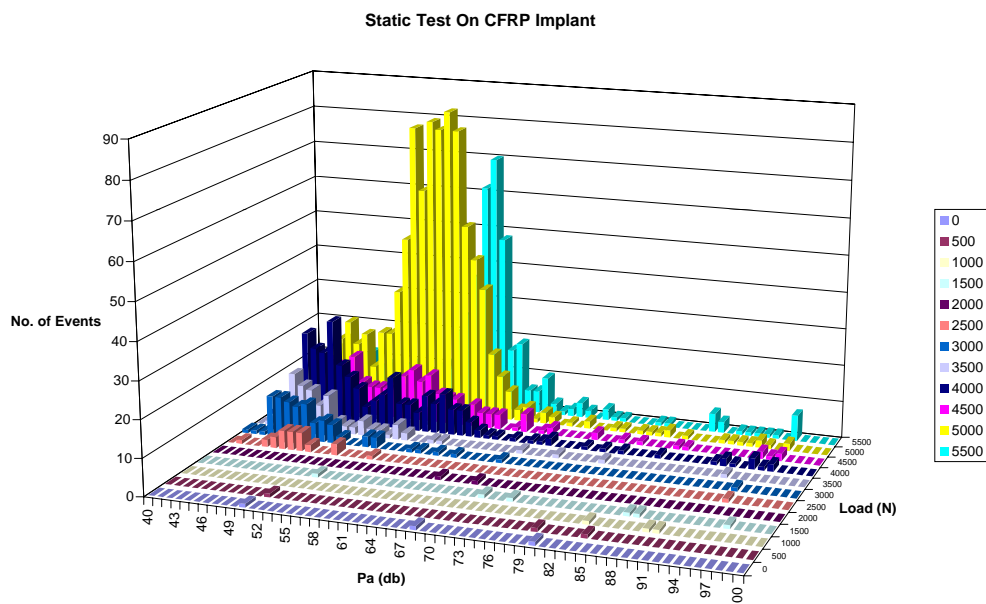


Fig. 1 The amplitude and energy of AE data.

Using intrinsic AE signatures recognised from the preceding specimens, an additional test was successfully terminated just prior to fast fracture (during the hold period at maximum load). The implant was then sectioned to determine the initial damaging failure mechanisms. An additional static test was stopped at a level, where the Felicity ratio was still 1 (80% of the ultimate) and again sectioned. Figure 8

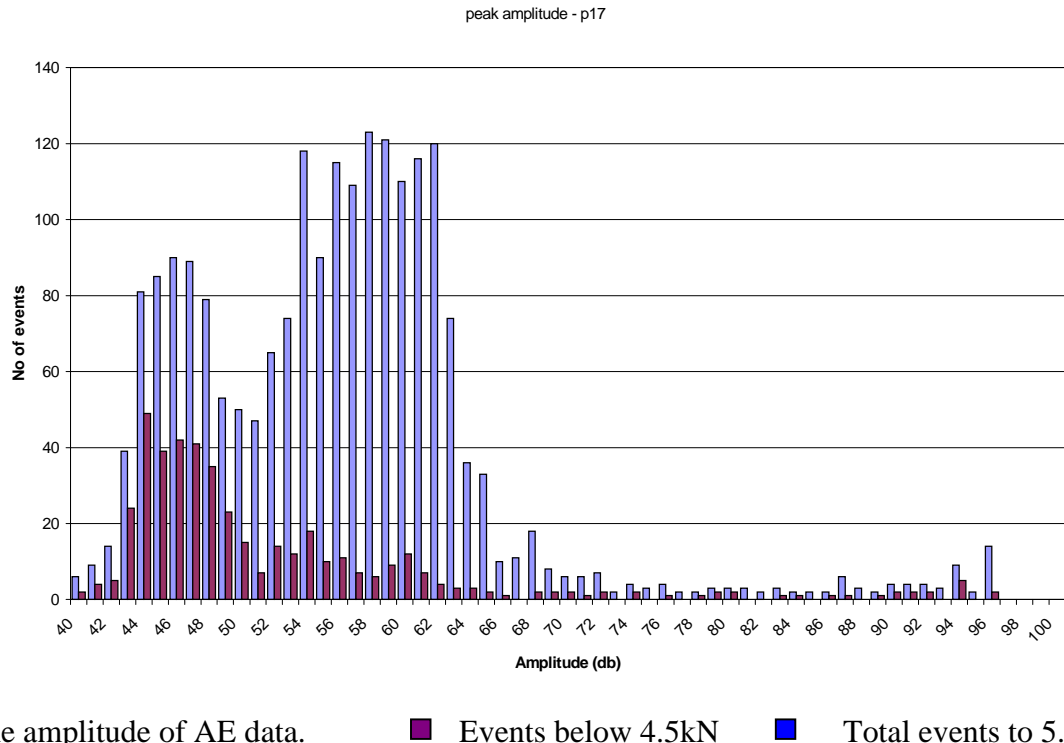


Fig. 2 The amplitude of AE data.

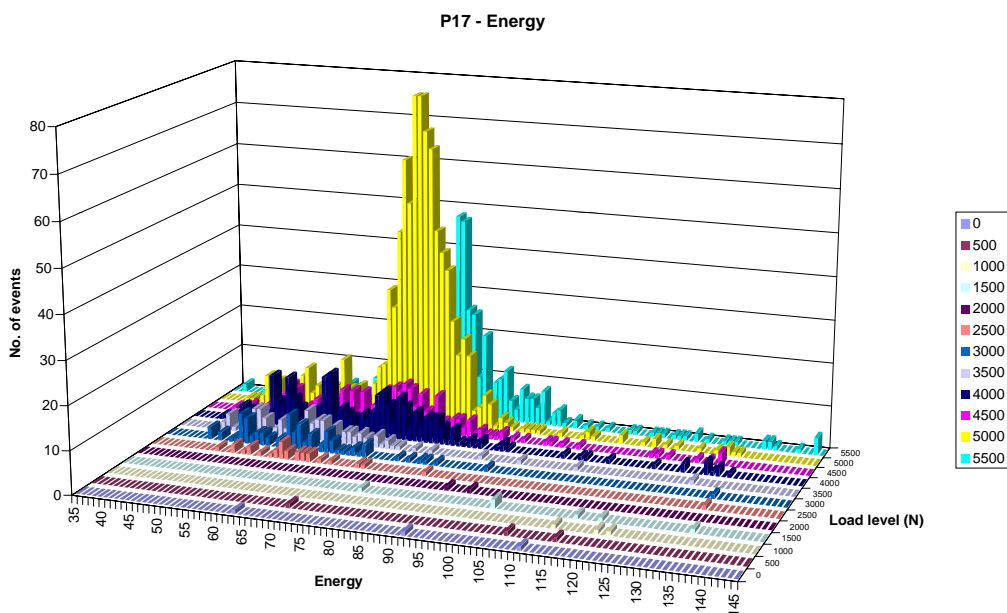


Fig. 3 The energy of AE data.

shows a typical section from the specimen loaded to 80% of the ultimate, displaying microcracking only in the resin-rich areas. This provided a correlation of the AE data (Fig. 6), with the extent of micro-

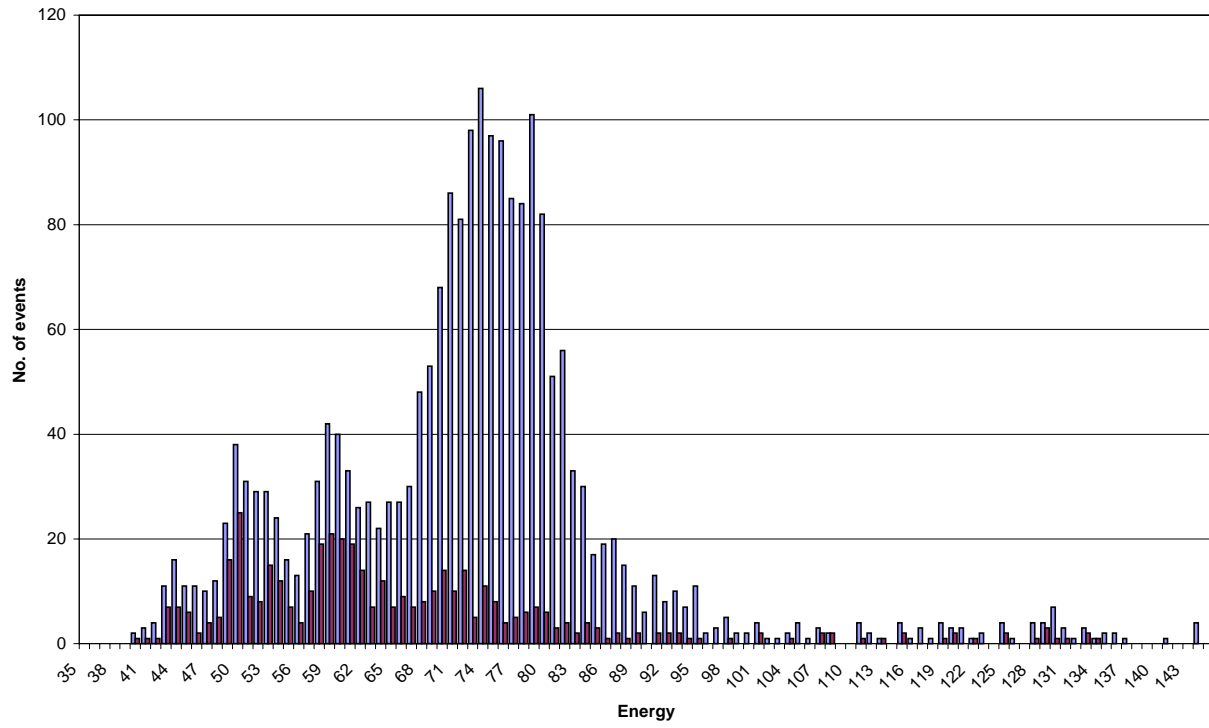


Fig. 4 The energy of AE data.      ■ Events below 4.5kN      ■ Total events to 5.5kN

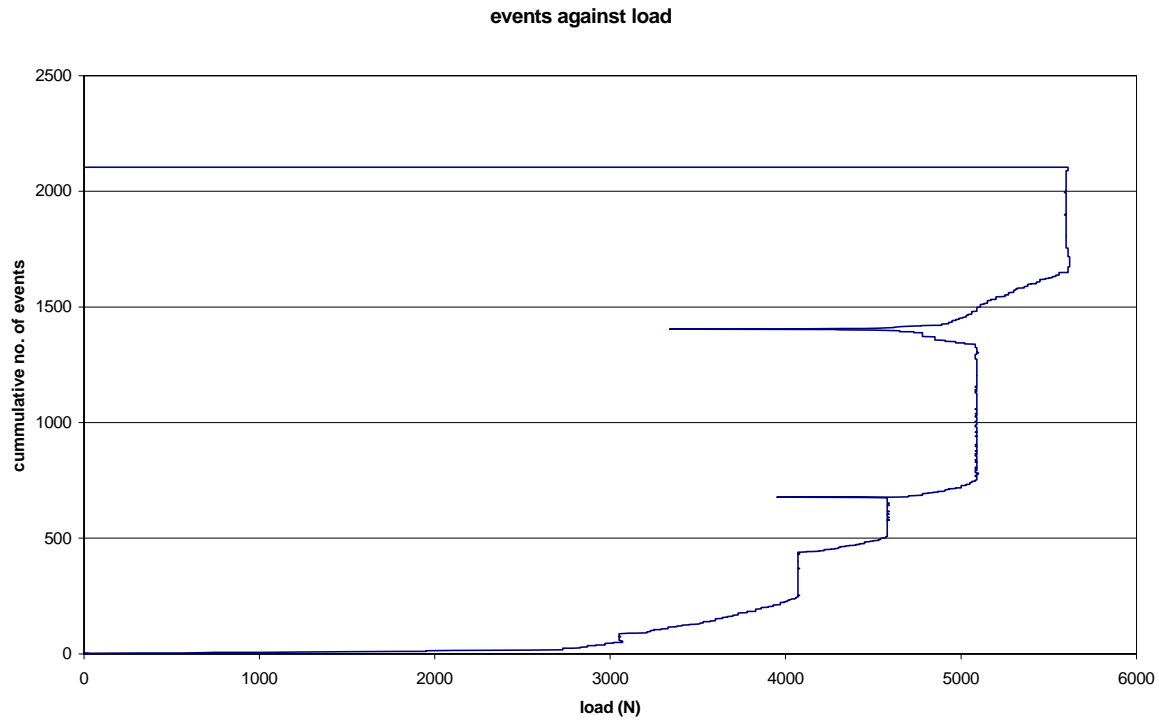


Fig. 5 Graph displaying cumulative events/load history during incremental static load test. The maximum applied load resulting in a felicity ratio of 1 was 4.5kN.

cracking, and also classified and distinguished the evolution of the additional failure mechanisms on previous micro-sections. The initial damage detected during static testing was a result of stable matrix

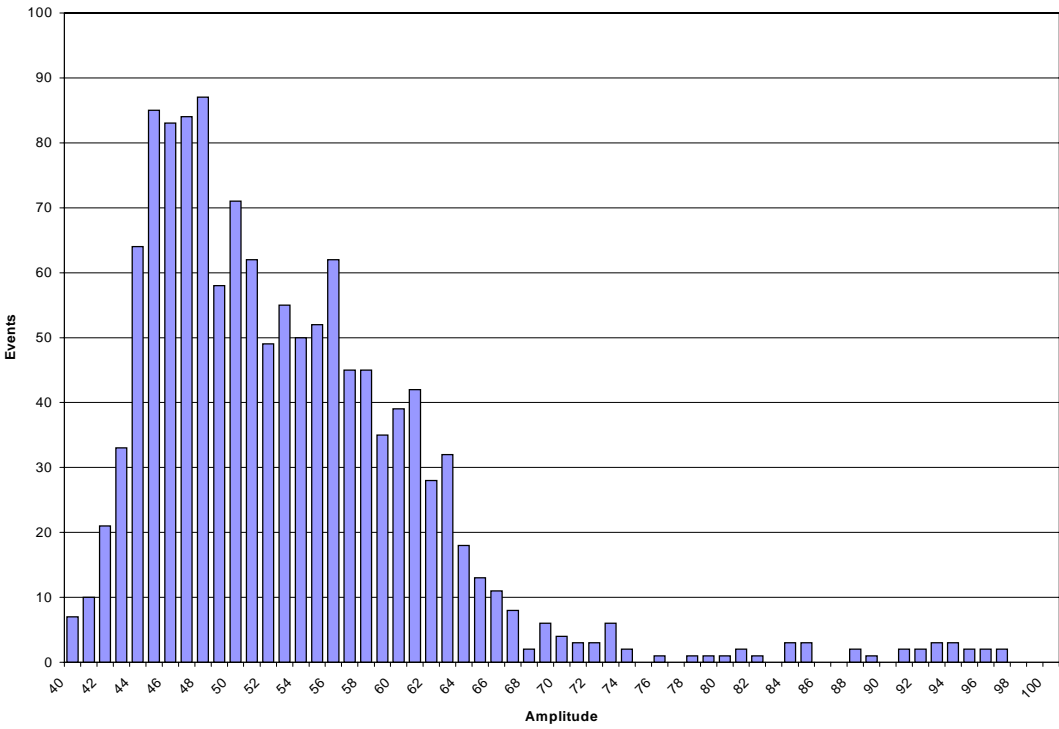


Fig. 6 Display of peak amplitude for a specimen loaded below the point where the Felicity ratio departed from 1 [4.5kN].

micro-cracking at the position of maximum stress adjacent to the implant mounting; these occurred early in the test and then diminished.

The relatively compliant PMMA-resin potting medium to implant interface also emitted emissions throughout the loading history as a result of a tensile/shear failure, and subsequent friction on the proximal implant surface and a creep/bearing failure at the distal location. These emissions predominantly occur on the unloading section of the incremental static test. A small degree of micro-cracking was observed on all the tested specimens and this correlates well with the lower amplitude emissions centred around 46dB. Figure 7 displays the onset of delamination between tows in resin rich areas and microcracking observed in the implant. These delaminations then propagated to form the trans-tow macro-cracking observed in Fig. 9. This permanent damage results in the Felicity ratio dropping below 1. This failure propagation mechanism resulted in acoustic emissions centering around 60dB.

## THE RESULTS OF THE FATIGUE TESTING

In order to record only useful data and make post-test analysis more efficient, a filter was set up to monitor events occurring during approximately 90% of the sine-wave fatigue cycle using a voltage-control gate. This eliminated most of the noise generated at the lowest load due to the movement at the potting interface.

A series of fatigue tests were conducted employing the same fixture configuration as with the static tests but at various load amplitudes. These established the signal/noise characteristics of the implant design and the fatigue threshold level of the implant (Fig. 12). With the cyclic tests loaded above the fatigue

threshold, and using the AE signatures recorded from the static tests, it was observed that damage initially developed with matrix cracks propagating to form stable delamination growth in the critical section. Evidence to support this theory can be gained from Fig. 10, which displays the striations left on a typical fracture surface along resin-rich areas in planes orthogonal to the loaded fibres. Figure 11 displays the AE amplitude-event history throughout the test that can be compared to those obtained from the static tests. As a result of this failure mechanism, the local stress distribution adjusts with the effect of superimposing additional matrix micro-cracking into the AE data as was observed in Fig. 11.

Once the local delaminations propagated due to continued cycling, friction-induced emissions were generated as the fracture surfaces rubbed against each other, this being most prominent on the unloading section of the cycle. These initial two stages dominated the useful life of the implant as can be observed in the discrete stage damage accumulation curve in Fig. 13. Stage 1, resulting from micro-cracking and the resulting propagation to form delamination in resin-rich areas adjacent to fibre tows. This produces cumulative events linearly increasing with cycle count. The number of micro-cracks and delamination initiation sites continue for approximately half the life of the specimen until the density promotes delamination to propagate. The result is the second stage displayed by the prominent increase of slope. This continues for the remaining life of the specimen until rapid final failure, stage 3, which occurs in the final few cycles. The rapid failure is characterised by a short burst of high amplitude, 92dB, emissions at the end of the test, Fig. 11.

In contrast to the predictable delamination propagation, the damage growth just prior to the final failure (stage 3) was very short consisting of fibre breakage and gross delamination making prediction of imminent failure difficult. Bursts of acoustic emissions with very high amplitude and duration dominated the stage. This stage is difficult to observe in Fig. 13 due to the very short duration.

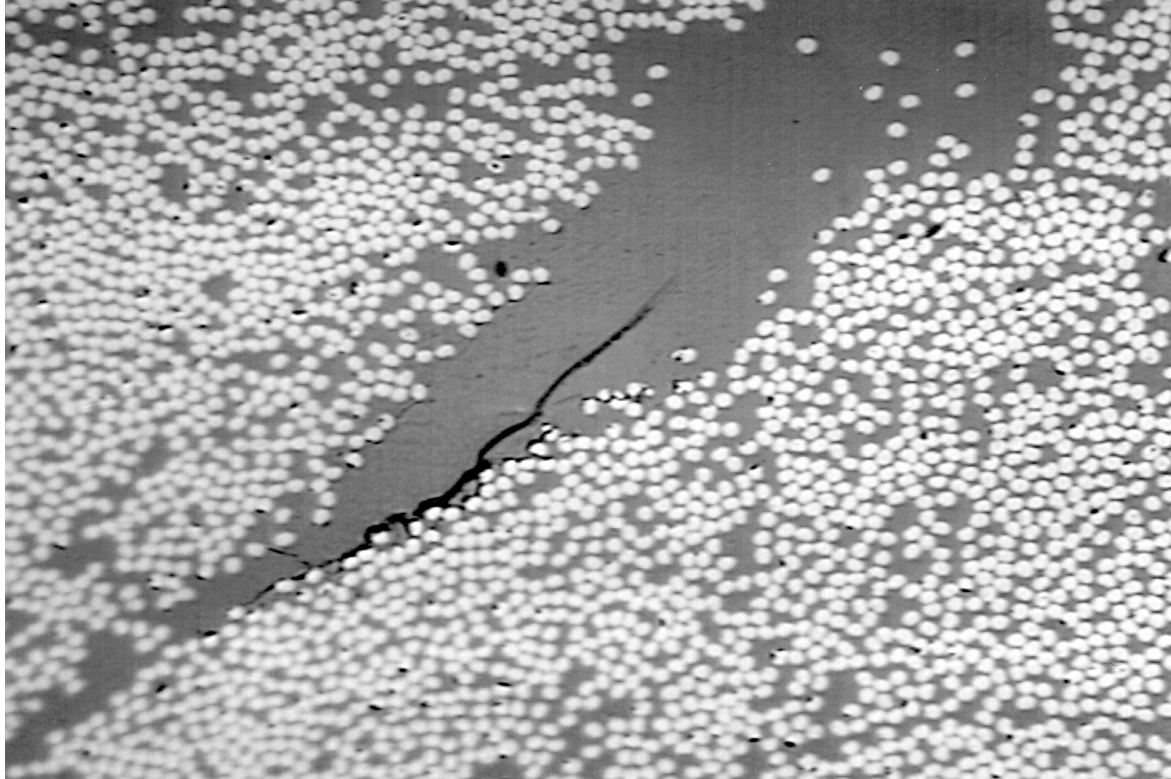


Fig. 7 Delamination in resin rich area and microcracking observed in samples before onset of permanent damage.

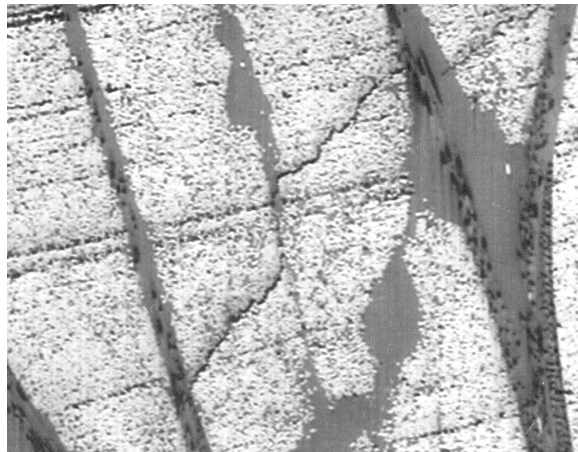


Fig. 8 Areas of high resin concentration often exhibit cracking prior to permanent damage. The initial microcracking, delamination and resin crack propagation in these areas result in an AE distribution centred around 46 dB.

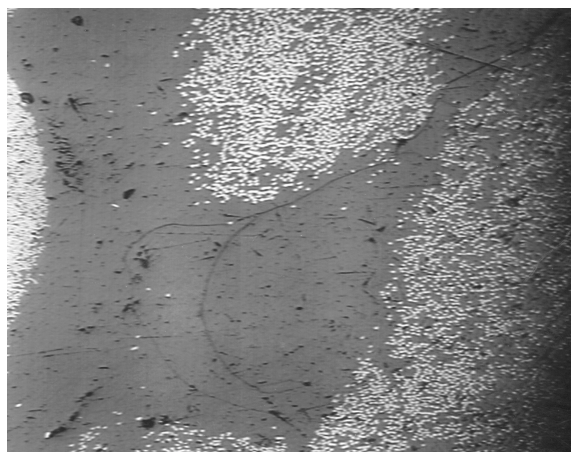


Fig. 9 Transtow macrocracks found when the Felicity ratio drops below 1, which during testing is characterised by an acoustic emission amplitude distribution centred around 60 dB.

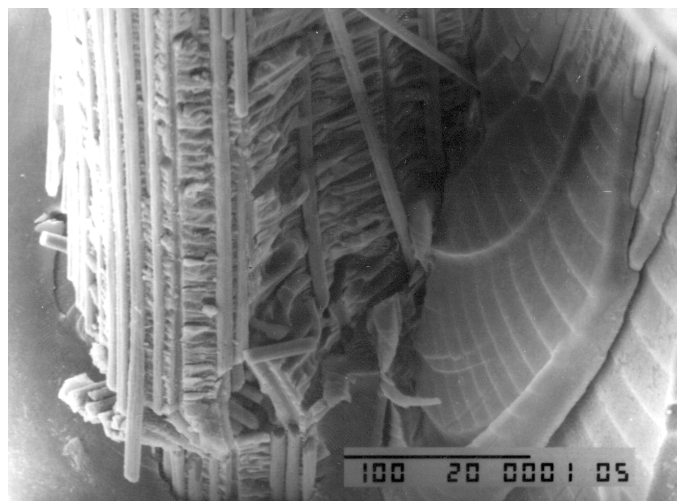


Fig. 10 Scanning electron microscope view of the striations found in the resin rich areas adjacent to the fibre tows.

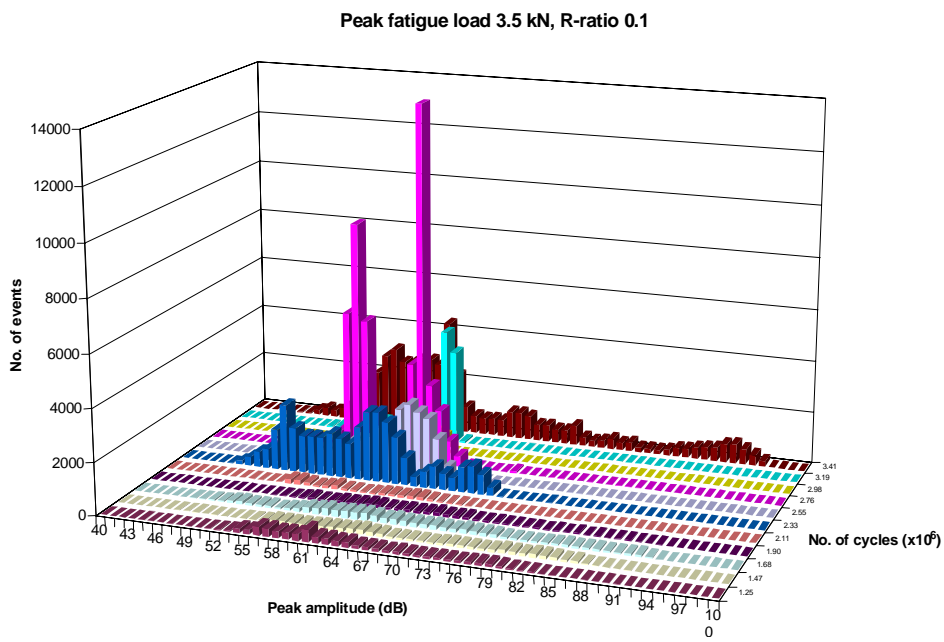


Fig. 11 AE response during a typical fatigue test displaying similar signatures to that observed during the static investigations.

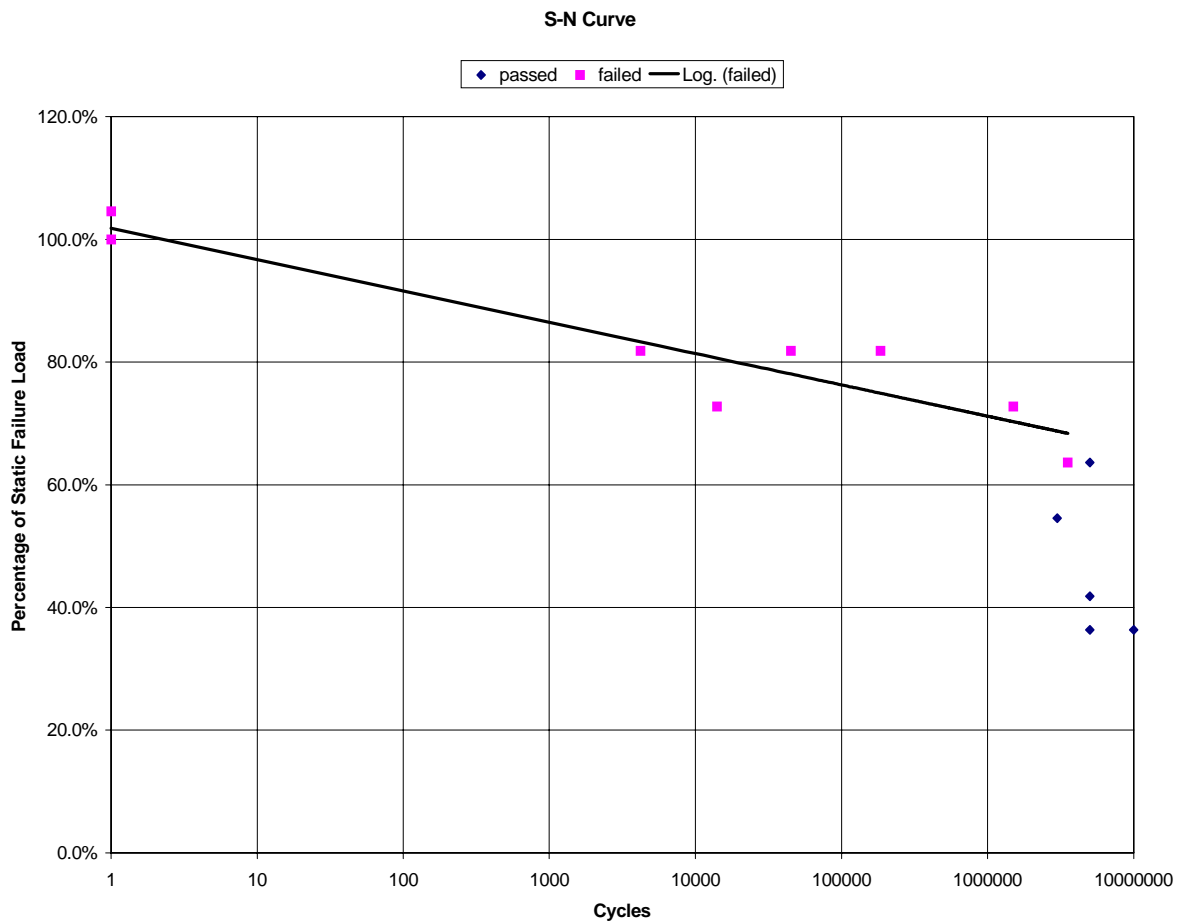


Fig. 12 S/N curve generated from the implant test program.

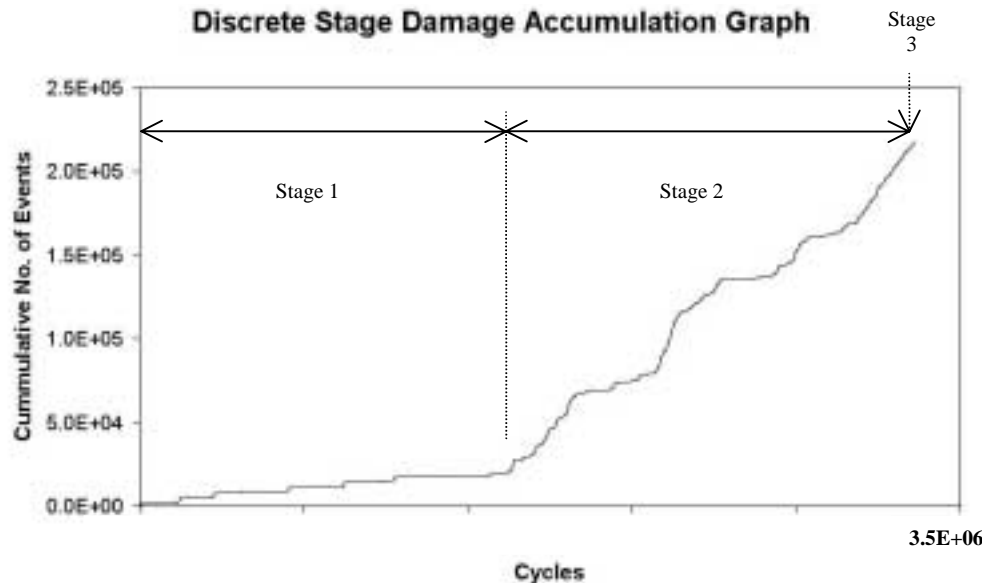


Fig. 13 AE fatigue test history graph. The onset of stage 2 damage propagation is accompanied by a distinct change in event rate. This would coincide with the point at which the Felicity ratio departed from 1.

## CONCLUSIONS

The use of acoustic emission health monitoring throughout this research has established the following:

- The characterisation and recognition of damage mechanisms.
- A reliable method for terminating a test prior to final catastrophic failure, to enable the fundamental initiation sites to be identified.
- The ability to detect the onset of permanent component damage by observation of the Felicity effect.
- A discrete three stage progressive damage accumulation mechanism is observed in fatigued specimens.

The CFRP implants displayed good fatigue immunity with a resulting threshold level equating to 70% of the average initial static failure load. The failure mechanisms observed in the fatigue investigation with corresponding AE data matched that of the static testing very well.

## REFERENCES

- [1] Evans, S.L., Gregson, P.J., Doherty, P.D., Osei, D., Revell, P.A., Taylor, A., Tuke, M.A., The design, development and testing of a novel femoral component using advanced composite technology. 5<sup>th</sup> World Biomaterials Congress, Toronto, 29 May – 2 June 1996; 2, p. 795.
- [2] ISO 7206-4 Implants for surgery – Partial and total hip joint prostheses – part 4: Determination of endurance properties of stemmed femoral components. 1997.
- [3] Hamstad, M.A., A Discussion of the Basic Understanding of the Felicity Effect in Fiber Composites. Journal of Acoustic Emission, 5(2), 95.

# CONTINUOUS MONITORING OF ROCK FAILURE BY A REMOTE AE SYSTEM

**Tomoki SHIOTANI, Shigenori YUYAMA\*, Mark CARLOS<sup>†</sup>, Sotirios J. VAHA VIOLOS<sup>†</sup>**

Tobishima Corporation, Chiba, Japan. \*Nippon Physical Acoustics Ltd., Tokyo, Japan.

<sup>†</sup>Physical Acoustics Corporation, Lawrenceville, NJ, USA.

## SUMMARY

*In Japan, rock failure is one of the most frequent disasters. Because rock materials are brittle, deformation due to micro to macro fracture is thought to be transient phenomenon. Acoustic emission known as a premonitory phenomenon is expected to be useful for prediction of eventual rock failure. In order to perform stable AE monitoring to evaluate rock failure, a remote AE system by modem communication has been successfully developed for continuous rock failure monitoring in field. A prospective method to install AE sensors into the rock slope (WEAD) has also been developed. A series of studies on the WEAD are conducted for evaluation of AE signals in the laboratory. Based on the experimental results, criteria for classifying fracture states are proposed. The remote AE systems have been used at three sites in field for monitoring rock slope failure for about two years. The proposed criteria for the fractures are applied to the field data and fracture state are evaluated comparing with internal slope behavior estimated by displacement, borehole-strain, temperature and so forth. Thus, the applicability of the remote AE system for continuous monitoring of rock failure with WEAD is demonstrated.*

## INSTALLATION OF AE SENSORS

In the case of AE monitoring in rock slope, effective detection of AE waves generated due to deformation of rock is usually difficult because AE waves are strongly attenuated when they propagate through joints of rock. In geotechnical application of the AE technique, to avoid energy attenuation of AE waves, waveguides are often employed to detect AE signals (Hardy and Taioli, 1988; Nakajima et al., 1988). There are two types of the waveguides. One is low-attenuation type of waveguides devised to lead weak AE signals to AE sensors. Metallic materials are generally adopted as the low-attenuation type of waveguides. Another is deformation-related waveguides designed to generate self-emissions due to deformation of the guide corresponding to the rock motion. Several types of rosin, fiberglass, PVC with sand, PVC with water, and so on, are employed as the self-deformation waveguides. The latter waveguides, however, are devised on soil materials, which have relatively ductile nature compared with rock materials. Thus, applications of these waveguides to rock materials are thought to be difficult. Desirable conditions of waveguide for rock materials are as follows: (a) AE waves can propagate up to the AE sensor to avoid strong attenuation influenced by rock conditions. (b) The characteristics of AE waves detected should reflect actual fracture mechanisms. (c) The stability of the rock slope can be reasonably evaluated by the AE signals acquired.

In order to meet the above conditions on the waveguide for rock materials, WEAD (waveguide for AE waves due to rock deformation) has been developed. The WEAD consists of cementitious materials and reinforcement with AE sensors. In the WEAD, borehole excavation is performed to install the AE sensors and to obtain mechanical properties of the rock. Mixture proportion of cementitious materials is

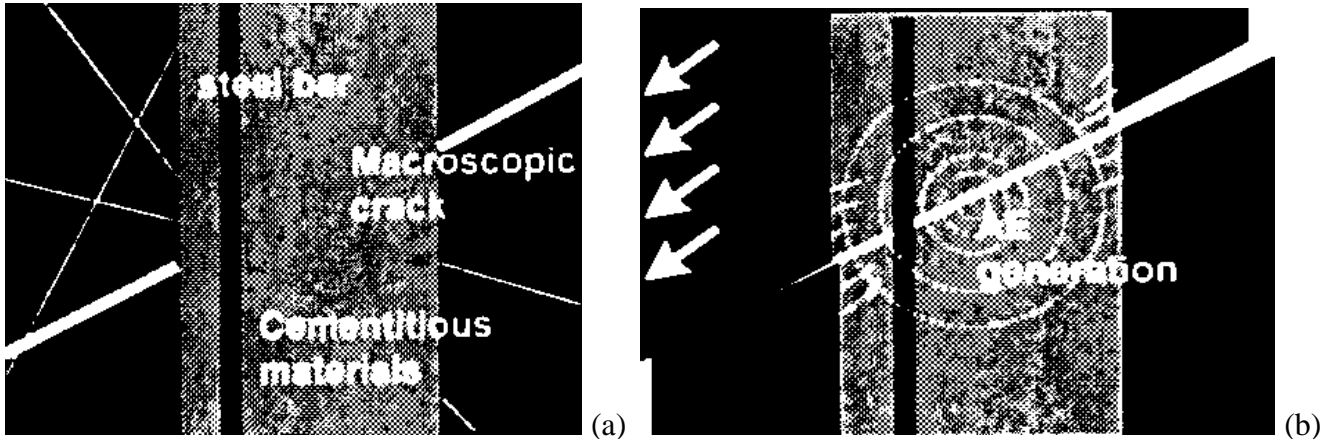


Fig. 1. Behavior of WEAD under deformation of rock. (a) Before. (b) After deformation.

designed with reference to the mechanical properties of core samples retrieved. Figure 1 shows behavior of the WEAD under deformation of rock. With the deformation of the rock, the WEAD simultaneously deforms along with the rock, and then AE wave is generated within the cementitious material. Fracture of the WEAD occurs similarly to those of the deformed rock. As a result, characteristics of the AE waves would be compatible to those due to actual rock deformation. Because initial state of the WEAD is intact, AE waves generated can efficiently propagate to the AE sensors. The WEAD can have other advantages. Because filler of cementitious materials in the borehole is mixed from cement, sand and chemical admixtures, AE characteristics of the filler can be experimentally obtained. Thus, comparing field data with empirical data, fracture state of the rock can be readily evaluated.

In the case that the WEAD contained many cracks due to damage, the rock conditions would be similar to those of surrounding rock. It may result in the difficulty to detect AE signals effectively. To solve this problem, reinforcement of steel bar is installed into the borehole with AE sensors. AE signals subsequent to the local motion would be detected until final failure with the reinforcement. It is noted that these AE waves may have nothing to do with the actual fracture mechanism of rock. However, AE counting and AE parameters could provide reasonable information on the fracture state. Figure 2 shows characteristics of wave attenuation in grouting materials with or without reinforcement. Also in the figure, results of the filler fractured by bending and shear are shown. Properties of the filler are discussed in the next session. The grouting material (filler) with reinforcement has more effective propagation characteristic than that without reinforcement. Even in the cases of the grouting materials failure, those propagation characteristics are comparable to that without reinforcement. Thus, the reinforcement plays an important role in the WEAD.

## **EXPERIMENTAL STUDIES**

In a monitoring site of rock failure, boreholes are excavated to investigate crack conditions and to determine mechanical properties. To make the strength of the grouting material compatible to the rock, to develop the strength promptly and to ensure high workability, grouting materials of fast-curing type are employed. Chemical components of  $\text{CaO}$ :  $\text{SiO}_2$ :  $\text{Al}_2\text{O}_3$ :  $\text{SO}_3$  are 51.5: 26.9: 11.8: 2.6 by weight. Beam-type specimens of dimensions 10 cm x 10 cm x 100 cm with reinforcement of 13 mm diameter installed in a neutral axis were cast. These specimens were moisture-cured in water for 28 days in the standard room ( $20^\circ\text{C}$ ). Figure 3 illustrates both bending and shear tests along with the arrangement of AE

sensors. These two types of failure tests were conducted by four-point loading. Ten AE sensors (60 kHz resonance) were set on the specimen in the bending, while eight AE sensors (60 kHz resonance) were used in the shear test.

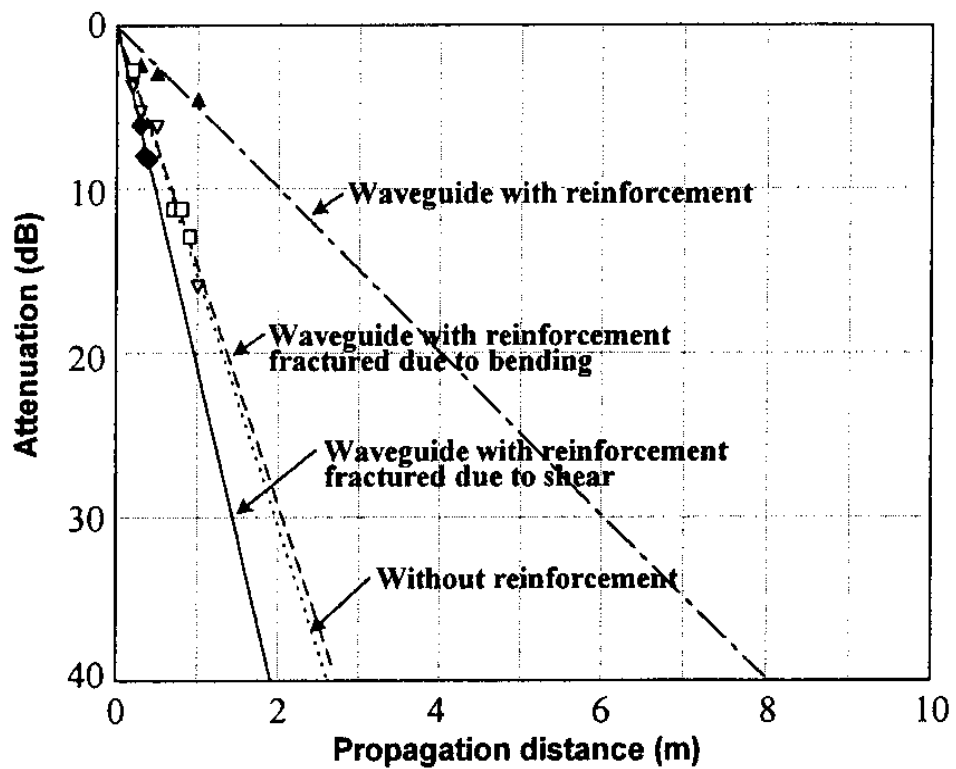


Fig. 2. Characteristics of wave attenuation in the waveguides.

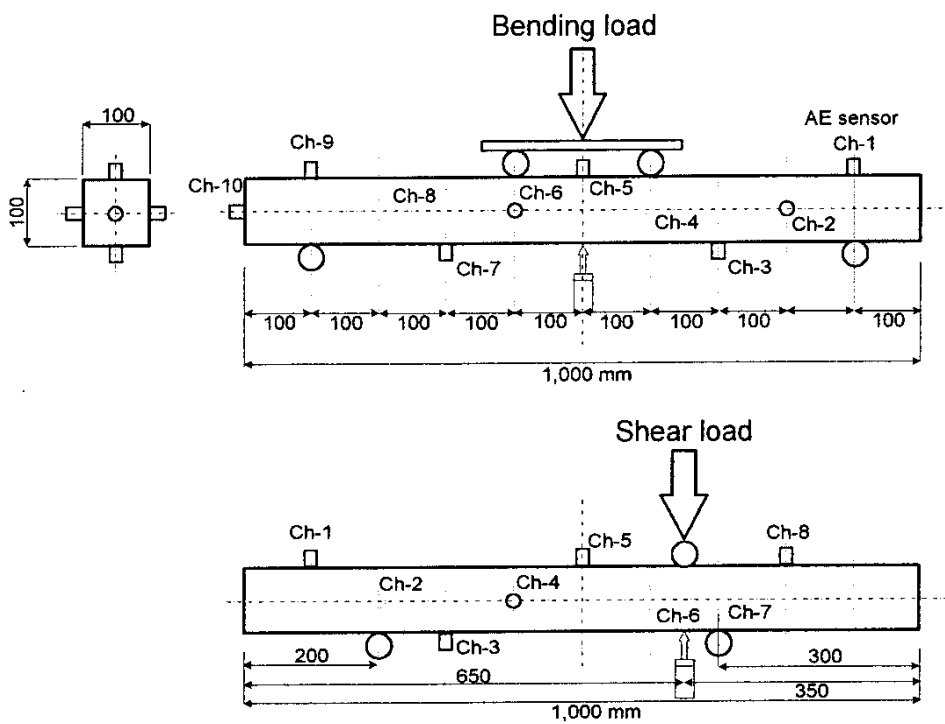


Fig. 3. Illustrations of bending and shear tests and arrangement of AE sensors.

AE signals over 40 dB were recorded as AE waves by a MISTRAS AE system (PAC). Classical AE parameters were also analyzed. Using sets of AE signals from more than six independent channels, AE sources were located in three-dimension. Applied load and deflection of the specimen were also measured.

## Results and discussions

Figure 4 shows averaged AE (ringdown) counts of the latest 100 data sets until the final failure. The dotted lines in Fig. 4 show the elapsed time reached 100 data sets. In both bending and shear tests, stable increase of the AE counts could not be observed. In the case of bending, the averaged AE counts less than 20 may imply the fracture state transferred from early stage to intermediate stage. The AE counts of the final stage would be from 20 to 30. In the result of shear test, the averaged ringdown counts ranged from 40 to 50 over the whole fracture stages.

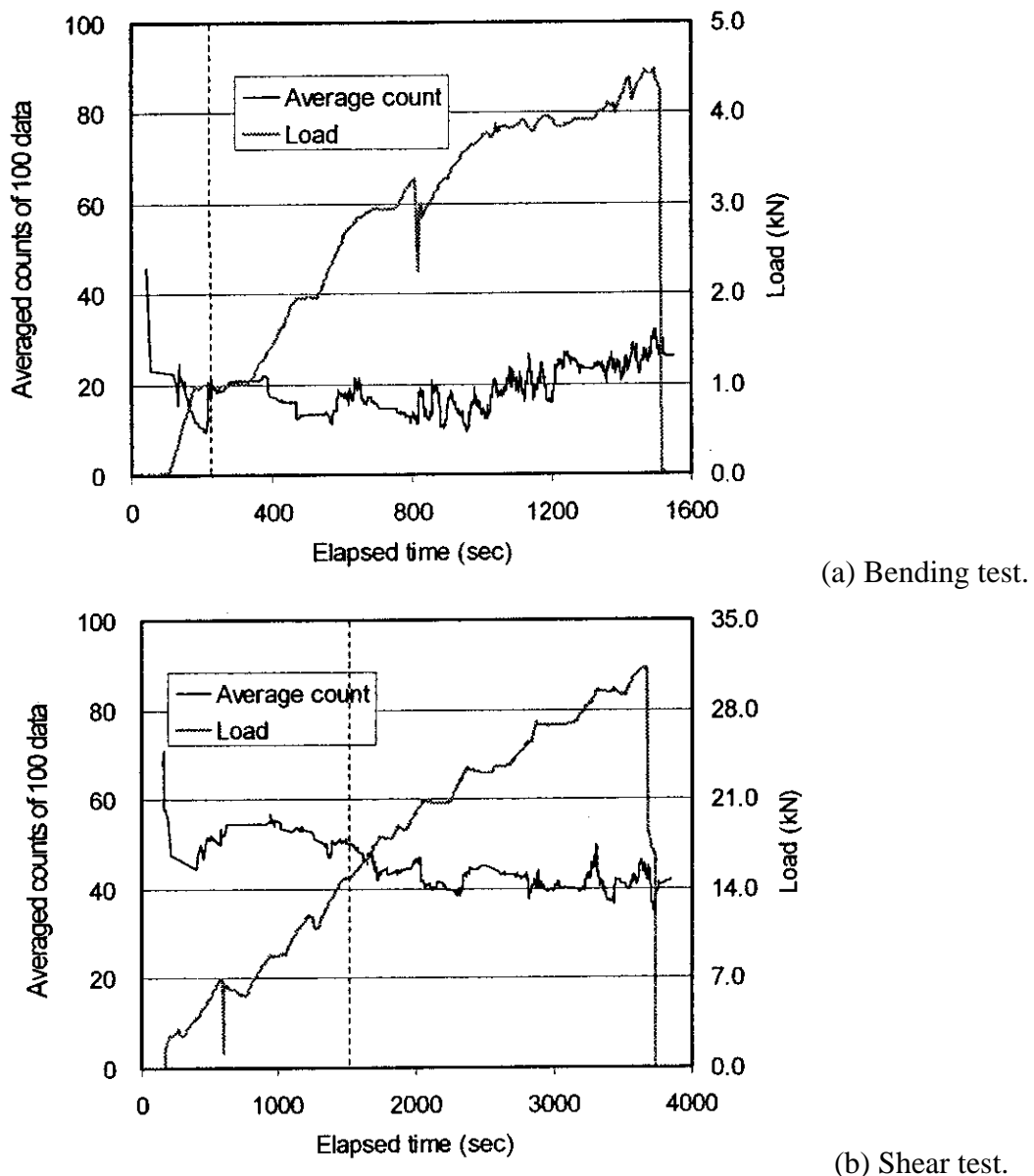


Fig. 4. Averaged AE (ringdown) counts of the latest 100 data sets until the final failure.

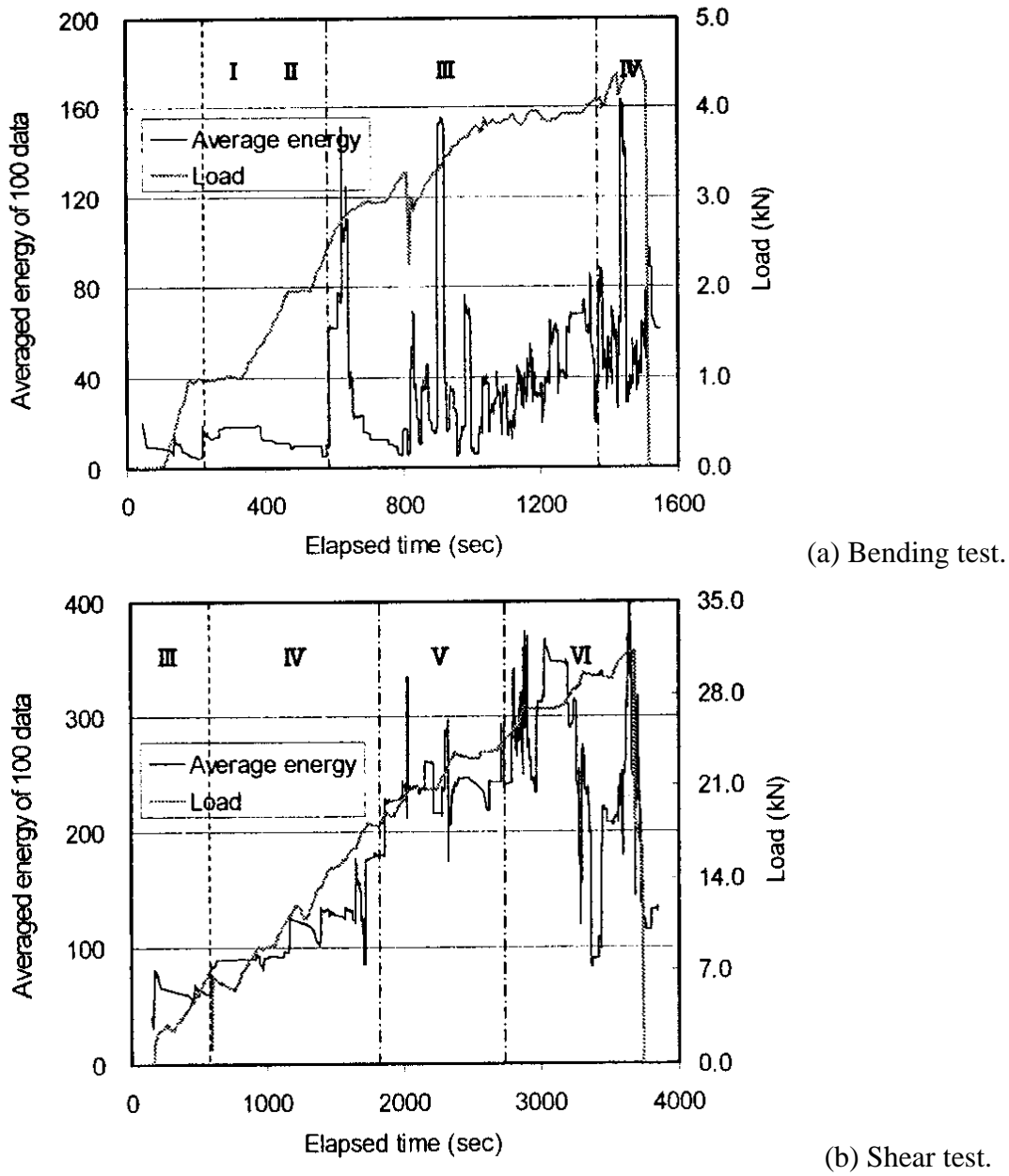


Fig. 5. Averaged energy counts of the latest 100 data sets until the final failure.

Figure 5 shows the averaged energy counts of the latest 100 data sets until the final failure. The energy counts are defined by the area of a rectified AE signal envelope, and is known as a parameter, which is closely related to the energy of AE sources. In the result of bending, it is found that energy counts in the early stage of fracture are less than 20. This is when mortar cracks would be generated in the specimen. The energy counts ranging from 20 to 40 are thought to represent the intermediate stage of fracture, although sudden increase up to 160 and a decrease are observed. In the intermediate stage of fracture, bond fracture between reinforcement and mortar would be generated. In the final stage of fracture suggesting crack coalescence and crack growth, the averaged AE energy counts of over 40 is observed. In the case of shear, it is obvious that the averaged energy counts successively increase up to the final fracture level. This implies that the average energy counts of 80, 200 and 300 would become the criteria to classify the fracture stages.

Because AE amplitude is associated with the magnitude of fracture, the b-value that is defined as a slope of the amplitude distribution is known as an effective index related to the fracture states (Mogi, 1964; Sholz, 1968). In order to apply the b-value to the AE technique, improved b-value is proposed (Shiotani et al., 1994). The improved b-value has successfully been applied not only to geotechnical materials (Shiotani and Ohtsu, 1999a; Shiotani et al., 1999b) but also to concrete materials (Shiotani et al., 1999c). Because the b-value is originally defined in seismology, it is difficult to determine the amplitude range and the number of AE data to obtain the proper b-value in AE application. The improved b-value is defined by utilizing such statistical values of the amplitude distributions as mean,  $\mu$ , and standard deviation  $\sigma$ . The improved b-value ( $I_b$ ) is proposed by,

$$I_b = \frac{\log_{10} N(w_1) - \log_{10} N(w_2)}{(\alpha_1 + \alpha_2)\sigma}, \quad (1)$$

where  $N(w_1)$  is the accumulated number of AE events, in which amplitude is more than  $\mu - \alpha_1$ ,  $N(w_2)$  is those of AE events, in which amplitude is more than  $\mu + \alpha_2$ ; and  $\alpha_1$  and  $\alpha_2$  are constants. Then, the amplitude range is given by  $(\mu - \alpha_1 + \alpha_2)$ . To compare with the seismic b-value, the improved b-value above should be multiplied by twenty.  $n(a)$  in equation (2) is the total number of AE events when the improved b-value analysis is performed.

$$\int n(a)da = \beta. \quad (2)$$

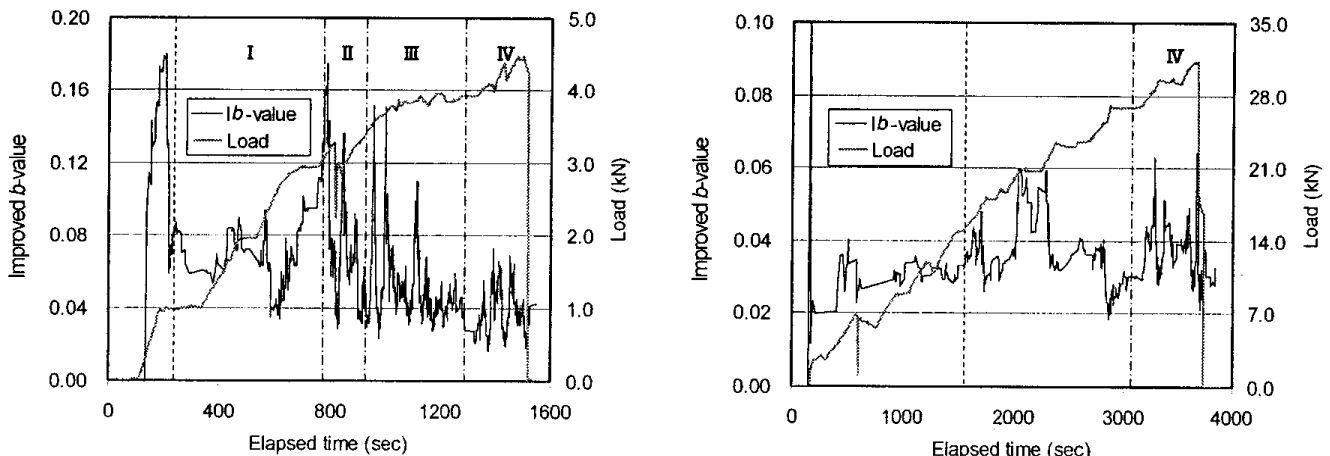


Fig. 6. Improved b-value due to bend and shear tests until the final failure.

Figure 6 shows the improved b-value due to bending and shear loads, where  $\alpha_1 = 1$ ,  $\alpha_2 = 0$  and  $\beta = 100$  are employed. Dotted lines in the figure represent the elapsed time when AE events reached  $\mu$ . In the result of bending, the improved b-value reached 0.17 in the intermediate stage of fracture, then it sharply dropped to 0.04. Afterwards, with progressing to the final stage of fracture, it rises and drops repeatedly ranging from 0.04 to 0.15. Finally, the variation becomes smaller between 0.02 to 0.06. In the result of shear, the improved b-value perpetually changes in the narrow range from 0.02 to 0.06 over the whole fracture stage. This implies that continuous fluctuations of the improved b-value from 0.02 to 0.06 correspond to the fracture stage where shear-type of fracture is more dominantly generated than tensile-type of fracture. Based on the experimental results, the criteria of fracture levels suggested are summarized as Table 1.

Table 1. Criteria of fracture level based on the experimental results.

AE parameters			Evaluated fracture level	Evaluated types and states of fracture (B: bending, S: shear E: early, I: intermediate, F: final)
Ringdown count	Energy count	Improved <i>b</i> -value		
-20	-20	increase up to 0.15	I	E in B, generation of mortar cracks
	20-40	decrease down to 0.04	II	I in B, bond fracture between reinforcement and mortar
20-40	40-80	repetition between level I and level II	III	F in B, crack coalescence and crack growth
40-	80-200	vary from 0.02 to 0.06	IV	L in B and E in S, nucleation of shear planes
	200-300		V	I in S, micro to macro fracture on shear planes
	300-		VI	F in S, macro fracture on shear planes

## APPLICATIONS

Geologically, a monitoring site is made of hornfels. The monitoring slope dips with angle of 80°. In the slope, it is observed that many diagonal joints are lying perpendicular to the slope surface. After removal of unstable rocks for disaster prevention, AE monitoring was performed with the WEAD. Making reference to mechanical properties of rock, grouting material, which is previously discussed, was used for the WEAD. Figure 7 shows the sensor arrangement and the joint condition. Five AE sensors (60 kHz) equally spaced on reinforcement 13 mm diameter by 1.5 m were installed into the slope and one AE sensor (60 kHz) was placed at control room to monitor background noise. To eliminate undesirable emissions due to natural phenomena induced by rain, sunshine and wind, a surface portion of the borehole was filled with sand down to 1.0 m. AE signals generated from the slope were amplified 40 dB at sensor-integrated preamplifiers, and the signals over the threshold 40 dB were acquired in a remote AE system (PAC). To collect data and to change test conditions remotely, an AE system with a modem connection was developed and deployed. A seismometer, crack gauges in three dimensions and borehole strain gauges were also set in the slope.

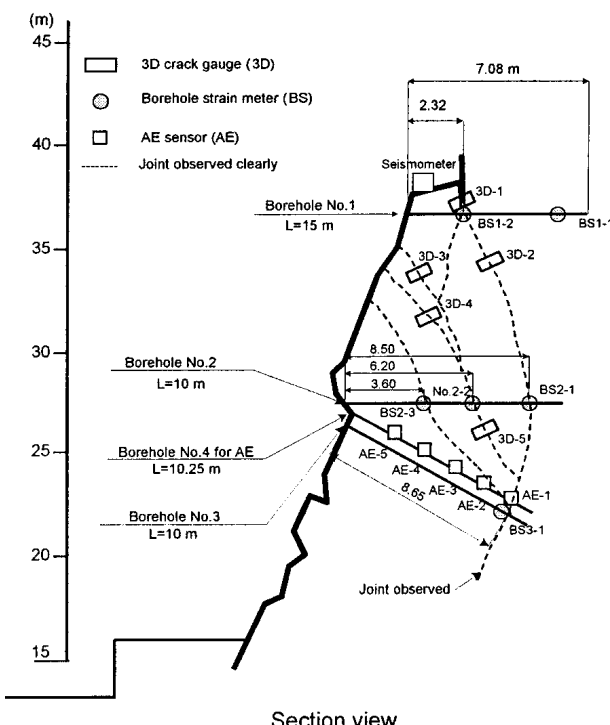


Fig. 7. Sensor arrangement in monitoring slope.

## **Results and Discussion**

AE activity between March and September 1999 is shown in Fig. 8, although AE monitoring is still in progress. Because AE activity during six months was mostly of the same trend at all sensors, only results of AE-4 are shown in Fig. 8. Figure 8(a) exhibits the averaged ringdown counts of the latest 100 data sets. A dotted line in the figure denotes the elapsed time reached when data number reaches 100. It is observed that the averaged ringdown counts stayed around 10. Thus, fracture level of the site was evaluated as level I/II from Table 1. Figure 8(b) shows the averaged energy counts. The same trend as the ringdown counts was confirmed. Because the averaged energy counts varied around 10, fracture level was evaluated as level I from the table.

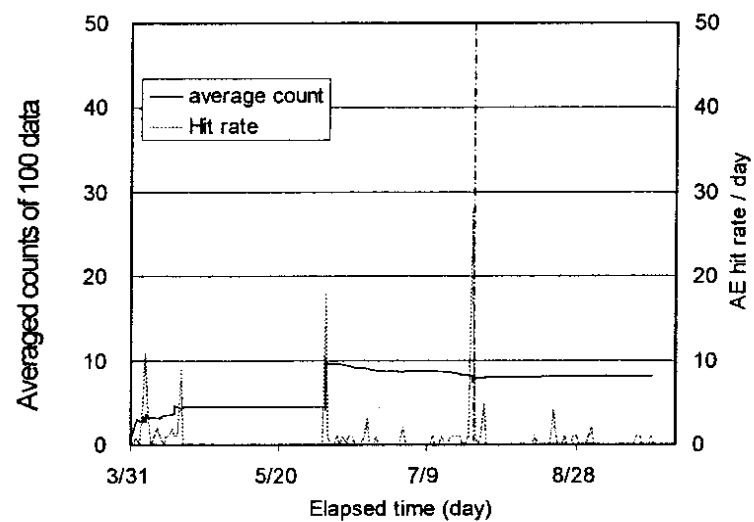
Figure 8(c) represents the variation of the improved b-value. Because remarkable increase and decrease could not be observed, the fracture level was evaluated as less than level I. Thus, fracture levels evaluated from these parameters agreed quite well. From all those results on the ringdown counts, the energy counts and the improved b-values, the monitoring slope was thought to be sound. Moreover, from the trends of temperature and crack gauges in three dimensions, emissions detected during the measured period were estimated as those due to volumetric expansion and shrinkage of the rock blocks induced by temperature variation.

## **CONCLUSIONS**

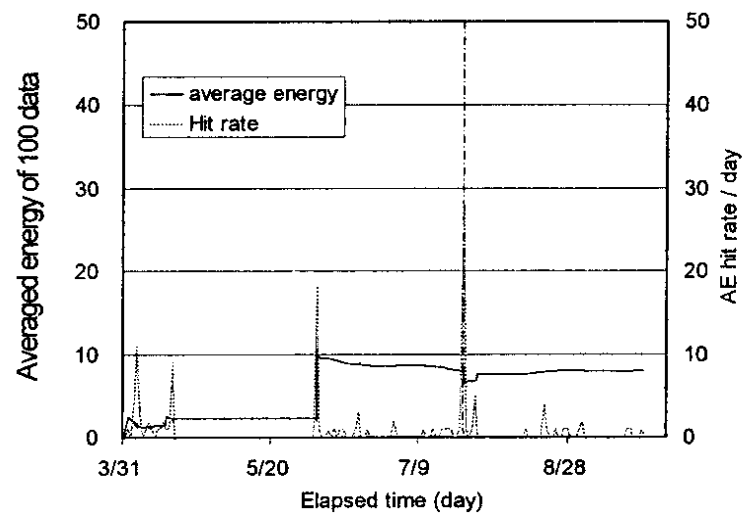
An installation method of AE sensors for the rock AE monitoring technique called WEAD is introduced. In order to evaluate the slope stability, the fracture criteria are proposed on the basis of experimental studies on the WEAD. A remote AE system has been developed. The WEAD and the remote AE system were applied to in-situ slope monitoring and then the AE data acquired are evaluated by the proposed criteria comparing with slope behavior. It is found that both fracture levels estimated from AE activity and slope behavior agreed quite well. Thus, reliability of the WEAD and the remote AE system is verified.

## **REFERENCES**

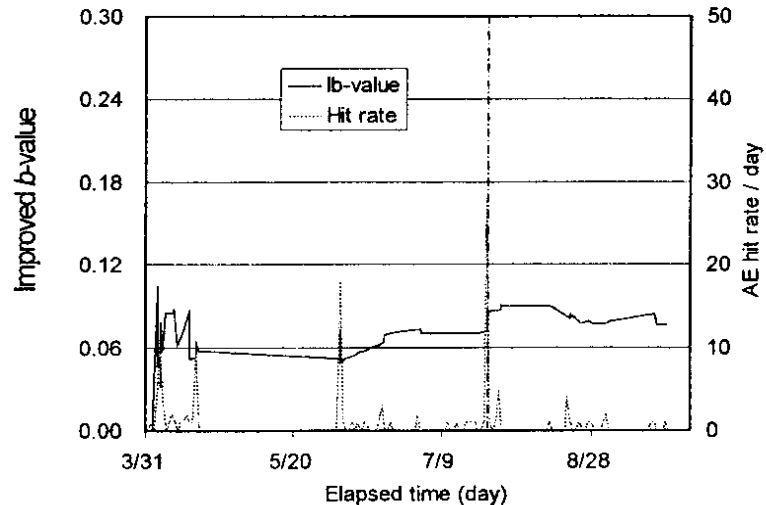
- Hardy, H.R. and Taioli, F. (1988). "Mechanical Waveguides for Use in AE/MS Geotechnical Application," *Progress in Acoustic Emission IV*, JSNDI, pp. 293-301.
- Mogi, K. (1964). "Magnitude-Frequency Relation for Elastic Shocks Accompanying Fracture of Various Materials and Some Related Problem in Earthquakes," *Bulletin of Earthquake Research Institute*, 40, pp. 831-853.
- Nakajima, L, Sato, J., Taira, N. and Kubota, N. (1988). "The Observation of Landslide by the Acoustic Emission Monitoring Rod," *Progress in Acoustic Emission IV*. JSNDI, pp. 273-281.
- Sholz, H. (1968). "The Frequency-Magnitude Relation of Microfracturing in Rock and Its Relation to Earthquakes" *Bulletin of Seismological Society of America*, Vol. 58, No. 1, pp. 399-415.



(a) Averaged ringdown counts



(b) Averaged energy counts



(c) Improved  $b$ -values

Fig. 8. AE activity in AE-4 between March and September, 1999.

Shiotani, T., Fujii, K., Aoki, T. and Amou, K. (1994). "Evaluation of Progressive Failure Using AE Sources and Improved b-Value on Slope Model Tests," *Progress in Acoustic Emission VII*, JSNDI, pp. 529-534.

Shiotani, T. and Ohtsu, M. (1999a). "Prediction of Slope Failure Based on AE Activity," *Acoustic Emission: Standards and Technology Update*, ASTM STP 1351 pp. 156-172.

Shiotani, T. Ohtsu M and Monma. K. (1999b). "Rock Failure Evaluation by AE Improved b-Value," *The Second Japan-US Symp. On Advances in NDT Proc. Book*, JSNDI & ASNT. pp. 421-426.

Shiotani, T., Yuyama, S., Li, Z., Okamoto, T. and Ohtsu M (1999c). Quantitative Evaluation of Fracture Process in Concrete by the Use of Improved b-value." *Proceedings of 6th Domestic Conf. on Subsurface and Civil Engineering Acoustic Emission*. MMIJ, pp. 123-128, (in Japanese).

# **NEW AE SIGNAL CONDITIONNER FOR INDUSTRIAL USE**

**Hartmut VALLEN, Jens FORKER and Jürgen VON STEBUT\***

**Vallen-Systeme GmbH, Icking (Munich) Germany,**

**\*Ecole des Mines, Lab. de Science et Genie des Surfaces, Nancy, France**

## **ABSTRACT**

*The analysis of transient acoustic emission bursts is used relatively rarely in industrial environments. Highly sophisticated AE-systems as available today are powerful tools for the development of new AE applications and the demonstration of their feasibility. Integrating these complex systems into industrial environments causes various fundamental problems. The ASCO-P Signal Conditioner presented here is made for rugged industrial environment. The ASCO-P is easy to handle and allows for detection and measurement of short AE-bursts, for example from crack growth, delamination, fibre breakage, partial discharge, etc.. The ASCO-P converts these short bursts into DC-signals that can be measured by simple devices. No complicated software setup is required whatsoever. The ASCO-P measures the peak amplitude levels of burst AE from the lowest that can be discriminated against background noise to that of a pencil lead break with approximately 1 dB accuracy and without any need to enter a threshold. A simple recorder can present the time and peak amplitude of a burst. Additionally, the ASCO-P possesses a digital output for external controls and an analog output that represents the continuous background signal. In addition to AE bursts the ASCO-P provides also information about continuous AE.*

## **INTRODUCTION – BURST AND CONTINUOUS SIGNALS**

An AE application works with either burst or continuous AE signals. AE burst signals are distinct signals where the beginning and end can be recognised. Common examples include crack growth, particle impact, partial discharge, or other source mechanisms of short duration. Continuous AE are endless although the amplitude and frequency content can change over time. Examples are flow noise from leaks and rubbing noise, among others. A rapid sequence of overlapping burst signals can also appear as a continuous signal, when the individual signals can no longer be separated. The measurement type is chosen according to whether burst or continuous signal types are being investigated.

For continuous signals, one measures usually the averaged amplitude. A signal conditioner amplifies, rectifies, and averages the high frequency AE-signal over an integration time and by a specific method. The RMS-value is often used, which is the square root of the averaged signal square. From burst signals one usually extracts a variety of features. These features include arrival time, peak amplitude, rise time, signal duration, counts and energy. The acquisition threshold is the most important criterion for discriminating AE burst signals.

## **PROBLEMS FROM THE INFLUENCE OF THRESHOLD ON MEASUREMENTS**

Signals whose peak amplitude is not large enough to cross the threshold are not detected. Setting the threshold too high will prevent potentially important signals from being recorded. Setting the threshold too low will cause the background noise to cross the threshold and will result in a great deal of unwanted data to be recorded.

If the background level rises during the test, the signals may remain above the threshold for long times, so that the AE system “sees” only a few especially long hits. In this case, despite a large number of burst

signals occurring, only a small amount of data will be produced. Possibly a lot of important information is lost.

Next to the severe influence of threshold on general detection of the signals is the dependence between the threshold setting and the values obtained for many measured features. An example is the value measured for the duration of the AE signals. The duration is defined as the time period between the first and last threshold crossing of a signal. A signal, which decays slowly, will result in a much longer duration for low thresholds than for higher thresholds.

The optimum threshold setting depends specifically on the amplitude of the AE signals of interest and on the actual noise signals. Further, the signal amplitude depends on many factors, such as sensor sensitivity, the sensor coupling quality, the source energy, the signal attenuation related to distance between source and sensor, changes in wave propagation conditions, and so forth. With presently available AE systems, the optimum threshold setting is of primary importance and fundamental for the success of every application that makes use of burst emission analysis. One needs experience to recognise if acquired data is plausible and then conclude a correct threshold setting.

There are numerous possible applications, where threshold independent detection of short AE burst-signals in a wide range of amplitudes would be helpful. These measurements should be both foolproof and require no special AE knowledge.

As an example the scratch tester application is presented.

## **SCRATCH TESTER APPLICATION EXAMPLE**

Scratch testers are used to determine failure limits of surface coatings. Consider the following: a test fixture set-up draws the tip of a diamond indenter with continuously increasing force and constant speed across a test surface. The linearly increasing contact load causes tensile stress behind the indenter tip (trailing edge) and compressive stress ahead of the cutting tip (leading edge). At some point during scratching, a crack is initiated. The position of the first crack within the scratch path is determined visually using a microscope. From the crack position within the scratch track one can determine the corresponding critical contact load

With modern coatings, the first cracks are so small that they are difficult to perceive even under the microscope. They may even close up within a few ms and thus become optically “undetectable”. This is a task just waiting for AE as a “crack damage warning – validation” indicator. However, this requires an AE system that is easy to use and cost effective.

In the course of an EC funded project (SMT4- CT97-2150), a better scratch test procedure is currently under development. Here, an AE module and a coupled video system are added to a conventional scratch tester. The AE module is used to determine the cracking and trigger the video system. These video images (potentially taken on-line, in the stressed state) will then be the material proof of AE signals caused by cracking.

For this application, it was necessary to study the relation between AE and different variables - such as different diamond tips, coatings and substrates. These measurements were made with the multipurpose Vallen AMSY4 instrument. Results were published by von Stebut et al. [1]

The goal was to find means to differentiate between crack emissions and noise such as friction, mechanical vibrations etc. For this purpose, many burst signals were studied, including investigation of waveforms and their frequency content.

For this application, the sensor has to be attached to the shaft of the scratch tester for practical reasons. In this position, the geometry of the shaft influences the wave propagation very strongly. It was not possible to find a waveform or frequency analysis criterion suited to differentiate crack signals from friction and mechanical vibration artefacts that could be obtained with a realistic and cost effective instrument.

The best criterion found for separating cracking and unwanted noise is the peak amplitude. It is easy to understand that the absolute peak amplitude is strongly dependent on the brittleness of the test sample, the shape and size of the diamond tip as well as the quality of the AE sensor coupling on the shaft, along with other factors.

Several requirements were established from the preliminary study and knowledge of how scratch testers are used. These requirements and the corresponding solutions are described hereafter.

## FIRST REQUIREMENT

The AE module should be as foolproof as possible. This means that as many conditions, which cause errors or mistakes, such as bad settings, should be eliminated. One cannot expect that a user will perform multiple tests on each new coating only for the reason of finding the optimum threshold. Despite these constraints, determining the instant of crack formation remains the goal, which must be reached in practice. This must even be true when the amplitude-dependent AE conditions change, as can be expected with every new test material. It must also hold true when the diamond-tip sharpness and the quality of the coupling changes.

### Solution:

The AE signal is converted into a DC-signal, which is proportional to the logarithm of the peak amplitude detected. The scaling factor is  $40 \text{ mV}/\text{dB}_{\text{AE}}$ . A noise signal at the input of  $20 \text{ dB}_{\text{AE}}$ , or  $10 \mu\text{V}$ , produces an ASCO-P output of  $800\text{mV}$  ( $40\text{mV}/\text{dB} * 20\text{dB}_{\text{AE}}$ ). A pencil lead break which generates a pulse of  $100\text{dB}_{\text{AE}}$  produces  $4\text{V}$  ( $40\text{mV}/\text{dB} * 100\text{dB}_{\text{AE}}$ ).

After each increase in amplitude, the peak signal remains for 50 ms at this last peak. This time period is called the peak stretching time (PST), because the peak output voltage is maintained constant for this period. This allows a slower, inexpensive data acquisition system to be used, such as one for measuring the force. If the amplitude increases still further during the 50-ms PST, the output increases immediately to this new value and the PST begins again. After the expiration of the PST, the signal quickly falls to the value of the input amplitude, thereby allowing further hits with lower amplitudes to be easily recognised.

Figure 1 shows the ASCO-output signal (upper curve) caused by a simulated AE signal (lower curve). To make this process clearer, the peak-stretching time was lowered from 50 ms to approximately 0.080 ms in this example.

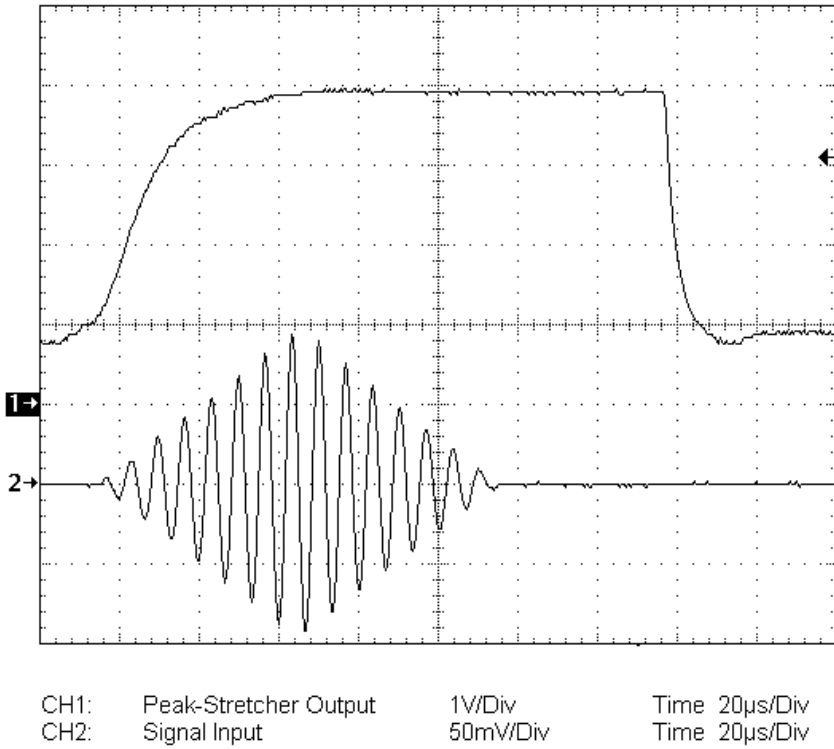


**Figure 1: ASCO-output reply to a short transient AE-signal**

following quickly after each other.

To further exploit these signals, a chart recorder or a simple data acquisition system can be used. The sampling rate should be shorter than the PST; with a 50 ms PST, a 25-50 Hz sampling rate is recommended. This combination will guarantee that short bursts can be measured with an arrival time resolution of 20-40 ms. If one acquires an additional test parameter, such as load or displacement, then one can read the activation point of the first crack in a simple load-time diagram. An example is shown in Fig. 2. The steadily increasing line curve shows the contact load of the diamond normal to the surface (right axis). Every bar represents the peak amplitude of at least one AE-signal. The dB scale (left axis) is

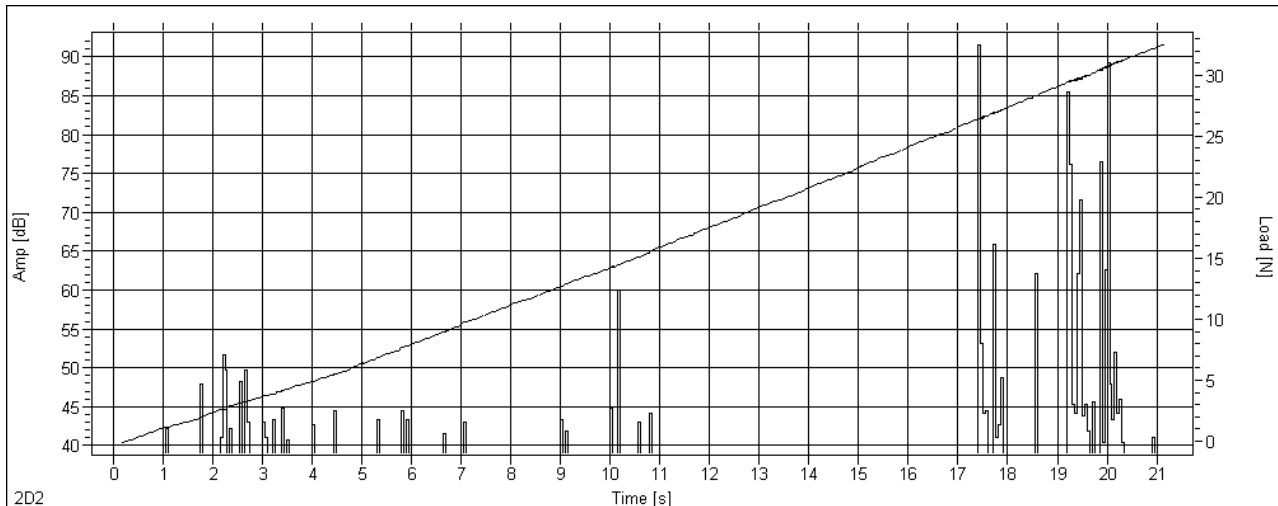


**Figure 2: ASCO-Output and Load vs. Time**

The arrows 1 and 2 on the left edge show the zero point of both signals. The ASCO output begins at the far left at about 0.8 V, before the AE signal begins. This corresponds to the peak value of the electrical noise, which is around 20 dB<sub>AE</sub> ( $40 \text{ mV/dB}_{\text{AE}} * 20 \text{ dB}_{\text{AE}} = 800 \text{ mV}$ ). The ASCO-output follows the rising AE-Signal without delay. The peak amplitude of the signal reaches approximately 99 dB<sub>AE</sub> (90 mV), which causes a corresponding increase in the output signal to 3960 mV (99 dB<sub>AE</sub> \* 40 mV/dB<sub>AE</sub> = 3960 mV) and remains at this value for the duration of the PST (here reduced to 0.08 ms; default is 50 ms). When the PST is over, the output signal falls immediately to the current value of the input signal. This allows short duration signals to be separated even when they are

obtained by the factor 40mV/dB.

The high amplitude signal at  $t = 17$  s was correlated unambiguously with a crack under the microscope. All activity before this peak was essentially low amplitude friction or other noise. The 60-dB signal at 10s could not be correlated to visible cracks either. The first crack is found to occur at 27 N from the correlation with the load curve shown here.

Materials behave differently. Most, however, follow a similar pattern: a clear increase of amplitude at a specific load. The actual value of the peak amplitude is not important, as long as crack signals rise above the amplitude range of the friction noise.

## **SECOND REQUIREMENT**

When crack growth occurs, a digital switch shall be activated. In the case of the scratch tester this switch triggers a video system.

### **Solution:**

To satisfy this requirement, an absolute threshold setting is used. This is defined as the level, which is expected for peak amplitudes of cracking. Because the measurements are completely independent of the threshold, the first test with a crack is already sufficient to show the optimum threshold for a reliable separation of useful signals from the noise. In the example shown in Fig. 2, one would set the threshold at about 75-80 dB.

The ASCO-P does not have a direct threshold setting; instead an alarm threshold is specified by an analogue input signal. A PC-plug-in-board used for data acquisition can normally also supply this analogue setting.

The ASCO-P compares the logarithmic AE signal with the supplied alarm threshold signal. When the AE signal exceeds the alarm threshold, a 50-ms long impulse is produced. With the scratch tester application, this alarm signal is used to trigger the video system to record crack initiation.

Triggering the mega-pixel video system by the AE module reduces the amount of video data considerably. Images are stored only when there is a high probability of crack activity. The recorded video verifies the indication of the AE-module. New knowledge of not yet understood artefacts then helps to improve the understanding of the AE-module indications. In other applications, this output can have other functions, for example to turn off a test or as an impulse for an event counter.

Presently available commercial instrumentation often requires a threshold setting that determines whether data is acquired and the values of the recorded features. On the contrary, the ASCO-P measurements are not influenced by a threshold. Merely the digital switch function is dependent on a threshold.

## **BLOCK DIAGRAM AND PRACTICAL INFORMATION**

Figure 3 shows the ASCO-P block diagram with essential functional groups of the ASCO-P. The filter module can be chosen appropriate for specific applications.

The frequency range which is best for crack detection is 100-300 kHz. Even higher frequency ranges are useful to get farther away from noise. For detection of leakage the frequency range of 20-100 kHz is recommended. The ASCO-P has the additional outputs, OutputFilter and OutputASL, which are useful for maximising potential applicability. The OutputFilter signal is the amplified and filtered high frequency AE signal. This can be used with a transient recorder, for example.

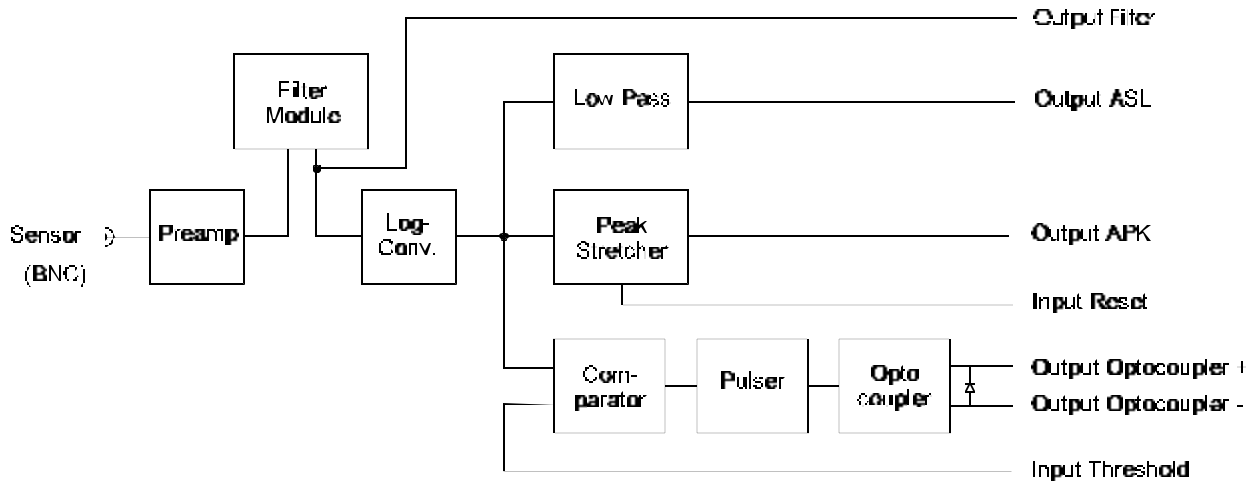


Figure 3: ASCO-P block diagram.

The logarithmic AE signal is fed through a low-pass filter and presented as OutputASL signal. On this output the influence of short burst signals is insignificant and it shows the essential features of the continuous background noise. It is especially useful in monitoring continuous AE signals

Figure 4 shows the actual device, cover removed. The module fastened by 2 screws is the filter module that can be easily replaced.

#### ASCO-P AND AMSY4

The ASCO-P is an analogue front-end, easy to use, and cost effective. It is suited for industrial applications as well as for research activities. But where more detailed information about the AE signals is required, a high-end system is needed.

The possibilities of the ASCO-P can be easily extended by changing the PST when industrial applications require this. The analogue output can then be combined with other instruments and the ACSO-P then becomes an AE front end providing filtered AE signal output that can be acquired and analysed with an external transient recorder.

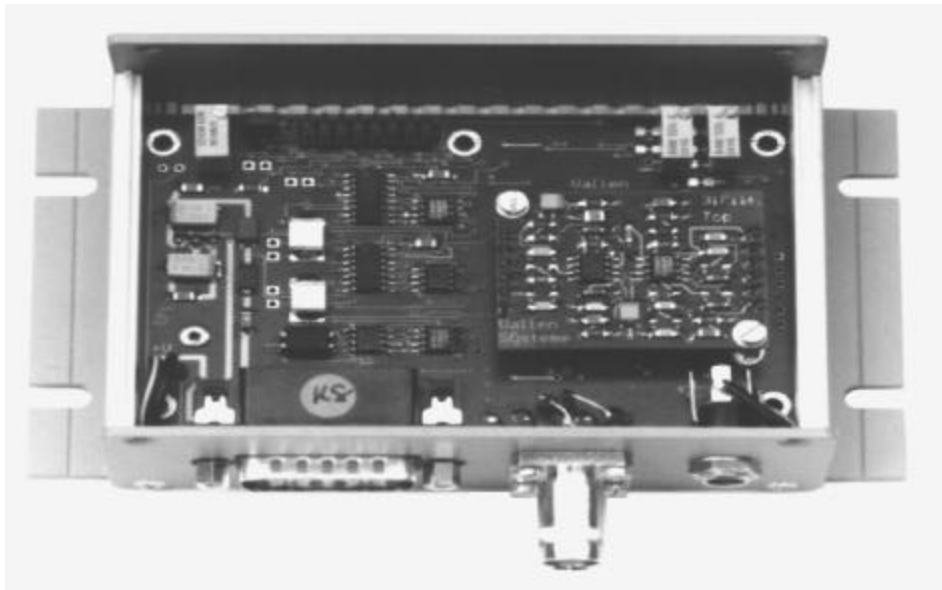


Figure 4: ASCO-P with removed cover

## FURTHER DEVELOPMENTS

The AMSY4 AE system has been extended to include a threshold independent mode that corresponds to the function of the ASCO-P. Thereby new applications of the ASCO-P can be developed and documented with both the convenience and greater possibilities of the AMSY4. When the initial work is completed, the ASCO-P is then ready to be put into service.

The ASCO-P is also the basis for a new battery-powered hand held instrument LSM1: The Leak Signal Monitor. The peak amplitude of the AE signals can be read in  $\text{dB}_{\text{AE}}$  on a digital display. With this device, the AE operator can test a structure for background noise levels before testing. Either the background level (ASL) or peak amplitude level can be chosen for display. Headphones can be used with an adjustable threshold so that even the smallest variations can be tracked. Differences in signal intensity can be used to find the direction from where noise signals arrive.

The LMS1 helps determining the origin of specific noise sources before a time-consuming multi-channel test set-up. The field-test engineer, and even the field test client, can use the LSM1 to find out if a structure is sufficiently “quiet” for AE testing. The device allows for scheduling only quiet tanks for AE field test and avoids costs that unnecessarily arise, when a AE test crew comes and cannot perform the test because the structure is too noisy.

## CONCLUSION

The ASCO-P allows for the measurement of short peak amplitude signals with large dynamic range in a simple, easy to use instrument. It makes the realisation of new, simpler and cost effective applications for the AE method possible.

The ASCO-P is an ideal accessory for any universal testing machine. This is especially true when the machine is already equipped with an existing data acquisition system for measuring load and/or displacement, to which the ASCO-P output can be added. One then possesses a simple, manageable, yet powerful AE system that shows the first onset of damage as it occurs.

## ACKNOWLEDGEMENTS

This work has been accomplished in the framework of the European programme “Standards, Measurements and Testing“ as part of an on-going EC funded project (SMT4- CT97-2150).

## REFERENCES

- [1] J. von Stebut, F. Lapostelle, M. Bucsa, H. Vallen, *Acoustic Emission Monitoring of Single Cracking Events and Associated Damage Mechanism Analysis in Indentation and Scratch Testing*. Surface and Coatings Technology, **116-119** (1999), 160.

# NEW SOFTWARE TOOLS FOR THE AE-PRACTITIONER

Hartmut VALLEN and Jochen VALLEN  
Vallen-Systeme GmbH, Icking (Münich), Germany

## ABSTRACT

The analysis of AE data is more complex compared to traditional forms of data acquisition. In addition to the presentation of measurement values against time, as one expects in any basic data acquisition system, AE analysis software is usually expected to perform extensive data processing, for example:

- Statistical distributions of AE signals according to AE features and/or external load parameters,
- Calculating the source location of each event based on the measured arrival time differences and the geometry of the structure under test,
- Automated cluster analysis emphasizing the places of high location density and more.

The capabilities stated above are basic features found in today's AE systems and frequently used. In addition to basic system capabilities, AE users desire a series of advanced tools. This paper describes some of the new tools that have been implemented in the VisualAE™ software package. These tools utilize extensively the graphical representation possibilities offered by the 32-bit Windows® software platform.

## Tools for Checking Sensor Coupling

Normally, before an AE test begins, the coupling between the sensors and the test structure is checked. Even though the auto-calibration feature of modern AE-systems is extensively in use today, it cannot replace the pencil-lead break calibration method that can be performed at any desired position of a test object. A pencil-lead break of known diameter and hardness produces an AE signal with sufficiently repeatable amplitude. It is usually best to read and judge these amplitudes in a listing. Unfortunately, additional unwanted signals are often produced from the pencil-lead breaks due to various reasons including the impact of the pencil-lead fragment with the surface, reflections and more. In many cases the number of unwanted signals that arrive after the pencil break shift the lines containing the pencil break signal out of the screen. One remedy is to use a higher threshold; however, this is inconvenient at best.

The tools in VisualAE offer a more efficient approach:

- 1a) A scrollbar in the listing,
- 1b) Direct addressing of listing lines by clicking on points in amplitude-time diagrams,
- 1c) Analysis filters which are setup quickly.

A few examples follow:

### 1a) Scrollbar in Listing

Figure 1 shows a screen with various diagrams and a listing window. With the vertical scrollbar on the right edge, the user can view the AE data with similar ease to the text in a word-processor (like MS-Word). Both upward and downward commands make it easy to display the desired listing line.

With the horizontal scrollbar, the area of the listing that is being displayed can be shifted sideways. This helps with data presentation when there are more desired result columns than fit onto one screen area. The user can position the display window to the currently desired columns, without disturbing simultaneously running data acquisition.

## 1b) Direct Addressing of Listing Lines

With a double click on an amplitude point within a correlation plot (or on a location point in a location plot), the user also positions the listing window on the selected line.

When waveforms were also recorded and a TR-diagram is present, the waveform diagram is also updated to the TR-data corresponding to the selected point. This allows for immediate visualization of the maximum amount of information from any selected data set.

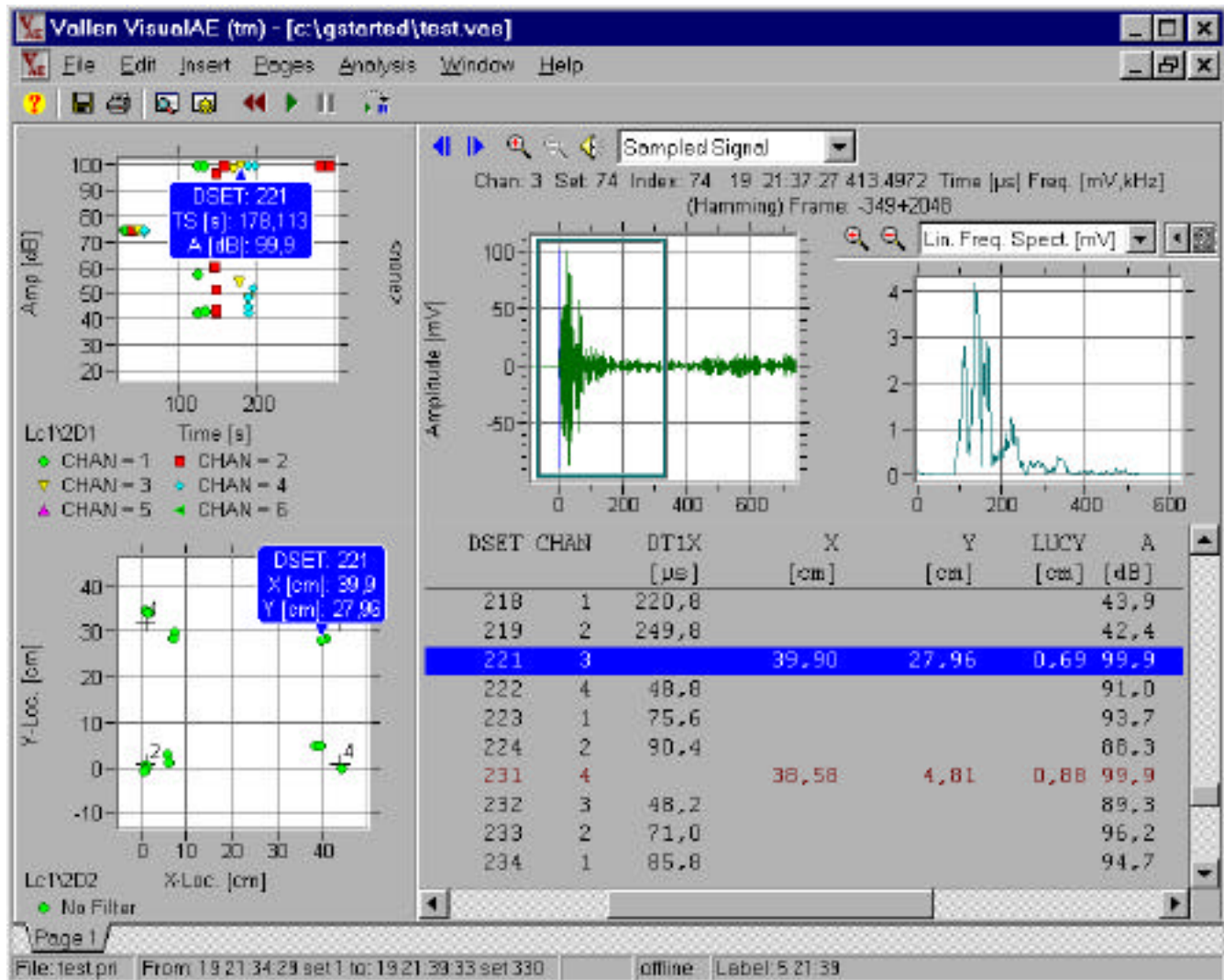


**Fig. 1: Listing with scrollbars. Diagram with identifying inset windows.**

Figure 1 shows data from a pencil-lead break. In the location diagram (below left) a point was selected with a double-click as the arrow in the small inset window shows. The data corresponding to the selected event has been automatically identified in other display areas with small inset windows. The mouse-click has also highlighted the line on the listing and brought the corresponding waveform and FFT from the first hit channel of the event into the TR-diagram display. With the forward and backward arrow symbols in the waveform diagram, one has a simple means to view the other channels in the event. The data acquisition can be running simultaneously to this analysis without any disturbance from on-screen manipulations. This makes possible both fast selection and visualization of data from any pencil-lead break.

### 1c) Analysis Filters

During breaking pencil leads, one can often produce many unwanted signals with smaller amplitude. For coupling checks, these signals need to be skipped quickly. VisualAE provides fast and easy means to insert, modify or remove a filter from within the analysis path.

Figure 2 shows a structure menu for a normal analysis process. An additional filter processor for  $A > 80$  dB has been prepared in the file TEST.PRI. There is, however, no element (diagrams, listings) attached to this filter, means the filter is not used. The location processor (Lc1...) has four elements (three diagrams and a listing) attached.

If one wants now to only locate data that passes through the filter  $A > 80$  dB, one can simply drag the location processor with the mouse and drop it under the filter processor. The structure menu will be modified as shown in Fig. 3.



Fig. 2: Structure menu where filter (FL1) has no attached elements

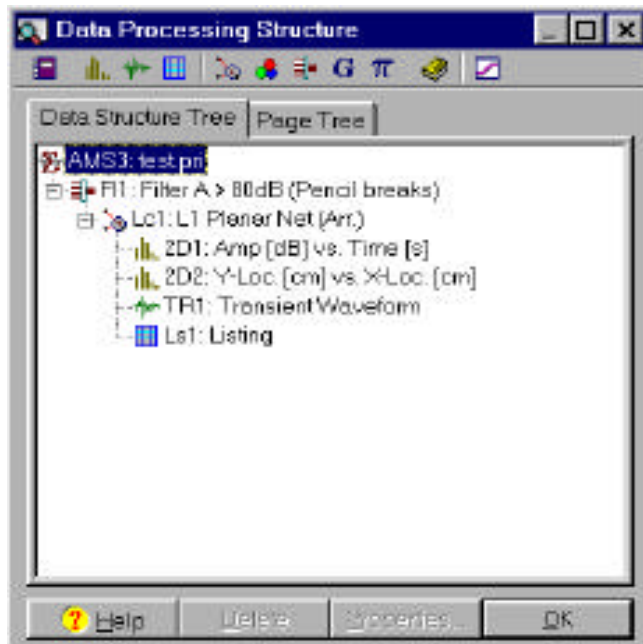


Fig. 3: Structure menu after moving location processor behind filter (FL1)

### Location Analyzer - a Tool for Verifying Calculated Location

The location calculation is increasingly important. The significant and numerous uses include:

- Recognition of signals from known and locatable noise sources. These signals should be eliminated from the data sets without being mistakenly assigned to potential failure processes.
- The location calculation shows the general area of suspected defects for focused, cost-effective follow-up NDT search.
- From the measured amplitude and determined distance between the sensor and the source, an amplitude correction can be calculated, which indicates the source amplitude before propagation. This higher, corrected value is already a part of the standard prEN13445-5 Appendix E.

To gain the most possible information from location analysis, it is necessary to understand why and where errors in location analysis occur and potentially eliminate them.

The correct settings and interpretation for location calculation requires experience. Without experience, it is difficult to tell which combinations of arrival times are at all plausible. The wave propagation starting from the source on its way to the sensor may be influenced by many different factors: pipe inlets and outlets, welded areas on the structure, and propagation through fluid within the test object, as well as many others. It is very difficult to judge how strongly such influences alter location results.

An understanding on how the various influences actually effect location results is highly desirable to a user. A user-friendly tool, with which the operator can quickly check location results is needed. This tool should use real data recorded from real structures and offer the possibility to manipulate values by the user. One such tool, the Location Analyzer in VisualAE, is presented here.

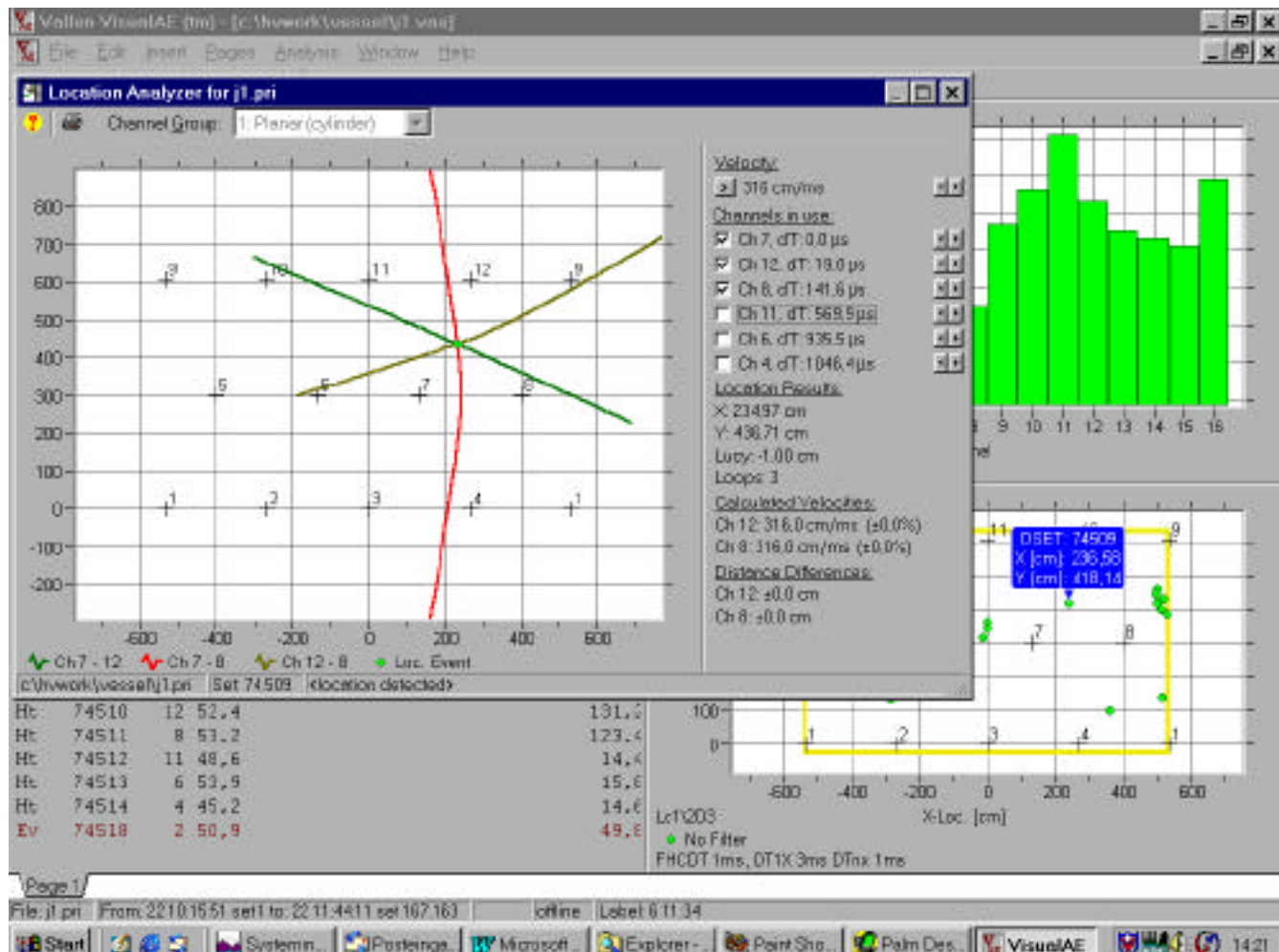


**Fig. 4: Location Analyzer from an analysis window with diverse diagrams and listings.**

Figure 4 shows data from a cylindrical pressure vessel, 3.4 m in diameter. The AE sensors are found in 3 rings with 4 sensors per ring. The location analyzer (window in foreground) shows the hyperbolae for a location after a mouse click. The location was selected by a double click on a location dot in the location plot below right. This dot is now indicated by an inset window. Every hyperbola shows all the points on the surface of the test object corresponding to a certain distance difference to two sensors. With isotropic wave propagation, one finds the difference in distances between each sensor pair by multiplying the arrival time difference by the sound velocity. The intersection of all three hyperbolae is the location

result. The legend beneath the graph is color-coded to show which hyperbola belongs to which sensor pair.

On the right side of the window of the location analyzer (Fig. 4), there is an entry point for different sound speeds (velocity, at top) and for individual arrival time differences for every channel (below). The time differences initially correspond to the measured values. The user can change these values and see immediately how these modifications change the location results.

From three hit channels are three pairs of channels possible, and there can only be one intersection within the sensor array. The selected event in Fig. 4 contains 6 hit-channels. Only the hyperbolae for the combinations of sensors 7, 12 and 8 are shown because these have been checked in the menu (Fig. 4, right above).

After checking channel 11 in that menu, the software shows the hyperbolae from four channels (7, 12, 8, 11), reproduced in Fig. 5. Four channels make six channel-pairs, hence Fig. 5 shows 6 hyperbolae. Here, the hyperbolae do not show a single common intersection point. This happens, when the effective velocity to at least one channel differs from the user-defined velocity that is used for location calculation. The location result represents the position that gives the least squared Distance Difference. The term Distance Difference is explained below. The RMS (root mean squared) value of all involved Distance Differences is called LUCY (Location Uncertainty) and its numerical value is shown in the legend, below of the location result.

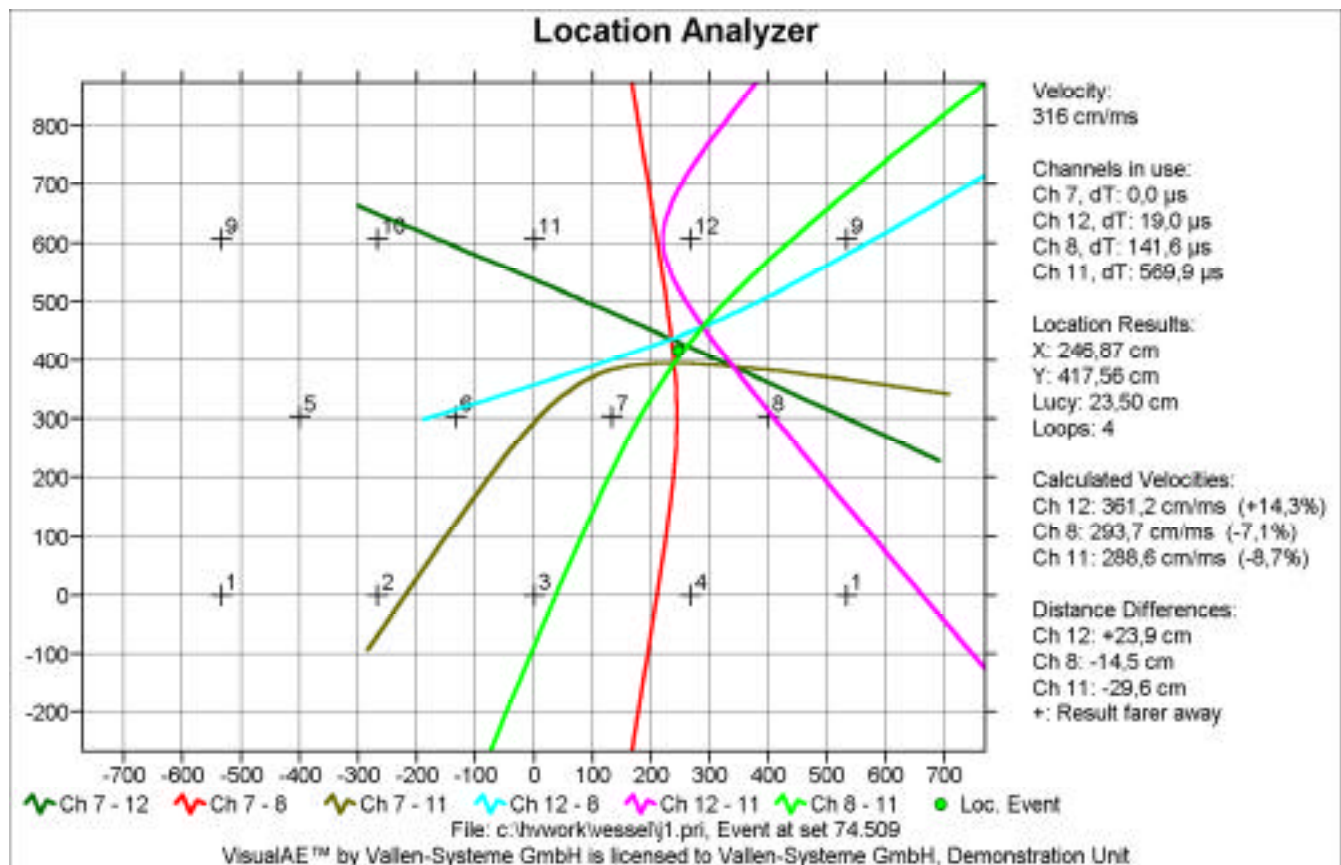
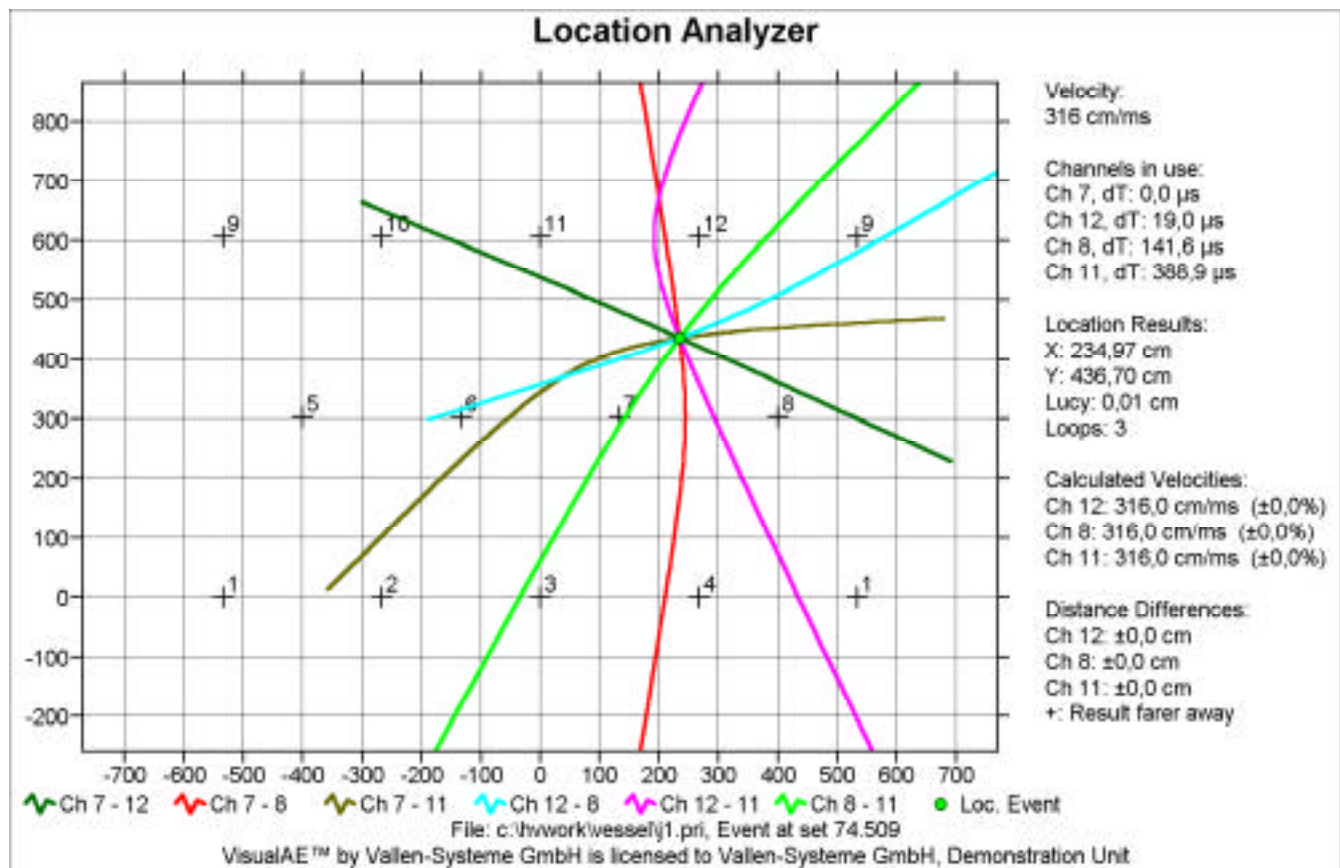


Fig. 5: Location Analyzer showing hyperbolae from 4 hit channels.

“Velocity: 316 cm/ms”, shown on top of the legend, defines the Used Velocity, the speed of sound the software uses for location calculation and for determining the time of source. The “Calculated Velocities” and “Distance Differences”, also shown in the legend, help the user interpret the uncertainty of the source position. These values are based on the time of flight (TOF) between assumed source location and sensor. The TOF is the difference between Time of Source (TOS) and Arrival Time (AT). The AT is measured for the channel, the TOS results from first hit AT minus first hit sensor-source distance divided by Used Velocity. “Calculated Velocity” means “source-to-sensor distance divided by TOF”. “Distance Difference” means “source-to-sensor distance minus TOF x Used Velocity”. A positive Distance Difference indicates that the shown result is too far away from the sensor, or, the hit was triggered by a wave mode faster than Used Velocity, or, the wave reached the sensor over a shorter path, e.g. through a liquid in the structure.



*Fig. 6: Intersection point obtained by decreasing the time difference from Channel 11*

The Location Analyzer lets the user play with alternative velocities and time differences to see how this influences the location result and the plausibility indicators. In Fig. 6, for example, a common intersection point is found, when the arrival time difference from channel 11 is reduced from 569.9 µs to 399.9 µs.

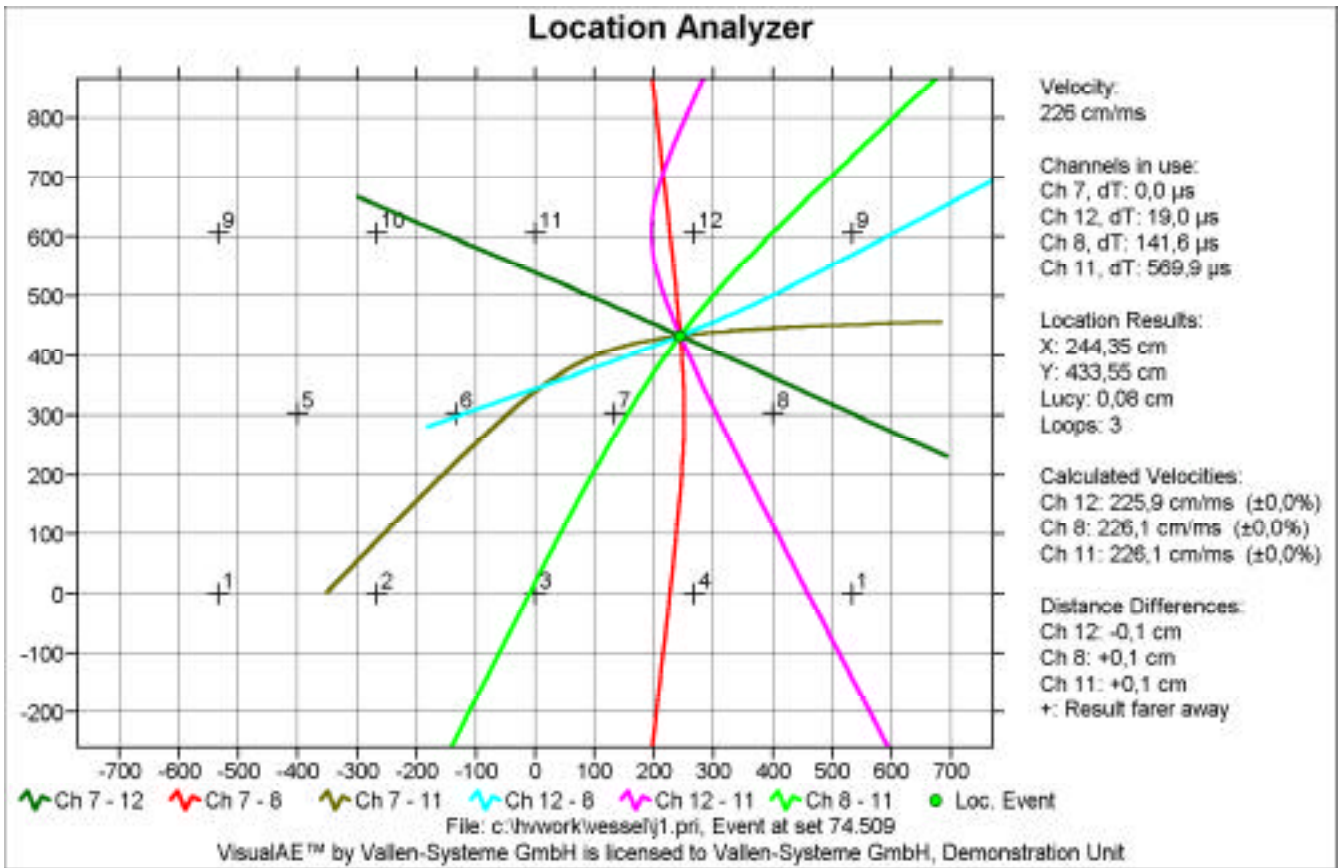


*Fig. 7: Intersection point obtained by changing the velocity to 226 cm/s.*

In Fig. 7, the velocity of 316 cm/ms is reduced to 226 cm/ms for all channels. This method also finds one common intersection for the four hyperbolae.

The location analyzer is a helpful tool that quickly develops experience on effects of errors of velocity used. At the same time, it helps to find out which location results are plausible and which are not. For non-plausible results, the user can quickly determine what plausible arrival-time differences would be, and whether this corresponds to certain conditions of the test object; e.g. a direct wave path through a liquid instead of over the structure wall.

Another purpose of the Location Analyzer is to improve the understanding of the capabilities and limits of today's location algorithms, and to generate feedback for improvement and further development.

# IMPROVED SOURCE LOCATION METHODS FOR PRESSURE VESSELS

Valery GODINEZ, Sotirios J. VAHAVIOLOS, Richard D. FINLAYSON,  
Ronnie K. MILLER and Mark F. CARLOS  
Physical Acoustics Corporation, Princeton Junction NJ, USA

## ABSTRACT

*In this work, results of an acoustic emission source location study using both linear and planar location strategies are presented. The study was performed on a submarine steel gas flask with pencil-lead breaks used as artificial acoustic emission sources. Plate wave propagation theory is used to analyze the effects of dispersive Lamb wave modes on source location accuracy. Narrow-band filtering techniques are used in conjunction with different sensor arrays of 2, 4, 6, and 8 sensors to improve source location accuracy. By combining these two factors, location accuracy of 1% of the length of the flask and 3% of its circumference can be achieved. The results are presented in the form of 2-D accuracy color maps. The total average error in source location for each one of the sensor configurations is calculated. Finally, a summary of the results is presented in the form of a table indicating the advantages and disadvantages of every sensor configuration studied.*

## INTRODUCTION

Acoustic emission (AE) source location in an extended structure, such as a pressure vessel, is subject to inaccuracies caused by two factors: the location method, i.e. linear or planar, and by the ratio of the acoustic signal frequency to the thickness of the structure under study. When AE signals received by two sensors are used to locate an AE source, i.e. linear location methods, the arrival times of the signal produced by an AE source will define a hyperbola with its foci located on the position of the sensors. Thus, the position of the AE source could be at any point along this hyperbola [1]. To avoid this problem, planar location methods must be used; that is, signals from a minimum of three sensors have to be used to calculate the position of the AE source [2].

The ratio of the AE signal wavelength ( $\lambda$ ) to the vessel wall thickness ( $T$ ) determines the nature of the wave propagation phenomena in the structure. In the case of a wavelength much smaller than the wall thickness,  $\lambda/T \ll 1$ , the stress waves produced by the AE source will propagate in the form of bulk longitudinal, bulk shear, and surface waves, with constant velocities. When the wavelength is comparable to the wall thickness,  $\lambda/T \approx 1$ , the situation becomes more complex. In this case, the stress waves produced by the AE source will propagate as multiple Lamb (plate) wave modes, each with a particular velocity and attenuation depending on its frequency; that is, the modes will be dispersive [3]. The immediate effect in the location method is, depending on the position of the AE source in relation to each of the sensors, that different wave modes, traveling with different speeds, may trigger different sensors.

In the case of very large structures, such as large storage tanks or civil structures, the problem of multiple wave mode propagation does not have an effect on AE source location due to the long paths that the wave modes have to travel to reach the sensors. However, in the case of AE inspection of relatively smaller pressure vessels, such as compressed gas cylinders, it is important to precisely locate AE sources. The solution of the problem becomes even more critical when these compressed gas cylinders are located inside large structures such as submarines and other ships. In submarines, for

instance, the cylinders are located behind bulkheads and the inspector must be certain of the location of any AE indications, as removal of the bulkheads is very time consuming and expensive. Therefore, it is important to study the effect of multiple wave mode propagation in these pressure vessels in order to improve the accuracy of source location techniques.

## EXPERIMENTAL SETUP

In order to study the effect of Lamb wave mode propagation in AE source location, a steel gas flask was removed from a Trident nuclear submarine. The cylindrical shell is 4.57 m (180") long, with an external diameter of 509 mm (20"), and spherical end caps. The flask was instrumented with eight PAC AE R15I sensors (with a peak resonance frequency at 150 kHz) as shown in Fig. 1. Figure 1(a) presents an unwrapped view of the flask with the approximate positions of the sensors on its surface and Fig. 1(b) shows the approximate position of the sensors around the circumference of the flask.

The wall thickness of the cylindrical shell of the flask was measured using an ultrasonic thickness gauge and was found to be 31 mm (1.2"). The sensors were connected to a PAC DiSP 52 channel AE system. According to the US Navy requirements, the maximum permissible error in AE source location is 127 mm (5") in the circumferential and axial directions. Accordingly, the entire surface of the flask was divided into a rectangular grid of 127 x 127 mm (5" x 5").

A series of five pencil-lead breaks (PLB) using a 2H/0.3 mm mechanical pencil with a Neilsen shoe, were performed at the center of every square on the grid. Files containing the amplitudes, arrival times, and waveforms of each PLB were stored on the DiSP AE system. Later, the data were processed using PAC's source location software in order to calculate the position of every PLB. The five readouts obtained for each PLB position were averaged and the result was assigned to the PLB location. The difference between the real and the measured locations of the PLB was calculated and then plotted on 2D-color maps of the extended surface of the flask.

## LINEAR LOCATION

The first case analyzed is that of linear location, in which the sensors are located along the axis of the flask. In this case, sensors 2 and 6 were used to calculate the positions of the PLB. In order to demonstrate the effect of the different wave modes propagating on the flask as a result of a simulated source, the averaged differences in arrival times ( T ) from the five PLB on each square of the grid were used to calculate the position of the simulated sources. For this purpose, a set of two values of the wave velocity was selected:  $3.10 \text{ mm/us}$  ( $122 \times 10^3 \text{ in/s}$ ) and  $4.88 \text{ mm/us}$  ( $192 \times 10^3 \text{ in/sec}$ ), which correspond to the  $a_0$  and  $s_1$  Lamb wave modes. These values were selected based on the group velocity dispersion curve for Lamb waves propagating along a steel plate with a thickness of 31 mm in the frequency range of the sensors used or 150 kHz. This group velocity dispersion curve is shown in Fig. 2.

Figure 3 presents accuracy maps of PLB location obtained using linear location. These maps present the error point by point on the surface of the flask. The x-axis represents the flask coordinates along the axial direction and the y-axis represents the flask coordinates along the circumferential direction. Each square on the error map, corresponding to a 13 cm square on the real flask, has been colored according to the difference between the real and calculated PLB for that particular point. Red and yellow tones indicate higher differences while blue tones represent small differences. The color bars situated by the maps indicate the numerical equivalence of the error in source location.

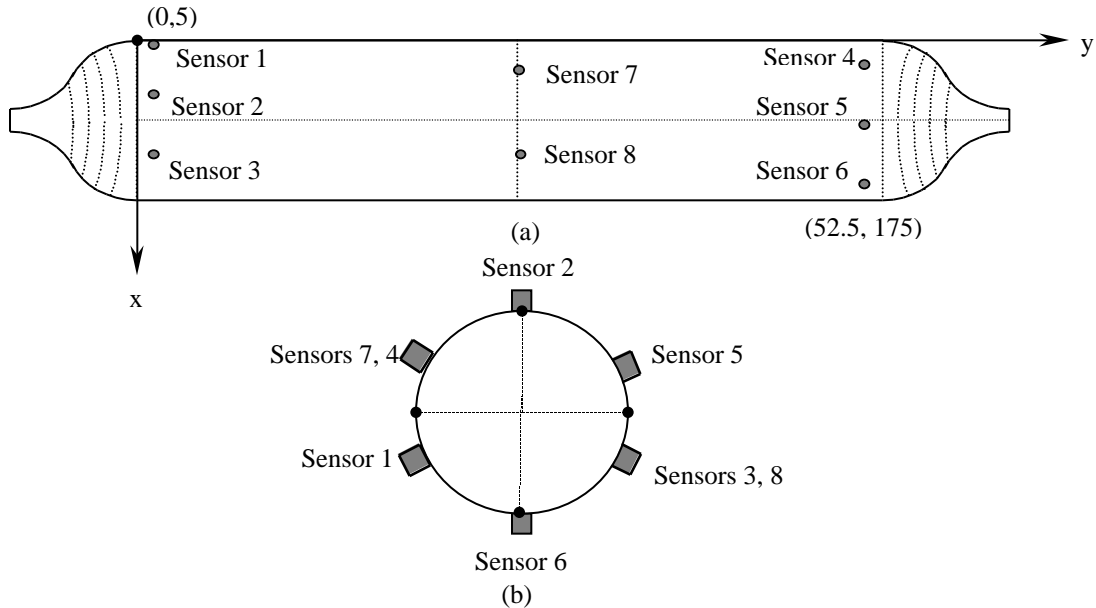


*Fig. 1. Position of the AE emission sensors on the Trident submarine steel gas flask. (a) Extended surface of the flask. (b) Position of the sensors around the circumference of the flask.*

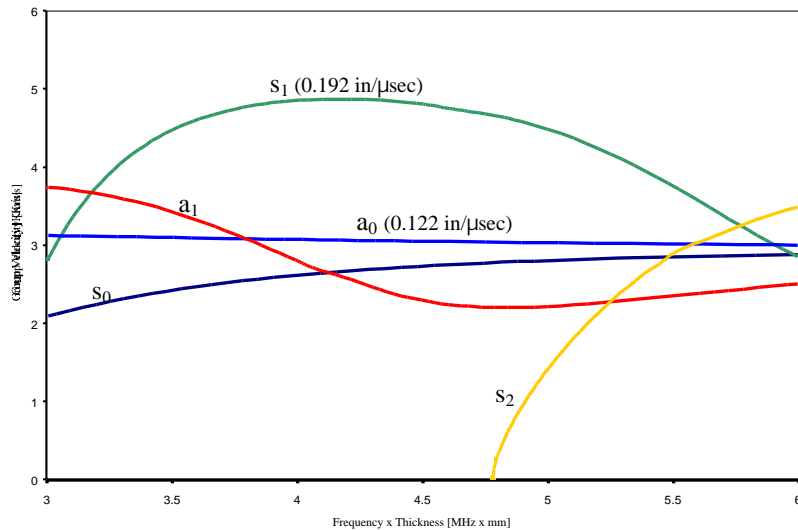


*Fig. 2. Lamb group velocity dispersion curves for a 31 mm (1.2") thick steel plate.*

Figures 3(a) and 3(b) clearly show the influence of wave-mode velocity choice on linear location and confirm the hypothesis of higher velocity modes arriving at nearby sensors, while the lower velocity modes are the ones that trigger the sensors furthest away. When the  $a_0$  wave mode group velocity (3.10 mm/μs) is used to calculate the positions of the sources, the areas close to sensors, located at the edges of the cylindrical shell, present an error in location as high as 76 cm (30"). The points located towards the center of the flask present errors below 25 cm (10"). When the  $s_1$  (4.88 mm/μs) wave mode velocity is used in the calculation, the large errors in location shift towards points in the center of the cylindrical shell, while the areas close to the sensors present errors below 13 cm.

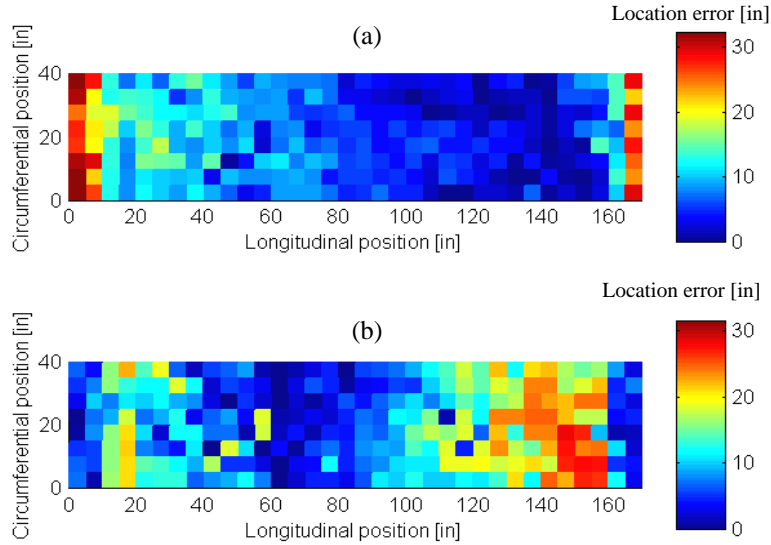


*Fig. 3. Accuracy maps for linear source location on a cylindrical gas flask. These maps were generated using: (a) the  $a_0$  wave mode group velocity, and (b) the  $s_1$  wave mode group velocity.*

## NARROW BAND FILTERING

In order to reduce the inaccuracy of source location due to the effect of Lamb waves, we have investigated the technique of narrow-band filtering. Previous studies at PAC have shown that by applying narrow-band digital filters to signals from simulated AE sources in a gas flask, accuracy in source location can be improved [4,5]. The dispersion curve shown in Fig. 2 indicates that in the frequency band of interest, the  $a_0$ ,  $a_1$ ,  $s_0$  and  $s_2$  modes have very similar group velocities, around 3.10 mm/ $\mu$ s, and the  $s_1$  mode has a maximum group velocity of 4.88 mm/ $\mu$ s. However, the  $s_1$  mode propagates with low amplitude when compared to that of the  $a_0$  mode. Therefore, if the signals from the AE source are narrow-band filtered in the frequency range of interest (before being processed by the AE system), the amplitude of the  $s_1$  mode will not be large enough to trigger the sensors while the  $a_0$  mode will. An accuracy map generated using narrow-band filtered signals and a group velocity of 3.10 mm/ $\mu$ s is presented in Fig. 4. In this case, the errors observed along the flask are below 13 cm for all the points.

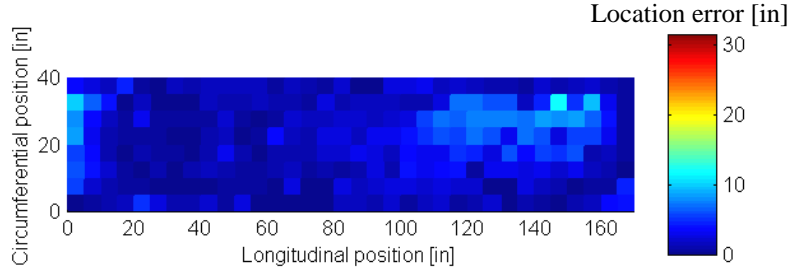


*Fig. 4. Accuracy map for linear source location on a cylindrical gas flask. This map was generated using the  $a_0$  wave mode group velocity and narrow-band filtered signals.*

## PLANAR LOCATION

Although linear location combined with narrow-band filtering can achieve good location accuracy, its main drawback is the fact that it only provides the source position along the longitudinal axis between two sensors. In order to obtain the axial and circumferential position of an AE source on the flask, planar location methods must be used.

In this work, three different configurations for planar location were studied. The first configuration was a “F-placement” using sensors 1, 2, 4, and 5 positioned at coordinates (0,5), (31.5,5), (15.75, 175), and (47.25,175), respectively, according to Fig. 1(a) coordinates (unit in inches). As in the case of linear location, the signals were narrow-band filtered. The results obtained with the F-placement configuration are shown in Figs. 5(a) and 5(b).

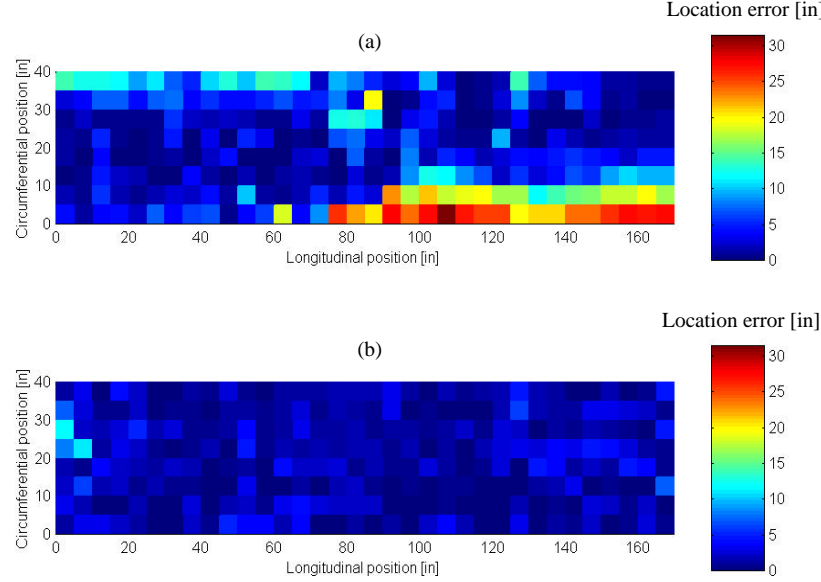


*Fig. 5. Accuracy map for planar source location on a cylindrical gas flask using an array of four sensors. (a) Along the circumference of the flask. (b) Along the axis of the flask.*

Figure 5(a) presents the accuracy map for source location in the circumferential direction of the flask. It is clear that two bands of high inaccuracy, where the error can be as high as 76 cm, appear on the surface of the flask. These bands are located symmetrically on opposite sides of a band of very low inaccuracy, where the error is lower than 13 cm, and which runs from the (0,5) to the (47.25, 175) position on the extended flask surface. The accuracy map of source location along the axial direction is shown in Fig. 5(b). In this case, the accuracy is very good and the error is below 13 cm in nearly all the positions of the simulated AE sources. A practical way of estimating the overall accuracy of the sensor configuration is to calculate the total average error (TAE) in both directions, circumferential and axial. In the case of the F-placement with 4 sensors, the TAE is 15.5 cm (6.11") and 4.30 cm (1.69") in the circumferential and axial directions, respectively. It is important to mention that the F-placement is an ideal configuration for a length-to-circumference ratio approximately equal to 1. In the present case, the length to circumference ratio is 2.77.

The second configuration studied was an array of six (6) sensors, with sensors 1 to 6 located according to Fig. 1. In this case, the PLB positions were calculated using PAC's arbitrary sensor configuration software. This software selects the three first arrival times, regardless of the sensor position, and calculates the intersection point of the three hyperbolae defined by the three sets of two-sensor combination. Figure 6(a) presents the accuracy map for source location along the circumference of the flask and Fig. 6(b) the corresponding one for the source location along the axis of the flask. The circumferential error decreases substantially when compared to the previous case. Except for a section on the center of the flask, the location error is less than 13 cm in the circumferential direction. For the axial direction, the map indicates errors below 13 cm in almost every point of the flask. The TAE in this case is 5.23 cm (2.06") for the circumferential direction and 4.55 cm (1.79") for the axial direction.

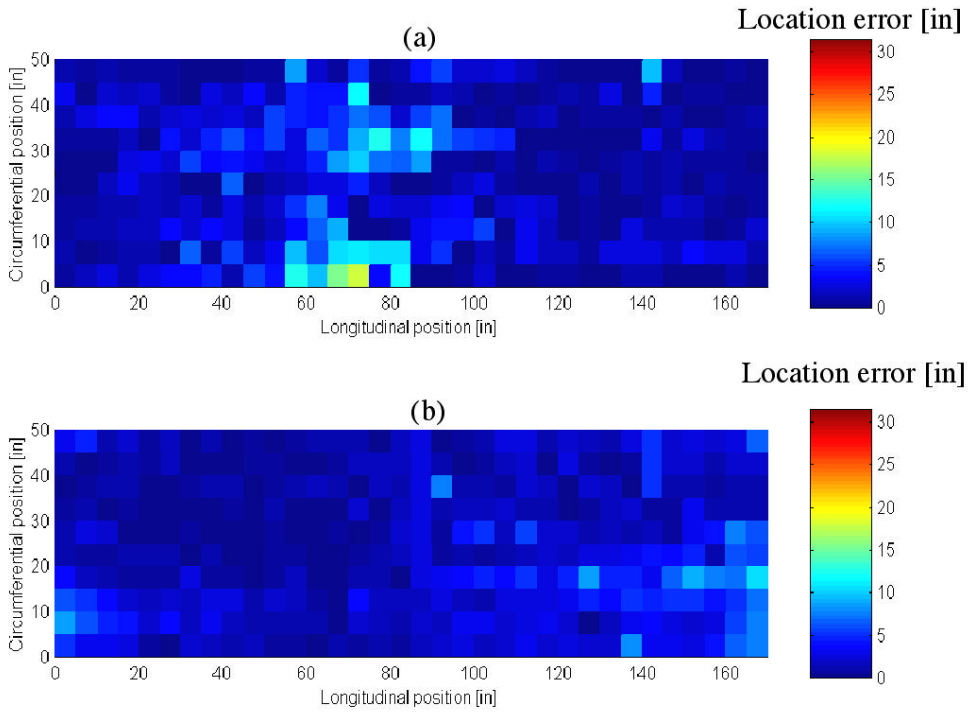


*Fig. 6. Accuracy map for planar source location on a cylindrical gas flask using an array of six sensors. (a) Along the circumference of the flask. (b) Along the axis of the flask.*

The last configuration analyzed is the array of eight sensors positioned as indicated in Fig. 1. Arbitrary location software was used for source location and Figs. 7(a) and 7(b) show the resulting accuracy maps for the axial and the longitudinal directions, respectively. Figure 7(a) shows no spots with errors above 13 cm, the same is observed in Fig. 7(b). The TAE is 4.04 cm (1.59") and 4.50 cm (1.77") for the circumferential and longitudinal direction, respectively.

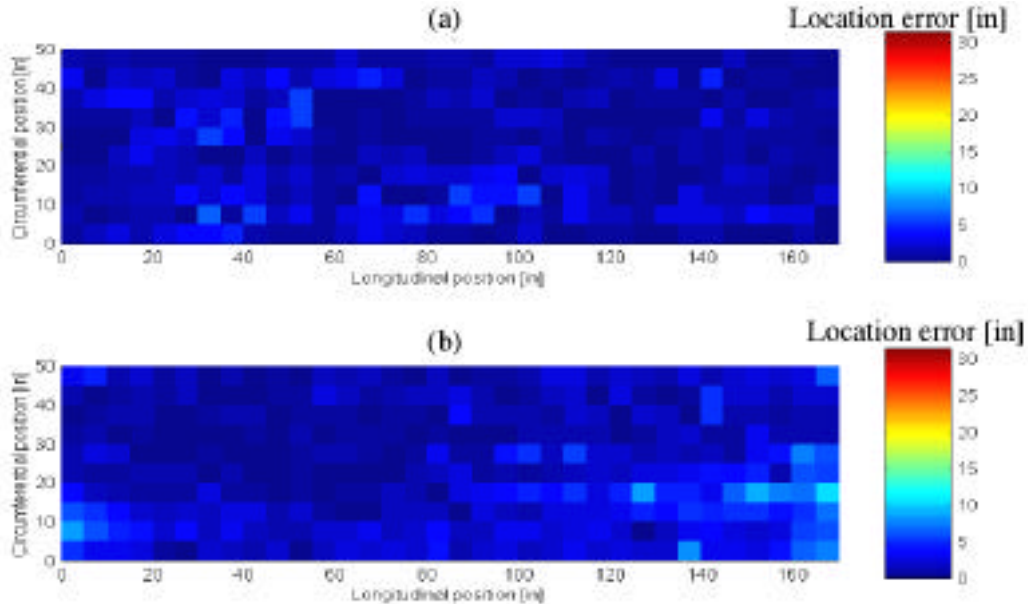


*Fig. 7. Accuracy map for planar source location on a cylindrical gas flask using an array of eight sensors. (a) Along the circumference of the flask. (b) Along the axis of the flask.*

## CONCLUSIONS

The results obtained in this study clearly demonstrate that the propagation of Lamb wave modes in plate-like structures has a serious impact on the accuracy of AE source location. The use of narrow-band filtering eliminates this problem by filtering out low amplitude higher velocity Lamb wave modes. In addition, if very accurate source location is required, such as in the case of the Trident nuclear submarine compressed gas cylinders, planar source location methods have to be implemented during inspection. Also, other factors have to be taken into account when a source location strategy is implemented, such as cost, availability of AE channels, number of cylinders to inspect, and access to the whole surface of the cylinders. Finally, Table 1 summarizes the practical advantages and disadvantages of using different source location strategies.

**Table 1. Comparison between advantages and disadvantages of linear and planar source location strategies**

Sensor number	Total Average Error (TAE) [in]			Advantages	Disadvantages
	Circumf	Longitudinal	Combined		
2	--	1.95	----	<ul style="list-style-type: none"> <li>Easiest Set Up</li> <li>Excellent longitudinal location</li> <li>26 tubes inspected in a single pressurization*</li> </ul>	<ul style="list-style-type: none"> <li>Does not provide circumferential position of the source</li> <li>It may require additional pressurization on suspected cylinders with 8 sensors</li> </ul>
4	6.1	1.69	6.88	<ul style="list-style-type: none"> <li>Excellent longitudinal location and fair circumferential location</li> <li>No access to the center of the tube is needed</li> </ul>	<ul style="list-style-type: none"> <li>180° “Flip Over” on the circumferential position of AE sources in certain areas of the tube</li> <li>13 tubes inspected in a single pressurization*</li> </ul>
6	2.06	1.79	3.25	<ul style="list-style-type: none"> <li>Excellent longitudinal location and very good circumferential location</li> <li>No access to the center of the tube is needed</li> </ul>	<ul style="list-style-type: none"> <li>Errors in circumferential location as large as 15 inches at the center of the tube</li> <li>8 tubes inspected in a single pressurization*</li> </ul>
8	1.59	1.77	2.39	<ul style="list-style-type: none"> <li>Excellent longitudinal and circumferential location</li> </ul>	<ul style="list-style-type: none"> <li>Access to the center of the tube is needed</li> <li>6 tubes inspected in a single pressurization*</li> </ul>

\*These percentages were calculated assuming PAC DiSP 52 channel system.

## ACKNOWLEDGEMENTS

The authors would like to acknowledge the support of Jon Fallick from the Naval Sea Systems Command in Arlington VA USA, for the completion of this work.

## REFERENCES

- Godínez-Azcuaga, Valery, “Acoustic Emission and Ultrasonic Testing for Periodic Inspection of Pneumatics Pressure Vessels: Comparison of Linear and Planar Source Location Methods for Gas Flask Inspection,” Physical Acoustics Corporation Project No. R-97-573 Final Report, March, 1999.
- Miller, Ronnie K. and McIntire, Paul, Editors, “Nondestructive Testing Handbook, Vol. 5, Acoustic Emission Testing,” American Society for Nondestructive Testing, Second Edition, 1987.
- Viktorov, Igor A., “Rayleigh and Lamb Waves. Physical Theory and Applications.” Plenum Press, 1967.
- Shen, Warren, “Acoustic Emission and Ultrasonic Testing for Periodic Inspection of Pneumatics Pressure Vessels: Waveform Analysis of Simulated AE Transient Signals,” Physical Acoustics Corporation Project No. R-97-573 Final Report, March, 1999.
- Promboon, Yajai, “Source Location Studies on a Tank Car,” Acoustic Emission Working Group Meeting, Princeton, NJ, June 1999.

# NEURAL NETWORK LOCALIZATION OF NOISY AE EVENTS IN DISPERSIVE MEDIA

**M. BLAHACEK, Z. PREVOROVSKY, J. KROFTA, and M. CHLADA**  
Institute of Thermomechanics AS CR, Prague, Czech Republic

## ABSTRACT

*New philosophy for AE source localization under high background noise is designed. The algorithm is based on probabilistic and fuzzy-neuro principles, so AE events may be classified according to their energy and location probability. AE signals recorded during the stamping processes of a thin metal sheet are used for new algorithm testing.*

## INTRODUCTION

Classical algorithms of AE event detection and localization give satisfactory results in relatively simple situations. Nevertheless, they can completely fail under conditions when dispersion and high background noise are present. For example, the detection and localization of AE events occurring during the stamping process of thin metal sheets is complicated by the dispersion of waves propagating in the sheet, and by the presence of noise produced during plastic deformation.

As an alternative approach, the artificial neural network localization algorithms based on signal arrival time differences were extensively studied ([1-3], theoretical aspects in [5]), but the accurate signal arrival time detection is still required. Therefore, a new philosophy of signal processing and AE source localization is suggested to solve the problems with noisy AE events where the signal arrival time detection is rather complicated. The philosophy is based on probabilistic and fuzzy principles reflecting some uncertainty of AE event detection and localization.

AE signals recorded during the stamping processes of a thin metal sheet (Fig. 1) are used for new algorithm testing. Both problems - AE event detection and source localization - are treated together. We monitored AE by four wideband transducers placed at appropriate positions on a cutting tool. Preprocessed AE signals were digitally recorded by a storage oscilloscope at 10 MHz sampling rate. Recorded signal length is up to 0.5 s, so huge data must be analyzed.

As we suppose that the AE events caused by shear deformation and cutting mode fracture in metal sheet are concentrated along the edge of a stamp, the localization may be reduced to a curvilinear 1-D problem. Redundant information obtained from four AE transducers (only two transducers are needed for 1-D localization) is used to reduce errors resulting from high background noise and wave dispersion.

## AE EVENT DETECTION

It is usually easier to recognize individual AE events in a signal envelop than in the original signal, especially if the high level noise is superimposed. The enveloping may be realized by convolution of the recorded AE signal with functions

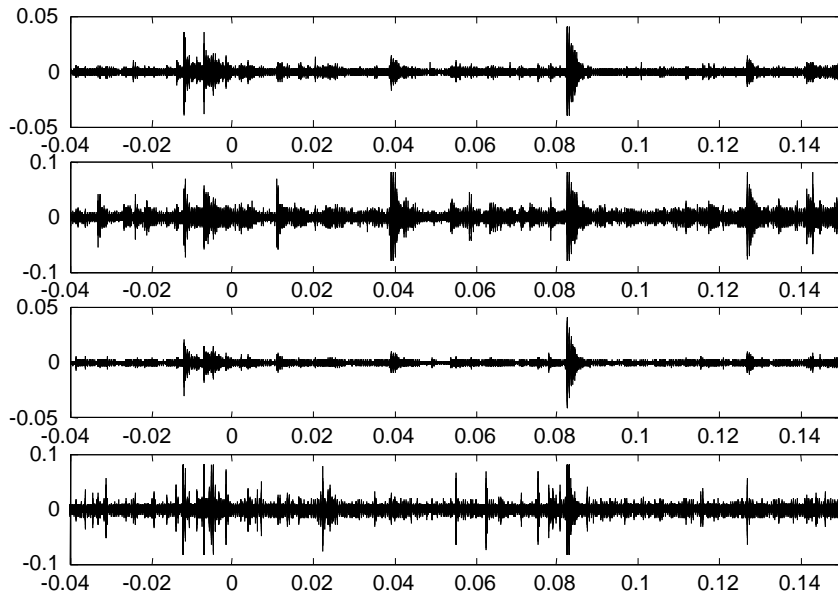


*Fig.1: AE signals recorded during the stamping process (4 channels; time in s).*

$$F_1(x) = \max(f(x), 0), \quad F_2(x) = -\min(f(x), 0), \quad f(x) = -\sqrt[3]{x}e^{-x^2}$$

Here,  $f(x)$  is a function used to enhance signal edges. The envelopes  $F_1$  and  $F_2$  of the AE signal are then divided to obtain new signal  $F$  with highlighted transient effects (see Fig. 2).

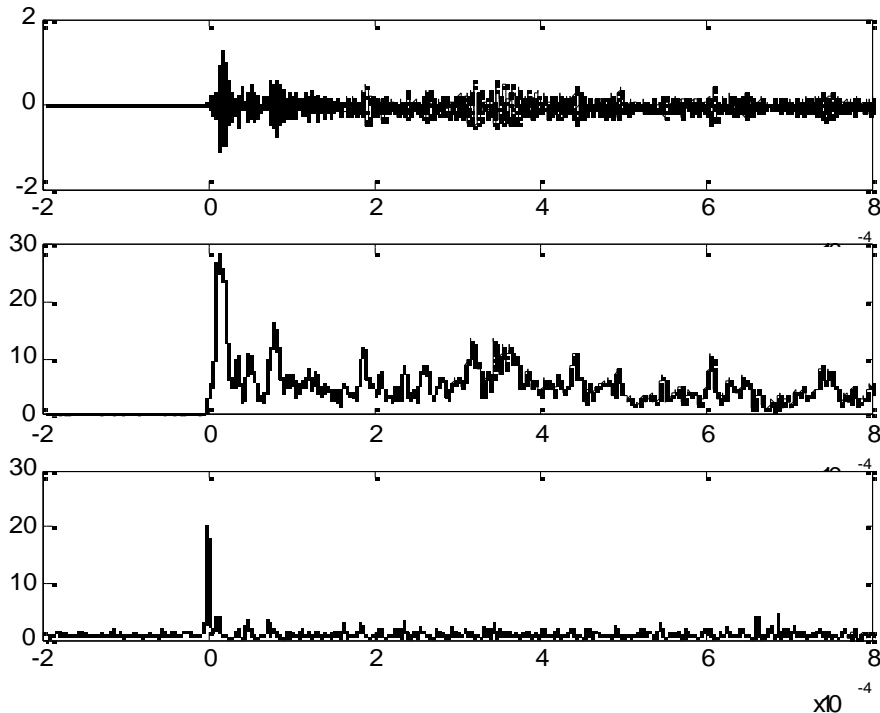


*Fig.2: Original AE signal, convoluted signal  $F_1$ , and ratio  $F$  of the signals  $F_1$  and  $F_2$ .*

To detect AE events, the function  $F$  applied on the whole AE record was searched for its maxima. Corresponding maxima in channels 1 to 4 have been determined, and if at least two maxima co-exist, the AE event is registered.

## AE SOURCE LOCALIZATION

The first problem that must be accounted in a source localization algorithm is high level background noise, and the second consists in the fact that many AE events must not be well pronounced at all transducer positions (the information redundancy helps to event recognition).

The signal  $F$  with enhanced transient effects is suitable for event arrival time  $t_i$  detection under the high level noise. Time differences  $t_{ij} = t_i - t_j$  are calculated for each pair of transducers (if the event is detected by all transducers) or only for those pairs of transducers at which the AE event is detected.

Time differences  $t_{ij}$  obtained by pencil-lead break calibration tests were used to construct localization matrices  $L_i$ ,  $i = 1, \dots, 4$  corresponding to channels 1, ..., 4 (Fig. 3). The stamp contour is split into 32 location sectors. Each row of matrix  $L_i$  corresponds to one location sector. The maximal arrival time difference allowed on the contour ( $50 \mu s$ ) has been divided into 50 equidistant intervals creating matrix columns.

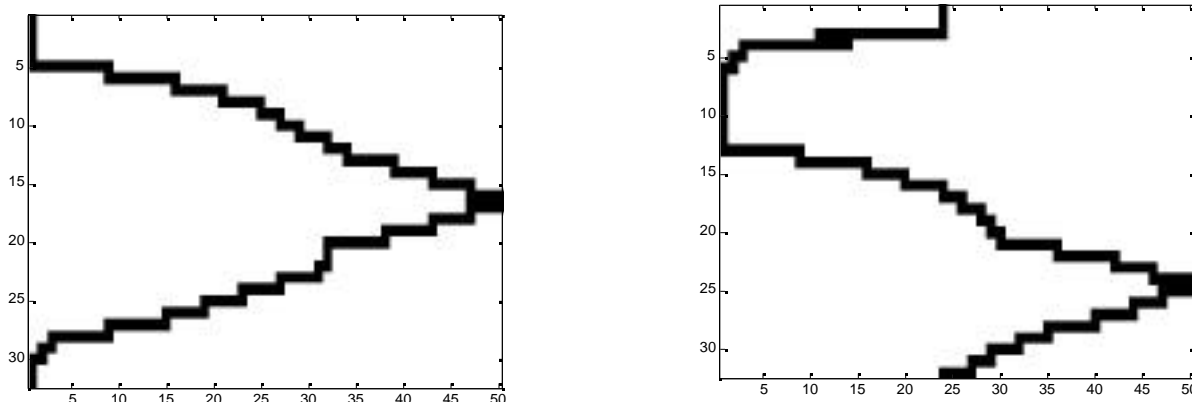


Fig.3: Localization matrices  $L_1$ ,  $L_2$ . Black color represents ones, and white color zeros.

The localization matrices can be treated in terms of neural networks (NN) - see schematic diagram in Fig. 4. In NN notation, the matrix  $L_i$  represents weight matrix of one layer neural network ( $NN_i$ ) with linear transfer function, i.e. associative memory type of NN. Each NN has 50 inputs corresponding to time differences  $t_{ij}$ , and 32 outputs corresponding to 32 location sectors.

If we put a signal without noise to the networks (e.g. pencil-lead break test signal), then each input vector will contain 31 zeros and one unit element, as it is possible to determine near exact time differences  $t_{ij}$  in this case. Quadratic mean  $P$  of output vectors  $P_i$  (see Fig. 4) will have more than one non-zero elements, but one of them is much higher than the others (supposing that the NN's are already well trained).

Dealing with the noisy AE events, the matrices  $L_i$  are convoluted with 2-D function

$$G(x, y) = e^{-x^2} \cdot e^{-y^2}$$

to include possible errors in time difference determination (see Fig. 5). Now the i-th element of output vector  $P$  corresponds to the probability that AE event occurs in the i-th location sector.

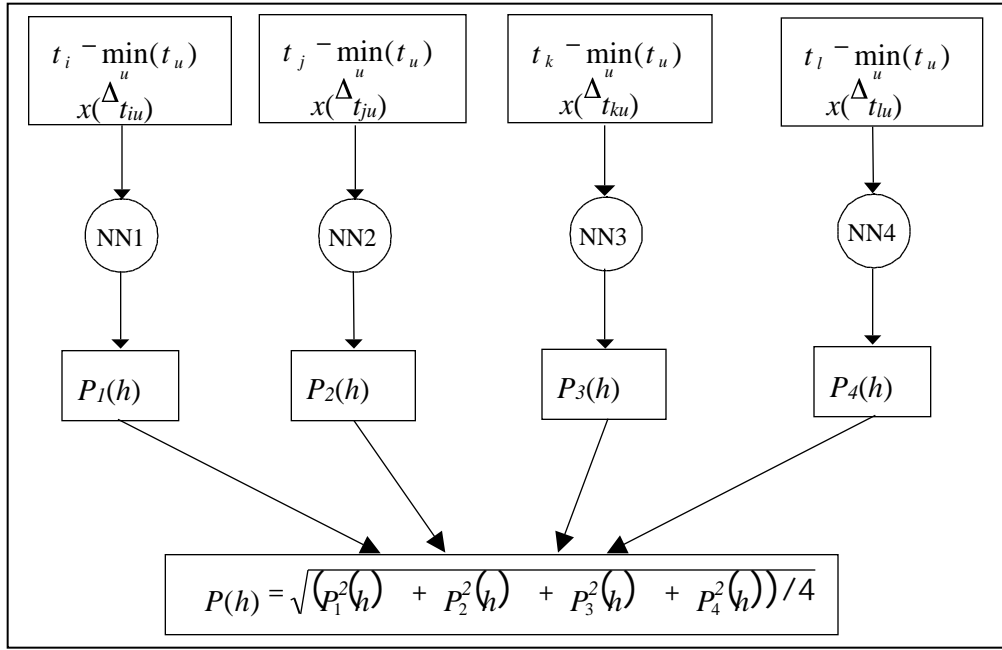


Fig. 4: Schematic diagram of the localization algorithm.

The input vectors were also “fuzzyfied” to include the uncertainties of individual AE event detection. All the above algorithms were programmed in MATLAB [4], and tested on recorded experimental data.

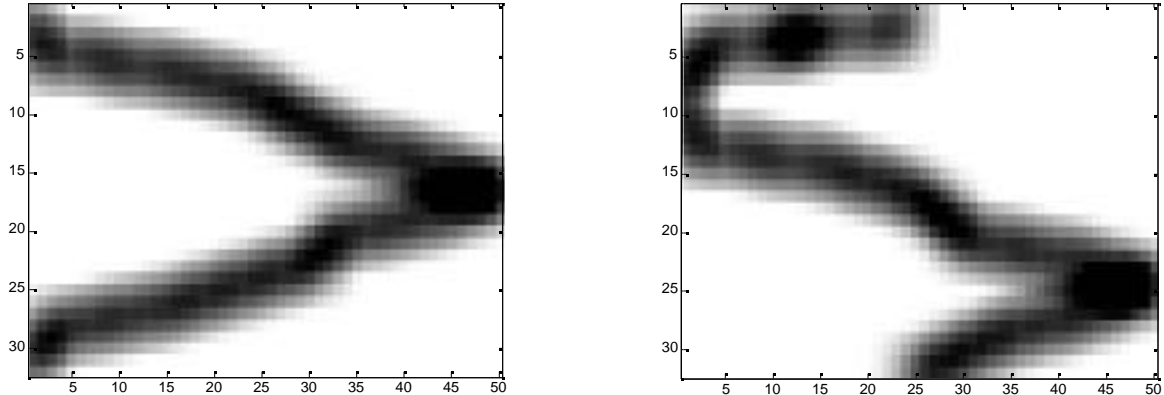


Fig. 5: Matrices  $L_1$ ,  $L_2$  after convolution with the function  $G$ .

## DISCUSSION OF RESULTS

The algorithms described above were used to detect and localize AE events in signals obtained during stamping processes. Time - location distributions of AE events were plotted for better understanding of running processes. Examples of two evaluated experimental results are shown in Fig. 6. The history of

loading force  $P$  is plotted in Fig. 6 along with localized AE events represented by point markers distributed in 16 circumferential sectors, and the energy of AE event is quantified by marker size.

The whole stamping process may be observed in first part of Fig. 6, while the second part shows only beginning of the process under different experimental conditions. Metal sheet thickness, sheet position in stamping machine, position of transducers, AE analyzer settings and process parameters are the main factors influencing the AE results. Stamping tool diagnostics and process parameters optimization can be supported by diagrams in Fig. 6.

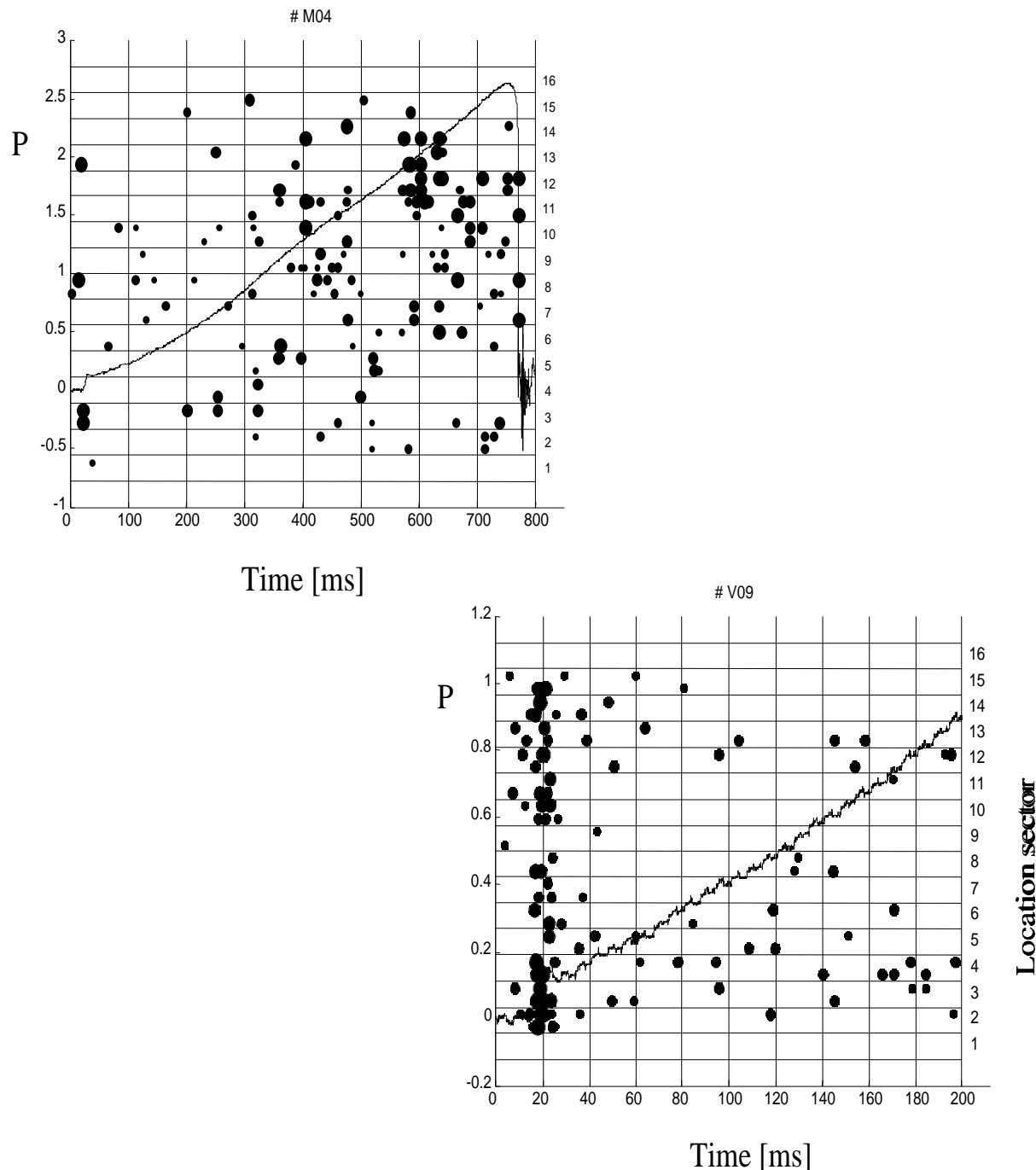


*Fig. 6: Loading history with time - location - energy plot of AE events.*

As the demonstrated examples represent very noisy processes of relatively short duration, the combined probabilistic and fuzzy-neural approach give more reliable diagnostic view than quasi-deterministic treatment charged by many unknown errors. In this new approach, the fixed localization of each individual AE event is substituted by the event occurrence probability distribution. In Fig.6, the marked source locations represent distribution maxima of individual events. Summation of fuzzy localized events registered during the whole experiment is illustrated in Fig. 7. Distributions of individual events have been weighted by event energy and summed to obtain distribution of the event energy density parameter Q in location sectors on the contour.

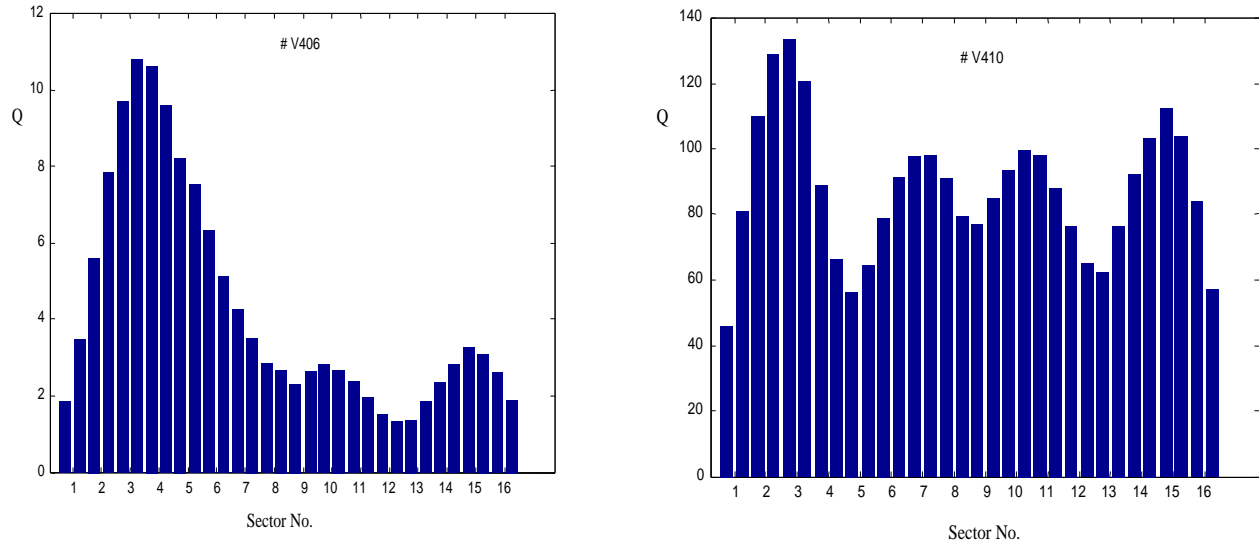


Fig. 7: AE event energy density (Q) distribution in location sectors 1 to 16

The left part of Fig. 7 illustrates typical experiment where the total AE energy is predominantly concentrated around defective place while in the right part experiment, the defect dominance is masked by near random distribution.

In some cases, it is not easy to perform enough pencil-lead break calibration experiments to the training of NN algorithms described above. Nevertheless, the localization procedure may be successfully applied in such situation, as the theoretically computed velocity diagram can be used to construct localization (weighting) matrices  $\mathbf{L}_i$  of time differences  $t_{ij}$ . Once determined, velocity diagram may be usually transferred from one case to another when the same geometry and material are used [3]. If the theoretical velocity diagram cannot be easily obtained, it is possible to establish localization matrix in one dummy application.

## CONCLUSIONS

New philosophy for AE source localization under high background noise is designed. The algorithm is based on probabilistic and fuzzy-neuro principles, so AE events may be classified according to their energy and location probability. It is shown that the AE source location distribution can bring more information about a complex process than erroneous localization of individual AE events. The another AE event characteristics may be also included into the algorithm (in the NN weight matrix) to enhance some important features of diagnosed process.

## **ACKNOWLEDGEMENT**

The present research has been supported by the project No. P4.30 of the European COST P4 action.

## **REFERENCES**

- [1] Z. Prevorovsky, M. Landa, M. Blahacek, D. Varchon, J. Rousseau, L. Ferry, D. Perreux : *Ultrasonic scanning and AE of composite tubes subjected to multiaxial loading*. Ultrasonics, 36(1-5), 1998, pp. 531-537.
- [2] Z. Prevorovsky, M. Blahacek : *Acoustic emission source location by artificial neural networks*. Tagungsband der IV.Kolloquium Technische Diagnostik, Dresden, 1996, p. 212.
- [3] M. Blahacek. Acoustic emission source location using artificial neural networks. PhD Thesis, Institute of Thermomechanics AS CR, Prague, 1999.
- [4] H. Demuth, M. Beale. *Neural Network Toolbox for Use with MATLAB*, The Mathworks, Inc., Natick, MA, (1994).
- [5] I. Grabec, W. Sachse. *Synergetics of Measurements, Prediction and Control*. Springer-Verlag, Berlin, (1995).

# DYNAMICS AND DAMAGE ASSESSMENT IN IMPACTED CROSS-PLY CFRP PLATE UTILIZING THE WAVEFORM SIMULATION OF LAMB WAVE ACOUSTIC EMISSION

Y. MIZUTAMI, H. NISHINO, M. TAKEMOTO and K. ONO\*

Aoyama Gakuin University, Setagaya, Tokyo, JAPAN

\*University of California, Los Angeles, CA, U.S.A.

## ABSTRACT

*Utilizing the simplex-assisted waveform simulation of the Lamb AE waves, we successfully estimated impact force histories in cross-ply CFRP plates impacted by 10–43 m/s steel ball. The force amplitudes estimated by the waveform simulation are compared with those calculated by energy balance and mass-spring models. The force estimated by the AE waveform simulation appears to represent the most realistic value. The maximum force estimated from the measured plate deflection agreed with that by the energy balance model at slower ball velocities, but deviated significantly at higher velocities. Critical ball velocity to cause large internal damage was detected by plate deflection monitoring.*

## INTRODUCTION

Cross-ply CFRP plates suffers various internal damages upon the collision with flying objects. The estimation of impact force history and the detection of damage onset are critical for transportation equipment. Impact force has been intensively studied based on the energy balance (1) and mass-spring models (2), (3). The former can calculate the force amplitude, and the latter the force history as well as the displacement response. In spite of extensive numerical calculations, propriety of estimated impact forces has not been verified by experimental work (4).

Accurate measurement of the impact force history was first attempted by the quantitative AE source characterization. Force amplitude, duration and momentum of elastic impact (ball drop) on an infinite elastic body were studied by direct inverse processing (deconvolution) of bulk mode waves (5),(6),(7). However, AE waves in a thin plate propagates as the Lamb waves. Source characterization of the Lamb waves is generally difficult due to their dispersive nature, more so due to large plate vibration induced by the impact (8). Direct deconvolution of Lamb waves often fails.

In this study, we estimated the force history by the simplex-assisted waveform simulation of Lamb waves, utilizing the experimental transfer function. The force amplitudes estimated for ball velocities from 10 to 43 m/s were compared with that estimated by energy balance and mass-spring models.

## TEST SPECIMEN AND EXPERIMENTAL METHOD

Impact test method is shown in Fig.1. CFRP plates of 100x100 mm square with 2 mm thick, (0<sub>4</sub>/90<sub>4</sub>)<sub>sym</sub>, was firmly supported by a circular steel flanges with an inside diameter of 61 mm. A 7-mm diameter steel ball (1.404 g mass) was accelerated by a nitrogen gas gun and guided by a steel pipe, hitting the plate at the center. Ball velocities, 10 to 43 m/s, were measured by a laser –photodiode pair near the end of the guide pipe. An AE transducer (PAC, PICO) was pressed to the plate via aluminum support, whose ends are firmly attached to the flange. Sensor output was attenuated by 20dB using a high impedance attenuator and digitized by an A/D converter at 50ns sampling interval with 4096 points at 10 bits. We monitored plate deflection by a laser displacement meter (frequency 50 kHz) from the bottom surface.

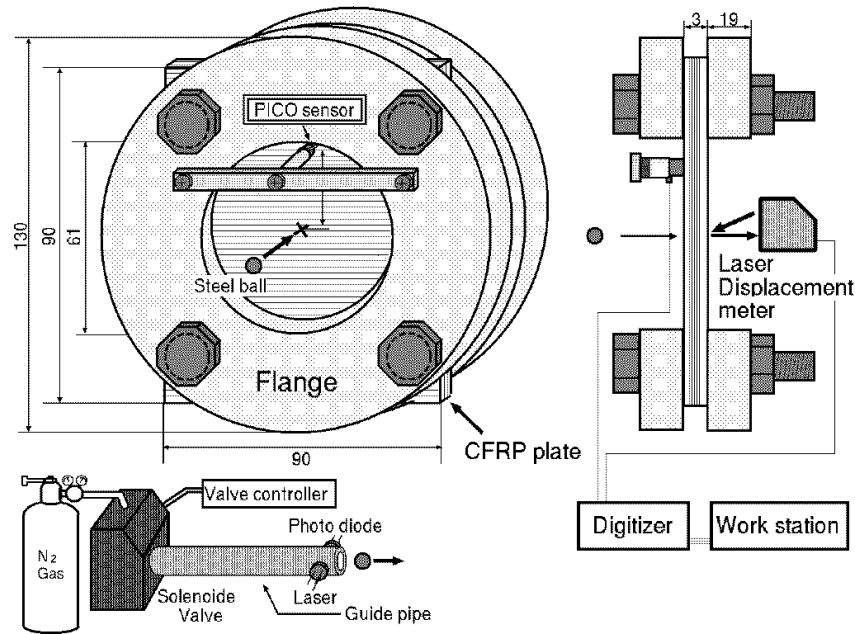


Fig.1 Experimental Setup for impact test.

## RESULTS AND DISCUSSION

### Force history estimated by waveform simulation

Figure 2 represents a flowchart for estimating the impact force history by simplex-assisted waveform simulation. An asymmetric bell-shaped source function, approximated by 11<sup>th</sup> order Fourier series, was optimized by iteration so that the error between the computed and monitored waveforms was minimized.

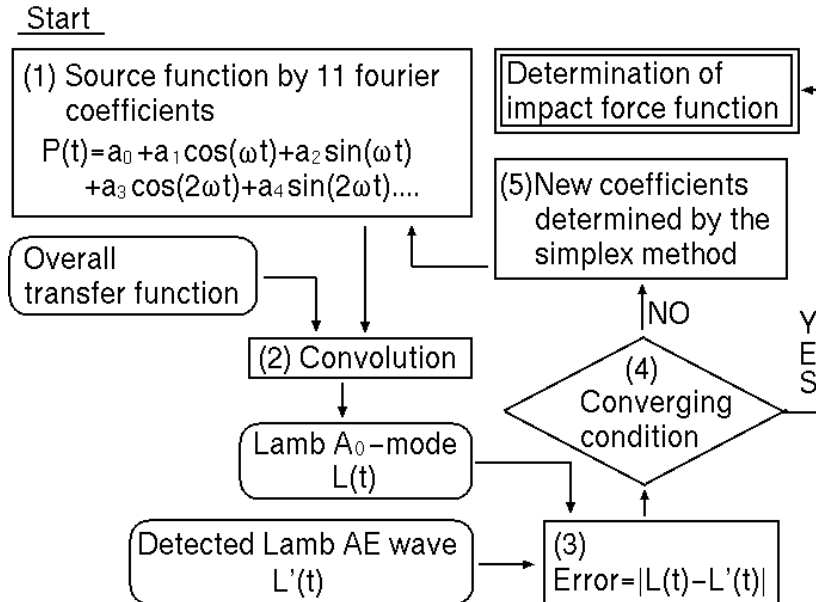


Fig.2 Lamb waveform simulation for estimating the impact force function by the simplex method.

The Lamb waveform was obtained by the time domain convolution of the source function with the overall transfer function determined as a response to a pencil-lead break<sup>(8)</sup>. An example for 16-ply CFRP impacted by 12 m/s ball is shown in Fig. 3.

The overall transfer function (a) was obtained by Gauss-Zeidel deconvolution of detected wave by a step-wise source function (lead break at angle  $60^\circ$ , force release of 5 N at  $0.9 \mu\text{s}$  rise time). By matching the synthesized waveform (c) to the detected one (b), asymmetric force history or the source function (d) with the maximum force of 245 N and duration of  $15 \mu\text{s}$  was obtained. Another examples at 20 and 23 m/s ball impact are shown in Fig. 4. Here, the waveforms were matched for  $S_0$ -mode and first portion of  $A_0$ -mode (to  $30 \mu\text{s}$ ), since the later portions are insensitive to the source function. Estimated force amplitudes are shown in Fig. 5, together with those estimated from plate deflection and two theoretical models.

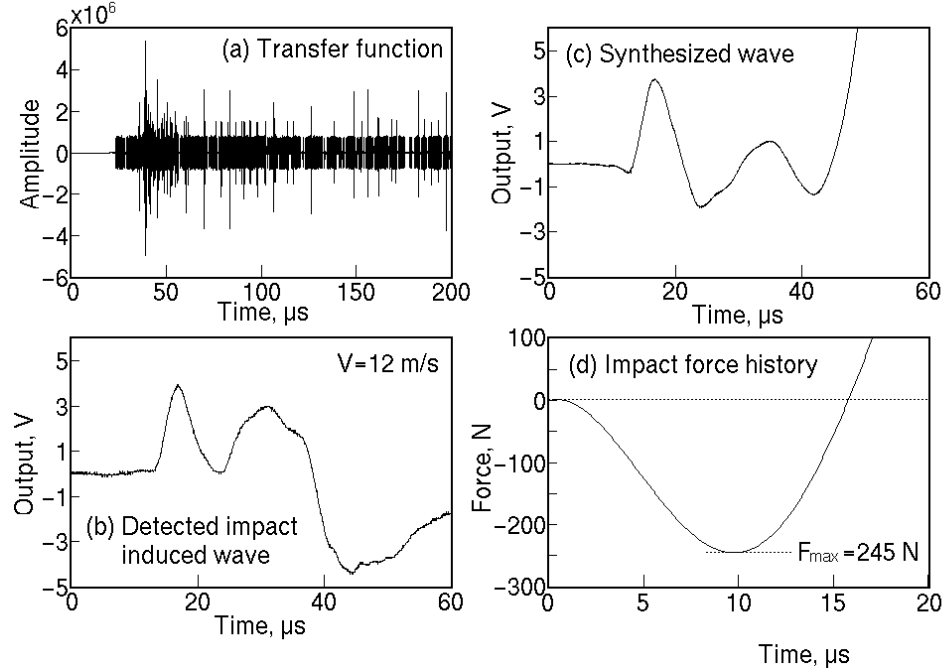


Fig.3 Procedure for estimating the impact force history for 12 m/s ball impact. (a) overall transfer function, (b) detected Lamb wave, (c) synthesized Lamb waves, (d) source wave (impact force history).

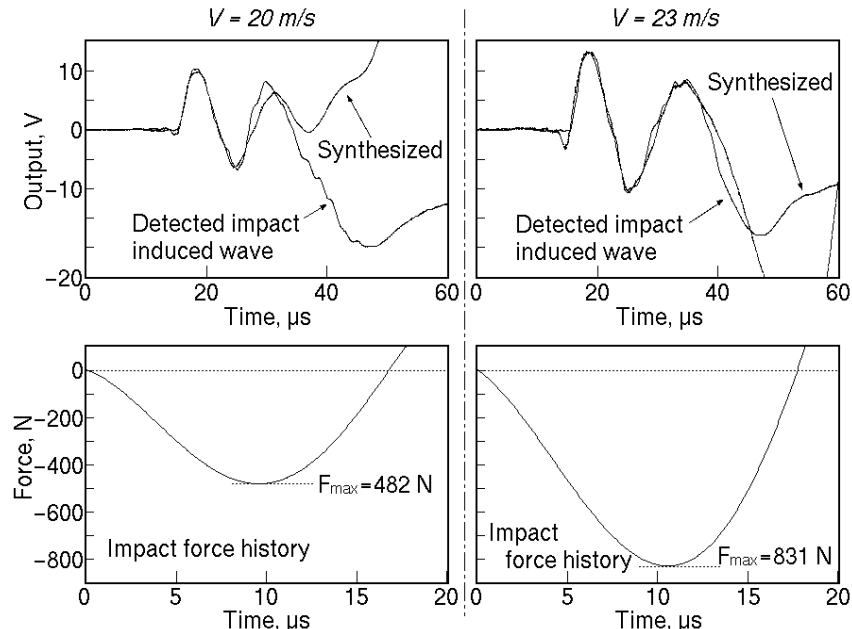


Fig.4 Overlapping of detected and synthesized waves (the upper) and estimated impact force history (the lower) by 20 and 23 m/s ball.

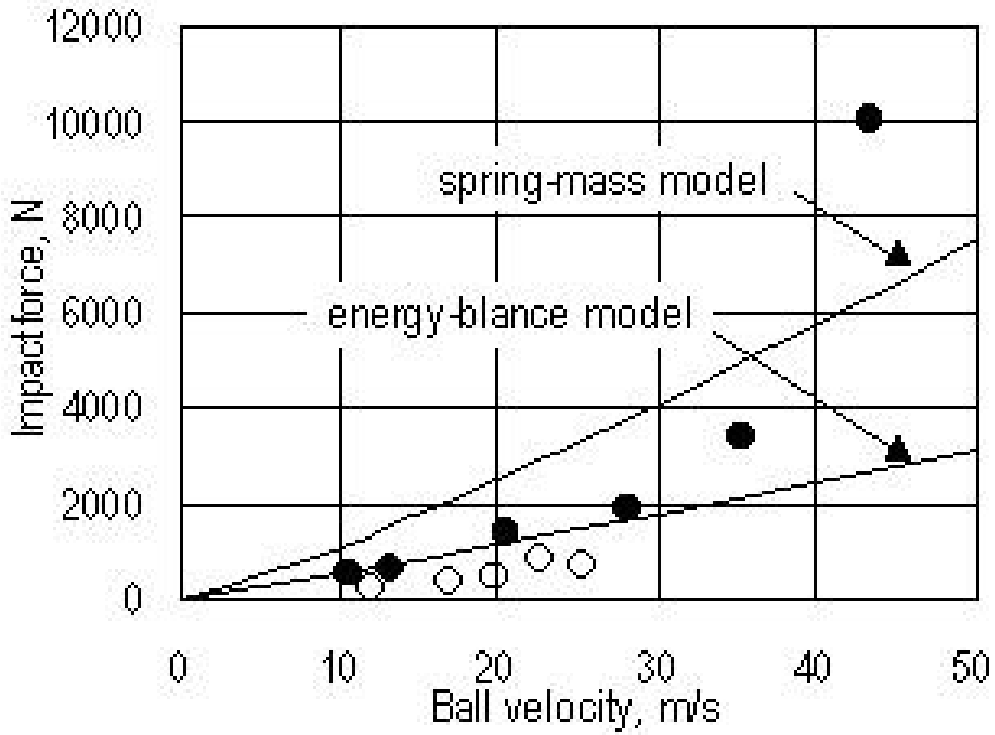


Fig. 5 Ball velocity vs. impact force  $F$  for cross-ply CFRP subjected to impact test.  
 (● : Estimated from plate deflection, ○ : Estimated from Lamb wave)

### Force history predicted by mass-spring model

Displacement responses of the plate and an impacting ball were obtained by solving the kinetic equations (1) and (2) for two-degree-of-freedom mass and spring model with the following initial conditions;  $\dot{x}_1 = Vx_1 = x_2 = \dot{x}_2 = 0$  (1).

$$M_i \ddot{x}_1 + \lambda n |(x_1 - x_2)|^{1.5} = 0 \quad (1)$$

$$M_p \ddot{x}_2 + K_{bs} x_2 + K_m x_2^3 - \lambda n |(x_1 - x_2)|^{1.5} = 0 \quad (2)$$

$$= 1 \text{ for } x_1 > x_2, \quad = -1 \text{ for } x_1 < x_2$$

$M_i$  and  $M_p$  designate the mass of the ball and one-quarter of plate mass, and  $x_1$  and  $x_2$  the displacements of the ball and plate, respectively. Displacement response, for the case of 21 m/s ball impact, is shown in Fig. 6. Intersection of the two curves occurs at 25  $\mu$ s indicating that the ball leaves the deflecting plate and flies off in the opposite direction. The maximum deflection of the plate occurs at 60  $\mu$ s. Shown in Fig. 7 is the force history estimated from the Hertz contact law  $F_I = n(x_1 - x_2)^{1.5}$ . It was obtained by using the instantaneous indentation depth:  $(x_1 - x_2)$  and  $n = 9.97 \times 10^8 \text{ Nm}^{2/3}$ . The source functions in Figs. 4 and 7 resemble each other with the almost same impact duration, which also agrees with the time of the ball-plate separation shown in Fig. 6. However, the force amplitude (831N) estimated by the AE waveform simulation for 23 m/s ball impact is 3.5 times smaller than that (2960N) predicted by the mass-spring model. This difference may be due to the model ignoring the wave propagation effect and also calculating the force from the maximum deflection when the ball had separated from the plate.

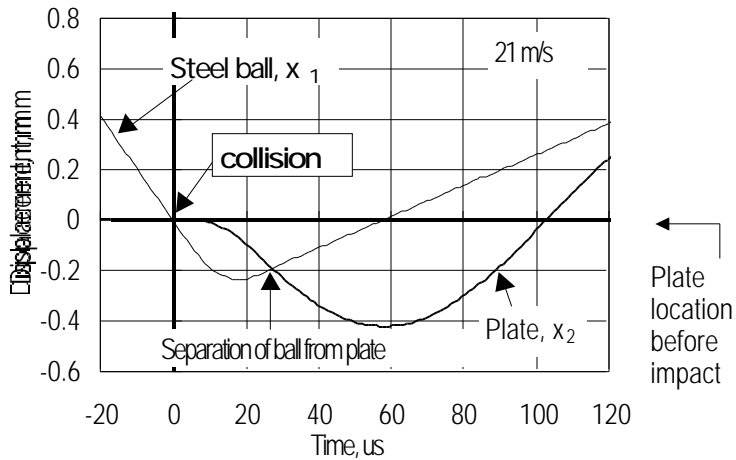


Fig.6 Displacement response of the ball and the plate predicted by the mass-spring model.

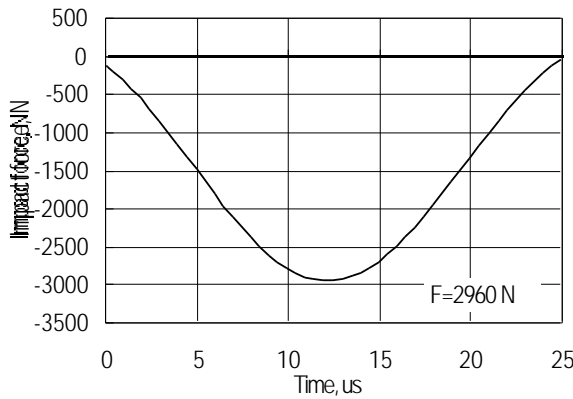


Fig.7 Impact force history of cross-ply CFRP plate predicted by the mass-spring model.  
( $V=23$  m/s)

### Force amplitude estimated by energy balance model and measured plate deflection

Force amplitude, denoted as  $F_2$ , can be estimated by the energy balance model; Eqs. (3) and (4), by equating the kinetic energy of the ball to the sum of the energies due to contact, bending, shear and membrane deformation.

$$M_i V_0^2 = K_{bs} W^2 + \frac{K_m W^4}{2} + \frac{4}{5} \left[ \frac{(K_{bs} W + K_m W^3)^5}{n^2} \right]^{\frac{1}{3}} \quad (3)$$

$$F_2 = K_{bs} W + K_m W^3 \quad (4)$$

$W$  designates the plate deflection at impact position. This model assumes that both  $x_1$  and  $x_2$  reach their maxima at the same timing, while the spring-mass model (Fig. 6) predicts different timing. Thus, the maximum force  $F_1$  estimated by the mass-spring model differs from  $F_2$  predicted by the energy balance model.

We measured the plate deflection  $w$  in Eq. (4) (see Fig. 8) by a laser displacement meter, and calculated the maximum force  $F_2$ . Results are shown in Fig. 5 as filled circles. These values agree with  $F_2$  predicted by the energy balance model (the lower curve in Fig. 5) up to 30 m/s velocity.

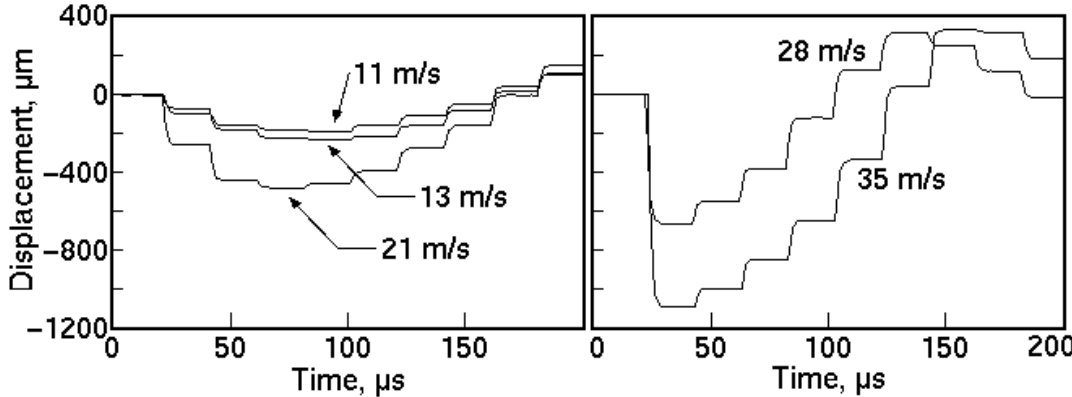


Fig. 8 Displacement response of CFRP plate impacted by 11 to 35 m/s ball.

It is noted that the plate deflection shows symmetric shape at lower velocities (the left of Fig. 8), but asymmetric shape with fast rise and slow recovery at higher ball velocities (the right). This transition appears to be due to the internal damages, as discussed later. The maximum deflection (488  $\mu\text{m}$ ) and timing (103  $\mu\text{s}$ ) by 21 m/s ball impact agreed fairly well with that (426  $\mu\text{m}$  and 163  $\mu\text{s}$  in Fig. 6) estimated by the mass-spring model.

### Change of impact force as a function of ball velocity

Impact forces estimated are represented in Fig. 5 as a function of ball velocities. The mass-spring models shows the largest values, since it calculated the idealized (and unrealistic) Hertz contact force. The force calculated from the measured deflection are on the curve of the energy balance model at ball velocities below 21 m/s, but deviates from the curve above 30 m/s. This deviation is found to be due to the onset of large internal damage. Post-impact ultrasonic C-scan inspection (Fig. 9) revealed a large extension of delamination at back surface (tension side) at around 28 m/s. Plate deflection monitoring can be used for inspecting the critical internal damage onset in impacted CFRP plates. The force amplitude calculated from the measured plate deflection is two times larger than estimated by the AE waveform simulation. This overestimate appears to be due to the continued deflection of the plate by inertia, as shown in Fig. 6. From the consideration, the force estimates by the AE waveform simulation appear to represent the most realistic values.

### CONCLUSION

We estimated the impact force histories in impacted cross-ply CFRP plate by the waveform simulation of Lamb AE signals, and compared them with those predicted by the mass-spring and energy balance models. Results are summarized below;

- 1) Waveform simulation method can correctly predict the force history, since AEs are monitored before the onset of plate deflection. Impact force increased with ball velocity, while the duration is almost constant, irrespective of the ball velocity.
- 2) The force estimated by the AE waveform simulation appears to represent the most realistic value. The present methodology of using experimental transfer function and simplex-assisted matching of calculated and observed waveforms can be a useful tool in other circumstances as well.
- 3) The impact force estimated from the measured plate deflection agreed with that estimated by the energy balance model at slower ball velocities, but deviates above the critical velocity where large delamination has occurred.

## ACKNOWLEDGMENTS

A part of this research was supported by the fellowship from the Japan Society for Promotion of Science to Y. Mizutani.

## REFERENCES

- <sup>1</sup> K.N. Shivakumar: Transactions of the ASME, Vol.52, 1985, pp.674-680
- <sup>2</sup> S. Abrate, IMPACT ON COMPOSITE STRUCTURES, Cambridge Univ. Press, (1998), p.85
- <sup>3</sup> Goldsmith, Impact: The Theory and Physical Behaviour of Colliding Solid, Arnold Publ., Ltd. London, (1960)
- <sup>4</sup> S. Abrate, IMPACT ON COMPOSITE STRUCTURES, Cambridge Univ. Press, (1998), p.85
- <sup>5</sup> N.N. Hsu and S.C. Hardy, AMD-Vol.29, ASME(1978)85.
- <sup>6</sup> T. Ohira and T. Kishi, The iron and Steel Institute of of Japan, 70(1984), pp. 2188-2195.
- <sup>7</sup> M. Takemoto and Y. Hayashi, J. Acoustic Emission, 7-4, (1988), p.185
- <sup>8</sup> Y. Mizutani, F. Nishiwaki, M. Takemoto and K. Ono, 2<sup>nd</sup> ESIS TC4 Conference on Polymers and Composites, Sept., 1999 (in press).

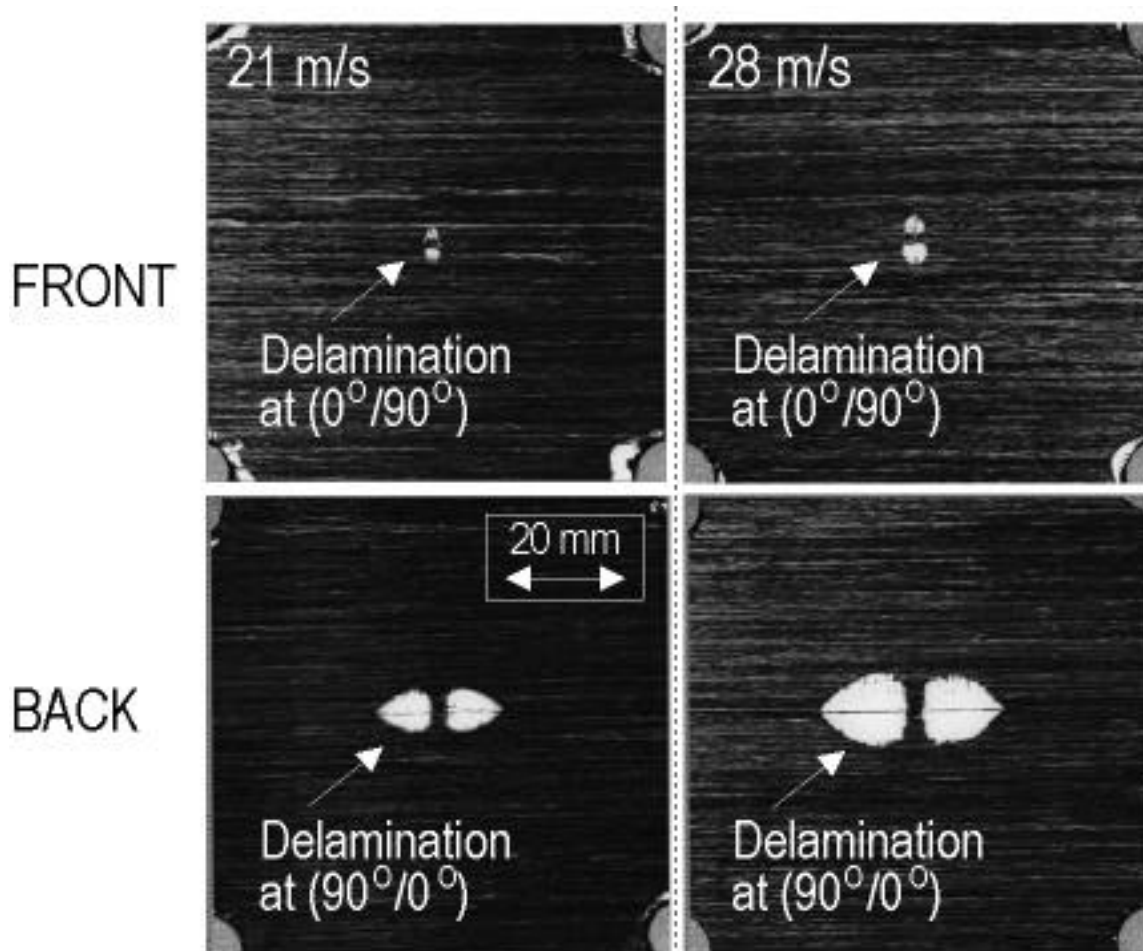


Fig. 9 C-scan images of internal damage in cross-ply CFRP plate impacted by 21 and 28 m/s ball.

# ACOUSTIC EMISSION DETECTION DURING STRESS CORROSION CRACKING AT ELEVATED PRESSURE AND TEMPERATURE

R. VAN NIEUWENHOVE and R. W. BOSCH

Studiecentrum voor Kernenergie – Centre d'Etude de l'Energie nucléaire,  
Reactor Materials Research, Mol, Belgium

## ABSTRACT

In order to test the feasibility of using acoustic emission for the detection of stress corrosion cracking under pressurized water reactor conditions, experiments were carried out on sensitised and solution annealed AISI 304 cylindrical samples, loaded by an SSRT unit in an autoclave. To enhance inter-granular cracking, the measurements were carried out in an oxygen containing solution of 0.01 M Na<sub>2</sub>SO<sub>4</sub>. Using the SSRT pull rods as waveguides, it has been demonstrated that acoustic emission events can be detected outside the autoclave, revealing increased activity during the elastic-plastic transition and in the plastic region before the actual failure of the sample. Whereas this increased activity could be caused both by dislocation movements and real cracking events, simultaneous electrochemical impedance spectroscopy measurements seem to favor the interpretation that real crack initiation events are being detected.

## INTRODUCTION

Due to the increasing age of nuclear power plants, stainless steel core components suffer from increasing radiation damage. These irradiated stainless steels are susceptible to stress corrosion cracking, in this case called irradiation assisted stress corrosion cracking (IASCC)[1]. To study this complex phenomenon, it is important to monitor not only the crack propagation rate but also the exact time of crack initiation. Acoustic emission (AE) is a powerful and sensitive technique [3,4], but its application to pressurized water reactor (PWR) conditions poses a real challenge. A feasibility test has been performed in an autoclave, equipped with a slow strain rate tensile testing (SSRT) unit at high temperature (300°C) and pressure (105 bar).

## EXPERIMENTAL SET-UP AND CONDITIONS

### Autoclave system and material

The experiments were carried out in a Hastelloy autoclave equipped with a double SSRT loading unit system (see Fig. 1). The experiments were carried out on AISI 304 cylindrical samples (length 10 mm, diameter 2.5 mm) in an oxygen containing solution of 0.01-M Na<sub>2</sub>SO<sub>4</sub> at 300°C, which should result in inter-granular stress corrosion cracking (IGSCC) [2]. Before heating the autoclave, the autoclave was pressurized with 10 bar of air to ensure that the test solution contains a large amount of oxygen. The experiments were conducted under static conditions, i.e. no recirculation of the test solution was performed. In each test, one sample was subjected to a constant elongation rate of  $1 \times 10^{-6} \text{ s}^{-1}$  while the other sample was free of stress. One experiment was performed on solution-annealed AISI 304, while a second one was carried out at 300 °C on sensitized (621°C) AISI 304.

## Acoustic emission detection system

The AE sensors (DECI SE25-P; broadband, single-ended) were mounted on the SSRT pull rods which served as waveguides (see Fig. 1). The sensor signals were amplified by preamplifiers (type AEP4; 34 dB) and fed to a Vallen AMSY4-PC system, equipped with a 300-kHz low-pass filter. The low frequency-limit was chosen deliberately to avoid high-frequency electrical noise generated by the autoclave heating system. Reducing the electrical noise to an acceptable level was found to be very difficult. An extra grounding pin was installed just outside the laboratory to provide a more effective grounding of the whole SSRT and autoclave structure. Even then, there was some correlation between the electrical-heating phases of the autoclave and the electrical noise. To reduce this effect on the measurement, a signal was derived from the heating system, which was fed into a data acquisition control input of the AMSY4 system, such that data were only recorded during relatively ‘quiet’ heating phases. In a next step, differential AE sensors will be used to reduce the noise even further.

## Electrochemical impedance spectroscopy system

Every hour, electrochemical impedance spectroscopy (EIS) measurements were performed quasi-simultaneously at both samples. The EIS measurements were performed with one potentiostat and one frequency response analyzer connected to a multiplexer. Pt wires were used as pseudo-reference electrodes while the autoclave was used as counter electrode. The impedance measurements were performed from 1000 to 1 Hz with amplitude of 10 mV RMS. One measurement (containing all frequencies) took about 3 min. The difference in phase shift between the stressed and the non-stressed sample, at low frequency (1 Hz) was found to be a sensitive indicator of cracking [5].

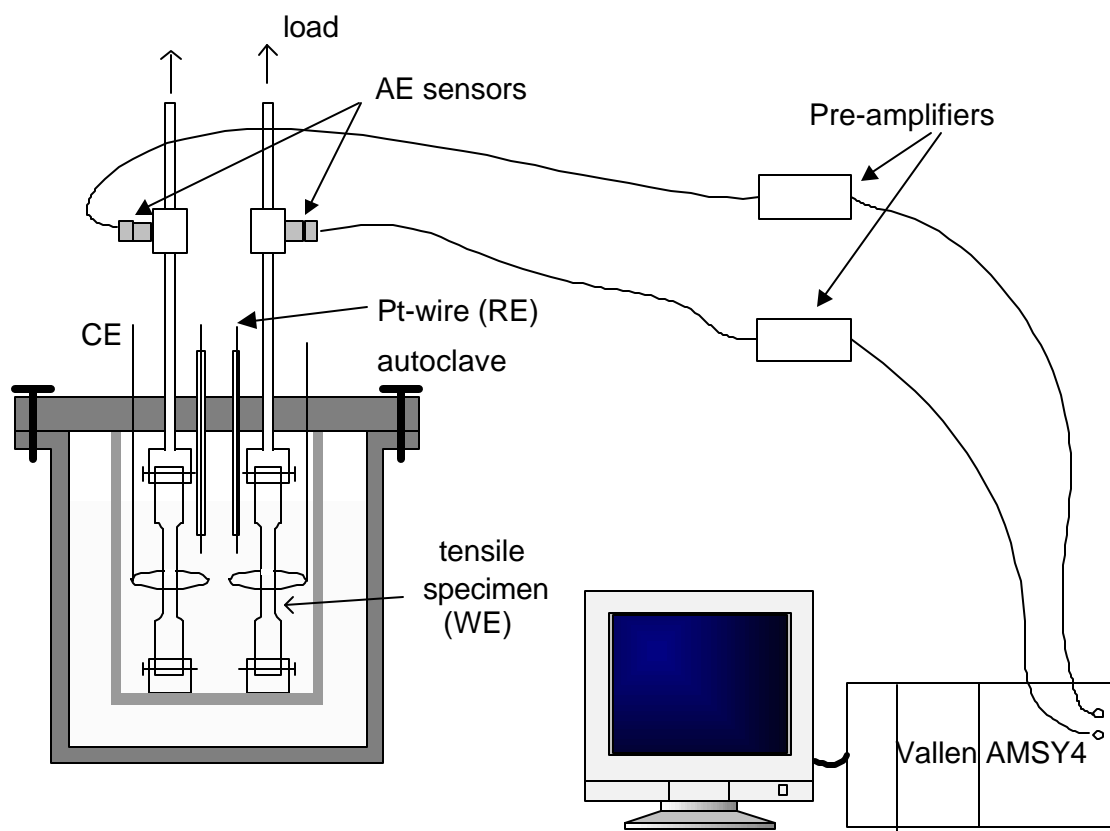
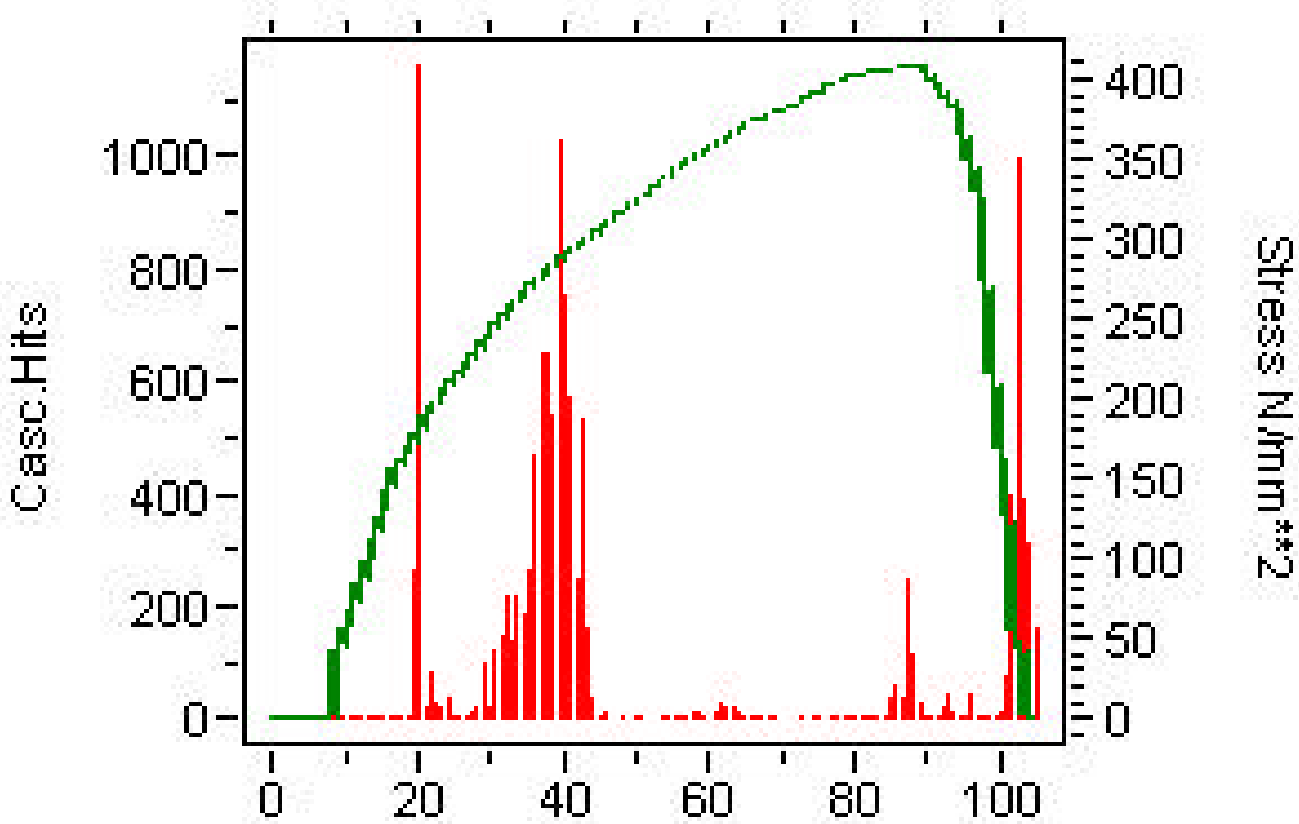


Fig. 1: Experimental set-up.

## MEASUREMENTS

For the case of the solution-annealed AISI 304, the rate of the cascaded hits and the amplitude (both with a time step of 0.2 h) are plotted in Figs. 2 and 3. Strong AE can be observed at  $t = \sim 20$  h, which corresponds to the transition between the elastic and plastic deformation regions. Between 30 and 40 h (already in the plastic region), again strong AE activity is observed and finally also before (around 87 h) the sample breaks (at  $t = 95$  h). Simultaneous EIS measurements on the solution-annealed AISI 304 are shown in Fig. 4, revealing also crack initiation at  $t = \sim 20$  h (deviation from zero phase difference). Often, AE at the elastic-plastic transition region is attributed to the motion of dislocations [3, 4], but the simultaneous observation of a phase shift by EIS seems to support the view that the AE events are mainly caused by cracking. SEM pictures of the fracture surface of the solution-annealed AISI 304 sample are shown in Fig. 5, revealing trans-granular stress corrosion cracking.

For the sensitized AISI 304, the rate of the cascaded hits and the amplitude (both with a time step of 0.2 h) are plotted in Figs. 6 and 7. An increased hit rate is already observed several hours before the final cracking of the sample. The amplitude of the hits in this period is, however, lower as compared to the elastic loading phase (from 0 to 13 hours).



*Fig. 2: Rate of cascaded hits (time step 0.2 h) during the SSRT test on solution annealed AISI 304 revealing several signatures of crack initiation (at 20 h, 30-40 h, 87-90 h).*

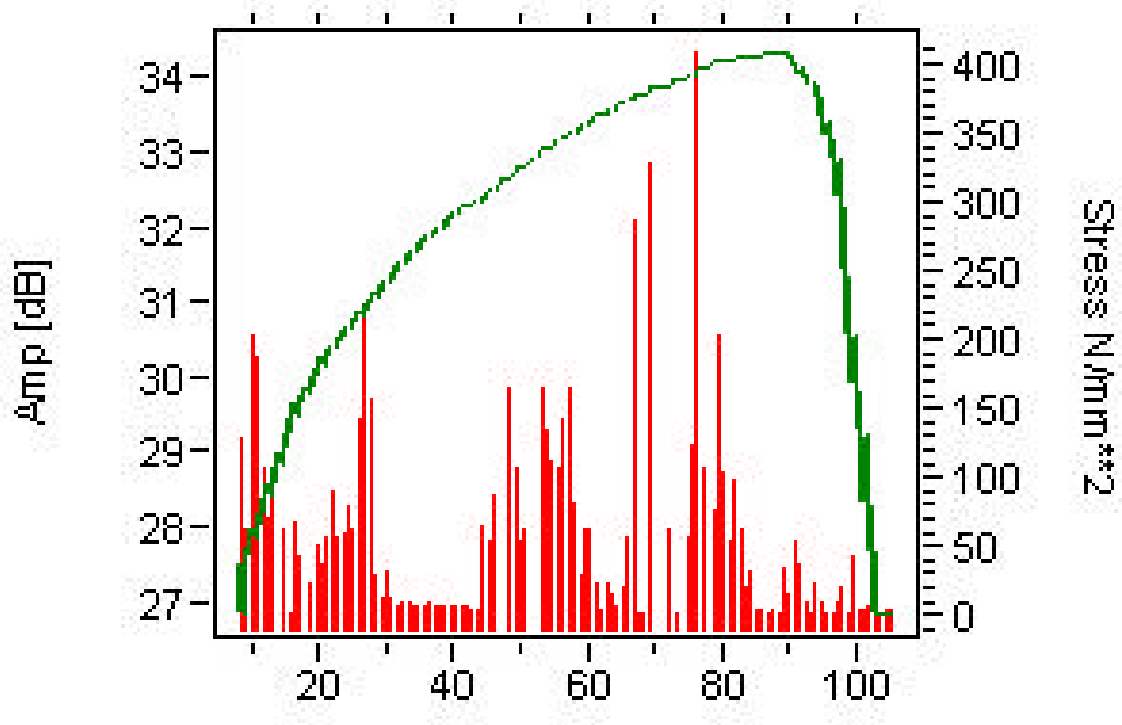


Fig. 3: Amplitude of hits (time step for averaging: 0.2 h) during the SSRT test on solution-annealed AISI 304 revealing signatures of crack initiation.

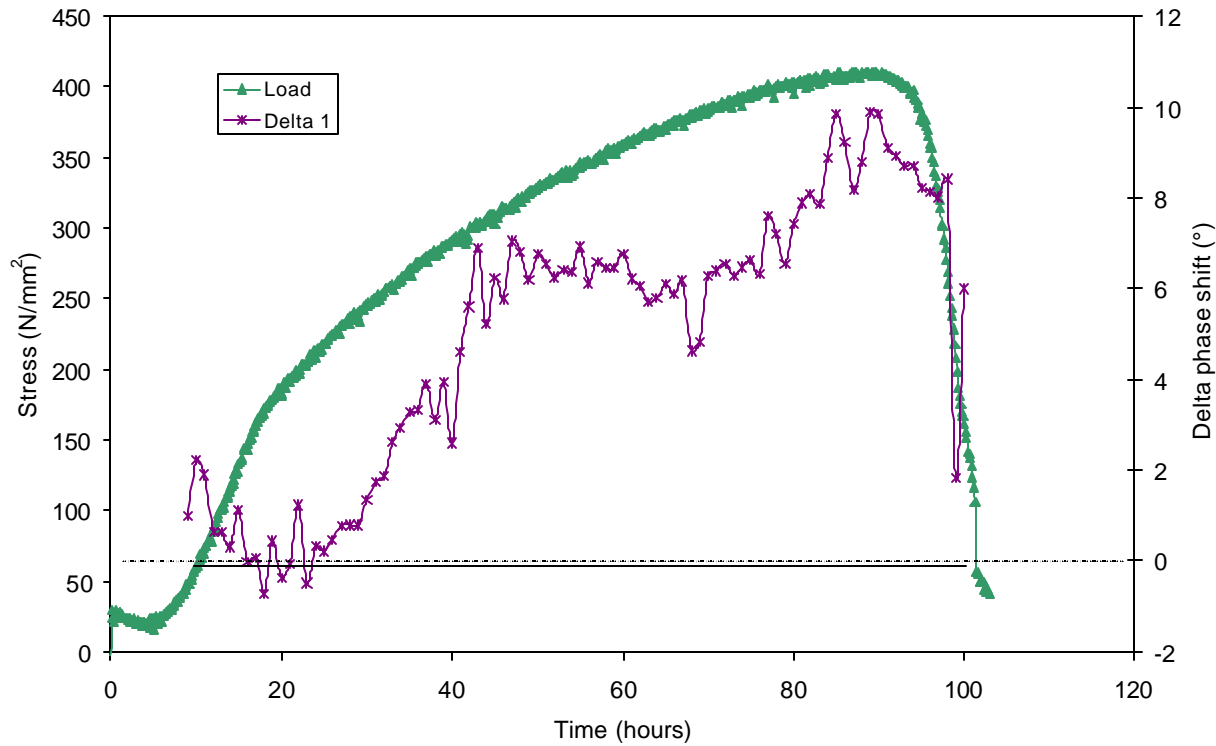
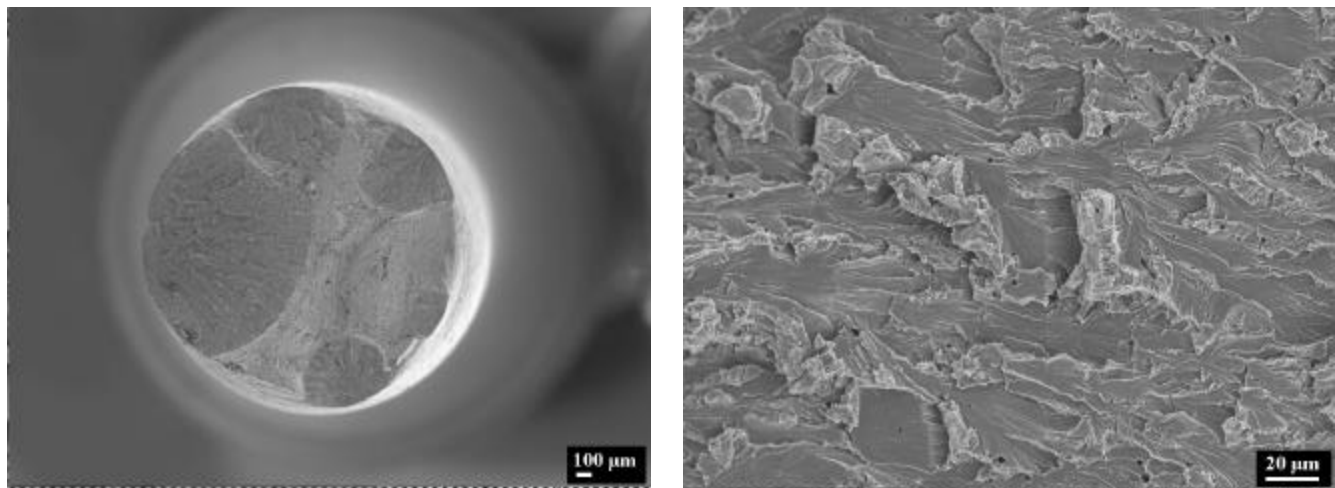
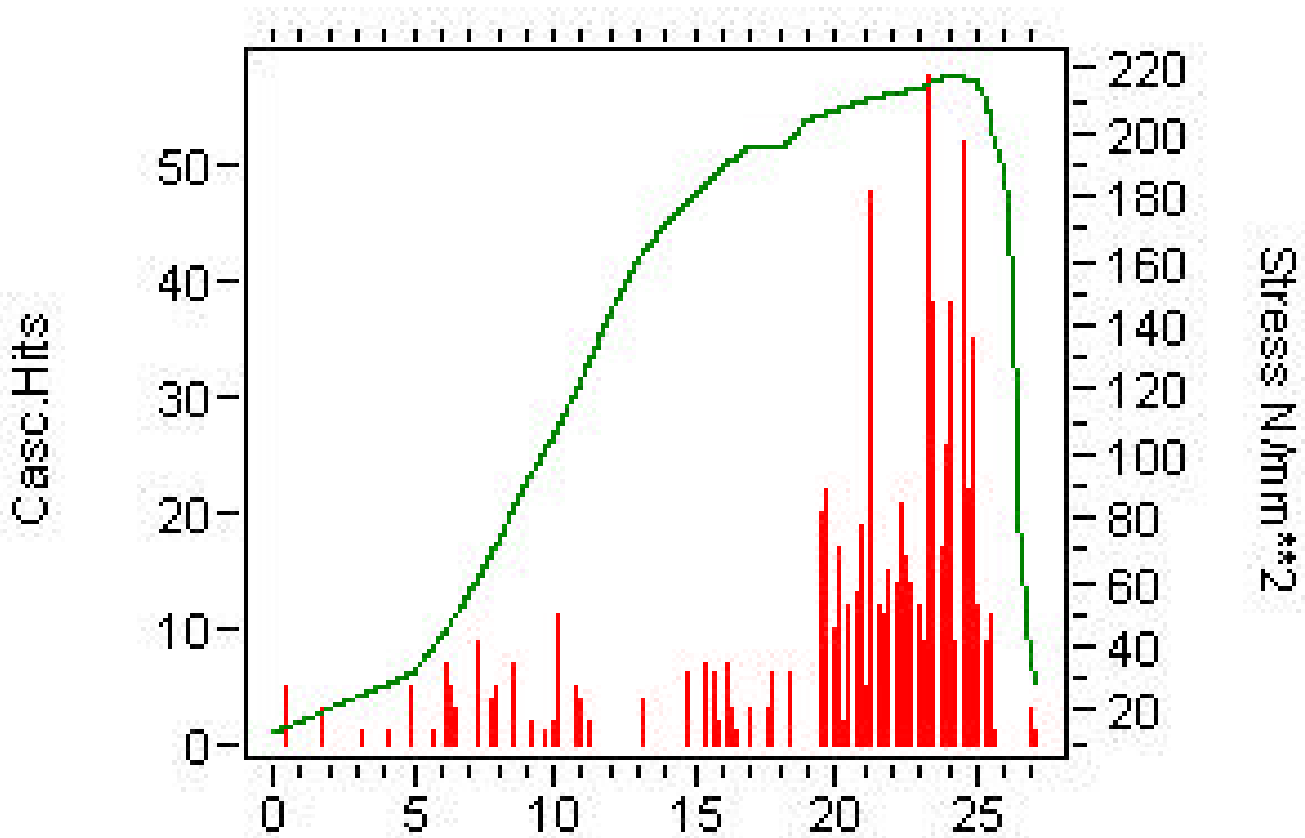


Fig. 4: Phase difference between a stressed and a non-stressed AISI 304 solution annealed sample, as obtained by EIS measurements, starts to deviate from zero at ~20 hours, providing a possible indication of crack initiation.



*Fig. 5: SEM pictures of fracture surface of the solution-annealed AISI 304 sample, showing transgranular fraction (stress corrosion cracking).*



*Fig. 6: Rate of cascaded hits (time step: 0.2 h) vs. time in h during the SSRT test on sensitized AISI 304 revealing several signatures of crack initiation (at 5-10 h, and at 20-25 h)*

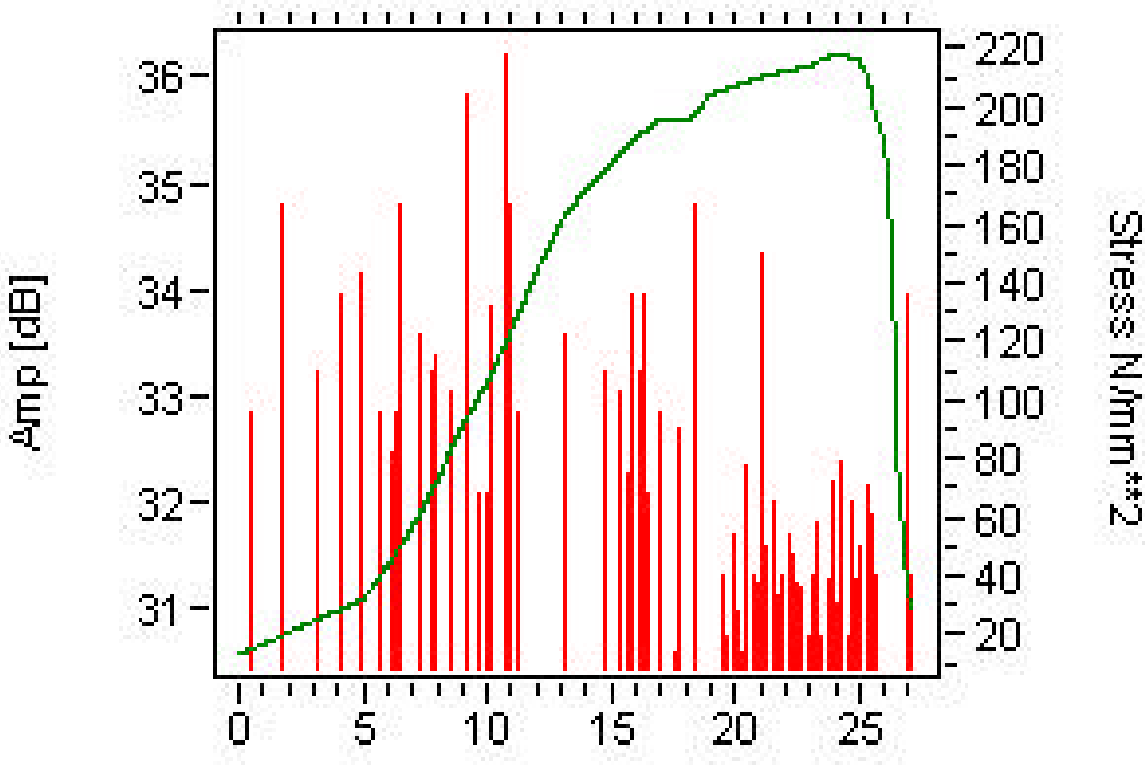


*Fig. 7: Amplitude of hits (time step for averaging: 0.2 h) vs. time in h during the SSRT test on sensitized AISI 304 revealing signatures of crack initiation.*

## CONCLUSION

Acoustic emission detection can be successfully applied to detect stress corrosion cracking on samples located in an autoclave at high temperature and pressure.

## ACKNOWLEDGEMENTS

The authors wish to acknowledge Ludo Eysermans for the autoclave and sample preparations.

## REFERENCES

1. S.M. Bruemmer, E.P. Simonen, P.M. Scott, et al., Radiation-induced material changes and susceptibility to intergranular failure of light water-reactor core internals, *Journal of Nuclear Materials*, **274** (1999), 299-314
2. M.E. Indig, A.R. McIlree, *Corrosion*, **35**(7), (1979), 288.
3. H.N.G. Wadley, C.B. Scruby, and J.H. Speake, Acoustic emission for physical examination of metals, *International Metals Review*, 1980, No. 2, Review 249, 41.
4. W.W. Gerberich, et al., Acoustic Emission Monitoring of Stress Corrosion Cracking, *Materials Science and Engineering*, **A103** (1988).
5. R.-W. Bosch, Investigation of stress corrosion cracking at elevated temperatures with Electrochemical Impedance Spectroscopy, *EUROCORR 99*, 1999, Aachen.

# **RELIABILITY OF ACOUSTIC EMISSION TECHNIQUE TO ASSESS CORROSION OF REINFORCED CONCRETE**

**H. IDRISI and A. LIMAM\***

**Physico-chimie Industrielle, I.N.S.A. Lyon, Lyon, FRANCE**

**\* U.R.G.C. "Structures", I.N.S.A. Lyon, Lyon, FRANCE**

## **ABSTRACT**

The deterioration of reinforced concrete structures is of major concern. Most of the damages are the consequences of reinforcement (steel-rebar) corrosion. Rebar corrosion can be induced by chloride or by carbonation. It is well known that the chloride rebar corrosion is more detrimental and that this process contains three basic components: chloride diffusion, electrochemical corrosion and concrete fracture. Therefore, the early detection and the checking of state of corrosion of reinforcing rebars by non-destructive techniques are important not only in an academic point of view but in practical applications concerning structure's maintenance and repair. This paper presents the results of an experimental investigation on the use of acoustic emission during the corrosion of steel rebars embedded in mortar and immersed in sodium chloride solution. The process of corrosion is accelerated by various imposed potentials and is followed by AE coupled to electrochemical techniques. The experimental results show that AE methods can detect the initiation steps damage and a perfect correlation between the evolution of the acoustic activity and the current of corrosion density. This could allow us to evaluate the corrosion rate and to simulate the long-term degradation behavior of reinforced concrete.

## **INTRODUCTION**

Nowadays, the durability of concrete structures has become a matter of concern, primarily because of the corrosion of steel reinforcement. The problem is not due to mechanical strength deterioration of rebar, as only a few percent of the steel cross-section is corroded after 10 years [1], but it is because the corrosion products exert stresses within the concrete, which cannot be supported by its limited plastic deformation, and the concrete therefore cracks [2], leading to delamination and spalling of the concrete cover. The break-down of the steel-concrete interface can lead to the failure of the structure. The tendency of steel rebars to corrode or not depends on its potential corrosion evolution in its environment. Hence, infrastructure corrosion is linked to the composition and to the fabrication process of the concrete; it depends particularly on the presence of aggressive agents such as chlorides, sulphates, acids, in the employed materials and in their environment of use.

The processes or mechanisms of rebar corrosion are well known [3-5]. The importance of both chloride and hydroxide ions in reinforcement corrosion process is studied by several authors [6,7]. While most of the concrete damage processes are well explained and studied with accuracy by laboratory techniques, current inspection methods of reinforced concrete structures lack accuracy and can provide sufficient information only after corrosion has occurred.

This study aims at establishing a laboratory technique, based on the coupling of acoustic emission with electrochemical methods allowing, on the one hand, early detection and control of the reinforcements corrosion in the concrete, and on the other hand, the simulation of the long-term behavior of reinforced concrete degradation. The degradation mechanism of mortar, and the reinforcement corrosion itself, was followed by acoustic emission. The acceleration of the corrosion process was carried out by various

imposed potentials. The obtained results first show a perfect correlation between the acoustic activity and the behavior of reinforcements when corroded in the NaCl solution.

## TEST SPECIMENS, EXPERIMENTAL DEVICE AND PROCEDURE

The samples used in this study are made from a normalized mortar with a water-cement ratio of 0.5. The composition of this mortar is given in Table 1. The dimension of these samples (Fig. 1) was defined in a way representative of the real structures, and the standard cover concrete dimension is preserved.

**Table 1: Chemical composition of concrete.**

Component	Weight (g)
Water / Cement	0.5
Water	225
Portland cement CPA 52-5	450
Normal sand ISO 679	1350

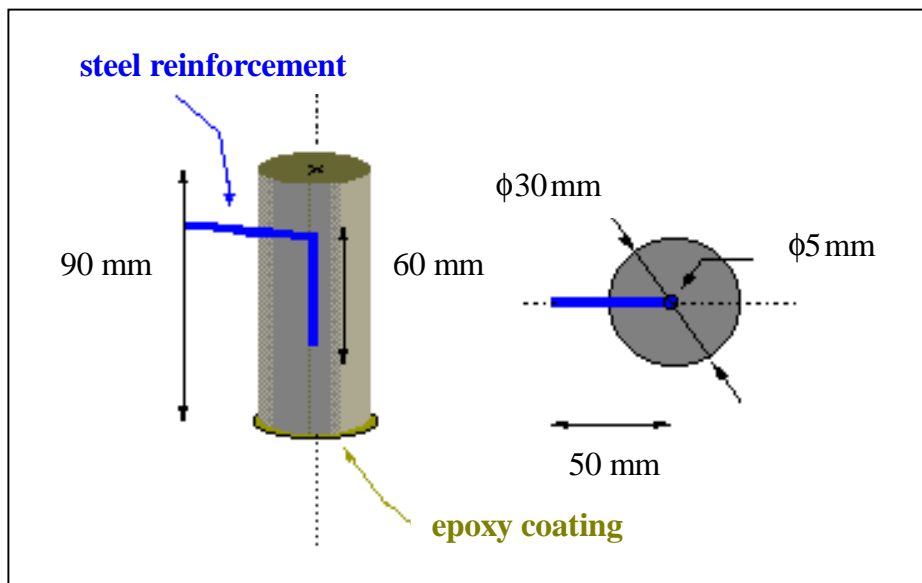


**Fig. 1: Test specimen.**

The mortar was mixed automatically and poured in PVC mould in which a carbon steel reinforcement, 5 mm in diameter and 60 mm length, was placed along the mould longitudinal axis. The sample is then compacted with the assistance of a vibrating table during 60 s, then cured in a climatic chamber, with a relative humidity higher than 50% during 4 weeks. The upper face of the cylinder is polished with a silicon carbide paper (standard P180) so as to obtain a smooth surface giving a better contact interface with the sensor of acoustic waves. The contact for electrochemical measurements is ensured by direct connection on the steel reinforcement. An epoxy resin coating is then applied to the lower face of the sample so as to impose the infiltration of the solution only by the side faces.

The experimental device used is composed of two systems (Fig. 2):

1. An electrochemical system of measurement consisted of a potentiostat Tacussel-Radiometeur PGZ 301 coupled to a computer and of a software of acquisition Voltamaster 4, with the sample being the working electrode, a platinum mesh as the counter-electrode and a saturated calomel electrode (Hg/Hg<sub>2</sub>Cl<sub>2</sub>/KCl) as a reference. In order to avoid acquisition of acoustic noise induced by hydrogen

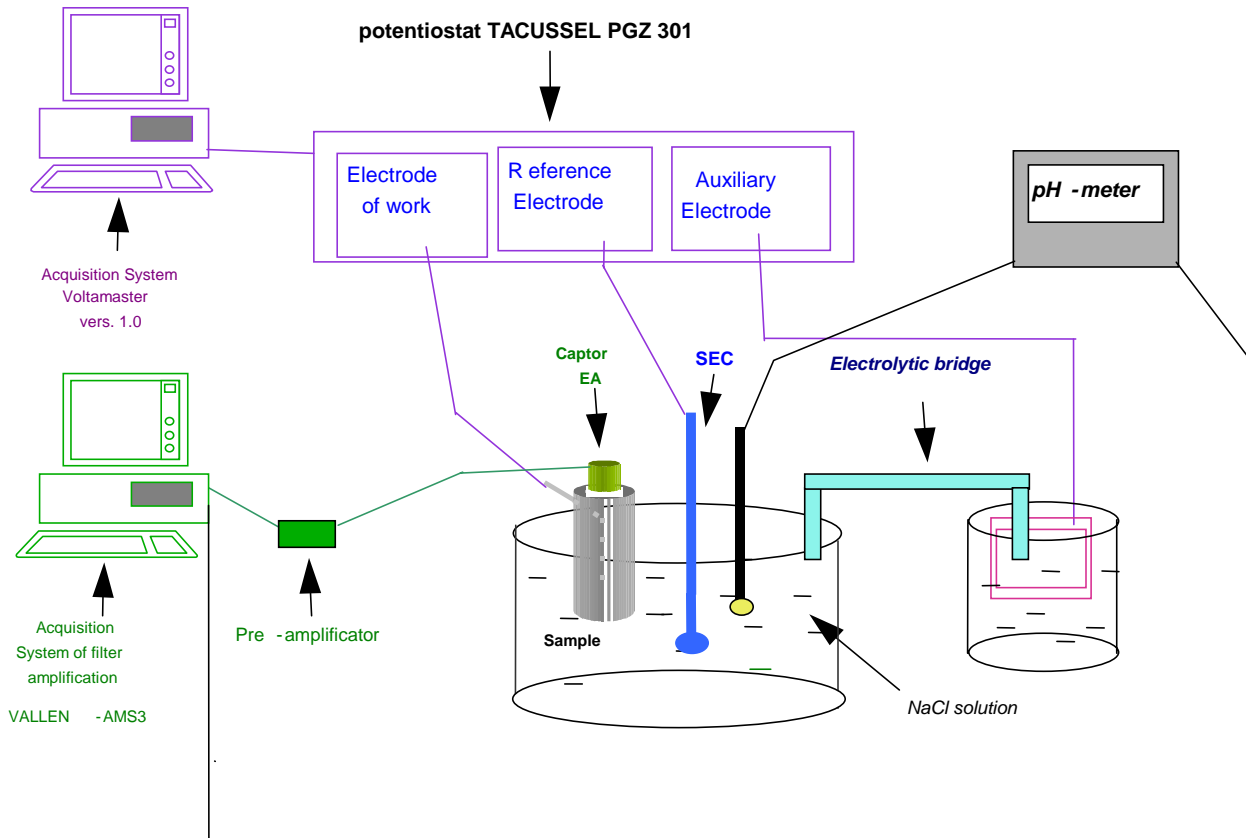


**Fig. 2: Experimental device.**

evolution from the counter-electrode during anodic polarization of the specimen, the platinum mesh had to be placed in a near-by annex cell connected to the corrosion cell via a salt bridge.

2. An instrumentation of AE consisted of a transducer, a preamplifier and an acquisition device (MISTRAS from Physical Acoustic Corp.). The transducer is resonant R15 type from PAC. It has been selected because of their high sensitivity around the value of 150 kHz. The acquisition system was completely computer controlled. The waveforms and the characteristic acoustic parameters (events, amplitude, rise-time, energy, counts number, duration) are stored on a hard disk as soon as detected, and are available for treatment under the form of ASCII files, as well as the electrochemical parameters.

The non-acoustic parameters such as the free potential of corrosion, the pH of the medium, and the current of corrosion density, were recorded during tests, through the analog input available on this system.

Potentiostatic tests were carried out on the standardized reinforced concrete in a 1M-NaCl (58.44 g/l) solution. The applied potential is 500 mV/SCE. It was selected according to the Pourbait diagram [8] in order to avoid the release of oxygen coming from the reaction of water reduction.

## RESULTS AND DISCUSSION

**pH Evolution:** The experiment consists in following the evolution of the medium pH, initially neutral, in order to study the action of the concrete on the reinforcement during the immersion of the sample in the solution. Indeed, Fig. 3 shows that, from the immersion, the pH increases quickly to reach a value of approximately 11.5. In the same way, a gradient of pH was measured in the mass of the mortar. With

this pH value, the steel reinforcement is naturally protected by the formation of a protective coating on its surface [8]. On the other hand, when the immersion is alternated every 24 h with drying of the sample and renewal of the medium, the pH decreases [9] to reach a value of approximately 8, for a test total duration of 200 h. Under these conditions, the deterioration of the protective coating is easier, particularly with the presence of chloride in a medium of low alkalinity.

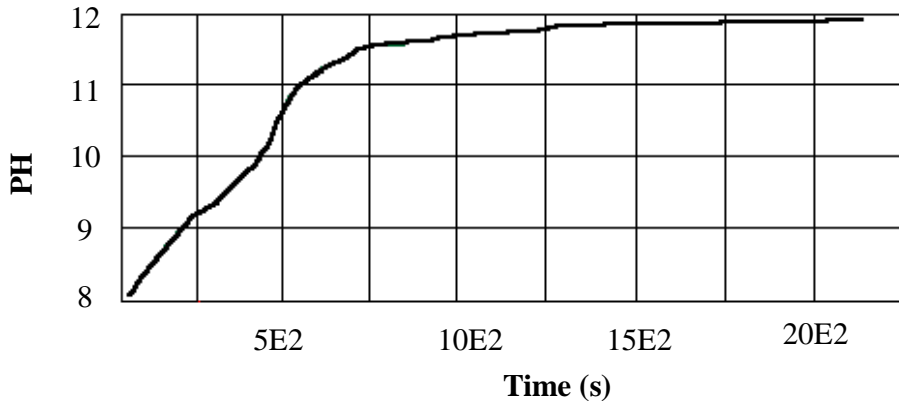


**Fig. 3: Evolution of medium pH during the immersion of the sample.**

**AE study:** The recording of the detected AE signals, under our experimental conditions, show three noted types of waves, A, B and C. The types A and B signals are characterized by shorter duration and rise times (lower than 20  $\mu$ s). This result is illustrated in the three-dimensional presentation of duration, time and rise time (Fig. 4). This presentation also shows that the AE activity starts after a latency time of approximately 10 h.

As for the follow-up of the current density and of the AE activity evolution recorded (Fig. 5), it shows that there is a close connection between electrochemical measurements and the AE activity. The shape of these curves can be divided into three steps:

1. A first step of relatively long duration, during which the current density I and the AE activity density remain low. This step can be associated with the infiltration of the medium through porosity and with the medium modifications in the vicinity of the reinforcement by diffusion of ions  $\text{Cl}^-$ . Under these conditions, the corrosion of the reinforcement is weak and the energy resulting from the electrochemical reaction is insufficient to be emissive. On the other hand, the rupture of the layer previously formed at free potential on the reinforcement surface can be responsible for the signals recorded during this step (Fig. 6a). Their duration is weak (<20  $\mu$ s) and their rise time is about 5  $\mu$ s.
2. A second step characterized by an increase in current density I and in AE (Fig. 6b). This activity can be explained if it is considered that the diffusion of chlorides, more particularly when the concentration ratio of the ions  $[\text{Cl}^-]/[\text{OH}^-]$  is higher than 0.6 [6,7], leads again to the dissolution of the reinforcement. Thus, the accumulation of corrosion products at the interface of reinforcement/concrete develops stresses on the internal surface of the concrete. This leads to the initiation of microscopic cracks, which are AE sources [10,11]. The population of signals is of type B and is characterized by a rise time lower than 20  $\mu$ s.

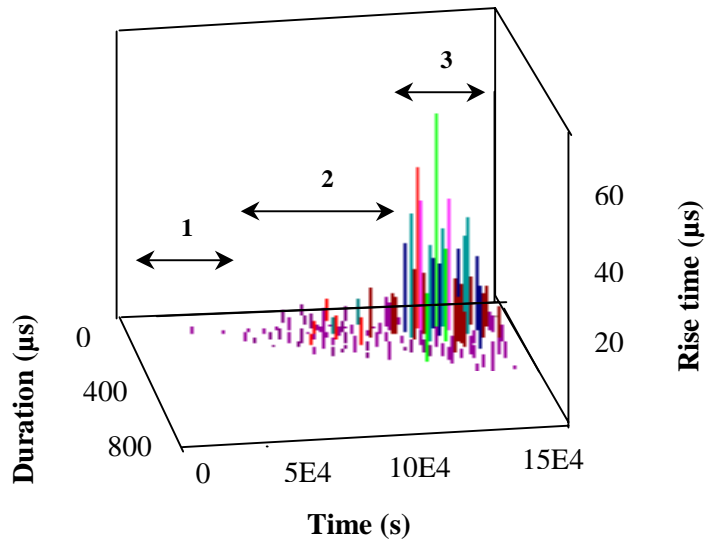


**Fig. 4:** 3D Correlation curve (Duration – Time – Rise time) for normalized reinforced concrete.

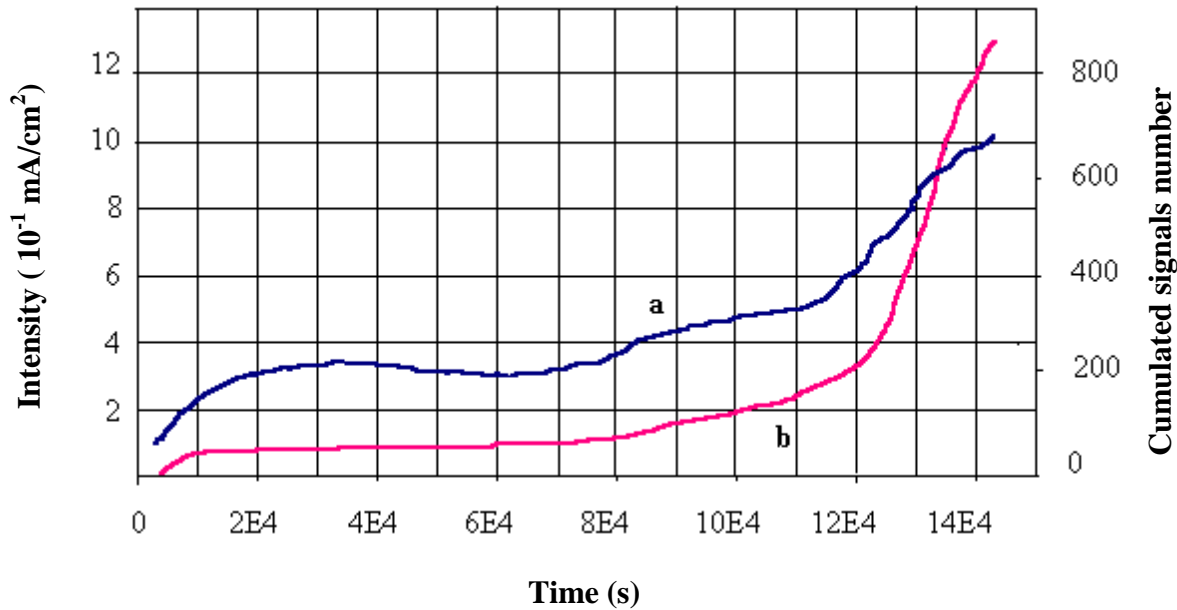


**Fig. 5:** Simultaneous evolution of current density (a) and AE (b) for normalized reinforced mortar.

3. A third step corresponding to a notable increase in the AE activity, which seems to be the consequence of the microscopic crack development and their propagation in the concrete to discharge the corrosion products. The friction of the latter against the walls of these cracks and pores may also be emissive source. The characteristics of the signals detected during this step (Fig. 6c) are different from those recorded beforehand in the second step, in particular in term of duration and rise time. The concrete matrix being fissured, and the infiltration of the electrolyte in the vicinity of the reinforcement is characterized by a new corrosion current increase and by signals of more diversified characteristics.

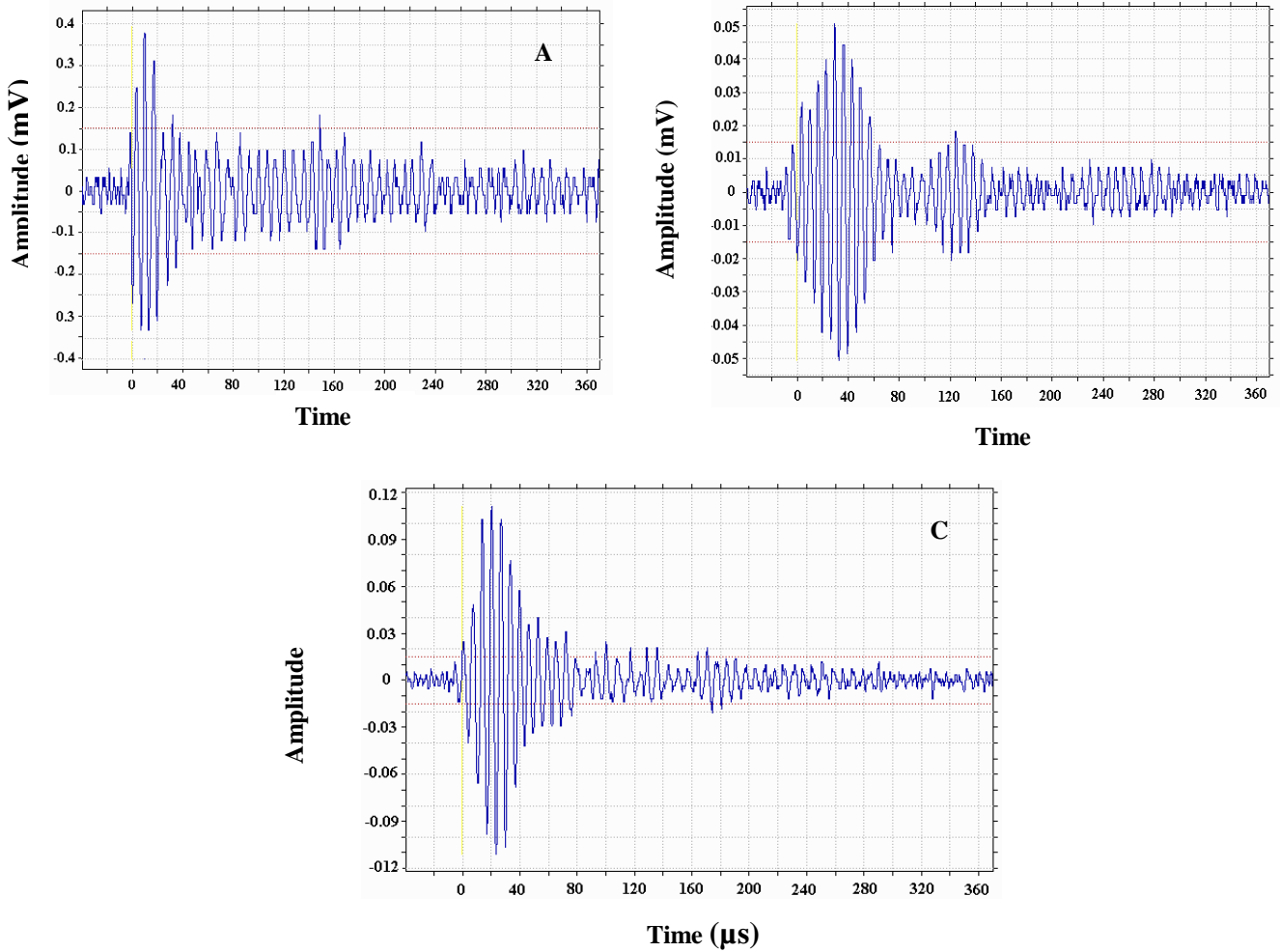


*Fig. 6: Waveform recorded for corrosion of rebar in concrete.*

## CONCLUSION

The corrosion current measured during the degradation of the samples shows that the protective part played by the concrete on the reinforcements is not always assured. This corrosion current is conditioned by the density of concrete open porosity, which represents the surface of reinforcement in contact with the electrolyte. The accumulation of corrosion products at the reinforcement/concrete interface causes microscopic cracks in the reinforced concrete matrix.

The perfect correlation between the AE activity and the corrosion current density shows that the AE detection of the degradation of the reinforced concrete infrastructures seems to be completely feasible. Furthermore, the AE parameters related to the detected AE signals, such as the rise time and energy, can constitute significant components to monitoring and even to qualify the damage.

The AE is a powerful non-destructive technique by its capacity to detect the degradation of reinforced concrete from the first step of the process. It appears necessary to look further into research in this field with an aim of controlling real reinforced concrete structures. For that purpose, the characteristics of the emitted signals need to be better correlated with the nature of the physical phenomena, which generate them during the various steps of corrosion.

## REFERENCES

- [1] R. DUVAL. La durabilité des armatures et du béton d'enrobage, in La durabilité des bétons. Presses de l'Ecole Nationale des Ponts et Chaussées. Edited by J. BARON and J.P. OLIVIER.
- [2] J.E. SLATER, Magnitude of the problem, ASTM – STP 818. Corrosion of Metals in Association with Concrete, pp. 5-9, 1983.
- [3] C.L. PAGE and K.W.J. TREADAWAY, Aspects of the electrochemistry of steel in concrete, Nature, 297 (1982), pp. 109-115.
- [4] L. HACHINI, J . CARPIO, E. TRIKI, C. FIAUD, A. RAHARINAVIO, Steel corrosion in concretes deteriorated by chlorures and sulphate : Electrochemical study using impedance spectrometry and stepping down the current method. Cement and Concrete Research, V. 22; 1992; pp. 56-66.
- [5] K. VIDEM, R. MYRDAL, Electrochemical Behaviour of steel in concrete and evaluation of the corrosion rate. Corrosion, V. 53; No. 9; 1998; pp. 734-743.
- [6] D. A. LEWIS, Some aspects of the corrosion of steel in concrete, Int. Proc. 1st International Conference Met. Corr., London, 1962, pp. 547-555.
- [7] S. VASANTH, N. S. RENGASWAMY, S. SRINIVASAN and K. BALUKRISHNAN, Evaluation of Indian Pozzolan Cements for their Corrosion Resistance, Transaction of the Society for Advancement of Electrochemical Science and Technology, 2 (1988), pp. 273-277.
- [8] H. POURBAIX. Atlas of electrochemical equilibria in aqueous solutions, Oxford, (1966).
- [9] L. HACHINI, E. TRIKI, D. MOUSSA, A. RAHARINAVIO, Etude expérimentale de la dégradation du béton armé dans diverses solution aqueuses. Bull. liaison Labo P et Ch- Réf. 3526, 169, (1990) , pp. 69-75.
- [10] A.PROUST, P. FLEISCHMANN, H. MAZILLE, R. ROTHEA, Acousitic emission monitoring of stress corrosion cracking on ferritic, austenitic and duplex stainless steels". Les Editions de Physique (France) (1993), pp. 925-934.
- [11] H. CIFLET, H. IDRISI, F. FERRER, F. DALART, Etude du claquage de la couche d'oxyde du zircaloy-4 en acide nitrique concentré et chaud par émission acoustique. Journées d'électrochimie, Toulouse, 1-4 June 1999.

## e-mail Address of Author

Surname	First name	e-mail
Anastasopoulos	Nassos	<a href="mailto:nassos@envirocoustics.gr">nassos@envirocoustics.gr</a>
BAYRAY	Mulu	<a href="mailto:mbayray@iaa1.iaa.tuwien.ac.at">mbayray@iaa1.iaa.tuwien.ac.at</a>
BLAHACEK	Michal	<a href="mailto:blahacek@bivoj.it.cas.cz">blahacek@bivoj.it.cas.cz</a>
CATTY	Johann	<a href="mailto:johann.catty@cetim.fr">johann.catty@cetim.fr</a>
COLE	Phil	<a href="mailto:ptc@pacuk.co.uk">ptc@pacuk.co.uk</a>
DUBIEL	Ryszard	<a href="mailto:dubiel@uranos.cto.us.edu.pl">dubiel@uranos.cto.us.edu.pl</a>
DVORACEK	Viri	<a href="mailto:dvoracek@cms.fme.vutbr.cz">dvoracek@cms.fme.vutbr.cz</a>
FERRER	Fréderic	<a href="mailto:frederic.ferrer@crde.elf-atochem.fr">frederic.ferrer@crde.elf-atochem.fr</a>
FINLAYSON	Richard	<a href="mailto:rfinlayson@pacndt.com">rfinlayson@pacndt.com</a>
GOMERA	Viktor	<a href="mailto:Gomera_V_P@kinet.ru">Gomera_V_P@kinet.ru</a>
HERVE	Catherine	<a href="mailto:catherine.herve@cetim.fr">catherine.herve@cetim.fr</a>
IDRISSI	Hassane	<a href="mailto:idrissi@insa-lyon.fr">idrissi@insa-lyon.fr</a>
IVANOV	Valery	<a href="mailto:pac.rus@g23.relcom.ru">pac.rus@g23.relcom.ru</a>
LENAIN	Jean-Claude	<a href="mailto:epa.jcl@wanadoo.fr">epa.jcl@wanadoo.fr</a>
MAJEWSKA	Zofia	<a href="mailto:majewska@geol.agh.edu.pl">majewska@geol.agh.edu.pl</a>
MAZAL	Pavel	<a href="mailto:mazal@cms.fme.vutbr.cz">mazal@cms.fme.vutbr.cz</a>
NISHINO	Hideo	<a href="mailto:nishino@me.aoyama.ac.jp">nishino@me.aoyama.ac.jp</a>
ONO	Kanji	<a href="mailto:ono@ucla.edu">ono@ucla.edu</a>
PININSKA	Joanna	<a href="mailto:joannap@geo.uw.edu.pl">joannap@geo.uw.edu.pl</a>
PRATEEPASEN	Asa	<a href="mailto:Asa.Prateepasen@brunel.ac.uk">Asa.Prateepasen@brunel.ac.uk</a>
RAUSCHER	Franz	<a href="mailto:f.rausch+e329@tuwien.ac.at">f.rausch+e329@tuwien.ac.at</a>
RAZUVAEV	Igor	<a href="mailto:alcor@alcor.nnov.ru">alcor@alcor.nnov.ru</a>
REUBEN	Bob	<a href="mailto:R.L.Reuben@hw.ac.uk">R.L.Reuben@hw.ac.uk</a>
ROWLAND	Chris	<a href="mailto:101750.2134@compuserve.com">101750.2134@compuserve.com</a>
SHIOTANI	Tomoki	<a href="mailto:shiotani@mx1.alpha-web.ne.jp">shiotani@mx1.alpha-web.ne.jp</a>
SKRABER	Alain	<a href="mailto:alain.skraber@cetim.fr">alain.skraber@cetim.fr</a>
SURGEON	Marnix	<a href="mailto:marnix.surgeon@metalogic.be">marnix.surgeon@metalogic.be</a>
TSCHELIESNIG	Peter	<a href="mailto:tsc@tuev.or.at">tsc@tuev.or.at</a>
TSIMOGIANNIS	Apostulos	<a href="mailto:envac@otenet.gr">envac@otenet.gr</a>
VALLEN	Hartmut	<a href="mailto:hartmut@vallen.de">hartmut@vallen.de</a>
VAN DE LOO	Peter J.	<a href="mailto:peter.j.vandeloo@opc.shell.com">peter.j.vandeloo@opc.shell.com</a>
VAN NIEUWENHOVE	Rudi	<a href="mailto:rvnieuwe@sckcen.be">rvnieuwe@sckcen.be</a>
WEBER	Zdenek	<a href="mailto:fypaz@fce.vutbr.cz">fypaz@fce.vutbr.cz</a>
WEVERS	Martine	<a href="mailto:martine.wevers@mtm.kuleuven.ac.be">martine.wevers@mtm.kuleuven.ac.be</a>
YOSHIDA	Kenichi	<a href="mailto:yoshida@me.tokushima-u.ac.jp">yoshida@me.tokushima-u.ac.jp</a>

# Theoretical Treatment of AE in Massive Solid

Masayasu Ohtsu

Graduate School of Science & Technology, Kumamoto University

2-39-1 Kurokami, Kumamoto 860-8555, Japan

[ohtsu@gpo.kumamoto-u.ac.jp](mailto:ohtsu@gpo.kumamoto-u.ac.jp)

## 1. Background

The generalized theory of acoustic emission (AE) has been established on the basis of elastodynamics (Ohtsu and Ono, 1984). Thus, it is clarified that AE waves are elastic waves due to dynamic failure in a solid. Here, AE waves due to microcracking are discussed in massive solids, in particular, in concrete. Theoretical treatment of AE in concrete was studied as elastic waves in a homogeneous medium (Ohtsu, 1982). The results were remarkably successful, whereas concrete is not homogeneous but heterogeneous. This is because elastodynamic properties of material constituents are physically dependent on the relation between the wavelengths and the characteristic dimensions of heterogeneity. In the case that the wavelengths are even larger than the sizes of heterogeneous inclusions, the effect of heterogeneity is inconsequential. This is the case of massive solids such as concrete and rock, if the sizes of specimens are large enough compared with the wavelengths.

For AE waves in concrete, the velocity of elastic waves is over 1000 m/s, and thus the waves of frequency range up to some 100 kHz correspond to the wavelengths of several centimeters. It results in the fact that the concrete specimen consisting of normal aggregate (of around 10 mm diameter) is reasonably referred to as homogeneous. The wavelengths to be detected should be shorter than characteristic lengths of the specimen or the propagating medium in order to detect body waves which are responsible for the source mechanisms. This is occasionally not the case of AE waves in plate specimens of steel, of ceramics, and of composites, where the thickness of the plate is normally shorter than the wavelengths. In the case, diffracted and dispersive waves are dominantly observed. Because these waves are not associated with generating mechanisms, source characterization of AE in the plate specimen is normally a difficult task.

## 2. Fundamentals

Elastodynamic solutions of wave motions  $\mathbf{u}(\mathbf{x},t)$  are mathematically represented as,

$$\mathbf{u}_k(\mathbf{x},t) = \int_S [G_{ki}(\mathbf{x},\mathbf{y},t)^* t_i(\mathbf{y},t) - T_{ki}(\mathbf{x},\mathbf{y},t)^* u_i(\mathbf{y},t)] dS, \quad (1)$$

where  $\mathbf{u}(\mathbf{x},t)$  and  $\mathbf{u}(\mathbf{y},t)$  are displacements, and  $\mathbf{t}(\mathbf{y},t)$  are tractions. The asterisk symbol \* represents the convolution integral in time.  $G_{ik}(\mathbf{x},\mathbf{y},t)$  are Green's functions and  $T_{ik}(\mathbf{x},\mathbf{y},t)$  are the associated tractions with Green's functions,

$$T_{ik}(\mathbf{x},\mathbf{y},t) = G_{ip,q}(\mathbf{x},\mathbf{y},t) C_{pqjk} n_j. \quad (2)$$

Here  $C_{pqji}$  are the elastic constants, and  $G_{ip,q}(\mathbf{x},\mathbf{y},t)$  are the spatial derivatives of Green's functions as they imply  $\partial G_{ip}(\mathbf{x},\mathbf{y},t)/\partial x_q$ .  $\mathbf{n}$  is the normal vector to the boundary surface S.

In the boundary element method (BEM), eq. 1 is directly digitized and numerically solved. For theoretical development, first, only one force  $\mathbf{f}(\mathbf{y},t)$  is applied at point  $\mathbf{y}$  on the boundary. Thus, eq. 1 becomes,

$$u_i(\mathbf{x},t) = G_{ij}(\mathbf{x},\mathbf{y},t)^* f_j(\mathbf{y},t). \quad (3)$$

This is the governing equation in the case where a dynamic force is applied to the specimen. From eq. 3, the physical meaning of Green's function is readily obtained as  $G_{ij}(\mathbf{x},\mathbf{y},t)$  is an

elastodynamic solution of the displacement in the  $x_i$  direction at point  $\mathbf{x}$  and at time  $t$  due to an impulsive force in the  $x_j$  direction at point  $\mathbf{y}$  and at time  $t$ . Since Green's functions are dependent on not only material properties but also on configuration of the medium, they have to be computed numerically except for an infinite space where analytical solutions are known. Semi-analytical solutions are also known in a half space (Ohtsu and Ono, 1984) and in an infinite plate (Pao and Ceranoglu, 1981). For a finite body, numerical solutions of Green's functions are reported as the waves due to a monopole source (Hamstad, O'Gallagher and Gary, 1999)

A famous experiment of pencil-lead break (Hsu and Hardy, 1978) is also represented by eq. 3. A pencil-lead break is known to generate a Heaviside step function force,  $H(t)\mathbf{e}_j(\mathbf{y})$ , where  $\mathbf{e}(\mathbf{y})$  is the unit direction vector at point  $\mathbf{y}$ . Since the convolution with the step function leads to the integration, eq. 3 becomes,

$$u_i(\mathbf{x},t) = \int G_{ij}(\mathbf{x},\mathbf{y},t)\mathbf{e}_j(\mathbf{y}) dt. \quad (4)$$

Accordingly, Green's function of the arbitrary specimen,  $G_{ij}(\mathbf{x},\mathbf{y})$ , due to the pencil-lead break at point  $\mathbf{y}$  in the  $x_j$  direction could be empirically obtained from,

$$G_{ij}(\mathbf{x},\mathbf{y},t) = du_i(\mathbf{x},t)/dt. \quad (5)$$

### 3. Crack Modeling

In order to model a crack as an AE source, the boundary surface  $S$  in eq. 1 is replaced by internal surface  $F$  of a crack surface. To introduce the discontinuity of the displacements, virtual two surfaces  $F^+$  and  $F^-$  are considered as shown in Fig. 1. Before a crack is nucleated, these two surfaces make a concurrent motion. Due to cracking, the discontinuity of displacement  $\mathbf{u}(\mathbf{y},t)$  is nucleated between the two surfaces and denoted by using superscripts + and - on surface  $F^+$  and  $F^-$ ,

$$\mathbf{b}_i(\mathbf{y},t) = u_i^+(\mathbf{y},t) - u_i^-(\mathbf{y},t). \quad (6)$$

Vector  $\mathbf{b}(\mathbf{y},t)$  is called the dislocation and is identical to Burgers vector. Setting  $t(\mathbf{y},t) = 0$  on the surface  $F$ , eq. 1 becomes,

$$u_k(\mathbf{x},t) = \int_{F^+} [-T_{ki}^+(\mathbf{x},\mathbf{y},t)^* u_i^+(\mathbf{y},t)] dF + \int_{F^-} [-T_{ki}^-(\mathbf{x},\mathbf{y},t)^* u_i^-(\mathbf{y},t)] dF. \quad (7)$$

Here  $T_{ik}^+$  and  $T_{ik}^-$  contain the normal vector  $\mathbf{n}^+$  and  $\mathbf{n}^-$ , respectively. Assuming  $\mathbf{n} = \mathbf{n}^- = -\mathbf{n}^+$ , and  $F = F^-$ ,

$$\begin{aligned} u_k(\mathbf{x},t) &= - \int_F T_{ki}(\mathbf{x},\mathbf{y},t)^* [-u_i^+(\mathbf{y},t)] dF + \int_F [-T_{ki}(\mathbf{x},\mathbf{y},t)^* [u_i^-(\mathbf{y},t)]] dF \\ &= \int_F T_{ki}(\mathbf{x},\mathbf{y},t)^* [u_i^+(\mathbf{y},t) - u_i^-(\mathbf{y},t)] dF = \int_F T_{ki}(\mathbf{x},\mathbf{y},t)^* b_i(\mathbf{y},t) dF. \end{aligned} \quad (8)$$

Comparing eq. 3 with eq. 8, it is noted that Green's functions empirically obtained from a pencil-lead break are not definitely applicable to AE waves due to cracking. From eqs. 2 and 8,

$$\begin{aligned} u_k(\mathbf{x},t) &= \int_F T_{ki}(\mathbf{x},\mathbf{y},t)^* b_i(\mathbf{y},t) dF \\ &= \int_F G_{kp,q}(\mathbf{x},\mathbf{y},t) C_{pqij} n_j^* b_i(\mathbf{y},t) dF \\ &= G_{kp,q}(\mathbf{x},\mathbf{y},t)^* S(t) C_{pqij} n_j l_i \int_F b(\mathbf{y},t) dF \\ &= G_{kp,q}(\mathbf{x},\mathbf{y},t)^* S(t) C_{pqij} n_j l_i \Delta V, \end{aligned} \quad (9)$$

where  $\mathbf{l}$  is the unit direction vector and  $S(t)$  is the source-time function of crack motion.  $\Delta V$  is the crack volume. As can be seen, the amplitude of AE waves,  $u(\mathbf{x}, t)$ , is directly associated only with the crack volume, neither with the area nor with the opening. This implies that some attempts to determine the crack area or the magnitude of shear slip (Enoki, Kishi and Kohara, 1986; Dai, Labuz and Carvalho, 2000) are not rational, because only a disk-shaped crack is taken into account. According to the simulation analysis (Ohtsu, Yuyama and Imanaka, 1987), the crack volume estimated as the penny-shaped crack was more than 30% different from that of the disk-shaped.

Equation 9 is the integral representation of AE wave due to cracking and can be applied to simulation analysis as shown in Fig. 2. Assuming a buried inclined crack ( $45^\circ$  to the surface), AE wave due to a tensile crack is synthesized. The spatial derivatives Green's functions,  $G_{kp,q}$ , in eq. 9 are computed in a half space. As can be seen, AE wave detected in concrete is in reasonable agreement with the synthesized. Here, the tensile crack is represented as the case that vector  $\mathbf{l}$  is parallel to vector  $\mathbf{n}$ , and elastic constants of an isotropic material are applied.

#### 4. Moment Tensor

Since eq. 9 is fairly complicated and contains two vectors  $\mathbf{l}$  and  $\mathbf{n}$ , it is not suitable for an inverse problem. Thus, introducing moment tensor  $M_{pq}$ , eq. 9 is simplified,

$$\int_F C_{pqkl} b(\mathbf{y}) l_k n_l dF = C_{pqkl} l_k n_l [ \int_F b(\mathbf{y}) dF ] = C_{pqkl} l_k n_l \Delta V = M_{pq} \quad (10)$$

$$u_k(\mathbf{x}, t) = G_{kp,q}(\mathbf{x}, \mathbf{y}, t) M_{pq} * S(t). \quad (11)$$

The moment tensor,  $M_{pq}$ , is defined by the product of the elastic constants [ $N/m^2$ ] and the crack volume [ $m^3$ ], which leads to the moment of physical unit [Nm]. In the case of an isotropic material,

$$M_{pq} = \begin{matrix} \lambda l_k n_k + 2\mu l_1 n_1, \mu(l_1 n_2 + l_2 n_1), \mu(l_1 n_3 + l_3 n_1) \\ \mu(l_2 n_1 + l_1 n_2), \lambda l_k n_k + 2\mu l_2 n_2, \mu(l_2 n_3 + l_3 n_2) \\ \mu(l_3 n_1 + l_1 n_3), \mu(l_3 n_2 + l_2 n_3), \lambda l_k n_k + 2\mu(l_3 n_3) \end{matrix} \quad \Delta V, \quad (12)$$

where  $\lambda$  and  $\mu$  are Lame constants. Originally, the seismic moment was defined by the product  $\mu b \Delta F$  of shear modulus  $\mu$ , shear displacement  $b$ , and area of fault  $\Delta F$ . Setting  $\mathbf{l} = (1, 0, 0)$ ,  $\mathbf{n} = (0, 1, 0)$  ( $\mathbf{l}$  is perpendicular to  $\mathbf{n}$ ) and  $\Delta V = b \Delta F$  in eq. 11,  $M_{pq} = 2\mu b \Delta F$ . Thus, the tensor is named the moment tensor. This suggests that the moment tensor is comparable to a stress due to crack nucleation, as a symmetric second-order tensor as shown in Fig. 3.

Crack kinematics are sometimes represented by such equivalent forces as dipole forces and couple forces. The dipole forces are known as two forces of the same magnitude and the opposite directions on the coincident straight line. The couple forces are two parallel and opposite-direction forces with infinitesimal distance. Mathematically, these forces correspond to particular components of the stress. As can be seen in Fig. 3 (b), normal components of the moment tensor are identical to dipole forces, while couple forces correspond to tangential (shear) components. The concept of the equivalent forces is sometime so misleading that nucleation of a tensile crack is represented by only a pair of dipole forces. In the case of a pure tensile crack, a scalar product  $l_k n_k = 1$ . Since all diagonal components contain the scalar product as given in eq. 12, the tensile crack should be modeled by three normal components (three pairs of dipole forces). In contrast, couple forces correspond to off-diagonal components in eq. 12. Since the moment tensor is symmetric, double-couple forces are rational.

An application of the moment tensor analysis to AE waves was previously reported on

cracking mechanisms of glass due to indentation (Kim and Sachse, 1984), where only diagonal components of the tensor were assumed. From eq. 12, it is realized that the presence of all components is not actually associated with the type of the crack, but closely related with the coordinate system. Although the crack orientations are often assumed as parallel to the coordinate system (Saito, Takemoto, Suzuki and Ono, 1998), they are generally inclined to the coordinate system mostly because of the configuration of the specimen. As a result, the presence of all the components is consequent whether the type of the crack is of tensile or of shear. In contrast, if the coordinate system is taken as parallel to the crack orientation, elastic waves in eq. 11 could be represented as the vector obliquely incident to the surface which further complicates the reflection at the surface and is not easily analyzed.

## 5. SiGMA Code

For the analysis of the inverse problem, the spatial derivatives of Green's functions are inevitably required. Accordingly, numerical solutions are obtained by FDM (Enoki, Kishi and Kohara, 1986) and by FEM (Hamstad, O'Gallagher and J. Gary, 1999). These solutions, however, need a vector processor for computation and are not readily applicable to processing a large amount of AE wave. Based on the far-field term of P wave, therefore, a simplified procedure was developed, which is suitable for a PC-based processor and robust in computation. The procedure is now implemented as a SiGMA (Simplified Green's functions for Moment tensor Analysis) code.

By taking into account only P wave motion of the far field (1/R term) of Green's function in an infinite space, the displacement  $U_i(\mathbf{x}, t)$  of P wave motion is obtained from eq. 11 as,

$$U_i(\mathbf{x}, t) = -1/(4\pi\rho v_p^3) r_i r_p r_q / R dS(t)/dt M_{pq}. \quad (13)$$

Here  $\rho$  is the density of the material and  $v_p$  is P-wave velocity.  $R$  is the distance between the source  $\mathbf{y}$  and the observation point  $\mathbf{x}$ , of which direction cosine is  $\mathbf{r} = (r_1, r_2, r_3)$ . Considering the effect of reflection at the surface and neglecting the source-time function, amplitude  $A(\mathbf{x})$  of the first motion is represented,

$$A(\mathbf{x}) = C_s \text{Ref}(\mathbf{t}, \mathbf{r})/R \quad (r_1, r_2, r_3) \quad \begin{matrix} m_{11}, m_{12}, m_{13} \\ m_{12}, m_{22}, m_{23} \\ m_{13}, m_{23}, m_{33} \end{matrix} \quad \begin{matrix} r_1 \\ r_2 \\ r_3 \end{matrix}, \quad (14)$$

where  $C_s$  is the calibration coefficient including material constants in eq. 13.  $\mathbf{t}$  is the direction of the sensor sensitivity.  $\text{Ref}(\mathbf{t}, \mathbf{r})$  is the reflection coefficient at the observation location  $\mathbf{x}$ . In the relative moment tensor analysis (Dahm, 1996), this coefficient is not taken into consideration, because the effect of the sensor locations are compensated. Since the moment tensor is symmetric, the number of independent unknowns  $m_{pq}$  to be solved is six. Thus, multi-channel observation of the first motions at more than six channels is required to determine the moment tensor components.

From AE waveform, two parameters of the arrival time (P1) and the amplitude of the first motion (P2) are determined. In the source location procedure, source location  $\mathbf{y}$  is determined from the arrival time differences. Then, distance  $R$  and its direction vector  $\mathbf{r}$  are determined. The amplitudes of the first motions at more than 6 channels are substituted into eq. 14, and the components of the moment tensor are determined. Since the SiGMA code requires only relative values of the moment tensor components, the relative calibration of the sensors is sufficient enough. Then, the classification of a crack is performed by the eigenvalue analysis of the moment tensor. Setting the ratio of the maximum shear contribution as  $X$ , three eigenvalues for the shear crack become  $X, 0, -X$ . Likewise, the ratio of the maximum deviatoric tensile component is set as  $Y$  and the isotropic tensile as  $Z$ . It is reasonably assumed that the principal axes of the shear crack is identical to those of the tensile crack. Then, the eigenvalues of the moment tensor for a general case are represented by the

combination of the shear crack and the tensile crack. In the SiGMA, eq. 16 is normalized and decomposed,

$$\begin{aligned}
 1.0 &= X + Y + Z, \\
 \text{the intermediate eigenvalue/the maximum eigenvalue} &= 0 - Y/2 + Z, \\
 \text{the minimum eigenvalue/the maximum eigenvalue} &= -X - Y/2 + Z,
 \end{aligned} \tag{15}$$

where  $X$ ,  $Y$ , and  $Z$  denote the shear ratio, the deviatoric tensile ratio, and the isotropic tensile ratio, respectively. In the present SiGMA code, AE sources of which the shear ratios are less than 40% are classified into tensile cracks. The sources of  $X > 60\%$  are classified into shear cracks. In between 40% and 60%, cracks are referred to as mixed mode. In the eigenvalue analysis, three eigenvectors are also determined, and then the vectors  $\mathbf{l}$  and  $\mathbf{n}$ , which are interchangeable, are recovered.

In a three-point bending test of a concrete beam, SiGMA analysis was performed (Ohtsu and Ohtsuka, 1998). Results are given in Fig. 4. The tensile crack is indicated by arrow symbol, while the shear crack is denoted by cross symbol. The directions of two vectors  $\mathbf{l}$  and  $\mathbf{n}$  are shown in their directions. It is found that both types of tensile cracks and shear cracks are observed in the fracture process zone ahead of the notch in concrete. Thus, the moment tensor analysis is very promising for practical applications to identify fracture mechanisms in concrete.

## REFERENCES

- Dai, S. T., J. F. Labuz and F. Carvalho (2000), "Softening Response of Rock Observed in Plane-Strain Compression," *Trends in Rock Mechanics, Geo SP-102, ASCE*, 152-163.
- Dahm, T. (1996), "Relative Moment Tensor Inversion based on Ray Theory: Theory and Synthetic Tests," *Geophys. J. Int.*, No. 124, 245-257.
- Enoki, M., T. Kishi and S. Kohara (1986), "Determination of Micro-cracking Moment Tensor of Quasi-cleavage Facet by AE Source Characterization," *Progress in Acoustic Emission III, JSNDI*, 763-770.
- Hamstad, M. A., A. O'Gallagher and J. Gary (1999), "Modeling of Buried Monopole and Dipole Source of Acoustic Emission with a Finite Element Technique, *Journal of AE*, 17(3-4), 97-110.
- Hsu, N. N. and S. C. Hardy (1978), "Experiments in AE Waveform Analysis for Characterization of AE Sources, Sensors and Structures, *Elastic Waves and Nondestructive Testing of Materials, AMD-Vol. 29*, 85-106.
- Kim, K. Y. and W. Sachse (1984), "Characterization of AE Signals from Indentation Cracks in Glass," *Progress in Acoustic Emission II, JSNDI*, 163-172.
- Ohtsu, M. (1982), "Source Mechanism and Waveform Analysis of Acoustic Emission in Concrete," *Journal of AE*, 2(1), 103-112.
- Ohtsu, M. and K. Ono (1984), "A Generalized Theory of Acoustic Emission and Green's Functions in a Half Space," *Journal of AE*, 3(1), 124-133.
- Ohtsu, M. , S. Yuyama and T. Imanaka (1987), "Theoretical Treatment of Acoustic Emission Sources in Microfracturing due to Disbonding," *J. Acoust. Soc. Am.*, 82(2), 506-512.
- Ohtsu, M. and M. Ohtsuka (1998), "Damage Evolution by AE in the Fracture Process Zone of Concrete," *J. Materials, Conc. Struct. Pavement, JSCE*, No. 599/V-40, 177-184.

Pao, Y. H. and A. N. Ceranoglu (1981), "Propagation of Elastic Pulse and Acoustic Emission in a Plate," *J. Appl. Mech.*, 48, 125-147,

Saito, N., M. Takemoto, H. Suzuki and K. Ono (1998), "Advanced AE Signal Classification for Studying the Progression of Fracture Modes in Loaded UD-GFRP," *Progress in Acoustic Emission IX, JSNDI, V-1 - V-10.*

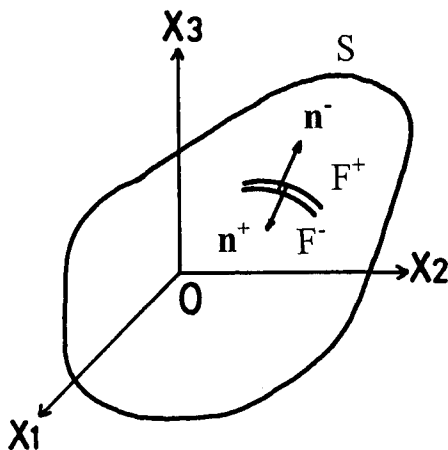


Fig. 1 Crack (dislocation) surfaces  $F^+$  and  $F^-$ .

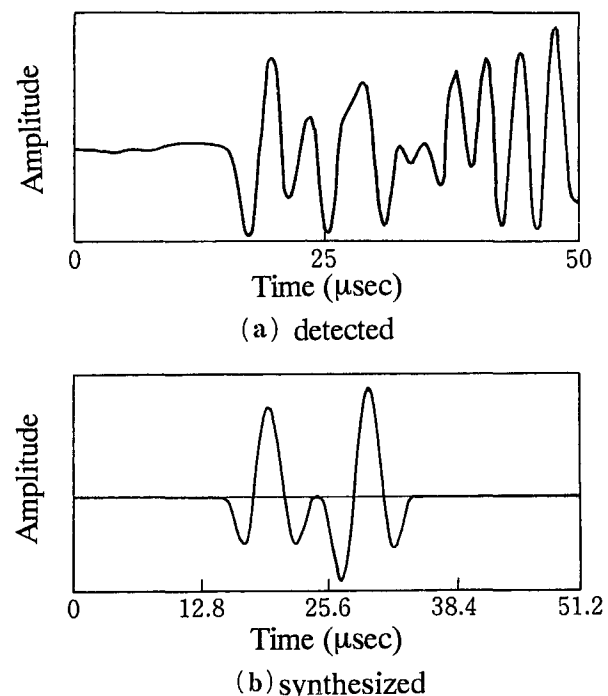


Fig. 2 AE waveforms in concrete.

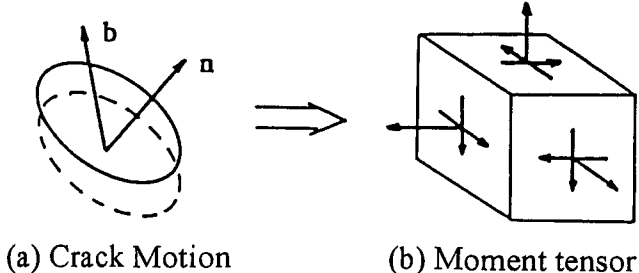


Fig. 3 Modeling crack motion by the moment tensor.

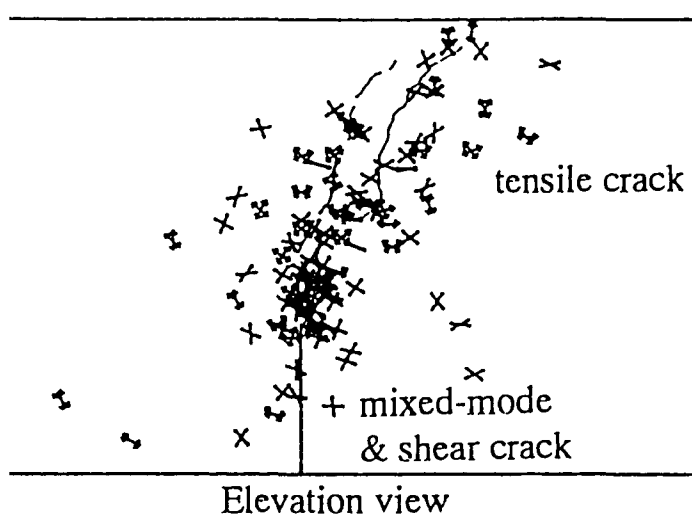


Fig. 4 Results of SiGMA analysis of the notched beam.

# Diagnosis of Concrete Structures by AE

**Masayasu Ohtsu**

Graduate School of Science and Technology,  
Kumamoto University, 2-39-1 Kurokami, Kumamoto 860-8555, JAPAN  
ohtsu@gpo.kumamoto-u.ac.jp

## 1. Scope

Acoustic emission (AE) techniques are extensively studied in concrete engineering and are recently going to be applied to practical use. In particular, the increase of aging structures and the disastrous damage due to earthquakes substantially demand for the maintenance of reinforced concrete (RC) structures in service. It results in the need for the development of advanced and effective inspection techniques. Accordingly, AE techniques draw an attention for diagnostic applications to RC structures. By several authorities In Japan, activities for the standardization of AE testing procedure are in progress.

The concrete structures have their particular functions in service, which may deteriorate due to heavy traffic loads, fatigue, chemical reactions, and other disasters. To perform their functions properly, repair and rehabilitation of the structures are eventually necessary. In this case, an inspection on the current state is necessary. Consequently, to estimate the degree of the damage or structural integrity of the existing concrete structures, in situ monitoring techniques by AE are going to be standardized. Some fundamental results associated with these actions are reviewed.

## 2. Measurement

According to extensive research on AE in concrete (Ohtsu, 1987), the following conditions are reported to properly detect AE signals.

- (1) AE device for concrete usually requires total amplification around 60 dB to 90 dB. To decrease the effect of noises on site, 1 MHz low-pass filter is desirable, as well as a high-pass filter over several kHz. The noise should be lower than 20 mV as input.
- (2) A monitoring system can measure at least some of the following parameters: count, hit, event, maximum amplitude, energy, rise time, duration, energy-moment, RMS voltage, frequency spectrum, and arrival-time difference.
- (3) Elimination of the noises shall be performed by setting the threshold level, filtering and post-analysis of the data. In any cases, the averaged amplitude of the noise should be managed to be lower than 10 mV as input.
- (4) Inspection of the operating system shall be carried out routinely, checking that the variation of sensitivities in the channels is within 3 dB. Sensor array shall be determined from the attenuation properties of AE waves, setting the distance where attenuation of travel is less than 30 dB. Then, the frequency range from 20 kHz to 100 kHz is recommended for in situ monitoring.

### 3. Monitoring

For AE monitoring of existing concrete structures, it is essential to confirm that any AE signals responsible for the damage are not observed under service conditions. In the case that AE signals not of noises but due to deterioration process are detected, the monitoring and the analyses shall be conducted. The monitoring shall be performed continuously or routinely, and sometimes temporarily after the disasters.

Due to the sudden increase of AE activity, the deterioration process and in many cases the impending failure can be estimated. There is a report on AE activity under freezing and thawing process (Murakami et al., 1991), where AE counts rapidly increase prior to the volumetric expansion associated with microcracking and scaling in concrete. Another result on continuous monitoring under corrosion of the reinforcement in RC beams is given in Fig. 1. By visual observation prior to the test, the beam at channel 5 was found to be sound without any cracks, while one surface crack running vertical to the reinforcement axis was observed at that of channel 6. These beams were exposed on shore for three months. Due to rainfall, some AE activities were observed simultaneously at both the beams as seen in the figure. At the beam of channel 5, AE activity always ceased right after the rain. In contrast, after heavy rain at 50 days elapsed and 60 days AE counts were periodically observed following the activities due to the rain. This was considered to be an evidence for corrosion of the reinforcement. Water of the rainfall permeated into the concrete along the existing crack and probably corroded the reinforcement, which could generate microcracks and AE signals in concrete around the rebars. In the test, the corrosion in the beam at channel 6 was confirmed after removing rebars. These findings confirm an applicability of AE monitoring to estimate nucleation of microcracks in concrete structures.

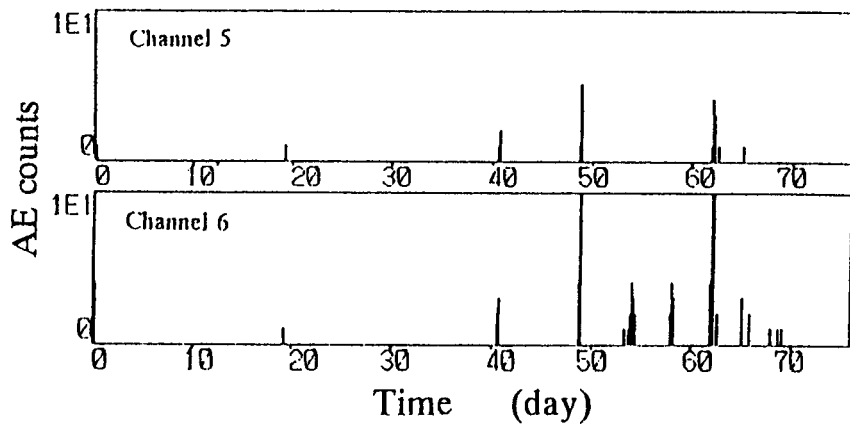


Fig. 1 In situ AE observation in RC beams.

### 4. Trend Analysis

From a relation between any AE parameters and other physical parameters, its trend can be analyzed and applied to the diagnosis. For example, the change of AE activity could be related with the rate of

the deterioration process. The rate-process analysis was introduced to evaluate quantitatively the change of the activity. When concrete contains a number of critical microcracks, active AE occurrence is expected under compression due to crack propagation from existing defects or microcracks. In contrast, AE activity in sound concrete is known to be stable and low prior to final failure. Thus, to formulate AE activity under loading, the rate process theory is introduced. Probability function of AE occurrence from stress level  $V(\%)$  to  $V + dV (\%)$  is formulated as a hyperbolic function. Eventually, a relationship between the number of total AE events  $N$  and stress level  $V(\%)$  is obtained as,

$$N = C V^a \exp(bV). \quad (1)$$

Here  $a$  and  $b$  are empirical coefficients and  $C$  is the integration constant.

From previous research, the rate  $a$  is, in particular, known to be sensitive to the damage degree. Core samples were taken from an aqueduct of a nuclear power plant. To drill core samples, three sites were selected: at the gate (Site A), 20 m inland (Site B), and 30 m inland from the gate (Site C). Then, a uniaxial compression test of the sample was conducted. Three samples at each site were tested. The uniaxial compressive strength and the rate  $a$  were determined as the averaged value of the three. In order to quantify microscopic damage, distribution of pore radii was also measured by the mercury intrusion method from concrete fragments at the three sites. After determining the pore distribution, the volume of pore radii over 0.5 mm was determined, because microvoids over 0.5 mm are predominantly responsible for deterioration of concrete. Results of the pore volumes over 0.5 mm radius, the rate  $a$ , and the compressive strength are summarized in Fig. 2. From Site A to Site C, the pore volume over 0.5 mm radius decreases with the increase of the distance from the sea. This implies that the heaviest damage was introduced in concrete at the gate (Site A), where concrete was frequently deteriorated by seawater. Apart from the seaside, it is expected that the damage of concrete decreases. In accordance

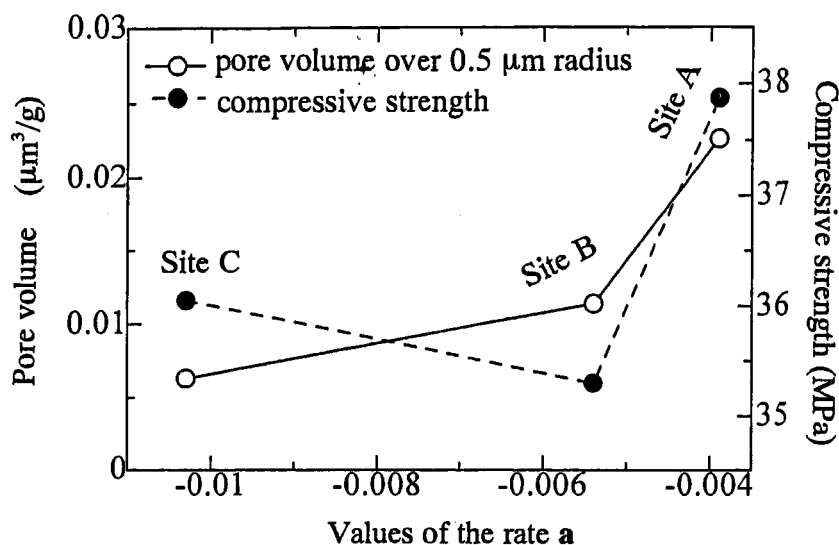


Fig. 2 Relation among the pore volume, compressive strength and the rate  $a$ .

with the increase of the pore volume over 0.5 mm radius, the rates a increase from Site C to Site A. Thus, the increase of the pore volume over 0.5 mm radius corresponds remarkably to the increase of the rate **a**. It suggests that with the increase in the rate **a**, the volume of the microvoids responsible for damage increases. Consequently, the trend analysis of AE occurrence could give us information on the deteriorated degree of concrete.

## 5. Distribution Analysis

Distribution of AE parameters is analyzed in relation to the occurrence of AE counts, hits, and events. The purpose of the analysis is variation of such AE parameters as RMS, energy, amplitude distribution and so forth. Concerning the variation of AE parameter during the deterioration process, it is found that the change of amplitude distribution is useful. In Fig. 3, amplitude distributions observed in RC beams under bending are shown. RC beams were damaged by cyclic loading of prescribed level. After particular loading cycles, the beam was statically loaded up to the service-load limit, and AE was measured. In Fig. 3(a), RC beam was repeatedly loaded at 85% static load-bearing capacity until final failure. After several cycles of loading, amplitude distributions of AE signals were measured under monotonous loading. With the increase of loading cycles, amplitude distributions shift to the distribution where AE signals of the larger amplitudes are dominant. In contrast, there exist no change of the amplitude distribution in RC beam (Fig. 3(b)) which was repeatedly loaded at only 75% until 2,500,000 cycles. The beam was not broken in the test. This implies that amplitude distribution can be applied to routinely inspection, investigating the variation of the distribution. The distribution is also quantitatively estimated from the gradient of the slope, which is called the b value (Shiotani et al. 1999).

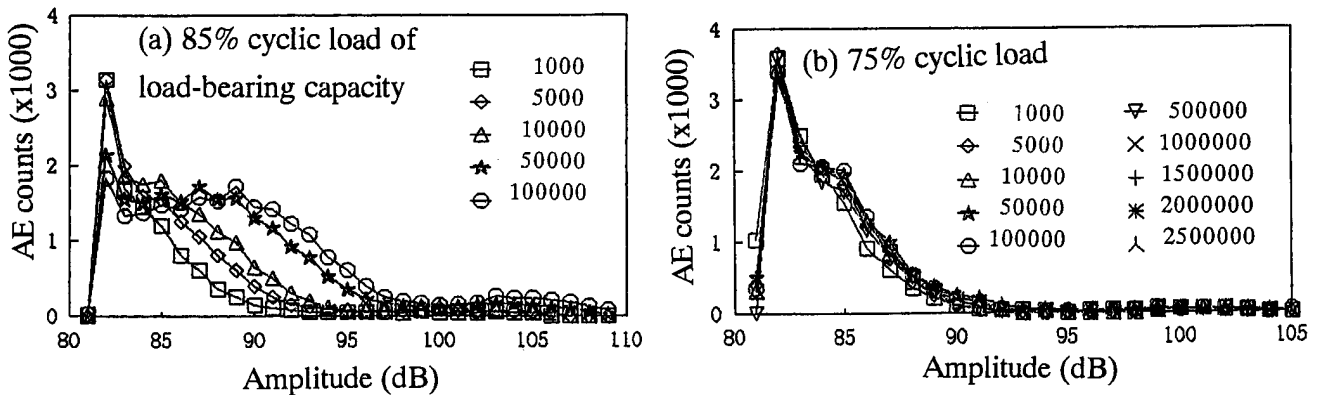


Fig. 3 AE amplitude distribution during the fatigue test.

## 6. Clustering Analysis

From the arrival time differences, AE sources are located one-dimensionally, two-dimensionally, or three-dimensionally. By applying AE location procedure, a relation between the location of AE cluster and existing defects is readily obtained. In Fig. 4, AE locations observed in a retaining wall are shown (Matsuyama et al., 1993). According to the two-dimensional locations of the raw data, wide scattering of

AE locations is observed. Eliminating the noises and compensating the effect of the existing surface cracks, AE locations are calibrated as shown in Fig. 4(b). All signals are mainly observed along the existing cracks. This implies that AE events are mostly nucleated due to fretting of the existing cracks. Thus, repair of the wall was carried out, just sealing the surface cracks. In addition to AE location, the moment tensor analysis is developed to classify the source into the tensile crack and the shear crack, and to determine crack orientations.

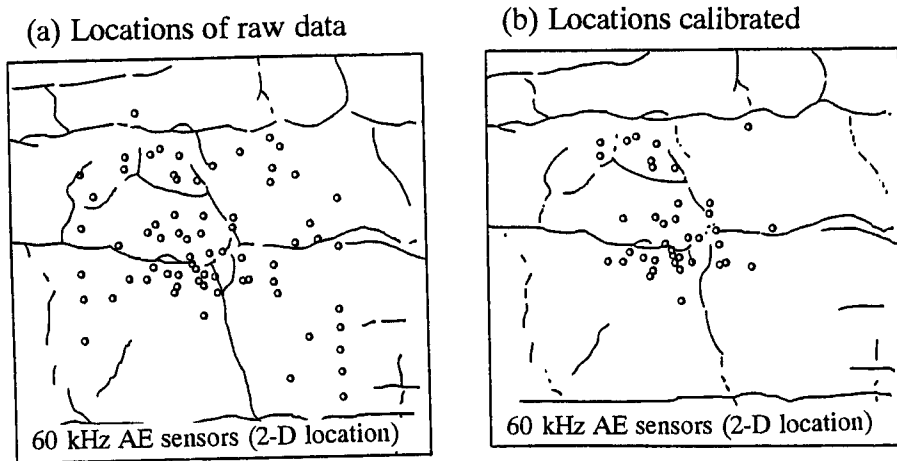


Fig. 4 AE source locations at a retaining wall.

## 7. Estimation Based on Kaiser Effect

Concerning AE activity under repeated loading, the Kaiser effect is well known. In RC beams, the relation between crack opening and the presence of the Kaiser effect was reported (Yuyama et al., 1996). In order to apply the Kaiser effect, further, to evaluate the damage of concrete structures, the following two parameters are proposed.

(a) Ratio of load at the onset of AE activity to previous load:

**Load ratio** = load at the onset of AE activity under the repeated loading / previous load.

(b) Ratio of cumulative AE activity under unloading to that of previous maximum loading cycle:

**Calm ratio** = the number of cumulative AE activity during unloading / total AE activity at the previous maximum loading cycle.

One result on the relation between these ratios and crack-mouth opening displacements (CMOD) observed in RC beams tested is given in Fig. 5. Based on the ratios, one criterion the damaged degree is presented in the figure. Agreement between the damage estimated from the maximum CMOD observed in the beams after the tests and the zone of the criterion is remarkable. This implies that the deterioration

process and the current conditions of the concrete structure could be estimated under repeated loading or traffic loading from this kind of criterion.

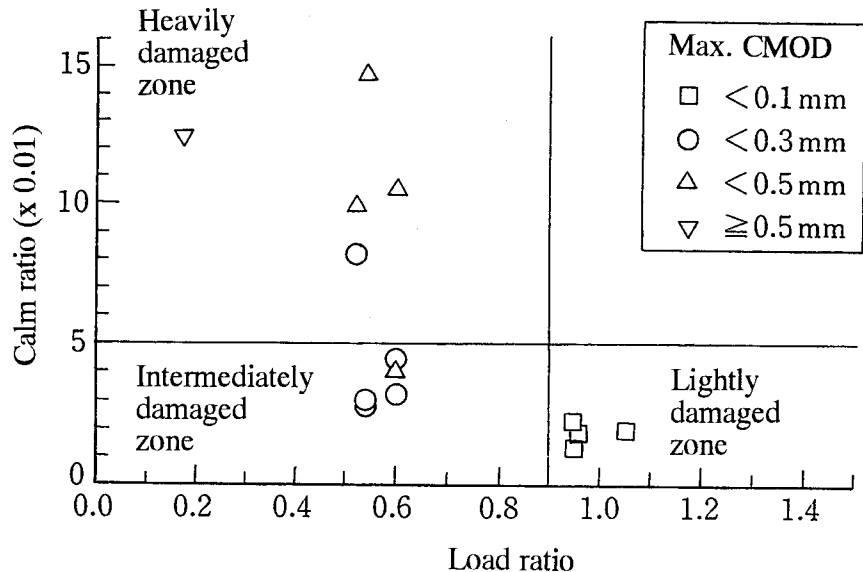


Fig. 5 Relation between CMOD and the ratios in RC beams tested.

## REFERENCES

- Akiyama, T., N. Mikami, H. Yokota and H. Hamada (1999),"AE Characteristics of Damaged Reinforced Concrete Beams due to Marine Environment," Proc. JCI, Vol. 21, No. 2, 1231-1236 (in Japanese).
- Matsuyama, K., T. Fujiwara, A. Ishibashi and S. Fukuchi (1993),"AE Measurement of Reinforced Concrete Retaining Wall," Proc. 9th AE Conf., JSNDI, 131-136 (in Japanese).
- Murakami, Y., H. Yamashita, T. Kita and H. Yoshikawa (1991),"Deformation and AE Characteristics of Concrete in freezing - Thawing Process," Proc. 4th AE Conf. in Subsurface and Civil Engineering, JSNDI, 47-51 (in Japanese).
- Ohtsu, M. (1987),"Acoustic Emission Characteristics in Concrete and Diagnostic Applications," *Journal of AE*, 6(2), 99-108.
- Shiotani, T., S. Yuyama, Z. Li and T. Okamoto (1999),"Fracture Process of Concrete Members by Improved b-Values," Proc. 6th AE Conf. in Subsurface and Civil Engineering, JSNDI, 123-128 (in Japanese).
- Yuyama, S., T. Okamoto, T. Kamada, M. Ohtsu and T. Kishi (1996),"A Proposed Standard for Evaluating Structural Integrity of Reinforced Concrete Beams by AE," *Progress in AE VIII*, JSNDI, 295-304.

# **EWGAE 2000**

## **24th European Conference on Acoustic Emission Testing, published by CETIM, Senlis, France**

### **SOMMAIRE**

Studies of the non-linear dynamics of acoustic emission generated in rocks by Z. Majewska, Z. Mortimer (Institute of Geophysics, University of Mining and Metallurgy- Poland)	1
Acoustic emission as result of tensil and shearing processes in stable and unstable fracturing of rocks by J. Pininska (Warsaw University - Poland)	9
Relation between acoustic emission signals sequences induced by thermal loading and the structure of sedimentary rocks by B. Zogala, R. Dubiel (University of Silesia - Poland)	15
Electromagnetic and Acoustic Emission from solids under ramp increasing pressure by J. Sikula, B. Koktavy, V. Sedlakova (Technical University - Czech Republic)	21
Acoustic emission/Acousto-Ultrasonic data fusion for damage evaluation in concrete by A. Tsimogiannis, B. Georgali, A. Anastassopoulos (Envirocoustics S.A. - Greece)	27
Concrete crossbeam diagnostic by acoustic emission method by Z. Weber, P. Svadbik, M. Korenska (Technical University of Brno - Czech Republic)	33
Fluctuation of ultrasonic beam in inhomogeneous media by S. Ahmed, R. Roberts, F. Margetan (Saint Louis University - USA)	39
Acoustic emission in PZT ceramics generated by electric fileds of high amplitude and low frequency by M. Aleksiejuk, V. Busko, F.R. Rejmund (Institute of Fundamental Technological Research PAS - Poland)	45
Amplitude analysis in the assay of impacted composites damage tolerance by F. Billi, C. Caneva, M. Valente (University of Rome « La Sapienza » - Italy)	51
A new acoustic parameter for the analysis of composite materials damages by F. Lachaud (LGMT - France)	57
Waveform based analysis techniques for the reliable acoustic emission testing of composite structures by M. Surgeon, C. Buelens, M. Wevers, P. De Meester (Metalogic and Katholieke University Leuven - Belgium)	63
Optical fibres for in situ monitoring the damage development in composites and the relation with acoustic emission measurements by M. Wevers, L. Rippert, S. Van Huffel (Katholieke University Leuven - Belgium).	69
Lamb-wave source location of impact on anisotropic plates by H. Yamada, Y. Mizutani, H. Nishino, M. Takemoto, K. Ono (Aoyama Gakuin University –Japan and UCLA - USA)	77

Characterisation of the damage and fracture mechanisms in $Ti_3SiC_2$ using acoustic emission by P.T. Cole, P. Finkel, R. Miller (Physical Acoustics Corp. - USA)	85
Crack microstructure and sources of acoustic emission in metals by L. Rogers (Lloyd's Register of Shipping - United Kingdom)	91
Evaluation of martensitic transformation dynamics of Cu-Al-Ni shape memory alloy single crystals by acoustic emission method by K. Yoshida, S. Kihara, K. Sakamaki (University of Tokushima - Japan)	107
The identification of basic fatigue parameters on electroresonance pulsator with help of acoustic emission technology by P. Mazal, J. Petras (Brno University of Technology - Czech Republic)	113
The phase of contact damage and its description by help of acoustic emission by J. Dvoracek, J. Pazdera, and L. Petras (Brno University of Technology - Czech Republic)	119
Acoustic emission monitoring of delayed hydride cracking in zirconium by A. Barron, C. Rowland (Pancom - United Kingdom)	125
Examination of plate valve behaviour in a small reciprocating compressor using acoustic emission by J.D. Gill, R.D. Douglas, Y.S. Neo, R.L. Reuben and J.A. Steel (Heriot-Watt University - United Kingdom)	133
A new method of acoustic emission source location in pipes using cylindrical guided waves by H. Nishino, F. Uchida, S. Takashina, M. Takemot, K. Ono (Aoyama Gakuin University - Japan and UCLA – USA)	139
Some approximate measurements of acoustic emission energy associated with dislocation motion in metal alloys by E.R. Brown, R.L. Reuben and J.A. Steel (Heriot-Watt University - United Kingdom)	145
Acoustic emission method for pressure vessel diagnostics at a refinery by V.L. Sokolov, B. Kabanov, V.P. Gomera, A.A. Okhotnikov (Kirishinefteorgsintez - Russia)	153
Optimisation of acquisition parameters for acoustic emission measurements on small pressure vessels by F. Rauscher (Vienna University of Technology - Austria)	161
Monitoring of weld's defects evolution submit to static and dynamic loading thanks to the acoustic emission method by C. Hervé, R. Pensec, A. Laksimi, (CETIM - France)	167
Acoustic emission due to cyclic pressurisation of vessels with partially penetrated longitudinal seams by M. Bayray (Institute of Pressure Vessels and Plant Technology - Austria)	175
Inspection of LPG vessels with AE examination by P. Tscheliesnig, G. Schauritsch (TÜV Austria - Austria)	183
Inspection of pressure vessels used in refrigeration and air conditioning systems by A. Amber, F. Zhang, M. Cherfaoui, L. Legin (CETIM - France)	189

The new Russian standards in the field of acoustic emission by V.I. Ivanov, I.E. Vlasov (Orgenergoneft - Russia)	195
The feasibility of using passive ultrasonic techniques for the analysis of active corrosion processes by M. Surgeon, C. Buelens (Metalogic - Belgium)	201
Using acoustic emission to monitor metal dusting by F. Ferrer, E. Andres, J. Goudiakas, C. Brun (Elf Atochem - France)	209
Use of acoustic emission to detect localised corrosion philosophy of industrial use, illustrated with real examples by A. Proust, J.C. Lenain (Euro Physical Acoustics - France)	215
Inspection of flat bottomed storage tanks by acoustical methods. Classification of corrosion related signals by M. Gori, P. Tscheliesnig, G. Lackner, H. Vallen and B. Herrmann (CESI – Italy, TUV – Austria, Vallen Systeme -Germany)	221
Screening of tank bottom corrosion with a single point AE detector : AE-simple by P. J. Van De Loo, D.A. Kronemeijer (Shell Global Solutions - The Netherlands)	227
Case histories from ten years of testing storage tank floors using acoustic emission by P.T. Cole, S.J. Schoorlemmer, S.N. Gautrey (Physical Acoustics Limited - United Kingdom)	233
Approach to the acoustic-emission diagnostics of main oil & gas pipeline systems by V.M. Belov, M.N. Podlevskikh (Eltest Company - Russia)	241
Acoustic emission detection of damage in reinforced concrete conduit by H.W. Shen, S. Iyer, M.A. Friesel, F. Mostert, R.D. Finlayson, R.K. Miller, M.F. Carlos and S. Vahaviolos (Physical Acoustics Corp. - USA)	247
Comparison of artificial acoustic emission sources as calibration sources for tool wear monitoring in single-point machining by A. Prateepasen, Y.H.J. Au, B.E. Jones (Brunel University - United Kingdom)	253
Development of an equipment to monitoring and control the quality of resistance welding by J. Catty and CRAFT Partners (CETIM - France)	261
Comparison of acoustic emission with sound waves generated in arc welding process by I. Polajanr, L. Grad (Faculty of mechanical engineering - Slovenia)	267
Monitoring aging structures with acoustic emission and acousto-ultrasonics by R.D. Finlayson, P.T. Cole, J.C. Lenain (Physical Acoustics Corp. - USA)	273
A study of small HSDI Diesel engine fuel injection equipment faults using acoustic emission by J.D. Gill, R.L. Reuben, J.A. Steel (Heriot-Watt University - United Kingdom)	281
Acoustic emission development at Rolls Royce Plc U.K. by S. Church (Rolls-Royce PLC - United Kingdom)	287

Unsupervised pattern recognition of acoustic emission from full scale testing of a wind turbine blade by D. Kourousis, A. Anastassopoulos, P. Vionis (Envirocoustics S.A. - Greece)	291
Acoustic emission proof testing of insulated aerial man lift devices by A. Anastassopoulos, A. Tsimogianis, D. Kourousis (Envirocoustics S.A. - Greece)	299
BOXMAP - Non-invasive detection of cracks in steel box girders by J.R. Watson, P.T. Cole, K.M. Holford (Physical Acoustics Ltd - United Kingdom)	305
Monitoring failure mechanisms in CFRP orthopaedic implants during fatigue testing by A. Taylor, C. Rowland, P. Gregson (Pancom - United Kingdom)	313
Continuous monitoring of rock failure by a remote AE system by T. Shiotani, S. Yuyama, M. Carlos (Research Institute of Technology, Tobishima Corp. - Japan)	321
Reciprocity calibration of acoustic emission transducers by H. Hatano (Science University of Tokyo - Japan)	327
Influence of mounting between acoustic emission sensor and tested surface by M. Korenska, L. Pazdera, L. Ritickova (Technical University of Brno - Czech Republic)	333
New AE signal conditionner for industrial use by H. Vallen, J. Von Stebut, J. Forker (Vallen Systeme GmbH - Germany)	339
New software tools for the AE-practitioner by H. Vallen, J. Vallen (Vallen Systeme GmbH - Germany)	347
Improved source location methods for pressure vessels by S. Vahaviolos, V. Godinez, R.D. Finlayson (Physical Acoustics Corp. - USA)	355
Neural Network localization of noisy AE events in dispersive media by M. Blahacek, Z. Prevorovsky, J. Krofta (Institute of Thermomechanics AS CR - Czech Republic)	363
Waveform analysis of simulated transient signals by S. Vahaviolos, H.W. Shen, R.D. Finlayson (Physical Acoustics Corp. - USA)	369
Waveform analysis of acoustic emission on thin composites structures by M. El Moudni, S. Benmedakhene, A. Laksimi (UTC - France)	375
Development of a moment tensor analysis system for quantitative waveform analysis of AE by S. Yuyama, M. Ohtsu, M.F. Carlos (Nippon Physical Acoustics Ltd - Japan)	381
The diagnostic of cutting tool wear by V. Poppeova (University of Zilina - Slovakia)	387
Dynamics and damage assessment in impacted cross-ply CFRP plate utilizing the waveform simulation of Lamb wave acoustic emission by Y. Mizutami, H. Nishino, M. Takemoto, K. Ono (Aoyama Gakuin University –Japan and UCLA - USA)	395

Acoustic emission detection during stress corrosion cracking at elevated pressure and temperature by Van Nieuwenhove, R.W. Bosch (Centre d'Etude de l'Energie nucléaire - Belgium)	403
Detection of pitting corrosion of aluminium alloys by acoustic emission technique by H. Idrissi, J. Derenne, H. Mazille (Laboratoire de Physico-chimie Industrielle - France)	409
Reliability of acoustic emission technique to assess corrosion of reinforced concrete by H. Idrissi, A. Limam (Laboratoire de Physico-chimie Industrielle - France)	417
The evaluation of the influence of metrological and constructural parameters on the acoustic emission generated by partial discharges by T. Boczar (Technical University of Opole - Poland)	425
The analysis of the possible use of the descriptors determined in the time and frequency domains for the characteristics of acoustic emission signals from partial discharges by T. Boczar (Technical University of Opole - Poland)	433
Determining the influence of mechano-electrical coupling of measuring transducers used in acoustic emission from partial discharges on the values of the registered descriptors by L. Marcin (Technical University of Opole - Poland)	439
Applied of acoustic emission during high temperature oxidation under stress of nickel by L. Gaillet, S. Benmedakhene, A. Laksimi, G. Moulin (Université de Techn. de Compiègne - France)	445

## **Proceedings volume, EWGAE 2000**

The 24th EWGAE Meeting (EWGAE 2000) was held May 24-26, 2000 at CETIM, Senlis, France. Program Chairs were C. Rigault and M. Cherfaoui. Over 90 participants from 15 countries attended the meeting. Proceedings "EWGAE 2000", containing 66 papers, 460 pages, can be purchased from CETIM. Contact: christel.rigault@cetim.fr

## **AVANT-PROPOS**

This is the 24th European Conference on Acoustic Emission Testing organised by the EWGAE (European Working Group on Acoustic Emission) at CETIM-Senlis from the 24th to 26th May 2000. In addition of the European contribution, the American and Asian contingents taking part in this conference is important. This gives the conference an international radiance.

The Proceedings are the result of a two and a half day programme, significantly over-subscribed. As the contributions are interesting, the EWGAE has tried to include as many papers as possible into programme.

The technical programme has been organised along traditional lines:

Day 1: is devoted essentially to fundamental aspects: calibration of transducers with dislocation, damage evaluation in concrete, rocks, ceramics and composite materials, cracks in metals, new multi-technique methods, pattern recognition, neural network, etc.

Day 2: is predominantly devoted to applications in traditional and new fields in industry:

- Pressure vessels, LPG vessels, storage tanks
- Pipes, pipeline
- Composites, ceramics, concrete
- Corrosion
- Aging structures
- Welding, cutting tool wear, etc.

Day 3: gives us an overview of the newest developments in the field of the AE instrumentation. Exhibitions and posters is held through the 3 day conference.

The EWGAE committee has tried to meet the needs of both:

- Industrialists worried about minimising cost and increasing availability while maintaining safe and efficient operations. Application sessions appeal to process, production, maintenance, quality-control engineers concerned with asset management.
- Scientists and technologists concerned with the fundamental mechanisms, fracture and crack propagation in materials and its measurement by acoustic emission.

The Proceedings provide an up-to-date reference on recent developments in AE technology throughout Europe and the wide world. Beside the technical programme, we prepare a social highlight where you have an opportunity to meet the colleagues within the AE community and to encourage exchanges and cooperation between laboratories and industries.

We hope this conference gives you strong image and encourage you to attend the first EWGAE meeting of the 3rd Millenium in the year 2002.

**Mohammed CHERFAOUI, Christel RIGAULT**  
Conference Organisers

## Présentation

Founded in 1972 by Dr Adrian Pollock, this year marks the 28th Anniversary of EWGAE (The European Working Group on Acoustic Emission). It has remained an important forum for exchange of scientific and technical information and for the promotion of quality AE testing practice. The Group is a charitable society and survives through the voluntary efforts of its committee and the support of its membership by attendance at its now biennal conference.

The Code Sub-Group of EWGAE published 5 codes of practice during the late 1970s and early 1980s. The work of this group has now been taken up by a new working group on AE within the Commission for European Norms (CEN), the European Standardisation Commission. The technical committee TC 138 is concerned with NDT in general and working group WG-7 within the committee is devoted to AE. The working group is comprised of national representatives from the European Union and from other European countries, which have been nominated by their respective National Standards Institutions. The convenor of WG-7 is Emilio Fontana of CISE and the group's first meeting was held in Milan in September 1991. Norms have been made in the standardisation of:

- AE technology
- General principles of AE testing and monitoring
- Equipment characterisation

AE testing in Europe is now well established in several important areas of proof testing, in-service monitoring and leak detection. Development of the technology continues to be driven by the needs of primary industry to reduce inspection and maintenance costs while preserving its assets and personnel safety.

The need to exchange ideas and experience is stronger than ever, as is the requirement for the standardisation of measurement and test procedures. EWGAE will continue as a focal point for the former with CEN now fulfilling the latter.

# Notes for Contributors

## 1. General

The Journal will publish contributions from all parts of the world and manuscripts for publication should be submitted to the Editor. Send to:

Professor Kanji Ono, Editor - JAE  
6531 Boelter Hall, MSE Dept.  
University of California  
Los Angeles, California 90095-1595 USA  
FAX (1) 818-990-1686  
e-mail: ono@ucla.edu

Authors of any AE related publications are encouraged to send a copy for inclusion in the AE Literature section to:

Mr. T.F. Drouillard, Associate Editor - JAE  
11791 Spruce Canyon Circle  
Golden, Colorado 80403 USA

Only papers not previously published will be accepted. Authors must agree to transfer the copyright to the Journal and not to publish elsewhere, the same paper submitted to and accepted by the Journal. A paper is acceptable if it is a revision of a governmental or organizational report, or if it is based on a paper published with limited distribution.

Compilation of annotated data files will be accepted for inclusion in CD-ROM distribution, so that others can share in their analysis for research as well as training. ASCII or widely accepted data formats will be required.

The language of the Journal is English. All papers should be written concisely and clearly.

## 2. Page Charges

No page charge is levied. One copy of CD-ROM will be supplied to the authors free of charge.

## 3. Manuscript for Review

Manuscripts for review need only to be typed legibly; preferably, double-spaced on only one side of the page with wide margins. The title should be brief. An abstract of 100-200 words is needed for Research and Applications articles. Except for short communications, descriptive heading should be used to divide the paper into its component parts. Use the International System of Units (SI).

References to published literature should be quoted in the text citing authors and the year of publication. These are to

be grouped together at the end of the paper in alphabetical and chronological order. Journal references should be arranged as below. Titles for journal or book articles are helpful for readers, but may be omitted.

H.L. Dunegan, D.O. Harris and C.A. Tatro (1968), Eng. Fract. Mech., 1, 105-122.

Y. Krampfner, A. Kawamoto, K. Ono and A.T. Green (1975), "Acoustic Emission Characteristics of Cu Alloys under Low-Cycle Fatigue Conditions," NASA CR-134766, University of California, Los Angeles and Acoustic Emission Tech. Corp., Sacramento, April.

A.E. Lord, Jr. (1975), Physical Acoustics: Principles and Methods, vol. 11, eds. W. P. Mason and R. N. Thurston, Academic Press, New York, pp. 289-353.

Abbreviations of journal titles should follow those used in the ASM Metals Abstracts. In every case, authors' initials, appropriate volume and page numbers should be included. The title of the cited journal reference is optional.

Illustrations and tables should be planned to fit a single page width (178 mm or 7"). For the reviewing processes, these need not be of high quality, but submit glossy prints or equivalent electronic files with the final manuscript. Lines and letters should be legible.

## 4. Review

All manuscripts will be judged by qualified reviewer(s). Each paper is reviewed by one of the editors and may be sent for review by members of the Editorial Board. The Board member may seek another independent review. In case of disputes, the author may request other reviewers.

## 5. Electronic Media

This Journal will be primarily distributed electronically by CD-ROM. In order to expedite processing and minimize errors, the authors are requested to submit electronic files or floppy disk copy of the paper. We can read Macintosh and IBM PC formats. On the INTERNET, you can send an MS Word file or the text portion to "ono@ucla.edu".

## 6. Color Illustration

We can process color illustration needed to enhance the technical content of an article. With the new format, authors are encouraged to use them.

## AUTHORS INDEX

- A. Anastassopoulos, 21, 217, 224  
E. Andres, 155  
J. Asquith, 211  
Y.H.J. Au, 196  
A. Barron, 87  
M.W. Barsoum, 61  
M. Bayray, 131  
M. Blahacek, 279  
R.W. Bosch, 293  
C. Brun, 155  
C. Buelens, 34  
M.F. Carlos, 189, 248, 272  
J. Catty, 205  
M. Cherfaoui, 144  
P.T. Cole, 61, 180, 232  
A.W. Davies, 232  
P. De Meester, 34  
J. Derenne, 299  
R.D. Douglas, 96  
R. Dubiel, 15  
J. Dvoracek, 81  
T. El-Raghy, 61  
F. Ferrer, 155  
P. Finkel, 61  
R.D. Finlayson, 61, 189, 272  
J. Forker, 258  
M.A. Friesel, 61, 189  
S.N. Gautrey, 180  
B. Georgali, 21  
J.D. Gill, 96, 211  
V. Godinez, 272  
V.P. Gomera, 111  
M. Gori, 167  
J. Goudiakas, 155  
P. Gregson, 239  
S. Gross, 239  
B. Herrmann, 167  
C. Hervé, 125  
K.M. Holford, 232  
H. Idrissi, 299, 307  
V.I. Ivanov, 144  
S. Iyer, 189  
B.E. Jones, 196  
B.S. Kabanov, 111  
S. Kihara, 68  
V. Kolovos, 217  
M. Korenska, 29  
D. Kouroussis, 217, 224  
J. Krofta, 279  
D.A. Kronemeijer, 174  
G. Lackner, 167  
A. Laksimi, 125  
L. Legin 144  
J. C. Lenain, 161  
A. Limam, 307  
Z. Majewska, 1  
P. Mazal, 75  
H. Mazille, 299  
R.K. Miller, 61, 189, 272  
Y. Mizutani, 51, 286  
Z. Mortimer, 1  
F. Mostert, 189  
Y.S. Neo, 96  
H. Nishino, 51, 102, 286  
M. Ohtsu, S1, S7  
A.A. Okhotnikov, 111  
K. Ono, 51, 102, 286  
L. Pazdera, 29  
J. Pazdera, 81  
R. Pensec, 125  
J. Petras, 75  
L. Petras, 81  
J. Pininska, 8  
A. Prateepasen, 196  
Z. Prevorovsky, 279  
A. Proust, 161  
F. Rauscher, 118  
R.L. Reuben, 96, 211

- L. Rippert, 41  
C. Rowland, 87, 239  
K. Sakamaki, 68  
M.W. Scaife, 211  
G. Schauritsch, 138  
S.J. Schoorlemmer, 180  
H.W. Shen, 189  
T. Shiotani, 248  
A. Skrabber, 144  
V.L. Sokolov, 111  
J.A. Steel, 96, 211  
M. Surgeon, 34  
P. Svadbik, 29  
S. Takashina, 102  
M. Takemoto, 51, 102, 286  
A. Taylor, 239  
P. Tscheliesnig, 138, 167  
A. Tsimogiannis, 21, 224  
F. Uchida, 102  
S. Vahaviolos, 189, 248, 272  
H. Vallen, 167, 258, 265  
J. Vallen, 265  
P.J. Van De Loo, 174  
S. Van Huffel, 41  
R. Van Nieuwenhove, 293  
P. Vionis, 217  
L.E. Vlasov, 150  
J. von Stebut, 258  
J.R. Watson, 232  
Z. Weber, 29  
M. Wevers, 34, 41  
H. Yamada, 51  
K. Yoshida, 68  
S. Yuyama, 248  
F. Zhang, 144  
B. Zogala, 15

# Journal of Acoustic Emission

## Contents of Volume 18, 2000

### Selected papers from “EWGAE 2000, 24th European Conference on Acoustic Emission Testing”, published by CETIM, Senlis, France

Studies of the non-linear dynamics of acoustic emission generated in rocks by Z. Majewska and Z. Mortimer (Institute of Geophysics, University of Mining and Metallurgy - Poland)	1
Acoustic emission as result of tensile and shearing processes in stable and unstable fracturing of rocks by J. Pininska (Warsaw University - Poland)	8
Relation between acoustic emission signals sequences induced by thermal loading and the structure of sedimentary rocks by B. Zogala, and R. Dubiel (University of Silesia - Poland)	15
Acoustic emission/Acousto-Ultrasonic data fusion for damage evaluation in concrete by A. Tsimogiannis, B. Georgali, and A. Anastassopoulos (Envirocoustics S.A. - Greece)	21
Concrete Crossbeam Diagnostic by acoustic emission method by Z. Weber, P. Svadbik, M. Korenska and L. Pazdera (Technical University of Brno - Czech Republic)	29
Waveform based analysis techniques for the reliable acoustic emission testing of composite structures by M. Surgeon, C. Buelens, M. Wevers, and P. De Meester (Metalogic and Katholieke University Leuven - Belgium)	34
Optical fibres for in situ monitoring the damage development in composites and the relation with acoustic emission measurements by M. Wevers, L. Rippert, and S. Van Huffel (Katholieke University Leuven - Belgium).	41
Lamb-wave source location of impact on anisotropic plates by H. Yamada, Y. Mizutani, H. Nishino, M. Takemoto and K. Ono (Aoyama Gakuen University - Japan and University of Calif., Los Angeles [UCLA] - USA)	51
Characterisation of the damage and fracture mechanisms in $Ti_3SiC_2$ using acoustic emission by P. Finkel, R.K. Miller, M.A. Friesel, R.D. Finlayson, P.T. Cole, M.W. Barsoum and T. El-Raghy (Physical Acoustics Corp. and Drexel University - USA)	61
Evaluation of martensitic transformation dynamics of Cu-Al-Ni shape memory alloy single crystals by acoustic emission method by K. Yoshida, S. Kihara, and K. Sakamaki (University of Tokushima - Japan)	68
The identification of basic fatigue parameters on electroresonance pulsator with help of acoustic emission technology by P. Mazal, and J. Petras (Brno University of Technology - Czech Republic)	75

The phase of contact damage and its description by help of acoustic emission by J. Dvoracek, J. Pazdera, and L. Petras (Brno University of Technology - Czech Republic)	81
Acoustic emission monitoring of delayed hydride cracking in Zirconium by A. Barron and C. Rowland (Bodycote and Pancom - United Kingdom)	87
Examination of plate valve behaviour in a small reciprocating compressor using acoustic emission by J.D. Gill, R.D. Douglas, Y.S. Neo, R.L. Reuben and J.A. Steel (Heriot-Watt University - United Kingdom)	96
A new method of acoustic emission source location in Pipes using cylindrical guided waves by H. Nishino, F. Uchida, S. Takashina , M. Takemoto and K. Ono (Aoyama Gakuen University - Japan and University of Calif., LA - USA)	102
Acoustic emission method for pressure vessel diagnostics at a refinery by B.S. Kabanov, V.P. Gomera, V.L. Sokolov, and A.A. Okhotnikov (Kirishinefteorgsintez - Russia)	111
Optimisation of acquisition parameters for acoustic emission measurements on small pressure vessels by F. Rauscher (Vienna University of Technology - Austria)	118
Monitoring of weld's defects evolution submit to static and dynamic loading thanks to the acoustic emission method by C. Hervé, R. Pensec, and A. Laksimi, (CETIM - France)	125
Acoustic emission due to cyclic pressurisation of vessels with partially penetrated longitudinal seams by M. Bayray (Institute of of pressure vessels and plant Technology - Austria)	131
Inspection of LPG vessels with AE examination by P. Tscheliesnig, and G. Schauritsch (TÜV Austria - Austria)	138
Inspection of pressure vessels used in refrigeration and air conditioning systems by A. Skrabec, F. Zhang, M. Cherfaoui, and L. Legin (CETIM - France)	144
The new Russian standards in the field of acoustic emission by V.I. Ivanov, and L.E. Vlasov (Orgenergoneft - Russia)	150
Using acoustic emission to monitor metal dusting by F. Ferrer, E. Andres, J. Goudiakas, and C. Brun (Elf Atochem - France)	155
Use of acoustic emission to detect localised corrosion philosophy of industrial use, illustrated with real examples by A. Proust, and J. C. Lenain (Euro Physical Acoustics - France)	161
Inspection of flat bottomed storage tanks by acoustical methods. Classification of corrosion related signals by P. Tscheliesnig, G. Lackner, M. Gori, H. Vallen and B. Herrmann (TÜV - Germany, CEST - Italy)	167
Screening of tank bottom corrosion with a single point AE detector: AE-Simple by P.J. Van De Loo, and D.A. Kronemeijer (Shell Global Solutions - The Netherlands)	174
Case histories from ten years of testing storage tank floors using acoustic emission by S.N. Gautrey, P.T. Cole, and S.J. Schoorlemmer, (Physical Acoustics Limited -United Kingdom)	180

Acoustic emission detection of damage in reinforced concrete conduit by H.W. Shen, S. Iyer, M.A. Friesel, F. Mostert, R.D. Finlayson, R.K. Miller, M.F. Carlos and S. Vahaviolos, (Physical Acoustics Corp. - USA)	189
Comparison of artificial acoustic emission sources as calibration sources for tool wear monitoring in single-point machining by A. Prateepasen, Y.H.J. Au and B.E. Jones (Brunel University - United Kingdom)	196
Development of an equipment to monitoring and control the quality of resistance welding (CRAFT Project) by J. Catty, (CETIM - France)	205
A study of small HSDI Diesel engine fuel injection equipment faults using acoustic emission by J.D. Gill, R.L. Reuben, J.A. Steel, M.W. Scaife and J. Asquith (Heriot-Watt University - United Kingdom)	211
Unsupervised pattern recognition of acoustic emission from full scale testing of a wind turbine blade by D. Kouroussis, A. Anastassopoulos, P. Vionis and V. Kolovos (Envirocoustics S.A. - Greece)	217
Acoustic emission proof testing of insulated aerial man lift devices by A. Anastassopoulos, A. Tsimogianis and D. Kourousis (Envirocoustics S.A. - Greece)	224
BOXMAP - Non-invasive detection of cracks in steel box girders by J.R. Watson, K.M. Holford, A.W. Davies and P.T. Cole, (Cardiff University, Physical Acoustics Ltd - United Kingdom)	232
Monitoring failure mechanisms in CFRP orthopaedic implants during fatigue testing by A. Taylor, S. Gross, C. Rowland and P. Gregson (Finsbury, University of Southampton, Pancom - United Kingdom)	239
Continuous monitoring of rock failure by a remote AE system by T. Shiotani, S. Yuyama, M. Carlos and S. Vahaviolos (Tobishima Corp. – Japan, PAC - USA)	248
New AE signal conditioner for industrial use by H. Vallen, J. Forker and J. von Stebut, (Vallen Systeme GmbH – Germany and Ecole des Mines - France)	258
New software tools for the AE-practitioner by H. Vallen and J. Vallen, (Vallen Systeme GmbH - Germany)	265
Improved source location methods for pressure vessels by V. Godinez, S. Vahaviolos, R.D. Finlayson, R.K. Miller, and M.F. Carlos (Physical Acoustics Corp. - USA)	272
Neural network localization of noisy AE events in dispersive media by M. Blahacek, Z. Prevorovsky, and J. Krofta (Institute of Thermomechanics - Czech Republic)	279
Dynamics and damage assessment in impacted cross-ply CFRP plate utilizing the waveform simulation of Lamb wave acoustic emission by Y. Mizutani, H. Nishino, M. Takemoto and K. Ono (Aoyama Gakuin University – Japan and UCLA - USA)	286
Acoustic emission detection during stress corrosion cracking at elevated pressure and temperature by R. Van Nieuwenhove, and R.W. Bosch (Centre d'Etude de l'Energie Nucléaire - Belgium)	293
Detection of pitting corrosion of aluminium alloys by acoustic emission technique by H. Idrissi, J. Derenne, and H. Mazille (INSA de Lyon - France)	299

Reliability of acoustic emission technique to assess corrosion of reinforced concrete  
by H. Idrissi, and A. Limam (INSA de Lyon - France)

307

## **AEWG43 Presentation**

Theoretical Treatment of AE in Massive Solid....by M. Ohtsu

S1

Diagnosis of Concrete Structures by AE....by M. Ohtsu

S7

## **EWGAE 2000 (EWGAE.pdf)**

**SOMMAIRE** -- Content of EWGAE 2000 Proceedings

i - v

**AVANT-PROPOS** Mohammed CHERFAOUI, Christel RIGAULT

vi

**Présentation - EWGAE**

vii

**Authors Index** (18Auindx.pdf)

I-1 – I-2

**Contents of Volume 18, 2000** (18Conts.pdf)

I-3 – I-6

e-mail Addresses of Authors (e-mail.pdf)

EWGAE 2000 Participant List (Senlis.pdf)

# Notes for Contributors

## 1. General

The Journal will publish contributions from all parts of the world and manuscripts for publication should be submitted to the Editor. Send to:

Professor Kanji Ono, Editor - JAE  
6531 Boelter Hall, MSE Dept.  
University of California  
Los Angeles, California 90095-1595 USA  
FAX (1) 818-990-1686  
e-mail: ono@ucla.edu

Authors of any AE related publications are encouraged to send a copy for inclusion in the AE Literature section to:

Mr. T.F. Drouillard, Associate Editor - JAE  
11791 Spruce Canyon Circle  
Golden, Colorado 80403 USA

Only papers not previously published will be accepted. Authors must agree to transfer the copyright to the Journal and not to publish elsewhere, the same paper submitted to and accepted by the Journal. A paper is acceptable if it is a revision of a governmental or organizational report, or if it is based on a paper published with limited distribution.

Compilation of annotated data files will be accepted for inclusion in CD-ROM distribution, so that others can share in their analysis for research as well as training. ASCII or widely accepted data formats will be required.

The language of the Journal is English. All papers should be written concisely and clearly.

## 2. Page Charges

No page charge is levied. One copy of CD-ROM will be supplied to the authors free of charge.

## 3. Manuscript for Review

Manuscripts for review need only to be typed legibly; preferably, double-spaced on only one side of the page with wide margins. The title should be brief. An abstract of 100-200 words is needed for Research and Applications articles. Except for short communications, descriptive heading should be used to divide the paper into its component parts. Use the International System of Units (SI).

References to published literature should be quoted in the text citing authors and the year of publication. These are to

be grouped together at the end of the paper in alphabetical and chronological order. Journal references should be arranged as below. Titles for journal or book articles are helpful for readers, but may be omitted.

H.L. Dunegan, D.O. Harris and C.A. Tatro (1968), Eng. Fract. Mech., 1, 105-122.

Y. Krampfner, A. Kawamoto, K. Ono and A.T. Green (1975), "Acoustic Emission Characteristics of Cu Alloys under Low-Cycle Fatigue Conditions," NASA CR-134766, University of California, Los Angeles and Acoustic Emission Tech. Corp., Sacramento, April.

A.E. Lord, Jr. (1975), Physical Acoustics: Principles and Methods, vol. 11, eds. W. P. Mason and R. N. Thurston, Academic Press, New York, pp. 289-353.

Abbreviations of journal titles should follow those used in the ASM Metals Abstracts. In every case, authors' initials, appropriate volume and page numbers should be included. The title of the cited journal reference is optional.

Illustrations and tables should be planned to fit a single page width (178 mm or 7"). For the reviewing processes, these need not be of high quality, but submit glossy prints or equivalent electronic files with the final manuscript. Lines and letters should be legible.

## 4. Review

All manuscripts will be judged by qualified reviewer(s). Each paper is reviewed by one of the editors and may be sent for review by members of the Editorial Board. The Board member may seek another independent review. In case of disputes, the author may request other reviewers.

## 5. Electronic Media

This Journal will be primarily distributed electronically by CD-ROM. In order to expedite processing and minimize errors, the authors are requested to submit electronic files or floppy disk copy of the paper. We can read Macintosh and IBM PC formats. On the INTERNET, you can send an MS Word file or the text portion to "ono@ucla.edu".

## 6. Color Illustration

We can process color illustration needed to enhance the technical content of an article. With the new format, authors are encouraged to use them.